

## **Related titles**

*A Comprehensive Guide to Successful Offshore Wind Farm Installation*  
(ISBN: 978-0-12-410422-8)

*Solar Energy Engineering 2e*  
(ISBN: 978-0-12-397270-5)

*Renewable Energy Integration: Practical Management of Variability, Uncertainty, and Flexibility in Power Grids*  
(ISBN: 978-0-12-407910-6)

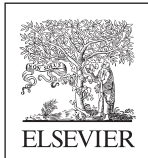
Woodhead Publishing Series in Energy

# Renewable Energy Forecasting

## From Models to Applications

*Edited By*

**George Kariniotakis**



**WP**

WOODHEAD  
PUBLISHING

An imprint of Elsevier

Woodhead Publishing is an imprint of Elsevier  
The Officers' Mess Business Centre, Royston Road, Duxford, CB22 4QH, United Kingdom  
50 Hampshire Street, 5th Floor, Cambridge, MA 02139, United States  
The Boulevard, Langford Lane, Kidlington, OX5 1GB, United Kingdom

Copyright © 2017 Elsevier Ltd. All rights reserved.

No part of this publication may be reproduced or transmitted in any form or by any means, electronic or mechanical, including photocopying, recording, or any information storage and retrieval system, without permission in writing from the publisher. Details on how to seek permission, further information about the Publisher's permissions policies and our arrangements with organizations such as the Copyright Clearance Center and the Copyright Licensing Agency, can be found at our website: [www.elsevier.com/permissions](http://www.elsevier.com/permissions).

This book and the individual contributions contained in it are protected under copyright by the Publisher (other than as may be noted herein).

### Notices

Knowledge and best practice in this field are constantly changing. As new research and experience broaden our understanding, changes in research methods, professional practices, or medical treatment may become necessary.

Practitioners and researchers must always rely on their own experience and knowledge in evaluating and using any information, methods, compounds, or experiments described herein. In using such information or methods they should be mindful of their own safety and the safety of others, including parties for whom they have a professional responsibility.

To the fullest extent of the law, neither the Publisher nor the authors, contributors, or editors, assume any liability for any injury and/or damage to persons or property as a matter of products liability, negligence or otherwise, or from any use or operation of any methods, products, instructions, or ideas contained in the material herein.

### Library of Congress Cataloging-in-Publication Data

A catalog record for this book is available from the Library of Congress

### British Library Cataloguing-in-Publication Data

A catalogue record for this book is available from the British Library

ISBN: 978-0-08-100504-0 (print)

ISBN: 978-0-08-100505-7 (online)

For information on all Woodhead Publishing publications visit our website at <https://www.elsevier.com/books-and-journals>



Working together  
to grow libraries in  
developing countries

[www.elsevier.com](http://www.elsevier.com) • [www.bookaid.org](http://www.bookaid.org)

*Publisher:* Joe Hayton

*Acquisitions Editor:* Maria Convey

*Editorial Project Manager:* Ashlie M. Jackman

*Production Project Manager:* Poulouse Joseph

*Designer:* Greg Harris

Typeset by TNQ Books and Journals

# List of contributors

**Stefano Alessandrini** National Center for Atmospheric Research (NCAR), Boulder, CO, United States

**Christophe Baehr** CNRM, Toulouse, France

**Ricardo Bessa** INESC Technology and Science (INESC TEC), Porto, Portugal

**Philippe Blanc** MINES ParisTech, PSL Research University, Sophia Antipolis, France

**Audun Botterud** Argonne National Laboratory, Argonne, IL, United States

**Edgardo D. Castronuovo** University Carlos III de Madrid, Leganés (Madrid), Spain

**Carlos F.M. Coimbra** University of California, San Diego, CA, United States

**Alain Dabas** CNRM, Toulouse, France

**Romain Dupin** MINES ParisTech PSL - Research University Centre PERSEE: Centre for Processes, Renewable Energies and Energy Systems, Sophia Antipolis, France

**Gregor Giebel** DTU Wind Energy, Roskilde, Denmark

**Robin Girard** MINES ParisTech, Sophia Antipolis, France

**Paula Gómez** Technical University of Denmark, Roskilde, Denmark

**Sven-Erik Gryning** Technical University of Denmark, Roskilde, Denmark

**Sue Ellen Haupt** Research Applications Laboratory, National Center for Atmospheric Research, Boulder, Colorado, United States

**Rich H. Inman** University of California, San Diego, CA, United States

**Pedro A. Jiménez** Research Applications Laboratory, National Center for Atmospheric Research, Boulder, Colorado, United States

**George Kariniotakis** MINES ParisTech, Sophia Antipolis, France

**Andreas Kazantzidis** University of Patras, Patras, Greece

**Branko Kosović** Research Applications Laboratory, National Center for Atmospheric Research, Boulder, Colorado, United States

**Kevin Laquaine** MINES ParisTech, Sophia Antipolis, France

**Jared A. Lee** Research Applications Laboratory, National Center for Atmospheric Research, Boulder, Colorado, United States

**Pierre Massip** MINES ParisTech, PSL Research University, Sophia Antipolis, France

**Manuel Matos** INESC Technology and Science (INESC TEC), Porto, Portugal; University of Porto, Portugal

**Nicoló Mazzi** University of Padova, Padova, Italy

**Andrea Michiorri** MINES ParisTech PSL - Research University Centre PERSEE: Centre for Processes, Renewable Energies and Energy Systems, Sophia Antipolis, France

**Torben Mikkelsen** Technical University of Denmark, Roskilde, Denmark

**Ewan O'Connor** Finnish Meteorological Institute, Helsinki, Finland

**Laura Frías Paredes** National Renewable Energy Centre (CENER), Sarriguren, Spain

**Hugo T.C. Pedro** University of California, San Diego, CA, United States

**Pierre Pinson** Technical University of Denmark, Kgs. Lyngby, Denmark

**Lourdes Ramirez-Santigosa** CIEMAT, Madrid, Spain

**Gordon Reikard** U.S. Cellular, Chicago, IL, United States

**Jan Remund** Meteotest, Berne, Switzerland

**Lucie Rottner** CNRM, Toulouse, France

**Javier Sanz Rodrigo** National Renewable Energy Centre (CENER), Sarriguren, Spain

**Mikael Sjöholm** Technical University of Denmark, Roskilde, Denmark

**Simone Sperati** Ricerca Sistema Energetico (RSE) SpA, Milano, Italy

**Nicole Stoffels** University of Oldenburg, Oldenburg, Germany

**Irene Suomi** Finnish Meteorological Institute, Helsinki, Finland

**Pierre-Julien Trombe** Vattenfall Vindkraft A/S, Esbjerg, Denmark

**Panagiotis Tzoumanikas** University of Patras, Patras, Greece

**Loïc Vallance** MINES ParisTech, PSL Research University, Sophia Antipolis, France; EDF R&D—STEP, Chatou, France

**Nikola Vasiljević** Technical University of Denmark, Roskilde, Denmark

**Claire L. Vincent** The University of Melbourne, Melbourne, VIC, Australia

**Lueder von Bremen** University of Oldenburg, Oldenburg, Germany

**Stefan Wilbert** German Aerospace Center (DLR), Institute of Solar Research, Plataforma Solar de Almería, Almería, Spain

**Zhi Zhou** Argonne National Laboratory, Argonne, IL, United States

# Principles of meteorology and numerical weather prediction

1

*Sue Ellen Haupt, Pedro A. Jiménez, Jared A. Lee, Branko Kosović*

Research Applications Laboratory, National Center for Atmospheric Research, Boulder, Colorado, United States

## 1.1 Introduction to meteorology for renewable energy forecasting

Renewable resources are fast becoming the predominant energy source of the future, but to harvest them requires an understanding of the causes of their variability and the ability to predict numerous atmospheric processes over a range of scales. This understanding of the atmosphere is the key to harvesting renewable energy, specifically wind and solar power, in at least three ways. First, one must be able to characterize the resource availability to appropriately site plants and elements (such as wind turbines) within those plants. Second, it is imperative to forecast the resource on time periods of minutes to seasons to properly plan how to blend the renewable resources into the grid while continuing to meet the load obligation. Third, forecasts of expected energy generation and variability, including forecasts of extreme weather or sudden changes in the weather that may affect energy generation, are helpful in planning operation and maintenance of the sites. Thus, understanding the atmospheric physics and dynamics that ultimately cause the wind and solar resource to vary is key to modeling and forecasting for renewable energy. In this section, we briefly review the causes of atmospheric motion and the basics of forecasting before getting into more detail in subsequent sections.

### 1.1.1 Atmospheric motion

The atmospheric circulation arises because the Earth is spherical and the Sun's rays impact the Earth more directly near the equator than at the poles. The warmer tropical atmosphere is less dense than the polar atmosphere, forcing the predominant motion from the polar regions toward the tropics at the surface. Thus, the tropical air converges and rises at the Inter-Tropical Convergence Zone near the thermal equator, while the movement of surface air out of the polar regions causes a polar subsidence. This resulting circulation includes a return flow aloft from the tropics toward the polar region as the primary solar-forced circulation, known as the Hadley circulation (Anthes et al., 1981). Because the Earth rotates on its axis, it is actually a bit more complicated than that. This rotation creates an apparent Coriolis force that turns the flow toward the right in the northern hemisphere and toward the left in the southern hemisphere.

In addition, this Coriolis force, due to the conservation of angular momentum, causes there to be not a single hemispheric-spanning Hadley cell, but rather three primary cells in each hemisphere (Fig. 1.1). The thermally indirect Ferrel cell encompasses the mid-latitudes and acts to mix the air through large-scale eddies and vertical instabilities. These instabilities generate waves that form the low- and high-pressure systems in the regions near the equator. Finally, the polar cell is a thermally direct circulation, exhibiting high pressure from subsiding air at the poles.

The Earth's  $23.5^{\circ}$ -tilted axis generates the seasonality of the flow, the diurnal heating patterns cause the rise and fall of the atmospheric boundary layer (the lowest kilometer or so of well-mixed air), differential ocean and land heating rates cause further instabilities, and mountain ranges impede atmospheric flow, frequently leading to the generation of new low-pressure systems in the lee of the mountains. All these forcings work together to form the variability of the atmospheric flow (Fig. 1.1). Introductory meteorology texts (e.g., Holton, 2004; Wallace and Hobbs, 2006) provide more details of this general circulation theory and demonstrate how it can be codified into a series of

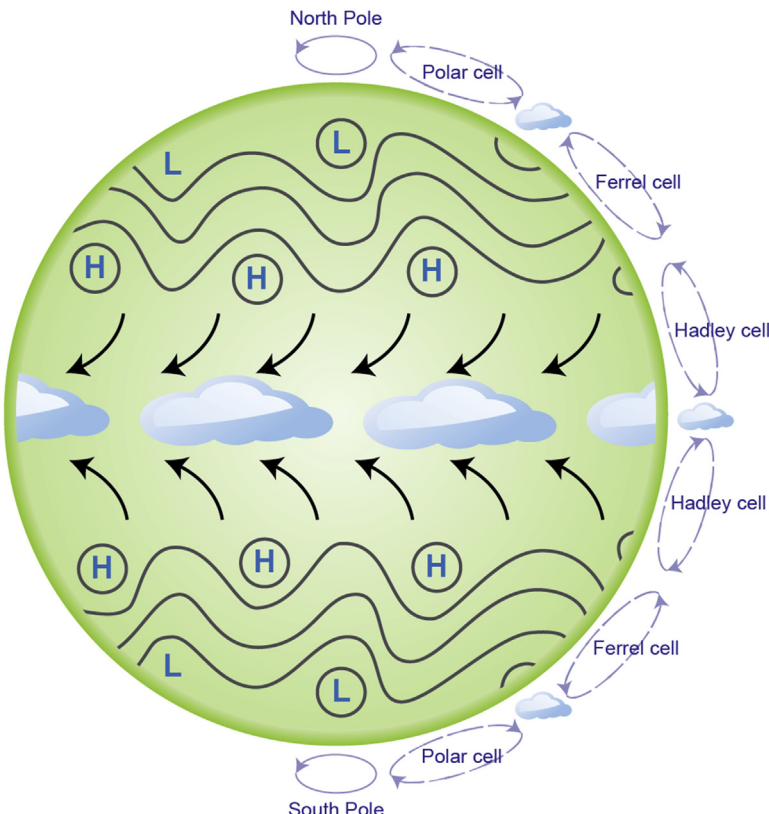


**Figure 1.1** Depiction of the general circulation of the atmosphere.

partial differential equations of conservation of mass, momentum, and energy to model the flow, known as the Navier–Stokes equations. These equations codify the changes in the wind, temperature, and other atmospheric properties due to the forcings and are the basis of numerical weather prediction (NWP) models ([Section 1.3](#)).

Although the solar radiation that hits the earth is the source of atmospheric motion, it is modified by atmospheric constituents including aerosols and water vapor, which are important to both the details of the circulation and to forecasting solar power. The large amount of water vapor in the atmosphere both impacts the flow and the cloudiness of the atmosphere. Because water vapor is less dense than air, moist air rises, generating adiabatic cooling, which can lead to condensation into clouds. Various processes cause this lifting of moist air and cloud formation. The most basic one is daily surface heating, which warms the moist air near the surface, causing it to become less dense and rise. Thus are formed the “popcorn” cumulus clouds that often grow, merge, and become more solid clouds at the top of the boundary layer. Another process that forces rising motion involves the weather fronts associated with the atmospheric waves, particularly the warm fronts leading the low-pressure cells and their attendant cold fronts. Although the processes that form clouds are well understood, due to the small scales of many of the processes, as well as the nonlinear and turbulent motions that make the problem chaotic and stochastic (as opposed to deterministic), it is difficult to predict the precise location and timing of cloud formation and its life cycle. These factors cause the largest variability around the solar resource.

### 1.1.2 Prediction across scales

It is important to understand the wide range of scales in weather forecasting and their impact on providing an accurate forecast. One can think of the atmospheric motion as being composed of a large number of nonlinearly interacting waves. [Fig. 1.2](#) shows the amount of energy contained in each scale ([Skamarock et al., 2014](#)). The largest scale of wave is those weather systems (lows followed by highs) that circle the globe in the mid-latitudes ([Fig. 1.1](#)), the Rossby waves that form the interesting daily weather in mid-latitudes. These weather systems have wavelengths on the order of about 10,000 km and their influence persists over a given region for a few days. Other circulations develop at smaller scales. The mesoscale is responsible for diurnal circulations usually originated by heterogeneities at the surface. The sea breeze associated with a differential heating of the land and the ocean is a clear example. Other waves exist, including gravity waves (like those waves observed on the surface of a water body), inertial waves that travel through the interior of the rotating atmosphere, and sound waves due to the compressibility of the air. Some of the smallest eddies in the boundary layer have wavelengths on the order of centimeters. This implies that the range of scales of atmospheric motion is on the order of eight decades. Given current computing power, one cannot resolve all these scales with a numerical model. Energy from variations in the smallest scales also can backscatter, or propagate to larger scales and can cause a numerical integration to “blow up” due to numerical instability.

In modeling for renewable energy, we need to understand these various scales and match our modeling to what is required by the end user, who often needs forecasts for a

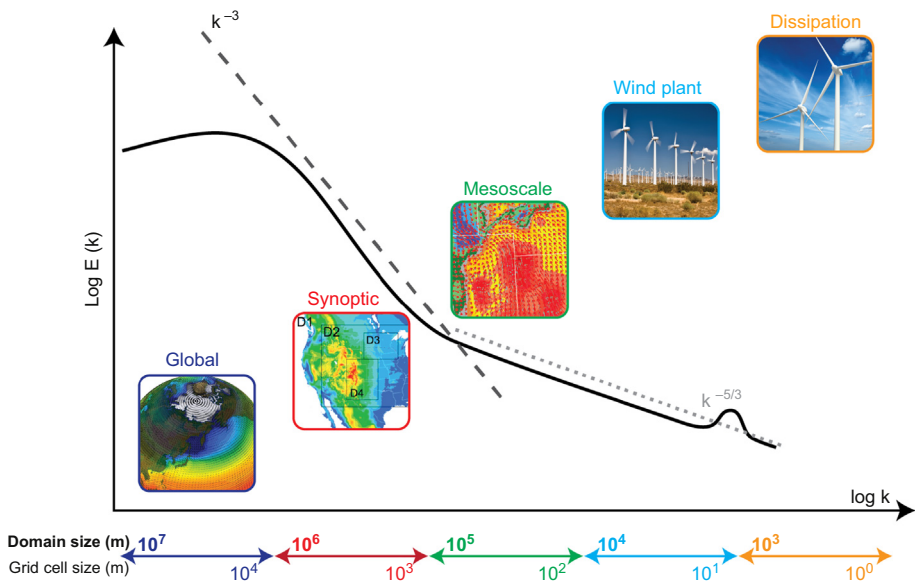


**Figure 1.2** Scales of motion in the atmosphere interact. This energy spectrum (*solid black line*) indicates the amount of energy at each scale. The *light dashed and dotted lines* indicate the slopes of the different portions of the spectrum. Also included is a depiction of the type of motion represented by each scale, the size of typical domains, and the typical grid cell spacing for modeling at that scale.

variety of temporal scales. For instance, utilities and Independent System Operators depend on accurate forecasts for the next few hours, several days, several weeks, or even seasons. They often need to plan operation and maintenance weeks to months in advance. Weather events may make it difficult to maintain power lines, wind turbines, and other infrastructure. Weather also impacts day-ahead planning of how to commit units.

Although weather impacts all types of power production, it actually drives the renewable units. It is important to be able to forecast the wind, solar, and hydro power available the next day, and often, the next several days as well. The marginal cost to run these renewable resources is quite low because the fuel is free, and it is economically advantageous to allocate as much power from those units as possible. But over-allocation of those units when the wind, irradiance, or water power is not available could lead to using much more expensive reserve units in real time. For timescales less than a day, it is important to know the most recent update to the forecast to balance the load in close to real time. Ramp events are sharp increases or decreases in power production, often caused by the passage of fronts (wind) and clouds (solar). If these ramps are predicted far enough in advance, grid operators can commit other units appropriately. On the other hand, these ramps in renewable energy generation must be balanced with the costly spinning reserve units if the grid operators were not expecting them. Finally, they are required to maintain a consistent transmission frequency,

and this becomes difficult with high penetrations of renewable energy; this is a problem on the order of seconds and lower. Note that these temporal needs correspond greatly to the spatial variability discussed earlier (Fig. 1.2), implying that one must be able to tailor the model to those needs. Thus, a full range of prediction often requires a variety of models that then must be seamlessly integrated to produce a coherent forecast (Giebel et al., 2007; Monteiro et al., 2009; Mahoney et al., 2012; Ahlstrom et al., 2013; Orwig et al., 2014; Tuohy et al., 2015; Wilczak et al., 2015; Haupt and Mahoney, 2015). It is also worth noting, however, that if the balancing area for the electrical grid covers a sufficiently large geographic area, then the complexity of the problem can be reduced because the renewable resource would be less variable as a whole over that area (St. Martin et al., 2015).

At the very short range, on the order of seconds or minutes to a couple hours, it is best to have situational awareness through measurements at the site, and also at short distances upwind from the site. It is difficult to improve on persistence forecasts at these temporal scales; that is, a forecast would assume that the current value of wind speed or irradiance persists to the next time period. Methods that improve on persistence tend to be statistical learning methods (Sharma et al., 2011; Marquez and Coimbra, 2011, among others) and methods to identify changes in regimes (McCandless et al., 2016a,b).

Beyond an hour or two, NWP becomes important. This is where we leverage the equations of motion and numerically integrate them forward in time (more details in Section 1.3). It is important to initialize those equations with the best estimate of the atmospheric state (also known as an analysis) via data assimilation (DA) (Section 1.2). Integrating the equations forward from the current analysis state provides an estimate at the future time. NWP continues to provide value until about 2 weeks, when predictability approaches climatology (Bauer et al., 2015).

Beyond a couple weeks, the specifics of the integrations are washed out, but one can still use general trends associated with long-range atmospheric oscillations, such as the El Niño/Southern Oscillation, which is associated with heating in the tropical Pacific that produces standing waves in the atmosphere that may persist for a period of time, affecting global weather patterns for months at a time. Understanding and predicting such oscillations lead to seasonal predictions that may be better than climatology. On the very longest (climatic) scales, there is a potential for long-term trends due to changes in atmospheric composition—these issues are dealt with in later chapters.

This chapter focuses on the short- and medium-range prediction methods.

### 1.1.3 Atmospheric chaos

At first, scientists saw initial successes at integrating the filtered equations of motion as an indication that with increases in computing power, one would eventually be able to resolve all scales and fully model the circulation of the Earth as accurately as the computer (and filters) would allow. But in the 1960s, Edward Lorenz found that these equations are extremely sensitive to initial conditions and that very small perturbations to the initial conditions (or boundary conditions or other forcings) could cause large

deviations in the computed flow conditions at a later time (Lorenz, 1963). This sensitivity to initial conditions has become known as “chaos” and has altered meteorologists’ views of predictability. The sensitivity is caused by an inability to accurately represent the current atmospheric state. Thus, resulting errors grow and saturate the energy spectrum. This inherent sensitivity means that because we cannot precisely know the conditions at all places at the initial time, we are doomed to a loss of predictability at future times. Because of this limitation, meteorologists have embraced probabilistic forecasting to quantify uncertainties in the forecast, as will be discussed further in [Section 1.5](#).

The remainder of this chapter lays out the details of how forecasting on the short to medium range is accomplished. We introduce approaches to forecasting at the scales that are important to forecasting for renewable energy. [Section 1.2](#) discusses how modelers incorporate or assimilate observational data into models to produce the best possible initial condition. [Section 1.3](#) discusses the models themselves, including the dynamical formulation and incorporation of the important physical mechanisms, emphasizing configuring the model for the needs of the problem. The use of postprocessing methods is treated in [Section 1.4](#) and probabilistic forecasting is introduced in [Section 1.5](#). [Section 1.6](#) provides some hints for modeling for renewable energy with a theme of planning for the validation process. The chapter is summed up and concluded in [Section 1.7](#) with a view of how modern forecasting for renewable energy has become a Big Data problem that requires bringing together the best models with the best observational data in innovative ways to produce the best deterministic and probabilistic forecast.

## 1.2 Observational data and assimilation into numerical weather prediction models

### 1.2.1 *Observational data*

There is a wealth of observational data of many variables that influence the weather and climate, and which NWP models are designed to predict, either directly with the prognostic equations, or indirectly with diagnostic equations. These include numerous meteorological (e.g., temperature, humidity, wind speed/direction, and barometric pressure), chemical/air quality (concentrations of various aerosol species, ozone,  $\text{NO}_x$ , etc.), land surface (e.g., soil moisture and soil temperature), and ocean (e.g., sea surface temperature, significant wave height) quantities, as well as turbulent heat, moisture, and momentum fluxes that govern surface–atmosphere exchanges.

These varied observations come from numerous platforms. At the surface there are several in situ networks. Meteorological Aerodrome Report (METAR) stations provide routine, standardized-format meteorological reports at airports worldwide, typically hourly or every 20 min. METAR observations are some of the most relied-upon observations of near-surface quantities, because the sensors tend to be well maintained. Filling in the gaps between the METAR stations there are numerous

mesonets (“mesoscale networks”) of varying quality on land, and on the surface of oceans or other large bodies of water there are networks of moored and drifting buoys, as well as ship-based observations. Various air quality mesonets also exist. Vehicles and smartphones can also provide tremendously rich observational datasets ([Mahoney and O’Sullivan, 2013; Mass and Madaus, 2014](#)).

Above the surface there are several additional in situ observation platforms. These include radiosondes (also called rawinsondes), which are instrument packages carried up through the troposphere and into the lower stratosphere by weather balloons. These radiosondes measure temperature, humidity, and pressure, while wind speed and direction are derived from Global Positioning System (GPS) tracking. Radiosondes are launched worldwide at 0000 and 1200 UTC daily from locations spaced several hundred kilometers apart. Many of these radiosonde sites are included in the World Meteorological Organization (WMO) Regional Basic Synoptic Network and Antarctic Observing Network sites, which are displayed in [Fig. 1.3](#). These radiosondes naturally tend to be heavily concentrated over continents, and especially in the United States, Europe, East Asia, and the Indian Subcontinent, with comparatively sparser coverage over South America and Africa. Dropsondes are similar to radiosondes, except they are dropped from a plane and take a profile of measurements down to the surface, and often measure upper-ocean properties. Additionally, commercial aircraft worldwide take flight-level and ascent/descent profile observations of temperature, humidity, and pressure via the Aircraft Communications and Reporting System (ACARS).

Distinct from the various in situ observation platforms, there are also several remote sensing observation platforms. The most obvious and prevalent of these are satellites.

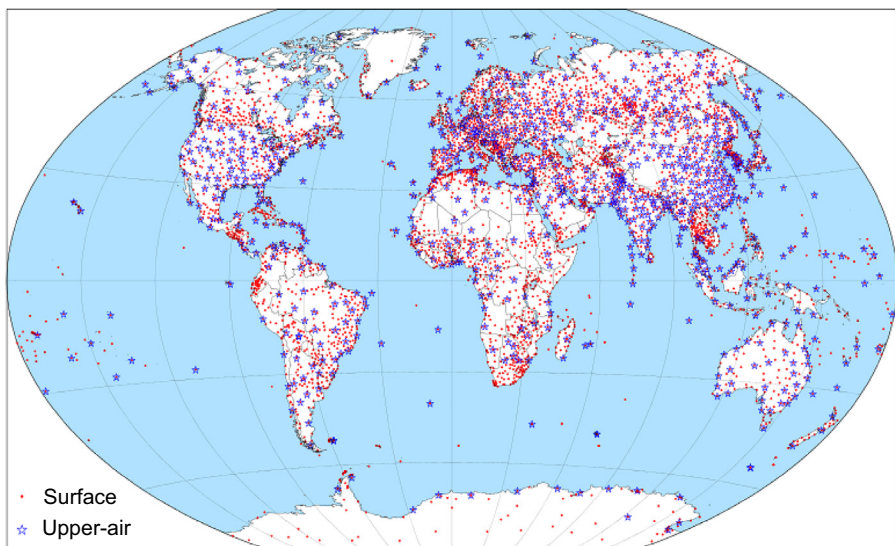


**Figure 1.3** Surface (red dots) and upper-air (blue stars) observation stations in the WMO Regional Basic Synoptic Network and Antarctic Observing Network.

Most satellites observe radiances at various wavelengths, from which quantities including temperature, moisture, cloud-top wind, and aerosol/chemical concentration can be derived. Each satellite makes a unique set of measurements with unique error characteristics that can change through time, and the spatial coverage and temporal frequency of these satellite observations are determined by the satellite's orbital path and plane (e.g., polar-orbiting, geostationary, etc.). In addition to satellites, there are various ground-based and aircraft-based remote sensing observations, including radars, sodars, and profilers.

As with any measurement of a physical quantity, no observation is perfect. Estimates of observation error, which combines the effects of both instrumentation error and representativeness error (how representative a point measurement is of the surrounding area), must be made and taken into account when using observations.

### **1.2.2 Data assimilation**

As mentioned in [Section 1.1](#), the atmosphere is chaotic. Therefore, a major key to reducing errors in NWP forecasts is to specify the initial state of the atmosphere as accurately as possible. Some form of DA is used for this task in NWP. As [Talagrand \(1997\)](#) put it, DA is the “process in which observations distributed in time are merged together with a dynamical numerical model of the flow in order to determine as accurately as possible the state of the atmosphere.” There are a few basic classes of DA algorithms in use today, all of which use observations from the numerous platforms mentioned earlier to increment from a background (prior) state to an analysis (posterior) state, and a few of these are highlighted below. The analysis state serves as the initial condition for a subsequent forecast.

#### **1.2.2.1 Nudging**

Observation nudging, or Newtonian relaxation, is an empirical analysis scheme in which the NWP model state is “nudged” toward an observation by means of adding a small extra term to the model prognostic equations ([Hoke and Anthes, 1976](#)). In modern four-dimensional data assimilation (FDDA) nudging schemes, this nudging term is weighted in both time and space around the observation to avoid introducing artificial gravity waves ([Stauffer and Seaman, 1990, 1994; Liu et al., 2008](#)). FDDA is a continuous DA technique, as it assimilates observations sequentially through time, rather than treating all observations within a given time window as being valid at a single analysis time. A limitation of FDDA is that it can only assimilate observations that can be converted to model prognostic variables.

#### **1.2.2.2 Variational assimilation**

Variational assimilation techniques are a form of statistical interpolation. All statistical interpolation techniques require an estimation of the error covariances between variables in the background state, as well as error covariances between the observed

variables. These techniques find the optimal analysis by globally minimizing a cost function that incorporates the distance between the analysis and observations within the assimilation window. This method also requires the observation error covariance matrix and the background error covariance matrix (e.g., [Talagrand, 1997](#); [Kalnay, 2003](#)), which at times may be difficult to compute accurately. In three-dimensional variational DA (3D-Var) schemes, these error covariance matrices come from a static climatology, and all observations within a given assimilation window are assumed to be valid at the analysis time. These assumptions reduce the computational burden. In contrast, four-dimensional variational DA (4D-Var) schemes seek to minimize the cost function, subject to the NWP model equations, to find the best model trajectory through the entire assimilation window, rather than just at the analysis time. In addition, the error covariance matrices are flow-dependent in 4D-Var. These differences make 4D-Var significantly more computationally intensive than 3D-Var, but also more accurate (e.g., [Klinker et al., 2000](#); [Yang et al., 2009](#)).

### 1.2.2.3 Ensemble Kalman filters

Kalman filters (KF; [Kalman, 1960](#); [Kalman and Bucy, 1961](#)) are another form of statistical interpolation. Like 3D-Var or 4D-Var, forward operators must be written to generate a model prediction of the observed quantity, which facilitates assimilation of a much wider set of variables than can be done with observation nudging. Unlike 3D-Var or 4D-Var, which globally correct a background to a set of observations, KF algorithms are sequential DA methods, meaning that the background is updated in sequence by each observation within the assimilation window. Background error covariance matrices also evolve with the flow in KF implementations, so they better represent the true “errors of the day” than do static error covariances. For large geophysical models, however, a true KF is computationally prohibitive, largely due to the flow-dependent background error covariance matrix. To reduce the computational cost, [Evensen \(1994\)](#) developed the ensemble Kalman filter (EnKF). By using an ensemble of nonlinear model simulations, each with uniquely perturbed initial and lateral boundary conditions, the forecasts can be considered to be a random sample of the model state’s flow-dependent probability distribution. The impact of an observation on the ensemble analysis estimate depends on the sample covariance between various components in the ensemble state vector. Multiple flavors of EnKF have been developed, and they are widely used by the community (e.g., [Anderson, 2001](#); [Yang et al., 2009](#); [Anderson et al., 2009](#); [Schwartz et al., 2015](#)).

### 1.2.2.4 Hybrid approaches

In addition to the basic classes of DA approaches outlined previously, there are many efforts to combine the best parts of each approach to further improve the resulting analysis state. Many of these hybrid approaches combine EnKF with variational DA (e.g., [Wang et al., 2008](#); [Zhang et al., 2013](#); [Pan et al., 2014](#); [Lorenc et al., 2015](#)), but some also combine nudging with an EnKF ([Lei et al., 2012](#)).

### 1.2.3 Coupled models

In addition to DA systems, another way to further reduce forecast errors from NWP models is to couple them to models that simulate other parts of the Earth system. For instance, it is known that both the wind and the waves mutually impact each other in the marine atmospheric boundary layer (Sullivan et al., 2014). Efforts to build two-way coupled atmosphere-wave models (e.g., Chen et al., 2013; Kuznetsova et al., 2015) are crucial to improving predictions for a number of applications, including offshore wind energy. Additionally, coupled atmosphere-hydrology models (e.g., Gochis et al., 2015) reduce forecast errors for several applications, including hydro energy and even wind energy, thanks to the impact of soil moisture on boundary layer winds (Maxwell et al., 2011).

## 1.3 Configuring numerical weather prediction to the needs of the problem

### 1.3.1 Fundamentals of numerical weather prediction

The rational basis for NWP was proposed at the beginning of the 20th century. Bjerknes (1904) suggested that the weather could be predicted using the fundamental conservation laws of nature. These equations, when expressed in mathematical form, form a system of equations with the same number of unknowns and equations. In principle a solution can be found, allowing a forecast of the evolution of the atmosphere. He anticipated that to solve this system of equations, the atmospheric equations of motion, one would need first to develop an analysis of the atmospheric state (i.e., temperature, humidity, winds, etc.) and then use this information to prognose subsequent states. The first step, the analysis, is facilitated by DA and was discussed in Section 1.2. The second step, the prognosis or forecast, is challenging because, among other things, the analytical solution of the atmospheric equations of motion is unknown. Hence, we need to numerically approximate the solution to the atmospheric equations of motion. The method used to approximate the solution is the NWP model.

The number of calculations necessary to approximate a solution is enormous and NWP was not feasible until the advent of digital computers. In a visionary work, Richardson (1922) approximated a solution to the atmospheric equations of motion using the basic ideas that we still use in modern NWP models. He discretized the model equations onto a grid, beginning with observed conditions (which at that time required wiring weather conditions from upstream locations), and envisioned that a team of human “calculators” could perform the numerical calculations. Although his method failed (he did not fully understand the impact of the small scales on the larger scales, and the unfiltered equations “blew up”), thus was born the concept of NWP. Based on this work, the development of digital computers, and with improved understanding of atmospheric dynamics, Charney et al. (1950) made the first successful NWP. A rapid increase in NWP model developments took place after this pioneering work, leading to modern NWP models (Lynch, 2006).

Current NWP models have two main components: a dynamic solver and a set of physical parameterization schemes. These components are described further.

### 1.3.1.1 *Dynamic solver*

The dynamic solver uses algebraic approximations to represent the differential terms in the atmospheric equations of motion. This requires the selection of appropriate spatial and temporal discretization. Typical terms approximated by the dynamic solver include advection, the pressure gradient force, and the Coriolis force resulting from Earth's rotation.

Different approaches have been proposed to represent the differential terms. The most common approach is to use finite difference schemes. These methods expand the spatial and temporal differential terms into a polynomial series (a truncated Taylor series). This type of dynamic solver is simple, relatively easy to code, and widely used in limited-area models. An alternative approach is to use spectral methods. The fundamental idea of spectral methods consists of expanding atmospheric variables (temperature, winds, moisture, etc.) in frequency (or wavenumber) space. Spectral methods provide the highest possible order of accuracy for a discretized set of partial differential equations, and therefore result in reduced errors in representing the transfer of energy toward the finest atmospheric scales. Spectral methods are most often used in global NWP models and in fine-scale large eddy simulations (LES).

### 1.3.1.2 *Parameterizations*

Regardless of the dynamic solver used, there are additional processes that need to be represented in an NWP model. These include physical processes that we cannot resolve at the selected grid spacing, processes that we do not know how to represent analytically, and processes that require large amounts of calculations to represent explicitly. In these situations, the model includes the effects of these terms in the form of physical parameterization schemes.

The model physics, therefore, can introduce larger approximations than those introduced in the dynamic solver.

## 1.3.2 *Standard physics available in numerical weather prediction models*

All NWP models parameterize a number of physical processes ([Stensrud, 2007](#); [Warner, 2011a](#)). These include atmospheric radiation, land–surface interactions, turbulent mixing, convective clouds, and cloud microphysics.

Radiation parameterizations provide atmospheric heating rates and downward irradiance at the surface. The radiative transfer calculations are divided into shortwave and longwave components. Longwave radiation accounts for the infrared radiation absorbed and emitted by atmospheric gases, clouds, and the Earth's surface. On the other hand, shortwave radiation accounts for the absorption, reflection, and scattering

by gases, clouds, and the Earth's surface of the solar spectrum centered in the visible region. Both shortwave and longwave radiative transfer are affected by the modeled water vapor, clouds, and gases such as ozone, oxygen, and carbon dioxide. Some advanced radiation schemes also model the interaction with various species of modeled atmospheric aerosols.

Land surface models (LSMs) represent the interactions between the land and atmosphere, and quantify soil properties (soil type, vegetation type, soil moisture, and soil temperature), as well as the surface turbulent fluxes of heat, moisture, and (sometimes) momentum. LSMs usually represent moisture and heat fluxes in multiple layers of the soil. More advanced LSMs include vegetation effects, urban effects, snow cover prediction, and hydrology. All of these processes ultimately determine the ground temperature, which is used to compute the longwave radiation emitted by the ground and passed to the radiation parameterization. LSMs also calculate the albedo, and thus provide feedback to the shortwave radiation package. In addition, the turbulent fluxes provide the lower boundary condition to the planetary boundary layer (PBL) parameterization (Stensrud, 2007).

PBL parameterizations account for the vertical mixing associated with atmospheric turbulence in the PBL (Wyngaard, 2010), which grows and decays with diurnal heating and cooling of the underlying surface. The turbulent mixing usually includes temperature, water vapor, horizontal momentum, and trace gases. The atmospheric turbulent fluxes are usually modeled as a combination of local and nonlocal mixing. The parameterizations require a quantification of the surface turbulent fluxes, which are usually computed via Monin-Obukhov similarity theory (Monin and Obukhov, 1954) in a surface layer parameterization, which models these fluxes below the lowest model layer of the PBL scheme, and/or in the LSM directly.

Cumulus parameterizations account for the effects on temperature and moisture profiles associated with unresolved deep convective and/or shallow convective clouds. In addition, the schemes provide surface precipitation that feeds back into the LSM. The deep convective schemes are usually based on closure assumptions valid for horizontal grid spacing higher than 10 km. These approximations are less accurate at finer grid spacing because the NWP starts to resolve the convective updrafts/downdrafts that are parameterized. The deep convective scheme is usually turned off at a grid spacing finer than about 5 km. However, shallow convection may still need to be parameterized at a grid spacing of about 1 km.

Finally, microphysics parameterizations represent processes involving cloud droplets and/or ice crystals and the effects of their life cycle on the temperature and moisture profiles, precipitation, and cloud radiative properties. Microphysics can account for processes in liquid water clouds (warm clouds) or clouds consisting in water and ice hydrometeors (mixed phase clouds). Hence, the parameterizations differ in the number of hydrometeors that are predicted and advected by the model dynamics. Microphysics parameterizations are usually based on a bulk approach wherein the size distribution of hydrometeors follows a functional form, and one or more parameters of the distribution are predicted by the parameterization (e.g., mixing ratios).

### 1.3.3 Configuration of numerical weather prediction models for specific applications

There are a number of aspects to consider when providing weather predictions tailored to a specific application, such as forecasting renewable energy. The first decision is which model to use. This is an important decision because one not only needs to learn how to run the model but also understand the approximations in the dynamical solver and the parameterizations. It is desirable to use a model under active development and widely used in the community, thus benefitting from potential advances in the field.

Once the model has been selected it is necessary to identify the meteorological data to provide the initial conditions (and boundary conditions if it is a regional model). The data are usually from a global model that assimilates observations over the entire Earth, or a previous forecast from a regional model typically run by national weather services. Important aspects to consider are the frequency of the forecasts, the length of the forecasts, and the vertical and horizontal grid spacing. One should also be aware of the observations that the model assimilates and the performance of the forecasts from retrospective analyses. Obtaining accurate initial conditions is the first step in the weather forecast process.

The spatial discretization in the model should be tailored to the specific problem under investigation. For example, if one is interested in simulating airflow through a wind turbine, it is desirable to have several vertical levels intersecting with the turbine rotor—otherwise, the interaction of the blades with the atmosphere will not be captured. Limitations in the algebraic approximations introduced by the dynamic solver should be taken into account—the use of algebraic expressions may distort the representation of the finest atmospheric scales. In these situations, the effective resolution of the model could be several grid spacing increments (Jiménez et al., 2016b). This numerical artefact should be taken into account when deciding the target grid spacing.

Frequently, differences in grid spacing between the forecast used to generate the initial conditions and the target resolution are large. In these situations NWP models can be configured as a nested set of domains to progressively reach the target grid spacing. This nesting approach requires a careful configuration of the size and location of each domain. In this direction, it is desirable to have boundaries as homogenous as possible to gradually capture heterogeneities. For example, it is more prudent to place a domain boundary over relatively flat terrain than intersecting a mountain range. Nesting has been used successfully to reach a horizontal grid spacing of a few hundred meters (e.g., Jiménez et al., 2015).

The selected grid spacing strongly conditions the choice of model physics schemes. Ideally, the parameterizations should be insensitive to the grid spacing (scale aware). However, in general this is not the case and some schemes perform better at certain grid spacings. Most schemes are designed based on assumptions valid only over a specific range of spatial scales corresponding to given grid spacings. Knowing the sensitivity of the various schemes to the grid spacing is an added bonus when configuring the physics of the model for specific applications.

The performance of a given parameterization scheme can also depend on the atmospheric state. For example, PBL parameterizations have been shown to be sensitive to the atmospheric stability. Being aware of this different performance can be of special relevance if the target location more frequently exhibits stable or unstable conditions, as in polar or tropical regions. In general, the modeler should be aware of the approximations introduced by the parameterizations. Previous sensitivity studies can guide the forecaster to optimize the simulation of a particular physical process.

There are some situations in which the available physical options are not sufficient to represent relevant processes for the target application. In these situations, the forecaster should be aware of the limitations of the forecast, and, if possible, try to “correct” model errors with some kind of postprocessing (see [Section 1.4](#)). If this correction is still not satisfactory and enough resources are available, then one can develop the model to include the missing physical process(es).

### **1.3.4 Model development: the WRF-Solar model**

The WRF-Solar model ([Jiménez et al., 2016a](#)) is a clear example of model development to fulfill a particular need. The Weather Research and Forecasting (WRF) model ([Skamarock et al., 2008](#)) provides an appropriate framework for weather prediction but certain limitations, mostly in the representation of the cloud-aerosol-radiation system, hampered its use for solar energy applications. The model upgrades described here made WRF-Solar into the first NWP model specifically designed to meet the increasing demand for specialized forecast products for solar energy applications.

A complete set of the WRF-Solar upgrades is depicted in [Fig. 1.4](#). The first set of augmentations specifically targeted solar applications. The first augmentation focused on improving the solar tracking algorithm. WRF-Solar includes the equation of time (EOT; [Muller, 1995](#)) to account for deviations associated with the eccentricity of the Earth’s orbit and the obliquity of the Earth. Omitting the EOT caused irradiance leads and lags of up to 16 min. This is normally inconsequential when running the radiation scheme approximately every half hour. However, solar energy applications require more frequent calls to the radiation package and the inaccuracies in the solar position cause a nonnegligible error.

Many solar applications require direct and diffuse solar irradiance components in addition to global horizontal irradiance (GHI). However, GHI is the only irradiance necessary to compute the surface energy budget and thus WRF previously only output this irradiance. WRF-Solar added the direct normal irradiance (DNI) and diffuse (DIF) components from the radiation parameterization to the model output when available, and parameterized them ([Ruiz-Arias et al., 2010](#)) when the radiative transfer scheme only accounts for GHI.

Another useful augmentation is irradiance output at arbitrary time intervals limited only by the model time step. First, WRF-Solar allows the user to output the complete irradiance time series at selected locations. Then, efficient parameterizations were implemented to either interpolate the irradiance in between calls to the radiative transfer parameterization, or to use a fast radiative transfer code that avoids computing

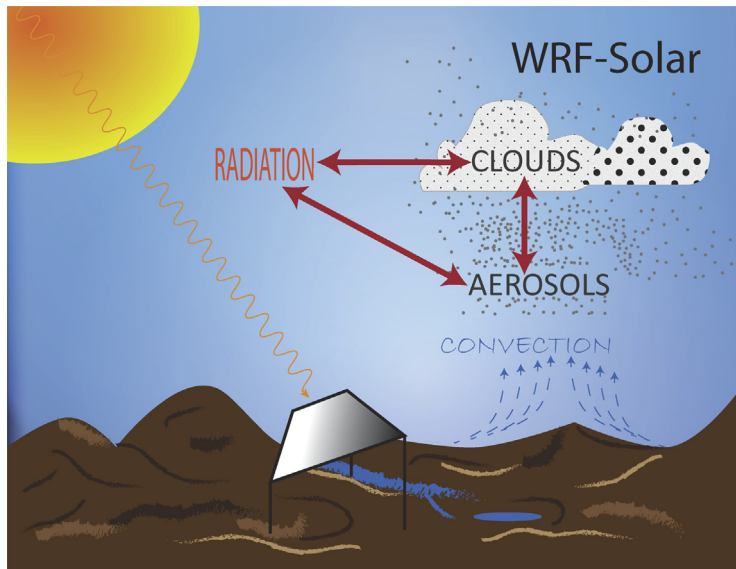


**Figure 1.4** Diagram showing the WRF-Solar augmentations that now include specific interactions between the radiation, clouds, and aerosols. The radiation scheme has been augmented with an improved solar tracking algorithm and explicitly calculates all irradiance components with a capability for high-frequency output of GHI, DNI and DIF. It additionally allows time variation in the irradiance components between function calls. The aerosols are also now allowed to vary in time, as well as to be advected by the winds, to allow feedback to the radiation scheme. The aerosols additionally become the microphysics species that determine the cloud condensation nuclei for cloud formation. Clouds in turn scavenge the aerosols. A new shallow convection scheme enhances the capability for the cloud feedback to the radiation. Both aerosols and clouds fully feed back to determining the scattering, absorption, and emission in the radiation scheme.

three-dimensional heating rates but provides the surface irradiance (Xie et al., 2016). The former interpolates the irradiance between successive calls to the radiation parameterization, considering the change in the solar position and keeping the contribution of the hydrometeors constant. The latter is based on a simplified radiative transfer algorithm and uses the current concentration of hydrometeors. Both are efficient algorithms that provide high-frequency irradiance calculations useful to analyze solar ramps, for instance.

A new parameterization was developed to improve the representation of absorption and scattering of radiation by aerosols (aerosol direct effect). This aerosol direct effect is usually represented via monthly climatologies of the aerosol optical properties. Such representation is not sufficient to capture the high spatio-temporal variability of aerosols. The treatment of aerosols in WRF-Solar (Ruiz-Arias et al., 2014) allows ingesting aerosol optical properties with time stamps to accurately model the temporal variations in aerosol loading. Atmospheric chemistry models are currently being run at the global

scale and even assimilate aerosol concentrations, which can be used to represent the aerosol optical properties in WRF-Solar.

Another advance is that the aerosols now interact with the cloud microphysics, altering the cloud evolution and radiative properties (aerosol indirect effect). This effect has been traditionally only implemented in atmospheric chemistry models, which are significantly more costly computationally than NWP models that do not include detailed chemistry. WRF-Solar uses a simplified treatment of the aerosols (only two aerosol species are allowed) that accounts for changes in the size of cloud hydrometeors to represent the aerosol indirect effect (Thompson and Eidhammer, 2014) with minimal increase in computational cost ( $\sim 16\%$ ). The aerosols are advected by the model dynamics and the parameterization is linked to the WRF-Solar aerosol parameterization to have a fully coupled representation of the cloud-aerosol-radiation system.

Another development accounts for the feedbacks that subgrid scale clouds produce in shortwave irradiance. The motivation for this development is to represent small-scale clouds at relatively coarse grid spacing ( $\sim 10$  km). This allows for significant speed up in the time required to complete a forecast. The development is implemented in a shallow cumulus parameterization (Deng et al., 2003, 2014). The scheme includes predictive equations for the subgrid cloud water/ice content and the cloud fraction.

Finally, WRF-Solar also allows assimilation of infrared irradiances from satellites to determine the three-dimensional cloud field (Auligné, 2014a,b). This allows for an improved initialization of the cloud field that increases the performance of short-range forecasts.

## 1.4 Postprocessing

Models have inherent biases. Different models often have different biases. If one can define these biases based on past performance, then one can correct the model with statistical or machine learning approaches. Modern forecasting includes postprocessing the NWP output to improve upon the results. At the basic level, a statistical regression model known as model output statistics (MOS) is applied to remove biases (Glahn and Lowry, 1972). More complex methods (such as artificial neural networks, autoregressive models, and others) also are used to provide nonlinear corrections to models (Myers et al., 2011; Myers and Linden, 2011; Giebel and Kariniotakis, 2007; Pelland et al., 2013). Ensemble MOS (Wilks and Hamill, 2007) not only corrects the individual models, but also optimizes weights for blending forecasts from multiple models. It is typical to blend multiple models together to produce a better forecast than any single model could produce consistently, often with a 10%–15% improvement over the best model forecast (Mahoney et al., 2012; Myers et al., 2011).

New methods are frequently advancing the state of postprocessing. For instance, some methods seek to identify atmospheric regimes and then train methods specific to each regime. An example in solar power forecasting leverages observations from both the surface and from satellites to determine the cloud regime, and then applies

the neural network that was trained for that specific regime (McCandless et al., 2016a,b).

These postprocessing techniques reduce the error of a deterministic forecast. However, additional techniques are necessary to quantify the uncertainty in the forecast.

## 1.5 Probabilistic forecasting

Section 1.1 of this chapter introduced the concept of sensitivity to initial conditions, the resulting chaotic nature of modeling atmospheric flow, and the need for probabilistic forecasts that quantify the uncertainty of the prediction. Some energy companies use the uncertainty information to help plan their reserve allocations. They find that if the forecasters are quite certain in their forecast, it may not be necessary to have as high a supply of spinning reserves as if they are less certain (Bartholomy et al., 2014; Bartlett, 2014).

To produce a probabilistic forecast requires an ensemble of model solutions with differing initial conditions or perturbations to other forcings that could impact the downstream solution. Fig. 1.5 illustrates the philosophy. An initial probability density function (pdf) of model conditions is initialized at time  $t = 0$ . At some later time,  $t = T$  in the figure, the spread of the pdf has increased. The rate of spread depends on the

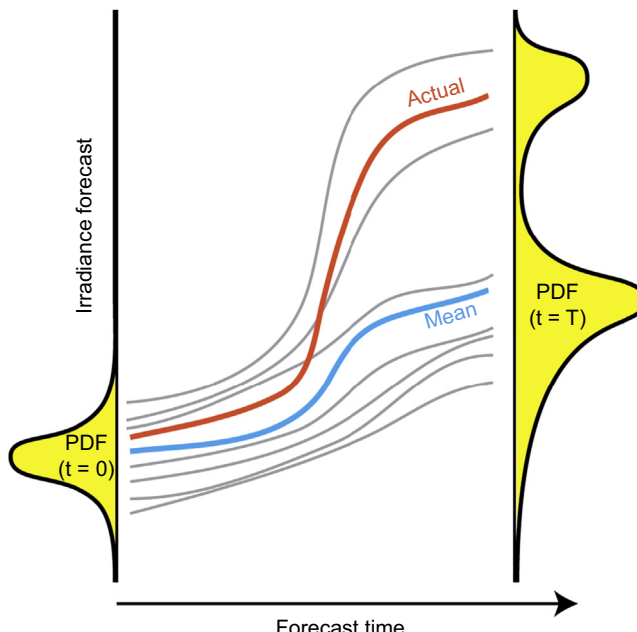


**Figure 1.5** The spread in the ensemble probability density function (pdf) at the initial time ( $t = 0$ ) increases in time, sometimes resulting in a different shape to the pdf at the later time ( $t = T$ ).

model and the atmospheric conditions. The goal of ensemble modeling is to sufficiently span the initial conditions so that the state of the final pdf is fully spanned. One finds, however, that if random initial conditions or other perturbations are used, it may require several hundred model simulations to fully span the resulting pdf ([Kolczynski et al., 2011](#)). With current computing power, this number is prohibitive. The solution, then, is to choose a sufficient number of conditions in a way that spans the pdf without including redundancies ([Lee et al., 2012, 2016](#)). For large-scale models, national centers have developed methods to find the fastest-growing modes (e.g., singular vectors) of the models, and use those modes as the ones to perturb ([Molteni and Palmer, 1993](#)). Today, many methods exist to initialize ensembles, as discussed in [Section 1.2](#).

As we saw earlier, NWP does not depend only on initial conditions, but also on the physics parameterizations and boundary conditions. There are several major techniques for generating an ensemble—the first adds perturbations to the initial state of a forecasting system, while the second type uses different physics parameterization schemes, and a third uses different numerical models altogether in a “poor man’s ensemble” ([Ebert, 2001](#)). The second type directly generates a set of model runs that approximate the uncertainty of specific processes of the atmosphere and are capable of simulating the uncertainty in the calculation of the state of the atmosphere in every time step of the forecast.

A good ensemble should be well calibrated, meaning that it should be centered (unbiased), sharp (narrow pdf), and reliable (the quantile predicted matches the quantile observed when averaged over time). There are various methods to do this, including linear variance calibration ([Kolczynski et al., 2011](#)), logistic regression, ensemble MOS ([Woodcock and Engel, 2005](#)), Bayesian model averaging ([Raftery et al., 2005](#)), and more.

Another interesting postprocessing method is the analog ensemble (AnEn) technique. In this case, however, rather than running multiple models, the historical output from a single, often high-resolution model is used to generate the ensemble. A search of the historical forecast records is made to identify the forecasts that are most similar to the current forecast. The observations corresponding to those forecasts form the AnEn. This AnEn is effective for both improving the deterministic forecast as well as using the multiple analogs to form an ensemble that can be used to quantify the uncertainty of the forecast ([Delle Monache et al., 2013; Haupt and Delle Monache, 2014; Alessandrini et al., 2015](#)). [Fig. 1.6](#) provides an example of a probabilistic wind power forecast generated using the AnEn technique.

## 1.6 Planning for validation

We would be remiss if we did not include discussion of the importance of planning NWP applications from a holistic point of view and the knowledge of the field required to do it correctly. [Warner \(2011b\)](#) wrote an excellent article that lays out the need for knowledge and skill to apply NWP to a problem. While it is relatively simple to

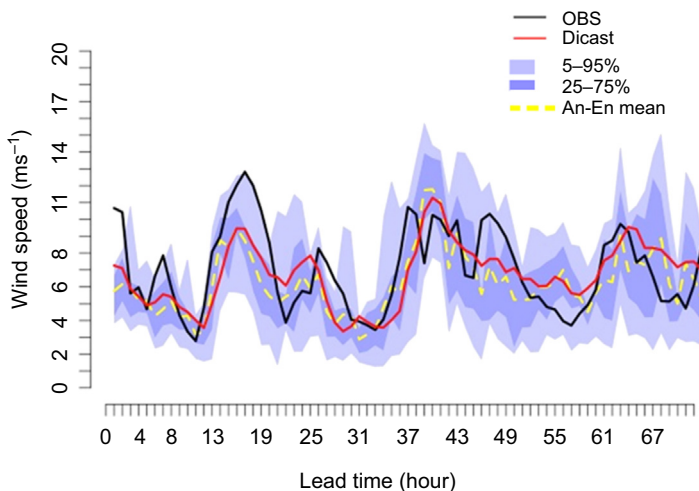


**Figure 1.6** Example of a probabilistic wind speed forecast for a power plant. The forecast has been made originally by blending various numerical weather prediction models with the DICast® consensus forecasting system (Mahoney et al. 2012), then further postprocessed using the analog ensemble (AnEn) technique. The DICast forecast is the *solid red line* and the *yellow dashed line* is the deterministic AnEn prediction. The *solid black line* is the actual wind speed that transpired. The *shaded blue regions* indicate the uncertainty estimates and their width varies with the prediction time.

download and run a model “out of the box,” it takes a great deal of modeler skill and knowledge to obtain useful model output. Warner offers a list of recommendations to plan and execute an NWP application, paraphrased below as a list of steps, and reiterating on some of the points made in previous sections:

1. Clearly define the objectives of the study and the model runs.
2. Identify and develop a physical understanding of the atmospheric processes that are to be simulated.
3. Analyze all available observations. Some of these may be assimilated into the model while others may be reserved for independent validation and verification.
4. Prepare the experimental design, including any series of model runs.
5. Choose the horizontal and vertical grid resolution to meet the objectives, remembering that the effective resolution will be coarser than the horizontal grid spacing, as discussed in [Section 1.3](#). Also know limitations of resolution and carefully avoid modeling in resolution regions where the assumptions that parameterizations are built on are violated ([Wyngaard, 2004](#)).
6. Avoid running the model prematurely, before planning well.
7. Choose the start time, initialization, and assimilation processes wisely for best results.
8. Run test simulations for limited-area models to evaluate the sensitivity to the computational domain boundaries and configuration.
9. Define the most appropriate combination of physics parameterizations for the application, using both sensitivity studies and review of the literature.

10. Understand the limitations to the predictability of what you are modeling, as discussed in [Sections 1.1 and 1.4](#).
11. Plan for verification. Just because a model runs successfully without crashing does not mean that it produces a correct or useful result.
12. Organize well and keep notes of model configurations, model runs, and their results.
13. Document your code well and use good coding practices. Consider using version control software.

When forecasting for renewable energy, all of these steps apply. As demonstrated in [Section 1.2](#), there are a plethora of observations to leverage for DA. There may also be local observations available at a wind or solar plant that should be included. Prior work demonstrates the value of including such observations ([Mahoney et al., 2012; Wilczak et al., 2015](#)). An independent validation is crucial to determining the accuracy of the forecast and to ascertaining the subsequent improvements that could be made.

## 1.7 Weather forecasting as a Big Data problem

We have briefly reviewed the origins of atmospheric motion as being forced by differential solar heating over the globe, the rotation of the Earth, and various forcings. The motions are codified in the Navier–Stokes equations that can be numerically discretized to provide forecasts. One can model the motion by configuring NWP with dynamics and parameterizations of the physical processes. An important consideration is selecting initial conditions that are informed by the observations and assimilated into the models. The flow is still chaotic due to imperfect representation of those initial and boundary conditions, finite time steps in the model discretization, and the approximations introduced by the physical parameterizations in the models. Meteorologists deal with the resulting deviation from exact solutions by postprocessing to improve the forecasts, by embracing the uncertainty and approaching the problem as a probabilistic one, seeking to quantify the uncertainty. When applying the NWP models, it is important to plan for the verification and validation through careful definition of the problem and the data available for comparison. We saw that it is critical to select the appropriate model and apply it correctly to meet the goals of the problem.

In practice, forecasting for NWP is a Big Data problem ([Haupt and Kosović, 2015, 2017](#)). One must assemble a plethora of data and models. This implies disparate data sources and real-time operational planning. NWP model data can be voluminous when simulations are accomplished on fine grids, or when ensembles of simulations are generated. The amount of data involved in assimilation can also be large, and arrive at different times, which adds complexity, variability, velocity, and variety to the forecasting process. There are often issues with the veracity of the data, requiring quality control of the observations that must be handled in the software systems. When data from multiple models with multiple methods of assimilation are combined, the issues all expand and require robust software systems to accomplish the forecasting process. Many of these issues will be elaborated on further in subsequent chapters.

## Acknowledgments

The authors are supported for this effort by a grant from the U.S. Department of Energy, award DE-EE0006016. They wish to thank Cindy Halley-Gotway, Karen Griggs, and Stefano Alessandrini for help with the figures that appear in this chapter.

## References

- Alessandrini, S., Delle Monache, L., Sperati, S., Cervone, G., 2015. An analog ensemble for short-term probabilistic solar power forecast. *Applied Energy* 157, 95–110. <http://dx.doi.org/10.1016/j.apenergy.2015.08.011>.
- Ahlstrom, M., Bartlett, D., Collier, C., Duchesne, J., Edelson, D., Gesino, A., Keyser, M., Maggio, D., Milligan, M., Mohrlen, C., O’Sullivan, J., Sharp, J., Storck, P., Rodriguez, M., 2013. Knowledge is power: efficiently integrating wind energy and wind forecasts. *IEEE Power and Energy Magazine* 11, 45–52. <http://dx.doi.org/10.1109/MPE.2013.2277999>.
- Anderson, J.L., 2001. An ensemble adjustment Kalman filter for data assimilation. *Monthly Weather Review* 129, 2884–2903. [http://dx.doi.org/10.1175/1520-0493\(2001\)129<2884:AEAKFF>2.0.CO;2](http://dx.doi.org/10.1175/1520-0493(2001)129<2884:AEAKFF>2.0.CO;2).
- Anderson, J., Hoar, T., Raeder, K., Liu, H., Collins, N., Torn, R., Avellano, A., 2009. The Data Assimilation Research Testbed: a community facility. *Bulletin of the American Meteorological Society* 90, 1283–1296. <http://dx.doi.org/10.1175/2009BAMS2618.1>.
- Anthes, R.A., Cahir, J.J., Fraser, A.B., Panofsky, H.A., 1981. *The Atmosphere*, third ed. Bell & Howell Co., Columbus, OH. 531 pp.
- Auligné, T., 2014a. Multivariate minimum residual method for cloud retrieval. Part I: theoretical aspects and simulated observations experiments. *Monthly Weather Review* 142, 4383–4398. <http://dx.doi.org/10.1175/MWR-D-13-00172.1>.
- Auligné, T., 2014b. Multivariate minimum residual method for cloud retrieval. Part II: real observations experiments. *Monthly Weather Review* 142, 4399–4415. <http://dx.doi.org/10.1175/MWR-D-13-00173.1>.
- Bartholomy, O., Vargas, T., Simone, M., Hansen, C., Fitchett, S., Pohl, A., 2014. Benchmarking solar power and irradiance forecasting accuracy at Sacramento Municipal Utility District. In: *IEEE Photovoltaic Specialist Conference*, June 8–13, pp. 63–68.
- Bartlett, D., February 25, 2014. What is the value of a variable generation forecast?. In: *Utility Variable Generation Group Forecasting Workshop*, Phoenix, AZ.
- Bauer, P., Thorpe, A., Brunet, G., 2015. The quiet revolution of numerical weather prediction. *Nature* 525, 47–55. <http://dx.doi.org/10.1038/nature14956>.
- Bjerknes, V., 1904. Das Problem der Wettervorhersage, betrachtet vom Standpunkt der Mechanik und der Physik. *Meteorologische Zeitschrift* 21, 1–7 (Translated and edited by Volken, E., Brönnimann, S., 2009. *Meteorologische Zeitschrift* 18, 663–667, doi:[10.1127/0941-2948/2009/416](https://doi.org/10.1127/0941-2948/2009/416)).
- Charney, J., Fjörtoft, R., von Neumann, J., 1950. Numerical integration of the barotropic vorticity equation. *Tellus* 2, 237–254. <http://dx.doi.org/10.1111/j.2153-3490.1950.tb00336.x>.
- Chen, S.S., Zhao, W., Donelan, M.A., Tolman, H.L., 2013. Directional wind–wave coupling in fully coupled atmosphere–wave–ocean models: results from CBLAST-Hurricane. *Journal of the Atmospheric Sciences* 70, 3198–3215. <http://dx.doi.org/10.1175/JAS-D-12-0157.1>.

- Delle Monache, L., Eckel, F.A., Rife, D.L., Nagarajan, B., Searight, K., 2013. Probabilistic weather prediction with an analog ensemble. *Monthly Weather Review* 141, 3498–3516. <http://dx.doi.org/10.1175/MWR-D-12-00281.1>.
- Deng, A., Seaman, N.L., Kain, J.S., 2003. A shallow-convection parameterization for mesoscale models. Part I: submodel description and preliminary applications. *Journal of the Atmospheric Sciences* 60, 34–56. [http://dx.doi.org/10.1175/1520-0469\(2003\)060<034:ASCPFM>2.0.CO;2](http://dx.doi.org/10.1175/1520-0469(2003)060<034:ASCPFM>2.0.CO;2).
- Deng, A., Gaudet, B.J., Dudhia, J., Alapaty, K., 2014. Implementation and evaluation of a new shallow convection scheme in WRF. In: 26th Conf. on Wea. Analysis and Forecast./22nd Conf. on Numer. Wea. Pred., Atlanta, GA, p. 13. Preprint available at: <https://ams.confex.com/ams/94Annual/webprogram/Paper236925.html>.
- Ebert, E.E., 2001. Ability of a poor man's ensemble to predict the probability and distribution of precipitation. *Monthly Weather Review* 129, 2461–2480. [http://dx.doi.org/10.1175/1520-0493\(2001\)129<2461:AOAPMS>2.0.CO;2](http://dx.doi.org/10.1175/1520-0493(2001)129<2461:AOAPMS>2.0.CO;2).
- Evensen, G., 1994. Sequential data assimilation with a nonlinear quasi-geostrophic model using Monte Carlo methods to forecast error statistics. *Journal of Geophysical Research Oceans* 99, 10143–10162. <http://dx.doi.org/10.1029/94JC00572>.
- Giebel, G., Kariniotakis, G., 2007. Best practice in short-term forecasting – a users guide. In: European Wind Energy Conference and Exhibition, Milan, Italy, May 7–10, 2007. Available online at: <http://powwow.risoe.dk/publ.htm>.
- Giebel, G., Meibom, P., Pinson, P., Kariniotakis, G., 2007. Towards smart integration of wind generation. In: Cutululis, N., Sørensen, P. (Eds.), Nordic Wind Power Conf. - NWPC'2007: Power System Integration and Electrical Systems of Wind Turbines and Wind Farms, Nov 2007. Roskilde, Denmark RISO, p. 7. ISBN 978-87-550-3640-6. Available online at: <https://hal.archives-ouvertes.fr/hal-00822869/>.
- Glahn, H.R., Lowry, D.A., 1972. The use of Model Output Statistics (MOS) in objective weather forecasting. *Journal of Applied Meteorology* 11, 1203–1211. [http://dx.doi.org/10.1175/1520-0450\(1972\)011<1203:TUOMOS>2.0.CO;2](http://dx.doi.org/10.1175/1520-0450(1972)011<1203:TUOMOS>2.0.CO;2).
- Gochis, D.J., Yu, W., Yates, D.N., 2015. The WRF-Hydro Model Technical Description and User's Guide, Version 3.0. NCAR Technical Document. 120 pp. Available online at: [http://www.ral.ucar.edu/projects/wrf\\_hydro](http://www.ral.ucar.edu/projects/wrf_hydro).
- Haupt, S.E., Delle Monache, L., 2014. Understanding ensemble prediction: how probabilistic wind power prediction can help in optimizing operations. *WindTech* 10 (6), 27–29.
- Haupt, S.E., Kosović, B., 2015. Big data and machine learning for applied weather forecasts: forecasting solar power for utility operations. In: IEEE Symp. Series on Comp. Intell., Cape Town, South Africa, December 9, 2015. <http://dx.doi.org/10.1109/SSCI.2015.79>.
- Haupt, S.E., Kosović, B., 2017. Variable generation power forecasting as a Big Data problem. *IEEE Transactions on Sustainable Energy*. <http://dx.doi.org/10.1109/TSTE.2016.2604679> (in press).
- Haupt, S.E., Mahoney, W.P., 2015. Taming wind power with better forecasts. *IEEE Spectrum* 52, 47–52. <http://dx.doi.org/10.1109/MSPEC.2015/7335902>.
- Hoke, J.E., Anthes, R.A., 1976. The initialization of numerical models by a dynamic-initialization technique. *Monthly Weather Review* 104, 1551–1556. [http://dx.doi.org/10.1175/1520-0493\(1976\)104<1551:TIONMB>2.0.CO;2](http://dx.doi.org/10.1175/1520-0493(1976)104<1551:TIONMB>2.0.CO;2).
- Holton, J.R., 2004. An Introduction to Dynamic Meteorology, fourth ed. Elsevier Academic Press. 535 pp.

- Jiménez, P.A., Navarro, J., Palomares, A.M., Dudhia, J., 2015. Mesoscale modeling of offshore wind turbine wakes at the wind farm resolving scale: a composited-based analysis with the Weather Research and Forecasting model over Horns Rev. *Wind Energy* 18, 559–566. <http://dx.doi.org/10.1002/we.1708>.
- Jiménez, P.A., Hacker, J.P., Dudhia, J., Haupt, S.E., Ruiz-Arias, J.A., Gueymard, C.A., Thompson, G., Eidhammer, T., Deng, A., 2016a. WRF-Solar: description and clear-sky assessment of an augmented NWP model for solar power prediction. *Bulletin of the American Meteorological Society* 97, 1249–1264. <http://dx.doi.org/10.1175/BAMS-D-14-00279.1>.
- Jiménez, P.A., Alessandrini, S., Haupt, S.E., Deng, A., Kosović, B., Lee, J.A., Delle Monache, L., 2016b. The role of unresolved clouds on short-range global horizontal irradiance predictability. *Monthly Weather Review* 144, 3099–3107. <http://dx.doi.org/10.1175/MWR-D-16-0104.1>.
- Kalman, R.E., 1960. A new approach to linear filtering and prediction problems. *J. Basic Eng.* 82, 35–45. <http://dx.doi.org/10.1115/1.3662552>.
- Kalman, R.E., Bucy, R.S., 1961. New results in linear filtering and prediction theory. *J. Basic Eng.* 83, 95–108. <http://dx.doi.org/10.1115/1.3658902>.
- Kalnay, E., 2003. Atmospheric Modeling, Data Assimilation, and Predictability. Cambridge University Press, New York, 341 pp.
- Klinker, E., Rabier, F., Kelly, G., Mahfouf, J.-F., 2000. The ECMWF operational implementation of four-dimensional variational assimilation. III: Experimental results and diagnostics with operational configuration. *Quarterly Journal of the Royal Meteorological Society* 126, 1191–1215. <http://dx.doi.org/10.1002/qj.49712656417>.
- Kolczynski, W.C., Stauffer, D.R., Haupt, S.E., Altman, N.S., Deng, A., 2011. Investigation of ensemble variance as a measure of true forecast variance. *Monthly Weather Review* 139, 3954–3963. <http://dx.doi.org/10.1175/MWR-D-10-05081.1>.
- Kuznetsova, A., Troitskaya, Y., Kandaurov, A., Baydakov, G., Vdovin, M., Papko, V., Sergeev, D., 2015. Wind waves modeling on the water body with coupled WRF and WAVEWATCH III models. In: European Geosciences Union General Assembly 2015, Vienna, Austria, April 12–17, 2015. Abstract available at: <http://meetingorganizer.copernicus.org/EGU2015/EGU2015-497.pdf>.
- Lee, J.A., Kolczynski, W.C., McCandless, T.C., Haupt, S.E., 2012. Objective techniques for configuring and down-selecting an NWP ensemble for low-level wind predictions. *Monthly Weather Review* 140, 2270–2286. <http://dx.doi.org/10.1175/MWR-D-11-00065.1>.
- Lee, J.A., Haupt, S.E., Young, G.S., 2016. Down-selecting numerical weather prediction multi-physics ensembles with hierarchical cluster analysis. *Journal of Climatology & Weather Forecasting* 4, 1000156. <http://dx.doi.org/10.4172/2332-2594.1000156>.
- Lei, L., Stauffer, D.R., Deng, A., 2012. A hybrid nudging-ensemble Kalman filter approach to data assimilation in WRF/DART. *Quarterly Journal of the Royal Meteorological Society* 138, 2066–2078. <http://dx.doi.org/10.1002/qj.1939>.
- Liu, Y., et al., 2008. The operational mesogamma-scale analysis and forecast system of the U.S. army test and evaluation command. Part I: overview of the modeling system, the forecast products, and how the products are used. *Journal of Applied Meteorology and Climatology* 47, 1077–1092. <http://dx.doi.org/10.1175/2007JAMC1653.1>.
- Lorenc, A.C., Bowler, N.E., Clayton, A.M., Pring, S.R., Fairbairn, D., 2015. Comparison of hybrid-4DEnVar and hybrid-4DVar data assimilation methods for global NWP. *Monthly Weather Review* 143, 212–229. <http://dx.doi.org/10.1175/MWR-D-14-00195.1>.
- Lorenz, E.N., 1963. Deterministic nonperiodic flow. *Journal of the Atmospheric Sciences* 20, 130–141. [http://dx.doi.org/10.1175/1520-0469\(1963\)020<0130:DNF>2.0CO;2](http://dx.doi.org/10.1175/1520-0469(1963)020<0130:DNF>2.0CO;2).

- Lynch, P., 2006. The Emergence on Numerical Weather Prediction: Richardson's Dream. Cambridge University Press, 290 pp.
- Mahoney, W.P., O'Sullivan, J.M., 2013. Realizing the potential of vehicle-based observations. Bulletin of the American Meteorological Society 94, 1007–1018. <http://dx.doi.org/10.1175/BAMS-D-12-00044.1>.
- Mahoney, W.P., Parks, K., Wiener, G., Liu, Y., Myers, B., Sun, J., Delle Monache, L., Johnson, D., Hopson, T., Haupt, S.E., 2012. A wind power forecasting system to optimize grid integration. IEEE Transactions on Sustainable Energy 3, 670–682. <http://dx.doi.org/10.1109/TSTE.2012.2201758>.
- Marquez, R., Coimbra, C.F.M., 2011. Forecasting of global and direct solar irradiance using stochastic learning methods, ground experiments and the NWS database. Solar Energy 85, 746–756. <http://dx.doi.org/10.1016/j.solener.2011.01.007>.
- Mass, C.F., Madaus, L.E., 2014. Surface pressure observations from smartphones: a potential revolution for high-resolution weather prediction? Bulletin of the American Meteorological Society 95, 1343–1349. <http://dx.doi.org/10.1175/BAMS-D-13-00188.1>.
- Maxwell, R.M., Lundquist, J.K., Mirocha, J.D., Smith, S.G., Woodward, C.S., Thompson, A.F.B., 2011. Development of a coupled groundwater–atmosphere model. Monthly Weather Review 139, 96–116. <http://dx.doi.org/10.1175/2010MWR3392.1>.
- McCandless, T.C., Haupt, S.E., Young, G.S., 2016a. A regime-dependent artificial neural network technique for short-range solar irradiance forecasting. Applied Energy 89, 351–359. <http://dx.doi.org/10.1016/j.apenergy.2015.12.030>.
- McCandless, T.C., Young, G.S., Haupt, S.E., M Hinkelmann, L., 2016b. Regime-dependent short-range solar irradiance forecasting. Journal of Applied Meteorology and Climatology 55, 1599–1613. <http://dx.doi.org/10.1175/JAMC-D-15-0354.1>.
- Molteni, F., Palmer, T.M., 1993. Predictability and finite time instability of the northern winter circulation. Quarterly Journal of the Royal Meteorological Society 119, 269–298. <http://dx.doi.org/10.1002/qj.49711951004>.
- Monin, A.S., Obukhov, A.M., 1954. Basic laws of turbulent mixing in the surface layer of the atmosphere. Trudy Akademii Nauk SSSR Geofizicheskogo Instituta 24, 163–187. English translation available online at: [http://mcnaughty.com/keith/papers/Monin\\_and\\_Obukhov\\_1954.pdf](http://mcnaughty.com/keith/papers/Monin_and_Obukhov_1954.pdf).
- Monteiro, C., Bessa, R., Miranda, V., Botterud, A., Wang, J., Conzelmann, G., 2009. Wind Power Forecasting: State-of-the-Art 2009. Argonne National Laboratory, Argonne, IL. ANL/DIS-10-1. Available online at: <http://www.ipd.anl.gov/anlpubs/2009/11/65613.pdf>.
- Muller, M., 1995. Equation of time – problem in astronomy. Acta Physica Polonica A 88 (Suppl.), 549–567. Available online at: <http://www.ifpan.edu.pl/firststep/aw-works/fsII/mul/mueller.html>.
- Myers, W., Linden, S., 2011. A turbine hub height wind speed consensus forecasting system. In: AMS 9th Conf. on Artificial Intelligence and Its Applications to the Environmental Sciences, Seattle, WA, January 23–27, 2011. Preprint available online at: <https://ams.confex.com/ams/91Annual/webprogram/Paper187355.html>.
- Myers, W., Wiener, G., Linden, S., Haupt, S.E., 2011. A consensus forecasting approach for improved turbine hub height wind speed predictions. In: AWEA Windpower 2011 Conf. & Exhib., Anaheim, CA, May 22–25, 2011.
- Orwig, K.D., Ahlstrom, M., Banunarayanan, V., Sharp, J., Wilczak, J.M., Freedman, J., Haupt, S.E., Cline, J., Bartholomy, O., Hamman, H., Hodge, B.-M., Finley, C., Nakafuji, D., Peterson, J., Maggio, D., Marquis, M., 2014. Recent trends in variable generation forecasting and its value to the power system. IEEE Transactions on Sustainable Energy 6, 924–933. <http://dx.doi.org/10.1109/TSTE.2014.2366118>.

- Pan, Y., Zhu, K., Xue, M., Wang, X., Hu, M., Benjamin, S.G., Weygandt, S.S., Whitaker, J.S., 2014. A GSI-based coupled EnSRF-En3DVar hybrid data assimilation system for the operational rapid refresh model: tests at a reduced resolution. *Monthly Weather Review* 142, 3756–3780. <http://dx.doi.org/10.1175/MWR-D-13-00242.1>.
- Pelland, S., Remund, J., Kleissl, J., Oozeki, T., De Brabandere, K., 2013. Photovoltaic and Solar Forecasting: State of the Art. IEA PVPS Task 14, Subtask 3.1 Report IEA-PVPS T14-01: 2013. Available online at: <http://iea-pvps.org/index.php?id=278>.
- Raftery, A.E., Gneiting, T., Balabdaoui, F., Polakowski, M., 2005. Using Bayesian model averaging to calibrate forecast ensembles. *Monthly Weather Review* 133, 1155–1174. <http://dx.doi.org/10.1175/MWR2906.1>.
- Richardson, L.F., 1922. Weather Prediction by Numerical Process. Cambridge University Press, 262 pp.
- Ruiz-Arias, J.A., Alsamanra, H., Tovar-Pescador, J., Pozo-Vazquez, D., 2010. Proposal of a regressive model for the hourly diffuse solar radiation under all sky conditions. *Energy Conversion and Management* 51, 881–893. <http://dx.doi.org/10.1016/j.enconman.2009.11.024>.
- Ruiz-Arias, J.A., Dudhia, J., Guemard, C.A., 2014. A simple parameterization of the shortwave aerosol optical properties for surface direct and diffuse irradiances assessment in a numerical weather model. *Geoscientific Model Development* 7, 1159–1174. <http://dx.doi.org/10.5194/gmd-7-1159-2014>.
- Schwartz, C.S., Romine, G.S., Sobash, R.A., Fossell, K.R., Weisman, M.L., 2015. NCAR's experimental real-time convection-allowing ensemble prediction system. *Weather and Forecasting* 30, 1645–1654. <http://dx.doi.org/10.1175/WAF-D-15-0103.1>.
- Sharma, N., Sharma, P., Irwin, D., Shenoy, P., 2011. Predicting solar generation from weather forecasts using machine learning. In: Proceedings of the 2nd IEEE International Conference on Smart Grid Communications, Brussels, October 17–20, pp. 32–37.
- Skamarock, W.C., Klemp, J.B., Dudhia, J., Gill, D.O., Barker, D.M., Duda, M.G., Huang, X.-Y., Wang, W., Powers, J.G., 2008. A Description of the Advanced Research WRF Version 3. NCAR Tech. Note NCAR/TN-475+STR. 113 pp. <http://dx.doi.org/10.5065/D68S4MVH>.
- Skamarock, W.C., Park, S.-H., Klemp, J.B., Snyder, C., 2014. Atmospheric kinetic energy spectra from global high-resolution nonhydrostatic simulations. *Journal of the Atmospheric Sciences* 71, 4369–4381. <http://dx.doi.org/10.1175/JAS-D-14-0114.1>.
- Stauffer, D.R., Seaman, N.L., 1990. Use of four-dimensional data assimilation in a limited-area mesoscale model. Part I: experiments with synoptic-scale data. *Monthly Weather Review* 118, 1250–1277. [http://dx.doi.org/10.1175/1520-0493\(1990\)118<1250:UOFD-DA>2.0.CO;2](http://dx.doi.org/10.1175/1520-0493(1990)118<1250:UOFD-DA>2.0.CO;2).
- Stauffer, D.R., Seaman, N.L., 1994. Multiscale four-dimensional data assimilation. *Journal of Applied Meteorology* 33, 416–434. [http://dx.doi.org/10.1175/1520-0450\(1994\)033<0416:MFDDA>2.0.CO;2](http://dx.doi.org/10.1175/1520-0450(1994)033<0416:MFDDA>2.0.CO;2).
- St. Martin, C.M.S., Lundquist, J.K., Handschy, M.A., 2015. Variability of interconnected wind plants: correlation length and its dependence on variability time scale. *Environmental Research Letters* 10, 044004. <http://dx.doi.org/10.1088/1748-9326/10/4/044004>.
- Stensrud, D.J., 2007. Parameterizations: Keys to Understanding Numerical Weather Prediction Models. Cambridge University Press, 478 pp.
- Sullivan, P.P., McWilliams, J.C., Patton, E.G., 2014. Large-eddy simulation of marine atmospheric boundary layers above a spectrum of moving waves. *Journal of the Atmospheric Sciences* 71, 4001–4027. <http://dx.doi.org/10.1175/JAS-D-14-0095.1>.
- Talagrand, O., 1997. Assimilation of observations, an introduction. *Journal of the Meteorological Society of Japan* 75, 191–209. Available online at: [https://www.jstage.jst.go.jp/article/jmsj1965/75/1B/75\\_1B\\_191/\\_article](https://www.jstage.jst.go.jp/article/jmsj1965/75/1B/75_1B_191/_article).

- Thompson, G., Eidhammer, T., 2014. A study of aerosol impacts on clouds and precipitation development in a large winter cyclone. *Journal of the Atmospheric Sciences* 71, 3636–3658. <http://dx.doi.org/10.1175/JAS-D-13-0305.1>.
- Tuohy, A., Zack, J., Haupt, S., Sharp, J., Ahlstrom, M., Dise, S., Grimit, E., Möhlren, C., Lange, M., Garcia Casado, M., Black, J., Marquis, M., Collier, C., 2015. Solar forecasting: methods, challenges, and performance. *IEEE Power and Energy Magazine* 13, 50–59. <http://dx.doi.org/10.1109/MPE.2015.2461351>.
- Wallace, J.M., Hobbs, P.V., 2006. *Atmospheric Science: An Introductory Survey*, second ed. Elsevier Academic Press. 483 pp.
- Wang, X., Barker, D.M., Snyder, C., Hamill, T.M., 2008. A hybrid ETKF-3DVAR data assimilation scheme for the WRF model. Part II: real observation experiments. *Monthly Weather Review* 136, 5132–5147. <http://dx.doi.org/10.1175/2008MWR2445.1>.
- Warner, T.T., 2011a. *Numerical Weather and Climate Prediction*. Cambridge University Press, 526 pp.
- Warner, T.T., 2011b. Quality assurance in atmospheric modeling. *Bulletin of the American Meteorological Society* 92, 1601–1610. <http://dx.doi.org/10.1175/BAMS-D-11-00054.1>.
- Wilczak, J., et al., 2015. The Wind Forecast Improvement Project (WFIP): a public–private partnership addressing wind energy forecast needs. *Bulletin of the American Meteorological Society* 96, 1699–1718. <http://dx.doi.org/10.1175/BAMS-D-14-00107.1>.
- Wilks, D.S., Hamill, T.M., 2007. Comparison of ensemble-MOS methods using GFS reforecasts. *Monthly Weather Review* 135, 2379–2390. <http://dx.doi.org/10.1175/MWR3402.1>.
- Woodcock, J.S., Engel, A.F., 2005. Operational consensus forecasts. *Weather and Forecasting* 20, 101–110. <http://dx.doi.org/10.1175/WAF-831.1>.
- Wyngaard, J.C., 2004. Toward numerical modeling in the “Terra Incognita.” *Journal of the Atmospheric Sciences* 61, 1816–1826. [http://dx.doi.org/10.1175/1520-0469\(2004\)061<1816:TNMITT>2.0.CO;2](http://dx.doi.org/10.1175/1520-0469(2004)061<1816:TNMITT>2.0.CO;2).
- Xie, Y., Sengupta, M., Dudhia, J., 2016. A Fast All-sky Radiation Model for Solar applications (FARMS): algorithm and performance evaluation. *Solar Energy* 135, 435–445. <http://dx.doi.org/10.1016/j.solener.2016.06.003>.
- Yang, S.-C., Corazza, M., Carrassi, A., Kalnay, E., Miyoshi, T., 2009. Comparison of local ensemble transform Kalman filter, 3DVAR, and 4DVAR in a quasigeostrophic model. *Monthly Weather Review* 137, 693–709. <http://dx.doi.org/10.1175/2009MWR2396.1>.
- Zhang, F., Zhang, M., Poterjoy, J., 2013. E3DVar: coupling an ensemble Kalman filter with three-dimensional variational data assimilation in a limited-area weather prediction model and comparison to E4DVar. *Monthly Weather Review* 141, 900–917. <http://dx.doi.org/10.1175/MWR-D-12-00075.1>.

## Further reading

- Wyngaard, J.C., 2010. *Turbulence in the Atmosphere*. Cambridge University Press, Cambridge, 393 pp.

# Measurement methodologies for wind energy based on ground-level remote sensing

2

Sven-Erik Gryning<sup>1</sup>, Torben Mikkelsen<sup>1</sup>, Christophe Baehr<sup>2</sup>, Alain Dabas<sup>2</sup>,  
Paula Gómez<sup>1</sup>, Ewan O'Connor<sup>3</sup>, Lucie Rottner<sup>2</sup>, Mikael Sjöholm<sup>1</sup>, Irene Suomi<sup>3</sup>,  
Nikola Vasiljević<sup>1</sup>

<sup>1</sup>Technical University of Denmark, Roskilde, Denmark; <sup>2</sup>CNRM, Toulouse, France; <sup>3</sup>Finnish Meteorological Institute, Helsinki, Finland

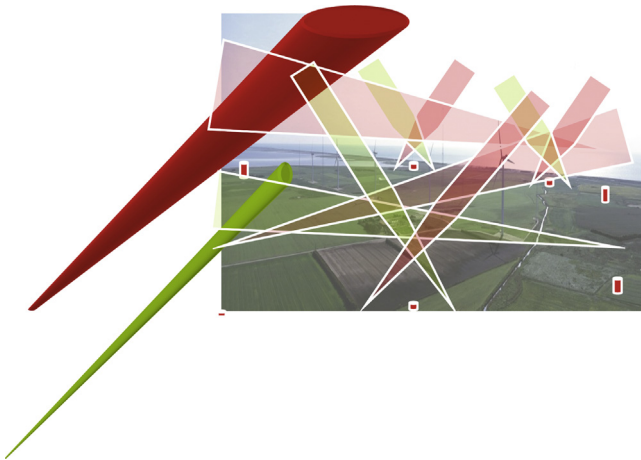
## 2.1 Introduction

Traditionally, wind measurements in connection with research and development for wind energy are obtained from meteorological masts. Meteorological masts (met masts), however, only measure the wind at a few discrete points of a vertical profile, typically in front of the wind turbines. Because current wind turbines are very tall (a Vestas V164 turbine tip height reaches 225 m above the ground) and tall met masts are expensive and not easy to move, detailed measurements of the entire atmospheric wind field surrounding the huge turbines are difficult if not impossible to acquire; on the other hand such measurements are of utmost importance for improving wind turbine performance and control. Experimental acquisitions of detailed three-dimensional (3D) wind field data over the entire rotor plane and within the turbine wakes enable research, testing, and characterization of individual wind turbines and of the entire wind farm performance.



Wind measurement using classical cup anemometry installed in tall immobile meteorological masts at Høvsøre test site for tall wind turbines - DTU Wind Energy.

Wind light detection and ranging (lidars), in the form of ground-based remote sensing wind measurement devices are, in contrast to met masts, easy deployable and mobile. When equipped with steerable scan heads, synchronized sets of simultaneously scanning lidars can measure the entire 3D wind velocity field at high-temporal and spatial resolution, providing for instance user-selected scan planes in front of or in the wakes of operating wind turbines. Today's 3D wind velocity scanning capability now provides researchers and wind engineers with detailed new 3D wind field experimental data and hence fundamental insight into wind and turbulence for the wind research community.



Three-dimensional (3D) wind field measurements from ground-based scanning wind light detection and ranging (lidars) - WindScanners.

### 2.1.1 *Historical background*

Lidars for meteorological applications emerged in the early 1960s shortly after the invention of the red ruby laser. Wind lidars based on the so-called coherent detection principle of Doppler-shifted frequency in backscattered radiation were one of the first applications of the emerging laser technology. The technology used in lidars has since expanded vastly in capability. Today, lidar-based remote sensing devices perform a wide range of measurements that include measuring winds, studying aerosols, profiling clouds, and quantifying a number of atmospheric components. Similar to a radar, the amount of light backscattered provides range-resolved information about the atmospheric content such as cloud density and aerosol concentrations. Determination of the wind speed based on the Doppler-shifted backscattered radiation, however, requires a precise detection of the Doppler shift in frequency by mixing the transmitted and backscattered radiation. Lidars measure the wind component of the instant velocity vector in the lidar sounding volume, projected along the laser line-of-sight (LOS) transmitted beam direction, by determining the small difference in frequency between the transmitted and the backscattered light. One of the first applications of a Doppler lidar system was in connection with the 2008 Summer Olympics in Beijing to measure wind fields during the sailing regatta.

Doppler lidar systems are now beginning to be successfully applied in the renewable energy sector to acquire meteorological quantities such as wind speed, wind veer, wind shear, and atmospheric turbulence. Both pulsed and continuous-wave systems are being used. Pulsed systems use time-of-flight to obtain distance resolution, whereas continuous-wave systems control their measurement range by changing the focus of the laser radiation to provide high intensity at the selected point of measurement.

Originally lidars were large heavy instruments, but owing to the use of components developed for use in optical fiber communication, lidars have improved in compactness, reliability, and ease of use. The development of eye-safe fiber-based lidars started in the mid-1990s and the first commercial available products became available about 15 years later.

The basic measuring principles for coherent fiber-based scanning wind lidars will be described in this chapter together with a number of examples on their use with an emphasis on renewable energy production.

## 2.1.2 *Measuring principles for a heterodyne wind lidar*

Remote sensing of several properties in the atmosphere can be achieved by using various laser-based techniques as, e.g., described in [Svanberg \(2004\)](#). For instance, range-resolved optical remote sensing can be achieved by lidar techniques that have been an active and expanding research area since the 1960s as reflected, among others, by the International Laser Radar Conference since 1968. The expansion of the coherent techniques over the years has been manifested by the introduction in 1980 of the additional Coherent Laser Radar Conference. Today, lidar systems are compact, robust, and easy to operate to a degree that they now have found acceptance for industrial use. In [Fig. 2.1](#) it is illustrated how today's commercially available human-sized wind lidars are in operation for wind energy applications.



**Figure 2.1** Two commercially available human-sized wind lidar profilers (first-generation ZephIR) deployed for wind energy applications at DTU Wind Energy test site for large wind turbines Høvsøre, Denmark, 2007.

This section focuses on lidars able to monitor the motion of the atmosphere by detecting the small Doppler shift in the frequency of the laser light scattered by the moving atmosphere. For most Doppler wind lidars currently realized, atmospheric aerosols are responsible for the scattering. However at ultraviolet wavelengths the scattering is dominated by molecular scattering which gives detectable signals even in very clean aerosol-free air. Regarding the detection scheme, it can either be built upon an incoherent direct detection principle or a coherent detection scheme can be used. The direct detection principle typically relies on a sharp frequency selective optical attenuation filter such as a Fabry-Pérot etalon or an absorption line of a gaseous substance (She et al., 2007).

The coherent detection is obtained by mixing the Doppler-shifted backscattered light optically with a reference fraction of the transmitted light such that the detector current,  $i(t)$  is proportional to the optical power detected, which is given by the square of the superimposed electrical fields of the backscattered light,

$$i(t) \propto (E_{Ref} \cos(\omega_{Ref}t) + E_{Sig} \cos(\omega_{Sig}t))^2, \quad (2.1)$$

where  $E_{Sig}$  and  $E_{Ref}$  are the amplitudes of the electrical fields of the backscattered light and the reference light, respectively,  $\omega_{Sig}$  and  $\omega_{Ref}$  are the corresponding angular frequencies of the light fields and  $t$  is the time. After expansion of the expression and low-pass filtering, there results a constant term and an oscillating term at the difference frequency between the two beating waves,

$$i(t) \propto E_{Ref}^2 + E_{Sig}^2 + 2E_{Ref}E_{Sig} \cos((\omega_{Ref} - \omega_{Sig})t). \quad (2.2)$$

The low-pass filtered detector signal is then Fourier transformed such that there results a power spectrum of difference frequency signals, corresponding to the Doppler frequency shifts depending on the frequency of the light,  $f_0$ , and the ratio between the speed of the atmosphere,  $v$ , and the speed of the light,  $c$ , by  $\Delta f = 2f_0v/c = 2v/\lambda_0$ . Applying the ratio between the atmospheric speed and the Doppler frequency,  $v/\Delta f = \lambda_0/2$ , to the often used wavelength,  $\lambda_0$ , of 1.55  $\mu\text{m}$  in the telecommunications near-IR band where optical components are readily available (Karlsson et al., 2000), a ratio of 0.775  $\text{m s}^{-1}/\text{MHz}$  is obtained. This means that the Doppler shifts for typical atmospheric speeds are easy to detect since they fall in the megahertz frequency region where data acquisition and real-time fast digital signal processing technology is mature and readily available.

A coherent wind lidar detects the Doppler shift of the projection of the wind velocity vector along the pointing direction of the laser beam. In the simplest implementation the direction of the speed, i.e., toward the lidar or away from the lidar is not resolved. However, by shifting the reference signal by the use of an acousto-optic modulator (i.e., a Bragg cell), the frequency corresponding to zero velocity can be shifted away from zero frequency such that the sign of the Doppler shift can be detected which for instance is of importance for studies of flows close to wind turbines (Simley et al., 2016). An alternative approach is to split up the signal, delay one of the replicas followed by an in-phase/quadrature-phase detection scheme (IQ detection), which nowadays can be implemented using readily available components (Abari et al., 2014; Pedersen et al., 2014; Simley et al., 2016).

### 2.1.3 Wind lidar calibration

One of the requirements for wind lidars, to be accepted as stand-alone instruments in wind resource assessment, is the need for a traceable calibration. A calibration, accredited (acc. [ISO/IEC 17025, 2005](#)) by the pertaining national standardization body, provides traceability of the measurements of a specific lidar instrument and associated measurement uncertainties, to international standards.

In metrology, the term “calibration” is defined in [JCGM 200 \(2012\)](#). In the context of wind lidars, a calibration is a comparison between measurements; one of known magnitude, and associated uncertainty, made with one instrument (usually, a cup anemometer) and another measurement made in as similar a way as possible with a second device (a wind lidar). Thus, a calibration generates a transfer function relating an input, such as an independently measured wind speed, to an output number, e.g., wind speed in meter per second, and associated uncertainties. A calibration is normally expressed by a calibration function or a table.

The most popular wind lidar types have reached production numbers exceeding several hundred units, and their use is not only restricted to wind resource assessments, but extend also to other fields of wind energy research, such as wind turbine testing. In particular, a method to perform lidar calibrations has recently been proposed in Annex L of [IEC 61400-12-1 Edition 2 FDIS \(June 2016\)](#).

A typical measurement campaign setup for the calibration of horizontal wind speeds at different heights for a ground-based wind lidar would be to deploy and operate the lidar close to a meteorological mast at a flat terrain site. The reference met mast is instrumented with cup anemometers at several heights, covering as high a proportion as possible of the range of heights the lidar will be configured to operate during its intended use (i.e., a wind resource assessment campaign). The cup anemometers must beforehand be calibrated in accredited wind tunnels and installed following guidelines on best practices for mounting of anemometers on meteorological masts (usually, [IEC 61400-12-1 Edition 1, December 2005](#), Annex G). Other sensors are normally present on the meteorological mast (e.g., wind vanes and temperature sensors), with the primary purpose of providing atmospheric filtering criteria to select appropriate data sets with respect to atmospheric stability, turbulence, etc., for the wind speed calibration. These sensors may serve in some cases to produce additional calibration results (e.g., for wind direction measurements). To obtain a meaningful calibration, the lidar is set up to measure at the same heights where there are cup anemometers on the meteorological mast; and the lidar is installed (regarding distance and orientation) so that it is as close as possible to the mast in an attempt to maximize the correlation between lidar and cup anemometer, while also screening any wakes impinging on the laser scanning volume from the mast itself, or other obstacles at the site.

A series of filters is applied, for each individual height, to obtain a calibration data set. First, a filter based on wind direction is applied, to exclude data where either the lidar probe volume or the reference cup anemometer is in the wake of a met mast or other obstacles. Next, filters are applied to discard data where the cup anemometer may not be functioning correctly (e.g., a temperature filter, to remove periods of data where the anemometer may be affected by icing). Additionally, only data sets

where the cup anemometer wind speeds is between  $4 \text{ m s}^{-1}$  and  $16 \text{ m s}^{-1}$  are selected, since this is the range of a standard cup anemometer wind tunnel calibration. Finally, filters based on lidar quality parameters are applied, to discard periods where the lidar is not functioning correctly, or where the measured 10-min wind speed averages are not representative. These filters are dependent on the particular lidar technology, but would usually consist of an internal “availability” or “quality” parameter [e.g., how many samples, in a 10-min period, have exceeded a lidar manufacturer predefined carrier-to-noise ratio (CNR) detection threshold] or the average number, in a 10-min period, of LOS trajectories used for the horizontal wind speed reconstruction.

Once a statistically significant data set is obtained, in terms of total amount of data and distribution of data along the wind speed range  $4\text{--}16 \text{ m s}^{-1}$ , the data (cup wind speed, lidar wind speed, and difference between lidar and cup wind speed) are binned into wind speed bins of width  $0.5 \text{ m s}^{-1}$ , an example is shown in Fig. 2.2. The calibration results may be presented as a table, which should also include the calibration uncertainty in each bin. This uncertainty, essentially, accounts for the uncertainty of the reference instrument (cup anemometer) and the uncertainty of the obtained transfer function. The cup anemometer uncertainty is obtained as the combination of the following uncertainty components: cup calibration uncertainty (which accounts for wind tunnel uncertainties, including the spread of calibration results between different wind tunnels); operational uncertainty (which is determined from the maximum errors associated to a particular cup operational class, corresponding to a defined set of turbulence intensity levels and inflow angle conditions, among others); and mounting uncertainty (which is determined by the mast geometry and solidity, and boom dimensions). As explained by Courtney (2015), the dominating term in the lidar calibration uncertainty budget is the uncertainty of the reference cup anemometer. Since the cup anemometer uncertainties mainly account for systematic errors that are not corrected for, but are instead included as uncertainties, investigations are ongoing to better

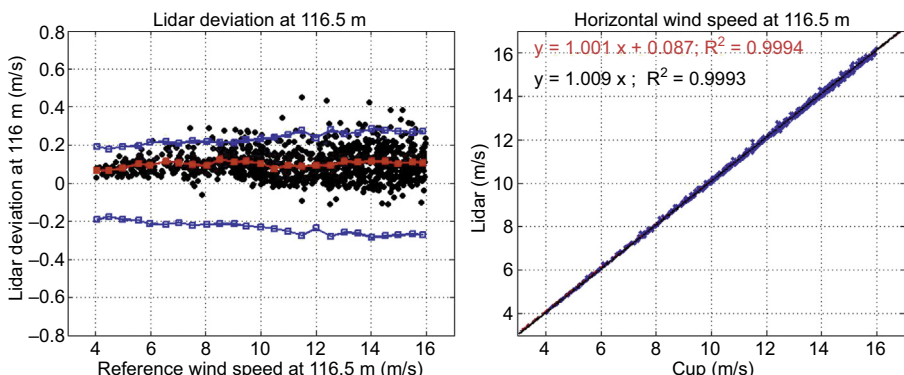


**Figure 2.2** Example of lidar calibration results. Left: deviation (lidar minus reference) versus reference wind speed. Each *black dot* represents a 10-min value; the *red dots* are the wind speed bin averages and the *blue squares* show the calibration uncertainty. The lines result from linear interpolation. Right: 1-parametric regression between the 10-min mean wind speed measurements from the lidar and the cup anemometer (with and without zero offset).

correct for these systematic effects. The result of this ongoing research could potentially lead to significant lower cup anemometer uncertainties and consequently lower lidar calibration uncertainties.

Finally, even though the calibration is a key factor for the use of wind lidars in wind resource assessment, it is not the only one. The first requirement, for a calibration result to be applicable to a specific lidar in a wind resource assessment campaign, is to follow best practices regarding installation, maintenance, and monitoring during the campaign ([IEA Wind, January 2013](#)). Additionally, documentation on the sensitivity of a given lidar type to specific site conditions (e.g., wind shear, turbulence; [Courtney et al., 2014](#)) should be available, since the lidar is usually deployed at a different site from where the calibration took place. Such sensitivities could, in principle, be derived from a classification test, which would aim at identifying the influential environmental conditions and quantify their effect on lidar measurements. A description for remote sensing classification tests is proposed in Annex L of the draft [IEC 61400-12-1 Edition 2 FDIS \(June 2016\)](#). However, the accuracy of this method is limited by the high degree of correlation between some environmental variables, as well as the difficulty in removing the effect of environmental variables (such as temperature and turbulence) on the reference instruments used in the classification (e.g., cup anemometers). Lastly, the long-term stability of lidar measurements should be documented, since wind resource assessment measurement campaigns usually have significantly longer durations (e.g., 1 year) than calibration campaigns (e.g., 2 months); and it is therefore necessary to know if a given lidar calibration is maintained over the longer period. [Courtney and Nygaard \(2014\)](#) reported several wind lidars which presented no evidence of calibration degradation (by means of comparing a precalibration and a postcalibration) after 2 years of field operation.

## **2.1.4 Climatological use of Doppler wind lidar measurements**

Long-term tall wind profile measurements were measured, analyzed, and reported by [Gryning et al. \(2016\)](#), including 9- to 11-month-long wind profile measurement campaigns in the atmospheric boundary layer (ABL) at a suburban (Hamburg) and a marine site in the North Sea (FINO3). The measurements consisted of combined tall met mast and wind lidar measurements obtained with a WLS70 lidar supplied by the French company Leosphere. Some of the experiences obtained from these campaigns are reported later. Wind lidar data quality can be quantified in terms of the lidar CNR, or signal-to-noise ratio (SNR), which are indicative of the strength of the back-scattered radiation carrying the Doppler signal per measurement relative to the inherent unavoidable noise level of the detection chain ([Fujii and Fukuchi, 2005; Cariou, 2013](#)). In [Gryning et al. \(2016\)](#) the consequences of filtering the data with a certain CNR value are discussed. When the signal strength is very weak, velocity estimates are distorted by noise and thus subject to estimation errors. The CNR depends not only on the characteristics of the specific wind lidar but also on the size and concentration of atmospheric particles that are responsible for the backscattered signal level. Lidars deployed at sites with clean air and thus low concentrations of aerosols are therefore retrieving wind data from power spectra measurements with generally lower CNR

value. According to Aitkin et al. (2012) the four most significant atmospheric factors influencing the wind lidar performance are aerosol backscatter, atmospheric refractive turbulence, relative humidity, and precipitation. For a pulsed wind lidar, such as the WLS70, the CNR is proportional to the aerosol cross-sectional area and at the longest measurement distances inversely proportional to the square of the measurement range. As a consequence the wind data availability decreases with measurement range when using a constant CNR value to filter the measurements.

Although the lidar in the study of Gryning et al. (2016) often measured to altitudes of 1 km above the surface, the wind lidar profiles were analyzed only up to 600 m to ensure a sufficiently large quality assured data set for the analysis. A complete, full profile was retrieved every time the CNR of concurrent measurements at all levels from 100 to 600 m was above a given threshold value.

Fig. 2.3 (left panel) uses an example from the marine site in the North Sea (FINO3) to illustrate the sensitivity of the mean wind speed as function of the CNR threshold value. It can be seen that the selection of a high CNR threshold favors higher mean wind speeds throughout the layer. Fig. 2.3 (right panel) shows the mean wind speed at 100-m height as a function of the CNR value for two sites with very different surface characteristics, the suburban site in Hamburg and the marine site in the North Sea (FINO3), respectively. It can be seen from Fig. 2.3 that the choice of CNR threshold has a significant consequence for the mean measured wind speed. When the wind lidar CNR is lower than a prescribed threshold value, the observations are not used as often because the uncertainty in the wind speed measurements increases. For the WLS70 wind lidar, selecting only measurements with a high value of the CNR implies that

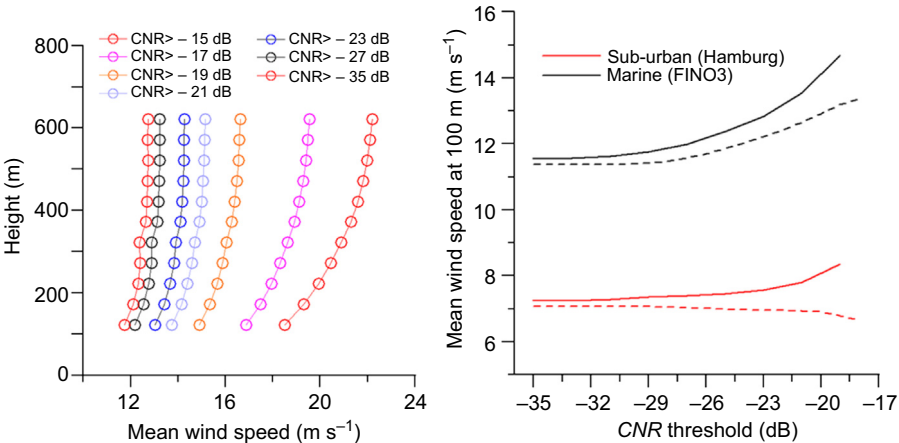


**Figure 2.3** The left panel shows the wind profile at a marine site in the North Sea (FINO3); circles represent observations by the wind lidar for a range of carrier-to-noise ratio (CNR) threshold values. The right panel illustrates the mean wind speed at 100 m as function of the CNR threshold value. The full lines are derived by filtering the wind lidar measurements with the same CNR threshold value imposed to all levels from 100 to 600 m. The *dashed lines* are derived by filtering the wind lidar measurements with the CNR threshold value only at 100 m.

predominantly high-speed measurements are favored. Using  $-22$  dB as a lower limit for the CNR as suggested by [Frehlich \(1996\)](#) results in an  $\approx 7\%$  overestimation of the long-term mean wind speed at  $100$  m at the suburban site, and an  $\approx 12\%$  overestimation at the marine site compared to the minimum internal threshold of  $-35$  dB set by the standard configuration of the wind lidar for recording measurements.

When the CNR of the wind lidar measurements at  $100$  m was used for data filtering, and not imposed to the full profile up to  $600$  m, the relationship between the CNR and the wind speed is illustrated by the dashed lines in [Fig. 2.3](#) (right panel). Use of a CNR threshold value of  $-22$  dB in these cases results in an overestimation of the long-term wind speed of  $\approx 9\%$  in the marine environment and a small overestimation at the suburban site.

[Gryning et al. \(2016\)](#) noticed that the quality of the wind speed measurements, when expressed in terms of CNR, is generally higher in an environment influenced by wind-induced sea spray combined with the fact that humid conditions allow hydroscopic aerosol growth. The nominal backscattered signal is an increasing function of both particle size and aerosol concentration. This is an important aspect for the use of lidars offshore. The best measuring conditions in the study of [Gryning et al. \(2016\)](#) were either during onshore winds, where wave breaking caused by the shallow seabed and coastline acted as an additional source of particles, or at the marine sites. The atmospheric particle cross-sectional area over land was generally the lowest at the sites investigated, as shown by the onshore-reduced CNR levels.

In conclusion, the selection of a CNR threshold should be done cautiously and with careful consideration to the characteristics of the individual wind lidars when creating wind speed climatologies.

## 2.1.5 **Turbulence estimated from wind lidar measurements**

Atmospheric turbulence impacts wind energy in several ways, specifically through power performance effects, impacts on turbine loads, fatigue and wake effects, and noise propagation. Considerable efforts have been made to estimate atmospheric turbulence from wind lidar measurements but all methods have advantages and drawbacks. Here three methods are reviewed and their ability to estimate turbulence is discussed; (1) estimates based on the time and volume-filtered horizontal wind speed, (2) Monte-Carlo techniques to restore the turbulence field, and (3) turbulence estimated from a stanning (vertical wind speed) lidar. Closely connected and equally important for wind energy are identifying gust levels in the atmosphere; the potential ability to derive gusts from lidar measurements are also considered.

### 2.1.5.1 **Filtering of the signal and its consequence for the estimation of turbulence**

Measurements from a lidar do by nature not originate from a single measurement point but rather from a volume, which means that turbulent fluctuations occurring at length scales on the order of magnitude of the sampling volume and less are affected by the spatial averaging of the lidar. The LOS component of the wind field provided

by the lidar in a measurement location at a distance  $r$  away from the lidar along the laser beam defined by the unit vector  $\mathbf{n}$  is given by,

$$v_{\text{LOS}}(r) = \int_{-\infty}^{+\infty} \varphi(s) \mathbf{n} \cdot \mathbf{u}(sn + r) ds, \quad (2.3)$$

where the projection of the 3D wind velocity field  $\mathbf{u}$  weighted by a range weighting profile  $\varphi(s)$  is integrated along the beam. The profile  $\varphi(s)$  is defined such that its line integral is unity, i.e.,  $\int_{-\infty}^{+\infty} \varphi(s) ds = 1$ . The effect of filtering the turbulence power spectra, i.e., the spectral transfer function  $H$ , can be obtained as the square of the Fourier transform of the range weighting profile (Sjöholm et al., 2009).

For a pulsed lidar, the range weighting function is given by the convolution between the laser pulse profile and the range gate profile. The laser pulse profile is often Gaussian with a width  $\sigma$  and if the range gate is a top-hat window of length  $L$ , the spectral transfer function expressed for spatial wave numbers,  $k$ , will be based on the product of their Fourier transforms, i.e.,

$$H_p = \text{sinc}^2\left(\frac{kL}{2}\right) \exp(-\sigma^2 k^2) \approx \exp\left(-l_p^2 k^2\right), \quad (2.4)$$

where the approximate expression has been achieved by using an expansion of the sinc function as described in detail in Kristensen et al. (2011) using the effective length scale  $l_p = \sqrt{\frac{L^2}{12} + \sigma^2}$ , which typically does not depend on the measurement distance.

The range-dependent sounding profile of a Doppler wind lidar, whether continuous or pulsed, is proportional to the laser beam radiation intensity ( $\text{Watt m}^{-2}$ ). For continuous-wave lidars, the range setting is obtained by focusing the transmitted laser radiation to its highest intensity at the measurement point and therefore the wind measurement depth or confinement about the measurement point behaves in a similar way to the depth of field of an imaging camera. The sampling profile is, to a first approximation, given by a Lorentzian function (Sjöholm et al., 2009) and consequently the spectral transfer function  $H$  of a continuous-wave lidar becomes an exponential function

$$H_{cw} = \exp(-l_{cw}k), \quad (2.5)$$

where  $l_{cw}$  is the full width at half maximum of the sounding profile given by  $l_{cw} = \frac{2\lambda r^2}{\pi a_0^2}$ , and where  $r$  is the measurement distance,  $\lambda$  the wavelength of the laser light, and  $a_0$  the radius ( $e^{-2}$ ) of the transmitted lidar beam, limited by the lidar lens size. This means that the effective probe length for a continuous-wave lidar increases quadratically with the measurement distance and thus more of the small-scale turbulence in the measurement signals are attenuated when measuring further away. As seen in the expression for  $l_{cw}$  the sounding profile effective probe length can be reduced by using larger optics in the lidar.

During the last three decades, various approaches with the aim of measuring unfiltered turbulence statistics from wind lidar measurements with a larger sounding volume than cup anemometers have been performed. Most of the processing algorithms developed rely on combining an isotropic turbulence model with the raw unfiltered lidar measurements to obtain the unfiltered turbulence statistics. A detailed treatment of these algorithms is outside the scope of this chapter and the reader is directed to the detailed review of turbulence measurements using ground-based wind lidars ([Sathe and Mann, 2013](#)).

### ***2.1.5.2 A numerical turbulence reconstruction method from Doppler lidar measurements***

Doppler lidars can provide precise mean wind profile measurements within the lower portion of the ABL. However, there are some well-known limitations when using a lidar to estimate turbulence ([Sathe and Mann, 2013](#)). Besides the inherent remote sensing-based instrument limitations, the estimation of turbulence relies on assumptions of stationary and ergodicity to compute wind velocity variances during sampling periods ranging from 10 to 30 min. To overcome these limitations, a Monte-Carlo method for turbulence estimation from wind lidar measurements has been developed by Baehr and Rottner ([Baehr, 2010; Rottner and Baehr, 2016](#)). Contrary to usual techniques for turbulence estimation, the method retrieves turbulence estimates at high sampling frequencies, typically 0.1 Hz. The estimation method uses a nonlinear filter to reconstruct the 3D wind and to estimate turbulence in real time. The method is based on a fluid particle motion approximation to the wind probability density function. The estimation algorithm consists of two main steps: first, a temporal evolution of the particle system where the particle evolution is given by the stochastic Lagrangian model suggested by [Baehr \(2010\)](#); then, the latest available wind observations are used to update the system. Particle velocities are compared to the observations, and particles are selected according to their likelihood. The wind and its spatial variability can in this way be described by the fluid particle distribution. As the estimation method uses a filter, observation errors are filtered with, for instance, spikes in the wind time series being removed. The power spectral densities of the reconstructed wind fit the Kolmogorov laws for turbulence ([Kolmogorov, 1941](#)).

The estimation method has been applied to 3D wind observations from 5-beam wind lidars (data from WindCube V2 provided by Leosphere have been used). The beams describe a conical volume, which is filled with numerical particles ([Fig. 2.4](#), left panel). Each particle carries information about the surrounding atmosphere. Under the assumption of a large number of particles, the method provides assessment of the local characteristics of the wind inside the volume filled by the observations. The particles complete the lidar observations by representing the spatial variability of the observed fluid. In this sense, it is a space-filling observation method. As an example, a comparison between a real-time turbulent kinetic energy level (TKE) from 0.25 Hz lidar sampling and TKE computed from the fluid particle model sampled during a 10-min sampling period is shown on the right panel of [Fig. 2.4](#).

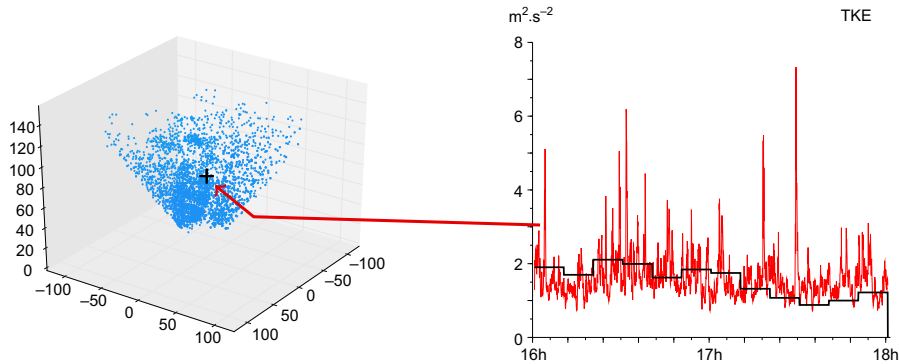


**Figure 2.4** On the left, the observed conical volume filled by numerical particles. On the right, real-time turbulent kinetic energy (TKE) estimates computed from the particles over 4 s (red) compared to the lidar-based TKE estimate computed over 10 min (black).

In addition to real-time turbulence estimates, the fluid particle method also improves the lidar turbulence intensity estimate. As lidars cover the lower ABL, they are powerful instruments for measuring turbulent intensities (TIs) at wind farm sites and at many vertical levels. The standard practice to measure TI for wind energy is based on cup anemometer variance measurements. Compared to cup anemometers, lidars can retrieve vertical profiles of turbulence without using a meteorological mast. However, lidar TI and cup anemometer TI are usually significantly different (Peña et al., 2009; Westerhellweg et al., 2010). These differences pose a strong limitation on the use of ground-based lidars for TI estimation. To evaluate the ability of the TI estimation method, the reconstructed wind field method has also been used to compute a lidar-based TI estimate. This TI estimate has then been compared to the 5-beam lidar TI and to cup anemometer TI, in Fig. 2.5, which compares the different TI averaged by wind speed classes for 7 days of observations. The TI obtained from raw lidar data is significantly higher than the cup anemometer TI, but the reconstructed TI has the right order over a large range of wind speed classes.

The turbulence estimation methodology can also be used for wind gust measurements. Recent comparisons between lidar and sonic anemometer observations have shown that the method improves wind gusts measurements.

### 2.1.5.3 *Turbulent properties from a vertically pointing Doppler lidar*

Vertically pointing Doppler lidars can provide high-temporal resolved vertical wind speed measurements required for deriving turbulent properties in the lower part of the ABL. There are a number of methods for assessing the dissipation rate of TKE from Doppler lidars: Doppler spectral width (Smalikho et al., 2005), temporal spectra or structure function methods (Davies et al., 2004; Smalikho et al., 2005), conical scanning (Banakh et al., 1999; Vakkari et al., 2015), and dual-Doppler lidar (Davies et al., 2005).

In the following a method is presented for estimation of the dissipation rate from unattended continuously operating Doppler lidars based on measured variances from

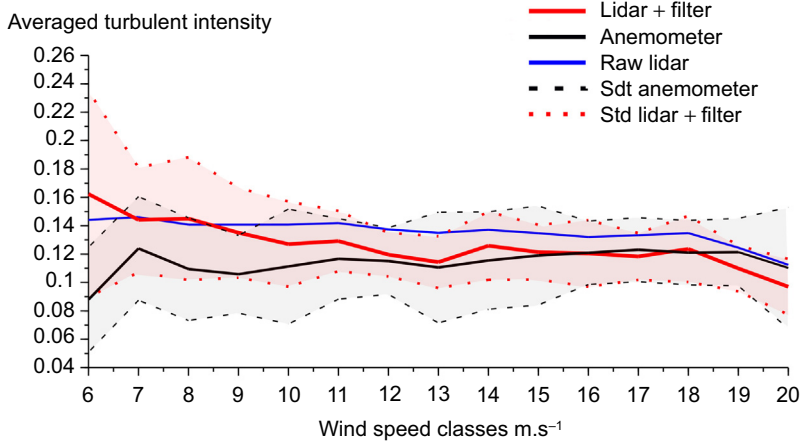


**Figure 2.5** Averaged turbulent intensity by wind speed class: raw lidar turbulent intensity (blue), cup anemometer turbulent intensity (black), and estimated turbulent intensity (red). The associated standard deviations are given by the *dashed lines*.

a number of sequential samples in conjunction with profile measurements of the horizontal wind speed.

The Kolmogorov hypothesis (1941) states that for homogeneous and isotropic turbulence within the inertial subrange, the turbulent energy spectrum  $S(k)$  is given by

$$S(k) = a\epsilon^{2/3}k^{-5/3}, \quad (2.6)$$

where  $a = 0.55$  is the Kolmogorov constant for the one-dimensional isotropic wind component spectra,  $\epsilon$  is the dissipation rate, and  $k$  is the wave number. O'Connor et al. (2005) introduced the parameter  $\sigma_v^2$ , which is the variance of the observed mean Doppler velocity over a number of sequential samples,  $N$ . If there are no other significant contributions then the observed vertical velocity variance  $\sigma_v^2$  corresponds to integrating  $S(k)$  over a specific portion of the spectrum defined by the measurement scales involved:

$$\sigma_v^2 = \int_k^{k_1} S(k) dk, = -\frac{3}{2}a\epsilon^{2/3}\left(k_1^{-2/3} - k^{-2/3}\right), = \frac{3a}{2}\left(\frac{\epsilon}{2\pi}\right)^{2/3}\left(L^{2/3} - L_1^{2/3}\right), \quad (2.7)$$

where wave number is related to a length scale by  $k = 2\pi/L$ . The two length scales are  $L_1$ , the scattering volume for the dwell time of a single sample and  $L$ , the length scale of the large eddies traveling through the lidar beam during the  $N$  sampling intervals. This can be rearranged to calculate  $\epsilon$  directly from  $\sigma_v^2$ ,

$$\epsilon = 2\pi\left(\frac{2}{3a}\right)^{3/2}\sigma_v^3\left(L^{2/3} - L_1^{2/3}\right)^{-3/2}, \quad (2.8)$$

assuming both length scales lie within the inertial subrange. Given the measured horizontal wind,  $U$ , and a dwell time,  $t$ , for an individual velocity sample, the length scale  $L_1$  for an individual sample is  $L_1 = Ut$ , and over  $N$  sampling intervals,  $L = NUt$ . Operating at 3 s per individual sample, and with 10 samples used to calculate  $\sigma_v^2$ , the length scales for a typical wind speed of  $U = 10 \text{ m s}^{-1}$  in the boundary layer are  $L_1 = 30 \text{ m}$  and  $L = 300 \text{ m}$ .

We now consider additional sources that can contribute to the observed velocity variance, such as noise. If the sources of variance are assumed to be independent and have a Gaussian distribution then the observed velocity variance is the sum of the variances from each of the sources (Doviak and Zrnic, 1993; Frehlich et al., 1998):

$$\sigma_v^2 = \sigma_w^2 + \sigma_e^2 + \sigma_d^2, \quad (2.9)$$

where  $\sigma_w^2$  is the turbulent contribution,  $\sigma_e^2$  is the contribution from noise, and  $\sigma_d^2$  is the contribution from the variation in still-air terminal fall speeds of particulates within the measurement volume from one sample to the next. For aerosol particles and liquid cloud droplets, the variance term  $\sigma_d^2$  can be neglected since aerosol particles and liquid cloud droplets have terminal fall speeds  $< 1 \text{ cm s}^{-1}$ . The noise contribution to the variance,  $\sigma_e^2$ , can be reliably estimated from the observed SNR (Pearson et al., 2009; O'Connor et al., 2010) so that the turbulent variance is obtained from the observed variance  $\sigma_w^2 = \sigma_v^2 - \sigma_e^2$ .

Note that precipitating particles (rain and ice) have significant terminal fall speeds with the potential for appreciable variation in particle fall speed from one sample volume to the next. Hence, estimating  $\varepsilon$  in precipitation is more uncertain since the  $\sigma_d^2$  contribution to  $\sigma_v^2$  should also be taken into account.

The relative size of the noise variance to the observed variance provides a measure of the confidence in the retrieval and the fractional uncertainty in  $\varepsilon$  is calculated as

$$\frac{\Delta\varepsilon}{\varepsilon} = \frac{3\Delta\sigma_w}{\sigma_w} + \frac{\Delta L}{L}, \quad (2.10)$$

where the measurement error in a variance is (Lenschow et al., 2000)

$$\Delta\sigma_w^2 \approx \sigma_w^2 \sqrt{\frac{4}{N} \frac{\sigma_e^2}{\sigma_w^2}}. \quad (2.11)$$

[Fig. 2.6](#) displays time–height plots of relevant Doppler lidar parameters from a 24-h period over Helsinki, Finland. The location is urban and coastal. During autumn this location can experience deep land boundary layers or shallow marine boundary layers, depending on the wind direction. On this day, the wind speeds were light ( $< 5 \text{ m s}^{-1}$ ) throughout the lowest 1 km so that a land boundary layer predominates. The early morning atmosphere is very calm before sunrise at 0430 UTC. A turbulent boundary layer begins to grow about an hour after sunrise with cumulus clouds (dark red in [Fig. 2.6](#)) forming on the top of the growing turbulent mixed layer. Surface-driven

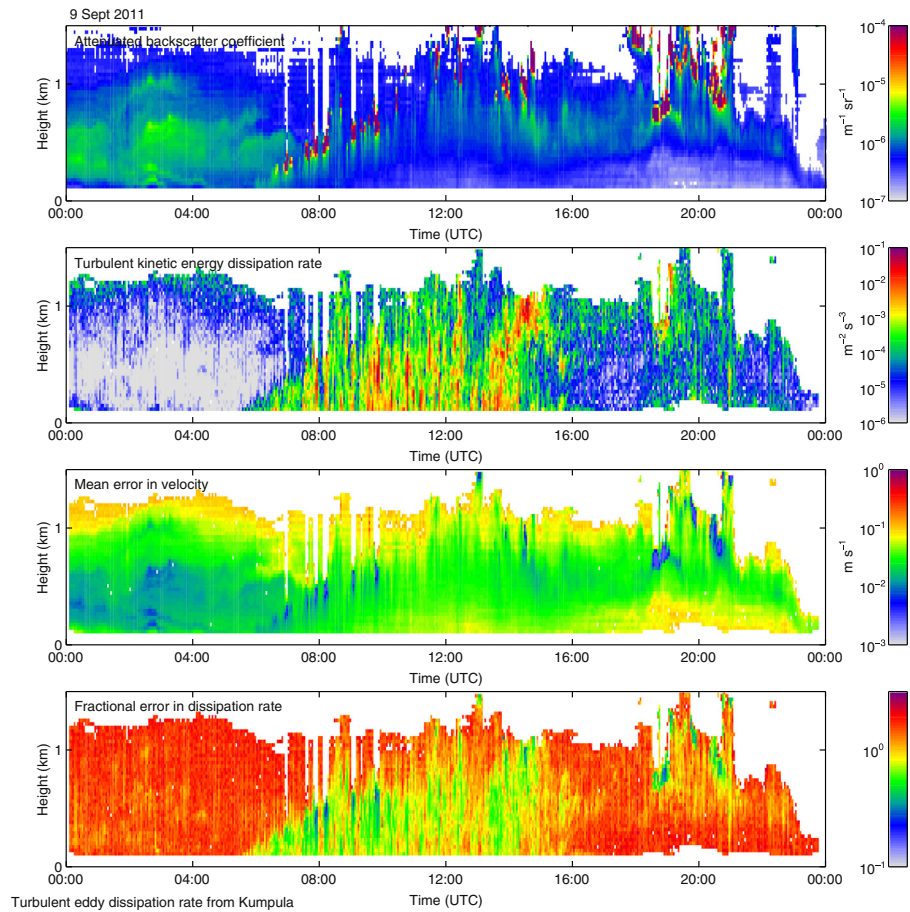


**Figure 2.6** Time–height plots of Doppler lidar parameters from Kumpula, Helsinki, Finland, on September 9, 2011. Local noon is at 1020 UTC. Top panel: attenuated backscatter coefficient. Second panel: derived dissipation rate. Third panel: theoretical uncertainty in observed velocities calculated from the signal-to-noise ratio. Lowest panel: fractional error in dissipation rate.

convection stops well before sunset (1800 UTC) and the turbulence dissipates, but there is still some elevated cloud-driven turbulence present after sunset. The calculated velocity uncertainty is  $<10 \text{ cm s}^{-1}$  throughout most of the lowest 1 km of the atmosphere and can be as low as  $1 \text{ cm s}^{-1}$  for strong signals such as clouds. Note that the fractional uncertainty in  $\varepsilon$  is clearly dependent on both the velocity uncertainty and  $\varepsilon$  itself, so that it is possible to retrieve reliable  $\varepsilon$  estimates in low signal but turbulent conditions. Since values of  $\varepsilon$  range over five orders of magnitude, measurements with fractional uncertainties of the order of one are still capable of providing useful information.

This method is most suitable for retrieval of dissipation rates within the convective well-mixed boundary layer where the scales of motion that the Doppler lidar probes

remain well within the inertial subrange. The results have been evaluated with balloon-borne sonic anemometers (O'Connor et al., 2010) and the range of dissipation rates agree well with those measured by Siebert et al. (2005). Caution must be applied when estimating dissipation rates in more quiescent conditions or in certain types of boundary layers where the transition between the inertial subrange and the outer scale may be rather small. Shorter integration times ensure that the length scales probed are always within the inertial subrange; however, this is at the expense of instrument sensitivity, which increases the Doppler velocity uncertainty. In locations with low atmospheric aerosol concentration, longer integration times must be used to improve the instrument sensitivity but there will be situations when the length scales are no longer within the inertial subrange limiting the method to convective boundary layers. This can be tested by examining the velocity spectra to determine the transition length scale (Tonttila et al., 2015).

#### 2.1.5.4 Wind gusts from a lidar

Measurement of wind gusts, which are short duration (seconds) wind speed maxima, has traditionally been limited to the lowest few hundred meters of the atmosphere, which can be reached by weather masts. Doppler lidars can potentially provide information from higher altitudes and thereby fill this knowledge gap. Measuring wind gusts requires wind speed observations at high-temporal resolution. In practice, such measurements have only been available from weather stations and masts where cup and sonic anemometers can be deployed. Due to the high sampling frequency (1 Hz or higher) of these instruments, the measurements cover the whole range of wind speed fluctuations—from a fraction of a second to several minutes—that contribute to wind gusts.

Doppler lidars provide wind speed measurements along each LOS. To measure the 3D wind vector, information from at least three different LOS pointing toward different directions are needed (e.g., Lane et al., 2013). The instrument sensitivity depends on the amount of aerosol present and the velocity measurement uncertainty is directly related to the amount of signal (Pearson et al., 2009). It typically takes several seconds to measure each LOS with sufficient sensitivity and therefore the temporal resolution of the wind measurement is of the order of tens of seconds, which is not sufficient for gusts (e.g., Suomi et al., 2015). Moreover, as the wind speed measurement is based on three different LOSs, it thereby combines information from three different measurement volumes, which can be hundreds of meters apart from each other, depending on the lidar measuring angles. From these reasons, the profile of wind speed maxima will differ from those that would be measured by a very tall weather mast with observations at every Doppler lidar measurement height.

If the aim is to estimate the gusts as measured at the weather mast, some assumptions on the high-frequency changes in the wind speed must be made. The wind speed maximum ( $U_{max}$ ) measured at the weather mast can be expressed in

terms of the mean wind speed ( $U$ ) and a maximum fluctuation from it. The fluctuation can further be estimated using turbulent information, for example, in terms of velocity variances ( $\sigma_u^2$ ,  $\sigma_v^2$ ,  $\sigma_w^2$ ) or as  $\varepsilon$ . At weather stations, it is typically the standard deviation of the along-wind speed that is used, and it is assumed that this is close to the standard deviation of the horizontal wind speed, i.e.,  $\sigma_u \approx \sigma_U$ . We can then write

$$U_{max} = U + g_x \sigma_u \quad (2.12)$$

where  $g_x$  is the peak factor defined as

$$g_x = \frac{U_{max} - U}{\sigma_u}. \quad (2.13)$$

The peak factor can be estimated by a statistical approach (Rice, 1944/1945; Beljaars, 1987; Kristensen et al., 1991; Wicher Schreur and Geertsema, 2008; Suomi et al., 2015) using information on the turbulence spectrum. In practical applications, it is relevant to know gusts with a certain duration, not just the absolute maximum of the time series. Therefore, gusts are usually measured as the maximum of the moving averaged wind speed time series, and the width of the moving average window determines the gust duration  $t_g$ , which is typically 3-s in meteorological applications. In the statistical method, the effect of  $t_g$  on  $g_x$  can be accounted for by filtering the turbulence spectrum.

[Eq. \(2.12\)](#) can be extended to estimate gusts from Doppler lidar measurements. As stated previously, Doppler lidars can determine the mean wind speed and turbulent properties with high, and known, accuracy. [Eq. \(2.12\)](#) can be rewritten as

$$U_{max} = U + g_x \tau_{\sigma,DL} \sigma_{u,DL} \quad (2.14)$$

where the second term on the right hand side includes the peak factor as in [Eq. \(2.12\)](#). The second component is the ratio of the standard deviations of the true turbulence ( $\sigma_u$ ) and of the one measured by the lidar ( $\sigma_{u,DL}$ ), i.e.,  $\tau_{\sigma,DL} = \sigma_u / \sigma_{u,DL}$ , which can be estimated from theoretical considerations (e.g., similar to Suomi et al. (2015), their [Eq. \(2.10\)](#); or by some other method described previously). Then, the only measurements needed to estimate the wind gust speed are the mean wind speed  $U$  and the standard deviation of the along-wind velocity  $\sigma_{u,DL}$ ; we can introduce a measured turbulent parameter in place of  $\sigma_{u,DL}$  such as  $\sigma_w^2$  or  $\varepsilon$  (Section 1.5.3).

Besides using these equations, there are also other possible methods to derive the gusts from lidar measurements. For example, the method by Baehr (2009) and Suzat et al. (2011) can potentially provide a gust estimate. [Fig. 2.7](#) shows the peak factor as a function of gust duration derived from sonic anemometer measurements, directly from the raw lidar measurements and from the reconstructed wind speed. In all cases, the

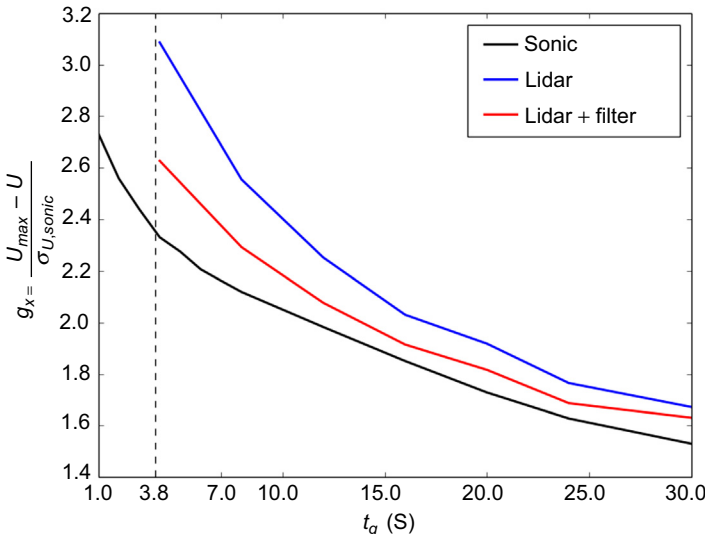


**Figure 2.7** Observed median peak factor relative to the true turbulence ( $\sigma_U$  from the sonic anemometer). Peak factors have been calculated from sonic anemometer (black), from raw lidar measurements (blue), and from reconstructed wind speed (red).

observed median peak factor (Eq. 2.13) is shown relative to the true turbulence, which is here from the sonic anemometer. The results show that maxima from raw Doppler lidar data are clearly higher than those from the sonic anemometer. The maxima from the reconstructed wind speed are closer to the ones from the sonic anemometer, but still slightly overestimated.

So far, we have discussed how to derive the gusts from the lidar similar to those observed at a weather mast. In the beginning of this section, we discussed that the lidar measurements of the 3D wind are based on combination of radial wind speeds from measurement volumes, which can be located far away from each other, while the mast measurements are always pointwise. The largest wind turbines today have a hub height of about 160 m, and their blade diameters typically are greater than 100 m. Therefore, the wind variability in both the horizontal and vertical directions can be important, because the turbulent fluctuations are not always isotropic in space. Large variations occur also on scales of 100 m corresponding to timescales from seconds to a minute (e.g., Suomi et al., 2015). These variations cause uneven load on the blades leading to structural fatigue over time. When these variations can be measured, sophisticated wind turbine operation algorithms could potentially be developed to take these variations into account, and thereby extend the turbine lifetime.

### 2.1.6 Boundary layer depth detection from lidars

The lowest part of the planetary boundary layer is termed the ABL and is the layer in which atmospheric turbulence dominates the mixing. Typically, this layer has a high

concentration of aerosols, most of which have been released from the ground. The layer is capped by an entrainment zone characterized by vigorous turbulence and a positive temperature jump during daytime ([Gryning and Batchvarova, 1994](#)) and a layer of stable air with little turbulence during nighttime. The top of the boundary layer constitutes an upper limit for the mixing ([Seibert et al., 2000](#)). It is therefore characteristic that the boundary layer has a high aerosol concentration with lower concentrations above in the free atmosphere. This phenomenon is used to determine the height of the boundary layer by remote sensing techniques.

During daytime, atmospheric mixing is driven by surface heating by the sun and the wind shear throughout the boundary layer ([Batchvarova and Gryning, 1991](#)). After sunset, the turbulence ceases and a new neutral and stable layer with little turbulence forms over the ground. This layer is much shallower than the daytime boundary layer. However, the temperature jump that was at the top of the daytime boundary layer still exists and prevents the aerosols from penetrating into the free atmosphere. It constitutes a layer of little turbulence but is still loaded with aerosol that was lofted during the day. The layer from the top of the stable layer up to the temperature jump is called the residual layer. In low wind speed conditions a low-level jet often forms at the top of the stable boundary layer.

Knowledge of the height of the boundary layer is essential in many contexts such as air pollution and wind energy where it is an important parameter, e.g., the parameterization of the wind profile ([Gryning et al., 2007](#)). A direct way to measure the boundary layer height does not exist which has led to the suggestion of a large number of proxies for the atmospheric mixing process. These proxies are typically adapted to available instrumentation.

Traditionally, the boundary layer height was estimated from radio-soundings which led to the development for procedures based on temperature profiles, humidity, and Richardson numbers; the latter combines wind speed and temperature profiles ([Seibert et al., 2000](#)).

However, the development of ground-based remote sensing instruments such as lidars lead to investigations on how to replace the traditional radiosonde-based methods for estimation of the boundary layer height. In a remote sensing system the aerosol backscatter and wind speed can be detected as function of height. The aerosol backscatter depends on number concentration, size, and optical properties of the particles in the air. If it is assumed that the particles originate from the surface or from chemical processes in the polluted air inside the boundary layer, the turbulent mixing in the boundary layer will result in a well-mixed layer that is limited upward by a distinct gradient in the particle concentration marking the zone between the top of the boundary layer and the much lower particle concentration in the free atmosphere. This suggests that the boundary layer depth can be estimated from gradients in the backscatter profile. This assumption resulted in the developments of a number of algorithms, the simplest is based on a threshold for the attenuated backscatter ([Harvey et al., 2013](#)), more elaborate methods are based on the gradient of the attenuated backscatter profile ([Endlich et al., 1979](#)). [Steyn et al. \(1999\)](#) took a different approach by fitting a function to the attenuated backscatter profile; this method was used by [Hannesdottir \(2013\)](#) to derive boundary layer depth climatology. An algorithm to detect the jump in the

attenuated backscatter profile has also been derived from wavelet analysis (Davies et al., 2000; Hajj et al., 2006). Although considerable efforts have been devoted, no consensus on a specific recommendation for an algorithm has yet been reached.

An alternative approach is based on wind profile measurements. Wind lidars can measure the vertical wind velocity and therefore offer, in addition to the attenuated backscatter profile, a direct approach for the determination of the depth of the turbulent boundary layer (Gürpinar, 2011). Procedures have been suggested based on measurements of the profiles of the standard deviation of the vertical wind speed  $\sigma_w$ . Somewhat in analogy with the proxies for the backscatter, the depth can be taken as the height where a distinct negative gradient for the  $\sigma_w$  profile (Martucci et al., 2012) or in the second derivative of the  $\sigma_w$  profile (Harvey et al., 2013). A simpler and more objective way is the use of a threshold value for  $\sigma_w$  (Tucker et al., 2009). O'Connor et al. (2010) suggested a quite different approach, which is based on the assumption that the measurements are performed in the inertial subrange of the wind velocity spectrum. Fig. 2.8 shows an example of the detection of boundary layer depth by use of the method suggested by Steyn et al. (1999), and Fig. 2.9 is an example of the boundary layer depth over a period of several days.

Developing approaches to determine the depth of the boundary layer from remote sensing measurements is an area of considerable activity. Currently, the agreement seems to be that the estimation is reliable during daytime when there exists a fully

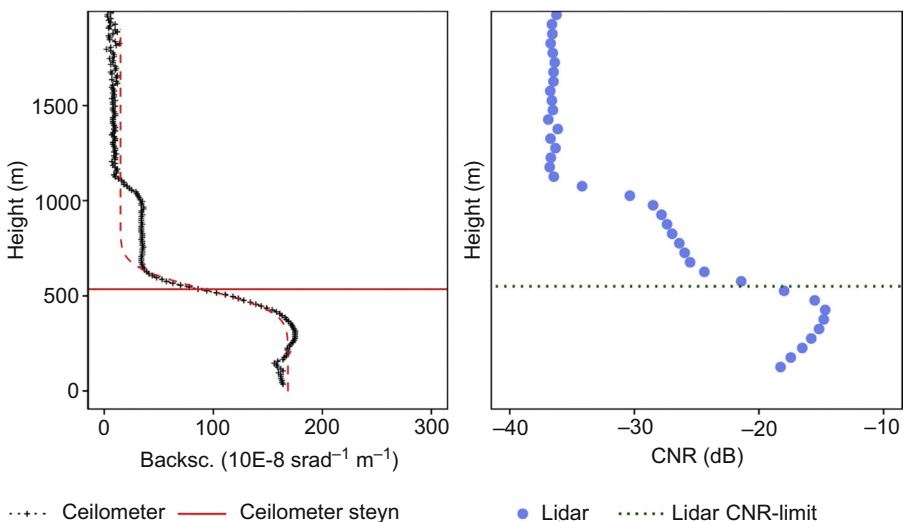


**Figure 2.8** Example of the boundary layer height estimated from attenuated backscatter profiles. The profile in the left panel is measured by a ceilometer and the right panel by a wind lidar. The carrier-to-noise ratio (CNR) is closely connected to attenuated backscatter. In the left panel the dashed red line shows the fitted profile used by the method of Steyn et al. (1999), and the horizontal line illustrates the height of the boundary layer. On the right panel the height of the boundary layer is determined by the threshold method ( $-22$  dB used as threshold) by Harvey et al. (2013). Good agreement can be observed between the two methods.

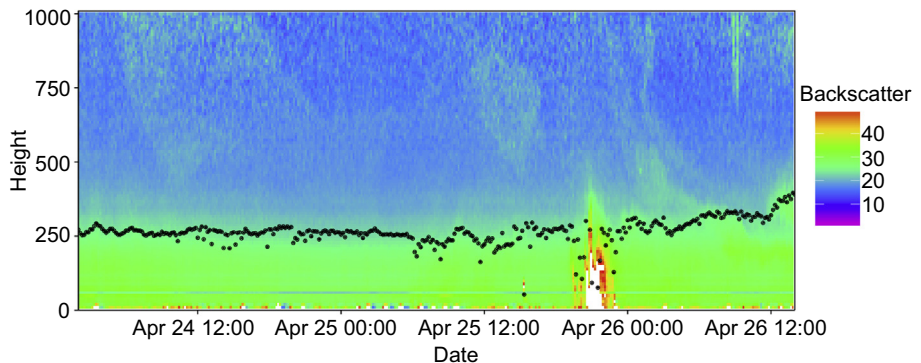


**Figure 2.9** Example of the temporal evolution of the height of the boundary layer, illustrated by the *black circles*. It is estimated by use of the method suggested by Steyn et al. (1999). The measurements of the backscatter are performed by a ceilometer located at Station Nord ( $81.65^{\circ}\text{N}$ ,  $16.65^{\circ}\text{W}$ ) in the High Arctic of Greenland (Batchvarova et al., 2014). The land surface during this part of the year is covered by snow and sun is visible throughout the whole diurnal cycle (24 h), therefore any pronounced diurnal variation is absent. This is in contrast to the characteristic behavior at midlatitudes where the diurnal variation is a characteristic feature of the behavior of the boundary layer.

developed convective boundary layer, which is topped by a distinct jump in the both attenuated backscatter and  $\sigma_w$  profiles. However for operational use, even under such ideal conditions the method can be hampered by low-level clouds where the cloud base can easily mistakenly be taken as the top of the boundary layer. A fully reliable operational method for the determination of the boundary layer depth still remains to be developed.

### 2.1.7 Long-range and short-range WindScanner systems

An inherent property of a single wind lidar is that it only measures the LOS projected wind velocity vector within an elongated measurement volume. To measure two or all three wind components of the wind velocity vector requires at least two or three independent LOS speeds at the measurement point, which is solely possible if two or three Doppler lidars are employed. In the existing body of literature we encounter use of dual-Doppler lidars (McCarthy et al., 1982; Allwine and Flaherty, 2005; Grubisic et al., 2008; Collier et al., 2005) and triple-Doppler wind lidar setups (Mann et al., 2009). What is common for these multilidar applications is that the Doppler lidars were typically owned by different parties and only combined for a short period of time; the lidars were operated individually without a central clock providing synchronization of the lidars. The development of fully time- and space-synchronized multi-lidar instruments commenced with the WindScanner.dk project (Mikkelsen et al., 2008). The outcomes of the WindScanner.dk project are two space-coordinated and time-synchronized triple-Doppler wind lidar instruments: the long-range and short-range WindScanner systems (Mikkelsen, 2014) described in the following sections.

### 2.1.7.1 The long-range WindScanner system

The long-range WindScanner (LRWS) system consists of three spatially separated pulsed coherent Doppler scanning lidars, known as the LRWS, and a remote master computer that coordinates them as illustrated in Fig. 2.10 (Vasiljevic, 2014). Each individual LRWS is built from a vertical profiling pulsed lidar Windcube 200, produced by Leosphere, which has a typical range of about 50–5000 m. The minimum probe length is 25 m and it is constant with range, while the maximum measurement rate, depending on aerosol content, is about 10 Hz. The maximum number of simultaneous LOS velocities acquired at any rate along each LOS is 500. The scanner head, illustrated in the right part of Fig. 2.11, designed by DTU Wind Energy assisted by IPU, a Danish SME, has been added to the lidar to provide full hemispheric, arbitrary,

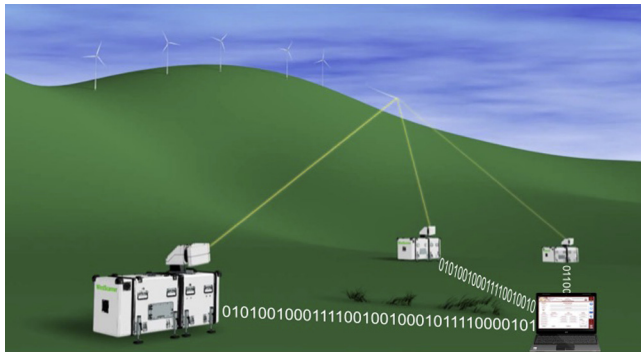


**Figure 2.10** The long-range WindScanner system concept—three lidars coordinated by the master computer.

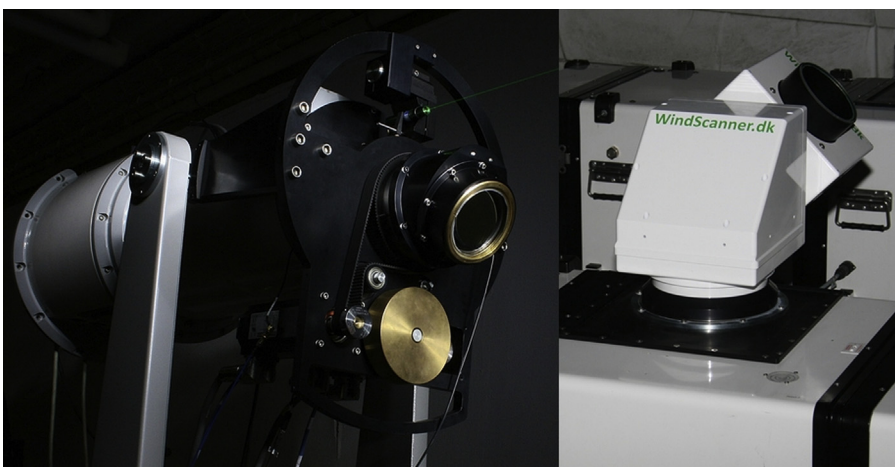


**Figure 2.11** Left: prism-based beam steering for the short-range WindScanners. Right: mirror-based beam steering for the long-range WindScanners.

and time-controlled steering of the laser beam. For the purpose of monitoring the synchronization of the three LRWSs in the WindScanner system, each LRWS is equipped with a GPS-driven clock with 250 ns time stamp accuracy. The LRWSs run DTU Wind Energy's WindScanner Client Software (WCS) that entirely governs the measurement process, while synchronizing the laser pulse emission, laser pulse steering, backscattered light acquisition and analysis.

The master computer represents a regular PC laptop that runs the long-range WindScanner master computer software (LRMCS) for the coordination of an ensemble of LRWSs. The role of the master computer in the LRWS system is to prepare the LRWSs to perform measurement strategies, issue the start of the measurements, monitor the LRWSs activities, and intervene if necessary (e.g., synchronization of LRWSs). The LRWSs take the control over the whole measurement process once the command to start measuring is received. The Doppler spectra are processed in real time, and the retrieved LOS velocity information, with the associated scanner head position and time stamp from the GPS-driven clock, are transferred to LRMCS.

The master computer coordination of the LRWSs is achieved by an exchange of network packets between the LRMCS and the WCS via any type of network interface (Vasiljevic et al., 2013, 2016a). Due to the typical separation of some kilometers between each WindScanner, a preferred choice for the network interface is 3G (Vasiljevic et al., 2016b).

#### 2.1.7.2 *The short-range WindScanner system*

The current implementation of the DTU-developed short-range WindScanner technology is based on continuous-wave wind lidars using coherent detection in the infrared spectral region at around 1.55  $\mu\text{m}$  for remote measurements of the LOS wind velocity. It targets short measurement ranges within 300 m of the lidar with high-spatial (starting from 0.1 m) and temporal (up to 400 Hz) resolution using a focused continuous-wave laser.

The laser beam is oriented by two freely steerable prisms (left side of Fig. 2.11); each prism deviates the focused continuous-wave lidar beam by about 30 degrees, which means that the scanning beam can be directed within a cone with a full opening angle of 120 degrees. The measurement range is determined by adjusting the distance between the optical fiber-end and the focusing lens and is steered by a compact linear motor stage. All the motors involved, i.e., in total nine motors for three wind components, are controlled synchronously by a common programmable multiaxis motion control system operating within an optical fiber ring network, cf. [www.WindScanner.eu](http://www.WindScanner.eu).

The backscattered light containing the coherent beating signal in the megahertz range is typically sampled at least twice the maximum Doppler frequency shift expected, e.g., at 100 M samples per second, and then partitions of, for instance, 512 samples are Fourier transformed to obtain the power Doppler spectra that subsequently are averaged. The first-generation short-range WindScanners were able to provide averaged spectra at a rate of up to about 400 Hz depending on the quality of the signals determined by the aerosol concentration.

Although the mobile short-range WindScanners originally were developed within the Wind Energy Department of the Technical University of Denmark targeting the

wind energy research sector with investigations of wind turbine inflow (Simley et al., 2016) and wakes (Sjöholm et al., 2015) in mind, they have also found applications within studies of aerodynamics around full-scale bridges (Jakobsen et al., 2015), downwash from helicopters (Sjöholm et al., 2014) as well as flow over complex terrain features (Lange et al., 2016). The short-range WindScanners have also proved useful in wind tunnels for measuring the flow field around scaled wind turbine farms and other structures (van Dooren et al., 2016).

## References

- Abari, C.F., Pedersen, A.T., Mann, J., 2014. An all-fiber image-reject homodyne coherent Doppler wind lidar. *Optics Express* 22 (21), 25880–25894.
- Aitkin, M.L., Rhodes, M.E., Lundquist, J.E., 2012. Performance of a wind-profiling lidar in the region of wind turbine rotor disks. *Journal of Atmospheric and Oceanic Technology* 29, 347–355.
- Allwine, K., Flaherty, J., 2005. Joint Urban 2003: Study Overview and Instrument Locations; Number August, 2006.
- Baehr, C., 2009. Stochastic modeling and filtering of discrete measurements for a turbulent field. Application to measurements of atmospheric wind. *International Journal of Modern Physics B* 23 (28–29), 5424–5433.
- Baehr, C., 2010. Nonlinear filtering for observations on a random vector field along a random path. Application to atmospheric turbulent velocities. *ESAIM: Mathematical Modelling and Numerical Analysis* 44 (05), 921–945.
- Banakh, V.A., Smalikho, I.N., Köpp, F., Werner, C., 1999. Measurements of turbulent energy dissipation rate with a CW Doppler lidar in the atmospheric boundary layer. *Journal of Atmospheric and Oceanic Technology* 16, 1044–1061.
- Batchvarova, E., Gryning, S.E., 1991. Applied model for the growth of the daytime mixed layer. *Boundary-Layer Meteorology* 56, 261–274.
- Batchvarova, E., Gryning, S.E., Skov, H., Sørensen, L.L., Hristina, K., Münkel, C., 2014. Boundary-layer and air quality study at “Station Nord” in Greenland. In: Steyn, D., Mahur, R. (Eds.), *Air Pollution Modeling and Its Application XXIII*. Springer Proceedings in Complexity, pp. 525–529. [http://dx.doi.org/10.1007/978-3-319-04379-1\\_86](http://dx.doi.org/10.1007/978-3-319-04379-1_86).
- Beljaars, A.C.M., 1987. The influence of sampling and filtering on measured wind gusts. *Journal of Atmospheric and Oceanic Technology* 4, 613626.
- Cariou, J.P., 2013. Pulsed lidars. In: Peña, A., Hasager, C.B., Lange, J., Anger, J., Badger, M., Bingöl, F., Bischoff, O., Cariou, J.P., Dunne, F., Emeis, S., Harris, M., Hofssäss, M., Karagali, I., Laks, J., Larsen, S., Mann, J., Mikkelsen, T., Pao, L.Y., Pitter, M., Rettenmeier, A., Sathe, A., Scanzani, F., Schlipf, D., Simley, E., Slinger, C., Wagner, R., Würth, I. (Eds.), *Remote Sensing for Wind Energy*, pp. 104–121. DTU Wind Energy-E-Report-0029(EN).
- Collier, C.G., Davies, F., Bozier, K.E., Holt, A.R., Middleton, D.R., Pearson, G.N., Siemen, S., Willetts, D.V., Upton, G.J.G., Young, R.I., 2005. Dual-doppler lidar measurements for improving dispersion models. *Bulletin of the American Meteorological Society* 2005 (86), 825–838.
- Courtney, M., 2015. Lidar calibration — what’s the problem?. In: European Wind Energy Association (EWEA) EWEA Annual Conference and Exhibition 2015, Paris, France, 17/11/2015.

- Courtney, M., Sathe, A., Nygaard, N.G., 2014. Shear and Turbulence Effects on Lidar Measurements. Report DTU Wind Energy E-0061.
- Courtney, M., Nygaard, N.G., 2014. The Long Term Stability of Lidar calibrations. Report DTU Wind Energy E-0033.
- Davies, K., Gamage, N., Hagelberg, C., Kiemle, C., Lenchow, D., Sullivan, P., 2000. An objective method for deriving atmospheric structure from airborne lidar observations. *Journal of Atmospheric and Oceanic Technology* 17, 1455–1468.
- Davies, F., Collier, C.G., Pearson, G.N., Bozier, K.E., 2004. Doppler lidar measurements of turbulent structure function over an urban area. *Journal of Atmospheric and Oceanic Technology* 21, 753–761.
- Davies, F., Collier, C.G., Bozier, K.E., 2005. Errors associated with dual Doppler lidar turbulence measurements. *Journal of Optics A: Pure and Applied Optics* 7, 280–289.
- van Dooren, M.F., Kühn, M., Petrovic, V., Bottasso, C.L., Campagnolo, F., Sjöholm, M., Angelou, N., Mikkelson, T., Croce, A., Zasso, A., 2016. Demonstration of synchronised scanning Lidar measurements of 2D velocity fields in a boundary-layer wind tunnel. *Journal of Physics, Conference Series (Online)* 753, p. 072032. <http://dx.doi.org/10.1088/1742-6596/753/7/072032>.
- Doviak, R.J., Zrnić, D.S., 1993. *Doppler Radar and Weather Observations*, second ed. Academic Press.
- Endlich, R., Ludwig, F., Uthe, E., 1979. An automatic method for determining the mixing depth from lidar observations. *Atmospheric Environment* 13, 1051–1056.
- Frehlich, R., 1996. Simulation of coherent Doppler lidar performance in the weak-signal regime. *Journal of Atmospheric and Oceanic Technology* 13, 646–658.
- Frehlich, R.G., Hannon, S., Henderson, S., 1998. Coherent Doppler lidar measurements of wind field statistics. *Boundary-Layer Meteorology* 86, 233–256.
- Fujii, T., Fukuchi, T., 2005. *Laser Remote Sensing*. Taylor & Francis Group, 912 pp.
- Grubisic, V., Doyle, J.D., Kuettner, J., Mobbs, S., Smith, R.B., Whiteman, C.D., Dirks, R., Czyzyk, S., Cohn, S.A., Vosper, S., Weissmann, M., Haimov, S., De Wekker, S.F.J., Pan, L.L., Chow, F.K., 2008. The terrain-induced rotor experiment. A field campaign overview including observational highlights. *Bulletin of the American Meteorological Society* 89, 1513–1533.
- Gryning, S.E., Batchvarova, E., 1994. Parametrization of the depth of the entrainment zone above the daytime mixed layer. *Quarterly Journal of the Royal Meteorological Society* 120, 47–58.
- Gryning, S.E., Batchvarova, E., Brümmer, B., Jørgensen, H., Larsen, S., 2007. On the extension of the wind profile over homogeneous terrain beyond the surface boundary layer. *Boundary-Layer Meteorology* 124 (2), 251–268.
- Gryning, S.E., Floors, R., Peña, A., Batchvarova, E., Brümmer, B., 2016. Weibull wind-speed distribution parameters derived from a combination of wind-lidar and tall-mast measurements over land, coastal and marine sites. *Boundary-Layer Meteorology* 159, 329–348. <http://dx.doi.org/10.1007/s10546-015-0113-x>.
- Gürpinar, M.A., 2011. Estimating Atmospheric Boundary Layer Height from Vertical Sigma W Profiles and Parameterization of Vertical Variances – by LIDARS at Høvsøre (Denmark). Technical Report EGI-2011-111MSC/EKV:859. KTH School of Industrial Engineering and Management, Stockholm, 85 pp.
- Haij, M., Wauben, W., Klein-Baltink, H., 2006. Determination of the mixing layer height from ceilometer backscatter profiles. In: Slusser Jr., , Schäfer, K., Comcrón, A. (Eds.), *Proceedings of the SPIE*, vol. 6362, p. 63620R.

- Hannesdóttir, A., 2013. Boundary-Layer Height Detection with a Ceilometer at a Coastal Site in Western Denmark (DTU Wind Energy Master thesis M-0039), 76 pp.
- Harvey, N.J., Hogan, R.J., Dacre, H.F., 2013. A method to diagnose boundary-layer type using Doppler lidar. *Quarterly Journal of the Royal Meteorological Society* 139 (676), 1681–1683.
- IEC 61400-12-1 Edition 1, December 2005. Power Performance Measurements of Electricity Producing Wind Turbines.
- IEC 61400-12-1 Edition 2, draft FDIS, June 2016. Power Performance Measurements of Electricity Producing Wind Turbines.
- ISO/IEC 17025, 2005. General Requirements for the Competence of Testing and Calibration Laboratories.
- Jakobsen, J.B., Cheynet, E., Snæbjörnsson, J., Mikkelsen, T., Sjöholm, M., Angelou, N., Hansen, P., Mann, J., Svardal, B., Kumer, V., Reuder, J., 2015. Application of lidars for assessment of wind conditions on a bridge site. In: Proceedings of the 14th International Conference on Wind Engineering. Brazil, Porto Alegre, 21 to 26 June 2015, 10 pp.
- JCGM 200, 2012. International Vocabulary of Metrology – Basic and General Concepts and Associated Terms (VIM), third ed.
- Karlsson, C.J., Olsson, F.A., Letalick, D., Harris, M., 2000. All-fiber multifunction CW 1.55 micron coherent laser radar for range, speed, vibration and wind measurements. *Applied Optics* 39, 3716–3726.
- Kolmogorov, A.N., 1941. Dissipation of energy in locally isotropic turbulence. *Doklady Akademii Nauk SSSR* 32, 16–18.
- Kristensen, L., Casanova, M., Courtney, M.S., Troen, I., 1991. In search of a gust definition. *Boundary-Layer Meteorology* 55, 91–107.
- Kristensen, L., Kirkegaard, P., Mikkelsen, T., 2011. Determining the Velocity Fine Structure by a Laser Anemometer with Fixed Orientation. Risø National Laboratory, Risoe-R. No. 1762(EN) 33 pp.
- Lane, S.E., Barlow, J.F., Wood, C.R., 2013. An assessment of a three-beam Doppler lidar wind profiling method for use in urban areas. *Journal of Wind Engineering and Industrial Aerodynamics* 119, 53–59.
- Lange, J., Mann, J., Angelou, N., Berg, J., Sjöholm, M., Mikkelsen, T., 2016. Variations of the wake height over the Bolund escarpment measured by a scanning lidar. *Boundary-Layer Meteorology* 159 (1), 147–159.
- Lenschow, D.H., Wulfmeyer, V., Senff, C., 2000. Measuring second- through fourth-order moments in noisy data. *Journal of Atmospheric and Oceanic Technology* 17, 1330–1347.
- Mann, J., Cariou, J.P., Courtney, M.S., Parmentier, R., Mikkelsen, T., Wagner, R., Lindelöw, P., Sjöholm, M., Enevoldsen, K., 2009. Comparison of 3D turbulence measurements using three staring wind lidars and a sonic anemometer. *Meteorologische Zeitschrift* 18, 135–140.
- Martucci, G., Chauvigne, A., O'Connor, E.J., Hirsikko, A., Ceburnis, D., Wobrock, W., O'Dowd, C., 2012. Ground-based remote sensing profiling of aerosols, boundary layer and liquid water clouds using synergistic retrievals. In: Proceedings of the 9th International Symposium on Tropospheric Profiling, L'Aquila, Italy, September 2012.
- McCarthy, J., Wilson, J.W., Fujita, T.T., 1982. The joint airport weather studies project. *Bulletin of the American Meteorological Society* 63, 15.
- Mikkelsen, T., 2014. Lidar-based research and innovation at DTU wind energy – a review. *Journal of Physics: Conference Series* 524, 012007.
- Mikkelsen, T., Mann, J., Courtney, M., Sjöholm, M., 2008. Windscanner: 3-D wind and turbulence measurements from three steerable Doppler lidars. *IOP Conference Series: Earth and Environmental Science* 1, U148–U156.

- O'Connor, E.J., Hogan, R.J., Illingworth, S.A.J., 2005. Retrieving stratocumulus drizzle parameters using Doppler radar and lidar. *Journal of Applied Meteorology* 44, 14–27.
- O'Connor, E.J., Illingworth, A.J., Brooks, I.M., Westbrook, C.D., Hogan, R.J., Davies, F., Brooks, B.J., 2010. A method for estimating the turbulent kinetic energy dissipation rate from a vertically pointing Doppler lidar, and independent evaluation from balloon-borne in situ measurements. *Journal of Atmospheric and Oceanic Technology* 27, 1652–1664.
- Pearson, G., Davies, F., Collier, C., 2009. An analysis of the performance of the UFAM pulsed Doppler lidar for observing the boundary layer. *Journal of Atmospheric and Oceanic Technology* 26, 204–250.
- Pedersen, A.T., Abasi, C.F., Mann, J., Mikkelsen, T., 2014. Theoretical and experimental signal-to-noise ratio assessment in a new direction sensing continuous-wave Doppler lidar, The Science of Making Torque from Wind 2014 (TORQUE 2014). *Journal of Physics, Conference Series* 524, p. 012004.
- Peña, A., Hasager, C.B., Gryning, S.E., Courtney, M., Antoniou, I., Mikkelsen, T., 2009. Offshore wind profiling using light detection and ranging measurements. *Wind Energy* 12 (2), 105–124.
- Rice, S.O., 1944/1945. Mathematical analysis of random noise. *Bell System Technical Journal* 23, 282–332, 24, 46–156.
- Rottner, L., Baehr, C., 2016. Real time turbulence estimation using Doppler lidar measurements. In: EPJ Web of Conferences. EDP Sciences, vol. 119, p. 14001.
- Sathe, A., Mann, J., 2013. A review of turbulence measurements using ground-based wind lidars. *Atmospheric Measurement Techniques* 6, 3147–3167.
- Seibert, P., Beyrich, F., Gryning, S.E., Joffre, S., Rasmussen, A., Tercier, P., 2000. Review and intercomparison of operational methods for the determination of the mixing height. *Atmospheric Environment* 34, 1001–1027.
- She, C., Yue, J., Yan, Z., Hair, J., Guo, J., Wu, S., Liu, Z., 2007. Direct-detection Doppler wind measurements with a Cabannes-Mie lidar: a Comparison between iodine vapor filter and Fabry-Perot interferometer methods. *Applied Optics* 46, 4434–4443.
- Siebert, H., Lehmann, K., Wendisch, M., 2005. Observations of small-scale turbulence and energy dissipation rates in the cloudy boundary layer. *Journal of the Atmospheric Sciences* 63, 1451–1466.
- Simley, E., Angelou, N., Mikkelsen, T., Sjöholm, M., Mann, J., Pao, L.Y., 2016. Characterization of wind velocities in the upstream induction zone of a wind turbine using scanning continuous-wave lidars. *Journal of Renewable and Sustainable Energy* 8, 013301.
- Sjöholm, M., Mikkelsen, T., Mann, J., Enevoldsen, K., Courtney, M., 2009. Spatial averaging-effects on turbulence measured by a continuous-wave coherent lidar. *Meteorologische Zeitschrift* 18 (3), 281–287.
- Sjöholm, M., Angelou, N., Hansen, P., Hansen, K.H., Mikkelsen, T., Haga, S., Silgjerd, J.A., Starsmore, N., 2014. Two-dimensional rotorcraft downwash flow field measurements by lidar-based wind scanners with agile beam steering. *Journal of Atmospheric and Oceanic Technology* 31 (4), 930–937.
- Sjöholm, M., Angelou, N., Hansen, K.H., Mikkelsen, T.K., Kluczewska-Bordier, J., Benedetti, P., Immas, A., Parneix, N., Silvert, F., 2015. 3D Measurements and Modelling of Wake Flow Around a Full-Scale Vertical Axis Wind Turbine (Nenuphar); Book of Abstracts – WindTech 2015. WindEEE Research Institute, pp. 71–72.
- Smalikho, I.N., Köpp, F., Rahm, S., 2005. Measurement of atmospheric turbulence by 2-μm Doppler lidar. *Journal of Atmospheric and Oceanic Technology* 22, 1733–1747.

- Steyn, D., Baldi, M., Hoff, R., 1999. The detection of mixed layer depth and entrainment zone thickness from lidar backscatter profiles. *Journal of Atmospheric and Oceanic Technology* 16, 953–959.
- Suomi, I., Gryning, S.-E., Floors, R., Vihma, T., Fortelius, C., 2015. On the vertical structure of wind gusts. *Quarterly Journal of the Royal Meteorological Society* 141, 1658–1670. <http://dx.doi.org/10.1002/qj.2468>.
- Suzat, F., Baehr, C., Dabas, A., 2011. A fast atmospheric turbulent parameters estimation using particle filtering: application to lidar observations. In: *Journal of Physics: Conference Series*, vol. 318. IOP Publishing, p. 072019.
- Svanberg, S., 2004. *Atomic and Molecular Spectroscopy – Basic Aspects and Practical Applications*, fourth ed. Springer, Heidelberg.
- Tonttila, J., O'Connor, E.J., Hellsten, A., Hirsikko, A., O'Dowd, C., Järvinen, H., Räisänen, P., 2015. Turbulent structure and scaling of the inertial subrange in a stratocumulus-topped boundary layer observed by a Doppler lidar. *Atmospheric Chemistry and Physics* 15, 5873–5885.
- Tucker, S.C., Senff, C.J., Weickmann, A.M., Brewer, W.A., Banta, R.M., Sandberg, S.P., Law, D.C., Hardesty, R.M., 2009. Doppler lidar estimation of mixing height using turbulence, shear, and aerosol profiles. *Journal of the Atmospheric Sciences* 26, 673–688.
- Vakkari, V., O'Connor, E.J., Nisantzi, A., Manouri, R.E., Hadjimitsis, G.G., 2015. Low-level mixing height detection in coastal locations with a scanning Doppler lidar. *Atmospheric Measurement Techniques* 8, 1875–1885.
- Vasiljevic, N., 2014. *A Time-Space Synchronization of Coherent Doppler Scanning Lidars for 3D Measurements of Wind Fields* (Ph.D. thesis). DTU Wind Energy. DTU Wind Energy Ph.D., no. 0027(EN).
- Vasiljevic, N., Lea, G., Courtney, M., Schneemann, J., Trabucchi, D., Trujillo, J.J., Unguran, R., Villa, J.P., 2013. The Application Layer Protocol: Remote Sensing Communication Protocol (RSComPro). DTU Wind Energy, Denmark.
- Vasiljević, N., Lea, G., Courtney, M., Cariou, J.-P., Mann, J., Mikkelsen, T., 2016a. Long-range WindScanner system. *Remote Sensing* 8 (11), 896.
- Vasiljevic, N., Lea, G., Hansen, P., Jensen, H., 2016b. Mobile network Architecture of the Long-Range WindScanner System. DTU Wind Energy, 15 pp. (DTU Wind Energy E; No. 0105).
- Westerhellweg, A., Cañadillas, B., Beeken, A., Neumann, T., 2010. One year of lidar measurements at FINO1-platform: comparison and verification to met-mast data. In: *Proceedings of 10th German Wind Energy Conference DEWEK*.
- Wichers Schreur, B., Geertsema, G., 2008. Theory for a TKE-Based Parameterization of Wind Gusts, vol. 54. HIRLAM Newsletter.
- Wind, I.E.A., January 2013. Expert Group Study on Recommended Practices 15. Ground-Based Vertically-Proiling Remote Sensing for Wind Resource Assessment, first ed.

# Wind power forecasting—a review of the state of the art

3

Gregor Giebel<sup>1</sup>, George Kariniotakis<sup>2</sup>

<sup>1</sup>DTU Wind Energy, Roskilde, Denmark; <sup>2</sup>MINES ParisTech, Sophia Antipolis, France

## 3.1 Introduction

This chapter gives an overview over past and present attempts to predict wind power for single turbines, wind farms or for whole regions, for a few minutes up to a few days ahead. It is based on a survey and report (Giebel et al., 2011) initiated in the frame of the European project ANEMOS, which brought together many groups from Europe involved in the field with long experience in short-term forecasting. It was then continued in the frame of the follow-up European projects SafeWind and ANEMOS.plus, which concentrated respectively on the forecasting of extreme events and the best possible integration of the forecasts in the work flow of end users.

Research in wind power forecasting emerged in the late 80's. In sync with the rise of wind power penetration in more and more countries, forecasting has risen from being a fringe topic for a few utilities with high levels of wind power in the grid, to being a central tool to many transmission system operators (TSOs) or power traders in or near areas with considerable levels of wind power penetration. At the same time, the amount of literature has risen dramatically. While the ANEMOS state of the art report was the first large review of short-term prediction literature, a considerable (though not necessarily overlapping) number of reviews have appeared since.

One of the most comprehensive reports to date comes from Argonne National Laboratory (Monteiro et al., 2009). It gives a good introduction to numerical weather predictions (NWP), has a detailed market overview of currently available commercial models, and closes with the integration of wind power forecasts into the unit commitment process, especially in the United States. Ernst et al. (2007) show some recent international use cases and conclude that using a combination of models and forecasting for larger regions and shorter horizons can reduce the average error of the forecasts. Lange and Focken put their emphasis on the developments in Germany in Lange and Focken (2005). Pinson et al. (2007a) gave an overview mainly on probabilistic forecasting, and concluded that the next breakthroughs were due in “models specific to different weather regimes, higher focus on potential use of ensemble forecasts, [and] spatio-temporal aspects of forecast uncertainty.” A review on 30 years of history of the wind power short-term prediction is also given by Costa et al. (2007). They concluded with a list of unsolved or even unexploited topics, among others “further research on the adaptive parameter estimation” and “new approaches on complex terrain (e.g., more accurate—and computationally feasible—turbulence

closure models for microscale tools).” The Canadian Wind Energy Association commissioned a study on international experiences in short-term forecasting ([Snodin, 2006](#)). This work, undertaken by Garrad Hassan (now part of Germanischer Lloyd Group), provides an overview of short-term wind energy forecasting including information about forecast models, their evaluation, forecasting experiences worldwide as well as a detailed summary of forecast providers. Additionally, a whole book devoted to short-term forecasting mainly focusing on the so-called physical approach that has appeared in [Lange and Focken \(2005\)](#), alongside some book chapters by [Ernst \(2005\)](#), [Lange et al. \(2007\)](#), and a chapter in the book by [Fox et al. \(2007\)](#). To the list of overviews also belongs our work on the best practice in the use of short-term forecasting ([Giebel and Kariniotakis, 2008](#)), which is a summary of the workshop series on the same topic ([powwow](#)).

This chapter goes extensively through the publications that appeared in the field from the very beginning. However, in the last years there is a high increase in the number of papers and for this reason only some highlight works are presented.

### **3.1.1 Forecast timescales**

One of the largest challenges of wind power, as compared to conventionally generated electricity, is its dependence on the volatility of the wind. This behavior happens on all time scales, but two of them are most relevant: One is for the turbine control itself (from milliseconds to seconds), and the other one is important for the integration of wind power in the electrical grid, and therefore determined by the time constants in the grid (from minutes to weeks). Turbine control is out of scope of this overview, as it involves mainly advection of a wind field measured a few seconds before it hits the turbine, usually using a lidar in the nose of the turbine, and therefore is qualitatively different from the rest of the approaches mentioned here.

One can distinguish the following types of applications:

- Optimization of the scheduling of conventional power plants by functions such as economic dispatch etc. The prediction horizons can vary between 3 and 10 h depending on the size of the system and the type of conventional units included (i.e., for systems including only fast conventional units, such as diesel gensets or gas turbines, the horizon can be below 3 h). Only a few fully integrated online applications of this type are met today. Typically, these systems are used for smaller or isolated power systems, like island systems, though the optimization for larger systems like Ireland is being evaluated.
- Optimization of the value of the produced electricity in the market and in large power systems. Such predictions are required by different types of end users (utilities, market operators, TSOs, DSOs, ESPs, IPPs, energy traders etc.) and for different functions such as unit commitment, economic dispatch, dynamic security assessment, congestion management, participation in the electricity market, etc. The prediction horizon can go up to 48 h ahead.
- Allocation of reserves based on the expected wind power feed. This aims at system security and is done for instance in Ireland ([Barry, 2006](#)) and Portugal ([Bessa et al., 2012](#)).
- Additionally, even longer time scales would be interesting for the maintenance planning of large power plant components, wind turbines, or transmission lines. However, the accuracy of weather predictions decreases strongly looking at 5–7 days in advance

(Moreno et al., 2003). As Still and Grainger (2001) reported, shorter horizons can also be considered for maintenance, when it is important that the crew can safely return from the offshore turbines in the evening. The north-western German Distribution System Operator EWE (Focken et al., 2009) is integrating wind forecasts into transformer maintenance routines to assess the line loading of the remaining rerouted electricity flows.

### 3.1.2 The typical model chain

In general, the models can be classified as either involving an NWP model or not. Whether the inclusion of an NWP model is worth the effort and expense of getting hold of it depends on the horizon one is trying to predict. Typically, prediction models using NWP forecasts outperform time series approaches after ca 3–6 h look-ahead time. Therefore, all models employed by utilities use this approach.

In most operational and commercial models, a **combination** of physics (atmospheric flow models) and statistics is used, as indeed both approaches can be needed for successful forecasts. In short, the physical models try to use physical considerations as long as possible to reach to the best possible estimate of the local wind speed before using model output statistics (MOS) or different relatively simple statistical techniques to reduce the remaining error. Statistical models in their pure form try to find the relationships between a wealth of explanatory variables including NWP results, and online measured power data, usually employing recursive techniques. Often, black-box models like advanced recursive least squares or artificial neural networks (ANNs) are used. The more successful statistical models actually employ gray-box models, where some knowledge of the wind power properties is used to tune the models to the specific domain. Some of the statistical models can be expressed analytically, some (like ANNs) cannot. The statistical models can be used at any stage of the modeling and more often than not combine various steps into one. The typical model chain for wind power forecasting models is illustrated in Fig. 3.1.

If the model is formulated rather explicitly, as is typical for the physical approach, then the stages are downscaling, conversion to power, and upscaling:

- The wind speed and direction from the relevant NWP level is scaled to the hub height of the turbine. This involves a few steps, first finding the best-performing NWP level (often the wind speed at 10 m a.g.l. or at one of the lowest model or pressure levels). However, recently, weather institutes like ECMWF deliver products like wind speed at 100 m a.g.l., which are well adapted to wind power forecasting applications.

The NWP model results can be obtained for the geographical point of the wind farm or for a grid of surrounding points. In the first case the models could be characterized as “advanced power curve models”, in the second case as a “statistical downscaling” model. LocalPred, for example, uses principal component analysis and artificial intelligence techniques from the surrounding NWP grid points (Pinson et al., 2008a; Frías et al., 2009).

The next step is the so-called **downscaling** procedure.

The physical approach uses a meso- or microscale model for the downscaling. If a mesoscale model is run, the mesoscale model can be run for various cases in a look-up table approach. The same procedure holds for microscale models [including computational fluid dynamics (CFD)]. The difference between the two is mainly the maximum and minimum domain size and resolution attainable. One of the reasons for microscale models with their

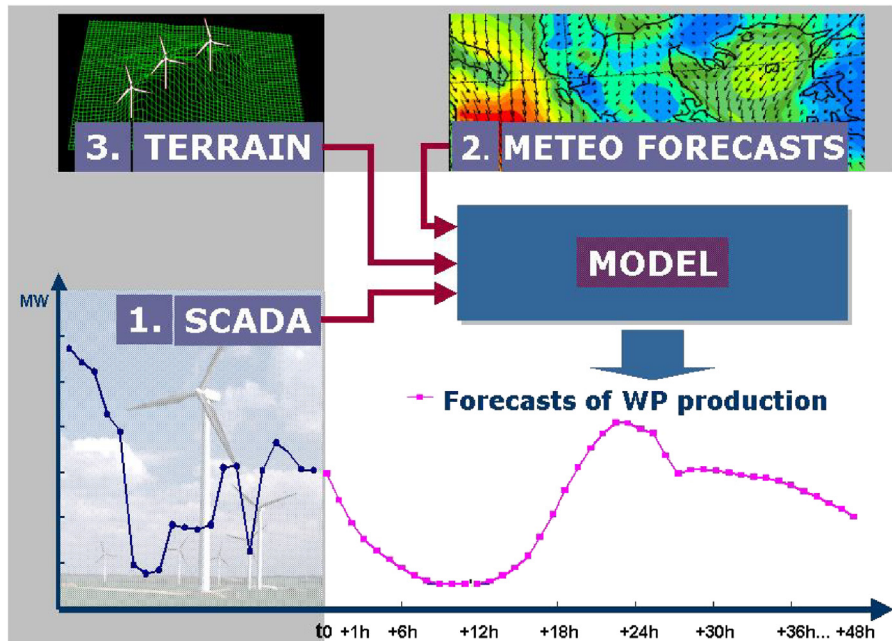


**Figure 3.1** The various forecasting approaches can be classified according to the type of input (SCADA indicates data available online). All models involving Meteo Forecasts have a horizon that is limited by the horizon of the NWP model, typically 48 h. (1): Short-term statistical approaches using only SCADA as input (horizons: <6 h). (2): “Physical” or “statistical” approaches. Good performance for >3 h. (2) + (3): “Physical” approach using NWP as input. Good performance for >3 h. (1) + (2): “Statistical” approach using NWP as input. (1) + (2) + (3): Combined approach.

ability to resolve scales down to tens of meters or even smaller, is that the effective resolution, which is the scale at which features are actually resolved in the NWP model, is some 4–7 grid points (Pielke and Kennedy, 1980; Young and Pielke, 1983; Skamarock, 2004). That is, even for a 2 km resolution, only features in the order of 10 km are really taken into account. This means that microscale models, except in cases of very simple terrain, are expected to be able to improve the NWP forecasts although this question remains a topic of research.

- The downscaling process yields a wind speed and direction for the turbine location. A power law has then to be applied to convert from the height the wind speed is given to the hub height of the wind turbine. This wind is then **converted to power** with a power curve. The use of the manufacturers’ power curve is the easiest approach, although research from a number of groups has shown it advantageous to estimate the power curve from the forecasted wind speed and direction and measured power.

Most actual statistical models leave this step out and do a direct prediction of the power production for single turbines or whole wind farms.

Depending on forecast horizon and availability, measured power data can be used as additional input. In most cases, actual data are beneficial for improving on the residual errors in a

MOS approach. If online data are available, then a self-calibrating recursive model is highly advantageous. This is part of the statistical approach. It can have the form of an explicit statistical model employed with advanced autoregressive statistical methods, or as an ANN type black-box. However, sometimes only offline data are available, with which the model can be calibrated in hindsight. In recent years, a number of system operators have demanded to get online data from wind farms specifically to be used in their online prediction tools.

- If only one wind farm is to be predicted, then the model chain stops here (maybe adding the power for the different turbines of a wind farm while taking the wake losses into account). Since utilities usually want a prediction for the total area they service, the **upscaling** from the single results to the area total is the last step. If all wind farms in an area were to be predicted, this would involve a simple summation. However, especially in some countries where not all wind farms have online data, some representative farms are chosen to serve as input data for an upscaling algorithm. Helpful in this respect is that the error of distributed farms is reduced compared to the error of a single farm.

Not all short-term prediction models involve all steps and/or all types of input. In the early days of forecasting, NWP data were not so widely available, therefore the first approaches were done with time series analysis techniques ([Kariniotakis et al., 1996](#)). But in an age where at least GFS forecasts from the United States are just a download away, there is no real incentive to not use it. Leaving out a few steps can be an advantage in some cases. For example, Prediktor ([Landberg, 1999](#)) is independent of online data, and can bring results for a new farm from day 1, while the advanced statistical models need historical data to learn the proper parameterizations.<sup>1</sup> However, this involves a reduced accuracy for rather short horizons. Alternatively, models using only SCADA data have a quite good accuracy for the first few hours, but without NWP input, they are generally useless for longer prediction horizons (except in very special cases of thermally driven winds with a very high pattern of daily recurrence). [Landberg \(1998\)](#) has shown that a simple NWP + physical downscaling approach is effectively linear, thereby being very easily amenable to MOS improvements—even to the point of overriding the initial physical considerations.

The opposite is a direct transformation of the input variables to wind power. This is done by the use of gray- or black-box statistical models that are able to combine input, such as NWPs of speed, direction, temperature etc., of various model levels together with online measurements such as wind power, speed, direction etc. With these models, even a direct estimation of regional wind power from the input parameters in a single step is possible. Whether it is better for a statistical model to leave out the wind speed step depends on a number of things, like the availability of data or the representativity of the wind speed and power for the area of the wind farm or region being forecasted. The optimal model can be potentially a combination of both, using physical considerations as far as necessary to capture the air flow in the region surrounding the turbines, and using advanced statistical modeling to make use of every bit of information given by the physical models.

<sup>1</sup> The commissioning behavior of wind farms does not lend itself easily to statistical recursive approaches, as different turbines will be offline for various reasons during the commissioning process, so that the power data coming from the wind farm tends to be nonrepresentative at many times.

## 3.2 Time series models

For very short-term horizons, the relevant time scales are given by:

- The mechanics of the wind turbine: typically the generator, gearbox, yaw mechanism, and most of all, the (blade) pitch regulation. The time scales involved are in the order of turbulence, i.e., seconds. The purpose is the active control of the wind turbines. Wind on those time scales is inherently nonstationary (compare also the excursion on why wind is nonstationary in [Vincent et al., 2010b](#)), and can best be forecasted with a lidar staring into the wind and a simple advection scheme of the measured wind field a few seconds ahead the rotor.
- The type of the power system into which the wind turbines are integrated. As mentioned in the introduction in small or medium isolated systems the relevant time scale is given by the type of conventional units (“fast” or “slow”) and the functions for which the forecasts are required (i.e., for economic dispatch horizons can be 10 min to 1 h while for unit commitment they can be a few hours ahead). It is typical for smaller island systems to consist of diesel generators with quite short time scales.

The typical approach is to use time series analysis techniques including methods based on data mining and artificial intelligence techniques like neural networks.

### 3.2.1 Time series models for very–short-term forecasting

If the forecasting horizon is not too long, wind speed and power can be forecast just using time series analysis methods, without resorting to actual weather forecasts. Direct time series models are models that use recent observed values of wind and other variables to predict the future wind speed.

While there had been attempts to forecast wind speeds before, the first paper considering wind power forecasts came from [Brown et al. \(1984\)](#). In retrospect, it is worth to acknowledge how complete the paper already was, using a transformation to a Gaussian distribution of the wind speeds, forecasting with an AR (AutoRegressive) process, upscaling with the power law (but discussing the potential benefit of using the log law), and then predicting power using a measured power curve. Additionally, the removal of seasonal and diurnal swings in the AR components is discussed, alongside prediction intervals and probability forecasts.

[Bossanyi \(1985\)](#) used a Kalman Filter (KF) with the last six values as input and got up to 10% improvement in the RMS error over persistence for 1-min averaged data for the prediction of the next time step. This improvement decreased for longer averages and disappeared completely for 1-hourly averages.

[Fellows and Hill \(1990\)](#) used 2-h ahead forecasts of 10-min wind speeds in a model of the Shetland Islands electricity grid. Their approach was to use optimized, iterative Box–Jenkins forecasting from detrended data, which then was subjected to central moving average smoothing. For 120 min look-ahead time, the RMS error reduction over persistence was 57.6%. [Nogaret et al., 1994](#) reported that for the control system of a medium size island system, the simple forecast with the best performance is an average of the last two or three values, i.e., 20–30 min. [Tantareanu \(1992\)](#) found that autoregressive moving average (ARMA) models can perform up to 30% better than persistence for 3–10 steps ahead in 4-sec averages of 2.5 Hz-sampled data.

[Torres et al. \(2005\)](#) use an ARMA model to forecast hourly average wind speeds for five sites in Navarra. They used site- and month-specific parameters for the ARMA model. The ARMA model usually outperformed persistence for the 1-h forecast, and always was better in RMSE and MAE for higher horizons up to 10 h ahead. The two complex sites have a slightly higher RMSE in general but are still in the same range as the other sites. In general, 2%–5% improvements for the 1-h forecast correspond to 12%–20% improvement for the 10-h forecast.

[Balouktsis et al. \(1986\)](#) used stochastic simulation models. They removed the annual and daily periodicities of the measured data and modeled transformed hourly average data with ARMA models. A similar approach is shown by [Daniel and Chen \(1991\)](#). They used stochastic simulation and forecast models of hourly average wind speeds, taking into account autocorrelation, non-Gaussian distribution, and diurnal nonstationarity and fit an ARMA process to wind speed data.

[Justus et al. \(1976\)](#) developed a method to compute power output from wind-powered generators, and they applied it to estimate potential power output at various sites across the United States. Values of the Weibull distribution parameters at approximately 135 sites have been evaluated and projected to a constant height of 30.5 and 61 m.

[Makarov et al. \(2005\)](#) describe a major California ISO-led project. Therein they developed prototype algorithms for short-term wind generation forecasting based on retrospective data (e.g., pure persistence models). The methods tested include random walk, moving average, exponential smoothing, auto-regression, Kalman filtering, “seasonal” differencing, and Box–Jenkins models. The latter one demonstrated the best performance. They also used a bias compensation scheme to minimize the look-ahead forecast bias. For forecasts for the next hour and 1 h ahead the total ISO-metered generation is predicted with MAE below 3% and 8% of the maximal observed generation correspondingly.

[Schwartz and Milligan \(2002\)](#) tested different ARMA models for forecasts up to 6 h for two wind farms in Minnesota and Iowa. Their main conclusion was that model performance was highly dependent on the training period—one should always try to have a parameter set-up procedure using data from a very recent period.

[Pinson et al. \(2008c\)](#) found that wind power and especially wind power variability from large offshore wind farms (Horns Rev and Nysted) occur in certain regimes, and therefore tested “regime-switching approaches relying on observable (i.e., based on recent wind power production) or nonobservable (i.e., a hidden Markov chain) regime sequences” for a one-step forecast of 1-min, 5-min, and 10-min power data. “It is shown that the regime-switching approach based on MSAR models significantly outperforms those based on observable regime sequences. The reduction in one-step ahead RMSE ranges from 19% to 32% depending on the wind farm and time resolution considered.”

Comparison of direct wind power prediction against wind speed forecasts with subsequent conversion to wind power ([Jensen et al.; ELSAM, 1996](#)) using autoregressive models showed that the use of wind speed predictions as explanatory variable is important for prediction horizons up to 8–12 h. For longer prediction horizons, use of separate wind speed forecasts offers no advantage over direct wind power prediction.

Madsen (1995) and Nielsen and Madsen (1996) found that two-stage modeling (conversion of wind speed predictions to wind power, in which correlation structure in power measurements is disregarded) are generally inferior to models that take the power correlation into account.

A number of models for the very short-term were proposed based on machine learning techniques including ANNs, fuzzy neural networks, and others. These approaches give more flexibility to consider explanatory variables as input. Reported improvements with respect to persistence are often comparable to classical time series models like AR, ARMA, etc. However, these models require particular effort to deal with dimensionality issues. A considerable effort is needed to appropriately select the most relevant input among the ensemble of available variables and also to select the structural parameters of the models (i.e., number of neurons, layers, etc.) so as to avoid overfitting.

Dutton et al. (1999) used a linear autoregressive model and an adaptive fuzzy logic-based model for the cases of Crete and Shetland. They found minor improvements over persistence for a forecasting horizon of 2 h, but up to 20% in RMS error improvement for 8 h horizon. However, for longer horizons, the 95% confidence band contained most of the likely wind speed values, and therefore a meteorological-based approach was deemed more promising on this time scale.

Kariniotakis proposed different types of prediction models based on ANNs and fuzzy logic in Kariniotakis (1996) and Kariniotakis et al. (1996). Emphasis is given on the selection of the structural parameters of the models through various approaches including cross-validation. In Kariniotakis et al. (1999) several methods are tested with data from islands in Greece. These included adaptive linear models, adaptive fuzzy logic models, and wavelet-based models. Adaptive fuzzy logic-based models were installed for online operation in the frame of the Joule II project CARE (JOR3-CT96-0119).

Beyer et al., 1994 found improvements in the RMSE criterion for next-step forecasting of either 1-min or 10-min averages to be in the range of 10% over persistence. This improvement was achieved with a rather simple topology, while more complex neural network structures did not improve the results further. A limitation was found in extreme events that were not contained in the data set used to train the neural network. Tande and Landberg (1993) examined 10 s forecasts for the 1 s average output of a wind turbine and found that the neural networks performed only marginally better than persistence. Alexiadis et al. (1998) used the differences of wind speeds from their moving averages (differenced pattern method) and found this technique to be superior to the wind speed normally used as input. They achieved improvements of up to 13% over persistence, while for the same time series the standard neural network approach yielded only 9.5% improvement. Bechrakis and Sparis (1998) used neural networks to utilize information from the upwind direction. Their paper does not give any numbers on the increase over persistence, since their aim is to predict the resource rather than to do short-term prediction.

Sfetsos (2001) applied ARIMA (Autoregressive Integrated Moving Average) and feed-forward neural net methods to wind speed time series data from the United Kingdom and Greece, comparing the results of using either 10-min or hourly averaged

data to make a forecast 1 h ahead. For both data sets, neither forecasting method showed a significant improvement compared to persistence using hourly averaged data, but both showed substantial (10%–20%) improvement using 10-min averages. The result is attributed to the inability of hourly averages to represent structure in the time series on the high-frequency side of the “spectral gap”, lying at a period of typically around 1 h.

[Mohandes et al. \(2004\)](#) show that support vector machines outperform multilayer perceptron neural networks for mean daily wind speed data from Medina city, Saudi Arabia. [Kretzschmar et al.](#) used neural network classifications for the forecasts of strong winds and wind gusts at Geneva and Sion in Switzerland. The quality of hit-and miss-rates was clearly improved from persistence for 1, 6, 12, and 24 h horizons. They also analyzed the benefits of using many meteorological observations of surrounding masts and found that “the correlations between speed or gusts to pressure or temperature were found to be more relevant than the correlations of speed or gusts to wind direction, humidity, radiation, or rain.” Despite that, and due to the facts that data usually cost money and that the same accuracy could be obtained just with the local observation, they decided against the use of surrounding data. Partly, this was due to the difficulty in determining the “upstream” station at all times.

[Sfetsos \(1999, 2000\)](#) compared a number of methods, including a Box–Jenkins model, feed-forward neural networks, radial basis function networks, an Elman recurrent network, ANFIS models (adaptive network based fuzzy inference system), and a neural logic network based on their ability to forecast hourly mean wind speeds. All nonlinear models exhibited comparable RMS error, which was better than any of the linear methods. For the 1 h ahead, the best model was a neural logic network with logic rules, reducing the error of persistence by 4.9%. [Wu and Dou \(1995\)](#) used a combination of a fuzzy classifier with a temporal neural network for nonlinear wind prediction.

[Potter and Negnevitsky \(2006\)](#) used an ANFIS model to predict just the u (northward) component of the direction 2.5 min ahead in Tasmania. On the 21-month test set, they were able to reduce the 30% mean absolute percentage error (without properly defining it) of persistence for the step-ahead prediction to 4%.

In a study for the Mexican Electric Utility Control Center [Cadenas and Rivera \(2009\)](#) compare different configurations of neural networks, and find that the simplest (two layers, two input neurons, one output neuron) outperformed more complex ones for one-step forecasts of hourly wind data in La Venta, Mexico. However, their way of presenting the findings, as MAE of 0.0399 without specifying what it is (m/s would be extremely low), makes one suspicious of the rest of the paper. In an earlier paper ([Cadenas and Rivera, 2007](#)), they had compared the merits of an ARIMA model and a neural network for the same test case and had concluded that a seasonal ARIMA model worked better than the relatively simple ANN they were using.

For an anemometer near Mumbai, [More and Deo](#) outperformed ARIMA models using neural networks for the 1-step ahead forecasts of mean daily, weekly, and monthly wind speeds. “Forecasting accuracy decreased as the interval of forecasting reduced from one month to one day.”

[Kusiak et al. \(2009b\)](#) explored the viability of five data mining algorithms for wind speed and wind power 1-step to 3-step ahead prediction. The 3-step ahead

uses the 1-step ahead and 2-step ahead predictions as input. “Two of the five algorithms performed particularly well. The support vector machine regression algorithm provides accurate predictions of wind power and wind speed at 10-min intervals up to 1 h into the future, while the multilayer perceptron algorithm is accurate in predicting power over hour-long intervals up to 4 h ahead.” They further muse: “One disadvantage of the proposed approach is that the time series model uses its own previously predicted values. As the number of prediction steps increases, the errors get accumulated. A possible approach for improving prediction accuracy is to build a set of prediction models for each time step.”

### ***3.2.2 An explanation of the time series model improvements***

*A general note on time series models (neural network or otherwise):* Some of the improvement of the time series approach over persistence can be explained with a term taking the time series (running) mean into account. [Nielsen et al. \(1998\)](#) tried a few years ago to introduce this as the new reference model. In essence, it predicts the power  $p(t)$  using the power  $p(t - n)$  ( $n$  being  $n$  time-steps back) and the mean  $\mu$  of the time series. Of course, disregarding  $\mu$  and having  $n = 1$ , this would be the persistence model itself. However, the new reference is written as

$$p(t) = a(n) \times p(t - n) + (1 - a(n)) \times \mu$$

where  $a(n)$  is the autocorrelation of the time series  $n$  steps back. This simple model can achieve the typically 10% RMS error improvements over persistence found by many authors using more or less advanced time series analysis techniques.

## **3.3 Meteorological modeling for wind power predictions**

The main error in the final forecast comes from the meteorological input. For example, [Sánchez et al. \(2002\)](#) show that the Spanish statistical tool Sipreolico run with on-site wind speed input has a much higher degree of explanation than HIRLAM forecasts. This means that given a representative wind speed, Sipreolico can predict the power quite well. It is the wind speed input from the NWP model that is decreasing the accuracy significantly. Therefore, it is logical to try to improve the NWP input to come up with significant improvement in forecasting accuracy (see [Fig. 3.2](#)).

### ***3.3.1 Improvements in NWP and mesoscale modeling***

[Möhrlen \(2001\)](#) has looked at the resolution needed for successful application of NWP forecasting. In a study with the Danish HIRLAM model for one site in Ireland she points out the reasons why NWP models are delivering inadequate accuracy of surface wind speeds. Among other things, these were so far, no customers made it necessary to increase the accuracy of surface winds, since for the existing ones the accuracy was

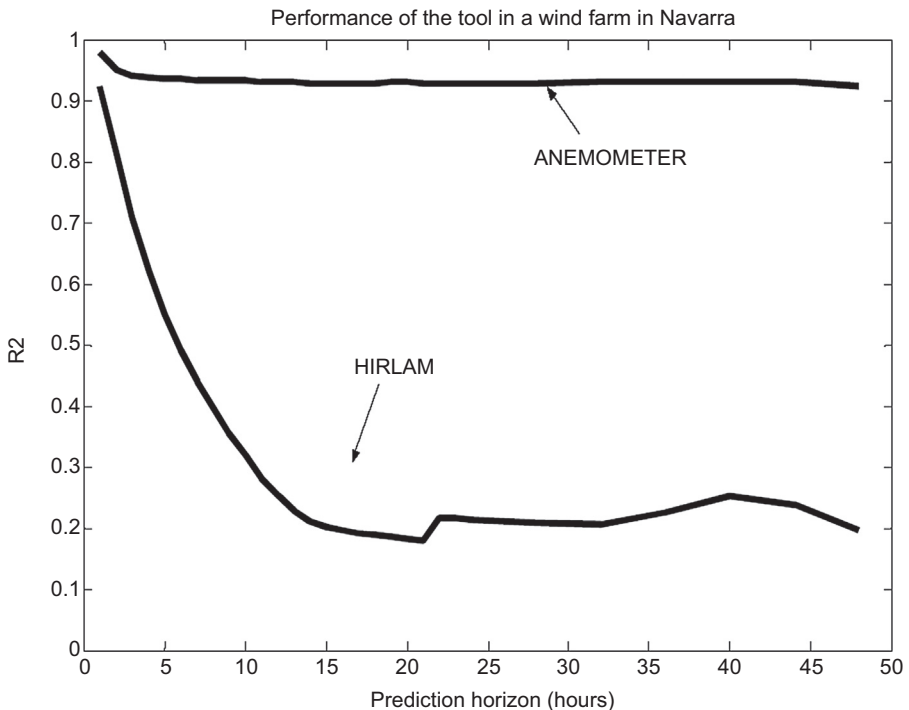


**Figure 3.2** The error comes from the numerical weather predictions. The figure shows the difference in degree of explanation between Sipreolico run with HIRLAM input (from an older version of the Spanish HIRLAM) and Sipreolico run with on-site wind speed input.

Source: Sanchez, I., Usaola, J., Ravelo, O., Velasco, C., Domínguez, J., Lobo, M.G., Gonzalez, G., Soto, F., June 2002a. SIPREOLICO—a wind power prediction system based on flexible combination of dynamic models. Application to the Spanish power system. In: Proceedings of the World Wind Energy Conference in Berlin, Germany.

good enough. The topography resolution is not good enough to account, e.g., for tunnel effects in valleys. Accurate predictions require high-resolution models covering a large area. However, running both is numerically very expensive. To improve on the state of things, she calculated the power directly inside the NWP model. This had the advantage that “major physical properties like direction dependent roughness, actual density, and stratification of the atmospheric boundary layer can be used in the calculations.”

In different runs with horizontal model resolutions of 30, 15, 5, and 1.4 km for two months in January 2001, the most common statistical accuracy measures (MAE, RMSE, correlation, etc.) did improve only slightly with higher resolution. However, peak wind speeds were closer to the measured values for the high-resolution forecasts. For the higher resolution forecasts, the best model layers were those closest to the ground. For the errors, she points out that phase errors (the timing of the frontal system) has a much larger influence on the error scores (and eventual payments)

than amplitude errors. As one possible remedy, she proposes to use free-standing turbine data as input for the NWP, thereby increasing the observational meteorological network.

A similar point is made by [Rife and Davis \(2005\)](#). They compared two otherwise identical model setups with horizontal resolution of 30 and 3.3 km, respectively, for wind speed variations at and near the White Sands Missile Range in New Mexico (US). “The authors hypothesize that the additional detail and structure provided by high-resolution becomes a ‘liability’ when the forecasts are scored by traditional verification metrics, because such metrics sharply penalize forecasts with small temporal or spatial errors of predicted features.” Therefore, they use three alternative skill scores, namely (in order of tolerance of timing errors) anomaly correlation, object-based verification, and variance anomalies. “The largest improvement of the fine-grid forecasts was in the cross-mountain component.” In general, the higher resolution forecasts exhibited more skill than their coarser counterparts.

Also for hurricanes [Davis et al. \(2010\)](#) find that 1.33 km grid spacing improves the results for “Intensity (maximum wind) and rapid intensification, as well as wind radii” over 4-km horizontal resolution, using the advanced research hurricane version of WRF.

In a follow-up paper on HIRLAM in Ireland ([Möhrlen et al., 2001a](#)), Möhrlen shows the difference between the usual 1-h average wind speed and the instantaneous wind speeds. She concludes that is important to calculate the power within the model itself, to make use of its significantly shorter time step (the difference comes of course because the energy in the wind is proportional to the cube of the wind speed, and does not depend linearly on it.). For the same setup, [Jørgensen et al. \(2002a\)](#) make a number of interesting points on the coupling of an NWP model to wind power forecasts. Examining 25 especially bad forecasted days from 15 months for the Western Danish TSO Eltra (now part of Energinet.dk), he found that in all cases the error came from the NWP model and not from the wind power predicting tool (WPPT) upscaling. Here too he found that using higher resolution in HIRLAM, the scores do not improve substantially, indicating that level errors are smaller and gradients sharper in the higher resolution. This leads to higher error measures for phase errors. On the weather dependence of the errors, he writes: “The more steady the flow is and the longer the controlling low pressure is towards the north, the better the quality of the forecast.” He also notes on the roughness (usually in NWP models just one value per grid box): “Most turbines are positioned such that the local roughness is lower than the average roughness in the corresponding NWP model grid box. This is at least true for the prevailing wind direction [...]. Thus, a NWP model will in average have a negative wind bias where turbines are installed unless direction dependent roughness is used.”

[Möhrlen et al. \(2002\)](#) describe the “Irish study”, where HIRPOM (HIRlAM POwer prediction Model) was implemented into HIRLAM to be run in prognostic and diagnostic mode with the aim of finding the most efficient resolution for wind energy forecasting in complex terrain. Ireland has Europe’s best wind resources and intends to use them. So the overall purpose of the Irish study was to surpass the island’s own target of 33% of renewable energy by 2020. The study showed that it is actually possible to generate 42% of Ireland’s electricity from renewable energy. The Irish study was

one of the biggest numerical experiments carried out in the wind energy domain at the time. For the actual forecasting, in Möhrlen et al. (2001b) they argued that high-resolution forecasting (down to 1.4 km) also needs high-resolution input databases for orography and roughness, and that due to the limited possibilities of data transfer (now a less relevant point) the power calculation should happen directly in the weather model. Jørgensen et al. (2002b) also found that coupling HIRLAM with a wave model and HIRPOM improves the forecasts over sea and also over land 100 km from the coast. For the North Sea coastline they found 2.5% improvement, further out in the North Sea they expect 5%.

Jørgensen et al. (2002c) describe the approach where they integrated the power prediction module within the NWP itself. They call it HIRPOM, also described by Möhrlen (2004). She used a simplified power conversion module using standard power curves from wind turbine manufactures, which was integrated into the NWP model. She also found through experiments with deterministic forecasts that increasing the horizontal resolution did not reduce the forecast errors. So using the same computational resources more economic benefit could be gained generating ensemble forecasts and derive uncertainty, the latter being as important as the wind speed and power itself. Jørgensen and Möhrlen therefore developed a 50-member Multi-Scheme Ensemble Prediction System (MSEPS) (more recently, WEPROG is running the system with 75 members) with an implicit forward–backward stepping algorithm (pmt-filter) to compute an uncertainty estimate for the forecasts (Möhrlen, 2001).

Sood et al. (2006) used WRF on a 3-km resolution grid over the German part of the North Sea. They found that stable and unstable conditions were less well forecasted than neutral conditions. On her own, Palomares and de Castro (2003) worked on the prediction using perfect prognosis to connect the too coarse fields of the 50-km resolution ECMWF global reanalysis model to the local flow at the strait, with quite reasonable results considering that the ECMWF global model did not even have a strait there.

Barstad (2001) used a library of precalculated mesoscale model results to downscale the wind from the large-scale weather situation to the actual site in Nord-Trøndelag county, Norway. The classification of the overall weather was derived from NCEP/NCAR Reanalysis data (Kalnay et al., 1996). For the 32 cases found, MM5 was run to transform the large-scale flow to the wind at the actual (very complex) site. This approach was used together with the reanalysis data to determine the resource in the vicinity and was also used in conjunction with the HIRLAM system of the Norwegian Meteorological Institute to yield short-term forecasts. Berge (2002) presented the whole system at a workshop in Norrköping in 2002. A larger report (Berge et al., 2003) additionally compares the performance of MM5 with results from the CFD model 3DWind. HIRLAM was run on a horizontal resolution of 10 km, MM5 on 1 km, and 3DWind with a resolution varying from 30 to 500 m. To compare these models, a statistical model has been developed. Bremnes (2002) reported during the Norrköping workshop on the use of probabilistic forecasts, to yield the uncertainty of a forecast. His approach was to transform the forecasts according to the error distribution, standardize the centered forecast errors using the variance estimate, and retransform the wind speed. This effectively gives a direct estimate of the frequencies,

or quantiles, of the resulting forecast. The larger report shows that the predicted frequencies actually are fairly reliable (i.e., the 95% fractile, defined as a 95% probability that the power production will be below this value, was reached ca. 95% of the time). The best selection of explanatory variables based on HIRLAM10 was to use the wind speed at 10 m a.g.l., the wind direction, the wind speed increase, and the time of day/horizon. One result of the comparison of the physical models was that despite the fact that the finer models did present more details of the forecasts, they were always fed with the initial and boundary conditions from the coarser HIRLAM model, and therefore were bound to have the same temporal development as the larger model. Also, the improvements in the details added by the mesoscale model and the CFD model did not show up in the error scores for a horizon of more than 20 h. As a side note, the model speed-ups from MM5 and WAsP were compared, showing that in the highly complex terrain of Norway, MM5 (on 1 km resolution) tended to underpredict the speed-up effects by around 20%.

[Enemoto et al. \(2001\)](#) used the LOCALS model (Local Circulation Assessment and Prediction System) to forecast the power production of the TAPPI wind farm in Aomori Prefecture, Japan. Despite using the model with a 500-m grid, the result is still a Root Mean Square Error (RMSE) of 15% of the installed capacity. Their results indicate that the significant differences in turbulence intensity between the turbines are not modeled correctly. [Murakami et al. \(2003\)](#) developed a numerical prediction model to obtain useful data for selecting suitable sites for windmill planting in Japan. They call it LAWEPS (Local Area Wind Energy Prediction System) and include CFD models for meteorological phenomena as well as a five-stage nesting method. [Hashimoto et al. \(2007\)](#) used WRF in conjunction with the local wind model NuWiCC. They found that every additional modeling step improved the accuracy. They also found that NuWiCC was able to express the differences between wind speeds at each turbine.

[Yamaguchi et al. \(2007\)](#) actually managed to reach nearly the same performance as a 1-km resolution RAMS downscaling of the 20-km resolution Japan Meteorological Agency met model with a simple transfer coefficient method. Using an ARXM (AutoRegressive with eXogenous input and multitemplescale parameter) with the operational condition of the wind farm as exogenous parameter, they even exceeded the performance of the RAMS downscaling.

The Meteorological Service of Canada developed a simulation toolkit ([Yu et al., 2006](#)) called WEST (Wind Energy Simulation Toolkit). It can look forward up to three days (with the mesoscale model MC2) and backward (through the reanalyzes of MC2) in time to generate a wind atlas for any location in Canada. They claim to also have modeled the wind power potential for whole Africa.

[Tammelin \(2002\)](#) reported for the Finnish case that the Finnish Meteorological Institute is working on wind power forecasts, using their version of the HIRLAM model plus a number of smaller scale models to scale the wind speed down to the surface. An additional problem appearing in Finland is the difference in power curve due to low temperatures and icing. [Dierer et al. \(2005\)](#) investigated the use of MM5 for wind energy purposes, not necessarily just with short-term forecasting in mind. They found no big differences in overall performance according to choice of planetary

boundary layer schemes, though the ETA and Blackadar scheme seemed generally quite good. An increase in horizontal resolution from 10 to 1 km did not bring about large improvements. “This is not an expected result, especially in orographically structured terrain, but it implies that the quality of the modelled wind profile is limited by other factors than the horizontal resolution, for instance, the forcing data.”

A large effort to the aim of meteorological forecasts for wind energy purposes has also been made by the original ANEMOS project. A long report ([Giebel, 2006](#)) details some work on especially downscaling techniques with microscale, mesoscale, and CFD models. The best parameterization for MM5 was found to be MRF, although it did not lead the competition at every forecast horizon and case study. If possible from a computational point of view, two-way nesting between domains is clearly preferred. While one group using mostly physical modeling reported increased accuracy down to 2-km grid spacing, another one using an advanced statistical model claimed no improvement when going from 9 to 3 km grid spacing. This is probably due to the fact that the forecasted time series become more “realistic” when increasing horizontal resolution, in the sense that the ups and downs of the time series have a similar amplitude to the original series in the high-frequency domain. However, this means a higher potential for phase errors, so for the usual RMS error or MAE the error goes up. Increasing the horizontal resolution beyond the resolution of the terrain database is fairly useless. On the other hand, increasing the vertical resolution in the lowest, say, 200 m of the atmosphere improved the results in all cases. The report closed with the following recommendations: “If you have a site in complex terrain, where you even after using an advanced MOS are not happy with the forecasts, then try to use higher resolution modelling. In many cases and with a large number of approaches, the models can improve the NWP results. When setting up a model yourself, make sure to use the best terrain DB available (e.g., SRTM data), and try to get good NWP input data. Set up the model to have good vertical resolution and reasonable horizontal resolution. Find out for yourself what ‘reasonable’ means in this context. Use a MOS. Use insights gleaned from high-resolution modelling to decide which parameters to employ in the MOS. In any case, setting up a model from scratch will take a long time before one is familiar with the model and its quirks; so do not plan on having a solution up and running immediately.”

For a real-time implementation of WRF (the successor of MM5) at DTU Wind Energy, [Peña and Hahmann \(2010\)](#) reported and described preliminary verification results for the modeling system using surface observations and tall mast observations from Denmark. “In general, below 80–100 m WRF overestimates wind and underestimates it above this level.” For the same setup, Draxl et al. set up a data assimilation system (WRFDA, 3DVAR) and performed initial tests. They investigated which model parametrizations would best capture wind conditions in the vicinity of the Horns Rev wind farm, and evaluated different model runs of the WRF model with seven different boundary layer schemes ([Draxl et al., 2010](#)). The main findings are that the YSU-scheme tends most of all to make the profiles neutral also when stable conditions were observed. The data assimilation system was then used to assimilate winds measured at the nacelle of the wind turbines at Horns Rev, to improve the mesoscale wind forecast for that wind farm ([Draxl, 2012](#)). Nacelle winds are a new data set and are not used so far for common assimilation systems. The data assimilation

experiments included the nudging technique and 3DVAR. The main findings here are that using the nudging technique the forecast could be improved for up to 2 h, with 3DVAR much longer.

An interesting option for dedicated data collection for assimilation in a mesoscale model has been presented by [Ágústsson et al. \(2010, 2011\)](#): they use the Small Unmanned Meteorological Observer (SUMO), a model airplane of 580 g total weight, as a “recoverable radiosonde” for ad hoc observations in the atmosphere, and assimilate the run in WRF. For the wind flow over the Eyjafjalla volcano in Iceland, they find a “major difference in flow pattern extending far above mountain top level.”

[Badger et al. \(2010\)](#) discussed the limitations of mesoscale modeling in the context of wind energy resource mapping and described a postprocessing procedure developed at DTU Wind Energy, where output from mesoscale models was linked to microscale modeling, such that correct verification of the models could be performed, and so that the application of mesoscale models could be extended for wind resource assessment, analysis of wind conditions, or short-term predictions. As an example, generalized winds for a specific storm event were calculated.

### **3.3.2 Ensemble Kalman filtering**

The KF methods have gained popularity for data assimilation tasks in recent years, because they account for the dynamic propagation of model errors. [Anderson and Anderson \(1999\)](#) found an ensemble Kalman filtering (EnKF) methodology to combine data assimilation with generation of ensembles to also account for the uncertainty in the forecasting step. However, the method only worked well in low-order systems and could not be applied to large atmospheric models.

This limitation of the KF technique in meteorological context was however found to not be a limitation in wind power context, because there, the area of observational distribution is also rather small, even if the area spans over an entire country. Therefore, [Möhrlen and Jørgensen \(2009\)](#) found that only a type of ensemble EnKF techniques can be adopted for wind power purposes. As described by [Anderson and Anderson \(1999\)](#) and [Houtekamer and Mitchell \(1998\)](#), the standard KF propagates the error covariance from one assimilation step to the next, which is computationally expensive.

In the EnKF, this procedure is approximated by using an ensemble of short-range forecasts, where the forecast error covariance is directly computed from the ensemble when they are needed for the data assimilation. [Meng and Zhang \(2008\)](#) found that it was beneficial to use a multischeme ensemble approach rather than a single-scheme approach, because it does not require such a large ensemble size to cover the uncertainties. They built an ensemble based on a Penn-State University WRF model kernel and different parameterization schemes.

[Möhrlen and Jørgensen \(2009\)](#) followed the same strategy and used an ensemble that is independent of the data assimilation system and also built upon a multischeme approach, their in-house MSEPS. Their MSEPS system has 75 ensemble members with various different parameterization schemes for the advection and the fast physical processes such as condensation and vertical diffusion. The authors developed the EnKF as part of the HREnsembleHR project, funded by the Danish PSO program

2006–09 and called it an “inverted Kalman Filter technique” (iEnKF). It was introduced it in 2009 (Gow, 2002) and became an operational short-term forecasting approach rolled out by WEPORG at the beginning of 2010 in Germany, Denmark, Ireland, and Canada. The approach is a generalized multidimensional state estimate methodology, which is capable of translating information between any kind of variables, that can be forecasted reasonably well by an ensemble prediction system like the MSEPS. The effect of each measurement is computed in the nondimensional ensemble percentile space and the time dependency is determined via the forecast covariance of the ensemble.

The strength of the iEnKF approach is the capability of combining different types of measurements. In this way meteorological SYNOP data, recorded data from wind farms and other power data can be combined to a consistent forecast.

### 3.4 Short-term prediction models with NWPs

This section deals with models using NWP data as input that includes a number of commercial models. Probably the earliest model was developed by McCarthy (1998) for the Central California Wind Resource Area. It was run in the summers of 1985–87 on an HP 41CX programmable calculator, using meteorological observations and local upper air observations. The program was built around a climatological study of the site and had a forecast horizon of 24 h. It forecasts daily average wind speeds with better skill than either persistence or climatology alone.

In 1990, Troen and Landberg (1990) and Landberg (1994) developed a short-term prediction model, now known as Prediktor, based on physical reasoning similar to the methodology developed for the European Wind Atlas (Troen and Petersen, 1998). The idea is to use the wind speed and direction from an NWP, transform this wind to the local site, use the power curve, and finally modify this with the park efficiency. Note that the statistical improvement module MOS can either be applied before the transformation to the local wind, before the transformation to power, or at the end of the model chain to operate on the power itself. A combination of all these is also possible.

The WPPT has been developed by the Institute for Informatics and Mathematical Modeling (IMM) of the Technical University of Denmark. In 2006, the original developer team founded the DTU spin-off company ENFOR, which now stands for all commercial activity with the model ([www.enfor.eu](http://www.enfor.eu)). WPPT has been running operationally in the western part of Denmark since 1994 and in the eastern part since 1999. The model uses adaptive RLSs estimation of the parameters of conditional parametric models to find the best connection between the NWP predicted wind speeds for the site and the measured power for each forecast horizon. A central part of this system is the statistical models for short-term prediction of the wind power production in wind farms or areas. For online applications it is advantageous to allow the function estimates to be modified as data become available. Furthermore, because the system may change slowly over time, observations should be down-weighted as they become

older. For this reason a time-adaptive and recursive estimation method is applied. Depending on the available data the WPPT modeling system employs a highly flexible modeling hierarchy for calculating predictions of the available wind power from wind turbines in a region. For a larger region this is typically done by separating the region into a number of subareas. Wind power predictions are then calculated for each sub-area and hereafter summarized to get a prediction for the total region. The predictions for the total region are calculated for a number of reference wind farms using online measurements of power production as well as NWPs as input.

A rather similar approach to Prediktor was developed at the University of Oldenburg (Beyer et al., 1999). They named it Previento (Focken et al., 2001a). A good overview over the parameters and models influencing the result of a physical short-term forecasting system has been given by Mönlich (2000). He found that the most important of the various submodels being used is the model for the atmospheric stability. The use of MOS was deemed very useful. However, since the NWP model changed frequently, the use of a recursive technique was recommended. A large influence was found regarding the power curve. The theoretical power curve given by the manufacturer and the power curve found from data could be rather different. Actually, even the power curve estimated from data from different years could show strong differences. The latter might be due to a complete overhaul of the turbine. The largest influence on the error was deemed to come from the NWP model itself. In 2004, the two principal researchers behind Previento, founded energy & meteo systems and further exploit the developed forecasting approach.

MINES ParisTech/ARMINES has developed work on short-term wind power forecasting since 1992. Initially, short-term models for the next 6–10 h were developed based on time series analysis to predict the output of wind farms in the frame of the LEMNOS project (JOU2-CT92-0053). In the frame of the project CARE (JOR-CT96-0119) (Wind Engineering, 1999), more advanced short-term models were developed for the wind farms installed in Crete. In the follow-up project MORE-CARE (ERK5-CT1999-00019), ARMINES developed models for the power output of a wind park for the next 48/72 h based on both online SCADA and NWPs (meteorological forecasts). An operational forecasting system (AWPPS) was developed. It integrates several deterministic and probabilistic models including modules for ramps, risk indices, etc. The developed forecasting system can generically accept as input different types of meteorological forecasts.

The IWES institute of Fraunhofer (Fraunhofer Institut für Windenergie und Energiesystemtechnik, previously ISET) has since 2000 operatively worked with short-term forecasting, using the DWD model and neural networks. It came out of the German federal monitoring program WMEP (Wissenschaftliches Mess- und EvaluierungsProgramm) (Durstewitz et al., 2001), where the growth of wind energy in Germany was to be monitored in detail. The system has been installed at several end users like E.On, RWE, and others (Ernst and Rohrig, 2002). In the last years IWES continued developments through the major national project in renewable energy forecasting EWELINE ([projekt-eweline.de](http://projekt-eweline.de)).

The Sustainable Energy Research Group (SERG) in University College Cork (UCC) has been researching and developing wind power forecasting methodologies

based on ensemble forecasts in the years 2002–06, see e.g., (Lang et al., 2006a,b,c). An operational forecasting system was developed by the principal researchers in UCC and brought to life in 2004 by WEPROG (Weather and wind Energy PROGnosis), which was founded in 2003. WEPROG's MSEPS contains a 2-step power prediction module. In the first step a physical reference power is computed and in a second step, the reference power is localized statistically and with the help of weather classes defined by the ensemble weather input.

eWind is a US-American model by TrueWind, Inc (now AWS TruePower) (Bailey et al., 1999). The current iteration of eWind uses ARPS, MASS, and WRF, fed by the global models GFS, GEM, and ECMWF, to yield an ensemble of nine different model runs (Vidal et al., 2010). For the average prediction of six wind farms in Europe, their results reveal that “the ensemble prediction outperforms the accuracy of [...] the MOS method applied to single NWP models, achieving between a 20 and 30% of improvement during the first three days of prediction.” Zack (2004) presented their high-resolution atmospheric model to operate in a rapid update cycle mode, called WEFRUC—Wind Energy Forecast Rapid Update Cycle. The model assimilates different types of data available in the local-area environment of a wind plant such as remotely sensed data, which is the starting point for a short-term simulation of the atmosphere. So, the atmospheric simulation produced by the physics based model is incrementally corrected through the use of the measured data as it evolves. Their update cycle is 2 h.

DNV GL's short-term energy forecasting service, previously known as GH Forecaster (Gow, 2002), is based on NWP forecasts. It uses “multiinput linear regression techniques” to convert from NWP to local wind speeds. For T + 24 h, they reach 35%–60% improvement over persistence.

A consortium of Portuguese universities and research institutes (Rodrigues et al., 2007) developed the EPREV tool and tested it at three wind farm sites in Portugal. MM5 was run as input to either a Wind Farm Power Curve model derived from WAsP, or from the CFD code Ventos, or to a statistical power curve. Salcedo-Sanz et al. (2009a) present an interesting study of three global NWP models downscaled with three different parameterizations of MM5 (with local data assimilation) as input to different neural networks (Salcedo-Sanz et al., 2009b). Unfortunately, their result “that the bank of neural networks obtains better results than the best of the models with a single neural network” is unreliable at best, as it is based on only one month of data. Sideratos and Hatziairgyriou (2008) have developed a wind power prediction model using neural networks emphasizing the importance to fit a different model for each part of the power curve. In addition, they combine RBF ANN with fuzzy logic to improve the use of NWP predictions into a final wind power prediction model (Sideratos and Hatziairgyriou, 2007).

In the Nordic countries, but also in Canada, icing of wind turbines can decrease the production as the turbines need to shut down, or as the aerodynamic efficiency is strongly reduced due to ice aggregation. The Winterwind conferences are specialized in icing predictions. Thompson (2008) talked on the potential of WRF and current developments for direct icing forecasts. Landberg (Duncan et al., 2008) showed an example of power curve degradation due to icing. Durstewitz et al. (2008) reported on the difficulties encountered in Germany.

The strong wind energy growth in Spain led Red Eléctrica de España (the Spanish TSO) to have the Sipreólico tool initially developed by the University Carlos III of Madrid. The tool is based on Spanish HIRLAM forecasts, taking into account hourly SCADA data from 80% of all Spanish wind turbines (Sánchez et al., 2002). These inputs are then used in adaptive nonparametric statistical models, together with different power curve models. These models are recursively estimated with both a recursive least squares (RLS) algorithm and a KF. The results of the multiple models are then used in a forecast combination (Sánchez, 2006), where the error term is based on exponentially weighted mean squared prediction error with a forgetting factor corresponding to a 24-h memory.

The optimal **combination** of forecasts is a field that has garnered attention in the last years. As Sánchez (2008) points out, “It is common in the wind energy industry to have access to more than one forecaster. It is well known that the relative performances of the alternative wind power forecasts can vary with the wind farm, and also with time. In these cases, an adaptive combination of forecasts can be useful to generate an efficient single forecast.” The combined approach was extensively studied within the ANEMOS project and was successfully implemented within the ANEMOS forecasting software platform. This platform, developed in the respective EU projects, was applied at different end users like the market and system operator of Australia (Kariniotakis et al., 2011).

### **3.4.1 Modeling wind speed versus wind power**

Wind power forecasting tools that consider “physical” modeling may integrate specific modules to predict initially wind speed and then converting it to power through a more or less advanced power curve model of the wind farm (i.e., integrating modeling of wake effects). It is likely that the model chain benefits from forms of statistical post-processing such as the MOS system. Any use of meteorological models must involve a two-stage process, so the MOS process should operate on the final result (the predicted wind power) instead of trying to optimize the local wind speed prediction.

Giebel (2001) showed that, when using NWP model winds and a fixed power curve in Prediktor, it is best to use MOS acting on the wind speed, i.e., before putting it through the power curve, rather than on the final power output. Likewise, Louka et al. (2008) showed that Kalman filtering SKIRON or RAMS results before feeding them into a power forecasting module significantly improves the forecast skill. The  $0.1 \text{ degrees} \times 0.1 \text{ degrees}$  SKIRON model had its bias removed and was thereby much better for power predictions than without the filter. The same held true for the RAMS model with runs down to 0.5 km horizontal resolution. Due to computing power limitations, only 2 days could be run. Using those results, it showed that Kalman filtering even the 12 km run gave a better power forecast than even the 0.5 km resolution run. “Therefore, this work suggests that the use of very expensive computational facilities to perform high-resolution (6 km) applications for wind energy predictions may be avoided by the combined use of moderate NWP model resolution and an adaptive statistical technique such as Kalman filtering; providing similar or even more accurate predictions at wind farm scale.”

Some models involve explicit modeling of the wind farm power curve. Such models may receive a wind speed forecast and convert it to power forecasts. Power curve modeling from wind speed was done by [Cabezon et al. \(2004\)](#). They used five methods based on statistical tools (linear models with binning methods and a fuzzy logic model) and found an improvement the more accurate the models were and the more effects they took into account.

[Collins et al. \(2009\)](#) point out that for large wind farms (>100 MW), the local effects vary so much across the site that a simple application of an upscaled manufacturers power curve is not good enough. An advanced wind farm power curve model taking air density, heterogeneous flow field, and wake effects into account and fine-tuned with local measurements reduced the power MAE for the power model being fed with on-site met mast wind speeds from 7.5% to 1.5% for a site in the UK. Fed with actual NWP forecasts, the day-ahead error was reduced by 1.2%. For a site in the United States, the numbers were 11.6%, 4.6%, and 0.9% improvement, respectively.

More recently, [Kusiak et al. \(2009a\)](#) used the data mining approaches from [Möhrlen \(2001\)](#) with NWP input to predict for up to 12 h and up to 84 h ahead. As input they used two US NWP models, the Rapid Update Cycle RUC and the North American Mesoscale (NAM) model, with the 16 data points around the wind farm. Both models had wind speed and direction at various levels plus air density and potential temperature difference. The NAM also had sensible heat flux and the percentage of vegetation in the grid point. Of this multitude of parameters, a boosting tree algorithm was used for feature selection, which reduced the number of data to the four nearest grid points. Data from those was then further reduced via principal component analysis, where all units with the same unit were collected in the first two principal components. The resulting values were then fed either to a model directly predicting the power output, or one predicting wind speed, which then was transformed into power. The direct approach was clearly better than using an intermediate wind speed forecast. Of the five models used, the multilayer perceptron outperformed k-Nearest Neighbor, support vector machine regression, radial basis function network, classification and regression tree, and random forest algorithms. Note that the available power measurement data were only 3 months long. In another paper, [Kusiak and Li \(2010\)](#) clustered 10-sec observations from only one week of data from a single wind turbine and compared the mentioned five models.

For statistical power curve modeling, [Pinson et al. \(2008a\)](#) demonstrated the advantage of orthogonal fitting at each point of the power curve, claiming that the usual way assumes noise only in the power, not in the predicted wind speed. “This assumption is not realistic for the wind power forecasting application, when the wind-to-power conversion function is estimated with meteorological forecasts as explanatory variables.”

An interesting hybrid approach was described by [H.Aa. Nielsen et al. \(2007a\)](#). The statistical power curve estimation of WPPT was initialized using the wind farm power curve from WAsP, in the way Prediktor uses it. The advantage was most pronounced for the first few months of operation of the model, and for wind power classes where only few data points were available. For example, for wind speeds above 10 m/s, the NRMSE is reduced with over 30% in the first 6 months.

[Barthelmie et al. \(2009\)](#) surveyed a number of short-term prediction providers as to their implementation of explicit wake modeling in the short-term prediction model,

and found that in most models, the direct estimation of a wind farm power curve from measured data and predicted wind data obviates the need for an actual wake model, as it is implicitly taken into account.

### 3.5 Upscaling models

Many larger end-users are more interested in the result for a region than for a single wind farm, e.g., an electrically defined region as for TSOs or a market region as for traders. In only very few cases, typically where wind power only took off in the last few years, there is online data available for all turbines in a region. In many cases though, like in Denmark, the production data for most wind turbines are only available from the accounting system for payments for the wind turbine owners, with a delay of up to a month. This means that for the purposes of an online forecast, it is useless (it can be used for a MOS system). Therefore, a correlation has to be found between a few wind farms delivering online data within a region, and the much later determined total regional production.

Since not all wind farms in a region see the same wind speed at the same time, and since the error made by the NWP is temporally and spatially distributed, the error for forecasting a region is smaller than the error for a single wind farm. In this context it is interesting to investigate the spatial correlations between both the wind power generation and the wind power forecasting errors, as it is the uncorrelated part of the error that generates the error improvement due to spatial smoothing.

The variability of an averaged time series, e.g., expressed as the relative standard deviation of this time series, depends on the respective variability of the single time series, and on the correlation between the various series. For wind power forecasting, there are two effects that reduce the forecast error for a region in comparison to the one of a single wind farm: the generation as such is already smoother for a region due to the uncorrelated frequencies of the single wind farm generation profiles, making it thereby more easily predictable, and the forecast errors are uncorrelated on an even smaller length scale. For the former issue, refer to the literature overview given by [Giebel \(2005a\)](#). In most studies, the generation correlation vanishes on a length scale of about 750 km.

The methodically most relevant study on the subject was made by [Lange and Focken \(2005b\)](#) and [Focken et al. \(2002\)](#). They applied power measurements on 30 wind farms in Germany to study the accuracy of the aggregated power output of wind farms distributed over given regions.

[Rohrig \(2005\)](#) presents the German experience from the day-ahead forecast (24–48 h ahead regarding the start of forecast model at the weather service): Single wind farm: 10%–20% (RMSE % of nominal capacity)—single control area: 3.5%–6.8%—all control areas (whole Germany): 2.6%–5.7%. Further reductions can be expected from combining different forecasting models: The first results from Germany show the best model performing at 5.1% RMSE, a “simple” combination 4.2% and “intelligent” combination 3.9%.

Likewise, for Finland [Holttilin et al. \(2006\)](#) present a reduction in forecasting error from up to 16% for the single site 24-h ahead forecast down to about 10% for the total

error of four wind farms with a maximum spacing of about 380 km. “The Mean Absolute Error (MAE) normalized by installed capacity is between 11%–15% for 12 h ahead for one site. Assuming the same installed wind power capacity in all 4 sites this drops the forecast error to 9%. For 36 h ahead, one site errors are 13%–18% and aggregated error drops to 11%.” For combining the predictions of East and West Denmark in 2001, [Holttinen \(2006\)](#) finds a reduction of prediction error of 9%.

Upscaling has also been a topic in the ANEMOS project ([Nielsen et al., 2006a](#)). For Jutland, a reduction down to 6.2% NMAE is reported, while for Ireland, the error only reduces to 11.6%. Within that framework, [Siebert and Kariniotakis \(2006\)](#) and [Siebert \(2008\)](#) in his PhD thesis have quantified the smoothing effect on the prediction errors from the aggregation of wind farms and looked into the optimal number of reference wind farms for the Jutland/Fyn area. Out of a total of 23 available wind farms, the optimal number of reference wind farms was shown to be only 5. This surprisingly low number is a combination of the sufficient coverage of those five farms of the main meteorological regions in the area, plus the very good data quality those five could offer. More wind farms would have led to more noise in the input signal for the upscaling algorithm.

## 3.6 Spatio-temporal forecasting

In the early days of the development, some models were developed using translatorial models, essentially trying to get an idea of the upstream wind field and just advecting the features found toward the site in question. More recently, with larger computing power and better data handling facilities, the addition of upstream data as additional model input has received some attention.

[Papke et al. \(1993\)](#) used a data assimilation technique together with three models to get a forecast of about 1 h ahead for the wind fed into the Schleswig grid in the German land of Schleswig–Holstein. These three models were a statistical model, analyzing the trend of the last 3 h, a translatorial model that moved a measured weather situation over the utility’s area, and a meteorological model based on very simple pressure difference calculations. No accuracy was given. The translatorial model developed into the Pelwin system. On a time scale of 1 h, the weather fronts coming over the North Sea to Schleswig–Holstein are predicted to anticipate high negative gradients due to the shutdown of wind turbines.

Another translatorial model was proposed by [Alexiadis et al. \(1998, 1999\)](#), which uses a cleaning of local influence much like the methodology used in the European Wind Atlas. The spatial correlation predictor avoids the drawback of the usual constant delay method and shows improvements over the latter of up to 30% and more. The same data have been analyzed by [Barbounis and Theocharis \(2007\)](#), using a local recurrent neural network, and by [Damousis et al. \(2004\)](#) using a fuzzy model trained by a genetic algorithm-based learning scheme.

[Larson and Gneiting \(2004\)](#) developed a forecast algorithm using off-site observations in the vicinity of the wind farm and applying statistical space-time modeling. They used linear regression, neural networks, conditional neural networks,

as well as support vector machines and found improvements over persistence in the range of 7%–37% in the best cases. Adding 5-km resolution MM5 forecasts helped the forecasts even further ([Larson and Westrick, 2006](#)).

[Tastu et al. \(2011\)](#) analyzed the auto- and cross-correlations of the forecast errors between five regions in Western Denmark, and found that “there exists in general a significant cross-correlation between forecast errors for neighbouring areas with lags of a few hours. For the present case study, lags with significant dependency are up to 5 h, while the lags with most effect are the 1- and 2-h lags. This cross-correlation pattern is clearly conditioned by the prevailing weather situation, mainly characterized by wind speed and direction. Wind direction is shown to play a crucial role.” Wind direction can be taken into account by a standard regime switching model, but the wind speed dependency required to use a conditional parametric regime switching models. [Tastu et al. \(2010\)](#) used a conditional parametric vector autoregressive model to take the other regional measurements into account in Western Denmark and found a reduction in RMSE for the hour ahead forecast of up to 18.5%.

[Lange et al. \(2008\)](#) and [Wessel et al. \(2009a,b\)](#) used data from the 30 m level of 30 wind measurement masts alongside the usual input of the WPMS, NWP fields from the DWD’s CosmoDE model and power data from 68 reference wind farms distributed over all of Germany. For the first few hours, the addition of wind speeds gives only a slight improvement in overall NRMSE. However, the “forecast accuracy is improved significantly for short forecast horizons especially at high wind speed cases” where the power signal does not contain any information, since the power curve is flat in that area. “The NRMSE for situations with more than 90% full load is reduced by up to 20%.”—“Remarkable is that the additional input from the measurements takes effect up to forecast horizon up to eight hours. This is hardly to explain, as one would expect an approximation of the nRMSE values of the different models at higher forecast horizons, when the influence of the measurements on the forecast decreases.”

[Jursa and Rohrig \(2008\)](#) developed a technique for the automatic choice of input parameters and internal model parameters, based on particle swarm optimization and differential evolution. “For the variable selection we constructed time delay vectors from data from 30 wind farm locations in an extended area. The optimization algorithms were used to find those time delay vectors which are optimal for the prediction of one wind farm.” For 10 wind farms in Germany, a marked improvement was seen in comparison to manually specified forecasting models.

A special case of this is the visualization proposed by [Cutler \(2008, 2009\)](#) and [Cutler et al. \(2009\)](#). He uses something akin to a measure-correlate-predict technique for the wind field coming from the grid points of the NWP, to yield a site-equivalent wind speed. In this way, the orographic and other surface effects are taken out of the upstream field, and it is easier for the operator to assess the incoming fronts. Even the superposition of those fields for a number of wind farms is possible. An assessment of the spatial uncertainty using several grid points similar to the temporal uncertainty used for the Meteo Risk Index of Armines/MINES ParisTech has also shown good potential ([Cutler et al., 2008](#)).

### 3.7 Ramp forecasting

In the early days of wind power, installations in, e.g., Denmark and Germany were small and well distributed. This led to a quite smooth wind power feed. In recent years though, especially in the new markets such as Australia, the United States, or Canada, wind farms (generally offshore) are installed in 400 MW or even larger blocks. This leads to a much larger possibility for quick variations or ramps. Those bring challenges to the personnel in the control room, as the wind feed can suddenly decrease several GW, going far out of the bounds of the usual spinning reserve requirements. Recently, there has been focus on developing dedicated short-term forecasting approaches for large and sharp wind power variations, so-called ramps. Accurate forecasts of specific ramp characteristics (e.g., timing, intensity, and probability of occurrence) are important, as related forecast errors may lead to potentially large power imbalances, with a high impact on the power system.

Ramps were first taken into account as a forecasting requirement in the pilot project of the Alberta Electric System Operator (AESO) in 2006. The purpose of the AESO pilot project was to trial different methods and vendors of wind power forecasting to determine the best approach to forecasting wind power in Alberta in the future. Three vendors were chosen with global forecasting experience: AWS Truewind (New York), energy & meteo systems (Germany), and WEPROG (Denmark). Each vendor forecasted for 12 geographically dispersed wind power facilities for one year (May 07 to May 08) providing a number of forecast products covering the next 48 h and an hourly refreshment rate. A final report written by ORTECH exists ([McKay, 2008](#)).

[Zack \(2007\)](#) pointed out the importance of understanding of the physical processes leading to large ramps, with the example of a complex meteorological phenomenon at the San Gorgonio pass in California. He then proposed to use event-based forecasting specifically for events important to the users. Those considerations eventually led to the development of the ELRAS, the ERCOT (Electricity Reliability Council Of Texas) Large Ramp Alert System ([Zack et al., 2010](#)). They use a 3DVAR data assimilation system of many freely available meteorological data in and around Texas as a starting point for the ELRAS-RUC (Rapid Update Cycle) model, which is an NWP model run every 2 h. The results of this feed a set of early detection mechanisms, which finally are used in a regime switching statistical model. As a metric for the ramp forecast, they use the Critical Success Index (CSI), defined as  $\text{number\_of\_hits}/(\text{number\_of\_hits} + \text{number\_of\_false\_alarms} + \text{number\_of\_misses})$ , and the Ranked Probability Skill Score (RPSS). [Greaves et al. \(2009\)](#) show a user-friendly way of showing up- and down-ramps with their timing uncertainty and projected level. A promising approach to ramps and variability forecasting is the use of state-transition or of regime-switching models.

[Bossavy et al. \(2013\)](#) and [Bossavy \(2012\)](#) proposed a method for the probabilistic forecasting of ramps based on ensemble NWPs. The aim is to predict the probability of occurrence of ramps as well as the ramps timing and intensity. An example is illustrated in [Fig. 3.3](#). Mapping the number of ensemble members forecasting a specific

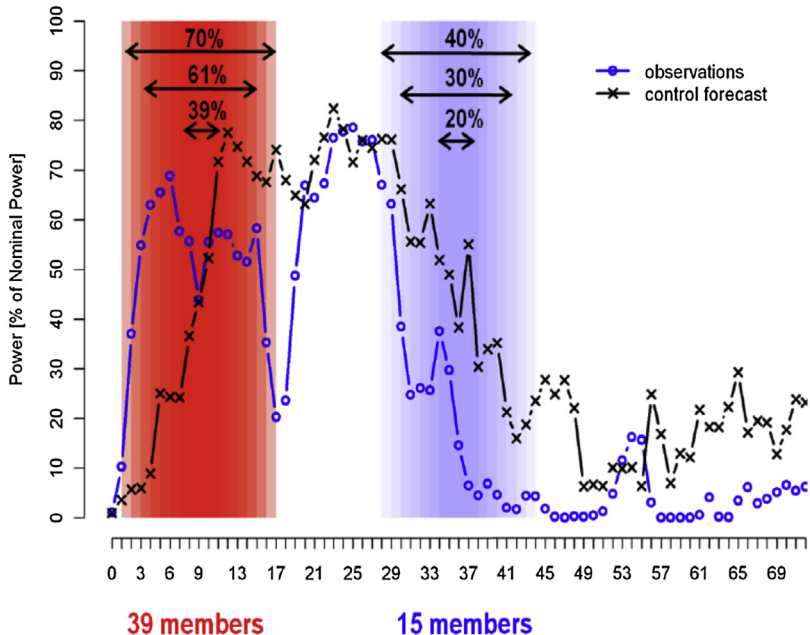


**Figure 3.3** Example of probabilistic forecast of upwards and downwards ramps based on ensemble numerical weather predictions ([Bossavy, 2012](#)).

ramp event to a probability of that ramp actually occurring, permitted to produce confidence intervals of ramps occurring. The authors recognize as a major challenge the definition or the characterization of a ramp itself. In the literature no common definition is available, while definitions range from a simple differentiation of wind power time series and consideration of a threshold for the differences above which a ramp is assumed to occur, up to more sophisticated definitions. [Bossavy et al. \(2015\)](#) propose a comprehensive framework for evaluating and comparing different characterization approaches of wind power ramps. As a first step, they introduce a theoretical model of a ramp inspired from edge-detection literature. The proposed model incorporates some important aspects of the wind power production process so as to reflect its nonstationary and bounded aspects, as well as the random nature of ramp occurrences. Then, they introduce adequate evaluation criteria from signal-processing and statistical literature, to assess the ability of an approach for reliably estimating ramp characteristics (i.e., timing and intensity). The evaluation results show that some practical choices in wind energy literature like the simple differentiation of the signal are inappropriate, while others, namely, from signal-processing literature, are preferable.

Bonneville Power Administration (BPA) ([Pease, 2008](#)) held a competition dedicated for ramp forecasting. The first results ([Pease, 2009](#)) indicated that for ramps, hourly predictions are not good enough, and shorter timings of the forecast lead to smaller deviations. However, as [Focken \(2010\)](#) points out, in the subsequent request for proposals for a short-term prediction system, ramps are not mentioned at all.

Focken (having been part of the ramp forecasting competition with his company energy & meteo systems) attributes this to the fact that a ramp does not have an action in the control room associated with it—“the operators don’t know what to do with a ramp forecast”. In the remainder of his talk he points out that the ramp forecast needs to be something separate from the usual RMS-optimized forecast, since this tends to be too smooth.

### 3.8 Variability forecasting

While ramp forecasting and variability forecasting bear some resemblance, the two are actually quite different. Variability forecasting refers to large amplitude, periodic changes in wind speed, and it is only recently that it has come into the sight of researchers. [Davy et al. \(2010\)](#) defined an index of variability based on the standard deviation of a band-limited signal in a moving window, and developed methods to statistically downscale reanalysis data to predict their index. Among the important predictors of variability, they found planetary boundary layer height, vertical velocity, and U-wind speed component during the months June–September (southern hemisphere winter), and U-wind speed, geopotential height, and cloud water for the months December–February (southern hemisphere summer).

[Vincent et al. \(2010a,b\)](#) defined a variability index as the sum of all amplitudes occurring within a given frequency range based on an adaptive spectrum. They studied the climatological patterns in variability on time scales of minutes to 10 h at the Horns Rev wind farm, and showed that there were certain meteorological conditions in which the variability tended to be enhanced. For example, variability had a higher average amplitude in flow from sea than in flow from the land, often occurred in the presence of precipitation and was most pronounced during the autumn and winter seasons.

[Von Bremen and Saleck \(2010\)](#) proposed the *totalfluc*, the sum of the absolute values of gradients exceeding a certain threshold within a, say, 6 h period, as a measure of variability. The variability of wind speed data from the FINO one site, converted to power with the power curve of the nearby Alpha Ventus offshore wind farm, was highest around 10 m/s wind speed. A clustering analysis of the principal components of the 500 hPa geopotential height showed that the largest variations occurred for north-western flow.

### 3.9 Uncertainty of wind power predictions

Spot predictions of the wind production for the next 48 h at a single wind farm or at a regional/national level are a primary requirement for end users. However, for an optimal management of the wind power production it is necessary to also provide end users with appropriate tools for online assessment of the associated prediction risk. Confidence intervals are a response to that need since they provide an estimation of the error linked to power predictions. Essentially, two main methodologies for

uncertainty forecasting have established themselves in the industry: statistical approaches working on single NWP forecasts and uncertainties derived from ensembles of predictions. A state of the art in probabilistic forecasting was published by the ANEMOS consortium ([Juban](#)).

The evaluation of probabilistic forecast is of primary importance to develop appropriate models. [Pinson et al. \(2007b\)](#) describe the properties of probabilistic forecasts and propose a framework for their evaluation composed of measures like reliability, sharpness, resolution, and skill. Practical examples are given.

### 3.9.1 Statistical approaches

While the estimation of confidence intervals for various types of mathematical models is an established field, in the area of wind power prediction first models were developed within the EU project ANEMOS (2002–06). While statistical models already have an estimate of the uncertainty explicitly integrated in the method, physical models need some additional processing to yield an uncertainty result as well.

Typical confidence interval methods, developed for models like neural networks, are based on the assumption that the prediction errors follow a Gaussian distribution. This however is often not the case for wind power prediction where error distributions may exhibit some skewness, while the confidence intervals are not symmetric around the spot prediction due to the form of the wind farm power curve. On the other hand, the level of predicted wind speed introduces some nonlinearity to the estimation of the intervals; e.g., at the cut-out speed, the lower power interval may suddenly switch to zero.

[Pinson and Kariniotakis \(2010\)](#) propose a generic method for the provision of prediction intervals based on the resampling approach. An example of such forecasts is shown in [Fig. 3.4](#). This approach provides situation-specific uncertainty information that can be associated to spot forecasts generated by either physical or statistical wind power forecasting models. To avoid a restrictive assumption on the shape of forecast error distributions, focus is given to an empirical and nonparametric approach

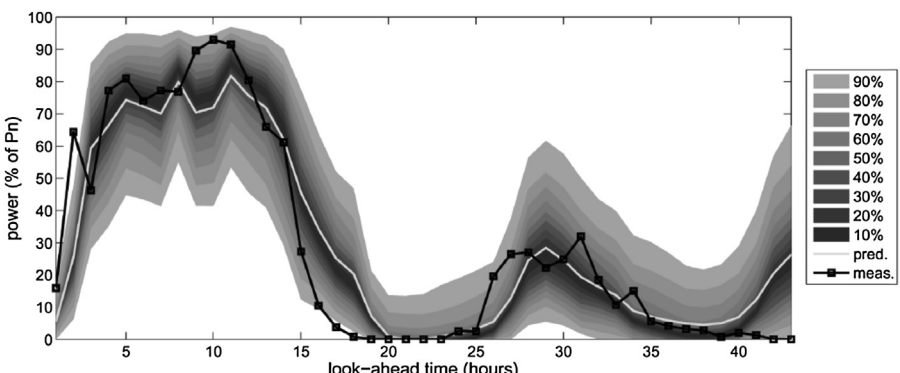


**Figure 3.4** Example of wind power point predictions associated with a set of interval forecasts ([Pinson and Kariniotakis, 2010](#)).

named adapted resampling. The approach employs a fuzzy inference model that permits to integrate expertise on the characteristics of prediction errors for providing conditional interval forecasts.

The limits introduced by the wind farm power curve (min, max power) are taken into account by the method proposed by [Luig et al. \(2001\)](#) and [Bofinger et al. \(2002\)](#). This method models errors using a  $\beta$ -distribution, the parameters of which have to be estimated by a postprocessing algorithm. This approach is applicable to models that use a well-defined wind park power curve.

[Lange and Waldl \(2001\)](#) and [Lange and Heinemann \(2002\)](#) classified wind speed errors as a function of look-ahead time. The errors in wind speed of the older DWD Deutschlandmodell are fairly independent of the forecast wind speed, except for significantly lower errors for the 0 and 1 m/s bins ([Lange and Waldl, 2001](#)). Another result was only for some wind farms did the error depend on the *Grosswetterlage* (a classification system with 29 classes for the synoptic situation in Europe), as classified by the DWD. Due to the nonlinearity of the power curve, wind speed forecasting errors are amplified in the high-slope region between the cut-in wind speed of the turbine and the plateau at rated wind speed, where errors are damped. [Landberg et al. \(2002\)](#) reported the same behavior. [Nielsen \(2002\)](#) also shows the WPPT error for western Denmark to have its peak at a forecast of half the installed capacity. This method is only applicable to models that provide intermediate forecasts of wind speed at the level of the wind park.

[Bremnes \(2002\)](#) developed a probabilistic forecasting technique, estimating the different quantiles of the distribution directly. [Bremnes \(2004\)](#) describes his method of local quantile regression (LQR) in more detail, and shows that for a test case in Norway, Hirlam forecasts have a lower interquantile range than climatology, which means that the Hirlam forecasts actually exhibit skill. LQR Hirlam features about 10% better in economic terms than pure Hirlam forecasts, increasing the revenue from ca 75%–79% of the ideal income (without any forecast errors) to ca 79%–86%, depending on the horizon. However, his pure Hirlam forecasting did not have an upscaling or MOS step, so this might have worked in favor of LQR in the comparison. He proposed to use the method to reduce the large amount of information found in meteorological ensembles. The motivation for this was that he could show that the economically optimal quantile was not the central (“best”) quantile, but one given by the relative prices of up- and down-regulation. [Bremnes \(2006\)](#) compares three different statistical models for quantile forecasts: LQR, the local Gaussian model (assuming that, around the forecasted values the distribution can be approximated with a Gaussian) and the Nadaraya–Watson Estimator. Applied to a wind farm in Norway with Hirlam10 forecasts, no clear preference of method is found, although the local Gaussian model produces slightly more uncertain forecasts than the other two methods. So if ease of implementation is an issue, the Nadaraya–Watson Estimator might be the best. Similar exhaustive comparison of probabilistic models is carried out also by [Juban et al. \(2008\)](#).

Nielsen and Madsen developed a stochastic model for Eltra, describing variance and correlation of the forecast errors of WPPT, version 2. [Nielsen et al. \(2004a, 2006b\)](#) tried a method similar to the LQR technique for the case of the small Danish

offshore wind farm Tunø Knob, using WPPT with various parameters as input. They concentrated on the 25% and 75% quantiles. Also here, the predictions proved “sharp” in comparison to historic data, meaning that the Inter-Quantile Range (IQR), given as the difference between the 75% and the 25% quantile, is much narrower than the historical average of the quantiles of the production distribution. There were deviations in quantiles between the training set and the test set.

These are results for single wind farms. Since the correlation between forecast errors is rather weak with distance, the forecasts for a region are much more accurate than the forecast for single wind farms [as Focken points out ([Focken et al., 2001b, 2002](#))]. This error reduction scales with the size of the region in question. This means that only a certain number of wind farms are needed to predict the power production in a region well enough. For regions, the error autocorrelation is also stronger on a time scale of days than for single wind farms.

[Dobschinski et al. \(2008\)](#) evaluated and compared five different models (multilinear regression, linear quantile regression, ANNs, simple classification, adaptive model) to estimate dynamic prediction intervals of existing wind power forecast systems. Their performance concerning reliability differs significantly but their sharpness is nearly equal. The results of all models have been combined in an ensemble model, which results in a higher quality of forecast uncertainty estimation. Regarding the sharpness it leads to an improvement of about 11% compared to the single models. Concerning the total German wind power generation an improvement of about 25% is obtained when using the up-scaled ensemble average prediction intervals compared to the reference static approach. It was also shown, that the advantage to use the ensemble model instead of each of the single models increases for higher reliabilities and decreasing quality of the underlying power prediction system.

In recent years, several works have been based on the use of the analog ensemble approach for both deterministic and probabilistic forecasting of different quantities like wind speed or power. The analog ensemble prediction of a given variable is constituted by a set of measurements of the past, concurrent to the past forecasts most similar to the current one. The method is found to compete well with other methods in the state of the art like quantile regression, while it is reported to exhibit more skill to rare events ([Alessandrini et al., 2015](#)). Although it involves the construction of ensembles from the historical data it is quite different from the approach described in the next section based on meteorological ensembles.

### **3.9.2 Ensemble forecasts, risk indices, and scenarios**

The increase in available computer power led to some progressive thinking on how to make the best use of these resources. Instead of just increasing the resolution more and more, the processing cycles might be better used in reducing the other errors. This can be done using ensembles of forecasts, either as a multimodel ensemble, using many different NWP models of different parameterizations within the same model, or by varying the input data and calculating an ensemble based on different forecast initializations. The use of this is to be able to quantify the uncertainty inherent in the forecasts. For example, if a slight variation in the initial state of the model (which still is

consistent with the measured data) leads to a larger variation a few days ahead, where, e.g., a low pressure system takes one of two distinct tracks, then the situation is different from one where all low pressure tracks more or less run over the same area. A number of groups in the field are currently investigating the benefits of ensemble forecasts.

[Giebel et al. \(1999\)](#) and [Waldl and Giebel \(2000\)](#) investigated the relative merits of the Danish HIRLAM model, the Deutschlandmodell of the DWD and a combination of both for a wind farm in Germany. There, the RMSE of the Deutschlandmodell was slightly better than the one of the Danish model, while a simple arithmetic mean of both models yields an even lower RMSE. [Giebel and Boone \(2004\)](#) extended this analysis to additional wind farms and used two different short-term prediction models for the analysis. The result is the same, that a combination of models is helpful. [H.Aa. Nielsen et al. \(2007b\)](#) showed that the combination of models can always be better than the best of the two input models, and that in most cases even a simple average outperforms the best of the models. In their paper, they develop the theory of how to combine forecasts if bias and variance/covariance of the individual forecasts are known. They try their approach for two wind farms in Denmark (Klim) and Spain (Alaiz) with up to four individual forecasts per wind farm, all done by WPPT with different NWP input. This “resulted in improvements as high as 15%, with an overall level of 9%, for the wind farm near Klim in Denmark. For the wind farm near Alaiz, the corresponding numbers are 9 and 4%, respectively. However, for Alaiz if one meteorological forecast and three different combinations of MOS and power curve are used, then no improvement is obtained.”

In the framework of the Danish PSO-funded project Intelligent Prognosis, [Nielsen et al. \(2007a\)](#) showed generic figures for the potential improvement of an additional NWP forecast depending on the correlation between the forecasts and the relative performance. The figures were verified for the Klim wind farm in Denmark and Alaiz in Spain. It “is recommended that two or three good meteorological forecasts are used and the forecast errors of these should have low correlation (less than approximately 0.8). This seems to be the case for meteorological forecasts originating from different global models.”

[Landberg et al. \(2002\)](#) used a poor man’s ensemble to estimate the error of the forecast for one wind farm. A poor man’s ensemble is formed using the overlapping runs of the forecasting model from different starting times for a given point in time. In his case, HIRLAM comes every 6 h with a model horizon of 48 h, leading to an ensemble size of up to eight members for the same time. The assumption is that when the forecasts change from one NWP run to the next, then the weather is hard to forecast and the error is large. However, no conclusive proof for this intuitive assumption could be found. Please also note that the term poor man’s ensemble in meteorological circles can also be used to denote a multimodel ensemble from various meteorological institutes. This probably reflects the fact that they do not have to pay the end user prices when exchanging data among themselves. Another expression occasionally used for this type of ensembles is lagged average ensembles or lagged initial conditions ensembles.

Möhrlen et al. (2002) use a multischeme ensemble of different parameterization schemes within HIRLAM. They make the point that, if the observational network has a spacing of 30–40 km, it might be a better use of resources not to run the NWP model in the highest possible resolution (in the study 1.4 km), but instead to use the computer resources for calculating a large amount of forecasts and generate an ensemble. A doubling of resolution means a factor 8 in running time (since one has to double the number of points in both horizontal grid components and time). The same effort could therefore be used to generate eight ensemble members. The effects of lower resolution would not be so bad, since effects well below the spacing of the observational grid are mainly invented by the model anyway, and could be taken care of by using direction-dependent roughnesses instead.

Their group was also coordinator of an EU-funded project called HONEYMOON—High resOlution Numerical wind EnergY Model for On- and Offshore forecastiNg using ensemble predictions. One part of the project was to reduce the large-scale phase errors using ensemble prediction.

WEPROG's MSEPS (see [weprog.com](http://weprog.com)) has been operational since 2004. Based on WEPROG's own NWP formulation, the system is built up with three different dynamics schemes, five different condensation schemes, and five different vertical diffusion schemes, which result in an ensemble of 75 members. The characteristic of the MSEPS system is that it has the capabilities to develop physical uncertainties with well-defined differences among the ensemble members. This is of advantage especially for wind energy predictions, because it means that the uncertainty is not dependent on the forecast horizon as in other ensemble approaches, but instead develops in every forecasts step as a result of the physically different formulations of the individual ensemble members (e.g., Möhrlen and Jørgensen, 2006 or <http://www.weprog.com/publications>).

Lange et al. (2006d) used input from 16 different European met services for Pre-viento to run a forecast combination. They tried to combine up to five different NWP forecasts and showed that the combination is quite advantageous if the forecasts based on different NWPs first have been individually tuned. This way, a reduction of forecast errors from 5% to 4.2% RMSE for all of Germany was achieved. Similar results have been reported from the IWES by Cali et al. (2008a,b), where the best combination coming out of the 75 members of the MSEPS is achieved after first tuning the ANNs individually for every member, and then training a second ANN to combine the optimized forecasts. Cali et al. (2008b) also showed that the combination of three NWP models for the whole of Germany reduces the RMSE from between 5.8% and 6.1% for the individual models to 4.6%. Using all 75 members of the MSEPS as input to the neural networks of WPMS, instead of just the ensemble mean or a single member, reduced the error considerably.

In Denmark, the Zephyr collaboration had a PSO-funded 3-year project (Giebel et al., 2004) on the use of different kinds of ensembles for utility grade forecasting. Among others, the NCEP/NCAR and ECMWF ensembles were used, multimodel ensembles (with input from both DMI and DWD) were compared, and some methods for a good visual presentation of the uncertainty were researched. One main result (Nielsen et al., 2004b) was the development of a technique to transform the quantiles

of the meteorological distribution to the quantiles of the power forecast distribution. The resulting quantiles were sharp and skillful. The use of pure meteorological ensemble quantiles was shown to be insufficient, since the ensemble spread is not probabilistically correct. Even using the transformation it was not possible to get satisfactory outer quantiles (e.g., below 15% and above 90%), since the meteorological ensemble spread is not large enough. This is especially relevant for the first days of the ensemble runs. However, in practice this might be less of a problem, since the ensemble runs also needed 17 h to complete, therefore making the first day impossible to use operatively. The model was used in a demo application run for two Danish test cases, the Nysted offshore wind farm and all of the former Eltra area (Denmark West). The results were quite satisfactory, have a horizon of one week, and were used for maintenance scheduling of conventional power plants, for the weekly coal purchase planning and for trading on the Leipzig electricity exchange, which is closed over the weekends. Besides a final project report (Giebel, 2005b), a number of more detailed reports on the model (Nielsen et al., 2005a), the experiences with the demo application (Nielsen et al., 2005b), the possibilities of nesting HIRLAM directly in the ECMWF ensemble members (Feddersen and Sattler, 2005), and some special turbulent kinetic energy parameterisations within HIRLAM (Boone et al., 2005) came out.

Roulston et al. (2003) evaluated the value of ECMWF forecasts for the power markets. Using a rather simple market model, they found that the best way to use the ensemble was what they called climatology conditioned on EPS (the ECMWF Ensemble Prediction System). The algorithm was to find 10 days in a reference set of historical forecasts for which the wind speed forecast at the site was closest to the current forecast. This set was then used to sample the probability distribution of the forecast. This was done for the 10th, 50th, and 90th percentile of the ensemble forecasts.

Taylor et al. (2009) create a calibrated wind power density from the ECMWF EPS system. “The resultant point forecasts were comfortably superior to those generated by the time series models and those based on traditional high-resolution wind speed point forecasts from an atmospheric model.”

Pinson and Madsen (2009) “describe, apply and discuss a complete ensemble-based probabilistic forecasting methodology” for the example, case of Horns Rev as part of the Danish PSO research project “HREnsembleHR—High Resolution Ensemble for Horns Rev, funded by the Danish PSO Fund from 2006 to 2009 (see [www.hrensemble.net](http://www.hrensemble.net)). The forecasts from WEPROG’s 75 member MSEPS ensemble are converted to power using the novel orthogonal fitting method. The single forecasts are then subjected to adaptive kernel dressing with Gaussian kernels, since “in theory, any probabilistic density may be approximated by a sum of Gaussian kernels”, meaning that the resulting probabilistic distribution can be “a non-symmetric distribution (and possibly multimodal), thus being consistent with the known characteristics of wind power forecast uncertainty”.

Pinson et al. (2008b) introduced a new concept for skill forecasting, named the **Prediction Risk Index**, that measures the spread of lagged average ensembles or classical ensembles and associates it to the level of prediction error of the forecasting

model. This model can be thus used to predict the level of error in a period in the future (i.e., day ahead).

In several applications it is necessary to have multiple alternative spot forecasts in the form of **scenarios**. Such forecasts can be generated from probabilistic (pdf) forecasts as proposed by [Pinson et al. \(2009\)](#). To generate such scenarios it is necessary to take into account the spatial correlations among the wind farms considered as well as the temporal correlations of the forecasts in consecutive look-ahead times. [Pinson and Girard \(2012\)](#) propose a formal method to evaluate the quality of such scenarios.

### 3.10 The ANEMOS projects and other major R&D activities

The ANEMOS project (“Development of a Next Generation Wind Resource Forecasting System for the Large-Scale Integration of Onshore and Offshore Wind Farms”) was a 4-years R&D project that started in October 2002. It was funded by the European Commission under the fifth Framework Program (ENK5-CT-2002-00665). A number of 22 partners participated from seven countries including research institutes, universities, industrial companies, utilities, TSOs, and energy agencies. This project put together for the first time the major European actors in the field under an ambitious research project that permitted significant advances in various topic including probabilistic models, physical modeling prestandardization of forecasting systems etc.

A coordination action called POW’WOW (Prediction of Waves, Wakes and Offshore Wind, see [powwow.risoe.dk](http://powwow.risoe.dk)) was the next step for the core partners, together with experts on waves and wakes. It ran from 2006 to 2009, funded also by the European Commission [Contract No 019898(SES6)].

As the major follow-up, two projects were developed [ANEMOS.plus](#) and [SafeWind](#) both supported by the European Commission. The former (Contract No 038692, sixth Framework Program, 2008–11, 22 partners) had a strong demonstration aspect, focusing on the maximum benefit for the end users through tools to schedule power plants and storage, to better trade on the markets, to integrate wind on shorter times, to manage congestions, to manage island systems, and other applications. The aim was to develop and demonstrate at real-world environments stochastic decision making and optimization tools capable to take into account uncertainties related to renewables forecasting.

More research studies were done in the latter, [SafeWind](#) (Grant Agreement no 213,740, 6th Framework Program, 2008–12, 22 partners). Here, the main emphasis was on extreme events, be it meteorologically, electrical system wise or financially extreme. [Pinson and the SafeWind Consortium \(2010\)](#) have compiled a catalog of extreme events, which resulted of a poll among project participants. Most importantly, an extreme event was very user dependent. A meteorologist would answer “a significant deviation from climatology”, an actor on the energy system would answer that it needs to have sizable consequences either financially or for the system safety, and an operator of wind farms is interested in small scale events that could be dangerous

for the turbines. As major new partner there is the ECMWF, to improve the use of ensemble products for wind power.

The above three R&D projects produced over the period 2002–12 more than 250 publications at peer reviewed journals and international conferences and gave several tools used in business practices.

A major national R&D project in Europe in the field of renewable energy forecasting in the last years has been the EWELINE project in Germany ([projekt-eweline](#)). The overarching goal of the project is to improve the wind and PV power forecasts by combining improved power forecast models and optimized weather forecasts. The technical objectives include among other the optimization of weather forecasts toward improved wind power and PV forecasts. Assimilation of new types of data in the NWP models, e.g., power production data, is considered. With regard to probabilistic forecasts, the focus is on the generation of ensembles and ensemble calibration. Emphasis is given also on the optimal use of forecasts.

Another major project was the Wind Forecast Improvement Project (WFIP) in the US (2011–13). Its goal was to improve the accuracy of short-term (0–6 h) wind power forecasts for the wind energy industry. WFIP was sponsored by the US Department of Energy (DOE), with partners that included the National Oceanic and Atmospheric Administration (NOAA), private forecasting companies, DOE national laboratories, grid operators, and universities. WFIP employed two avenues for improving wind power forecasts: first, through the collection of special observations to be assimilated into forecast models and, second, by upgrading NWP forecast models and ensembles ([James Wilczak et al., 2015](#)).

In terms of networking, the COST Action WIRE ES1002 (Weather Intelligence for Renewable Energies) brought together actors from 27 countries (2010–14, <http://www.wire1002.ch>). This network developed a number of activities including an international competition for wind and solar power forecasting.

A large grouping of international experts in short-term prediction gathered in the IEA Wind Task 36 (see [ieawindforecasting.dk](#)) has recently come up with a list of research topics for the coming years ([Giebel et al., 2016](#)). Among other things, rapid update cycle methods are recommended, a better modeled interaction between wind farms, NWP model improvements, and data assimilation of, e.g., wind turbine power.

## 3.11 Conclusions

Short-term forecasting has come a long way since the first attempts at it. Often, running the grid would not be possible without it, in situations with more than 100% instantaneous power from wind in the grid. The current crop of models, typically combining physical and statistical reasoning, is fairly good, although the accuracy is limited by the employed NWP model.

Short-term prediction consists of many steps. For a forecasting horizon of more than 6 h ahead, it starts with an NWP model. Further steps are the downscaling of the NWP model results to the site, the conversion of the local wind speed to power,

and the upscaling from the single wind farms power to a whole region. On all these fronts, improvements have been made since the first models. Typical numbers in accuracy are an RMSE of about 9%–14% of the installed wind power capacity for a 24 h horizon. When it goes up to regional or national forecasting performance is in the order of 3%–5% of installed capacity.

The main error in a short-term forecasting model stems from the NWP model. One current strategy to overcome this error source, and to give an estimate of the uncertainty of one particular forecast, is to use ensembles of models, either by using multiple NWP models or by using different initial conditions within those.

Information and communication technology is expected to play a major role in integrating wind power predictions in the market infrastructure. Another aspect of the “commodification” of short-term prediction is the integration of or into decision making tools for the end users, like the scheduling optimization module or the trading module developed and integrated by ANEMOS.plus.

Although it is recognized today that probabilistic predictions should be considered as input in the various power system management functions, today they are still not as largely used as the deterministic predictions.

Wind power prediction software is not “plug-and-play” since it is always site-dependent. To run with acceptable accuracy when installed to a new site, it is always necessary to devote considerable effort for tuning the models (in an offline mode) based on the characteristics of the local wind profile the local environment of the wind farms. It is here where the experience of the installing institute makes the largest difference. Due to the differences in the existing applications (flat, complex terrain, offshore) it is difficult to compare prediction systems based on available results. An evaluation of prediction systems needs however to take into account their robustness under operational conditions and other factors.

Despite the appearance of multiple similar approaches today, further research is developed in several areas to further improve the accuracy of the models but also to assess the uncertainty of the predictions. Combination models have received due attention. So have ramp and variability forecasts. Efforts to produce efficient probabilistic models and exploit spatio-temporal information continue. Optimal use of the forecasts by the end-users remains a topic. The feedback from existing online applications continues to lead to further improvements of the state of the art prediction systems.

The aim of this chapter was to contribute to the current research on wind power forecasting through a thorough review of the work developed in the area in the last decades. Wind power forecasting is a multidisciplinary area requiring skills from meteorology, applied mathematics, artificial intelligence, energy, software engineering, information technology, and others. It appears as a fairly mature and nearly off-the-shelf technology today, thanks not the least to some European Union Institutes and companies nurturing the field for more than a decade. This has been the result of an early recognition by the EU, as well as the pioneer countries in wind energy, of the necessity to anticipate efficient solutions for an economic and secure large-scale integration of wind power. The expectations from short-term wind power forecasting

today are high since it is recognized as the means to allow wind power to compete on equal footing with the more traditional energy sources in a competitive electricity marketplace. In that perspective, R&D will remain important in the future for improving not only the accuracy of the forecasts but also their value.

## Glossary

<b>a.g.l.</b>	Above ground level.
<b>ANN</b>	Artificial neural network.
<b>DMI</b>	Danish Meteorological Institute.
<b>DTU</b>	Technical University of Denmark.
<b>DSO</b>	Distributor System Operator
<b>DWD</b>	Deutscher Wetterdienst (German Weather Service).
<b>ECMWF</b>	European Center for Medium Range Weather Forecasts, Reading, UK.
<b>EPS</b>	(The ECMWF) Ensemble prediction system.
<b>ESP</b>	Energy service provider.
<b>ETA</b>	One of NCEP's mesoscale models.
<b>FINO</b>	Forschungsplattformen in Nord- und Ostsee, currently three offshore measurement masts in the North Sea (1 and 3) and the Baltic Sea (FINO 2).
<b>GFS</b>	Global forecasting system, an NWP provided globally for free by NOAA.
<b>HIRLAM</b>	High-resolution limited area model, an NWP model developed by the met. Institutes of Denmark, France, Norway, Finland, Spain, and Ireland.
<b>Horizon</b>	The look-ahead time, sometimes used for the maximum an NWP can deliver.
<b>IMM</b>	Informatics and Mathematical Modeling at DTU, Lyngby, Denmark.
<b>IPP</b>	Independent power producer.
<b>ISO</b>	Independent system operator (like a TSO, but does not own the transmission system).
<b>LM</b>	Lokalmodell (an NWP model of the DWD).
<b>LQR</b>	Local quantile regression.
<b>MAE</b>	Mean absolute error.
<b>MM5</b>	Mesoscale Model 5, a formerly popular mesoscale code developed at Pennsylvania State University and NCAR (successor is WRF).
<b>MOS</b>	Model output statistics, a means to remove residual error.
<b>MSEPS</b>	Multi-Scheme Ensemble Prediction System (75 members, by WEPROG).
<b>NCEP/NCAR</b>	National Center for Environmental Protection/National Center for Atmospheric Research, Golden, Colorado, US.
<b>NWP</b>	Numerical weather prediction, usually run by meteorological institutes.
<b>NOAA</b>	National Oceanic and Atmospheric Administration, US.
<b>PBL</b>	Planetary boundary layer, the lowest part of the atmosphere.
<b>Persistence</b>	Simple prediction method assuming that the wind production in the future will be the same as now.
<b>PSO</b>	Public Service Obligation (a research funding scheme in Denmark).
<b>RMSE</b>	Root mean square error.
<b>SCADA</b>	Supervisory control and data acquisition.
<b>TSO</b>	Transmission system operator.
<b>WRF</b>	Weather research and forecasting model, successor to MM5.

## Acknowledgments

Many people in the ANEMOS consortium for comments. Cyril Nedaud for hard surfing. Nuno Pais for finding the complete list of forecasting papers from selected journals. Ben Lumby for typo finding. This work was made possible through financial support from the European Commission, especially in the frame of a Marie-Curie Fellowship JOR3-CT97-5004 granted to Dr. Gregor Giebel and also with the European projects ANEMOS (ENK5-CT-2002-00665), ANEMOS.plus (Grant No. 038692), and SafeWind (Grant No. 213740) funded in part by the European Commission under the fifth, sixth, and seventh Framework Programmes.

The report has gotten input from some colleagues outside the ANEMOS consortium—especially Corinna Möhrlen of WEPROG and Bernhard Lange of IWES. Within ANEMOS, Pierre Pinson (DTU) is acknowledged for additional input and links to papers, as is Ricardo Bessa (INESC TEC). Claire Vincent (DTU Wind Energy) is acknowledged for thorough reviews.

## References

- Ágústsson, H., Ólafsson, H., Rögnvaldsson, Ó., Jonassen, M.O., September 15–16, 2010. On the importance of high spatial resolution and in-situ observations in simulations of the atmosphere in the vicinity of mountains. In: Proceedings of the Atlantic Conference on Eyjafjallajökull and Aviation, Keflavik (IS).
- Ágústsson, H., Ólafsson, H., Jonassen, M., Reuder, J., Rasol, D., Rögnvaldsson, Ó., April 3–8, 2011. Improving high-resolution atmospheric simulations of local weather using in-situ realtime observations from small unmanned aircraft. In: European Geophysical Union General Assembly, Vienna (AT).
- Alessandrini, S., Delle Monachea, L., Sperati, S., Nissen, J.N., April 2015. A novel application of an analog ensemble for short-term wind power forecasting. *Renewable Energy* 76, 768–781. <http://dx.doi.org/10.1016/j.renene.2014.11.061>.
- Alexiadis, M.C., Dokopoulos, P.S., Sahsamanoglou, H.S., Manousaridis, I.M., 1998. Short-term forecasting of wind speed and related electrical power. *Solar Energy* 63, 61–68.
- Alexiadis, M.C., Dokopoulos, P.S., Sahsamanoglou, H.S., 1999. Wind speed and power forecasting based on spatial correlation models. *IEEE Transactions on Energy Conversion* 14 (3), 836–842.
- Anderson, J.L., Anderson, S.L., 1999. A Monte Carlo implementation of the nonlinear filtering problem to produce ensemble assimilations and forecasts. *Monthly Weather Review* 127, 2741–2758.
- <http://www.anemos-plus.eu/>.
- Badger, J., Guo Larsén, X., Mortensen, N.G., Hahmann, A., Hansen, J.C., Jørgensen, H., April 20–23, 2010. A universal mesoscale to microscale modelling interface tool. In: Proceedings of the European Wind Energy Conference, Warsaw (PL).
- Bailey, B., Brower, M.C., Zack, J., March 1–5, 1999. Short-term wind forecasting. In: Proceedings of the European Wind Energy Conference, Nice, France, ISBN 1 902916 00 X, pp. 1062–1065. See also <https://www.awtruepower.com/>.
- Balouktsis, A., Tsanakas, D., Vachtsevanos, G., 1986. Stochastic simulation of hourly and daily average wind speed sequences. *Wind Engineering* 10 (1), 1–11.

- Barbounis, T.G., Theocharis, J.B., 2007. Locally recurrent neural networks for wind speed prediction using spatial correlation. *Information Sciences* 177, 5775–5797.
- Barry, D., October 25, 2006. The Irish experience. In: Talk on the Workshop for Best Practice in the Use of Short-term Forecasting of Wind Power, Delft (NL).
- Barstad, I., June 2–6, 2001. Down-scaling of wind in a dynamic framework. In: Proceedings of the European Wind Energy Conference, Copenhagen, Denmark, ISBN 3-936338-09-4, pp. 713–716.
- Barthelmie, R.J., Giebel, G., Cabezon, D., Martí, I., 2009. WP4: An Overview of Wind Turbine Wakes and Short-term Forecasting. Project report for the POW'WOW project. Risø, Roskilde, 19 pp.
- Bechrakis, D.A., Sparis, P.D., 1998. Wind speed prediction using artificial neural networks. *Wind Engineering* 22 (6), 287–295.
- Berge, E., December 2002. Experiences with wind forecasting techniques in Norway. In: Proceedings of the First IEA Joint Action Symposium on Wind Forecasting Techniques, Norrköping, Sweden. FOI - Swedish Defence Research Agency, pp. 59–64.
- Berge, E., Nyhammer, F., Tallhaug, L., Villanger, F., Bremnes, J.b., Køltzow, M.Ø., Smits, J., Knauer, A., 2003. Forecasting Wind and Wind Energy Production in Norwegian Wind Farms. Final report of the NFR project: 138848/212 “Korttidsprognosser for energiproksjon fra vindkraft”. Kjeller Vindteknikk Report number KVT/EB/2003/005. Kjeller (NO).
- Bessa, R.J., Matos, M.A., Costa, I.C., Bremermann, L., Franchin, I.G., Pestana, R., Machado, N., Waldl, H.-P., Wichmann, C., October 2012. Reserve setting and steady-state security assessment using wind power uncertainty forecast: a case study. *IEEE Transactions on Sustainable Energy* 3 (4), 827–837.
- Beyer, H.G., Degner, T., Hausmann, J., Hoffmann, M., Ruján, P., October 10–14, 1994. Short term prediction of wind speed and power output of a wind turbine with neural networks. In: Proceedings of the EWEC '94 in Thessaloniki, pp. 349–352.
- Beyer, H.G., Heinemann, D., Mellinghoff, H., Mönnich, K., Waldl, H.-P., March 1–5, 1999. Forecast of regional power output of wind turbines. In: Proceedings of the European Wind Energy Conference, Nice, France, ISBN 1 902916 00 X, pp. 1070–1073.
- Bofinger, S., Luig, A., Beyer, H.G., April 2–5, 2002. Qualification of wind power forecasts. In: Poster, P. (Ed.), GWP093 on the Global Windpower Conference and Exhibition, Paris, France.
- Boone, A., Giebel, G., Sattler, K., Feddersen, H., 2005. Analysis of HIRLAM Including Turbulent Kinetic Energy. Project report.
- Bossanyi, E.A., 1985. Short-term wind prediction using Kalman filters. *Wind Engineering* 9 (1), 1–8.
- Bossavy, A., December 2012. Characterization and Probabilistic Forecasting of Wind Power Production Ramps (Ph.D. thesis in Energetics). MINES ParisTech (131 pages), Accessible online at: <https://tel.archives-ouvertes.fr/pastel-00803234/document>.
- Bossavy, A., Girard, R., Kariniotakis, G., January 2013. Forecasting ramps of wind power production with numerical weather prediction ensembles. *Wind Energy* 16 (1), 51–63. <http://dx.doi.org/10.1002/we.526>.
- Bossavy, A., Girard, R., Kariniotakis, G., July 2015. An edge model for the evaluation of wind power ramps characterization approaches. Article first published online: 4 May 2014 *Wind Energy* 18 (7), 1169–1184.
- Bremnes, J.B., December 2002. Probabilistic wind power forecasts by means of a statistical model. In: Proceedings of the First IEA Joint Action Symposium on Wind Forecasting Techniques, Norrköping, Sweden. FOI - Swedish Defence Research Agency, pp. 103–114.

- Bremnes, J.B., 2004. Probabilistic wind power forecasts using local quantile regression. *Wind Energy* 7 (1), 47–54.
- Bremnes, J.B., 2006. A comparison of a few statistical models for making quantile wind power forecasts. *Wind Energy* 9 (1–2), 3–11.
- Brown, B.G., Katz, R.W., Murphy, A.H., August 1984. Time series models to simulate and forecast wind speed and wind power. *Journal of Climate and Applied Meteorology* 23 (8), 1184–1195.
- Cabezon, D., Martí, I., San Isidro, M.J., Perez, I., 2004. Comparison of methods for power curve modeling. In: Proceedings to Global Windpower 2004, Chicago (USA).
- Cadenas, E., Rivera, W., 2007. Wind speed forecasting in the South Coast of Oaxaca, Mexico. *Renewable Energy* 32, 2116–2128.
- Cadenas, E., Rivera, W., 2009. Short term wind speed forecasting in La Venta, Oaxaca, México, using artificial neural networks. *Renewable Energy* 34 (1), 274–278.
- Cali, Ü., Jursa, R., Kurt, M., Lange, B., Möhrlen, C., Jørgensen, J., Ernst, B., March 30–April 3, 2008a. Artificial neural network based wind power forecasting using a multi-scheme ensemble prediction model. In: Proceedings of the EWEC, Brussels (BE).
- Cali, Ü., Lange, B., Dobschinski, J., Kurt, M., Möhrlen, C., Ernst, B., May 2008b. Artificial neural network based wind power forecasting using a multi-model approach. In: Proceedings of the 7th International Workshop on Large-Scale Integration of Wind Power and on Transmission Networks for Offshore Wind Farms, Madrid (ES).
- Collins, J., Parkes, J., Tindal, A., 2009. Short term forecasting for utility-scale wind farms - the power model challenge. *Wind Engineering* 33 (3), 247–258.
- Costa, A., Crespo, A., Navarro, J., Lizcano, G., Madsen, H., Feitosa, E., 2007. A review on the young history of the wind power short-term prediction. *Renewable and Sustainable Energy Reviews* 12 (6), 1725–1744.
- Cutler, N., May 2008. Seeing a bigger picture from NWPs to assist power system management during uncertain periods. In: Talk on the 2nd Workshop on Best Practice in the Use of Short-term Forecasting, Madrid (ES), 28.
- Cutler, N., 2009. Characterising the Uncertainty in Potential Large Rapid Changes in Wind Power Generation (Ph.D. thesis). The University of New South Wales, School of Electrical Engineering and Telecommunications, 290 pp.
- Cutler, N., Kepert, J.D., Outhred, H.R., MacGill, I.F., 2008. Characterizing wind power forecast uncertainty with numerical weather prediction spatial fields. *Wind Engineering* 32 (6), 509–524.
- Cutler, N., Kepert, J., Outhred, H., MacGill, I., Kay, M., 2009. Characterising future large changes in aggregated wind power using numerical weather prediction spatial fields. *Wind Energy* 12 (6), 542–555.
- Damousis, I.G., Alexiadis, M.C., Theocharis, J.B., Dokopoulos, P.S., June 2004. A fuzzy model for wind speed prediction and power generation in wind parks using spatial correlation. *IEEE Transactions on Energy Conversion* 19 (2).
- Daniel, A.R., Chen, A.A., 1991. Stochastic simulation and forecasting of hourly average wind speed sequences in Jamaica. *Solar Energy* 46 (1), 1–11.
- Davis, C., Wang, W., Dudhia, J., Torn, R., 2010. Does increased horizontal resolution improve hurricane wind forecasts? *Weather and Forecasting* 25 (6), 1826–1841.
- Davy, R.J., Woods, M.J., Russell, C.J., Coppin, P.A., 2010. Statistical downscaling of wind variability from meteorological fields. *Boundary Layer Meteorology* 135 (1), 161–175.
- Dierer, S., Paus, T.de, Durante, F., Gregow, E., Lange, B., Lavagnini, A., Strack, M., Tammelin, B., 2005. Predicting wind speed for wind energy; progress of the WINDENG project. *Wind Engineering* 29 (5), 393–408.

- Dobschinski, J., Wessel, A., Lange, B., Rohrig, K., Bremen, L.V., Saint-Drenan, M., 2008. Estimation of wind power prediction intervals using stochastic methods and artificial intelligence model ensembles. In: Proceedings of the German Wind Energy Conference DEWEK, Bremen (DE).
- Draxl, C., Hahmann, A.N., Peña, A., Nissen, J.N., Giebel, G., October 18/19, 2010. Validation of boundary-layer winds from WRF mesoscale forecasts with applications to wind energy forecasting. In: Poster and Proceedings at the 9th International Workshop on Large-Scale Integration of Wind Power into Power Systems as Well as on Transmission Networks for Offshore Wind Power Farms, Quebec City (CA).
- Draxl, C., 2012. On the Predictability of Hub Height Winds (Ph.D. thesis). DTU Wind Energy, Risø. [http://orbit.dtu.dk/ws/files/10246050/Ris\\_PhD\\_84.pdf](http://orbit.dtu.dk/ws/files/10246050/Ris_PhD_84.pdf).
- Duncan, T., LeBlanc, M., Morgan, C., Landberg, L., December 9, 2008. Understanding icing losses and risk of ice throw at operating wind farms. In: Proceedings of the Winterwind Conference, Norrköping (SE).
- Durstewitz, M.C., Ensslin, B., Hahn, M., Kilpper, H., 2001. Annual Evaluation of the Scientific Measurement and Evaluation Programme (WMEP). Kassel.
- Durstewitz, M., Dobschinski, J., Khadiri-Yazami, Z., December 9, 2008. Wind power forecast accuracy under icing conditions - general approach, practical applications and options for considering effects of wind turbine icing. In: Proceedings of the Winterwind Conference, Norrköping (SE).
- Dutton, A.G., Kariniotakis, G., Halliday, J.A., Nogaret, E., 1999. Load and wind power forecasting methods for the optimal management of isolated power systems with high wind penetration. *Wind Engineering* 23 (2), 69–87.
- ELSAM, 1996. Final Report on EU JOULE II Project JOU-CT92-0083.
- Enemoto, S., Inomata, N., Yamada, T., Chiba, H., Tanikawa, R., Oota, T., Fukuda, H., June 2–6, 2001. Prediction of power output from wind farm using local meteorological analysis. In: Proceedings of the European Wind Energy Conference, Copenhagen, Denmark, ISBN 3-936338-09-4, pp. 749–752.
- Ernst, B., 2005. Wind power forecast for the German and Danish networks. In: Ackermann, T. (Ed.), *Wind Power in Power Systems*. John Wiley & Sons, Chichester (UK), ISBN 978-0-470-85508-9, pp. 365–382.
- Ernst, B., Rohrig, K., December 2002. Online-monitoring and prediction of wind power in German transmission system operation centres. In: Proceedings of the First IEA Joint Action Symposium on Wind Forecasting Techniques. FOI - Swedish Defence Research Agency, Norrköping, Sweden, pp. 125–145.
- Ernst, B., Oakleaf, B., Ahlstrom, M.L., Lange, M., Möhrlen, C., Lange, B., Focken, U., Rohrig, K., 2007. Predicting the wind. *IEEE Power & Energy Magazine* 5 (6), 78–89.
- Feddersen, H., Sattler, K., 2005. Verification of Wind Forecasts for a Set of Experimental DMI-HIRLAM Ensemble Experiments. DMI Scientific Report 05–01.
- Fellows, A., Hill, D., September 10–14, 1990. Wind and load forecasting for integration of wind power into a meso-scale electrical grid. In: Proceedings of the European Community Wind Energy Conference, pp. 636–640. Madrid, Spain.
- Focken, U., October 16, 2010. Experiences with extreme event warning and ramp forecasting for US wind farms. In: Talk on the 4th Workshop on Best Practice in the Use of Short-term Prediction of Wind Power, Quebec City (CA).
- Focken, U., Lange, M., Waldl, H.-P., June 2–6, 2001a. Previento — a wind power prediction system with an innovative upscaling algorithm. In: Proceedings of the European Wind Energy Conference, Copenhagen, Denmark, ISBN 3-936338-09-4, pp. 826–829.

- Focken, U., Lange, M., Waldl, H.-P., June 2–6, 2001b. Reduction of wind power production error by spatial smoothing effects. In: Proceedings of the European Wind Energy Conference, Copenhagen, Denmark, ISBN 3-936338-09-4, pp. 822–825.
- Focken, U., Jahn, J., Schaller, M., October 14–15, 2009. Transformer congestion forecast based on highly localized wind power. In: Talk on the 8th International Workshop on Large-Scale Integration of Wind Power into Power Systems as Well as on Transmission Networks for Offshore Wind Farms, Bremen (DE).
- Focken, U., Lange, M., Mönnich, K., Waldl, H.-P., Beyer, H.G., Luig, A., March 2002. Short-term prediction of the aggregated power output of wind farms – a statistical analysis of the reduction of the prediction error by spatial smoothing effects. *Journal of Wind Engineering and Industrial Aerodynamics* 90 (3), 139–249.
- Fox, B., Flynn, D., Bryans, L., Jenkins, N., Milborrow, D., Malley, M.O.', Watson, R., Anaya-Lara, O., 2007. Wind Power Integration: Connection and System Operational Aspects. The Institution of Engineering and Technology, London, ISBN 978-0-86341-449-7.
- Frías, L., Pascal, E., Irigoyen, U., Cantero, E., Loureiro, Y., Lozano, S., Fernandes, P.M., Martí, I., 2009. Support Vector Machines in the wind energy framework. A new model for wind energy forecasting. In: Proc. of the 2009 European Wind Energy Conference EWEC'09 Marseille (FR).
- Giebel, G., 2001. On the Benefits of Distributed Generation of Wind Energy in Europe. PhD thesis from the Carl von Ossietzky Universität Oldenburg. Fortschr.-Ber. VDI Reihe 6 Nr. 444. Düsseldorf, VDI Verlag, ISBN 3-18-344406-2.
- Giebel, G., 2005a. Wind power has a capacity credit -a catalogue of 50+ supporting studies. WindEng EJournal. [windeng.net](http://windeng.net).
- Giebel, G., September 2005b. In: Badger, J., Landberg, L., Nielsen, H.A., Nielsen, T.S., Madsen, H., Sattler, K., Feddersen, H., Vedel, H., Tøfting, J., Kruse, L., Voulund, L. (Eds.). Wind Power Prediction Using Ensembles. Risø-R-1527.
- Giebel, G., December 2006. Results from Mesoscale, Microscale and CFD Modelling. Deliverable D4.1b of the Anemos Project. In: Badger, J., Louka, P., Kallos, G., Martí Perez, I., Lac, C., Palomares, A.-M., Descombes, G. (Eds.). Available online from: [Anemos.cma.fr](http://Anemos.cma.fr), 101 pages.
- Giebel, G., Boone, A., November 22–25, 2004. A comparison of DMI-Hirlam and DWD-Lokalmodell for short-term forecasting. In: Poster on the European Wind Power Conference and Exhibition, London (UK).
- Giebel, G., Kariniotakis, G., 2008. Best Practice in the Use of Short-term Forecasting. A Users Guide. Project report for the POW'WOW project, online, 6 pp.
- Giebel, G., Landberg, L., Mönnich, K., Waldl, H.-P., March 1–5, 1999. Relative performance of different numerical weather prediction models for short term prediction of wind energy. In: Proceedings of the European Wind Energy Conference, Nice, France, ISBN 1 902916 00 X, pp. 1078–1081.
- Giebel, G., Badger, J., Landberg, L., Nielsen, H.Aa, Madsen, H., Sattler, K., Feddersen, H., March 28–31, 2004. Wind power forecasting using ensembles. In: Paper Presented on the Global Wind Power Conference and Exhibition, Chicago (US).
- Giebel, G., Brownsword, R., Kariniotakis, G., Denhard, M., Draxl, C., 2011. The State of the Art in Short-term Prediction of Wind Power: A Literature Overview, 110 pages, second ed. Available online at: [http://www.safewind.eu/images/Articles/Deliverables/swind\\_deliverable\\_dp-1.4\\_sota\\_v1.1.pdf](http://www.safewind.eu/images/Articles/Deliverables/swind_deliverable_dp-1.4_sota_v1.1.pdf).
- Giebel, G., Cline, J., Frank, H.P., Shaw, W., Pinson, P., Hodge, B.-M., Kariniotakis, G., Madsen, J., Möhrlen, C., 2016. Wind power forecasting: IEA Wind Task 36 & future research issues. *Journal of Physics: Conference Series* 753 (3), 032042 (Online).

- Gow, G., December 2002. Short term wind forecasting in the UK. In: Proceedings of the First IEA Joint Action Symposium on Wind Forecasting Techniques, Norrköping, Sweden. FOI - Swedish Defence Research Agency, pp. 3–10.
- Greaves, B., Collins, J., Parkes, J., Tindal, A., 2009. Temporal forecast uncertainty for ramp events. *Wind Engineering* 33 (4), 309–320.
- Hashimoto, A., Hattori, Y., Kadokura, S., Wada, K., Sugimoto, S., Hirakuchi, H., Tanaka, N., May 7–10, 2007. Effects of numerical models on local-wind forecasts over a complex terrain with wind farm prediction model. In: Proceedings of the European Wind Energy Conference, Milano (IT).
- Holttinen, H., June 11–15, 2006. Handling of wind power forecast errors in the Nordic power market. In: 9th International Conference on Probabilistic Methods Applied to Power Systems, KTH, Stockholm (SE).
- Holttinen, H., Saarikivi, P., Repo, S., Ikäheimo, J., Koreneff, G., 2006. Prediction errors and balancing costs for wind power production in Finland. In: Global Wind Power Conference, Adelaide.
- Houtekamer, P.L., Mitchell, H.L., 1998. Data assimilation using an ensemble Kalman filter technique. *Monthly Weather Review* 126, 796–811.
- James Wilczak, et al., October 2015. The wind forecast improvement project (WFIP): a public–private partnership addressing wind energy forecast needs. *AMS, Bulletin of the American Meteorology Society* 96 (10). <http://dx.doi.org/10.1175/BAMS-D-14-00107.1>.
- Jensen, U.S., Pelgrum, E., Madsen, H. The development of a forecasting model for the prediction of wind power production to be used in central dispatch centres. In: Proceedings of the EWEC '94 in Thessaloniki, 10.-14. Okt, 353–356.
- Jørgensen, J., Möhrlen, C., McKeogh, E., June 2002a. A new generation operational on- and offshore numerical prediction system. In: Talk on the World Wind Energy Conference in Berlin, Germany.
- Jørgensen, J.U., Möhrlen, C., Sattler, K., December 2002b. HIRPOM-WAM: an on - and offshore prediction system for real-time prediction and climatic studies. In: Offshore Wind Energy, EWEA Special Topic Conference, Brussels.
- Jørgensen, J., Möhrlen, C., Ó Gallaghóir, B., Sattler, K., McKeogh, E., April 2–5, 2002c. HIRPOM: description of an operational numerical wind power prediction model for large scale integration of on- and offshore wind power in Denmark. In: Poster on the Global Windpower Conference and Exhibition, Paris, France, 5 p. on the Proceedings CDROM.
- Juban, J. State of the Art on Probabilistic Forecasting. Deliverable 1.2b of the ANEMOS.Plus Project. Available: [www.Anemos-plus.eu](http://www.Anemos-plus.eu).
- Juban, J., Fugon, L., Kariniotakis, G., March 31–April 3, 2008. Uncertainty estimation of wind power forecasts. Comparison of probabilistic modelling approaches. In: Proceedings of EWEC2008, European Wind Energy Conference, Brussels, Belgium.
- Jursa, R., Rohrig, K., 2008. Short-term wind power forecasting using evolutionary algorithms for the automated specification of artificial intelligence models. *International Journal of Forecasting* 24 (4), 694–709.
- Justus, C.G., Hargraves, W.R., Yacin, A., 1976. Nation-wide assessment of potential output from wind power generators. *Journal of Applied Meteorology* 15 (7), 673–678.
- Kalnay, E., Kanamitsu, M., Kistler, R., Collins, W., Deaven, D., Gandin, L., Iredell, M., Saha, S., White, G., Woollen, J., Zhu, Y., Leetmaa, A., Reynolds, B., Chelliah, M., Ebisuzaki, W., Higgins, W., Janowiak, J., Mo, K.C., Ropelewski, C., Wang, J., Jenne, R., Joseph, D., 1996. The NCEP/NCAR 40-year reanalysis project. *Bulletin of the American Meteorological Society* 77 (3), 437–471. See also <http://wesley.wwb.noaa.gov/reanalysis.html>.

- Kariniotakis, G.N., December 1996. Contribution to the Development of a Control System for Autonomous Wind-Diesel Power Systems (Ph.D. thesis in Energetics). Ecole des Mines de Paris, France.
- Kariniotakis, G., et al., 2011. Optimal management of wind generation in power systems & markets – the ANEMOS.plus project. In: On-line Proc. of the 2011 European Wind Energy Association Annual Event (EWEA 2011), Brussels, Belgium March 14–17.
- Kariniotakis, G.N., Stavrakakis, G.S., Nogaret, E.F., December 1996. Wind power forecasting using advanced neural network models. *IEEE Transactions on Energy Conversion* 11 (4), 762–767.
- Kariniotakis, G.N., Nogaret, E., Dutton, A.G., Halliday, J.A., Androutso, A., March 1–5, 1999. Evaluation of advanced wind power and load forecasting Meghods for the optimal management of isolated power systems. In: Proceedings of the European Wind Energy Conference, Nice, France, ISBN 1 902916 00 X, pp. 1082–1085.
- Kretzschmar, R., Eckert, P., Cattani, D., Eggimann, F., 2004. Neural network classifiers for local wind prediction. *Journal of Applied Meteorology* 43 (5), 727–738.
- Kusiak, A., Li, W., 2010. Short-term prediction of wind power with a clustering approach. *Renewable Energy* 35, 2362–2369.
- Kusiak, A., Zheng, H., Song, Z., 2009a. Wind farm power prediction: a data-mining approach. *Wind Energy* 12 (3), 275–293.
- Kusiak, A., Zheng, H., Song, Z., March 2009b. Short-term prediction of wind farm power: a data mining approach. *IEEE Transactions on Energy Conversion* 24 (1), 125–136.
- Landberg, L., 1994. Short-term Prediction of Local Wind Conditions (Ph.D. thesis). Risø-R-702(EN), Risø National Laboratory, Roskilde, Denmark, ISBN 87-550-1916-1.
- Landberg, L., 1998. A mathematical look at a physical power prediction model. *Wind Energy* 1, 23–28.
- Landberg, L., 1999. Short-term prediction of the power production from wind farms. *Journal of Wind Engineering and Industrial Aerodynamics* 80, 207–220.
- Landberg, L., Giebel, G., Myllerup, L., Badger, J., Nielsen, T.S., Madsen, H., June 2–5, 2002. Poor Man's Ensemble Forecasting for Error Estimation. AWEA, Portland/Oregon (US).
- Lang, S., Möhrlen, C., Jørgensen, J., Gallachóir, B.Ó., McKeogh, E., February 27–March 2, 2006a. Application of a multi-scheme ensemble prediction system for wind power forecasting in Ireland and comparison with validation results from Denmark and Germany. In: Proceedings of the European Wind Energy Conference and Exhibition EWEC, Athens (GR).
- Lang, S., Möhrlen, C., Jørgensen, J., Gallachóir, B.Ó., McKeogh, E., 2006b. Forecasting total wind power generation on the Republic of Ireland grid with a multi-scheme ensemble prediction system. In: Proc. Global Wind Energy Conference GWEC, Adelaide (AU).
- Lang, S., Möhrlen, C., Jørgensen, J., Gallachóir, B.Ó., McKeogh, E., April 26–28, 2006c. Aggregate forecasting of wind power generation on the Irish grid using a multi-scheme ensemble prediction system. In: Proceedings, Renewable Energy in Maritime Island Climates, 2nd Conference, Dublin (IE).
- Lange, M., Focken, U., Meyer, R., Denhardt, M., Ernst, B., Berster, F., 2006d. Optimal combination of different numerical weather models for improved wind power predictions. In: 6th International Workshop on Large-Scale Integration of Wind Power and Transmission Networks for Offshore Wind Farms, Delft.
- Lange, M., Focken, U., December 15–16, 2005a. State-of-the-Art in wind power prediction in Germany and international developments. In: Prediction of Wind Power and Reducing the Uncertainty for Grid Operators, Second Workshop of International Feed-in Cooperation. Berlin (DE).

- Lange, M., Focken, U., 2005b. Physical Approach to Short-term Wind Power Prediction. Springer-Verlag, Berlin.
- Lange, M., Heinemann, D., April 2–5, 2002. Accuracy of short term wind power predictions depending on meteorological conditions. In: Poster, P. (Ed.), GWP091 on the Global Windpower Conference and Exhibition, Paris, France.
- Lange, M., Waldl, H.-P., June 2–6, 2001. Assessing the uncertainty of wind power predictions with regard to specific weather situations. In: Proceedings of the European Wind Energy Conference, Copenhagen, Denmark, ISBN 3-936338-09-4, pp. 695–698. Available online at: [https://www.researchgate.net/publication/228404650\\_Assessing\\_the\\_uncertainty\\_of\\_wind\\_power\\_predictions\\_with REGARD\\_to\\_specific\\_weather\\_situations](https://www.researchgate.net/publication/228404650_Assessing_the_uncertainty_of_wind_power_predictions_with REGARD_to_specific_weather_situations).
- Lange, B., Rohrig, K., Schlögl, F., Cali, Ü., Jursa, R., 2007. Wind power forecasting. In: Boyle, G. (Ed.), Renewable Electricity and the Grid. Serling, VA: Easthscan, London, pp. 95–120.
- Lange, B., Wessel, A., Jiang, J., Conz, A., Werner, H., March 30–April 3, 2008. Improving very short-term forecast of wind power by using an online wind measurement network. In: Proceedings of the EWEC, Brussels (BE).
- Larson, K.A., Gneiting, T., March 28–31, 2004. Advanced short-range wind energy forecasting technologies – challenges, solutions, and validation. In: Proceedings of the Global Wind Power Conference and Exhibition, Chicago (US).
- Larson, K.A., Westrick, K., 2006. Short-term wind forecasting using off-site observations. Wind Energy 9 (1–2), 55–62.
- Louka, P., Galanis, G., Siebert, N., Kariniotakis, G., Katsafados, P., Pytharoulis, I., Kallos, G., 2008. Improvements in wind speed forecasts for wind power prediction purposes using Kalman filtering. Journal of Wind Engineering and Industrial Aerodynamics 96, 2348–2362.
- Luig, A., Bofinger, S., Beyer, H.G., June 2–6, 2001. Analysis of confidence intervals for the prediction of regional wind power output. In: Proceedings of the European Wind Energy Conference, Copenhagen, Denmark, ISBN 3-936338-09-4, pp. 725–728.
- Madsen, H. (Ed.), 1995. Wind Power Prediction Tool in Control Dispatch Centres. ELSAM, Skaerbaek, Denmark, ISBN 87-87090-25-2.
- Makarov, Y., et al., 2005. Incorporation of Wind Power Resources into the California Energy Market. California ISO (CAISO). [http://www.caiso.com/docs/2005/04/05/20050405083\\_70111356.pdf](http://www.caiso.com/docs/2005/04/05/20050405083_70111356.pdf).
- McCarthy, E., March 23, 1998. Wind speed forecasting in the central California wind resource area. In: Paper Presented in the EPRI-DOE-NREL Wind Energy Forecasting Meeting. Burlingame, CA.
- McKay, D.C., August 2008. Wind Power Forecasting Pilot Project Part B: The Quantitative Analysis - Final Report. ORTECH Power Report no 70093–4.
- Meng, Z., Zhang, F., 2008. Tests of an ensemble Kalman filter for mesoscale and regional-scale data assimilation. Part III: comparison with 3DVAR in a real-data case study. Monthly Weather Review 136, 522–540.
- Mohandes, M.A., Halawani, T.O., Rehman, S., Hussain, A.A., 2004. Support vector machines for wind speed prediction. Renewable Energy 28 (4), 939–947.
- Möhrlen, C., 2001. On the benefits of and approaches to wind energy forecasting. In: Invited Speaker at the Irish Wind Energy Association Annual Conference “Towards 500MW”.
- Möhrlen, C., May 2004. Uncertainty in Wind Energy Forecasting (Ph.D. thesis). Department of Civil and Environmental Engineering, University College Cork, Ireland.

- Möhrlen, C., Jørgensen, J.U., 2006. Forecasting wind power in high wind penetration markets using multi-scheme ensemble prediction methods. In: Proc. German Wind Energy Conference DEWEK, Bremen (DE).
- Möhrlen, C., Jørgensen, J., October 14–15, 2009. A new algorithm for upscaling and short-term forecasting of wind power using ensemble forecasts. In: Proceedings of the 8th International Workshop on Large Scale Integration of Wind Power and on Transmission Networks for Offshore Wind Farms, Bremen, Germany.
- Möhrlen, C., Jørgensen, J., Sattler, K., McKeogh, E., June 2–6, 2001a. On the accuracy of land cover data in NWP forecasts for high resolution wind energy prediction. In: Proceedings of the European Wind Energy Conference, Copenhagen, Denmark, ISBN 3-936338-09-4, pp. 854–857.
- Möhrlen, C., Jørgensen, J.U., Sattler, K., McKeogh, E.J., June 2–6, 2001b. On the accuracy of land cover data in NWP forecasts for high resolution wind energy prediction. In: Proceedings of the European Wind Energy Conference, Copenhagen, Denmark, ISBN 3-936338-09-4, pp. 703–706.
- Möhrlen, C., Jørgensen, J.U., McKeogh, E.J., 2002. Power predictions in complex terrain with an operational numerical weather prediction model in Ireland including ensemble prediction. In: Proc. World Wind Energy Conference “Clean Power for the World”, Berlin, Germany.
- Mönnich, K., 2000. Vorhersage der Leistungsabgabe netzeinspeisender Windkraftanlagen zur Unterstuetzung der Kraftwerkseinsatzplanung (Ph.D. thesis). Carl von Ossietzky Universität Oldenburg.
- Monteiro, C., Bessa, R., Miranda, V., Botterud, A., Wang, J., Conzelmann, G., November 2009. Wind Power Forecasting: State-of-the-Art 2009. Argonne National Laboratory ANL/DIS-10-1. See also: <http://www.dis.anl.gov/projects/windpowerforecasting.html>.
- More, A., Deo, M.C., January–February 2003. Forecasting wind with neural networks. Marine Structures 16 (1), 35–49. [http://dx.doi.org/10.1016/S0951-8339\(02\)00053-9](http://dx.doi.org/10.1016/S0951-8339(02)00053-9).
- Moreno, P., Benito, L., Borén, R., Cabré, M., June 16–20, 2003. Short-term wind forecast. Results of first year planning maintenance at a wind farm. In: Poster Presented on the European Wind Energy Conference and Exhibition, Madrid (ES).
- Murakami, S., Mochida, A., Kato, S., 2003. Development of local area wind prediction system for selecting suitable site for windmill. Journal of Wind Engineering and Industrial Aerodynamics 91, 1759–1776.
- Nielsen, H.Aa, February 20, 2002. Analyse og simulering af prædiktionsfejl for vindenergi-produktion ved indmelding til NordPool. Report, IMM, DTU.
- Nielsen, T.S., Madsen, H., 1996. Using Meteorological Forecasts in On-line Predictions of Wind Power. ELSAM, Skaerbaek, Denmark.
- Nielsen, T.S., Joensen, A., Madsen, H., Landberg, L., Giebel, G., 1998. A new reference for predicting wind power. Wind Energy 1, 29–34.
- Nielsen, H.Aa, Madsen, H., Nielsen, T.S., November 22–25, 2004a. Using quantile regression to extend an existing wind power forecasting system with probabilistic forecasts. In: Paper in the Scientific Track of the European Wind Energy Conference, London (UK).
- Nielsen, H.Aa, Nielsen, T.S., Madsen, H., Badger, J., Giebel, G., Landberg, L., Feddersen, H., Sattler, K., March 28–31, 2004b. Wind power ensemble forecasting. In: Paper Presented on the Global Wind Power Conference and Exhibition, Chicago (US).
- Nielsen, H.Aa, Madsen, H., Nielsen, T.S., Badger, J., Giebel, G., Landberg, L., Sattler, K., Feddersen, H., 2005a. Wind Power Ensemble Forecasting Using Wind Speed and Direction Ensembles from ECMWF or NCEP. Project report. Lyngby.

- Nielsen, H.Aa, Yates, D., Madsen, H., Nielsen, T.S., Badger, J., Giebel, G., Landberg, L., Sattler, K., Feddersen, H., 2005b. Analysis of the Results of an On-line Wind Power Quantile Forecasting System. Project report. Lyngby.
- Nielsen, T.S., Madsen, H., Nielsen, H.Aa, Pinson, P., Kariniotakis, G., Siebert, N., Marti, I., Lange, M., Focken, U., von Bremen, L., Louka, P., Kallos, G., Galanis, G., February 27–March 2, 2006a. Short-term wind power forecasting using advanced statistical methods. In: European Wind Energy Conference and Exhibition, Athens (GR).
- Nielsen, H.Aa, Madsen, H., Nielsen, T.S., 2006b. Using quantile regression to extend an existing wind power forecasting system with probabilistic forecasts. *Wind Energy* 9 (1–2), 95–108.
- Nielsen, H.Aa, Pinson, P., Christiansen, L.E., Nielsen, T.S., Madsen, H., Badger, J., Giebel, G., Ravn, H.F., May 7–10, 2007a. Improvement and automation of tools for short term wind power forecasting. In: Scientific Proceedings of EWEC 2007. European Wind Energy Conference and Exhibition, Milan, Italy.
- Nielsen, H.Aa, Nielsen, T.S., Madsen, H., San Isidro Pindado, M.J., Marti, I., 2007b. Optimal combination of wind power forecasts. *Wind Energy* 10 (5), 471–482.
- Nogaret, E., Stavrakakis, G., Bonin, J.C., Kariniotakis, G., Papadias, B., Contaxis, G., Papadopoulos, M., Hatziyargyriou, N., Papathanassiou, S., Garopoulos, J., Karagounis, E., Halliday, J., Dutton, G., Pedas-Lopes, J., Androutsos, A., Pligoropoulos, P., October 10–14, 1994. Development and implementation of an advanced control system for medium size wind-diesel systems. In: Proceedings of the EWEC '94 in Thessaloniki, pp. 599–604.
- Palomares, A., de Castro, M., June 16–20, 2003. Short-term wind prediction model at the Strait of Gibraltar based on a perfect prognosis statistical downscaling method. In: Paper 164 Presented on the European Wind Energy Conference and Exhibition, Madrid (ES).
- Papke, U., Petersen, A., Köhne, V., March 8–12, 1993. Evaluation and Short-Time-Forecast of WEC-Power within the power grid of SCHLESWAG AG. In: Proceedings of the 1993 ECWEC in Travemünde, ISBN 0-9521452-0-0, pp. 770–773.
- Pease, J., May 28, 2008. Wind power forecasts in the US context. In: Talk on the 2nd Workshop on Best Practice in the Use of Short-term Forecasting, Madrid (ES).
- Pease, J., October 13, 2009. Critical short-term forecasting needs for large and unscheduled wind energy on the BPA system. In: Talk on the 3rd Workshop on Best Practice in the Use of Short-term Forecasting, Bremen (DE).
- Peña, A., Hahmann, A., April 20–23, 2010. Validation of boundary layer winds from WRF mesoscale forecasts over Denmark. In: Proceedings of the European Wind Energy Conference, Warsaw (PL).
- Pielke, R.A., Kennedy, E., January 1980. Mesoscale Terrain Features. report Uva Env. Sci meso 1980-1 University of Virginia Dept of Environmental Science.
- Pinson, P., Madsen, H., 2009. ensemble-based probabilistic forecasting at Horns Rev. *Wind Energy* 12 (2), 137–155.
- Pinson, P., Girard, R., 2012. Evaluating the quality of scenarios of short-term wind power generation. *Applied Energy* 96, 12–20.
- Pinson, P., Kariniotakis, G., November 2010. Conditional prediction intervals of wind power generation. *IEEE Transactions on Power Systems* 25 (4), 1845–1856.
- Pinson, P., the SafeWind Consortium, April 20–23, 2010. Defining a catalogue of complex to extreme events. In: Proceedings of the European Wind Energy Conference, Warsaw (PL).

- Pinson, P., Madsen, H., Giebel, G., Kariniotakis, G., von Bremen, L., Martí, I., May 7–10, 2007a. Forecasting of wind generation — recent advances and future challenges. In: Proceedings of the European Wind Energy Conference and Exhibition, Milan (IT).
- Pinson, P., Nielsen, H.Aa, Møller, J.K., Madsen, H., Kariniotakis, G.N., 2007b. Non-parametric probabilistic forecasts of wind power: required properties and evaluation. *Wind Energy* 10 (6), 497–516.
- Pinson, P., Nielsen, H.Aa, Madsen, H., Nielsen, T.S., 2008a. Local linear regression with adaptive orthogonal fitting for the wind power application. *Statistics and Computing* 18 (1), 59–71.
- Pinson, P., Nielsen, H.Aa, Madsen, H., Kariniotakis, G., 2008b. Skill forecasting from ensemble predictions of wind power. *Applied Energy* 86, 1326–1334.
- Pinson, P., Christensen, L.E.A., Madsen, H., Sørensen, P.E., Donovan, M.H., Jensen, L.E., 2008c. Regime-switching modelling of the fluctuations of offshore wind generation. *Journal of Wind Engineering and Industrial Aerodynamics* 96 (12), 2327–2347.
- Pinson, P., Papaefthymiou, G., Klockl, B., Nielsen, H.Aa, Madsen, H., 2009. From probabilistic forecasts to statistical scenarios of short-term wind power production. *Wind Energy* 12, 51–62.
- Potter, C.W., Negnevitsky, M., 2006. Very short-term wind forecasting for Tasmanian power generation. *IEEE Transactions on Power Systems* 21 (2), 965–972.  
[powwow.risoe.dk/BestPracticeWorkshop.htm](http://powwow.risoe.dk/BestPracticeWorkshop.htm).  
<http://www.projekt-eweline.de/>.
- Rife, D.L., Davis, C.A., 2005. Verification of temporal variations in mesoscale numerical wind forecasts. *Monthly Weather Review* 133 (11), 3368–3381.
- Rodrigues, A., Peças Lopes, J.A., Miranda, P., Palma, L., Monteiro, C., Bessa, R., Sousa, J., Rodrigues, C., Matos, J., 2007. EPREV — a wind power forecasting tool for Portugal. In: Proceedings of the European Wind Energy Conference EWEC'07, Milan (IT).
- Rohrig, K. (Ed.), 2005. Entwicklung eines Rechenmodells zur Windleistungsprognose für das Gebiet des deutschen Verbundnetzes, Abschlussbericht Forschungsvorhaben Nr. 0329915A. gefördert durch Bundesministeriums für Umwelt, Naturschutz und Reaktorsicherheit (BMU), Kassel, Germany.
- Roulston, M.S., Kaplan, D.T., Hardenberg, J., Smith, L.A., 2003. Using medium-range weather forecasts to improve the value of wind energy production. *Renewable Energy* 28, 585–602.
- Salcedo-Sanz, S., Pérez-Bellido, A.M., Ortiz-García, E.G., Portilla-Figueras, A., Prieto, L., Correoso, F., 2009a. Accurate short-term wind speed prediction by exploiting diversity in input data using banks of artificial neural networks. *Neurocomputing* 72, 1336–1341.
- Salcedo-Sanz, S., Pérez-Bellido, Á.M., Ortiz-García, E.G., Portilla-Figueras, A., Prieto, L., Paredes, D., 2009b. Hybridizing the fifth generation mesoscale model with artificial neural networks for short-term wind speed prediction. *Renewable Energy* 34, 1451–1457.
- Sánchez, I., 2006. Short-term prediction of wind energy production. *International Journal of Forecasting* 22 (1), 43–56.
- Sánchez, I., 2008. Adaptive combination of forecasts with application to wind energy. *International Journal of Forecasting* 24 (4), 679–693.
- Sánchez, I., Usaola, J., Ravelo, O., Velasco, C., Domínguez, J., Lobo, M.G., González, G., Soto, F., June 2002. SIPREÓLICO—a wind power prediction system based on flexible combination of dynamic models. Application to the Spanish power system. In: Proceedings of the World Wind Energy Conference in Berlin, Germany.

- Schwartz, M., Milligan, M., December 2002. Statistical wind forecasting at the U.S. National renewable energy laboratory. In: Proceedings of the First IEA Joint Action Symposium on Wind Forecasting Techniques. FOI - Swedish Defence Research Agency, Norrköping, Sweden, pp. 115B–124B.
- <http://www.safewind.eu>.
- Sfetsos, A., 1999. Time Series Forecasting of Wind Speed and Solar Radiation for Renewable Energy Sources (Ph.D. thesis). Imperial College, UK.
- Sfetsos, A., 2000. A comparison of various forecasting techniques applied to mean hourly wind speed time series. *Renewable Energy* 21, 23–35.
- Sfetsos, A., 2001. A novel approach for the forecasting of mean hourly wind speed time series. *Renewable Energy* 27, 163–174.
- Sideratos, G.N., Hatziairgyriou, N., February 2007. An advanced statistical method for wind power forecasting. *IEEE Transactions on Power Systems* 22 (1), 258–265.
- Sideratos, G.N., Hatziairgyriou, N., November 2008. An advanced radial base structure for wind power forecasting. In: *International Journal on Power and Energy Systems*, vol. 12. ACTA Press.
- Siebert, N., March 2008. Development of Methods for Regional Wind Power Forecasting (Ph.D. thesis in Energetics). MINES ParisTech (265 p.). Available online at: <https://hal-mines-paristech.archives-ouvertes.fr/tel-00287551>.
- Siebert, N., Kariniotakis, G., February 27–March 2, 2006. Reference wind farm selection for regional wind power prediction models. In: European Wind Energy Conference and Exhibition, Athens (GR).
- Skamarock, W.C., December 2004. Evaluating mesoscale NWP models using kinetic energy spectra. *Monthly Weather Review* 132, 3019–3032.
- Snodin, H., 2006. Short-term Wind Energy Forecasting: Technology and Policy. S.L.: Garrad Hassan and Partners Limited.
- Sood, A., Suselj, K., Heinemann, D., February 27–March 2, 2006. High resolution NWP North Sea wind forecasts in the marine atmospheric boundary layer. In: Proceedings of the European Wind Energy Conference, Athens (GR).
- Still, D., Grainger, B., June 2–6, 2001. Demanding seas – the UK's first offshore wind farm. In: Proceedings of the European Wind Energy Conference, Copenhagen, Denmark, ISBN 3-936338-09-4, pp. 169–171. Note: This statement was done during the talk.
- Tammelin, B., December 2002. Wind power forecasting. In: Proceedings of the First IEA Joint Action Symposium on Wind Forecasting Techniques, Norrköping, Sweden. FOI - Swedish Defence Research Agency, pp. 75–81.
- Tande, J.O., Landberg, L., March 8–12, 1993. A 10 sec. Forecast of wind turbine output with neural networks. In: Proceedings of the 1993 ECWEC in Travemünde, ISBN 0-9521452-0-0, pp. 774–777.
- Tantareanu, C., October 1992. Wind prediction in short term: a first step for a better wind turbine control. In: Nordvestjysk Folkecenter for Vedvarende Energi, ISBN 87-7778-005-1.
- Tastu, J., Pinson, P., Madsen, H., April 20–23, 2010. Multivariate Conditional Parametric Models for a spatio-temporal analysis of short-term wind power forecast errors. In: Scientific Proceedings of the European Wind Energy Conference, Warsaw (PL), pp. 77–81.
- Tastu, J., Pinson, P., Kotwa, E., Madsen, H., Nielsen, H.Aa, 2011. Spatio-temporal analysis and modeling of short-term wind power forecast errors. *Wind Energy* 14 (1), 43–60.

- Taylor, J.W., McSharry, P.E., Buizza, R., 2009. Wind power density forecasting using ensemble predictions and time series models. *IEEE Transactions on Energy Conversion* 24 (3), 775–782.
- Thompson, G., December 9, 2008. Using the Weather Research and Forecasting (WRF) atmospheric model to predict explicitly the potential for icing. In: Proceedings of the Winterwind Conference, Norrköping (SE).
- Torres, J.L., Garcia, A., De Blas, M., De Francisco, A., 2005. Forecast of hourly average wind speed with ARMA models in Navarre (Spain). *Solar Energy* 79 (1), 65–77.
- Troen, I., Landberg, L., September 10–14, 1990. Short-term prediction of local wind conditions. In: Proceedings of the European Community Wind Energy Conference, Madrid (ES), ISBN 0-9510271-8-2, pp. 76–78.
- Troen, I., Petersen, E.L., 1998. European Wind Atlas. Published for the EU Commission DGXII by Risø National Laboratory, Denmark, ISBN 87-550-1482-8.
- Vidal, J., Tortosa, A., Lacave, O., Aymamí, J., Zack, J., Meade, D., April 20–23, 2010. Validation of a wind power forecast system - the multi-model NWP ensemble strategy. In: Proceedings of the European Wind Energy Conference, Warsaw (PL).
- Vincent, C.L., Pinson, P., Giebel, G., 2010a. Wind fluctuation over the north sea. *International Journal of Climatology*.
- Vincent, C., Giebel, G., Pinson, P., Madsen, H., February 2010b. Resolving non-stationary spectral information in wind speed time series using the Hilbert-Huang transform. *Journal of Applied Meteorology and Climatology* 49 (2), 253–267.
- Von Bremen, L., Saleck, N., 2010. Minimizing the risk in offshore wind power integration induced by severe wind power fluctuations. In: Proceedings of the EAWE Special Topic Conference the Science of Making Torque from Wind, Crete (GR).
- Waldl, H.-P., Giebel, G., September 25–27, 2000. The quality of a 48-hours wind power forecast using the German and Danish weather prediction model. In: Wind Power for the 21st Century, EUWEC Special Topic Conference, Kassel (DE).
- Wessel, A., Jiang, J., Dobschinski, J., Lange, B., March 16–19, 2009a. Improving short-term forecast with online measurements. In: Proceedings of the European Wind Energy Conference EWEC, Marseille (FR).
- Wessel, A., Dobschinski, J., Lange, B., October 14–15, 2009b. Integration of offsite wind speed measurements in Shortest-term wind power prediction systems. In: 8th International Workshop on Large Scale Integration of Wind Power into Power Systems as Well as on Transmission Networks for Offshore Wind Farms, Bremen (DE).
- Wind Engineering, 1999. CARE Special Issue, 23 (2).
- Wu, G., Dou, Z., 1995. Non linear wind prediction using a fuzzy modular temporal neural network. *Windpower* 95, 285–294.
- Yamaguchi, A., Ishihara, T., Sakai, K., Ogawa, T., Fujino, Y., May 7–10, 2007. A physical-statistical approach for the regional wind power forecasting. In: Proceedings of the European Wind Energy Conference EWEC, Milan (IT).
- Young, G.S., Pielke, R.A., 1983. Application of terrain height variance spectra to meso scale modelling. *Journal of the Atmospheric Sciences* 40, 255–2560.
- Yu, W., et al., 2006. Wind Energy Simulation Toolkit (WEST): A wind mapping system for use by the wind-energy industry. *Wind Engineering* 30 (1), 15–33. <http://dx.doi.org/10.1260/030952406777641450>.
- Zack, J.W., March 28–31, 2004. A new technique for short-term wind energy forecasting: a rapid update cycle with a physics-based atmospheric model. In: Proceedings of the Global Wind Power Conference and Exhibition, Chicago (US).

- Zack, J., May 8, 2007. Optimization of wind power production forecast performance during critical periods for grid management. In: Proceedings of the European Wind Energy Conference EWEC, Milano (IT).
- Zack, J.W., Young, S., Cote, M., Nocera, J., Aymami, J., Vidal, J., April 20–23, 2010. Development and testing of an innovative short-term large wind ramp forecasting system. In: Proceedings of the European Wind Energy Conference and Exhibition, Warsaw (PL).

# Mathematical methods for optimized solar forecasting

4

Hugo T.C. Pedro, Rich H. Inman, Carlos F.M. Coimbra  
University of California, San Diego, CA, United States

## 4.1 Introduction

Effective ways to integrate increasing levels of solar penetration into the power grid typically involve a combination of resource and load forecasting combined with dispatchable and energy storage reserves. The need for reliable forecasting arises from the variable nature of the solar resource, seasonal deviations in generation and load profiles, the high cost of energy storage, and industry requirements that must balance grid flexibility with reliability (Denholm and Margolis, 2007a,b). Mostly due to absence of effective solar forecasting, solar plants are often backed by ancillary generators for periods of high variability, which increases the capital and operational costs of solar generation.

Reliable solar forecasts over several time horizons are required so that independent system operators (ISOs) or equivalent grid balancing authorities are able to successfully integrate increased levels of solar power production while maintaining reliability (Lew and Piwko, 2010; Sundar, 2010; Rodriguez, 2010). Solar forecasts on multiple time horizons become increasingly important as solar penetration grows for the purposes of grid regulation, load-following production, power scheduling and unit commitment. Short-term, intrahour solar forecasts are particularly useful for power plant operations, grid balancing, real-time unit dispatching, automatic generation control, and trading. Forecasts for longer time horizons are of interest to utilities and ISOs for unit commitment, scheduling and for improving balance area control performance. Ultimately, a spectrum of solar forecasts is required to address the planning, operational, and balancing needs of both the distribution and the transmission grids. Solar forecasting is therefore an enabling technology for the integration of ever-increasing levels of solar penetration into the grid because it improves the quality of the energy delivered to the grid and reduces the ancillary costs associated with weather dependency. The combination of these two factors (better energy quality through information that is capable of lowering integration and operational costs) has been the driving motivation for the development of a complex field of research that aims at producing better solar forecasting capabilities for the solar resource at the ground level and for the power output from different solar technologies that depend on the variable irradiance at the ground level. Solar, wind, and load forecasting have become integral parts of the so-called “smart grid concept.”

To date, high-fidelity, robust solar forecast systems that work for widely different microclimates remain evasive, even though this field has advanced substantially in

the last decade. The problem at hand is of great complexity due to the nonlinear and chaotic effect of cloud motion on solar irradiance and solar generation at the ground level. However, a number of promising approaches have been developed in the past few years, and the incipient research field of solar meteorology for renewable generation has grown considerably by aggregating diverse areas of knowledge such as atmospheric physics, solar instrumentation, machine learning, forecasting theory, and remote sensing in its quest to better predictive skills. This chapter presents an overview of best practices in solar forecasting, both for the solar resource and for solar power generation, as well as the theoretical basis for some of the most promising and widely used methods. A short discussion on the effectiveness of such methods for operational use is also included.

It should be noted that the techniques such as remote sensing, local sensing, and Numerical Weather Prediction (NWP) also find applications in solar forecasting, but these are covered in greater detail in other chapters in this book. For a detailed description of several other methods in the context of solar forecasting, see [Inman et al. \(2013\)](#). This reference also covers a number of fundamental considerations relevant to solar forecasting development and solar power engineering, including clear-sky models (CSMs) and the evaluation of forecasting performances, which are not included here.

## 4.2 Regression methods

Prior to stochastic techniques, solar radiation models focused on the extrapolation of data from long-term averages and steady-state values resulting in essentially static models, which described only seasonal and diurnal changes. In those primordial times, models, whether graphical or mathematical, ignored the short-term time-dependent patterns of solar radiation data which result from changing local weather conditions and cause fluctuations on timescales ranging from seconds to days. However, forecasting of such fluctuations is essential to the operation of, for example, concentrating photovoltaic systems due to their relatively small apertures and strong dependence on direct normal irradiance (DNI) ([Yogi et al., 2000](#)).

A second shortcoming of the prestochastic models was the use of common regression techniques to develop mathematical relationships. The statistical theory at the foundation of these regression techniques assumes that the individual observations of solar irradiance change independently ([Walpole and Meyers, 1972](#)). However, the reverse is true and changes due to local weather conditions generate data time series that are strongly dependent. Thus, the correlated nature of solar irradiance data is another essential characteristic, which must be addressed by any successful forecasting model. It is evident from the discussion that models that are based on long-term averages and employ independent regression techniques could be improved through the use of stochastic models, which account for short-term fluctuations and the correlated nature of the data.

In the 1920s G.U. Yule began to establish new approaches for the analysis of stationary time series. Yule pioneered the first of two new approaches for stationary time series analysis which he called moving averages (MA). The theory originates from two papers regarding the regular fluctuations of purely random series, which are given, for

instance, by throwing dice (Yule, 1921, 1926). The second of Yule's approaches, linear autoregression (AR), came in 1927 in a well-known paper, which discussed the periodicities of disturbed series with special reference to Wolfer's sunspot numbers (Yule, 1927). Shortly after, in the 1930s, the work of Yule was furthered by H. Wold who applied the theory to business cycles and econometric statistics (Wold, 1938). It was not until the 1960s that G.E.P. Box and G.M. Jenkins, motivated by the principle of parsimony, would popularize what would become two of the most widely used models in time series analysis (Box and Jenkins, 1998). The first, known as autoregressive moving averages (ARMA), advanced from the combination of the schemes established by Yule and Wold for stationary time series analysis. The second utilized an evolutive component and gave way to a class of models known as autoregressive integrated moving averages (ARIMA), which are useful for the analysis of nonstationary processes (Wold, 1938). The use of ARMA and ARIMA provides a basis for many problems outside the realm of solar forecasting including economic and business planning, production planning, inventory and production control, and optimization of industrial processes (Box and Jenkins, 1998).

Before beginning a discussion of the various stochastic models, it will be useful to review some simple operators and terminology. One operator that will be used frequently is the forward shift or advance operator  $q$  which, when applied to a time series  $\{z\}$  at time  $t$ , is defined as

$$qz_t = z_{t+1}. \quad (4.1)$$

The forward shift operator can be applied successively to yield

$$q^k z_t = z_{t+k}. \quad (4.2)$$

The inverse of the forward shift operator is the backward shift or delay operator  $q^{-1}$  which, when applied to a time series, is given by

$$q^{-1} z_t = z_{t-1}, \quad (4.3)$$

which in turn yields,

$$q^{-k} z_t = z_{t-k}. \quad (4.4)$$

The backward shift operator can be used to construct the backward difference operator  $D$  as follows,

$$Dz_t = z_t - z_{t-1} = (1 - q^{-1})z_t. \quad (4.5)$$

Its inverse, the summation operator  $S$ , can be written as

$$Sz_t = D^{-1} z_t = z_t + z_{t-1} = (1 + q^{-1})z_t. \quad (4.6)$$

The stochastic models that follow are based on the result from [Yule \(1927\)](#) that if a strong dependency exists between successive terms in a time series which is, for example, a characteristic of solar irradiance data, it can be effectively generated by a series of independent shocks, which are assumed to have nonpermanent effects and are drawn at random from a stationary distribution having zero mean and variance  $\sigma_\omega^2$ . Any series of such random shocks  $\{\omega\}$  is referred to as a white noise process. A linear filter can be used to transform the white noise process into the time series  $\{z\}$ .

The linear filter is defined by the following operation

$$z_t = \mu + \omega_t + g_1\omega_{t-1} + g_2\omega_{t-2} + \dots = \mu + G(q)\omega_t \quad (4.7)$$

where  $\mu$  is a parameter that determines the level of the process. The level of a stationary process can be thought of as the average value about which the series fluctuates. However, the level of a nonstationary process is time dependent and varies from section to section as exemplified in [Fig. 4.1](#). The operator that transforms  $\omega_t$  into  $z_t$  is coined the transfer function  $G(q)$  of the filter and is given by

$$G(q) = \sum_{k=0}^{\infty} g_k q^{-k} = 1 + g_1 q^{-1} + g_2 q^{-2} + \dots \quad (4.8)$$

where  $g_0 = 1$ . It should be noted that we choose the less-obvious  $q$  as the argument of  $G$  rather than  $q^{-1}$  for clarity. The sequence of weights  $g_1, g_2, \dots$  may be finite or infinite, which gives us an interpretation for the level  $\mu$  and determines the nature of the process; stationary or nonstationary.

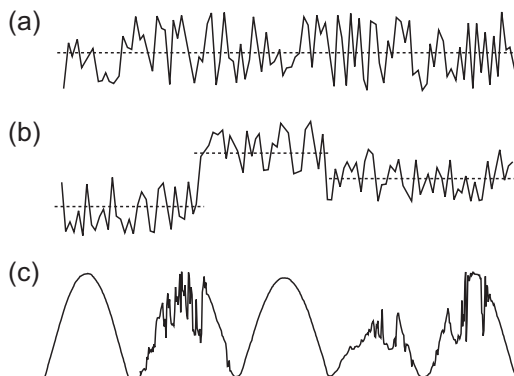


**Figure 4.1** (a) An example stationary time series fluctuating about a static level  $\mu$ , which can be represented by the model  $\Phi_m(q)\tilde{z}_t = \Theta_n(q)\omega_t$ . (b) An example time series showing nonstationary behavior in local level can be represented by the model  $\Phi_m(q)\tilde{\nabla}z_t = \Theta_n(q)\omega_t$ . (c) Global horizontal irradiance data at 5 min resolution with night values removed showing nonstationary behavior in local level and slope, which can be represented by the model  $\Phi_m(q)\tilde{\nabla}^2z_t = \Theta_n(q)\omega_t$ .

### 4.2.1 Linear stationary models

Observational series that describe a changing physical phenomenon with time can be classified into two main categories: stationary and nonstationary. If the sequence of weights in Eq. (4.8) is finite, or infinite and convergent, the linear filter is said to be stable and the time series  $\{z\}$  to be stationary. Stationary time series are static with respect to their general shape. The fluctuations may appear, to the user, as clearly ordered or totally random, nonetheless the character of the series is, on average, quite similar in different segments. In this case, the parameter  $\mu$  may be interpreted as the average value about which the series fluctuates as seen in Fig. 4.1(a). Stationary time series find applications in many areas of the physical sciences, for instance, observational time series and series involving deviations from a trend are often stationary (Wold, 1938). In fact, the stochastic component of a solar radiation data set is often framed as a stationary process (Sulaiman et al., 1997).

#### 4.2.1.1 Autoregressive models

The AR models get their name from the fact that the current value of the process can be expressed as a finite, linear combination of the previous values of the process and a single shock  $\omega_t$ . Thus, the process is said to be regressed on the previous values. If we define the stochastic portion of the time series  $\tilde{z}_t, \tilde{z}_{t-1}, \tilde{z}_{t-2}, \dots$  as deviations from the mean value  $\mu$  as

$$\tilde{z}_t = z_t - \mu \quad (4.9)$$

then the AR process of order  $m$  can be written as

$$\tilde{z}_t + \varphi_1 \tilde{z}_{t-1} + \varphi_2 \tilde{z}_{t-2} + \dots + \varphi_m \tilde{z}_{t-m} = \omega_t \quad (4.10)$$

We can simplify the previous expression by defining the AR transfer function of order  $m$ ,  $\Phi_m(q)$ , as

$$\Phi_m(q) = \sum_{k=0}^m \varphi_k q^{-k} = 1 + \varphi_1 q^{-1} + \varphi_2 q^{-2} + \dots + \varphi_m q^{-m}, \quad (4.11)$$

where  $\varphi_0 = 1$ . It follows that the AR( $m$ ) model may be written conveniently as

$$\Phi_m(q) \tilde{z}_t = \omega_t. \quad (4.12)$$

Here it is clear that the process is regressed on the previous values of  $\{\tilde{z}\}$ . To implement this model, one must determine the  $m + 2$  unknown parameters  $\varphi_1, \varphi_2, \dots, \varphi_m, \mu$  and  $\sigma_\omega^2$ . Typically these are calculated from the data using the techniques covered in Section 4.2.1.3. It is illustrative to note that Eq. (4.12) implies

$$\tilde{z}_t = \Phi_m^{-1}(q) \omega_t. \quad (4.13)$$

Therefore, it is helpful to think of the AR( $m$ ) process as the output of a linear filter with transfer function  $\Phi_m^{-1}(q)$  and white noise  $\omega_t$  as the input.

For the AR( $m$ ) process to be stationary a set of conditions must be satisfied. In [Box and Jenkins \(1998\)](#) the authors point out that the general AR( $m$ ) process has the inverse transfer function

$$\Phi_m(q) = (1 - \Gamma_1 q^{-1})(1 - \Gamma_2 q^{-1}) \dots (1 - \Gamma_m q^{-1}) \quad (4.14)$$

which allows expansion of the process in partial fractions,

$$\tilde{z}_t = \Phi_m^{-1}(q)\omega_t = \sum_{i=1}^m \frac{\kappa_i}{(1 - \Gamma_i q^{-1})} \omega_t \quad (4.15)$$

where it is clear that if  $\Phi_m^{-1}(q)$  is to be a convergent series for  $|q^{-1}| \leq 1$ , then we must have  $|\Gamma_i| < 1$ , where  $i = 1, 2, \dots, m$ . This is equivalent to saying that the roots of the equation  $\Phi_m(q) = 0$  must lie outside the unit circle. For a discussion of stationary conditions of AR( $m$ ) processes, see [Wold \(1938\)](#), [Box and Jenkins \(1998\)](#), and [Ljung \(1987\)](#).

#### 4.2.1.2 Moving average models

While the AR techniques model the stochastic portion of the time series  $\{\tilde{z}\}$  as a weighted sum of previous values  $\tilde{z}_{t-1}, \tilde{z}_{t-2}, \dots, \tilde{z}_{t-m}$ , MA methods model  $\{\tilde{z}\}$  as a finite sum of  $n$  previous shocks  $\omega_t, \omega_{t-1}, \omega_{t-2}, \dots, \omega_{t-n}$ . The MA process of order  $n$ , MA( $n$ ), is defined as

$$\tilde{z}_t = \omega_t + \theta_1 \omega_{t-1} + \theta_2 \omega_{t-2} + \dots + \theta_n \omega_{t-n}. \quad (4.16)$$

Let us pause here and note that the terminology MA can be a bit misleading due to the fact that the weights in Eq. (4.16) neither, in general, need to be positive nor do their sum necessarily equal unity ([Box and Jenkins, 1998](#)). Nonetheless, the name is used for historic convention. The MA( $n$ ) operator is defined as

$$\Theta_n(q) = \sum_{k=0}^n \theta_k q^{-k} = 1 + \theta_1 q^{-1} + \theta_2 q^{-2} + \dots + \theta_n q^{-n}, \quad (4.17)$$

where  $\theta_0 = 1$ . As a result we can write the MA model in an economic fashion

$$\tilde{z}_t = \Theta_n(q)\omega_t. \quad (4.18)$$

The MA process can be thought of as the output  $\tilde{z}_t$  of a linear filter whose transfer function is  $\Theta_n(q)$ , with white noise  $\omega_t$  as the input. Like its counterpart, the MA model contains  $n + 2$  undetermined parameters  $\theta_1, \dots, \theta_n, \mu$  and the variance of the white noise process  $\sigma_\omega^2$ , which must be determined from the data using the techniques described in the next section. Unlike AR models, MA models are unconditionally stable ([Wold, 1938](#)).

#### 4.2.1.3 Mixed autoregressive moving average models

Linear processes represented by an infinite or an extraneous number of parameters are clearly not practical. However, it is possible to introduce parsimony and still obtain useful models. A well-known result in time series analysis is the relationship between the  $\Theta$  weights and  $\Phi$  weights (Box and Jenkins, 1998). Operating on both sides of Eq. (4.12) by  $\Theta(q)$  and making use of Eq. (4.18) yields

$$\Theta(q)\Phi(q)\tilde{z}_t = \Theta(q)\omega_t = \tilde{z}_t \quad (4.19)$$

which implies

$$\Theta(q)\Phi(q) = 1 \quad (4.20)$$

that is

$$\Phi^{-1}(q) = \Theta(q). \quad (4.21)$$

Eq. (4.21) indicates that the  $\Phi$  weights may be arrived at from knowledge of the  $\Theta$  weights and vice versa. Thus the *finite* MA( $n$ ) process  $\tilde{z}_t = \Theta_n(q)\omega_t$  can be written as an *infinite* AR process

$$\tilde{z}_t = \omega_t - \theta_1\tilde{z}_{t-1} - \theta_1^2\tilde{z}_{t-2} - \dots \quad (4.22)$$

However, if the process were really MA( $n$ ), we would arrive at a nonparsimonious representation in terms of the AR expression. By the same reasoning, a *finite* AR( $m$ ) model could not be parsimoniously represented using an *infinite* MA expression. Therefore, in practice, to realize a parameterization, which is parsimonious, both AR and MA terms are often used in the model development. Hence,

$$\tilde{z}_t + \varphi_1\tilde{z}_{t-1} + \dots + \varphi_m\tilde{z}_{t-m} = \omega_t + \theta_1\omega_{t-1} + \dots + \theta_n\omega_{t-n} \quad (4.23)$$

or

$$\Phi_m(q)\tilde{z}_t = \Theta_n(q)\omega_t. \quad (4.24)$$

Eq. (4.24) is referred to as the mixed ARMA process of order  $(m, n)$ . It is illustrative to note that the ARMA( $m, n$ ) model can be written

$$\tilde{z}_t = \frac{\Theta_n(q)}{\Phi_m(q)}\omega_t = \frac{1 + \theta_1q^{-1} + \dots + \theta_nq^{-n}}{1 + \varphi_1q^{-1} + \dots + \varphi_mq^{-m}}\omega_t \quad (4.25)$$

where it is clear that  $\tilde{z}_t$  is the output from a linear filter, whose transfer function is the ratio of two polynomials  $\Theta_n(q)$  and  $\Phi_m(q)$ , with white noise  $\omega_t$  as the input (Fig. 4.2(a)).

In practice, it is frequently true that adequate representation of actually occurring stationary time series can be obtained from models in which  $n$  and  $m$  are not greater than two and often less than two (Box and Jenkins, 1998; Sulaiman et al., 1997). The order of the model, that is the values of  $m$  and  $n$ , is determined using the sample autocorrelation function and partial autocorrelation function of the time series (Goh and Tan, 1977). The model parameters are estimated by least-squares methods, and the resulting model is said to adequately describe the statistical information contained in the series in a parsimonious manner.

These techniques have been used since the 1970s to analyze time series resulting from solar irradiance data. Some of the recent works in this area include works such as Al-Awahdi et al. (Al-Awadhi and El-Nashar, 2002) in which the authors proposed an ARMA model that uses a bilinear time series to generate daily irradiance models for Kuwait. Mora-Lopez et al. (Mora-Lopez and Sidrach-De-Cardona, 1998) employed a multiplicative ARMA model for global radiation time series with diurnal and seasonal components. The multiplicative nature of these models enabled the acquisition of two types of relationships observed in recorded hourly series of global irradiation: the relationship between the value at 1 h and the value at the previous hour; and the relationship between the value at 1 h in one day and the value at the same hour in the previous day. Moreno-Muñoz et al. (2008) used multiplicative ARMA models to generate instantaneous series of global irradiance in southern Spain during a 4-year period. Lately, however, ARMA methods typically find applications as components of a robust hybrid system (HS) architecture (Chaabene and Ben Ammar, 2008; Sfetsos and Coonick, 2000; Wu and Chan, 2011; Voyant et al., 2011; Mellit et al., 2005), see Section 4.4.

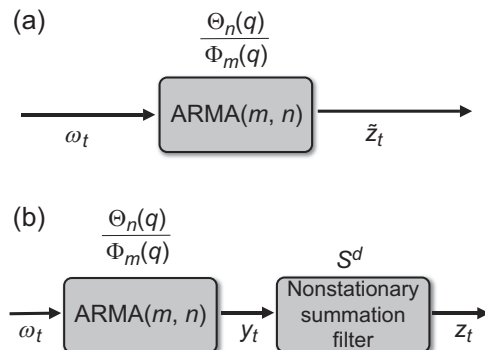


**Figure 4.2** (a) ARMA( $n, m$ ) modeled as a linear filter with transfer function  $\Phi_m^{-1}(q)\Theta_n(q)$ . (b) ARIMA( $n, d, m$ ) modeled as a stationary ARMA( $m, n$ ) linear filter in series with a nonstationary summation filter  $S^d$ .

#### 4.2.1.4 Mixed autoregressive moving average models with exogenous variables

All of the linear stationary stochastic techniques discussed so far have been univariate; meaning the technique uses previous values of only the time series it is attempting to model. However, the accuracy of ARMA( $m, n$ ) models may be improved by including information external to the time series under analysis. For example, in the case of solar irradiance and solar generation forecasting, the error of a forecasting model may be reduced by including information about the evolution of the local temperature, relative humidity, cloud cover, wind speed, wind direction, etc. Variables such as these, which are independent of the models but affect its value, are referred to as exogenous variables. We can include into the ARMA( $m, n$ ) models  $p$  exogenous input terms, which allows us to write the ARMAX( $m, n, p$ ) (autoregressive moving average models with exogenous variables) process as

$$\begin{aligned} \tilde{z}_t + \varphi_1 \tilde{z}_{t-1} + \dots + \varphi_m \tilde{z}_{t-m} &= \omega_t + \theta_1 \omega_{t-1} + \dots + \theta_n \omega_{t-n} \\ &\quad + \lambda_1 e_{t-1} + \dots + \lambda_p e_{t-p}. \end{aligned} \quad (4.26)$$

The above model contains AR( $m$ ) and MA( $n$ ) models as well as the last  $p$  values of an exogenous time series  $e_t$ . Defining the exogenous input operator of order  $p$  as

$$\Lambda_p(q) = \sum_{k=1}^p \lambda_k q^{-k} = \lambda_1 q^{-1} + \lambda_2 q^{-2} + \dots + \lambda_p q^{-p} \quad (4.27)$$

allows us to write the ARMAX( $m, n, p$ ) model conveniently as

$$\Phi_m(q) \tilde{z}_t = \Theta_n(q) \omega_t + \Lambda_p(q) e_t. \quad (4.28)$$

The careful reader might already be aware of the fact that all of the linear stationary models discussed so far have a similar structure. In fact, many models in linear system analysis can be considered a special case of the general discrete time model structure

$$\Phi(q) \tilde{z}_t = \frac{\Theta(q)}{\Psi(B)} \omega_t + \frac{\Lambda(q)}{\Xi(q)} e_t \quad (4.29)$$

where  $\Phi(q)$ ,  $\Theta(q)$ ,  $\Lambda(q)$ ,  $\Psi(q)$ , and  $\Xi(q)$  are polynomials of the shift operator  $q$  (Ljung, 1987; Suykens et al., 1996). Table 4.1 summarizes some of the commonly used discrete time models, which can be considered special cases of Eq. (4.29); however, the current study is limited to models we have discussed so far.

**Table 4.1 Special cases of the generalized linear model (Eq. 4.29). Polynomials of the shift operator that are not listed for a model are assumed to equal unity**

Polynomials	Model
$\Phi, (\Lambda/\Xi = 0)$	AR (autoregressive)
$\Theta, (\Lambda/\Xi = 0)$	MA (moving average)
$\Theta, \Phi, (\Lambda/\Xi = 0)$	ARMA (autoregressive moving average)
$\Phi, \Lambda$	ARX (AR-eXogenous)
$\Theta, \Phi, \Lambda$	ARMAX (ARMA-eXogenous)
$\Phi, \Theta, \Psi$	ARARX (autoregressive-ARX)
$\Phi, \Theta, \Lambda, \Xi$	ARARMAX (autoregressive ARMAX)
$\Theta, \Psi, \Lambda, \Xi$	BJ (Box–Jenkins)

## 4.2.2 Linear nonstationary models

If the sequence of weights in Eq. (4.8) is infinite but not convergent, the linear filter's transfer function  $G(q)$  is said to be unstable and the process  $z_t$  to be nonstationary. In this case,  $\mu$  has no physical meaning except as a reference to the level of the process (Fig. 4.1(b)). Nonstationary processes are different in one or more respects throughout the time series due to the time-dependent nature of the level. As a result, in the analysis of nonstationary time series, time must play a fundamental role, for example, as the independent variable in a progression function, or as a normalization factor in the analysis of the evolution of a phenomenon from an initial state (Wold, 1938). Several observed time series behave as if they have no specified mean about which they fluctuate, for example, daily stock prices or hourly readings from a chemical process (Box and Jenkins, 1998).

### 4.2.2.1 Autoregressive integrated moving average models

While nonstationary processes do not fluctuate about a static mean, they still display some level of homogeneity to the extent that, besides a difference in local level or trend, different sections of the time series behave in a quite similar way. These nonstationary processes may be modeled by particularizing an appropriate difference, for example, the value of the level or slope, as stationary (Fig. 4.1(b) and (c)). What follows is a description of an important class of models for which it is assumed that the  $d$ th difference of the time series is a stationary ARMA( $m, n$ ) process.

We have seen that the stationarity condition of an ARMA( $m, n$ ) process is that all roots of  $\Phi_m(q) = 0$  lie outside the unit circle, and when the roots lie inside the unit circle, the model exhibits nonstationary behavior. However, we have not discussed the

situation for which the roots of  $\Phi_m(q) = 0$  lie on the unit circle. Let us examine the following ARMA( $m, n$ ) model

$$\Phi_m(q)\tilde{z}_t = \Theta_n(q)\omega_t \quad (4.30)$$

and specify that  $d$  of the roots of  $\Phi_m(q) = 0$  lie on the unit circle and the residuum lie outside. We can then express the model as

$$\Phi_m(q)\tilde{z}_t = \Theta_n(q)(1 - q^{-1})^d \tilde{z}_t = \Theta_n(q)\omega_t \quad (4.31)$$

where  $\Phi_m(q)$  is a stationary and invertible AR( $m$ ) operator. Seeing that  $S^d\tilde{z}_t = S^d z_t$  when  $d \geq 1$ , we can write

$$\Phi_m(q)S^d z_t = \Theta_n(q)\omega_t. \quad (4.32)$$

Defining  $y_t = S^d z_t$  allows one to express the model in a more illustrative way

$$\Phi_m(q)y_t = \Theta_n(q)\omega_t \quad (4.33)$$

where it is clear that the model is in agreement with the assumption that the  $d$ th difference of the time series can be regarded as a stationary ARMA( $p, q$ ) process. We refer to Eq. (4.32) as the ARIMA process. Because the AR transfer function  $\Phi_m(q)$  is of order  $m$ ,  $d$  differencing steps are taken, and the MA transfer function  $\Theta_n(q)$  is of order  $n$  in Eq. (4.32), we refer to the process as ARIMA( $m, d, n$ ). In practice,  $d$  is typically 0, 1, or at most 2 (Box and Jenkins, 1998). As mentioned above, the ARIMA( $m, d, n$ ) model is equivalent to representing the process  $z_t$  as the output of a linear filter with transfer function  $\Phi_n^{-1}S^d\Theta_n$  and takes white noise  $\omega_t$  as an input, see Fig. 4.2.

In the past, ARIMA models have found applications in many areas of research; however, only recently have they been employed to model problems involving solar radiation. Craggs et al. (2000) used ARIMA models to compare 10, 20, 30 min, and 1 h averages of solar irradiance levels for a site in the United Kingdom. Santos et al. (2003) used an ARIMA(1, 1, 1) model to calculate synthetic daily solar radiation values using the monthly average radiation as the input for locations in Spain. Kärner (2002) carried out an ARIMA analysis for satellite-based global tropospheric and stratospheric temperature anomaly and solar irradiance data sets. Kärner's results emphasized a dominating role of the solar irradiance variability in variations of the tropospheric temperature. Yürekli et al. (2007) imposed ARIMA-based techniques to generate solar irradiance, temperature, and relative humidity forecasts for use in the control strategy of agricultural facilities. Stanhill and Cohen (2008) used a first-order ARIMA model to describe the time course of annual sunshine duration and global irradiance to study trends and changes in solar forcing at the Earth's surface and reported a 0.5% increase in solar forcing per decade during the 20th century. Kärner (2009) later employed ARIMA models to compare the variability of the total solar irradiance at the top of the atmosphere to surface air temperature series, which

he reports are strongly correlated. [Reikard \(2009\)](#) compared ARIMA models with a number of other methods, including transfer functions, neural networks, and hybrid models, for six data sets at resolutions of 5, 15, 30, and 60 min using the global horizontal component of solar irradiance. Reikard found that, in nearly all the tests, the best results are obtained using the ARIMA in logs, with time-varying coefficients. In [Perdomo et al. \(2010\)](#) the authors used daily solar radiation measurements carried out in Bogotá, Colombia, from 2003 to 2009 as inputs for an ARIMA(1, 0, 0) model for forecasting the mean daily global solar radiation. Like its stationary counterpart, the ARIMA model has, as of late, also found many applications in the construction of HSs ([Wu and Chan, 2011](#); [Voyant et al., 2011](#); [Mellit et al., 2005](#); [Reikard, 2009](#)).

#### **4.2.2.2 Autoregressive integrated moving average models with exogenous variables**

In a similar way to the ARMAX( $m, n, p$ ) model, the previous  $p$  values of an exogenous time series  $e_t$  may also be included into the ARIMA( $m, d, n$ ) model to yield the autoregressive integrated moving average models with exogenous variable (ARIMAX) process of order  $(m, d, n, p)$

$$\begin{aligned}\tilde{z}_t = & \varphi_1 S^d z_{t-1} + \dots + \varphi_m S^d z_{t-m} + \omega_t + \theta_1 \omega_{t-1} + \dots + \theta_n \omega_{t-n} + \lambda_1 e_{t-1} + \dots \\ & + \lambda_p e_{t-p}\end{aligned}\tag{4.34}$$

As we did before, defining  $y_t = S^d z_t$  in terms of the backward shift operator allows us to express the model in a more compact form

$$\Phi_m(q)y_t = \Theta_n(q)\omega_t + \Lambda_p(q)e_t\tag{4.35}$$

which again looks very similar to [Eq. \(4.29\)](#).

## **4.3 Artificial intelligence techniques**

The development of artificial intelligence (AI) techniques began in the early 1950s with a number of experiments conducted by Herbert Simon, Allen Newell, and Cliff Shaw ([Krishnamoorthy and Rajeev, 1996](#)). Simon was consulting at the RAND Corporation when he saw a printer using customary text and punctuation symbols to produce images ([Crevier, 1993](#)). Motivated by this, he recognized that machines could be used to simulate the decision-making process and possibly, if given enough resources, the human thought process. Simon enlisted the help of Allen Newell, the RAND Corporation logistics scientist who generated the code that printed the images, and Cliff Shaw to develop a program with the ability to provide proofs to mathematical theorems. The resulting program, called Logic Theorist, used heuristics to draw from a knowledge base of previously proved axioms to discover new proofs and would

ultimately solve 38 of the 52 problems presented by Bertrand Russell and Alfred Whitehead in their *Principia Mathematica* ([Russel and Whitehead, 1925](#)). Meanwhile, Claude Shannon demonstrated how a machine could be used to play a reasonable game of chess ([Shannon, 1950](#)). Shannon's chess program relied on the optimization of a weighted function dependent on the position of the chess pieces using a minmax procedure.

Another set of AI techniques that were motivated by a living organism's ability to adapt and evolve was developed in the 1970s by John Holland, a professor of Psychology and Electrical Engineering at the University of Michigan, Ann Arbor. In his book titled "Adaptation in Natural and Artificial Systems" [Holland \(1975\)](#), motivated by Darwinian views of evolution, conceptualized an algorithm that would identify an optimal solution through the combination and reproduction of the strongest individuals in a solution space. Holland's work was the first in a branch of AI techniques known as genetic algorithms (GAs). Neural and genetic computing remained relatively unpopular during the 1970s, however, with an increase in available computing power and technological advancements such as multilayer perceptrons (MLPs), the 1980s saw a renewed interest in artificial neural networks (ANNs) and GAs ([Mellit and Kalogirou, 2008; Goldberg, 1989](#)).

In contrast to the symbolic approach, these "evolutionary" approaches emphasize learning and adaptation over the representational power of symbolic processing. The "intelligence" of these systems is attributed to the ability to distinguish between two general classes of patterns without being directly programmed ([Stender and Addis, 1990](#)). For example, a set of solar irradiance measurements in one location forms a class of patterns which is different from a set at another location, as long as these sites are far enough away from each other as to not be correlated through local weather patterns ([Lave and Kleissl, 2010](#)). Evolutionary techniques are much more systematic than symbolic approaches, and it should be noted that the internal structure of the system itself is critical inasmuch as it determines the type of function the ANN is able to approximate ([Stender and Addis, 1990](#)).

### 4.3.1 Artificial neural networks

ANNs were motivated from the observations of a special type of cell known as a neuron. Neurons are responsible for a number of signal processing tasks in our bodies such as responding to touch, sound, light, or other external stimuli and receiving signals from the brain and spinal chord, which control muscles, glands and arteries. Neurons are located in the brain, spinal chord, and the autonomic ganglion found just outside of the spinal chord. Neurons are furnished with a number of antenna-like structures that stretch out from the cell body, or soma, which allow the cell to send and receive signals from other cells and the environment. The structures that allow the neuron to accept input signals are called dendrites; whereas the structures that carry signals away from the neuron are called axons. A neuron may possess numerous dendrites but it never has more than one axon. Nonetheless, the dendrites and axon may branch hundreds of times before they terminate forming complex treelike structures, see [Fig. 4.3\(a\)](#). By actively regulating calcium, chloride, potassium, and sodium ion

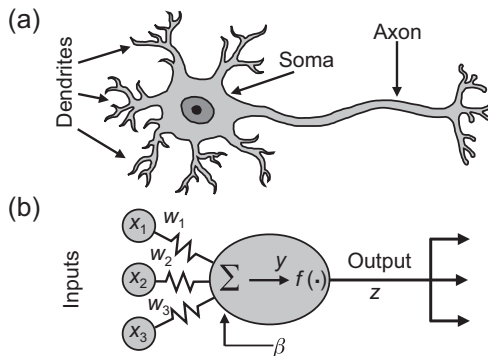


**Figure 4.3** (a) Simplified diagram of a biological neuron. Antenna-like structures which extend from the cell body, or soma, allow the neuron to communicate with other cells. The structures that allow the neuron to accept input signals are called dendrites. The structure that carries signals away from the neuron is called an axon. A neuron may possess numerous dendrites but it never has more than one axon. (b) Artificial neuron with inputs  $x_1$ ,  $x_2$ , and  $x_3$  weighted by  $w_1$ ,  $w_2$ , and  $w_3$ . The neuron has an embedded net function  $\beta + \sum_{i=1}^3 w_i x_i$  and transfer function  $f(\cdot)$  which are used to calculate output  $z$ .

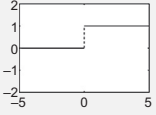
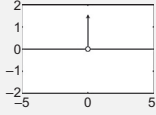
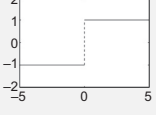
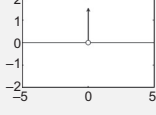
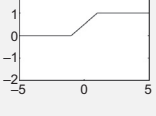
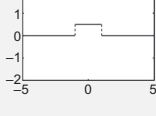
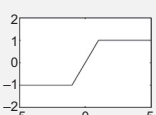
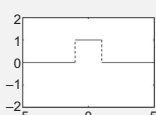
concentrations inside the cell, the neuron is able to maintain electrical potential gradients across its membrane. When a neuron's electric potential exceeds a specific threshold, an all-or-none electrochemical impulse called an action potential is generated. The action potential speeds down the neuron's axon and triggers synaptic communications at the tips of the axonic tree. This process is known as the "firing" of a neuron. The rate at which the neuron fires, which can reach up to 300 Hz, is regulated by adrenaline which acts as a bias for the neuron, making it much more likely to fire in the presence of a stimulus (Priddy and Keller, 2005).

Once the architecture of a biological neuron is understood, one can begin to construct an artificial neuron. Similar to their biological counterparts, artificial neurons can be connected to each other to form a network. A simple model of an artificial neuron which takes inputs  $x_1$ ,  $x_2$ , and  $x_3$  from three other neurons and processes a corresponding output  $z$  is detailed in Fig. 4.3(b). The quantity  $\beta$  is known as the bias and is used to model adrenaline's ability to lower the threshold. Because not every input is equally relevant to whether the neuron fires or not, we assign weights  $w_1$ ,  $w_2$ , and  $w_3$  to each of the inputs. Here we use a linear net function to sum the inputs which is given by

$$y = \beta + \sum_{i=1}^3 w_i x_i. \quad (4.36)$$

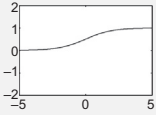
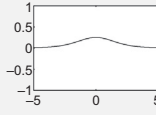
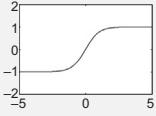
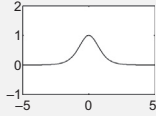
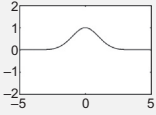
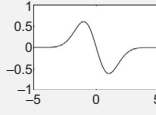
The firing rate of the action potential is modeled through the use of a transfer function  $f(\cdot)$ . Several different transfer functions have been suggested over the years, see Table 4.2. The most commonly used transfer function is the sigmoid or logistic

**Table 4.2 Artificial neuron transfer functions**

Class	Expression	Derivative	$f(z)$	$f'(z)$
Unipolar step or heavyside (threshold)	$f(y) = H(y) = \begin{cases} 1, & \text{if } y > 0 \\ 0, & \text{if } y \leq 0 \end{cases}$	$\delta(y) = \begin{cases} 0, & \text{if } y \neq 0 \\ \infty, & \text{if } y = 0 \end{cases}$		
Bipolar step (threshold)	$f(y) = \text{sign}(y) = 2H(y) - 1$	$\delta(y) = \begin{cases} 0, & \text{if } y \neq 0 \\ \infty, & \text{if } y = 0 \end{cases}$		
Unipolar linear	$f(y) = \begin{cases} 0, & \text{if } y < -1 \\ \frac{1}{2}(y+1), & \text{if } -1 \leq y < 1 \\ 1, & \text{if } y > 1 \end{cases}$	$\frac{1}{2}[H(y+1) - H(y-1)]$		
Bipolar linear	$f(y) = \begin{cases} -1, & \text{if } y < -1 \\ y, & \text{if } -1 \leq y < 1 \\ 1, & \text{if } y > 1 \end{cases}$	$H(y+1) - H(y-1)$		

*Continued*

**Table 4.2 Continued**

Class	Expression	Derivative	$f(z)$	$f'(z)$
Unipolar sigmoid (logistic)	$f(y) = \frac{1}{1+e^{-y}}$	$f(y)(1-f(y))$		
Bipolar sigmoid (hyperbolic tangent)	$f(y) = \tanh(y)$	$(1 -  f(y) ^2)$		
Gaussian radial basis	$f(y) = \exp\left(- y-m ^2/\sigma^2\right)$	$-2(y-m)f(y)/\sigma^2$		

function due to its attractive mathematical properties such as monotonicity, continuity, and differentiability (Mellit and Kalogirou, 2008; Priddy and Keller, 2005). Employing the sigmoid transfer function with the linear net function, the output  $z$  of the artificial neuron in Fig. 4.3(b) can be written in a very simple manner:

$$z = \frac{1}{1 + e^{-(\beta + \sum_i w_i x_i)}} \quad (4.37)$$

The attractiveness of ANNs stem directly from their likeness to their biological counterpart. Specifically, ANNs allow for very low-level programming (net and transfer functions) to solve a wide variety of complex, nonlinear, nonanalytic, nonstationary, stochastic, or general mathematically ill-defined problems in a self-organizing manner that requires little or no interference with the program itself.

#### 4.3.1.1 Simple perceptron

Arguably one of the first ANNs, simple perceptrons were developed by Frank Rosenblatt to act as electronic analogs to the human retina. Rosenblatt connected the input layer of the perceptron to a rectangular array of light sensors. A directed graph of a simple perceptron network is shown in Fig. 4.4(a). The weight connecting input node  $i$  to output node  $j$  is denoted by the matrix component  $w_{ij}$ . The goal of Rosenblatt's system was to trigger the relevant response unit given a class of input patterns. The input layer used a unipolar liner transfer function and the output was passed to the response layer by way of trainable weights.

The simple perceptron is said to use a form a supervised learning due to the fact that the weights were adjusted when an undesired response was triggered. The perceptron learning rule begins with a definition of the change made to the weight matrix component  $w_{ij}$  during the  $n$ th training set,

$$\Delta w_{ij}^{(n)} = \alpha \left( d_j^{(n)} - z_j^{(n)} \right) x_i^{(n)}, \quad (4.38)$$

where  $d_j^{(n)}$  is the desired output value for input  $x_i^{(n)}$ ,  $z_j^{(n)}$  is the actual output from the  $j$ th neuron with input  $x_i^{(n)}$ ,  $\epsilon^{(n)}$  is the output error of the  $n$ th set, and  $\alpha$  is referred to as the learning rate coefficient. Updating of the weight matrix  $\mathbf{W}$  proceeds as

$$\mathbf{W}^{(n+1)} = \mathbf{W}^{(n)} + \Delta \mathbf{W}. \quad (4.39)$$

The result after  $n$  training sets is that each of the weights  $w_{ij}$  will have been updated according to the rule outlined in Table 4.3. The perceptron learning rule can be optimized through the tuning of the learning rate coefficient  $\alpha$ . Small  $\alpha$  corresponds to a stable and slow learning scheme. Therefore, in practice, one would like to make  $\alpha$  as large as possible to ensure quick learning without introducing unstable oscillations about the desired value which result from overrelaxation.

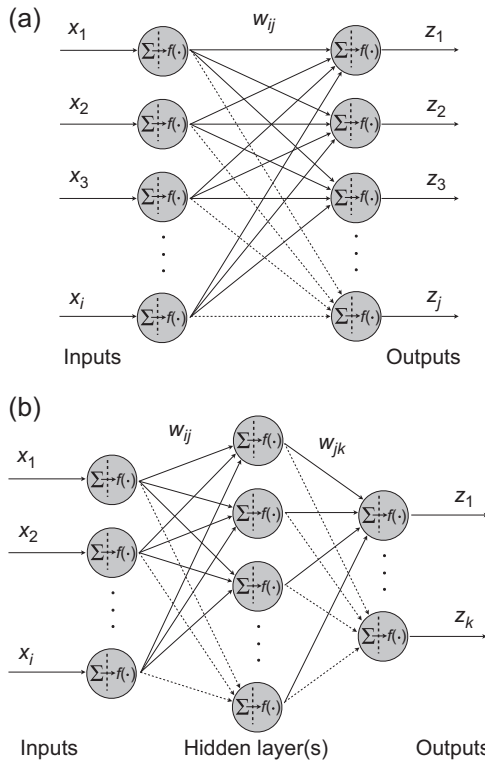


**Figure 4.4** (a) Simple perceptron logic only capable of mapping, which requires linear separability. (b) Multilayer artificial neural network capable of mapping, which requires nonlinear separability.

**Table 4.3 Perceptron learning rule**

$w_{ij}^{(n+1)} = w_{ij}^{(n)} + \alpha x_i^{(n)}$ $w_{ij}^{(n+1)} = w_{ij}^{(n)} - \alpha x_i^{(n)}$ $w_{ij}^{(n+1)} = w_{ij}^{(n)}$	If the output is zero and should be one If the output is one and should be zero If the desired output was achieved
---	--

In addition to the perceptron learning rule, Rosenblatt also proved a perceptron convergence theorem which states that given a finite set of inputs  $\mathbf{x}_N$  and desired output training sets  $\mathbf{d}_N$ , each presented with a positive probability, the perceptron learning rule provides guaranteed convergence of the weight matrix to values, which give the correct outputs if and only if the said set of weights exists. For a detailed outline of the proof see Patterson (1996).

**Table 4.4 XOR state table**

<b>State</b>	<b>Quadrant</b>	<b>Inputs</b>		<b>Output</b>	<b>Parity</b>
		$x_1$	$x_2$	$z$	
$\alpha$	1	1	1	0	Even
$\beta$	2	0	1	1	Odd
$\gamma$	3	0	0	0	Even
$\delta$	4	1	0	1	Odd

$$(x_1 \text{ or } x_2) \cap (\bar{x}_1 \text{ or } \bar{x}_2), \quad \text{where } \bar{x} \equiv \text{not } (x)$$

However, there are many tasks for which a set of weights do not exist and, as mentioned before, in 1969 Minsky and Pappert published a book concerning the strengths and limitations of single layer perceptron networks ([Minsky and Papert, 1969](#)). Included in this book, and the less popular earlier text by [E.B. Carne \(1965\)](#), was a criticism of the single-layer perceptron's inability to solve the simple two-state eXclusive-OR (XOR) problem, which is described in [Table 4.4](#). Solution of the XOR problem would require a nonlinear partitioning of even parity points from odd parity points. This is impossible for single-layer perceptrons that can only partition regions into two linearly separable spaces. As a result, researchers lost interest in neural computing, and work on perceptrons was effectively wiped out for almost two decades.

In the 1980s, almost 20 years after Minsky and Pappert's criticism of the simple perceptron's inability to solve the XOR problem, Bernard Widrow and Rodney Winter considered a new multilayer network which consisted of Many ADALINEs (MADALINE) ([Widrow and Winter, 1988](#)). In addition to the input and output layers of simple ANN structures in [Fig. 4.4\(a\)](#), the MADALINE architecture included additional layers, see [Fig. 4.4\(b\)](#). These additional neural layers are termed hidden due to the fact that no partial outputs are available for the training of these nodes. The use of multiple layers is one way of circumventing the problem of computing mappings, which require nonlinear separability. It is the introduction of hidden layers that enabled the MADALINE architecture to solve the XOR problem and renew interest in neural computing.

#### 4.3.1.2 Multilayer perceptron

MLPs with back propagation-learning (BPL) are some of the most established ANN architectures due to their ability to perform arbitrary nonlinear mappings. MLPs are also sometimes referred to as multilayer feed-forward networks to emphasize the forward flow of information with respect to the backward direction of weight adjustment used in BPL algorithm. The structure of MLPs consists of layered neurons possessing only forward connections to successive layers, see [Fig. 4.5](#).

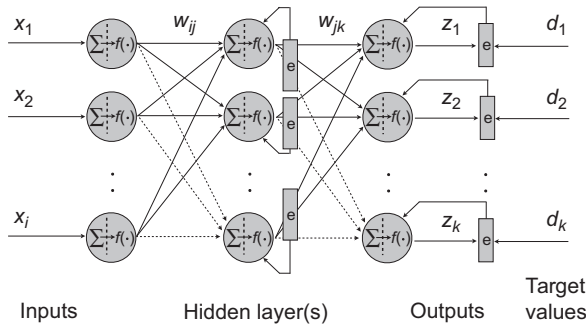


**Figure 4.5** Modification of a multilayer perceptron (MLP) network with a single hidden layer for the application of the back propagation-learning (BPL) algorithm. The use of partial derivatives of errors with respect to the weights upstream of the flow of information allows the algorithm to overcome the problem of inaccessible hidden layer data and is at the core of the BPL. The resulting algorithm may then be generalized to an MLP with an arbitrary number of hidden layers.

Several authors independently derived the BPL method in the 1970s and 1980s. Paul J. Werbos (1974) proposed the BPL method first in his 1974 Harvard University doctoral dissertation. Almost 10 years later, in 1985, D.B. Parker rederived the BPL method in his MIT technical report (Parker, 1985). Even so, credit for developing the BPL algorithm into a realizable procedure is typically assigned to David Rummelhart and the other members of his distributed processing group at the University of California, San Diego, in 1985 (Rumelhart and Zipser, 1985). In the BPL algorithm, for a given input pattern  $x_n$ , the information flows forward through the network until it reaches the output layer where node  $k$  calculates its output  $z_k$ . Subsequently, errors are calculated from knowledge of the desired output pattern  $d_n$ . The resulting errors are then propagated “backward” through the network every time a training pattern is presented, and weights  $w_{jk}$  are adjusted to minimize some error function. For a detailed discussion of the BPL algorithm, see Inman et al. (2013) and references therein.

### 4.3.2 *k*-nearest neighbors

Despite the similarity in the acronym, the *k*-nearest neighbors (*k*-NN) method is not related to ANNs. Although both methods belong to the family of AI techniques the origins of the *k*-NN stem from classification theory and its origins can be tracked back to an unpublished technical report by Fix and Hodges regarding the density estimation for classification theory (Duda et al., 2001; Ripley, 1996; Silverman et al., 1951).

As an algorithm for pattern classification in classification theory the *k*-NN method is one of the several nonparametric techniques for estimating the density functions from sample patterns. Within the confines of classification theory the *k*-NN has a very specific place and its mathematical derivation and properties can be derived precisely. Outside of the confines of classification theory the *k*-NN is often defined more

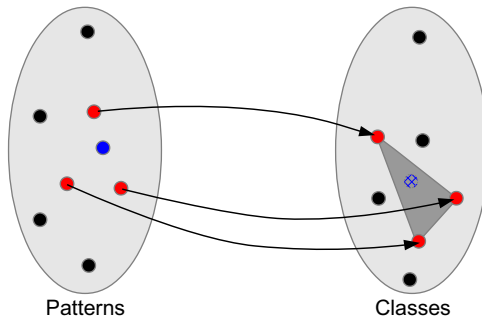


**Figure 4.6** The schematic of the  $k$ -nearest neighbors ( $k$ -NN) classification. The triangle represents the unclassified pattern and gray circles represent the three nearest neighbors. The class for the new pattern can be computed from some aggregation method (e.g., weighted average) from the  $k$ -NN classes. If a weighted average is used, the new class—represented by the star symbol, can assume values anywhere in the shaded area depending on the weights.

heuristically by the following statement (or some version thereof): an initial set of objects is created in which each object is classified by a property or value; new objects are classified based on a decision rule that assigns to the unclassified objects the class/value of the nearest  $k$  objects (hence the designation  $k$ -nearest neighbors), where  $k$  is a positive integer, typically small. If  $k = 1$ , then the object is simply assigned to the class of its nearest neighbor. Fig. 4.6 depicts this heuristic definition graphically.

The  $k$ -NN is one of the simplest methods among the machine learning algorithms. In contrast to the statistical methods presented before that attempt to find models from the available data, the  $k$ -NN uses the training data as the model, and unlike the ANN models there are no unknown model coefficients that need to be determined through training.

Despite the fact that the  $k$ -NN model was originally developed for pattern classification, its simplicity allows it to be applied to regression problems for time series (Yakowitz, 1987), such as the forecast of solar radiation. Although there are few articles in literature that apply  $k$ -NN to the forecasting of solar irradiation [see, for instance, (Paoli et al., 2010; Pedro and Coimbra, 2012)],  $k$ -NN has been extensively applied as a forecasting technique to problems such as the forecast of electricity load and electricity market price (Lora et al., 2002, 2003), the forecast of daily river water temperature (St-Hilaire et al., 2012), the forecast of water inflow (Akbari et al., 2011), and weather forecast (Bannayan and Hoogenboom, 2008), just to cite some of the most recent publications. In the field of meteorology and weather forecasting the  $k$ -NN method is also known as the analog method (Zorita and von Storch, 1999; Singh et al., 2008; Xavier and Goswami, 2007). The analog method searches a database of past weather patterns that resemble most closely the current weather conditions. The patterns are described either in terms of circulation patterns or in terms of various surface weather parameters. The selected past weather conditions, also known as analogs, are then used for predicting weather and its various components such as maximum, minimum and ambient temperatures, average wind speed, atmospheric

pressure, etc. Likewise, for the propose of forecasting time series, the  $k$ -NN model consists of looking into the time series history and identifying the time stamps in the past that resemble the “current” conditions most closely—the nearest neighbors. Once they are determined the forecasting is computed from the time series values subsequent to the matches. In essence, the  $k$ -NN model resembles a lookup table for which previous patterns are used as indicators of sequential behavior.

The first step in developing a  $k$ -NN model is to construct the database of features that will be used in the comparison with “current” conditions. For a univariate  $k$ -NN (no exogenous variables), examples of features used are values of the time series, averaged values of the time series, entropy of the time series, the cumulative sum of the time series, etc. If significant exogenous variables are available, they can easily be added to the set of patterns in the  $k$ -NN database. Fig. 4.7 exemplifies some of the patterns derived from a univariate time series in this case the global horizontal irradiance (GHI) clear-sky index,  $k_t$ .

With respect to the implementation of  $k$ -NN the algorithm can be easily summarized thus assuming that the  $n$  features or patterns for time  $t$  are assembled in the vector  $\vec{p}$  with components  $p_i$ ,  $i = 1, \dots, n$ , and that the features for historical data are assembled in a matrix  $A_{ij}$  whose rows correspond to the vector of features for each time in the historical data set, the  $k$  nearest neighbors to  $p_i$  can be determined in two steps:

1. compute the distance between  $p_i$  and all the rows from  $A_{ij}$ . Using the Euclidian distance that yields (other metrics such as Manhattan distance can be used in this calculation):

$$d_j = \sum_i \sqrt{(p_i - A_{ij})^2}. \quad (4.40)$$

2. extract the  $k$  indices that return smallest elements of  $d_j$  and their associated  $k$  time stamps  $\{\tau_1, \dots, \tau_k\}$ .

Once the set of nearest neighbors is determined the forecast can be obtained as:

$$z_{t+\Delta t} = \frac{\sum_{i=1}^k \alpha_i z_{\tau_i + \Delta t}}{\sum_{i=1}^k \alpha_i} \quad (4.41)$$

In other words, the prediction  $z_{t+\Delta t}$  is computed from a linear combination of the time series values that follow the nearest neighbors  $\tau_i$ . The weights  $\alpha_i$  often are a function of the distance  $d_j$  (Fig. 4.6).

## 4.4 Hybrid systems

A HS is characterized by a combination of any two or more of the methods described in the chapters of this book. As we will see below, currently HSs dominate the field of solar irradiance and solar power generation forecasting. One of the motivations for the development of hybrid models is that often it is possible to increase the forecasting

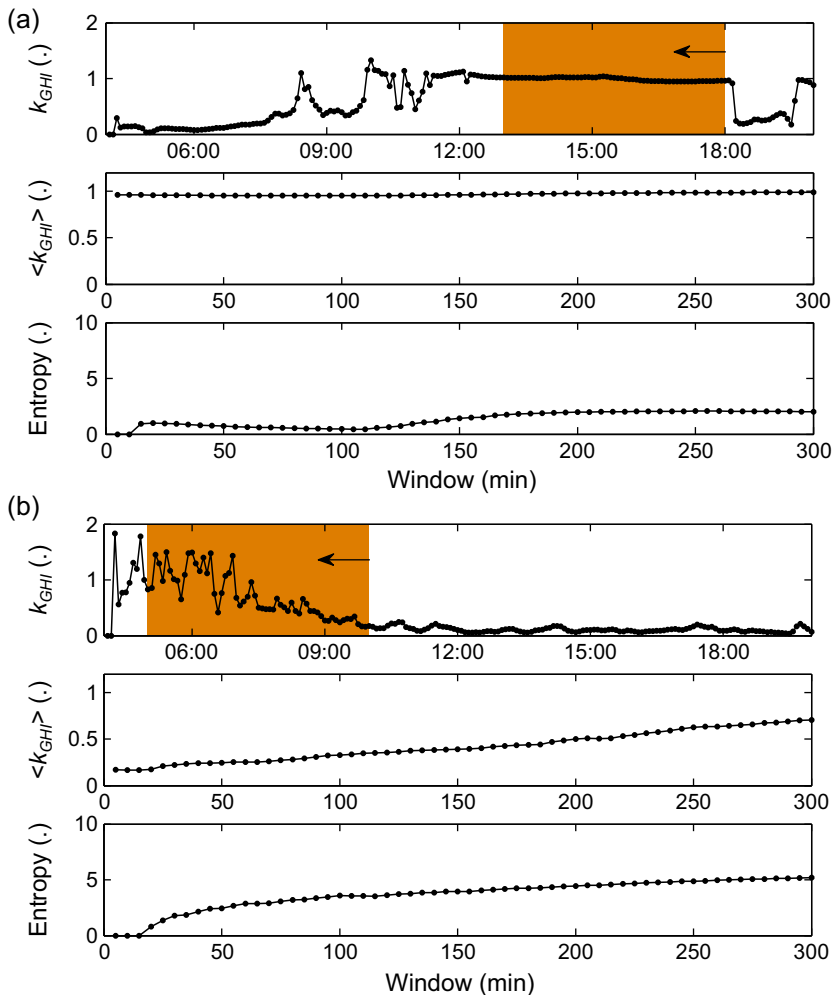


**Figure 4.7** Examples of preprocessing operations used to create patterns from the time series. Only the last 300 min are used in the computation of the patterns. (a) Examples of patterns of the  $k_{GHI}$  time series for a section of the time series with low variability. Top: the time series; middle: the backward cumulative sum for windows from 5 to 300 min; bottom: the entropy for windows from 5 to 300 min. (b) Same as (a) but for a section of the time series with high variability.

accuracy by taking advantage of the strengths of each methodology. A typical example for this is the pairing of cloud cover information derived from satellite images with ANNs as implemented in Marquez et al. (2013). Another reason to develop HSs concerns the situation illustrated in Fig. 4.8. This figure shows the approximate spatial and temporal limitations of each of the forecasting techniques described in this work. Noticeably, none of the individual methodologies is able to span all relevant areas

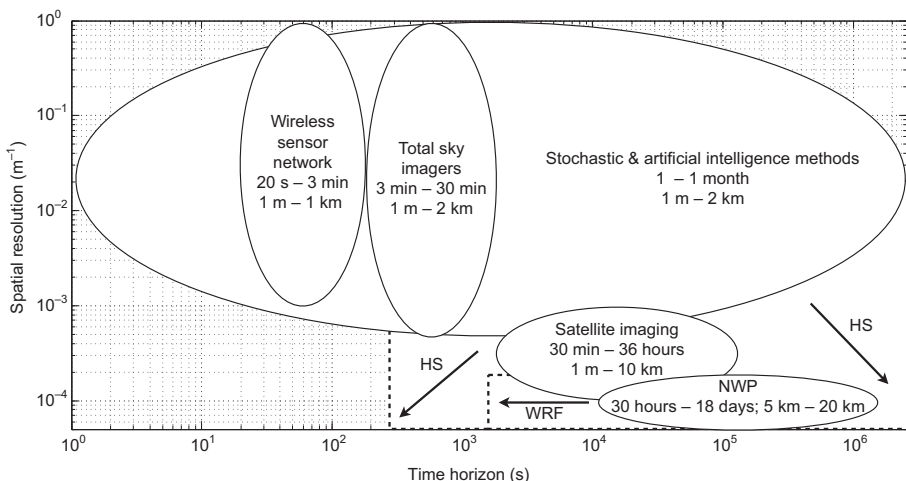


**Figure 4.8** Comparison of time horizon and spatial resolution. Solid lines indicate current limits of techniques while the dashed lines and arrows indicate the future progress of work. Artificial intelligence techniques will continue to include local, mesoscale, and global meteorological data, which will allow for both shorter time horizons and greater areas of interest. In addition, recent trends in Numerical Weather Prediction (NWP) suggest that shorter time horizons will be available through the development of the Weather Research and Forecasting (WRF) models.

of interest. For this reason, it is clear that a high-fidelity, robust forecasting engine would need to incorporate several of these techniques to appropriately forecast on several spatial and temporal resolutions.

Earlier examples of hybrid models for solar forecasting include the [Zarzalejo et al. \(2005\)](#) and [Mellit et al. \(2005\)](#). In [Zarzalejo et al. \(2005\)](#) the authors paired ANNs with satellite-derived cloud indexes for the forecasting of hourly mean GHI ([Zarzalejo et al., 2005](#)). [Mellit et al. \(2005\)](#) developed a hybrid model to predict the daily GHI by combining an ANN and a library of Markov transition matrices.

[Marquez and Coimbra \(2011\)](#) developed and validated a medium-term solar irradiance forecast for both GHI and DNI based on stochastic learning methods, ground experiments, and the National Weather Service database. A GA was used as an input selector to their ANN to select the most relevant input patterns. [Voyant et al. \(2012\)](#) used a hybrid ARMA/ANN with NWPs to predict hourly mean GHI. [Marquez et al. \(2012\)](#) also used cloud indexes obtained from a total sky imager as well as cloud indexes derived from infrared radiometric measurements to improve result for hourly forecasts of GHI. Marquez, Pedro, and Coimbra have developed a forecast based on satellite images and ANNs for time series predictions of GHI up to 2 h ahead ([Marquez et al., 2013](#)).

It is noteworthy in [Fig. 4.8](#) that stochastic and ANN techniques have a much broader coverage than other techniques especially in terms of time horizon. This is a direct result from these techniques relying on observational time series, and therefore their time horizon is generally limited only by the sampling frequency used for data acquisition. However, this does not imply that an appropriate ratio between time horizon and

temporal resolution, or data granularity, should not be conserved. In other words, as the data granularity changes, so should the time horizon. For instance, a sampling frequency of 2 Hz would imply the same bound on temporal resolution; therefore, a forecast horizon on the order of seconds would be appropriate. If high-frequency data are available, it is possible to preprocess the data to produce, for example, hourly or daily averages, lowering granularity and allowing for an effective extension of the temporal horizon. Having said that, the reciprocal argument does not hold: data initially logged at low sampling frequencies, daily averages, for instance, cannot be preprocessed in a manner which would make it appropriate for forecasting short time horizons, e.g., 30 min. In conclusion, meaningful time horizons should be of the same order of magnitude as the temporal resolution of the data. The degradation of forecasting quality with increased temporal extrapolation is a common issue in the area of forecasting and is not unique to irradiance prediction. In addition to the limitations imposed on spatial and temporal resolution, it should be noted that the forecasting skill of each of the individual techniques is a function of these resolutions; most notably the time horizon.

## 4.5 State of the art in solar forecasting

In this section, we review recent works that illustrate the state of the art in solar forecasting. The timeline for the papers included here starts in 2013 [for articles published prior to 2013, we refer the reader to the comprehensive reviews by [Mellit and Kalogirou \(2008\)](#) and [Inman et al. \(2013\)](#)].

**Table 4.5** summarizes some of these works and lists their main features such as the type of data used, the forecasting horizon and the methodology used. The analysis of recent works in solar forecasting research reveals broad trends:

- expansion of the set of input variables with exogenous data relevant to the forecasting;
- prepossession of the input variables into data more amenable to the forecasting tools;
- exploration of probabilistic forecasting tools instead of the classic point forecast;
- expansion of the forecasting to large spatial domains;
- creation of models dedicated to forecast extreme events such as solar and power ramps;
- exploration of new performance metrics to allow for a better assessment of forecast models.

### 4.5.1 Exogenous data

By far, the most common approach to improve solar irradiance and power generation forecasts consists in expanding the input variables with exogenous data. The most popular exogenous data streams include the output data from NWP models, satellite images, and local telemetry such as meteorological variables or sky images.

NWP exogenous data is, in most cases, simply obtained from public services. Examples of public NWP data used in this research include NOAA's North American Mesoscale Forecast System (NAM), NOAA's National Digital Forecast Database (NDFD), and the European Centre for Medium-Range Weather Forecast (ECMWF). In other cases, researchers opt to use in-house NWP models usually by running the

**Table 4.5 List of recent works (since 2014) in the forecasting solar irradiance and photovoltaic (PV) power generation**

Authors	Variable	Spatial domain	Probability	Granularity/horizon	Exogenous data	Methodology	Preprocessing
Bracale et al. (2013)	PV	Single point	Yes	1 h/1 h	Solar irradiance, meteorology, cloud cover	$k_t$ PDF forecasted with Bayesian autoregressive model; Monte Carlo using the PDF and a PV system model	—
Dong et al. (2013)	GHI	Single point	Yes	5–60 min/ 5–60 min	—	Exponential smoothing state space (ESSS) model	Fourier trend model to stationarize the time series
Huang et al. (2013)	GHI	Single point	No	1 h/1 h	—	CARDS and Lucheroni model	Fourier trend model to stationarize the time series
Lonij et al. (2013)	PV	80 rooftop PV	No	15 min/ 15–90 min	GHI	Frozen cloud model	—
Voyant et al. (2013)	GHI	Single point	No	1 h/1 h	—	Hybrid ANN/ARMA; model depends on the antecedent forecast error	Three approaches to stationarize data based on clear-sky normalization

Yang et al. (2013)	GHI	Ten weather stations	No	1 h/1 h	—	Time-forward kriging	Clear-sky normalization and coordinate transformation for stationarity	
Dambreville et al. (2014)	GHI	Single point	No	15 min/ 15–60 min	Satellite- derived GHI	ARX	Clear-sky normalization	
De Giorgi et al. (2014)	PV	Single point	No	1 h/1–24 h	Meteorological data	Multiregression analysis; Elmann artificial neural network	—	
Li et al. (2014)	PV	Single point	No	1 day/1 day	Meteorological data, GHI	Generalized ARMAX model	Moving average and exponential smoothing	
Nonnenmacher and Coimbra (2014)	GHI	Single point	No	1–3 h/1–3 h	Satellite images	Cloud advection along quasisteady streamlines. Optical flow model to determine cloud motion	—	
Quesada-Ruiz et al. (2014)	DNI	Single point	No	1–20 min/ 1–20 min	Sky images	Frozen cloud motion	Clear-sky normalization	
Yang et al. (2014)	GHI	Ten weather stations	No	5 min/ 5–20 min	—	Space–time kriging and vector autoregressive models based on long-term threshold distance of the spatiotemporal irradiance	—	

*Continued*

**Table 4.5 Continued**

Authors	Variable	Spatial domain	Probability	Granularity/horizon	Exogenous data	Methodology	Preprocessing
Yang et al. (2014)	GHI	Single point	No	30 s/30 s-15 min	Sky images	Frozen cloud method based on high-resolution sky images	Clear-sky normalization
Yang et al. (2014)	PV	Single point	No	1 h/24 h	Solar irradiance, meteorology, NWP data	SVR for different weather classes	Self-organizing map (SOM) and learning vector quantization (LVQ) networks are used to classify the data
Alessandrini et al. (2015)	PV	Single point	Yes	1 h/1–72 h	NWP output data	Analog ensemble ( $k$ -NN) based on an historical data; quantile regression for the probability forecast	—
Pinho Almeida et al. (2015)	PV	Single point	Yes	1 h/1–24 h	NWP output data	Quantile regression forests	Inputs selection: previous days, similar $k_t$ , similar irradiance PDF
Alonso-Montesinos and Batllés (2015)	GHI, DNI, DHI	Single point	No	15 min/15–180 min	Satellite images	Frozen cloud method	—

Chu et al. (2015a)	DNI	Single point	Yes	5 min/ 5–20 min	Sky images	Hybrid ANN/SVR model; Bootstrap-ANN model for the prediction intervals	Clear-sky normalization	
Chu et al. (2015b)	GHI, DNI	Single point	No	1 min/10 min	Sky images	ANN optimized with genetic algorithm	Clear-sky normalization	
Chu et al. (2015c)	PV	Single point	No	5 min /5–15 min	PV forecasts from a cloud tracking model	ARMA, <i>k</i> -NN, ANN optimized with genetic algorithm	Clear-sky normalization	
De Giorgi et al. (2015)	PV	Single point	No	1 h/1–24 h	Solar irradiance, temperature	Least square support vector machines (LS-SVM)	Wavelet decomposition	
Lipperheide et al. (2015)	PV	1 km <sup>2</sup> PV plant	No	1 s/20–180 s	—	Cloud speed persistence method; AR model	Clear-sky normalization	
Mazorra Aguiar et al. (2015)	GHI	Regional	No	1 h/1–6 h	Gridded satellite-derived GHI	ANN	Clear-sky normalization	
McCandless et al. (2015)	GHI	Distributed (8 weather stations)	No	15 min/ 15–180 min	Meteorological data	Model tree with nearest neighbors	—	
Pedro and Coimbra (2015a)	GHI, DNI	Single point	Yes	5–30 min/ 5–30 min	Sky images	Nearest neighbors; feature optimization	Clear-sky normalization	

*Continued*

**Table 4.5 Continued**

Authors	Variable	Spatial domain	Probability	Granularity/horizon	Exogenous data	Methodology	Preprocessing
Rana et al. (2015)	PV	Single point	Yes	1–30 min/ 30 min–6 h	Solar irradiance, meteorology	SVR	—
Thorey et al. (2015)	GHI	Regional	No	6 h/12–42 h	NWP	Optimized ensembles of GHI NWP forecasts	—
Zagouras et al. (2015)	GHI	Single point	No	1 h/1–3 h	Satellite-derived GHI	Linear models, ANN, SVR, and GA optimized linear model	Clear-sky normalization; correlation analysis to select lagged satellite- derived GHI
Aguiar et al. (2016)	GHI	Single point	No	1 h/1–6 h	Satellite-derived GHI; NWP GHI and cloud cover	ANN; Bayesian framework and automatic relevance determination for ANN optimization	Clear-sky normalization; Pearson correlation to select ANN inputs
Aybar-Ruiz et al. (2016)	GHI	Single point	No	1 h/1–3 h	NWP output data	Extreme learning machine algorithm with GA feature selection	—

Cheng (2016)	GHI	Single point	No	2–10 min/ 10–20 min	Sky images	Kalman filter; autoregression; time-varying adaptive Kalman filter to deal with ramp-down	—	
Chu et al. (2016)	DNI	Single point	No	1 min/ 5–20 min	Sky images (sun-centered and zenith- centered)	ANN	—	
David et al. (2016)	GHI	Single point	Yes	10–60 min/ 10 min–6 h	—	ARMA, GARCH, ANN, Gaussian processes, SVM	Clear-sky normalization	
Golestaneh et al. (2016)	PV	Single point	Yes	1 min/ 1–60 min	—	Extreme learning machine	—	
Grantham et al. (2016)	GHI	Single point	Yes	1 h/1 h	—	Nonparametric bootstrapped statistical ensemble	—	
Gutierrez- Corea et al. (2016)	GHI	Single point	No	1 h/1–6 h	Meteorological data	ANN; system for automated learning modeling operative networks used to select ANN parameters	Clear-sky normalization	
Jiménez-Pérez and Mora- López (2016)	GHI	Single point	No	1 h/2 4h	NWP data	Decision trees, ANN, SVM	Clustering analysis	

*Continued*

**Table 4.5 Continued**

<b>Authors</b>	<b>Variable</b>	<b>Spatial domain</b>	<b>Probability</b>	<b>Granularity/horizon</b>	<b>Exogenous data</b>	<b>Methodology</b>	<b>Preprocessing</b>
Larson et al. (2016)	PV	Single point	No	1 h/1–24h	NWP cloud cover and GHI from neighboring nodes	Least-squares optimization of NWP data	—
McCandless et al. (2016)	GHI	Single point	No	15 min/15–180 min	Meteorological data and observed cloud cover	ANN trained for each regime	K-means clustering used to determine cloud regime
Nonnenmacher et al. (2016)	DNI	Single point	No	1 h/1–24 h	NWP cloud cover	Linear relation between DNI and NWP cloud cover	Clear-sky normalization with aerosol correction based on measured data
Pierro et al. (2016)	PV	Single point	Yes	1 h/24 h	NWP output data	Multimodel ensemble, MOS correction, ARIMA, SVM, ANN	Clear-sky normalization; empirical mode decomposition; wavelet decomposition
Scolari et al. (2016)	GHI	Single point	Yes	500 ms–5 min/500 ms–5 min	—	Nearest neighbors	K-means clustering

Sperati et al. (2016)	PV	Single point	Yes	1 h/1–72 h	Ensembles from NWP model (ECMWF)	NN used to reduce bias; variance deficit; ensemble model output statistics	—	—
Vaz et al. (2016)	PV	Single point	No	15 min/ 15–60 min	GHI, temperature, and data from neighboring PV systems	Nonlinear autoregressive model with exogenous inputs	—	—
Wolff et al. (2016)	PV	Single point	No	15 min/ 15 min–5 h	GHI, DNI, NWP output data	SVR	Clear-sky normalization	—

*ANN*, artificial neural network; *ARIMA*, autoregressive integrated moving averages; *ARMA*, autoregressive moving averages; *ARMAX*, autoregressive moving average models with exogenous variables; *ARX*, AR-exogenous; *DHI*, diffuse horizontal irradiance; *DNI*, direct normal irradiance; *GA*, genetic algorithm; *GHI*, global horizontal irradiance; *MOS*, model output statistics; *NWP*, Numerical Weather Prediction; *PDF*, probability density function; *SVR*, support vector regression.

popular Weather Research and Forecasting (WRF) model. In these cases, “future” information is ingested into the forecasting algorithms through the data computed with the NWP models (Alessandrini et al., 2015; Pinho Almeida et al., 2015; Aguiar et al., 2016; Aybar-Ruiz et al., 2016; Larson et al., 2016; Nonnenmacher et al., 2016; Pierro et al., 2016). However, due to the low temporal resolution of these data (usually larger than 1 h), forecast models that use this information can only target coarse hourly intraday and day(s)-ahead forecast.

For higher-resolution forecasts, researchers often use local telemetry as exogenous data. These consist in meteorological data such as temperature, wind speed and direction, dew point, etc. These variables often are used, simply, as predictors for the forecasting models (Bracale et al., 2013; Lonij et al., 2013; De Giorgi et al., 2014; Vaz et al., 2016). In other cases, the meteorological variables are used in classification and clustering algorithms that allow to create forecasting models specific for some pre-defined condition or to identify highly correlated exogenous variables (Yang et al., 2014; Zagouras et al., 2015; Scolari et al., 2016). Local telemetry can be used, for instance, to classify the weather as clear sky or cloudy sky and adapt the forecasting model accordingly.

Due to the significance of clouds to irradiance and solar generation, another type of local sensing has become very popular: sky images. In this type of research, authors make use of image processing tools to identify clouds and detect cloud motion. This information is then used as a predictor to the forecast model.

In some cases the authors use cloud cover information or sky image features (red-to-blue ratio, image entropy, etc.) in machine learning models (Pedro and Coimbra, 2015a; Chu et al., 2016; Cheng, 2016). In other cases they use a physical-based approach in which the clouds are advected into the future, thus determining the irradiance and solar generation (Yang et al., 2014). The limited field of view restricts the time horizon for these methodologies to less than 30 min. On the other hand, the forecast temporal resolution can be very high, limited only by the image acquisition time.

Similar procedures are used for forecasting models that use satellite images such as the ones provided by NOAA’s geostationary satellite server. Due to low spatial and temporal resolutions, those images are appropriated for intraday forecasts with temporal resolutions higher than 15–30 min. On the plus side, the geographical coverage provided by those images allows for longer forecast horizons and wider forecast coverage than the sky images (Alonso-Montesinos and Batles, 2015; Nonnenmacher and Coimbra, 2014).

#### **4.5.2 Data preprocessing**

Another approach followed in many recent works is to explore preprocessing techniques that enhance the forecast. A traditional approach in this regard is the clear-sky normalization. In this technique the solar irradiance or power generation are normalized by some CSM. This allows to remove deterministic fluctuations in the time series and targeting the stochastic component.

Recent works show that researchers are actively pursuing other preprocessing techniques such as wavelet and Fourier transformations and mode decomposition. The trust behind these approaches is to transform the original time series into a set of

time series “easier” to forecast (Dong et al., 2013; Huang et al., 2013). For instance, by decomposing the time series into low- and high-frequency time series, researchers can use different forecasts models tailored for each case (Pierro et al., 2016). The final forecast is then the aggregation of the low- and high-frequency forecasts.

### **4.5.3 Probabilistic forecasts**

Another recent development in this area of research is related to providing some uncertainty measure for the forecast. Traditionally, forecast models would provide a single value valid for some future time. Efforts to integrate forecasting models into the management of power grids revealed that a probabilistic forecast is, in many cases, more useful than a single point forecast. The research community has put some effort in this problem, and in recent years, many forecast algorithms have been created to provide the point forecast, the prediction intervals, and/or the prediction probability distribution function. Methodologies used for this problem include Monte Carlo simulations or the ensembling or bootstrapping of a large number of point forecasts (Bracale et al., 2013; Scolari et al., 2016; Pedro and Coimbra, 2015a; Chu et al., 2015a; Rana et al., 2015; Sperati et al., 2016).

### **4.5.4 Increasing forecasting spatial coverage**

Another recent avenue pursued in solar energy consists in expanding the geographical domain of the forecasts. Traditionally, forecast models produce a prediction for a single point in space and do not extrapolate well outside of a close vicinity. Naturally, with the proliferation of solar farms that can cover very large areas, there was a need to expand the spatial domain of the forecast. Techniques used to extend the forecast use satellite images for low temporal resolution forecasts. For high resolution, researchers typically use multiple sky cameras, irradiance sensors spread across the area of interest or inverter data from the solar farm (Lonij et al., 2013; Lipperheide et al., 2015; Yang et al., 2013).

### **4.5.5 Ramp forecasts**

Another recent development in this research consists in optimizing the forecasting models for specific extreme events. In the past, virtually every forecast algorithm was trained or optimized to minimize some bulk error metric between the predictions and the measured values. Recently, while developing high-resolution intrahour forecasts, researchers realized that extreme events may not be well captured by the models. In particular, ramp events in which the irradiance or solar generation vary wildly in a matter of minutes tend to be poorly predicted. Given that in most training data sets, those events are underrepresented their impact in the bulk error metric that defines the fitness of the model is small, leading to models optimized for the average behavior of the time series. Naturally, such models tend to underpredict ramps. To address this issue a small number of researchers have started to include some ramp metrics in the analysis of the forecasting model (Cheng, 2016; Lipperheide et al., 2015; Chu et al., 2015b).

#### **4.5.6 Forecast assessment**

Finally, motivated by the large number of forecasting models in the literature and the difficulty in comparing competing models based on a few bulk error metrics, researchers are investigating new ways to characterize forecasting performance and the volatility of the irradiance and solar generation time series. Some authors attempt to define some predictability metrics that assess the level of difficulty in the forecasting (Pedro and Coimbra, 2015b; Voyant et al., 2015), while others develop a large set of error metrics to improve the validation of solar forecasting (Gueymard, 2014).

### **4.6 Conclusions**

A number of regressive, statistical, and stochastic methods for solar forecasting and their applications are covered in this chapter. From the description of the numerous approaches presented, it is clear that some level of predictive success has been experienced for a number of different spatial and temporal resolutions. This review indicates that a robust number of techniques and best practices have been developed in the past few years.

Regression methods, which take advantage of the correlated nature of the irradiance observations, tend to work well in both data-poor and data-rich environments. In data-poor environments, one might only have access to historical point sensor or power output data in which case endogenous stochastic methods can be used such as AR, MA, ARMA, and/or ARIMA. On the other hand, in a data-rich environment, one may have access to a wide number of additional data such as the time evolution of observations of meteorology and cloud cover. In these environments, exogenous inputs are included through a careful input selection process. These stochastic learning methods have been applied to a wide variety of time horizons ranging from intrahour to yearly averages.

ANN modeling offers improved nonlinear approximator performance and provides an alternative approach to physical modeling for irradiance data when enough historical data are available. ANNs are generic nonlinear approximators that deliver compact solutions for several nonlinear, stochastic, and multivariate problems. Like regression methods, ANNs perform well in both data-rich/poor environments and are not typically temporally limited. These techniques have been applied successfully to the modeling and forecasting of irradiance and solar power generation.

Recently, various hybrid methods incorporating two or more of the techniques discussed in this work have been presented. These methods offer many advantages over traditional approaches, including the ability to combine stochastic and deterministic forecast. Integration of NWP/satellite models with stochastic learning methods results in higher accuracy forecasts for several time horizons of interest. By the same reasoning, assimilating local meteorological information from sky imagers and wireless sensor networks through stochastic learning methods should result in higher-fidelity coverage of intrahour time horizons. Thus, a complete system in the form of a high-fidelity solar forecast engine that spans the entire spectrum of temporal and

spatial horizons, from intraminate to multiple days, and from single point radiometers to continental regions, is possible when multiple data inputs are combined with stochastic learning.

## References

- Aguiar, L.M., Pereira, B., Lauret, P., Díaz, F., David, M., November 2016. Combining solar irradiance measurements, satellite-derived data and a numerical weather prediction model to improve intra-day solar forecasting. *Renewable Energy* 97, 599–610.
- Akbari, M., Overloop, P., Afshar, A., 2011. Clustered k nearest neighbor algorithm for daily inflow forecasting. *Water Resources Management* 25 (5), 1341–1357.
- Al-Awadhi, S.A., El-Nashar, N., November 2002. Stochastic modelling of global solar radiation measured in the state of Kuwait. *Environmetrics* 13 (7), 751–758.
- Alessandrini, S., Delle Monache, L., Sperati, S., Cervone, G., November 2015. An analog ensemble for short-term probabilistic solar power forecast. *Applied Energy* 157, 95–110.
- Alonso-Montesinos, J., Batlles, F.J., April 2015. Solar radiation forecasting in the short- and medium-term under all sky conditions. *Energy* 83, 387–393.
- Aybar-Ruiz, A., Jiménez-Fernández, S., Cornejo-Bueno, L., Casanova-Mateo, C., Sanz-Justo, J., Salvador-González, P., Salcedo-Sanz, S., July 2016. A novel Grouping Genetic Algorithm – Extreme Learning Machine approach for global solar radiation prediction from numerical weather models inputs. *Solar Energy* 132, 129–142.
- Bannayan, M., Hoogenboom, G., 2008. Predicting realizations of daily weather data for climate forecasts using the non-parametric nearest-neighbour re-sampling technique. *International Journal of Climatology* 28 (10), 1357–1368.
- Box, G.E.P., Jenkins, G.M., 1998. *Time Series Analysis, Forecasting and Control*. Wiley.
- Bracale, A., Caramia, P., Carpinelli, G., Di Fazio, A.R., Ferruzzi, G., February 2013. A Bayesian method for short-term probabilistic forecasting of photovoltaic generation in smart grid operation and control. *Energies* 6 (2), 733–747.
- Carne, E.B., 1965. *Artificial Intelligence Techniques*. Spartan Press, Washington, DC.
- Chaabene, M., Ben Ammar, M., July 2008. Neuro-fuzzy dynamic model with Kalman filter to forecast irradiance and temperature for solar energy systems. *Renewable Energy* 33 (7), 1435–1443.
- Cheng, H.-Y., June 2016. Hybrid solar irradiance now-casting by fusing Kalman filter and regressor. *Renewable Energy* 91, 434–441.
- Chu, Y., Li, M., Pedro, H.T.C., Coimbra, C.F.M., 2015a. Real-time prediction intervals for intra-hour DNI forecasts. *Renewable Energy* 83, 234–244.
- Chu, Y., Pedro, H.T.C., Li, M., Coimbra, C.F.M., April 2015b. Real-time forecasting of solar irradiance ramps with smart image processing. *Solar Energy* 114, 91–104.
- Chu, Y., Urquhart, B., Gohari, S.M.I., Pedro, H.T.C., Kleissl, J., Coimbra, C.F.M., February 2015c. Short-term reforecasting of power output from a 48 MWe solar PV plant. *Solar Energy* 112, 68–77.
- Chu, Y., Li, M., Coimbra, C.F.M., October 2016. Sun-tracking imaging system for intra-hour DNI forecasts. *Renewable Energy* 96 (Part A), 792–799.
- Craggs, C., Conway, E.M., Pearsall, N.M., February 2000. Statistical investigation of the optimal averaging time for solar irradiance on horizontal and vertical surfaces in the UK. *Solar Energy* 68 (2), 179–187.

- Crevier, D., 1993. AI: The Tumultuous Search for Artificial Intelligence. Basic Books, New York, NY.
- Dambreville, R., Blanc, P., Chanussot, J., Boldo, D., December 2014. Very short term forecasting of the global horizontal irradiance using a spatio-temporal autoregressive model. *Renewable Energy* 72, 291–300.
- David, M., Ramahatana, F., Trombe, P.J., Lauret, P., August 2016. Probabilistic forecasting of the solar irradiance with recursive ARMA and GARCH models. *Solar Energy* 133, 55–72.
- De Giorgi, M.G., Congedo, P.M., Malvoni, M., May 2014. Photovoltaic power forecasting using statistical methods: impact of weather data. *IET Science, Measurement Technology* 8 (3), 90–97.
- De Giorgi, M.G., Congedo, P.M., Malvoni, M., Laforgia, D., August 2015. Error analysis of hybrid photovoltaic power forecasting models: a case study of Mediterranean climate. *Energy Conversion and Management* 100, 117–130.
- Denholm, P., Margolis, R.M., 2007a. Evaluating the limits of solar photovoltaics (PV) in traditional electric power systems. *Energy Policy* 35 (5), 2852–2861.
- Denholm, P., Margolis, R.M., 2007b. Evaluating the limits of solar photovoltaics (PV) in electric power systems utilizing energy storage and other enabling technologies. *Energy Policy* 35 (9), 4424–4433.
- Dong, Z., Yang, D., Reindl, T., Walsh, W.M., 2013. Short-term solar irradiance forecasting using exponential smoothing state space model. *Energy* 55, 1104–1113.
- Duda, R.O., Hart, P.E., Stork, D.G., 2001. Pattern Classification. Wiley.
- Goh, T.N., Tan, K.J., 1977. Stochastic modeling and forecasting of solar-radiation data. *Solar Energy* 19 (6), 755–757.
- Goldberg, D.E., 1989. Genetic Algorithms in Search, Optimisation and Learning. Addison-Wesley Publishing Co., Reading, Mass.
- Golestaneh, F., Pinson, P., Gooi, H.B., September 2016. Very short-term nonparametric probabilistic forecasting of renewable energy generation — with application to solar energy. *IEEE Transactions on Power Systems* 31 (5), 3850–3863.
- Grantham, A., Gel, Y.R., Boland, J., August 2016. Nonparametric short-term probabilistic forecasting for solar radiation. *Solar Energy* 133, 465–475.
- Gueymard, C.A., November 2014. A review of validation methodologies and statistical performance indicators for modeled solar radiation data: towards a better bankability of solar projects. *Renewable and Sustainable Energy Reviews* 39, 1024–1034.
- Gutierrez-Corea, F.V., Manso-Callejo, M.A., Moreno-Regidor, M.P., Manrique-Sancho, M.T., September 2016. Forecasting short-term solar irradiance based on artificial neural networks and data from neighboring meteorological stations. *Solar Energy* 134, 119–131.
- Holland, J.H., 1975. Adaptation in Natural and Artificial Systems. The University of Michigan Press.
- Huang, J., Korolkiewicz, M., Agrawal, M., Boland, J., January 2013. Forecasting solar radiation on an hourly time scale using a Coupled AutoRegressive and Dynamical System (CARDS) model. *Solar Energy* 87, 136–149.
- Inman, R.H., Pedro, H.T.C., Coimbra, C.F.M., 2013. Solar forecasting methods for renewable energy integration. *Progress in Energy and Combustion Science* 39 (6), 535–576.
- Jiménez-Pérez, P.F., Mora-López, L., October 2016. Modeling and forecasting hourly global solar radiation using clustering and classification techniques. *Solar Energy* 135, 682–691.
- Kärner, O., September–October 2002. On nonstationarity and antipersistency in global temperature series. *Journal of Geophysical Research (Atmospheres)* 107 (D20).

- Kärner, O., Jun. 2009. ARIMA representation for daily solar irradiance and surface air temperature time series. *Journal of Atmospheric and Solar-Terrestrial Physics* 71 (8–9), 841–847.
- Krishnamoorthy, C.S., Rajeev, S., 1996. Artificial Intelligence and Expert Systems for Engineers. CRC Press.
- Larson, D.P., Nonnenmacher, L., Coimbra, C.F.M., June 2016. Day-ahead forecasting of solar power output from photovoltaic plants in the American Southwest. *Renewable Energy* 91, 11–20.
- Lave, M., Kleissl, J., 2010. Solar variability of four sites across the state of Colorado. *Renewable Energy* 35 (12), 2867–2873.
- Lew, D., Piwko, R., 2010. Western Wind and Solar Integration Study. Technical report. National Renewable Energy Laboratories.
- Li, Y., Su, Y., Shu, L., June 2014. An ARMAX model for forecasting the power output of a grid connected photovoltaic system. *Renewable Energy* 66, 78–89.
- Lipperheide, M., Bosch, J.L., Kleissl, J., February 2015. Embedded nowcasting method using cloud speed persistence for a photovoltaic power plant. *Solar Energy* 112, 232–238.
- Ljung, L., 1987. System Identification: Theory for the User. Prentice-Hall.
- Lonij, V.P.A., Brooks, A.E., Cronin, A.D., Leuthold, M., Koch, K., November 2013. Intra-hour forecasts of solar power production using measurements from a network of irradiance sensors. *Solar Energy* 97, 58–66.
- Lora, A., Santos, J., Santos, J., Ramos, J., Exposito, A., 2002. Electricity market price forecasting: neural networks versus weighted-distance k nearest neighbours. In: Hameurlain, A., Cicchetti, R., Traunmüller, R. (Eds.), Database and Expert Systems Applications, Lecture Notes in Computer Science, vol. 2453. Springer, Berlin, Heidelberg, pp. 157–211.
- Lora, A.T., Riquelme, J.C., Ramos, J.L.M., Santos, J.M.R., Exposito, A.G., 2003. Influence of kNN-based load forecasting errors on optimal energy production. In: Pires, F.M., Abreu, S. (Eds.), Progress in Artificial Intelligence, vol. 2902. Springer-Verlag, Berlin, pp. 189–203.
- Marquez, R., Coimbra, C.F.M., 2011. Forecasting of global and direct solar irradiance using stochastic learning methods, ground experiments and the NWS database. *Solar Energy* 85 (5), 746–756.
- Marquez, R., Gueorguiev, V.G., Coimbra, C.F.M., 2012. Forecasting of global horizontal irradiance using sky cover indices. *ASME Journal of Solar Energy Engineering* 135 (1).
- Marquez, R., Pedro, H.T.C., Coimbra, C.F.M., 2013. Hybrid solar forecasting method uses satellite imaging and ground telemetry as inputs to ANNs. *Solar Energy* 92, 176–188.
- Mazorra Aguiar, L., Pereira, B., David, M., Díaz, F., Lauret, P., December 2015. Use of satellite data to improve solar radiation forecasting with Bayesian Artificial Neural Networks. *Solar Energy* 122, 1309–1324.
- McCandless, T.C., Haupt, S.E., Young, G.S., October 2015. A model tree approach to forecasting solar irradiance variability. *Solar Energy* 514–524.
- McCandless, T.C., Haupt, S.E., Young, G.S., April 2016. A regime-dependent artificial neural network technique for short-range solar irradiance forecasting. *Renewable Energy* 89, 351–359.
- Mellit, A., Kalogirou, S.A., October 2008. Artificial intelligence techniques for photovoltaic applications: a review. *Progress in Energy and Combustion Science* 34 (5), 574–632.
- Mellit, A., Benghanem, M., Arab, A.H., Guessoum, A., 2005. A simplified model for generating sequences of global solar radiation data for isolated sites: using artificial neural network and a library of Markov transition matrices approach. *Solar Energy* 79 (5), 469–482.
- Minsky, M., Papert, S., 1969. Perceptrons. MIT Press, Cambridge, MA.

- Mora-Lopez, L.L., Sidrach-De-Cardona, M., November 1998. Multiplicative ARMA models to generate hourly series of global irradiation. *Solar Energy* 63 (5), 283–291.
- Moreno-Muñoz, A., de la Rosa, J.J.G., Posadillo, R., Bellido, F., May 2008. Very short term forecasting of solar radiation. In: Photovoltaic Specialists Conference, 33rd IEEE, pp. 1–5.
- Nonnenmacher, L., Coimbra, C.F.M., October 2014. Streamline-based method for intra-day solar forecasting through remote sensing. *Solar Energy* 108, 447–459.
- Nonnenmacher, L., Kaur, A., Coimbra, C.F.M., February 2016. Day-ahead resource forecasting for concentrated solar power integration. *Renewable Energy* 86, 866–876.
- Paoli, C., Voyant, C., Muselli, M., Nivet, M.L., 2010. Forecasting of preprocessed daily solar radiation time series using neural networks. *Solar Energy* 84 (12), 2146–2160.
- Parker, D.B., 1985. Learning Logic. Technical report TR-47. Center for Computational Research in Economics and Management Science, MIT.
- Patterson, D.W., 1996. Artificial Neural Networks: Theory and Applications. Prentice-Hall.
- Pedro, H.T.C., Coimbra, C.F.M., 2012. Assessment of forecasting techniques for solar power production with no exogenous inputs. *Solar Energy* 86 (7), 2017–2028.
- Pedro, H.T.C., Coimbra, C.F.M., August 2015a. Nearest-neighbor methodology for prediction of intra-hour global horizontal and direct normal irradiances. *Renewable Energy* 80, 770–782.
- Pedro, H.T.C., Coimbra, C.F.M., December 2015b. Short-term irradiance forecastability for various solar micro-climates. *Solar Energy* 122, 587–602.
- Perdomo, R., Banguero, E., Gordillo, G., 2010. Statistical modeling for global solar radiation forecasting in Bogotá. In: Photovoltaic Specialists Conference (PVSC), 2010 35th IEEE, pp. 2374–2379.
- Pierro, M., Bucci, F., De Felice, M., Maggioni, E., Moser, D., Perotto, A., Spada, F., Cornaro, C., September 2016. Multi-Model Ensemble for day ahead prediction of photovoltaic power generation. *Solar Energy* 134, 132–146.
- Pinho Almeida, M., Perpiñán, O., Narvarte, L., May 2015. PV power forecast using a nonparametric PV model. *Solar Energy* 115, 354–368.
- Priddy, K.L., Keller, P.E., 2005. Artificial Neural Networks: An Introduction. SPIE Press.
- Quesada-Ruiz, S., Chu, Y., Tovar-Pescador, J., Pedro, H.T.C., Coimbra, C.F.M., April 2014. Cloud-tracking methodology for intra-hour DNI forecasting. *Solar Energy* 102, 267–275.
- Rana, M., Koprinska, I., Agelidis, V.G., December 2015. 2D-interval forecasts for solar power production. *Solar Energy* 122, 191–203.
- Reikard, G., March 2009. Predicting solar radiation at high resolutions: a comparison of time series forecasts. *Solar Energy* 83 (3), 342–349.
- Ripley, B.D., January 1996. Pattern Recognition and Neural Networks, first ed. Cambridge University Press.
- Rodriguez, G.D., 2010. A utility perspective of the role of energy storage in the smart grid. In: Power and Energy Society General Meeting, IEEE, pp. 1–2.
- Rumelhart, D.J., Zipser, D., 1985. Feature discovery by competitive learning. *Cognitive Science* 9, 75–112.
- Russel, B., Whitehead, A.N., 1925. Principia Mathematica, second ed., vols. 1–3. The University Press.
- Santos, J.M., Pinazo, J.M., Canada, J., August 2003. Methodology for generating daily clearness index index values  $K_t$  starting from the monthly average daily value  $\bar{K}_t$ . Determining the daily sequence using stochastic models. *Renewable Energy* 28 (10), 1523–1544.
- Scolari, E., Sossan, F., Paolone, M., December 2016. Irradiance prediction intervals for PV stochastic generation in microgrid applications. *Solar Energy* 139, 116–129.

- Sfetsos, A., Coonick, A.H., February 2000. Univariate and multivariate forecasting of hourly solar radiation with artificial intelligence techniques. *Solar Energy* 68 (2), 169–178.
- Shannon, C.E., 1950. Programming a computer for playing chess. *Philosophical Magazine* 256–275.
- Silverman, B.W., Jones, M.C., December 1989. E. Fix and J.L. Hodges (1951): an important contribution to nonparametric discriminant analysis and density estimation: commentary on Fix and Hodges (1951). *International Statistical Review/Revue Internationale de Statistique* 57 (3), 233–238. Article Type: research-article/Full publication date: December 1989/ Copyright © 1989 International Statistical Institute (ISI).
- Singh, D., Dimri, A.P., Ganju, A., 2008. An analogue method for simultaneous prediction of surface weather parameters at a specific location in the Western Himalaya in India. *Meteorological Applications* 15 (4), 491–496.
- Sperati, S., Alessandrini, S., Delle Monache, L., August 2016. An application of the ECMWF Ensemble Prediction System for short-term solar power forecasting. *Solar Energy* 133, 437–450.
- St-Hilaire, A., Ouarda, T.B.M.J., Bargaoui, Z., Daigle, A., Bilodeau, L., 2012. Daily river water temperature forecast model with a k-nearest neighbour approach. *Hydrological Processes* 26 (9), 1302–1310.
- Stanhill, G., Cohen, S., February 2008. Solar radiation changes in Japan during the 20th century: evidence from sunshine duration measurements. *Journal of the Meteorological Society of Japan* 86 (1), 57–67.
- Stender, J., Addis, T. (Eds.), 1990. Symbols Versus Neurons?. IOS Press, Amsterdam.
- Sulaiman, M.Y., Hlaing, W.M., Wahab, M.A., Sulaiman, Z.A., May 1997. Analysis of residuals in daily solar radiation time series. *Renewable Energy* 11 (1), 97–105.
- Sundar, V., 2010. Integration of Renewable Resources: Operational Requirements and Generation Fleet Capability at 20 Percent RPS. Technical report. Independent System Operator (CAISO), California.
- Suykens, J.A.K., Vandewalle, J.P.L., Moor, B.L.R., 1996. Artificial Neural Networks for Modelling and Control of Non-linear Systems. Kluwer Academic, P.O. Box 17, 3300 AA Dordrecht, The Netherlands.
- Thorey, J., Mallet, V., Chaussin, C., Descamps, L., Blanc, P., October 2015. Ensemble forecast of solar radiation using TIGGE weather forecasts and HelioClim database. *Solar Energy* 120, 232–243.
- Vaz, A.G.R., Elsinga, B., van Sark, W.G.J.H.M., Brito, M.C., January 2016. An artificial neural network to assess the impact of neighbouring photovoltaic systems in power forecasting in Utrecht, The Netherlands. *Renewable Energy* 85, 631–641.
- Voyant, C., Muselli, M., Paoli, C., Nivet, M.L., January 2011. Optimization of an artificial neural network dedicated to the multivariate forecasting of daily global radiation. *Energy* 36 (1), 348–359.
- Voyant, C., Muselli, M., Paoli, C., Nivet, M.L., 2012. Numerical weather prediction (NWP) and hybrid ARMA/ANN model to predict global radiation. *Energy* 39 (1), 341–355.
- Voyant, C., Muselli, M., Paoli, C., Nivet, M.-L., 2013. Hybrid methodology for hourly global radiation forecasting in Mediterranean area. *Renewable Energy* 53, 1–11.
- Voyant, C., Soubdhan, T., Lauret, P., David, M., Muselli, M., October 2015. Statistical parameters as a means to a priori assess the accuracy of solar forecasting models. *Energy* 671–679.
- Walpole, R.K., Meyers, R.H., 1972. Probability and Statistics for Engineers and Scientists. Macmillian, New York.
- Werbos, P.J., 1974. Beyond Regression: New Tools for Prediction and Analysis in the Behavioral Sciences (Ph.D. thesis). Harvard University.

- Widrow, B., Winter, R., 1988. Neural nets for adaptive filtering and adaptive pattern recognition. *Computer* 21, 25–39.
- Wold, A., 1938. Analysis of Stationary Time Series. Almqvist and Wicksell, Uppsala.
- Wolff, B., Kühnert, J., Lorenz, E., Kramer, O., Heinemann, D., October 2016. Comparing support vector regression for PV power forecasting to a physical modeling approach using measurement, numerical weather prediction, and cloud motion data. *Solar Energy* 135, 197–208.
- Wu, J., Chan, C.K., May 2011. Prediction of hourly solar radiation using a novel hybrid model of ARMA and TDNN. *Solar Energy* 85 (5), 808–817.
- Xavier, P.K., Goswami, B.N., December 2007. An analog method for real-time forecasting of summer monsoon subseasonal variability. *Monthly Weather Review* 135 (12), 4149–4160.
- Yakowitz, S., 1987. Nearest-neighbour methods for time series analysis. *Journal of Time Series Analysis* 8 (2), 235–247.
- Yang, D., Gu, C., Dong, Z., Jirutitijaroen, P., Chen, N., Walsh, W.M., December 2013. Solar irradiance forecasting using spatial-temporal covariance structures and time-forward kriging. *Renewable Energy* 60, 235–245.
- Yang, H.T., Huang, C.M., Huang, Y.C., Pai, Y.S., July 2014. A weather-based hybrid method for 1-day ahead hourly forecasting of PV power output. *IEEE Transactions on Sustainable Energy* 5 (3), 917–926.
- Yang, H., Kurtz, B., Nguyen, D., Urquhart, B., Chow, C.W., Ghonima, M., Kleissl, J., May 2014. Solar irradiance forecasting using a ground-based sky imager developed at UC San Diego. *Solar Energy* 103, 502–524.
- Yang, D., Dong, Z., Reindl, T., Jirutitijaroen, P., Walsh, W.M., May 2014. Solar irradiance forecasting using spatio-temporal empirical kriging and vector autoregressive models with parameter shrinkage. *Solar Energy* 103, 550–562.
- Yogi, D., Kreith, F., Kreider, J.F., 2000. Principles of Solar Engineering, second ed. Taylor and Francis, 270 Madison Ave, New York, NY 10016.
- Yürekli, K., Simsek, H., Cemek, B., Karaman, S., October 2007. Simulating climatic variables by using stochastic approach. *Building and Environment* 42 (10), 3493–3499.
- Yule, G.U., July 1921. On the time-correlation problem, with special reference to the variate-difference correlation method. *Journal of the Royal Statistical Society* 84, 497–537.
- Yule, G.U., January 1926. Why do we sometimes get nonsense-correlations between time-series? — A study in sampling and the nature of time-series. *Journal of the Royal Statistical Society* 89, 1–69.
- Yule, G.U., July 1927. On a method of investigating periodicities in disturbed series, with special reference to Wolfer's sunspot numbers. *Philosophical Transactions of the Royal Society of London Series A – Containing Papers of a Mathematical or Physical Character* 226, 267–298.
- Zagouras, A., Pedro, H.T.C., Coimbra, C.F.M., June 2015. On the role of lagged exogenous variables and spatio-temporal correlations in improving the accuracy of solar forecasting methods. *Renewable Energy* 78, 203–218.
- Zarzalejo, L.F., Ramirez, L., Polo, J., 2005. Artificial intelligence techniques applied to hourly global irradiance estimation from satellite-derived cloud index. *Energy* 30 (9), 1685–1697.
- Zorita, E., von Storch, H., August 1999. The analog method as a simple statistical downscaling technique: comparison with more complicated methods. *Journal of Climate* 12 (8), 2474–2489.

# Short-term forecasting based on all-sky cameras

5

Andreas Kazantzidis<sup>1</sup>, Panagiotis Tzoumanikas<sup>1</sup>, Philippe Blanc<sup>2</sup>, Pierre Massip<sup>2</sup>, Stefan Wilbert<sup>3</sup>, Lourdes Ramirez-Santigosa<sup>4</sup>

<sup>1</sup>University of Patras, Patras, Greece; <sup>2</sup>MINES ParisTech, PSL Research University, Sophia Antipolis, France; <sup>3</sup>German Aerospace Center (DLR), Institute of Solar Research, Plataforma Solar de Almería, Almería, Spain; <sup>4</sup>CIEMAT, Madrid, Spain

## 5.1 Introduction

Solar resource and forecasting in very short spatial and time scales (0–100 m, 0–30 min) is a challenging task that cannot be accurately achieved by satellite products or numerical weather predictions due to technical and methodological restrictions. For this reason, sky images from ground-based cameras are widely used in recent years to deal with the high spatial and temporal variability of clouds and provide the needed inputs for numerical models for the current and forecasted (in short-term) solar irradiance.

In this chapter, the available types of all-sky cameras/imagers are shortly presented. The chapter is focused on the state-of-the-art methodologies used to derive parameters needed for the estimations of solar resource and forecasting by a calibrated all-sky camera: cloud coverage, type, height, and velocity as well as aerosol optical properties. The application of these methodologies at Plataforma Solar de Almeria (PSA), in the frame of project: “Direct Normal Irradiance Nowcasting methods for optimized operation of concentrating solar technologies” (DNICast, <http://www.dnicast-project.net/>) is discussed. Finally, the chapter finishes with some propositions for future work in the recent, but quickly, developed research area.

## 5.2 Sky camera systems

An all-sky camera/imager is a ground-based camera, which captures pictures of the whole sky at scheduled time intervals. An all-sky camera is an automated imaging system for sky observations and estimation of the cloud coverage that covers a 180° view. A typical all-sky camera and the images provided are presented in Fig. 5.1.

A typical all-sky camera has two major components. The first component is a weather proof box with the optical assembly, and the second is the computer control assembly. At the heart of the optical assembly is a color charge-coupled device (CCD) or Complementary Metal Oxide Semiconductor (CMOS) camera, pointing upward to mirror the whole sky. A typical arrangement of an all-sky camera consists of the



**Figure 5.1** A typical all-sky camera and the images provided.

camera and a fisheye lens positioned on top of the camera. Neutral density or spectral filters can be used to block the Sun's intense direct normal radiation. An alternative arrangement of the all-sky camera consists of the camera pointing downwards to a hemispherical mirror that images the sky image into the lens. Furthermore, some commercial models include an image-processing algorithm running on a computer workstation that captures images at user-defined intervals and saves them for analysis. Most of the algorithms processing data from sky cameras use a “color ratio threshold” to distinguish whether a pixel represents a clear or cloudy portion of the sky image.

### 5.2.1 All-sky camera types

- *Cloud Imager (ICI)* is comprised by an IR camera, one or two blackbody calibration sources, a gold-plated beam-steering mirror, and control electronics. The ICI system records radiometrically calibrated images of the sky in the thermal IR window band of 8000–14,000 nm at a field of view (FoV) of approximately  $18^\circ \times 13.5^\circ$  (Smith and Toumi, 2008). The display of the camera on the screen is color coded according to the brightness

temperature of the black body. Within the ICI optical bandwidth, the most highly variable emission source other than clouds is water vapor that has to be removed from the ICI images to obtain the residual radiance that is used to identify clouds. A similar instrument to the ICI was developed by [Maghrabi et al. \(2009\)](#), specifically designed for cloud detection.

- The *VIS/IR Whole Sky Imager (WSI)* is a passive automated digital imaging system that obtains both visual and Near IR (NIR) images of the sky at a 180° view under day and night conditions and estimates radiance, cloud fraction, and morphology ([Feister et al., 2010](#)). It is a modification of the all-sky camera, consisting of additional spectrum and neutral density filters on a mechanical filter changer. A weather proof box covers the optical and computer control assembly. The core of the optical assembly consists of the camera sensor whose focal plane is cooled to reduce electronic noise. On top, there is an optical stack that consists of spectral and neutral density filters. An occulter is positioned between the dome and the Sun (or the Moon) to prevent direct sunlight/moonlight from producing artifacts in the image. The system is accompanied by an algorithm that compares, pixel-by-pixel, each acquired image to a matching clear-sky image from a library of background images that covers the full range of solar zenith angles. In case that the image pixel varies from the matching clear-sky pixel, then it is identified as a cloud.
- The *Solmirus All Sky Infrared Visible Analyzer (ASIVA)* is another hybrid camera used for cloud detection and classification that provides measurements from two cameras, one in the VIS and the other in the IR (8000–1300 nm). The VIS camera consists of a CCD or CMOS sensor and a 180° fisheye lens. The IR camera consists of a microbolometer IR sensor, a filter wheel, a blackbody calibration source, and a 180° fisheye diamond coated lens ([Sebag et al., 2008](#)).
- The *Whole-sky InfraRed Cloud-Measuring System (WSIRCMS*, proposed by [Liu et al., 2011](#)) is an IR camera in the range of 8000–1400 nm that uses an azimuthal tracker to obtain IR images of the sky at nine different positions to achieve a whole sky image.
- The *Whole Sky Camera*, developed by the University of Girona in Spain ([Long et al., 2006](#)), uses a small 1/3 in. CCD (752 × 582 pixel), a 1.6 mm focal-length fisheye lens and a shadow band that requires adjustment to match latitude and declination.
- The *All-Sky Imager (Cazorla et al., 2008)*, developed at the University of Granada in Spain, is built with a QImaging RETIGA 1300C, which uses a Sony ICX085AK 2/3 in., thermoelectrically cooled CCD that captures 36-bit images (12 bits per channel) with a Fujinon FE185C057HA fisheye lens. The optics are shaded from direct Sun using a shadowball and the camera system is enclosed in a weatherproof assembly that tracks the Sun. The system has been calibrated to measure sky radiance and characterize optical properties of the atmosphere.
- The Leibniz Institute of Marine Sciences at the University of Kiel, Germany (IFM-GEOMAR) developed a high-resolution camera with no shading devices designed specifically for shipboard sky photography ([Kalisch and Macke, 2008](#)). The system was based on a CCD sensor and captured 30-bit (10 bits per channel) color images in JPEG format.
- To address the specific imaging needs of short-term solar forecasting using ground-based observations, the University of California, San Diego Sky Imager (USI) is designed to perform in hot desert environments, the primary siting location for utility-scale solar plants, and it can reliably retrieve images with high resolution in both spatial and intensity dimensions ([Yang et al., 2014; Urquhart et al., 2015](#)).
- The United States Geological Survey has developed a CMOS-based camera called HDR-ASIS (high-dynamic-range all-sky imaging system) that merges multiple exposures to create a HDR composite image ([Dye, 2012](#)). It is developed for ecosystem and canopy research but the HDR technology is similar to that being developed at University California San Diego (UCSD) for its USI system.

- Several authors used inexpensive surveillance cameras with fisheye lenses. An example for such a system will be presented in [Section 5.5](#).

## 5.3 Image processing techniques

### 5.3.1 Cloud properties

#### 5.3.1.1 Cloud coverage

The all-sky imaging for cloud determination is an important advantage compared to zenith observations, because the instrument's FoV corresponds to conventional cloud observations by meteorological observers. In recent years, ground-based sky imaging systems have been developed and used for obtaining continuous information about the cloud conditions.

In most cases, image processing algorithms have been developed and tested to estimate the total cloud coverage, e.g., the percentage of sky that is covered by clouds. The cloud detection methods have been based on the fact that clouds, because they scatter similarly blue (B) and red (R) light, appear with whitish or gray colors. However, cloud-free skies in digital color images, show relatively higher values of B intensity, due to the enhanced scattering of blue light by air molecules. [Long et al. \(2006\)](#) proposed a method for the estimation of total cloud coverage based on using the Red-Green-Blue (RGB) image to determine thresholds according to a certain ratio of R and B intensities. Specifically, pixels with R/B signal ratio greater than 0.6 were classified as cloudy, while pixels with lower values as cloud-free. [Long et al. \(2006\)](#) reported that with the use of a unique threshold, some problems occurred with circumsolar pixels in high aerosol conditions (note that the Sun was obscured by a shadow band) and mis-detection of thin clouds. With that methodology, the fractional sky cover could be estimated with an uncertainty of about 0.2. When compared with visual observations, greater values of image-derived cloud cover were revealed for amounts lower than 0.2 and smaller for amounts ranging between 0.2 and 0.8. The two methods agreed virtually always for overcast conditions. [Kreuter et al. \(2009\)](#) used a diverse set of images with typical cloud situations (low and high clouds, illuminated and dark clouds, different solar zenith angles) and found a suitable threshold of 1.3 on the B/R ratio for marking cloudy pixels, which was relatively far from the previously mentioned value of 0.6. They compared their results with synoptic (SYNOP) observations at a meteorological station (3 km away from the camera site) and reported that 73% of the total number of analyzed images agreed to within one octa with the SYNOP observations. [Heinle et al. \(2010\)](#) considered the threshold  $R-B = 30$  instead of any R/B ratio and showed that, despite minor errors that still exist in the estimation of total cloud coverage, the difference threshold outperforms the ratio methods. For all cases, the determination of the threshold values is dependent of the digital camera (e.g., the color response of the CCD sensor) and of aerosol conditions, since less aerosols result in more B intensity.

In contrast with the aforementioned methods, [Martins et al. \(2003\)](#) and [Souza-Echer et al. \(2006\)](#) proposed a method for the estimation of cloud coverage, based on the

transformation of the digital image from RGB to hue saturation intensity (HSI). The main idea behind this method is that the cloudy pixels are characterized by high reflectance of a predominantly white color with hues from blue to red, which is characteristic of a mixture of various wavelengths. However, the cloud-free pixels display a much higher saturation of colors and are predominantly blue during daytime with hues ranging from green to red.

[Kazantzidis et al. \(2012\)](#) presented a method for the detection of clouds and the estimation of total cloud coverage that is based on the fact that color is the primary property that allows the visual detection of clouds on the sky. Using a diverse set of images with a variety of cloud conditions (including cases with different types and coverage) under different solar zenith angles, they found that the use of a ratio or a difference of R and B intensities results in errors for cases of broken or overcast cloudiness under large solar zenith angles ([Fig. 5.2](#)). In these cases, the comparison of results with the original image reveals that a multicolor criterion (including all R, G, and B intensities) outperforms the R-B difference method and provides results much closer to real conditions. The total cloud coverage values, derived from the proposed method, were compared to the SYNOP observations at 6, 9, 12, and 15 UT at a nearby airport. For this comparison, they excluded images obtained during the period May–September, when most images are taken under clear skies or under skies with very

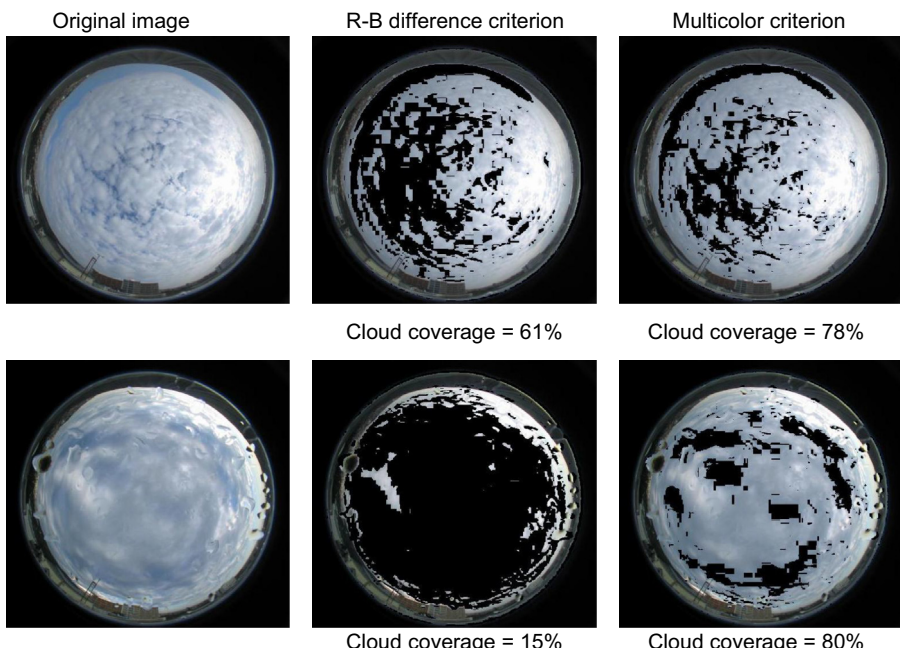


**Figure 5.2** Two typical examples of images with significant differences in the estimation of total cloud cover percentage. The original photos are presented in the left panel. The cloud-free areas (in *black color*) and the cloud coverage percentages, as estimated with the use of the R-B difference and the multicolor criterion are presented in the middle and right panel, respectively.

few clouds. According to results, the 83% and the 94% of the analyzed images agree with the SYNOP observations to within 1 and 2 octas respectively. The differences are mostly related to fast changing cloud coverage over the camera site, e.g., due to a coming thunderstorm or when fog is reported over the airport area.

In such a method, the total cloud cover is defined as the ratio of cloud-marked pixels to the total number of pixels. However, from the point of view of the observer, the fractional sky cover is an angular measurement, defined as the ratio between the solid angle occulted by clouds and the total solid angle of the visible sky hemisphere. [Long et al. \(2006\)](#) provided a correction method and computed the possible error in the calculation of total cloud cover. The needed correction is growing with increasing solar zenith angle but the introduced error in total cloud cover is slightly greater than 1% for most situations. As a result, negligible differences are expected in the presented results when the total cloud coverage values from the camera and visual observations are compared due to this approximation of the algorithm.

Although the use of a multicolor criterion could generally improve the accuracy of the total cloud cover from a digital image, the discrimination of very thin cirrus or cumulus is still problematic. Two typical examples are presented in [Fig. 5.3](#). In case

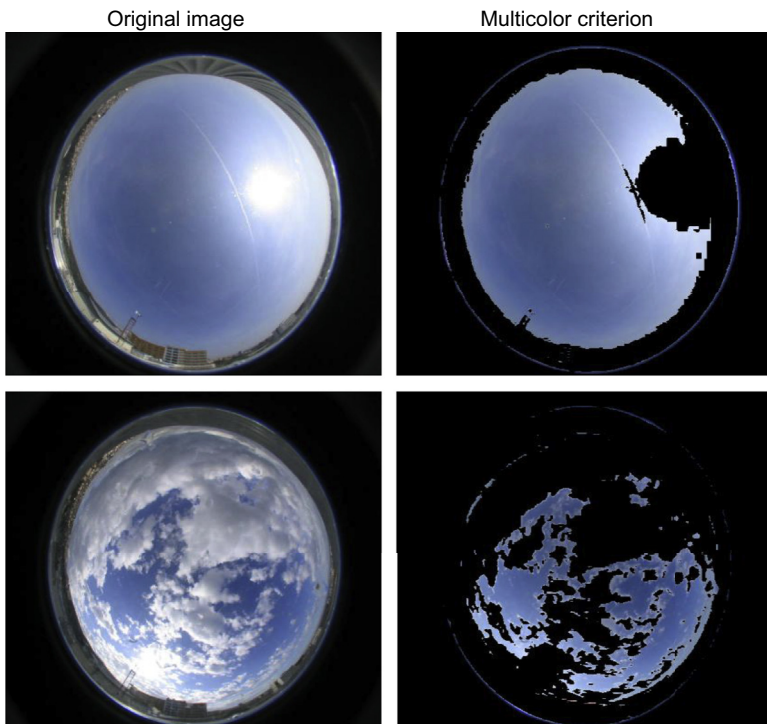


**Figure 5.3** Two examples of whole-sky images where the limitations of the proposed method are depicted. The existence of very thin cirrus (upper panel) and cumulus (lower panel) clouds cannot be detected correctly. The original photos and the cloudy areas (in *black color* including also the pixels containing the solar disk) are presented in the left and right panels, respectively.

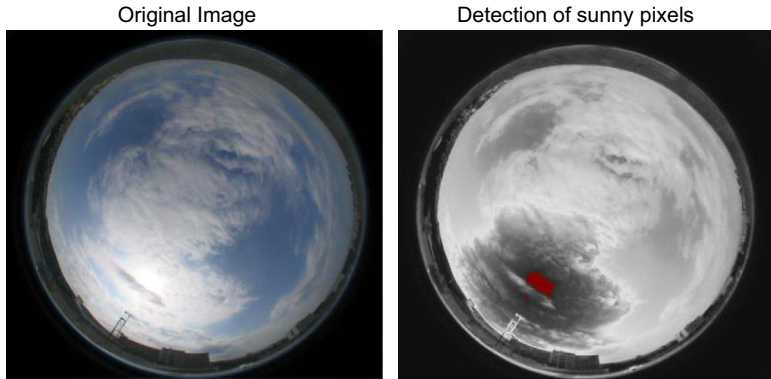


**Figure 5.4** A graphical example for the detection of cloudy pixels close to the Sun. The original image and the pixels that contain parts of the solar disk are presented.

of thin cirrus cloud (upper panel) only a part of the contrail and the cloud close to the Sun is detected, resulting in significant underestimation of the total cloud coverage. However, in case of cumulus clouds (lower panel) the total cloud cover result is only slightly affected.

The discrimination of clouds close to the Sun is another source of possible uncertainty for the calculation of cloudiness and solar irradiance. Another multicolor criterion could be applied to estimate the pixels that are covered by clouds. The image is converted to a full-scale color image, i.e., we scale the image to the full range of the current color map to isolate high color density pixels, and a threshold is for the detection of pixels that do not contain the solar disk (Fig. 5.4). The proposed threshold could provide a qualitative estimation about the cloudy pixels close to the Sun. The cases when the Sun is totally visible or not visible at all in the image can be successfully detected. Then, the synergetic use of these measurements with radiative transfer model outputs for cloud-free conditions could provide an estimation of the percentage of direct irradiance at the ground.

### 5.3.1.2 Detection of raindrops

For the detection of raindrops, the hemispherical shape and structure of the dome as well as the fact that it is not self-cleaned during rain is taken into account. As a result, the raindrops standing on the perimeter of the hemispheric dome distort the circular shape of the perimeter of the image during dry conditions. For these cases, the “circle factor” (CF), a factor indicative of the circle’s perfectness can be calculated. In Fig. 5.5, two examples of CF values that have been calculated are presented. For each image (left), the average perimeter ( $P$ ) and the area ( $A$ ) of the corresponding circle (right) is measured. CF is calculated from the equation  $CF = 4\pi A/P^2$ . For a perfect circle, CF should be equal to one. For images without raindrops (Fig. 5.5, upper panel), CF equals 0.88 and this is considered as a reference number for the specific camera and

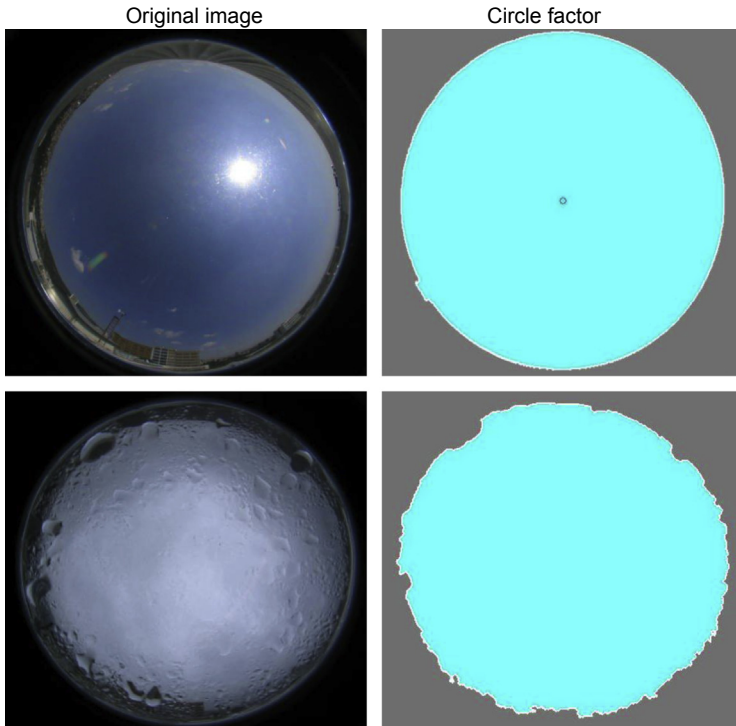


**Figure 5.5** The proposed method to detect raindrops on the camera images. For dry conditions (upper panel) the calculated circle factor (CF) equals 0.88. On the contrary, the CF value is reduced to 0.62 when raindrops appear (lower panel).

location. When raindrops are present, CF is reduced and in this case is equal to 0.62 (Fig. 5.5, lower panel).

The use of this metric can improve the cloud classification algorithms, since rain is related only to certain cloud types. However, the method can lead to false conclusions when the Sun is close to the horizon (sunrise, sunset), when the raindrops stay over the dome for quite some time although the weather conditions have been improved, and during cases with morning drizzle. For this reason, the total cloud coverage and the image luminance should be also taken into account, since they are significantly different between rainy and dry conditions.

### 5.3.1.3 Cloud classification

Referring to cloud types, some attempts have been made to develop algorithms for cloud-type classification from all-sky images. Most of those methods are used for the estimation of cloud base height (CBH) (Kassianov et al., 2005) or the identification of high or low clouds (Long et al., 2006; Cazorla et al., 2008; Parisi et al., 2008). Singh and Glennen (2005) used five different feature extraction methods (namely

autocorrelation, cooccurrence matrices, edge frequency, Law's features, and primitive length) in an automatically training classifier system to recognize cumulus, towering cumulus, cumulonimbus clouds, sky, and other clouds from common digital images. Although the authors judged their results as modest, they gave us a better understanding of the strengths and limitations of different feature extraction methods and classification techniques on the given problem. [Calbó and Sabburg \(2008\)](#) showed that the recognition of different cloud types from processing digital images taken by sky cameras is possible. In their work, they used features based on statistics, on Fourier transform of the image and features that need the distinction of cloudy pixels and sky pixels. Their automatic classification method agreed within 62% and 76% with visual inspection of the sky images when eight or five types of sky conditions were considered respectively. [Heinle et al. \(2010\)](#) presented a cloud classification algorithm, based on a set of mainly statistical features describing the color as well as the texture of an image. They proposed the use of a k-Nearest-Neighbor (kNN) classifier, due to its high performance in solving complex issues, simplicity of implementation, and low computational complexity. The assignment of an image to a specific class using kNN classifiers was performed by majority vote. They selected 12 features, separated in three teams, containing the color information (at R, G, B) and gray levels of each image. For a set of preclassified images, they computed the features and stored them with the assigned cloud class. Then, an additional test sample of random images was selected to assess the performance of the classifying algorithm. For each image of the test sample, the class associated with the majority of the k closest matches determines the unknown class. In cases that this majority is not unique, the absolute smallest distance to the unknown image specifies the target class. The method was applied for distinguishing seven cloud classes: cumulus, cirrus-cirrostratus, cirrocumulus-altocumulus, stratocumulus, stratus-altostratus, cumulonimbus-nimbostratus, and clear sky. They reported an accuracy of about 75% on a test run of random images. The best recognized classes were clear sky and cirrus. Confusions between cirrus and cumulus occurred primarily in cases of total cloud coverage less than 30%, between cumulus and high cumulus and among stratocumulus, stratus, and thick clouds.

[Kazantzidis et al. \(2012\)](#), are based on that cloud classifier. Twelve features, separated into three groups are used, but only the absolute smallest distance for the classification of each image is taken into account. The seven color features are exactly the same between the two methods. The existence of raindrops in the image is taken into as an additional metric. The selected features and their role in the cloud classification algorithm are presented in [Table 5.1](#). A set of images is used for training and testing the cloud classifier. All images are selected by visual inspection to be representative for different cloud types that we would like to identify and for a variety of solar zenith angles and fractions of the solar disk. Additionally, the selected images are carefully inspected to comprise clouds of only one class. In real world, it is usual to see a variety of cloud types on the sky at the same time. However, the simultaneous appearance of more than one cloud class could lead to incorrect class assignment and classification. When using the average values of all 12 metrics in each cloud class, the best result is not achieved because clouds belonging to the same type may vary a lot regarding their metrics used for classification. To overpass this problem, a number of subclasses for

**Table 5.1 The selected features and their role in the cloud classification algorithm**

Features		Name	Role
1	<b>Spectral</b>	Mean R	They describe the average color and total variation of an image. They are useful to distinguish between thick dark clouds and brighter clouds and to separate high and transparent cirrus clouds from others. Due to the color of the sky and the different translucency of clouds, the color component B has the highest separation power
		Mean B	
		Standard deviation B	
		Skewness B	
		Difference R-G	
		Difference R-B	
		Difference G-B	
8	<b>Textural</b>	Energy B	It shows the homogeneity of gray level differences
		Contrast B	
		Homogeneity B	
		Cycle factor	
		Cloud cover	

R, G, B correspond to color information of Red, Green and Blue channels respectively. The full description of the features 1–10 can be found in [Heinle et al. \(2010\)](#).

every cloud class are created, based on parameters that affect greatly the distribution of light in the sky. These parameters are the solar zenith angle, the cloud coverage, and the visible fraction of the solar disk. First, the 12 metrics are measured in all images of each cloud class and separated in subclasses, based on these three parameters. The following intervals for the subclassification are selected:

- solar zenith angle: < 40, 40–65, >65°,
- cloud coverage: < 3, 3–6, 7–8 octas, and
- visible fraction (%) of the solar disk: < 20, 20–80, >80.

The 12 metrics for each subclass are calculated and in cases that those averages are close, the subclasses are merged. The final number of subclasses depends on the cloud class: Sky images with stratus-altostratus and cumulonimbus-nimbostratus are divided into four and six subclasses respectively. More subclasses (8 and 9) are needed for cumulus and cirrocumulus-altocumulus respectively. Stratocumulus and cirrus-cirrostratus are divided in 10 and 12 subclasses respectively. No subclasses were detected for clear skies.

The accuracy of the classifier ranges between 78% and 95% ([Table 5.2](#)). The rate of successful detection of cumulus clouds is 91.9% while the remaining images are assigned as cirrus-cirrostratus and cirrocumulus-altocumulus (5.1% and 3%

**Table 5.2 Classification matrix of the selected cloud types**

True cloud class	Cloud classification						
	1	2	3	4	5	6	7
1. Cumulus	<b>91.9</b>	5.1	3.0	0.0	0.0	0.0	0.0
2. Cirrus-Cirrostratus	1.8	<b>94.6</b>	3.0	0.6	0.0	0.0	0.0
3. Cirrocumulus-Altocumulus	8.5	8.4	<b>78.0</b>	5.1	0.0	0.0	0.0
4. Stratocumulus	0.0	0.0	0.0	<b>92.9</b>	1.8	5.3	0.0
5. Stratus-Altostratus	0.0	0.0	0.0	6.9	<b>93.1</b>	0.00	0.0
6. Cumulonimbus-Nimbostratus	0.0	0.0	0.0	17.4	0.0	<b>82.6</b>	0.0
7. Clear sky	0.0	5.0	0.0	0.0	0.0	0.0	<b>95.0</b>

The average performance of the classifier is 87.9%.

respectively). The misclassified cases correspond to all-sky images with only a few clouds close to the horizon, far away from the camera site. Cirrus-cirrostratus clouds are successfully detected in the 94.6% of the images. Some images picturing overcast skies with these high clouds are classified to one of the three kinds of cumulus clouds. The lowest performance of the classifier (78%) is revealed for cirrocumulus-altocumulus. In this case, the rest of the images are distributed in all classes except stratus and cumulonimbus-nimbostratus. Stratocumulus and cumulonimbus-nimbostratus are correctly detected in 92.9% and 82.6% of cases, respectively. There is a small confusion between these two cloud classes, since the rest of images are classified to the other class and not the correct one. A high score of our classifier (93.1%) is revealed also for stratus-altostratus, while the rest of them (6.9%) are assigned as stratocumulus. Finally, the clear skies can be successfully detected in 95% of cases. The rest of the images correspond to days with considerably high values of aerosol optical depth (AOD), an optical parameter that has not been taken into account in the classification algorithm.

Based on the same methodology, [Wacker et al. \(2015\)](#) presents observations of total cloud cover and cloud-type classification results from a sky camera network comprising four stations in Switzerland. It is reported that over 90% of the images were correctly classified when the algorithm is trained to be site specific and only one cloud class occurs in the image. However, when the algorithm is applied to the remaining sites and/or multiple cloud classes occurred in the image, the mean success rate decreases substantially to 50%–80% depending on the randomness of the image selection procedure and the visual misclassification of the clouds in the sky camera image by the observers. Moreover, the current cloud type algorithm is sensitive to site and camera characteristics (e.g., site altitude and camera settings) and site-specific atmospheric conditions. The algorithm can be trained at one site and applied to different locations as long as the cloud classes are representative and the same camera system is used.

A similar methodology can be also applied in cases that when more than one cloud class is occurred in the all-sky image. In this case, the image is separated in segments and the algorithm is retrained. A typical example is presented in Fig. 5.6. The image is separated in 36 blocks; for everyone (except for the ones close to the edges) a single result is provided.

#### 5.3.1.4 Cloud height estimation

The triangulation procedure used to estimate the CBH is depicted in Fig. 5.7, where two pictures of the overhead sky are obtained from ground-based cameras 1 and 2. The distance between the two cameras and the CBH are  $d$  and  $h$ , respectively. The same cloud feature is identified on the pictures obtained from the two sites and the zenith angles  $\theta_1$  and  $\theta_2$  can be calculated. The CBH is given by:

$$h = \cos(\theta_1)\cos(\theta_2)d/\sin(\theta_1 + \theta_2)$$

#### 5.3.1.5 Aerosol optical properties

All-sky images can be analyzed per pixel, to extract information about the atmosphere, such as aerosol optical properties. Olmo et al. (2008), used a linear pseudoinverse algorithm to retrieve the spectral radiance from the all-sky images. The AOD, at 500 nm, was estimated as the value that minimizes the residuals between the image-derived the calculated (by a model) zenith spectral radiances. Various situations were tested, including the presence of nonspherical particles. The optical depths were

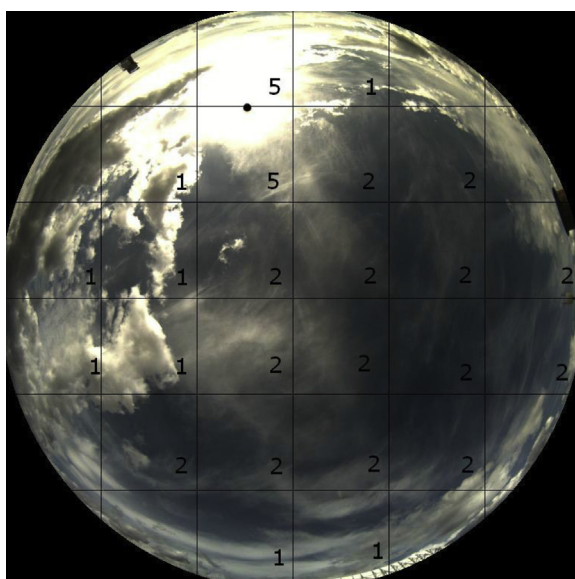


**Figure 5.6** A typical example of image segmentation and cloud classification when more than one cloud types appear in the sky. The image is separated in 36 blocks and a single result is provided for all except of those being close to the sky horizon. In this image, pixels numbered with 1, 2, and 5 correspond to cases that cumulus, cirrus-cirrostratus, and clear skies (or Sun) appear.

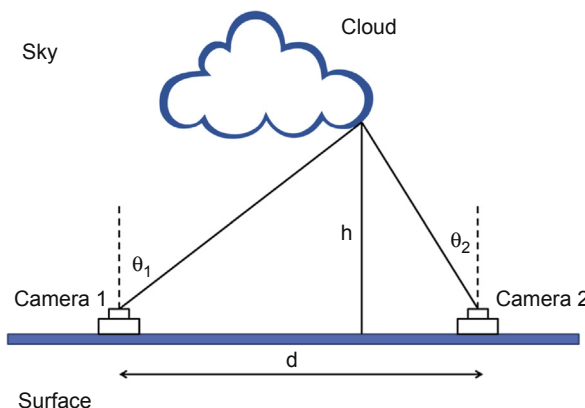


**Figure 5.7** Graphical presentation of the cloud height estimation method.

compared by those derived from a nearby sun photometer and the differences were similar to the nominal error of the retrievals of the sun photometer. [Huo and Lü \(2010\)](#) investigated the relationship between the radiance ratio at two wavelengths (450 and 650 nm) and AOD, using numerical simulations. The error in the AOD retrieval was depended mostly on the assumption of aerosol types and was found around 15%–20%. Based on the results from the comparison with the values from a colocated CIMEL photometer, they concluded that the method can be used for the retrieval of AOD, from all-sky images. The aerosol optical properties were determined by [Cazorla et al. \(2009\)](#), using a calibrated sky imager. AOD was calculated at three different wavelengths by different neural network-based models, using the radiance from the principal plane of sky images as input. The models were trained and validated, using data from a CIMEL photometer. The deviation between AOD from the all-sky camera and the sun photometer was found to be less than  $\pm 0.01$  for the 80% of the cases. The method of polarized all-sky imaging, regarding aerosol characterization, was investigated by [Kreuter and Blumthaler \(2013\)](#). According to their results, polarized all-sky imaging could improve aerosol characterization in combination with sky scanning radiometers, especially at low AOD values and low solar zenith angles.

[Kazantzidis et al. \(2016\)](#) developed a training algorithm, based on aerosol measurements from a CIMEL sun photometer at PSA, Spain, to provide AOD from cloud camera images. Images of a standard exposure time are used to achieve a good correlation between the change in brightness and the change in radiance for different solar zenith angles. For the training of the algorithm,  $\sim 3500$  CIMEL AOD values are used in synergy with the closest in time images for a 4-month time period. The brightness at the zenith point is selected due to its independency from the azimuth angle and the relative simple to define it in the image or to export it form the model calculations. The RGB radiance values at the zenith point are dependent not only from the AOD but also from other atmospheric variables, especially from the precipitable water (PW) and the aerosol single scattering albedo (SSA). Typical examples of the changes in Red radiance due to PW and Blue radiance due to SSA are presented in [Fig. 5.8](#). The presentation of changes in Red and Blue radiances for PW and SSA respectively are selected because the specific atmospheric parameters are expected to affect the

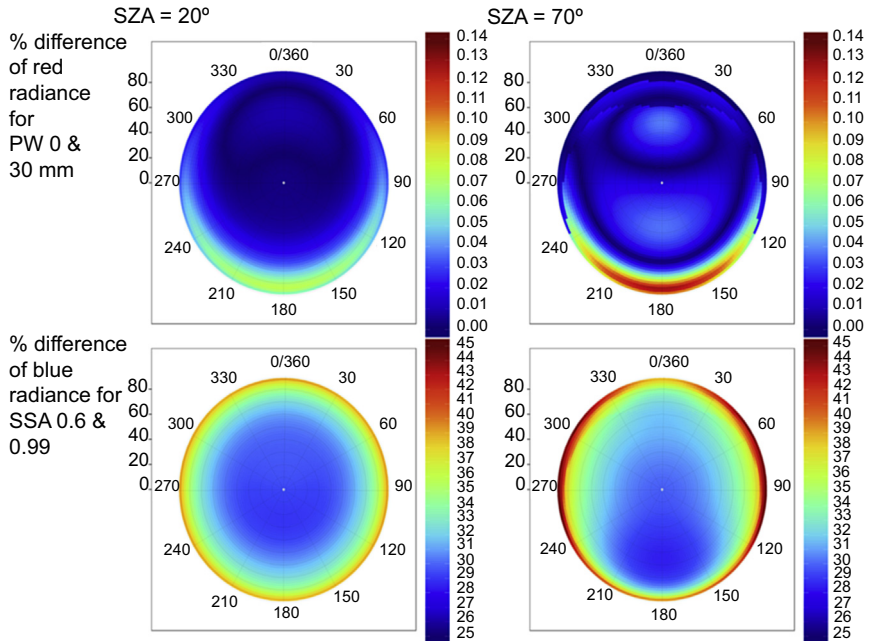


**Figure 5.8** Percentage (%) differences in Red and Blue radiances due to precipitable water and single scattering albedo respectively for in the sky for two solar zenith angles ( $20^\circ$  and  $70^\circ$ ).

radiance values especially for these colors. The percentage (%) differences are presented for a low ( $20^\circ$ ) and a high ( $70^\circ$ ) solar zenith angle. Based on the results, the effect of changing PW affects negligibly the zenith point radiance. Taken into account that the SSA values at PSA change between 0.9 and 0.99, the effect of changing SSA on zenith radiance is expected to be around 5%.

To improve the AOD results, the saturated area around the Sun is taken into account. Sample images showing how this area is different when aerosols are changing are presented in Fig. 5.9. The two photographs correspond to the same time at 2 consecutive days (7/23/2014 and 7/24/2014) but for different aerosol conditions. According to the AERONET measurement, the AOD value at 500 nm is quite low (0.09) on the first day. On the contrary, the AOD value at the same wavelength is 0.43 on the second day. The Sun saturated area is calculated as a percentage (%) of a greater area around the Sun, where the saturated pixels are counted. For the presented cases, the percentages are 9% and 95% for low and high AODs, respectively.

Finally, both the RGB intensities at the zenith point and the percentage (%) area of saturation are taken into account in a multilinear approach to estimate the AOD values at 440, 500, and 675 nm. The three relations are as follows:

$$\begin{aligned} \text{AOD (440)} &= a_{440} + b_{440} * B + c_{440} * \text{SAT} \\ \text{AOD (500)} &= a_{500} + b_{500} * G + c_{500} * \text{SAT} \\ \text{AOD (675)} &= a_{675} + b_{675} * R + c_{675} * \text{SAT} \end{aligned}$$

The comparison of the estimated AODs from the sky camera and the AERONET measurements and the statistics for all cases included in this study are presented in

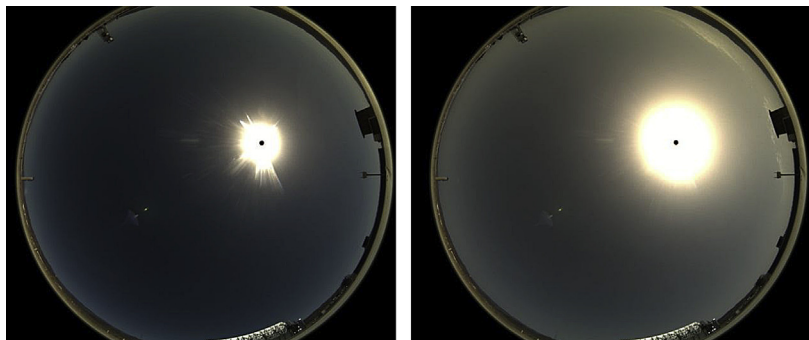


**Figure 5.9** All-sky images at the same time (11:16UT) for 2 days (23 and 24/7/2014) with low (left panel) and high (right panel) aerosol optical depth values.

[Fig. 5.10](#) and [Table 5.3](#), respectively. According to results, the mean/median difference and the standard deviation are less than 0.01 and 0.03 for all wavelengths. The results are comparable with those from similar methods and satellite-derived methodologies and provide substantial evidence that all-sky cameras could be efficiently used for the estimation of AOD.

## 5.4 Geometrical calibration of all-sky cameras

Geometric calibration is notably very important for the 3D reconstruction using multiple all-sky imagers in stereoscopic mode and the localization of the Sun position in cloudy situation. With two or more calibrated all-sky cameras at different geographic locations in a large solar plant, it is possible to determine on a real-time basis the position and the base height of the detected clouds and therefore to provide 3D map of clouds. With this time series of 3D cloud maps, position, and speed of cloud shadow can be estimated, thus enabling spatially resolved solar irradiance short-term forecasting.

This calibration for an all-sky camera is done in two steps. The first one is the intrinsic calibration, to determine the internal parameters of the camera, characterizing notably the focal plane, the focal and the optical distortions, that may be slightly different from another camera of the same model. This calibration is done by doing the acquisition of several hemispherical images of checkerboard pattern on a flat support with different orientations and covering different part of the FoV. The flatness of the support and the variety of acquired orientations and FoV parts of the pattern are key points for the intrinsic calibration precision. In [Fig. 5.11](#) an example of checkerboard pattern acquired by an all-sky camera is presented.

The OcamCalib toolbox ([Scaramuzza et al., 2006; Scaramuzza, 2008](#)) is a well-known toolbox available on Matlab to characterize the intrinsic calibration of the camera with checkerboard patterns. The camera's model compute by the toolbox is obtained thanks to the position of all the corners of squares on the chessboard in

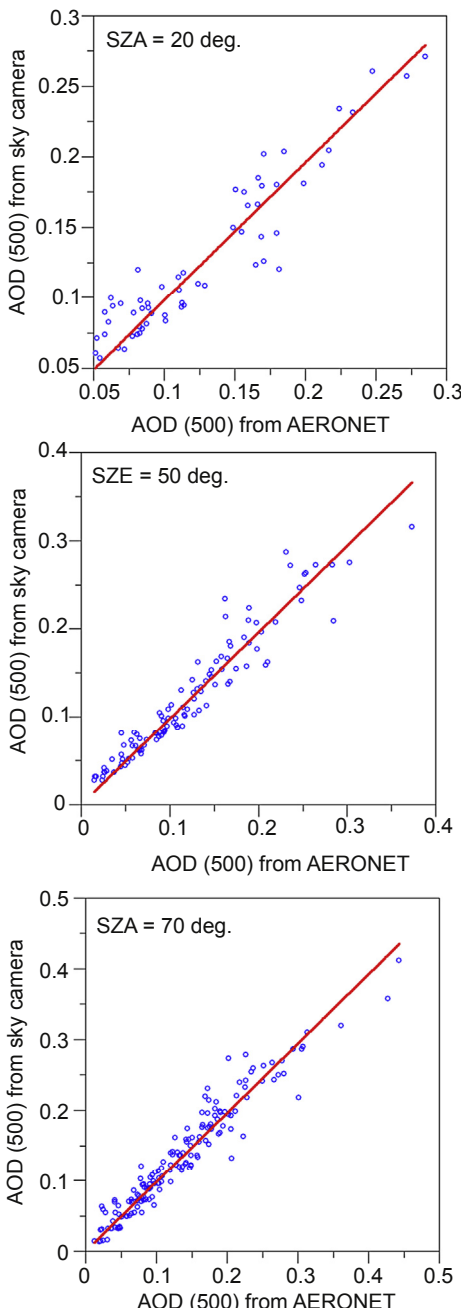


**Figure 5.10** Comparison of the aerosol optical depth (AOD) values at 500 nm from the all-sky camera with those from the AERONET measurements for solar zenith angles of 20° (upper panel), 50° (middle panel), and 70° (lower panel). The estimated AODs from the all-sky camera are based on the RGB intensities at the zenith point and the percentage (%) area of saturation around the Sun.

**Table 5.3 The statistical results of the differences between the estimated aerosol optical depth values from the sky camera and the corresponding measurements from AERONET**

Statistics/Wavelengths	440 nm	500 nm	675 nm
Mean differences	-0.009	0	-0.01
Median differences	-0.004	0	-0.01
Standard deviation	0.03	0.02	0.02

The results are presented for 440, 500 and 675 nm.

each position. The various positions and orientations of the checkerboard pattern in front of the camera are illustrated by Fig. 5.11. After optimization, the residue of the geometric calibration is around 0.1 degree in term of root mean square error.

The second step is the extrinsic calibration: it consists in the determination of the orientation of the camera in the local reference frame. This orientation is defined by three angles: the pitch, roll, and yaw angles, as illustrated in Fig. 5.12. These angles define three successive 3d-rotations in the following order: yaw first, then roll, and finally pitch. This extrinsic calibration is done by comparing the theoretical angular position and the center of the Sun detected in the time series of hemispherical images acquired during clear-sky days for different dates.

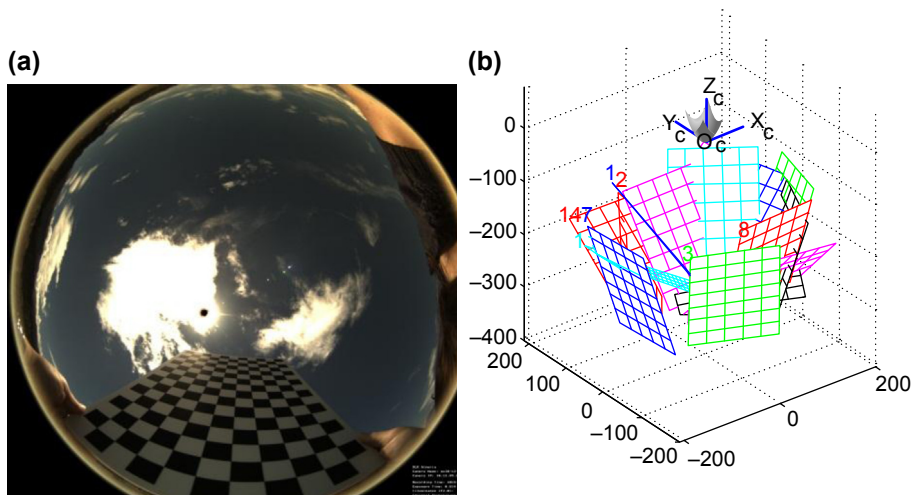


**Figure 5.11** (a) Example of a hemispherical image of the checkerboard pattern used for the intrinsic calibration. (b) Various positions and orientations of the checkerboard to establish the intrinsic model of the camera.

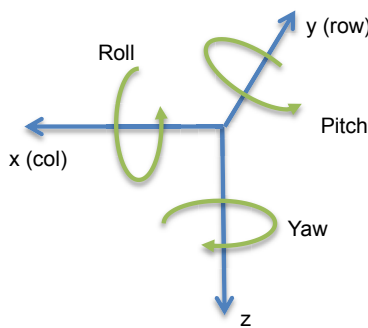


**Figure 5.12** Pitch, roll, and yaw angles for the orientation of a camera in the local reference frame.

## 5.5 Case study: solar resource and forecasting methodology in the frame of DNICast project

The predescribed methodologies have been applied at PSA in the framework of the European project “Direct Normal Irradiance Nowcasting methods for optimized operation of concentrating solar technologies” (DNICast, <http://www.dnicast-project.net/>).

PSA is a research center for solar energy focused on concentrating solar thermal technologies and its related applications. It is located in the Tabernas Desert in the south of Spain and belongs to CIEMAT (Centro de Investigaciones Energéticas, Medioambientales y Tecnológicas). Scientists from CIEMAT and DLR (Deutsches Zentrum für Luft- und Raumfahrt) jointly operate several meteorological measurement stations at PSA including an all-sky camera system within the collaboration METAS (Meteorological Station for Solar Energy Applications).

The locations of the stations at PSA are shown in Fig. 5.13. The basis for the image is an orthogonalized and merged image of six shadow cameras (Oberländer et al., 2015). The shadow cameras acquire photos of the ground from the top of the CESA-1 solar tower (position marked as square). This orthogonal image and the irradiance measurements are also used to create irradiance maps of PSA and for the validation of all-sky camera based nowcasts. Black areas mark pixels for which the irradiance maps are not derived from the shadow camera information. These areas are excluded due to higher buildings and reflective surfaces.

The all-sky camera system consists of four Mobotix Q24 cameras (circles). The Q24 is a weatherproof surveillance camera with a CMOS sensor and a fisheye lens. The cameras take one image series consisting of three exposure times every 30 s. Each image is saved as a 3.1 MPixel RGB jpg with 8 bit color resolution. The cameras are mounted on fixed horizontal surfaces without shading and are geometrically calibrated as explained earlier. As an alternative to the external calibration using the Sun also the Moon can be detected and used for the calibration. The all-sky images are obtained in real time for further processing.

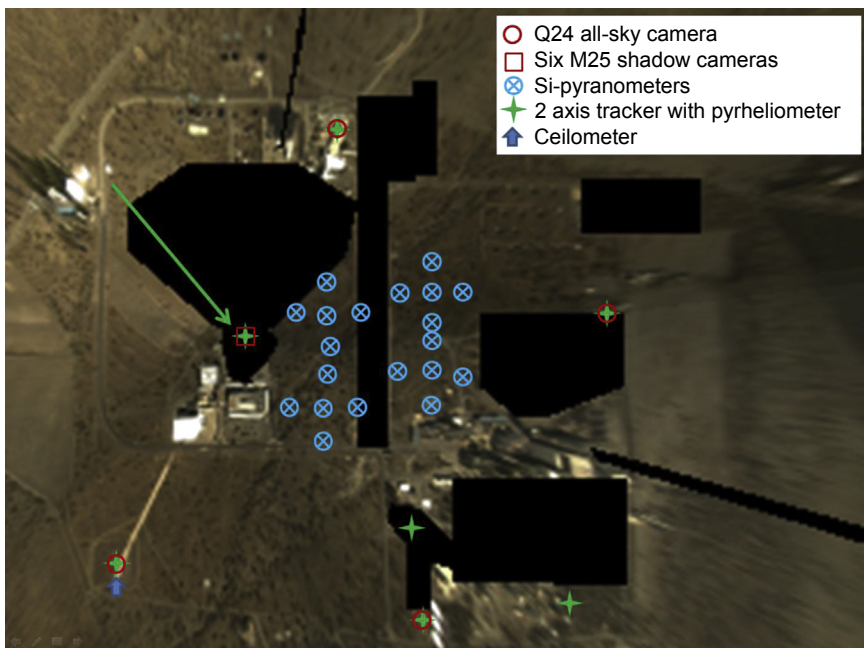


**Figure 5.13** All-sky camera system and validation setup at Plataforma Solar de Almería.

All all-sky imagers are set up next to two axis trackers equipped with thermopile radiometers (green crosses). First class pyrheliometers for Direct Normal Irradiance (DNI) measurements and secondary standard pyranometers for GHI (Global Horizontal Irradiance) and/or Diffuse Horizontal Irradiance measurements are used. Further two axis trackers are also shown in the figure. Also, six semiautomatic trackers with pyrheliometers are available that are not shown as they are used only in occasional cases. In addition to the tracker-based radiometric stations, 20 Si-pyranometers are shown as blue circles with crosses. The distance between the Si-pyranometers within each cross-shaped group of five instruments is approximately 50 m. Although the Si-pyranometers have a higher uncertainty compared to thermopile sensors, they are used in this case because of their lower maintenance requirements and their significantly faster response time. GHI is logged in 1 s resolution while the response time of most of the used thermopile sensors is approximately 5 s. A Jenoptik CHM 15k ceilometer is also operated next to one of the all-sky imagers (arrow). It can be used to obtain cloud heights either for the processing of the nowcast or the validation of cloud height derived by all-sky imagers.

Having past and real-time updated time series of spatially and temporally highly resolved DNI maps is very important for the transient modeling of the thermal energy production of large-scale concentrated solar power (CSP) plants for performance analysis and monitoring purposes. In addition, the nowcasting—i.e., the very short-term forecasting from 1 to 30 min—of these DNI maps is very useful for the dynamic

operation of these CSP plants, namely to control, in an optimal and safe way, the flow rate of the working fluid, the energy storage, or the command for the defocusing of the concentrating mirrors.

To answer this need, the objective of this case study in the framework of DNICast is to obtain a real-time estimation and nowcasting of 10-m resolution map of 1-min DNI from all-sky cameras, covering the site of PSA and its vicinity. At least two all-sky cameras are needed in this processing to provide stereoscopic information about the clouds. Images from PSA have been processed by University of Patras and ARMINES as explained in the following paragraphs.

The different stages to derive the real-time estimation and nowcasting from the all-sky cameras are schematically presented in Fig. 5.14 and are described in more detail by Massip et al., 2015.

The processing is sequential and done in near real-time. One all-sky camera serves as the master camera that enables to provide, for each frame, every 30 s:

- The cloud cover segmentation and the cloud classification into two simple optical thickness types: thin and thick clouds. To mitigate the problem of limited dynamic range in the image acquisition compared to the huge dynamic of sky radiance from the circumsolar region to the horizon, the master camera get sequentially, every 30 s, three images with three different exposure times as mentioned earlier.
- The apparent—*i.e.*, in the image geometry of the master all-sky camera—cloud motion vectors (CMV) thanks to a robust block-matching algorithm applied to two consecutive images. The robust block-matching is based on local maximization of the normalized cross-

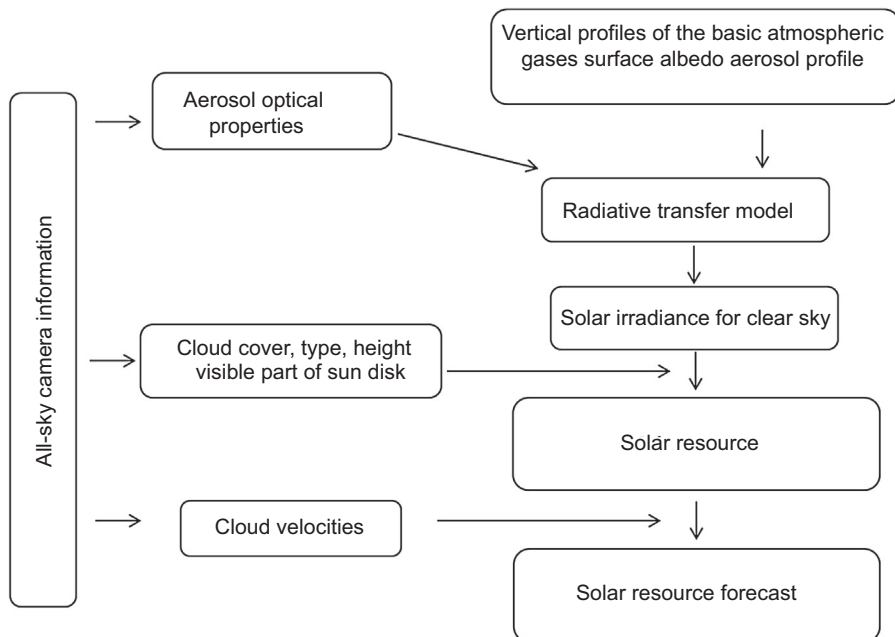


**Figure 5.14** Flowchart showing basic steps to derive solar resource and forecasting.

correlation. This block-matching is only applied on pixels (1) that have been classified as cloudy pixel and (2) that fit to a local contrast condition-based on local L2-norm of the image gradient.

The other available distant all-sky cameras provide concomitant hemispherical images. The geometric parallax disparities with respect to the master all-sky camera can be exploited using stereoscopic photogrammetry techniques to retrieve 3D information of the clouds. The same robust block-matching as the one used for subsequent images for the cloud motion vector is used to estimate the parallax disparities for some contrasted cloudy pixels in the master image. To reduce the research domain of the block-matching, images are beforehand resampled on the geometry of the master camera, assuming an average CBH. The latter can be adapted with the median value of the estimated CBH in the past. The intersections of corresponding lines of sight for each matched pixels then provide CBH information of the cloudy pixels in the master image that have been successfully matched. The prior thorough geometric calibrations of the different all-sky cameras are crucial for the accuracy of the 3D retrieval. To regularize these scattered CBH estimations, the kNN clustering method is applied to set the CBH estimations to a limited number of layers. A spatial interpolation from these scattered CBH estimations is then applied for each cloudy pixels of the current image of the master camera, to get their 3D positions.

[Fig. 5.15](#) shows an example of CBH estimations of successfully matched cloudy pixels, from stereoscopic images provided by two cameras at PSA compared to the CBH measured from a collocated ceilometer. There are two main differences between the estimated CBH by the two methods:

- The ceilometer only measures at the very vertical—nadir—of its position, whereas all-sky camera stereoscopy provides spatially resolved CBH estimations over a much larger FoV—up to approximately 80 degrees half angle with respect to the nadir of the master camera.
- The ceilometer is able to assess the CBH for different superimposed layers whereas stereoscopic photogrammetry with all-sky cameras is generally limited to the height of the lowest cloud layer due to cloud occlusion.

By knowing the 3D positions of the detected clouds and the direction of sunrays, it is straightforward to determine, in real-time, the shadow projections on the ground of the contour polygons of each detected clouds. [Fig. 5.16](#) illustrates the shadow projection of one cloud contour on the ground.

The concomitant 3D positions of the cloudy pixels with the estimation of their apparent CMV in the geometry of the master image enable the estimation of the corresponding 3D CMV. These 3D CMVs are then used, under the assumption of their short-term persistence, to forecast the future 3D positions of the clouds. These forecasted clouds are then projected as shadows to the ground using the angular direction of the sunrays at the forecasted time.

The real-time (resp. the forecasted) cloud shadows map on the ground along with the corresponding cloud types for each interior shadow pixels are used to assess corresponding real-time (resp. forecasted) DNI ([Fig. 5.17](#)). More precisely, direct clear-sky index maps are estimated from the shadow maps. The direct clear-sky index is defined as the ratio of the DNI on the ground with the corresponding modeled DNI under clear-sky—cloudless—condition.

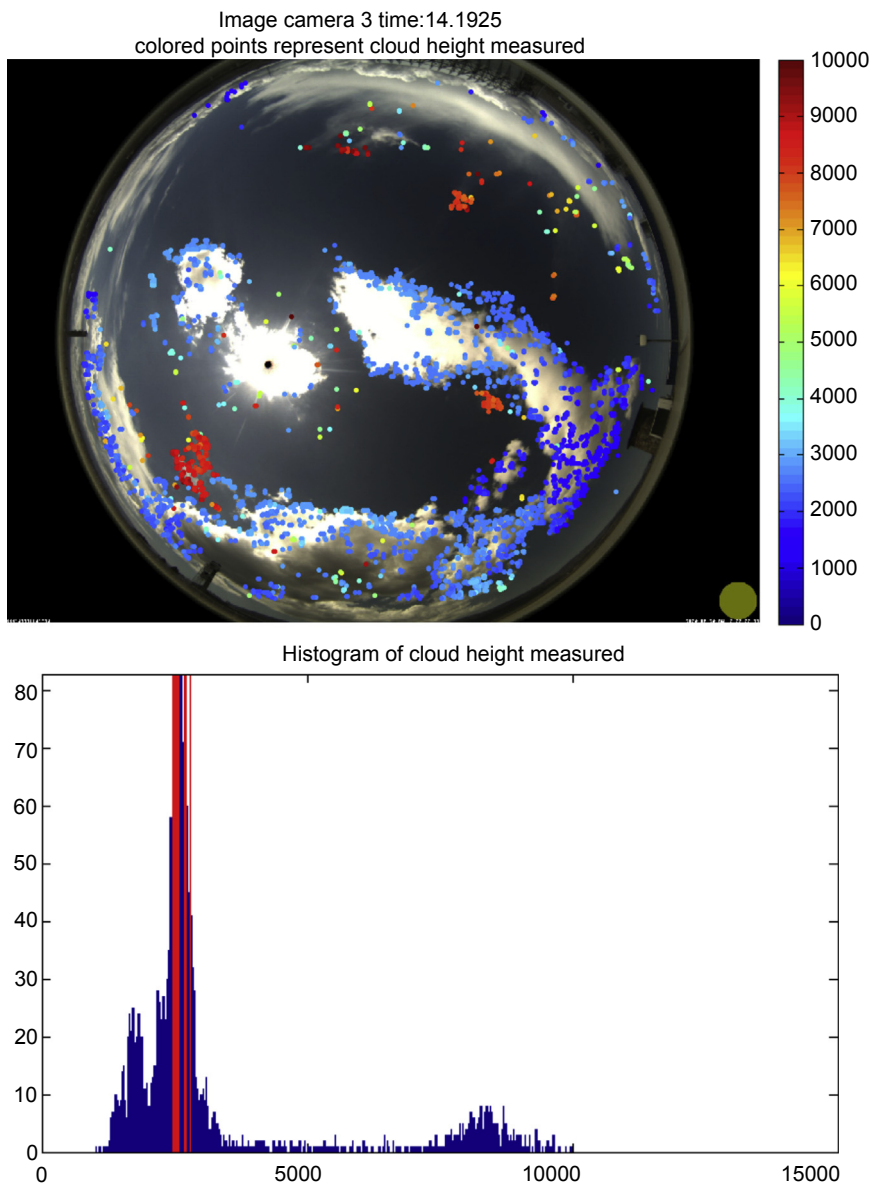


**Figure 5.15** Upper panel: example of cloud base height estimations of successfully matched cloudy pixels, from stereoscopic images provided by two cameras at Plataforma Solar de Almeria. Lower panel: the histogram of cloud base height estimated at a given time (blue lines) and the measurements provided by the ceilometer  $\pm 10$  min (red lines).

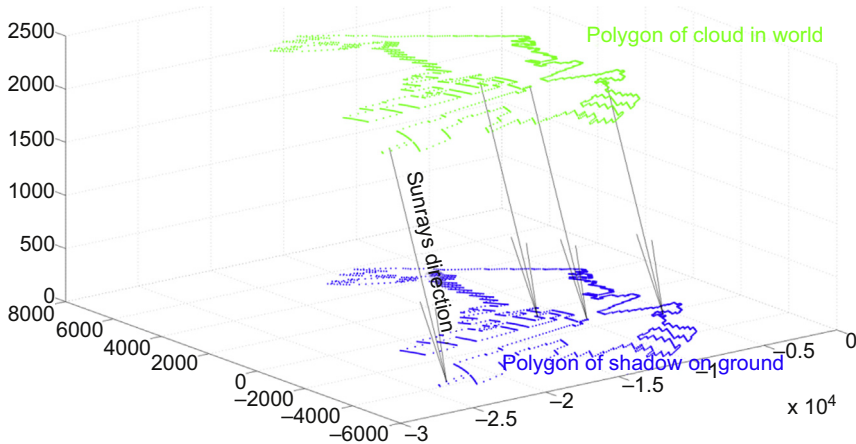


**Figure 5.16** Example of shadow projection of one cloud on the ground.

These maps of direct clear-sky index are computed from the ground-projected shadow and corresponding cloud types applying a simple linear regression model. This simple linear regression model maybe determined following two “operational” cases:

- Case 1: the regression model is beforehand determined on the basis of a training past period with concomitant DNI measurements from one in situ pyranometric station on the site.
- Case 2: the regression model is determined in a recursive manner, using real-time logged DNI measurements from one in situ pyranometric stations on the site.

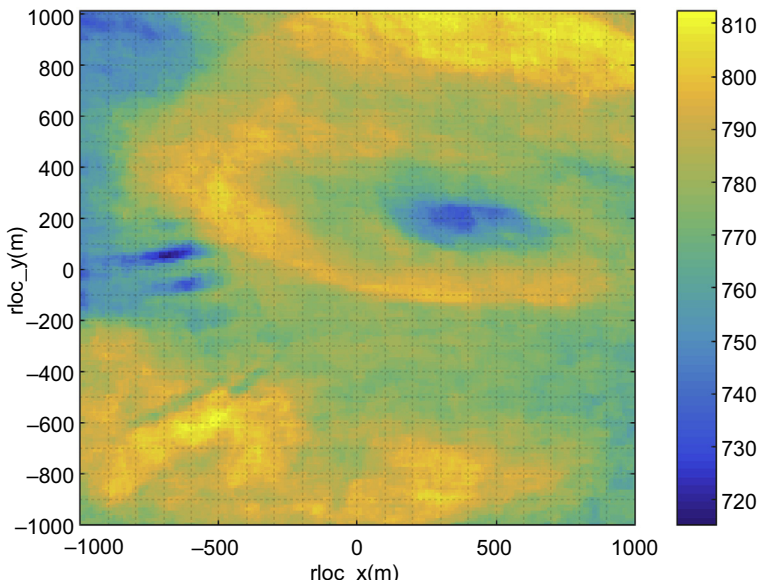


**Figure 5.17** Example map of short-term forecasted direct normal irradiance over the Plataforma Solar de Almeria site.

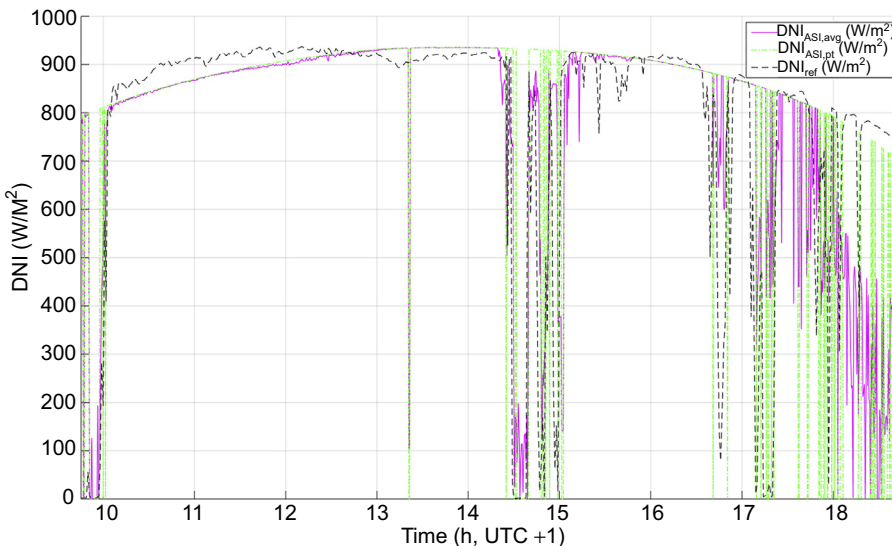


**Figure 5.18** Exemplary comparison of all-sky imager derived direct normal irradiance to measurements with a pyrheliometer.

The modeled clear-sky DNI is assessed using the McClear models (Lefevre et al., 2013) for which the required AOD can be retrieved in real-time from the all-sky cameras or provided by MACC AOD forecasting product. A comparison of the all-sky imager derived DNI to pyrheliometer measurements is shown in Fig. 5.18 for one exemplary day (6/24/2014). The DNI from the pyrheliometer is shown as  $DNI_{ref}$ , the average DNI in the 4-km surface derived from the all-sky imager is depicted as  $DNI_{ASI,\text{avg}}$ , and  $DNI_{ASI,\text{pt}}$  is the DNI for the pixel of the all-sky imager's DNI map that belongs to the coordinates of the pyrheliometer. The all-sky imager data are derived for the time of the image acquisition. The attenuation by thin clouds is at times not detected, e.g., around 15:30. Major cloud passages are detected by the all-sky imager.

## 5.6 Conclusions and future trends

In recent years, an extensive use of all-sky cameras and accompanied algorithms to estimate cloud and aerosol properties as well as solar resource and forecasting has been observed. The results seem promising, and significant progress has been gained during the last decade. However, an in-depth and extensive validation of results is needed. The application of methods at specific sites/atmospheric conditions during a limited time and for selected cases does not provide that the use of all-sky cameras could be successful across the globe. In all studies, the need for calibrated all-sky camera that fulfills the high standards of other instruments used in atmospheric sciences and solar energy application is revealed. The usefulness of all-sky cameras is significantly emerged when more than one camera is used at a site: the detection of different cloud layers and the 3D reconstruction of the cloud field in synergy with advanced radiative

transfer models could improve the proposed methodologies toward better results and provide valuable information in such detail that could establish the all-sky cameras as reference and standard instruments for the solar energy research community and the operators of solar power applications.

## References

- Calbó, J., Sabburg, J., 2008. Feature extraction from whole-sky ground-based images for cloud-type recognition. *Journal of Atmospheric and Oceanic Technology* 25, 3–14.
- Cazorla, A., Olmo, F.J., Alados-Arboledas, L., 2008. Using a sky imager for aerosol characterization. *Atmospheric Environment* 42, 2739–2745.
- Cazorla, A., Shields, J.E., Karr, M.E., Olmo, F.J., Burden, A., Alados-Arboledas, L., 2009. Technical note: determination of aerosol optical properties by a calibrated sky imager. *Atmospheric Chemistry and Physics* 9, 6417–6427.
- Dye, D., 2012. Looking skyward to study ecosystem carbon dynamics. *Eos, Transactions of the American Geophysical Union* 93 (14), 141–143.
- Feister, U., Möller, H., Sattler, T., Shields, J., Görtsdorf, U., Güldner, J., 2010. Comparison of macroscopic cloud data from ground-based measurements using VIS/NIR and IR instruments at Lindenberg, Germany. *Atmospheric Research* 96, 395–407.
- Heinle, A., Macke, A., Srivastav, A., 2010. Automatic cloud classification of whole sky images. *Atmospheric Measurement Techniques* 3, 557–567.
- Huo, J., Lü, D., 2010. Preliminary retrieval of aerosol optical depth from all-sky images. *Advances in Atmospheric Sciences* 27 (No. 2), 421–426.
- Kalisch, J., Macke, A., 2008. Estimation of the total cloud cover with high temporal resolution and parametrization of short-term fluctuations of sea surface insolation. *Meteorologische Zeitschrift* 17, 603–611.
- Kassianov, E., Long, C.N., Christy, J., 2005. Cloud-base-height estimation from paired ground-based hemispherical observations. *Journal of Applied Meteorology* 44, 1221–1233.
- Kazantidis, A., Tzoumanikas, P., Nikitidou, E., Salamalikis, V., Wilbert, S., Prahl, C., 2016. Application of simple all-sky imagers for the estimation of aerosol optical depth. Solar-PACES Conference, October 11–14, 2016. Abu Dhabi, United Arab Emirates.
- Kazantidis, A., Tzoumanikas, P., Bais, A.F., Fotopoulos, S., Economou, G., 2012. Cloud detection and classification with the use of whole-sky ground-based images. *Atmospheric Research* 113, 80–88.
- Kreuter, A., Blumthaler, M., 2013. Feasibility of polarized all-sky imaging for aerosol characterization. *Atmospheric Measurement Techniques* 6, 1845–1854.
- Kreuter, A., Zengerl, M., Schwarzmüller, M., Blumthaler, M., 2009. All-sky imaging: a simple, versatile system for atmospheric research. *Applied Optics* 48 (6), 1091–1097.
- Lefèvre, M., Oumbe, A., Blanc, P., Espinar, B., Gschwind, B., Qu, Z., Wald, L., Schröderter-Homscheidt, M., Hoyer-Klick, C., Arola, A., Benedetti, A., Kaiser, J.W., Morcrette, J.J., 2013. McClear: a new model estimating Downwelling solar radiation at ground level in clear-sky conditions. *Atmospheric Measurement Techniques* 6, 2403–2418. <http://dx.doi.org/10.5194/amt-6-2403-2013>.
- Liu, L., Sun, X., Chen, F., Zhao, S., Gao, T., 2011. Cloud classification based on structure features of infrared images. *Journal of Atmospheric and Oceanic Technology* 28, 410–417.
- Long, C.N., Sabburg, J., Calbó, J., Pagès, D., 2006. Retrieving cloud characteristics from ground-based daytime color all-sky images. *Journal of Atmospheric and Oceanic Technology* 23, 633–652.

- Maghrabi, A., Clay, R., Wild, N., Dawson, B., 2009. Design and development of a simple infrared monitor for cloud detection. *Energy Conversion and Management* 50, 2732–2737.
- Martins, F.R., Souza, M.P., Pereira, E.B., 2003. Comparative study of satellite and ground technique for cloud cover detection. *Advances in Space Research* 32, 2275–2280.
- Massip, P., Blanc, P., Kazantzidis, A., Tzoumanikas, P., 2015. Report on Algorithms for Nowcasting Methods Based on Sky Imagers. Technical report D3.1, DNICast (Grant agreement no: 608623), p. 29.
- Oberländer, D., Prahl, C., Wilbert, S., Müller, S., Stanicki, B., Hanrieder, N., 2015. Cloud shadow maps from whole sky imagers and voxel carving. In: Paper Read at ICEM, at Boulder.
- Olmo, F.J., Cazorla, A., Alados-Arboledas, L., López-Álvarez, M.A., Hernández-Andrés, J., Romero, J., 2008. Retrieval of the optical depth using an all-sky CCD camera. *Applied Optics* 47 (No. 34).
- Parisi, A.V., Sabburg, J., Turner, J., Dunn, P.K., 2008. Cloud observations for the statistical evaluation of the UV index at Toowoomba, Australia. *International Journal of Biometeorology* 52, 159–166.
- Scaramuzza, D., 2008. Omnidirectional Vision: From Calibration to Robot Motion Estimation. ETH Zurich (Ph.D. Thesis).
- Scaramuzza, D., Martinelli, A., Siegwart, R., 2006. A toolbox for easily calibrating omnidirectional cameras. In: IEEE/RSJ International Conference on Intelligent Robots and Systems, pp. 5695–5701. <http://dx.doi.org/10.1109/IROS.2006.282372>.
- Sebag, J., Krabbendam, V.L., Claver, C.F., Andrew, J., Barr, J.D., Klebe, D., 2008. LSST IR camera for cloud monitoring and observation planning. In: SPIE Proceedings, vol. 7012.
- Singh, M., Glennen, M., 2005. Automated ground-based cloud recognition. *Pattern Analysis and Applications* 8, 258–271.
- Smith, S., Toumi, R., 2008. Measuring cloud cover and brightness temperature with a ground-based thermal infrared camera. *Journal of Applied Meteorology and Climatology* 47, 683–693.
- Souza-Echer, M.P., Pereira, E.B., Bins, L.S., Andrade, M.A.R., 2006. A simple method for the assessment of the cloud cover state in high-latitude regions by a ground-based digital camera. *Journal of Atmospheric and Oceanic Technology* 2, 437–447.
- Urquhart, B., Kurtz, B., Dahlin, E., Ghonima, M., Shields, J.E., Kleissl, J., 2015. Development of a sky imaging system for short-term solar power forecasting. *Atmospheric Measurement Techniques* 8 (2), 875–890.
- Wacker, S., Groebner, J., Zysset, C., Diener, L., Tzoumanikas, P., Kazantzidis, A., Vuilleumier, L., Stockli, R., Nyeki, S., Kampfer, N., 2015. Cloud observations in Switzerland using hemispherical sky cameras. *Journal of Geophysical Research* 120 (2), 695–707.
- Yang, H., Kurtz, B., Nguyen, D., Chow, C.W., Ghonima, M., Kleissl, J., 2014. Solar irradiance forecasting using a ground based sky imager developed at UC San Diego. *Solar Energy* 103, 502–524.

# Short-term solar power forecasting based on satellite images

6

Philippe Blanc<sup>1</sup>, Jan Remund<sup>2</sup>, Loïc Vallance<sup>1,3</sup>

<sup>1</sup>MINES ParisTech, PSL Research University, Sophia Antipolis, France; <sup>2</sup>Meteotest, Berne, Switzerland; <sup>3</sup>EDF R&D—STEP, Chatou, France

## 6.1 Introduction

The scope of this chapter is the use of satellite-derived surface solar irradiance (SSI) from geostationary meteorological satellites to produce solar power nowcasting defined, according the World Meteorological Organization (WMO), as forecasts for a period ranging from 0 to 6 h ahead.<sup>1</sup>

By definition, the geostationary meteorological satellites remain always over the same geographical point, following the Earth's rotation. Using radiance images acquired by imaging sensors born by such satellites enable to scan several times per hour very large areas—typically a third of the surface of the Earth—thus capturing, in a persistent way, the spatial and temporal distribution of information about ground reflectance and optical state of the atmosphere. In particular, these satellites represent a source of large-scale information of great spatial and temporal density and resolution that enable continuous observations of cloud cover evolution, over a long period of times. Combining the different geostationary meteorological satellites on operation (namely, the METEOSAT, GOES, FENG YUN, and HIMAWARI families of satellites), these continuous and dense observations are available almost worldwide, except for the North and South Polar extended areas (see Fig. 6.1).

Thanks to this characteristics, satellite-based forecasting fills the gap both in the spatial and temporal resolution between in situ measurements from pyranometric sensors, photovoltaic (PV) production monitoring systems, sky cameras, and numerical weather prediction (NWP) models. Fig. 6.2 proposes a schematic view of the different spatial and time scales for the different Earth observation systems that can be used for solar forecasting.

More precisely, owing to Inman et al. (2013), satellite-based nowcasting is ideal for the time periods ranging from 30 min to 6 h. For shorter time periods, in situ

<sup>1</sup> <https://www.wmo.int/pages/prog/amp/pwsp/Nowcasting.htm>.

<sup>2</sup> OSCAR: Observing Systems Capability Analysis and Review tool of the WMO (<http://www.wmo-sat.info/oscar/>).

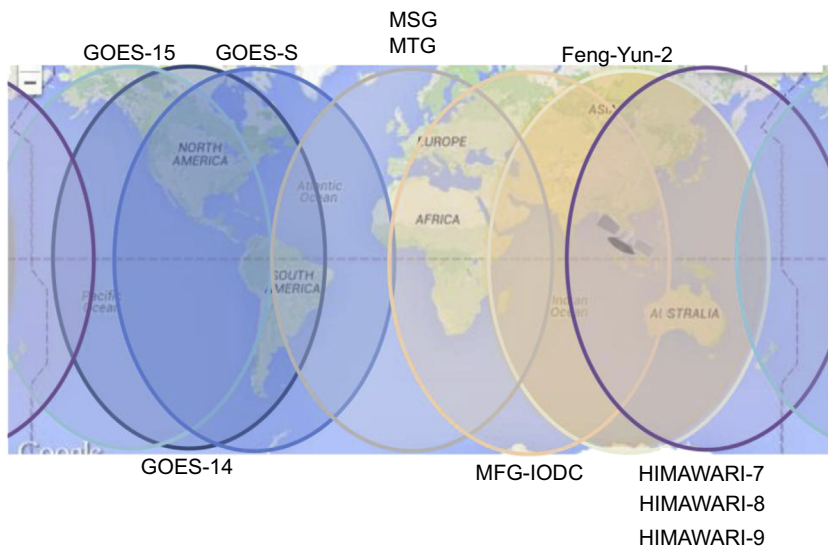


**Figure 6.1** Field of view of the main families of geostationary meteorological satellites (GOES, Meteosat first, second, and third generation, Feng-Yun, and Himawari) for a worldwide coverage.

Source: WMO OSCAR.<sup>2</sup>

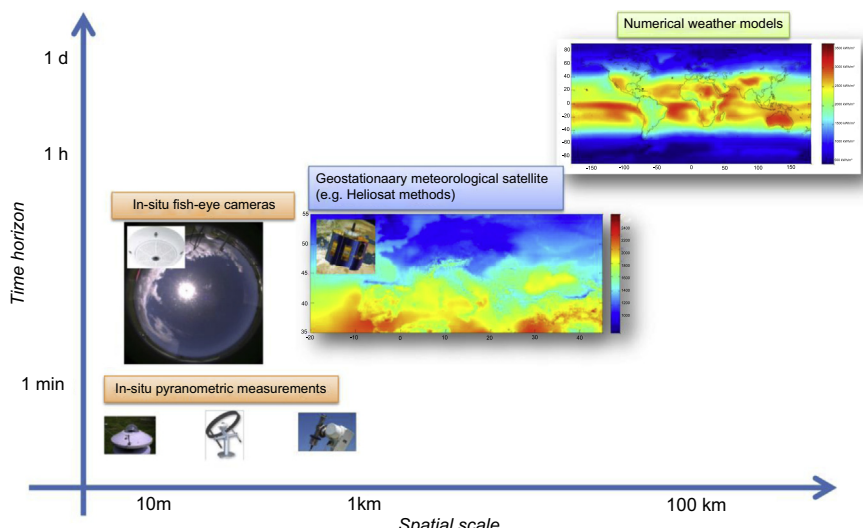


**Figure 6.2** Spatial (y-axis) and time (x-scales) scales of Earth observation systems (in situ sensors, satellite, and NWP) for solar forecasting.

measurements, even with persistence-based techniques—for horizon less than 10–15 min—are usually very effective. On contrary, NWP-based forecasts achieve their full capability for period ranging from 4 to 6 h ahead, and more.

Typical temporal resolution of satellite-based solar nowcasting is 2–10 km and typical temporal resolution is 15 min, both depending of course on the corresponding resolutions of satellite images. Most of the cases, such satellite-based nowcasting is done for specific sites since the main advantage of those methods is the ability of a better location of clouds. However these methods can be also used for regional forecasts.

The basis of the satellite-based forecasts is the SSI retrieval from the geostationary satellite. Therefore we first describe the different approaches of those retrievals (Section 6.2) before coming to the forecasting methods themselves (Section 6.3).

## 6.2 Surface solar irradiance retrieval from meteorological geostationary satellite

### 6.2.1 Different approaches

The models used for SSI retrieval with satellite images can be schematically separated in two groups.

The first group corresponds to the empirical and semiempirical methods based on cloud-index such as the first versions 1, 2, and 3 of the Heliosat methods (Cano et al., 1986; Diabate et al., 1989; Beyer et al., 1996; Perez et al., 2002; Rigollier et al., 2004; Cebecauer et al., 2010). These methods will be named hereinafter the cloud-index methods.

The second group corresponds to the physical approaches based on the explicit modeling the radiative transfer through the atmosphere, both for clear and cloudy situations. Examples of such models are the Heliosat-4 method used for the MACC-RAD database in the framework of the MACC projects<sup>3</sup> (Hoyer-Klick et al., 2014), the cloud physical properties (CPP) algorithm (Roebeling et al., 2006) used for the MSGCPP<sup>4</sup> product by the *Koninklijk Nederlands Meteorologisch Instituut* (KNMI) or the Physical Solar Model used by the *National Renewable Energy Laboratory* (NREL) for the new version of the NSRDB<sup>5</sup> database (Sengupta et al., 2015b).

The physical models are more complex and more computationally demanding than the cloud-index methods. Though not currently as accurate as the empirical cloud-index-based models, which are older and have been efficiently empirically tuned using networks of ground-based measurements. Indeed, cloud-index models have the advantage to be overall almost bias-free and are resulting therefore, in many cases, in lower uncertainty values in benchmarks (Richter et al., 2015). Nevertheless, the

<sup>3</sup> MACC (Monitoring Atmosphere Composition and Climate): <https://www.gmes-atmosphere.eu/>.

<sup>4</sup> MSGCPP (Meteosat Second Generation Cloud Physical Properties) product from the KNMI: <http://msgcpp.knmi.nl>.

<sup>5</sup> NSRDB (National Solar Radiation Database): <https://nsrdb.nrel.gov/current-version>.

physical models offer more space for improvement toward an increase in quality of the estimates for the future, namely in the spectral definition of SSI and its angular distribution for a better determination of the direct, circumsolar, and diffuse components.

In this chapter, only the cloud-index methods have been considered since these approaches are currently used by most of the operational satellite-based databases of SSI, such as those from the companies GeoModel Solar, 3TIER for most of the world, SOLEMI for Europa, Africa and Western Asia, SolarAnywhere for the USA, HelioClim for Europe and Africa, EnMetSol for Europe.

For cloud-index methods, satellite images of reflectance are first compared to corresponding ground albedo and typical cloud reflectance—modeled or empirically estimated—to produce a cloud index. This cloud-index  $n$  is then related to the clear-sky index  $K_c$  defined as the ratio of the global horizontal irradiance (GHI) with the concomitant modeled GHI under clear-sky—i.e., cloud-free—condition. The relation between the cloud index and the clear-sky index is based on an empirical decreasing function such as  $K_c = 1 - n$  in his simplest linear form. The GHI is then calculated by multiplying this clear-sky index by an exogenous model or database of clear-sky irradiance (Gueymard, 2012; Sengupta et al., 2015a, Section 4.4).

[Fig. 6.3](#) shows the basic method to obtain global radiation by cloud-index method.

### 6.2.2 From surface solar irradiance to solar power

Many users in the field of photovoltaic (PV) energy need solar power forecasts and not only the GHI. To obtain PV power forecasts, the following additional three steps are needed:

- Step 1: “Splitting” or transposition of GHI into diffuse horizontal irradiance (DHI) and direct normal irradiance (DNI), used for concentrated-PV (CPV) or concentrated solar thermal electricity (CSTE) systems or for Step 2.
- Step 2: Calculation of the global tilted irradiance (GTI) of the PV modules also named the plane-of-array irradiance (POAI). Those PV planes may be static or mounted on a solar tracking system with one or two axes.
- Step 3: Simulation of PV production notably based on POAI.

To account for variation of the Sun position, these steps should be applied typically at 1-min time resolution, using ad hoc temporal interpolation of clear-sky index.

For all three steps, many methods are available and well documented in the bibliography.

The splitting is either done based on available GHI data (Ruiz-Arias et al., 2010a; Gueymard and Ruiz-Arias, 2015) or directly based on satellite image processing (Hammer et al., 2009).

For the computation of the POAI, many models are available to estimate the GTI from the GHI and DHI (Ineichen, 2011; Efim and Kudish, 2009). The direct tilted component is “easily” determined from the DHI, considering the cosine of the incident angle—the angle between the direction of Sun and the normal to the PV planes. The diffuse tilted component is much more complex to assess since it theoretically requires the diffuse sky radiance—and possibly the ground reflectance—to be able to compute

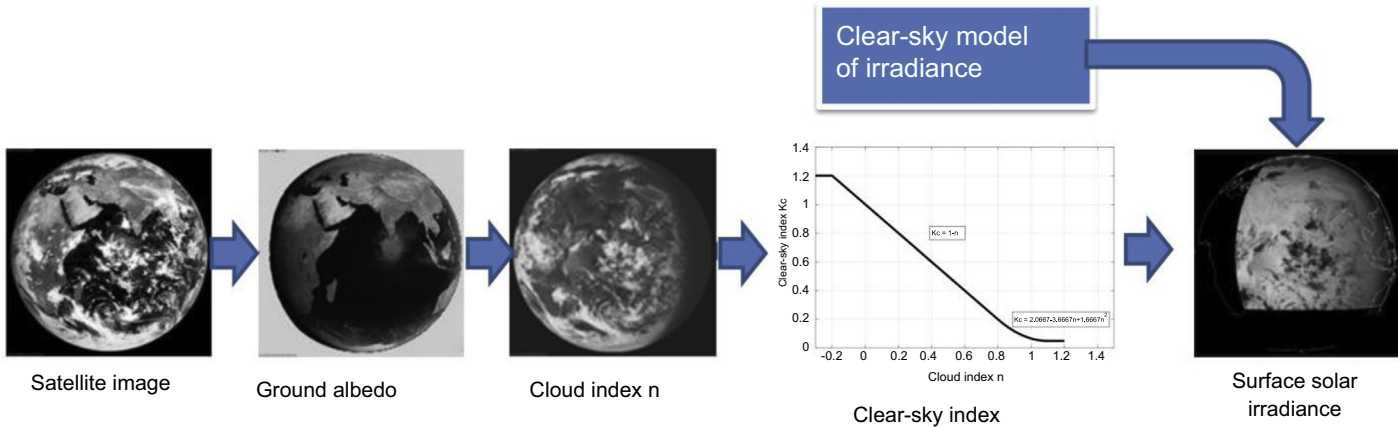


**Figure 6.3** Principle of surface solar irradiance retrieval with the cloud-index method Heliosat-2.

the sum of the all the infinitesimal flux contributions of each sky—and ground—infinitesimal solid angle element in front of the PV panels. The different approaches to assess this component are using in fact—explicitly or implicitly—empirical models of the diffuse sky radiance. This sky radiance model can be a fully isotropic model or, on contrary, a parametric one proposing a radiance model depending on the solar zenith angle and the angular distance of each sky element from the sun position (Perez et al., 1993). This step may be also used to account for potential surrounding buildings, vegetation, natural orography, etc., which may induce shadow on the power plants (Ruiz-Arias et al., 2010b or Remund et al., 1998).

Finally, the PV production can be modeled from the POAI either with very simple methods—more or less linear to the POAI with possible correction of the PV cell temperature effects—or with complex models including the physics and the processing of inverters and modules. Often rather simple models are used in the combination of forecasts since the uncertainty of the GHI forecasts are generally much larger than the PV modeling uncertainties. Moreover, the technical information of the PV installations needed for complex models are often not known. High-end modeling would include also spectral information and variability of the POAI, which is only seldom available and not yet standard for PV modeling.

For the calculation of PV production, air temperature and wind speed can be used to take into account the effects of lowered efficiency with increased module temperatures (Ceylan et al., 2014; Beyer et al., 2004). Both meteorological surface parameters are often provided as a forecast by NWP output rather than local measurements. The higher uncertainty of NWP temperature data of typically 2°C is acceptable as the conversion models are not so sensitive concerning the air temperature.

### **6.2.3 Characteristics of surface solar irradiance retrieval from satellite**

The basis of the solar power forecasts based on satellite images are the estimation of the current situation. Almost all errors of the initial state will be kept for the forecasted time steps and forecasted values can hardly have lower uncertainties, aside some smoothing effects that can slightly lower the root mean square errors (RMSE).

It is a reason why a short overview of the available databases is given here. However it is not possible to include all available datasets as the number of them is evolving quickly. Table 6.1 shows some of the available SSI databases that are ready for nowcasting, requiring the ability of near real-time processing of satellite images, typically every 15 min or 30 min.

All models listed in Table 6.1 belong to the empirical cloud-index methods. Up to now, physical models are not yet ready for nowcasting usage. The uncertainty of the cloud-index method defined here by the standard deviation is in the range of 15%–20% for hourly values, which equals also to the uncertainty of the starting point for the satellite-based forecast.

**Table 6.1 Examples of available near real-time surface solar irradiance databases including spatial and temporal resolutions and uncertainty information (relative standard deviation of hourly global horizontal irradiance)**

Database	Provider/source	Spatial coverage	Spatial resolution (km)	Temporal resolution (min)	Uncertainty (standard deviation) (%)
SolarGIS	<a href="http://www.solargis.info">www.solargis.info</a>	Worldwide	5	15	17
HelioClim-3 v4	<a href="http://www.soda-is.com">www.soda-is.com</a>	Europe, Africa	4	15	20
Enmetsol	<a href="https://www.uni-oldenburg.de/en/physics/research/ehf/energiemeteorology/enmetsol">https://www.uni-oldenburg.de/en/physics/research/ehf/energiemeteorology/enmetsol</a>	Europe, Africa	4	15	17
Irsolav	<a href="http://www.irlsolav.com">www.irlsolav.com</a>	Europe, Africa	4	15	24
SolarAnywhere	<a href="http://www.solaranywhere.com">www.solaranywhere.com</a>	USA, lower 48°N, Mexico	10	30	—

The uncertainty values are taken from the benchmark of IEA SHC Task 46. Ineichen, P., 2013. Long term satellite hourly, daily and monthly global, beam and diffuse irradiance validation. Interannual Variability Analysis. Data from IEA SHC Task 46 report, access: <http://archive-ouverte.unige.ch/unige:29606>.

### 6.2.4 Local combination with *in situ* pyranometric measurements

Solar radiation estimations based on satellites can be locally improved by combination with *in situ* pyranometric measurements. The combination can be used, for example, to correct systematic and seasonal deviations due to local and specific aerosol loads or cloud effects on the SSI. For the production of historical time series, the combination of short-term *in situ* measurement overlapping with the long-term satellite SSI data is a standard procedure (Ruiz-Arias et al., 2015; Cebecauer and Suri, 2015; Vernay et al., 2013).

The techniques used to do this calibration with *in situ* pyranometric measurement are generally based on model output statistics (MOS) (Glahn and Lowry, 1972) and include parametric calibration model with respect known exogenous variables such as the solar zenith and azimuth angles, the air mass, the incident angle, or the day angle.

## 6.3 Different approaches for satellite-based forecasting

### 6.3.1 Forecast based only on temporal information

For any given location—for single point solar forecast—or aggregated spatial region—for regional forecast—in the field of view of the geostationary satellite, satellite-based methods can be able to provide already existing long-term—10 years and more—historical dataset of intrahourly SSI along with near real-time estimation.

This information available in any location in the field of view of the geostationary satellites can be used for forecasting methods based on statistical modeling of the temporal variability. In principle, the same type of forecasting techniques used with *in situ* measurements can be applied to the satellite-based time series of irradiance.

An overview of different time series approaches used for solar irradiance forecasting is given notably by Coimbra et al. (2013), Inman et al. (2013) and Diagne et al. (2013):

- Persistence (clear-sky index—based and smart persistence—see explanation below).
- Autoregressive models (AR, ARMA, ARIMA) (Dambreville et al., 2014).
- Artificial neural network (ANN) (Voyant et al., 2014).
- Analog or k-nearest-neighbor (kNN) approaches (Pedro and Coimbra, 2015; Boilley et al., 2015).

All these time series methods can be generically written as:

$$\widehat{Kc}(p, k + dk|k) = F(Kc^{sat}(p, k), Kc^{sat}(p, k - 1), \dots) \quad (6.1)$$

where  $\widehat{Kc}(p, k + dk|k)$  is the forecasted clear-sky index at the location  $p$ , issued at the time  $k$  for the time horizon  $dk$ . The time is expressed hereinafter as integer index with respect the time resolution of the SSI retrieval. This forecasted clear-sky index is determined from series of lagged—or historical—past clear-sky indexes

$\{Kc^{sat}(p, k), Kc^{sat}(p, k - 1), \dots\}$  from the satellite-based SSI database, for the issue time  $k$ , for the same location  $p$ , thanks to a specific function  $F$  a priori defined for the persistence or the kNN approach or determined from a training period, for autoregressive models or for the ANN models.

Compared to in situ pyranometric stations, the ability of satellite-based database to provide long-term historical dataset of intrahourly SSI for any location, systematically enables long training periods that are required by these statistical temporal models of forecast, except for the persistence. These long-term historical datasets also enable consistent forecast uncertainty a posteriori analysis, using the satellite SSI dataset as a reference.

Nevertheless, the performances of the satellite-based statistical time series models are intrinsically limited by the uncertainties of the satellite-based estimations themselves (Section 6.2.3), even if the use of short-term overlapping in situ pyranometric measurements is possible to locally reduce these uncertainty, mainly for the bias (Section 6.2.4).

Clear-sky index-based persistence forecast is often used as a baseline for benchmarks of more sophisticated forecast approaches, especially for very short-term forecasts—in the range of minutes to 1 h. The simplest way to calculate this clear-sky-based persistence is to propagate the last clear-sky index estimated with the satellite images. More “sophisticated” persistence versions exists, named smart persistence. The idea is to use a sliding averaging window to calculate the clear-sky index to be propagated with a length consistent with the time horizon of the forecast, limited to the daylight period.

The statement of [Sengupta et al. \(2015a,b\)](#) about the statistical time series models with local irradiance measurements as input is of course still valid as a guideline for this type of satellite-based forecasting. These approaches “benefit from the high auto-correlation for short time lags in time series of solar irradiance; however, changes in cloud conditions, such as by approaching clouds, can hardly be predicted.”

Even if these statistical time series models for satellite-based forecasting present the advantage of being simple with a relatively good trade-off between complexity and performance—at least for time horizon of less than 1 h—, they are missing the available spatial information provided by the satellite that may be a breakthrough to the limitation stated by [Sengupta et al. \(2015a,b\)](#).

It is the reason why the next section presents forecasting methods based on this spatial and temporal information specifically provided by geostationary satellites.

### 6.3.2 Forecast based on spatial and temporal information

For any given location in the field of view of the geostationary satellite, satellite-based method provides in near real-time long-term intrahourly time series of kilometric maps of SSI, in the vicinity of the region of interest. The combination of spatial and temporal information can be used as information for different forecasting approaches:

- The forecasting approaches based on cloud motion vectors (CMVs) (cloud advection).
- The forecasting approaches based on a statistical modeling of the spatiotemporal variability.

### 6.3.2.1 Forecasting approaches based on cloud motion vectors

Generally, CMV techniques are used to forecast solar radiation based on time series of geostationary satellite images. Of course, these techniques can be also applied to do forecasting with hemispherical sky images from in situ sky imagers (see Chapter 5). The CMV techniques have a long scientific and technical track records—going back to Fujita (1968)—and are well documented by Menzel (2001). Lorenz et al. (2004) introduced this method for solar radiation forecasts. As shown in Law et al. (2014), forecasts between 1 and 5 h ahead were recommended to be obtained from satellite-based CMV techniques (Kleissl, 2010; Diagne et al., 2013; Coimbra et al., 2013).

The method is based on the determination of cloud vectors based on the analysis of consecutive images. Assuming that the features do not change significantly over a short interval, the CMV techniques are computed using pattern-matching or optical-flow techniques applied to successive images. The future cloud situation is then estimated by the extrapolation of motion assuming persistence of cloud speed, size, shape, and optical properties (Lorenz et al., 2004). This CMV-based forecasting can be schematically written as:

$$\widehat{Kc^{CMV}}(p, k + dk|k) = Kc^{sat}(p - dk.dp(p, k), k) \quad (6.2)$$

where  $\widehat{Kc^{CMV}}(p, k + dk|k)$  is the CMV-based forecasted clear-sky index at the location  $p$ , issued at the time  $k$  for the time horizon  $dk$ . This forecasted clear-sky index is determined from the clear-sky index  $Kc^{sat}(.,k)$  from the satellite-based database, at the issue time  $k$  for a location translated from the location  $p$  by the corresponding estimated CMV  $dp(p,k)$  linearly extrapolated on the horizon time  $dk$ . It is to be noted that CMV-based forecast approach may also be constructed with clearness or cloud index.

In other word, the CMV techniques therefore aim at explicitly and solely “capturing” the local advections of already existing clouds.

Block-matching or optical flow techniques are applied on time series of images from satellite to get local cloud advections. The optical flow techniques, such as the Lucas–Kanade method (Lucas and Kanade, 1981), are differential methods: following the brightness constancy constraint, the differences between two consecutive images are assumed to be only due to local translation of clouds. The corresponding displacement vectors are then locally determined with these differences thanks a local Taylor series approximation. The Soleksat forecast described by Cros et al. (2015) makes use of this technique. For the block-matching technique, the displacement vectors are calculated based on normalized cross-correlations between blocks of fixed size between two consecutive images. This technique is notably used for CMV-based solar forecasting by Lorenz et al. (2004) or by Dazhi et al. (2013).

Some CMV-based forecast methods do not use consecutive satellite images to assess the field of the local CMV: the CMV are, in this case, provided by NWP with gridded wind speeds vectors for different altitudes (Alvarez et al., 2010; Miller and Combs, 2012; Müller and Remund, 2013; Kühnert et al., 2013). In this case,

only the spatial information of SSI from the satellite-based database is used and temporal information is not taken into account.

This approach is computationally faster and allows forecasting of nonlinear changes of wind vectors: the persistence of cloud speed over the forecast horizon is not an assumption in that case.

It raises up the issue of choosing wind vectors at a wrong altitude level for the corresponding clouds and, for example, to transport fog or lee waves across mountain chains. Kühnert et al. (2013) has shown that altitude of wind speed information is not a sensitive parameter. Indeed, wind speed at 2–5 km altitude is rather stable in altitude and the optimal—in the sense of RMSE of the resulting forecast—altitude level for the wind vector to consider for the cloud advection is between 3 and 4 km. The usage of multi cloud layers has not yet been demonstrated as useful, but is currently still under investigation.

Lorenz et al. (2015) proposed a short review of two independent CMV models tested at 18 German sites. Uncertainty values are in the range of 16%–20% for 15 min and 30% for 3 h of forecast horizon. For the horizon of 0.25–1.5 to 2 h the CMV methods were better than the NWP-based forecasts (Fig. 6.4).

As measure of uncertainty, relative standard deviation or relative RMSE are often used. However these measures do not “show the whole picture”. With strong penalty to squared differences, notably for even slightly time-shifted of forecasted ramps, these uncertainty measures have some tendency to promote spatially and temporally smoothed forecasts. Therefore an additional performance criterion based on the “variability index” was proposed by Lorenz et al. (2015): the variability test. The variability index is the one proposed by Skartveit et al. (1998) that includes the relative ramp rates defined as the deviation of two consecutive values of the clearness index:

$$var_{Kc,2N+1}(t) = \sqrt{\frac{1}{2N+1} \sum_{i=-N+1}^N (Kc(k+1) - Kc(k))^2} \quad (6.3)$$

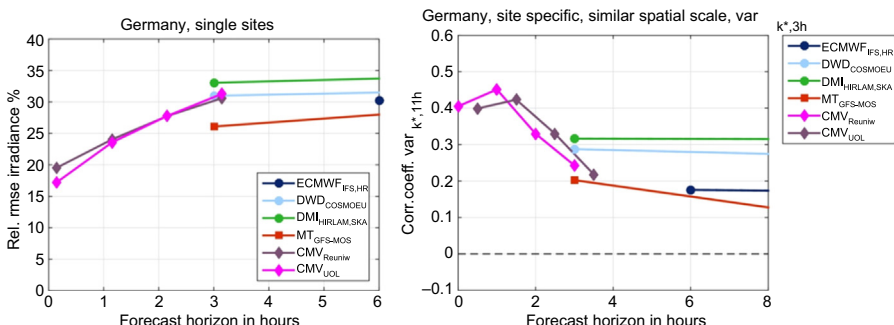


**Figure 6.4** Benchmark of CMV forecasts for 18 German sites (Lorenz et al., 2015). Left: relative RMSE, right: correlation coefficients of the forecasted and reference variability indexes. For RMSE, lowest values are best (ideal value: 0%), for the correlation coefficient of variability index, test highest values are best (ideal value: 1).

The variability test is then defined as the Pearson correlation of the variability indexes within blocks of 3–11 h of both measured and forecasted time series.

[Fig. 6.4](#) shows the relative RMSE and the variability index in dependence on time horizon. Nowcasting based on satellite show clearly lower uncertainty values for both measures (RMSE and variability test) than the NWP-based methods, for the first 3 h of time horizon. The results of both models (CMV<sub>UOL</sub> = Univ. Oldenburg and CMV<sub>Reuniwatt</sub> = CMV of Reuniwatt, the Soleksat model) are very similar. The NWP models show different ranks concerning RMSE and variability tests: For RMSE of global smoothed or statistically enhanced models like MT<sub>GFS-MOS</sub> or ECMWF<sub>IHS,HR</sub> show the best results. For variability models with higher spatial and temporal resolution DMI<sub>HIRLAM,SKA</sub> and DWD<sub>COSMOEU</sub> show the best results.

### 6.3.2.2 *The forecasting approaches based on a statistical modeling of the spatiotemporal variability*

The CMV-based forecasting approaches “only” address the cloud advection: the underlying spatiotemporal variability model is very simple: locally to the region of interest, the spatial field of cloud or clear-sky indexes at the time  $k + dk$  is assumed to correspond to a—locally—translated version of the field at the time  $k$ .

[Dambreville et al. \(2014\)](#) proposed, for very short-term horizon from 15 to 120 min of 15-min GHI, another satellite-based forecasting approach based on a statistical autoregressive model of the spatiotemporal variability. This approach takes into account lagged past clear-sky indexes of a set  $Q(p)$  of surrounding pixels to the location  $p$ , provided by the satellite-based database  $\{Kc^{sat}(q, k), Kc^{sat}(q, k - 1), \dots\}_{q \in Q(p)}$ . In addition, [Dambreville et al. \(2014\)](#) proposed to integrate an autoregressive model with lagged clear-sky indexes of the past,  $\{Kc(k), Kc(k - 1), \dots\}$  derived from the in situ pyranometric measurement:

$$\widehat{Kc^{AR_{st}}}(p, k + dk | k) = \alpha_0 + \sum_{\substack{q \in Q(p) \\ 0 \leq l \leq L}} \alpha_{q,l} Kc^{sat}(q, k - l) + \sum_{0 \leq n \leq N} \beta_n Kc(k - n) \quad (6.4)$$

where  $\widehat{Kc^{AR_{st}}}(p, k + dk | k)$  is the spatiotemporal autoregressive forecasted clear-sky index at the location  $p$ , issued at the time  $k$  for the time horizon  $dk$ .

The autoregressive parameters  $\{\alpha_0, \{\alpha_{q,l}\}\}$  and  $\{\beta_n\}$  are determined, thanks to an historical training period, in an optimal way, in the sense of the minimization of the RMSE for a given horizon of time  $dk$ .

[Dambreville et al. \(2014\)](#) drew the conclusion that, compared to a “simple” autoregressive temporal forecast model based on in situ pyranometric measurements, the spatiotemporal information from the satellite database in vicinity of the location of interest, significantly improves—up to 19% in term of RMSE—the quality of the forecast. This improvement from the satellite images is effective without any

calculation of CMV from them. Nevertheless, the choice of the set  $Q(p)$  of surrounding pixels to be taken into account for the spatiotemporal autoregressive model Eq. (6.4), is sensitive and depends on the time horizon. Dambreville et al. (2014) proposed methods based on correlation analysis on a training period to define, for a given time horizon  $dk$ , this set of pixels. Briefly, these methods consist of selecting the pixels of which the satellite-based clear-sky index present, on the training period, the highest Pearson correlation with the  $dk$ -lagged clear-sky index from the in situ pyranometric station.

Mazorra Aguiar et al. (2015) proposed, for short-term horizons from 1 to 6 h of hourly GHI, a similar satellite-based forecasting. In that case, an ANN model has been used instead of the autoregressive model. In different locations in Gran Canaria Island, the use of the satellite-based spatiotemporal information improves—up to 7% of the RMSE—the quality of the forecast compared to the ANN model only fed by the lagged in situ pyranometric measurements.

### **6.3.3 Postprocessing of satellite-based forecasts with in situ measurements**

If in situ pyranometric—or PV production—measurements are available, they can be included in a postprocessing scheme and the resulting forecast can be statistically improved. Depending on the operational constraints and the availability of the in situ measurements, this postprocessing can be based on different approaches.

If only past historical dataset of in situ measurements is available, the “raw” forecasted results are a posteriori analyzed for a given time horizon on this past period. Generally using MOS, a parametric calibration model is defined with respect known exogenous variables such as the solar zenith and azimuth angles, the air mass, the incident angle, or the day angle. The raw satellite-based forecast is then postprocessed by applying this calibration model.

In the case of availability of real-time in situ measurements, closed-loop correction of the raw satellite-based forecasted with real-time feedback may be defined. In most of the case, this closed-loop correction resort to the technique of the optimal predictor-corrector type estimator: the Kalman filter.

Such closed-loop postprocessing of raw satellite CMV forecast has been, for example, proposed by Müller and Remund (2013) as depicted by Fig. 6.5. Indeed, they used a simple offset correction based on Kalman filter technique, which can correct, e.g., errors induced by incorrect aerosol data. The postprocessing uses the last hour of measurements and starting points of the forecasts. If the forecasts are constantly lower or constantly higher than the measurements during that past hour, then the average difference in cloud index is calculated and added to the actual forecast. The adaption is not applied in case of variable conditions as this can enhance the error.

However, in the framework of satellite-based solar forecasting, the use of in situ pyranometric or PV production measurements is not standardized yet. The main reasons for this are the constraints of real-time data logging and access to those local data and the difficulties to have gap-free and high quality measurements that require high level of human maintenance.

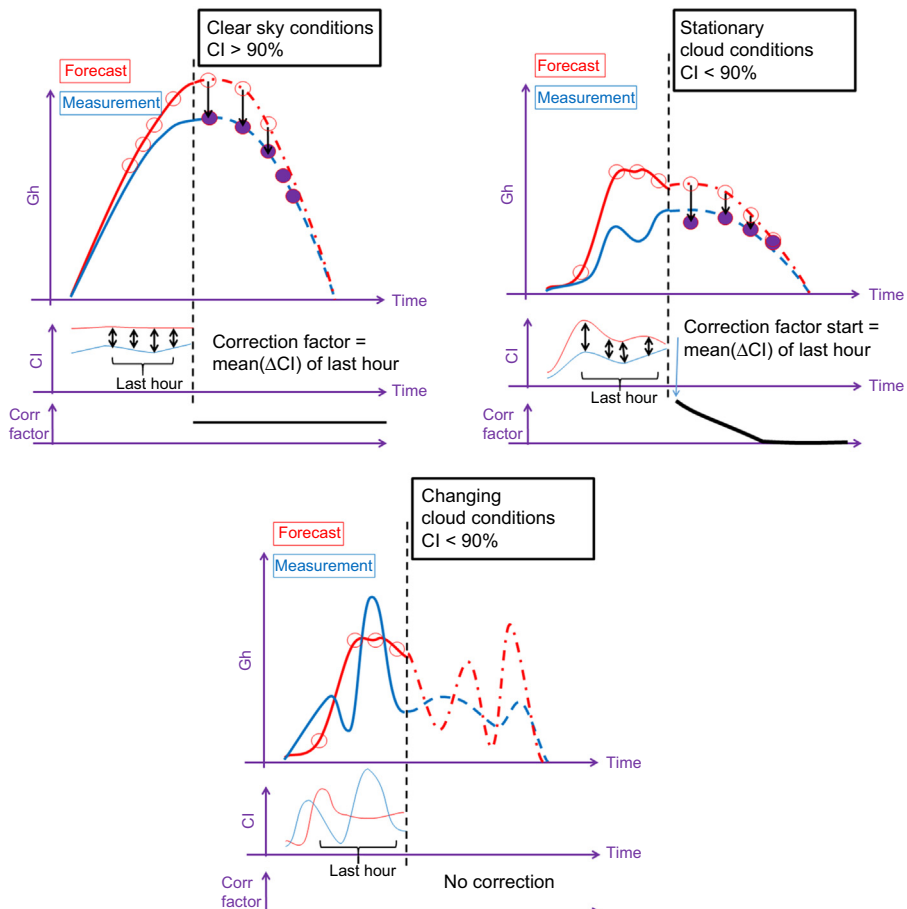


Figure 6.5 Kalman filter technique used by Müller and Remund (2013).

## 6.4 Conclusion and perspectives

The domain of the solar power nowcasting based on geostationary meteorological satellite images is very active in the research domain of the solar forecasting since it corresponds to real and present needs of operational end-users, asking for reliable, accurate, and easy-to-use forecast solutions.

In this chapter, multiple approaches have been described to benefit from meteorological geostationary satellite for solar power nowcasting, namely by using systematically preexisting long-term intrahourly SSI dataset for the training, global, or very large spatial coverage at kilometric spatial resolution for specific sites, and also spatio-temporal information on SSI available on the near real-time basis.

Some satellite-based approaches, such as simple persistence or CMV techniques, are already operationally and commercially used. Concerning the CMV-based

nowcasting, benchmarks have globally shown that they introduce additional benefit compared to single in situ measurements or NWP, for forecast horizons from 15 min to 3 h.

There are unfortunately not many independent validations and benchmarks of solar nowcasting approaches. Perez et al. (2010) showed a comparison of forecasts within the USA and Law et al. (2014) showed results mainly for DNI forecasts. The outlines of the benchmark at 18 German sites proposed by Lorenz et al. (2015) have been presented in Section 6.3.2.1. Nevertheless, benchmarks are strongly dependent on region—topography, specific local climate typically more prone to cloud advection or convection, etc.—seasons, time resolutions, and forecast horizons of interest. Moreover, additional in situ measurement can be used in the forecast (preprocessing local calibration of the satellite-based SSI time series, MOS, or Kalman filter postprocessing). Therefore it is difficult—if not impossible—to compare different benchmarks.

The sources of improvement of the use of geostationary meteorological satellite images for the solar nowcasting are multiple.

Firstly, improvements should be made for the satellite-based SSI retrieval to be more dedicated to PV simulation models with improved characterization of POAI—on tilted planes—and spectral distributions. The use of physical models for the SSI satellite retrieval (see Section 6.2.1) could be a solution for such required improvements, provided that they enable near real-time computation.

Secondly, improvements should be made in the combination of satellite images and NWP products. A first approach would be, for example, a better postprocessing of satellite-based and NWP forecasts to produce “seamless” forecast in time horizons ranging from 15 min to 6 h. Such a combination postprocessing has been notably proposed by Lorenz et al. (2014). This postprocessing is based on cloud-variability and forecast horizon dependent linear combination of the different forecasting results to provide “optimal” seamless forecasting for a large range of forecast horizon. This combination of satellite images and NWP products could be more intricate than a seamless blending postprocessing. For example, Thorey et al. (2015) proposed an optimal sequential aggregation—weighted linear combination—of elements of NWP ensemble forecast using near real-time satellite-based SSI estimations as observations.

Finally, better use of ground measurement and in particular fusion approaches between satellite imagery and sky imagers should be performed to achieve a “seamless” short-term and very short forecasting. Due to their geometry and location, the use of hemispherical sky images acknowledges limitation in terms of forecast horizon: this limit ranges from 10 to 20 min and mainly depends on cloud speeds. However, the high spatial and temporal resolutions of these images make it a suitable tool for nowcasting. Such a fusion with satellite-based approaches would enable an overlapping between the two different forecast horizons intervals. This fusion process would aim at combining the advantages of each method, either by using a pixel-by-pixel analysis, or by merging some attributes—or decisions—on spatial data from these various sources of information. Examples of attributes that may contribute to the forecast are CMV on each set of images, fractal descriptors of the cloud cover, or even more intrinsic properties of the clouds (cloud optical depth, cloud classification,

cloud phase, etc.). As seen in [Section 6.3.2.1](#), the quality of the resulting fusion should not rely only on standard statistical criteria, but also on other metrics as the characterization of the forecast variability or the ability to detect and follow ramp events.

## Acronyms

ANN	Artificial Neural Networks
CMV	Cloud motion vector
CPP	Cloud physical properties
CPV	Concentrated photovoltaic
CSTE	Concentrated solar thermal electricity
DHI	Diffuse horizontal irradiance
DNI	Direct normal irradiance
GHI	Global horizontal irradiance
GTI	Global tilted irradiance
KNMI	<i>Koninklijk Nederlands Meteorologisch Instituut</i>
kNN	k-nearest neighbor
MOS	Model output statistics
NREL	<i>National Renewable Energy Laboratory</i>
NSRDB	National solar radiation database
NWP	Numerical weather prediction
POAI	Plane-of-array irradiance
PV	Photovoltaic
RMSE	Root mean square error
SSI	Surface solar irradiance
WMO	World Meteorological Organization

## References

- Álvarez, L., Castaño Moraga, C.A., Martín, J., 2010. A Computer Vision Approach for Solar Radiation Nowcasting Using MSG Images. EMS 2010, Zurich access: <http://meetingorganizer.copernicus.org/EMS2010/EMS2010-495-3.pdf>.
- Beyer, H.G., Costanzo, C., Heinemann, D., 1996. Modifications of the Heliosat procedure for irradiance estimates from satellite images. *Solar Energy* 56, 207–212.

- Beyer, H.G., Heilscher, G., Bofinger, S., 2004. A Robust Model for the MPP Performance of Different Types of PV-Modules Applied for the Performance Check of Grid Connected Systems. *Eurosun*, Freiburg.
- Boilley, A., Blanc, P., Wey, E., Thomas, C., 2015. The solar forecast similarity method: a new method to compute solar radiation forecast for the next day. In: SHC 2015, International Conference on Solar Heating and Cooling for Buildings and Industry, Istanbul, Turkey.
- Cano, D., Monget, J.-M., Albuission, M., Guillard, H., Regas, N., Wald, L., 1986. A method for the determination of the global solar radiation from meteorological satellites data. *Solar Energy* 37, 31–39.
- Cebecauer, T., Suri, M., Perez, R., 2010. High performance MSG satellite model for operational solar energy applications. In: Proc. Solar 2010. ASES Annual Conference, Phoenix, AZ.
- Cebecauer, T., Suri, M., 2015. Site-adaptation of satellite-based DNI and GHI time series: overview and SolarGIS approach. In: SolarPACES 2015 Conference, Cap Town, South Africa.
- Ceylan, I., Erkaymaz, O., Gedik, E., Gurel, A.E., 2014. The prediction of photovoltaic module temperature with artificial neural networks. *Case Studies in Thermal Engineering* 3, 11–20. <http://dx.doi.org/10.1016/j.csite.2014.02.001>.
- Coimbra, C.F.M., Kleissl, J., Marquez, R., 2013. Overview of solar-forecasting methods and a metric for accuracy evaluation. In: Kleissl, J. (Ed.), *Solar Energy Forecasting and Resource Assessment*. Academic Press, Boston, ISBN 9780123971777, pp. 171–194. <http://dx.doi.org/10.1016/B978-0-12-397177-7.00008-5> (Chapter 8).
- Cros, S., Turpin, M., Lallemand, C., Sébastien, N., Schmutz, N., 2015. Soleksat: a flexible solar irradiance forecasting tool using satellite images and geographic web-services. EU PVSEC Proceedings 2128–2131. <http://dx.doi.org/10.4229/EUPVSEC20152015-SBV.1.42>.
- Dambreville, R., Blanc, P., Chanusso, J., Boldo, D., 2014. Very short term forecasting of the global horizontal irradiance using a spatio-temporal autoregressive model. *Renewable Energy* 72, 291–300. <http://dx.doi.org/10.1016/j.renene.2014.07.012>.
- Dazhi, Y., Walsh, W.M., Zibo, D., Jirutitijaroen, P., Reindl, T.G., 2013. Block matching algorithms: their applications and limitations in solar irradiance forecasting. *Energy Procedia* 33, 335–342. <http://dx.doi.org/10.1016/j.egypro.2013.05.074>.
- Diabaté, L., Moussu, G., Wald, L., 1989. Description of an operational tool for determining global solar radiation at ground using geostationary satellite images. *Solar Energy* 42, 201–207.
- Diagne, M., David, M., Lauret, P., Boland, J., Schmutz, N., 2013. Review of solar irradiance forecasting methods and a proposition for small-scale insular grids. *Renewable and Sustainable Energy Reviews* 27, 65–76. <http://dx.doi.org/10.1016/j.rser.2013.06.042>.
- Efim, G.E., Kudish, A.I., 2009. The assessment of different models to predict the global solar radiation on a surface tilted to the south. *Solar Energy* 83 (3), 377–388. <http://dx.doi.org/10.1016/j.solener.2008.08.010>.
- Fujita, T.T., 1968. Present status of cloud velocity computations from ATS-1 and ATS-3. *COSPAR Space Research* 9, 557–570.
- Glahn, H.R., Lowry, D.A., 1972. The use of model output statistics (MOS) in objective weather forecasting. *Journal of Applied Meteorology* 11, 1203–1211.
- Guemard, C., 2012. Clear-sky irradiance predictions for solar resource mapping and large-scale applications: improved validation methodology and detailed performance analysis of 18 broadband radiative models. *Solar Energy* 86 (8), 2145–2169. <http://dx.doi.org/10.1016/j.solener.2011.11.011>.

- Gueymard, C.A., Ruiz-Arias, J.A., 2015. Extensive worldwide validation and climate sensitivity analysis of direct irradiance predictions from 1-min global irradiance. *Solar Energy*. <http://dx.doi.org/10.1016/j.solener.2015.10.010>.
- Hammer, A., Lorenz, E., Kemper, A., Heinemann, D., Beyer, H.G., Schumann, K., Schwandt, M., 2009. Direct normal irradiance for CSP based on satellite images of Meteosat second generation. *SolarPACES 2009*, 15-18.9 (Berlin).
- Hoyer-Klick, C., Lefèvre, M., Schroedter-Homscheidt, M., Wald, L., 2014. User's Guide to the MACC-RAD Services on Solar Energy Radiation Resources. <http://dx.doi.org/10.13140/RG.2.1.5016.7521>.
- Ineichen, P., 2011. Global irradiance on tilted and oriented planes: model validations. Technical report, 77 pages, access: <http://archive-ouverte.unige.ch/unige:23519/ATTACHMENT01>.
- Ineichen, P., 2013. Long term satellite hourly, daily and monthly global, beam and diffuse irradiance validation. Interannual Variability Analysis. IEA SHC Task 46 report, access: <http://archive-ouverte.unige.ch/unige:29606>.
- Inman, R., Pedro, H., Coimbra, C., 2013. Solar forecasting methods for Renewable energy integration. *Progress in Energy and Combustion Science*. <http://dx.doi.org/10.1016/j.pecs.2013.06.002>.
- Kleissl, J., 2010. Current State of the Art in Solar Forecasting. *California Renewable Energy Forecasting, Resource Data and Mapping*. University of California.
- Kühnert, J., Lorenz, E., Heinemann, D., 2013. Satellite - based irradiance and power forecasting for the German energy Market. In: Kleissl, J. (Ed.), *Solar Energy Forecasting and Resource Assessment*. Academic Press, Boston, ISBN 9780123971777, pp. 267–297. <http://dx.doi.org/10.1016/B978-0-12-397177-7.00008-5> (Chapter 11).
- Law, E.W., Prasad, A.A., Kay, M., Taylor, R.A., 2014. Direct normal irradiance forecasting and its application to concentrated solar thermal output forecasting – a review. *Solar Energy* 108, 287–307. <http://dx.doi.org/10.1016/j.solener.2014.07.008>.
- Lorenz, E., Hammer, A., Heinemann, D., 2004. Short term forecasting of solar radiation based on satellite data. In: Proc. ISES Europe Solar Congress EUROSUN2004, Freiburg, Germany.
- Lorenz, E., Kühnert, J., Wolff, B., Hammer, A., Heinemann, D., 2014. Local and regional PV power forecasting based on PV measurements, satellite data and numerical weather prediction. In: 4th PV Modelling Workshop. Köln, Germany.
- Lorenz, E., Kühnert, J., Heinemann, D., Nielsen, K.P., Remund, J., Müller, S.C., 2015. Comparison of Irradiance Forecasts Based on Numerical Weather Prediction. In: 31st EU PVSEC 2015, 14–18 September, Hamburg, Germany.
- Lucas, B.D., Kanade, T., 1981. An iterative image registration technique with an application to stereo vision. In: Proceedings of DARPA Image Understanding Workshop, pp. 121–130.
- Mazorra Aguiar, L., Pereira, B., David, M., Díaz, F., Lauret, P., 2015. Use of satellite data to improve solar radiation forecasting with Bayesian Artificial Neural Networks. *Solar Energy* 122, 1309–1324. <http://dx.doi.org/10.1016/j.solener.2015.10.041>.
- Menzel, P.W., 2001. Cloud tracking with satellite imagery: from the pioneering work of Ted Fujita to the present. *Bulletin of the American Meteorological Society* 82, 33–47.
- Miller, S.D., Combs, C.L., 2012. Toward evaluating short - term predictions of solar irradiance at the surface: persistence, satellite - based trajectory and numerical weather prediction models. In: ASES 2012.

- Müller, S.C., Remund, J., 2013. Shortest term solar energy forecast for the next 1 to 6 hours. In: PVSEC 2013.
- Pedro, H.T.C., Coimbra, C.F.M., 2015. Short-term irradiance forecastability for various solar micro-climates. *Solar Energy* 122, 587–602. <http://dx.doi.org/10.1016/j.solener.2015.09.031>.
- Perez, R., Seals, R., Michalsky, J., 1993. All-Weather model for sky luminance distribution - preliminary configuration and validation. *Solar Energy* 50 (3), 235–245.
- Perez, R., Ineichen, P., Moore, K., Kmiecik, M., Chain, C., George, R., Vignola, F., 2002. A new operational satellite-to-irradiance model. *Solar Energy* 73 (5), 307–317. [http://dx.doi.org/10.1016/S0038-092X\(02\)00122-6](http://dx.doi.org/10.1016/S0038-092X(02)00122-6).
- Perez, R., Kivalov, S., Schlemmer, J., Hemker, K., Renné, D., Hoff, T.E., 2010. Validation of short and medium term operational solar radiation forecasts in the US. *Solar Energy* 84 (12), 2161–2172. <http://dx.doi.org/10.1016/j.solener.2010.08.014>.
- Remund, J., Salvisberg, E., Kunz, S., 1998. On the generation of hourly shortwave radiation data on tilted surfaces. *Solar Energy* 62 (5), 331–344. ISSN: 0038-092X. [http://dx.doi.org/10.1016/S0038-092X\(98\)00020-6](http://dx.doi.org/10.1016/S0038-092X(98)00020-6).
- Richter, M., De Brabandere, K., Kalisch, J., Schmidt, T., Lorenz, E., 2015. Best Practice Guide on Uncertainty in PV Modelling. Performance Plus. WP2 Deliverable 2.4 of EU FP7 project. [www.perfplus.eu](http://www.perfplus.eu).
- Rigollier, C., Bauer, O., Wald, L., 2004. On the clear sky model of the 4th European Solar Radiation Atlas with respect to the Heliosat method. *Solar Energy* 68, 33–48. <http://dx.doi.org/10.1016/j.solener.2004.04.017>.
- Roebeling, R.A., Feijt, A.J., Stammes, P., 2006. Cloud property retrievals for climate monitoring: implications of differences between SEVIRI on METEOSAT-8 and AVHRR on NOAA-17. *Journal of Geophysical Research* 111, D20210. <http://dx.doi.org/10.1029/2005JD006990>.
- Ruiz-Arias, J.A., Alsamamra, H., Tovar-Pescador, J., Pozo-Vázquez, D., 2010a. Proposal of a regressive model for the hourly diffuse solar radiation under all sky conditions. *Energy Conversion and Management* 51 (5), 881–893. <http://dx.doi.org/10.1016/j.enconman.2009.11.024>.
- Ruiz-Arias, J.A., Tomáš Cebecauer, Tovar-Pescador, J., Šúri, M., 2010b. Spatial disaggregation of satellite-derived irradiance using a high-resolution digital elevation model. *Solar Energy* 84 (9), 1644–1657. <http://dx.doi.org/10.1016/j.solener.2010.06.002>.
- Ruiz-Arias, J.A., Quesada-Ruiz, S., Fernández, E.F., Gueymard, C.A., 2015. Optimal combination of gridded and ground-observed solar radiation data for regional solar resource assessment. *Solar Energy* 112, 411–424. <http://dx.doi.org/10.1016/j.solener.2014.12.011>.
- Sengupta, M., Habte, A., Kurtz, S., Dobos, A., Wilbert, S., Lorenz, E., Stoffel, T., Renné, D., Myers, D., Wilcox, S., Blanc, P., Perez, R., 2015a. Best practices handbook for the collection and use of solar resource data for solar energy applications. access: <http://www.nrel.gov/docs/fy15osti/63112.pdf>.
- Sengupta, M., Habte, A., Lopez, A., Xi, Y., Weekley, A., 2015b. Introducing NREL's Gridded National Solar Radiation Data Base (NSRDB). In: International Conference on Energy Meteorology, Boulder (CO), US access: [http://icem2015.org/wp-content/uploads/2015/07/1110\\_ManajitSengupta.pdf](http://icem2015.org/wp-content/uploads/2015/07/1110_ManajitSengupta.pdf).
- Skartveit, A., Olseth, J.A., Tuft, M.E., 1998. An hourly diffuse fraction model with correction for variability and surface albedo. *Solar Energy* 63, 173–183.

- Thorey, J., Mallet, V., Chaussin, C., Descamps, L., Blanc, P., 2015. Ensemble forecast of solar radiation using TIGGE weather forecasts and HelioClim database. *Solar Energy* 120, 232–243. <http://dx.doi.org/10.1016/j.solener.2015.06.049>.
- Vernay, C., Blanc, P., Pitaval, S., 2013. Characterizing measurements campaigns for an innovative calibration approach of the global horizontal irradiation estimated by HelioClim-3. *Renewable Energy* 57, 339–347. <http://dx.doi.org/10.1016/j.renene.2013.01.049>.
- Voyant, C., Haurant, P., Muselli, M., Paoli, C., Nivet, M.L., 2014. Time series modeling and large scale global solar radiation forecasting from geostationary satellites data. *Solar Energy* 102, 131–142. <http://dx.doi.org/10.1016/j.solener.2014.01.017>.

# Wave energy forecasting

7

Gordon Reikard

U.S. Cellular, Chicago, IL, United States

## 7.1 Introduction

Wave energy is an emerging field. Studies have found that waves can provide substantial energy in coastal regions ([Arinaga and Cheung, 2012](#); [Esteban and Leary, 2011](#); [Robertson et al., 2014](#)). Wave energy has been under development in several countries over the last decade. As of 2016, the most successful venture has been in Western Australia.

There is a long history of forecasting waves, dating back to the late 1940s. The literature falls into two general categories. Physics-based models operate on the principle that the sea surface can be characterized as an ensemble of waves at varying frequencies, separated by their direction of propagation. The model domain can range from individual regions to wider areas. Smaller domains can be nested within larger ones for higher resolution. The second branch of the literature, time series models, emerged in the 1990s. The methods here range from regressions to neural networks and more advanced techniques such as genetic programming and artificial intelligence.

The two approaches were developed for entirely different purposes, although both can be adapted for energy planning. Short-term forecasts, ranging from horizons as short as a few minutes to as long as several hours, are regularly used by utilities for reserve planning, peak load matching, switching sources, and electricity trading. Medium-term forecasts, on the order of a few days to a week, are used to plan energy storage and maintenance of generators.

This chapter summarizes the current methods used in wave forecasting, with a particular emphasis on wave energy. [Section 7.2](#) overviews the characteristics of the data. [Section 7.3](#) covers the physics models. [Section 7.4](#) describes time series models. [Section 7.5](#) compares the two methods. [Section 7.6](#) looks at wave energy converters. [Section 7.7](#) looks at simulating wave farms. [Section 7.8](#) concludes.

## 7.2 Characteristics of the data

In calculating the energy, the two most important parameters are the wave height and period. The significant wave height ( $H_s$ , in meters), is the average height of the highest one-third of the waves. The period ( $T$ , in seconds), is the time between the arrival of consecutive crests. Buoy records often include both the mean wave period ( $T_M$ ), and the peak period ( $T_p$ ), which is higher and more volatile. The standard measure of wave power is the wave energy flux,  $E_F$ , denominated in kilowatts per meter of crest length.

Let  $g$  denote the acceleration caused by gravity ( $9.8066 \text{ m/s/s}$ ),  $\rho$  denote the density of seawater ( $1025 \text{ kg/m}^3$ ), and the subscript  $t$  denote time variation. For regular sea states in deep water, the flux is defined using the identity:

$$E_{Ft} = [(g^2 \rho / 64\pi) H_{St}^2 T_t] \approx 0.491 (H_{St}^2 T_t) \quad (7.1)$$

**Figs. 7.1–7.6** show data for the wave height, period, and flux at two locations, for the year 2013. The resolution of the data is hourly. **Figs. 7.1–7.3** are for a buoy off the south coast of Iceland, northwest of Surtsey Island. The buoy is located at latitude  $63.31^\circ\text{N}$ , longitude  $20.31^\circ\text{W}$ . The depth is 130 m. Some 220 values were missing—a common problem with buoy data. These were interpolated using a physics model.

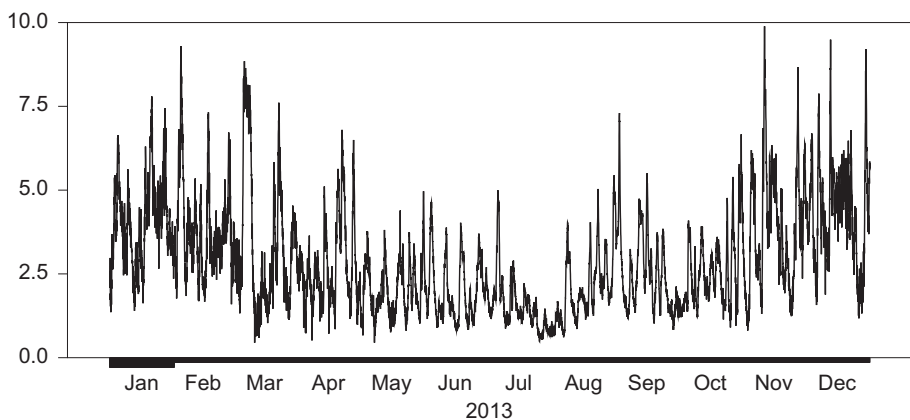


**Figure 7.1** The significant wave height, Surtsey, Iceland. Left scale: meters. Resolution: hourly. Dates: January 1 to December 31, 2013.

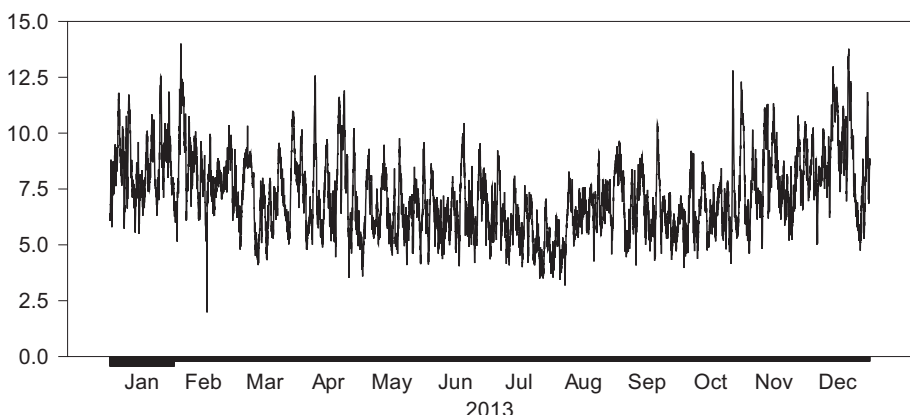


**Figure 7.2** The mean wave period, Surtsey, Iceland. Left scale: seconds. Resolution: hourly. Dates: January 1 to December 31, 2013.

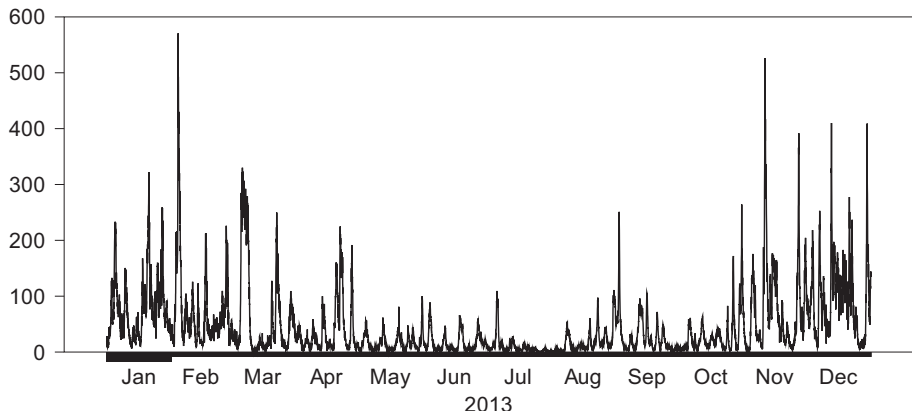


**Figure 7.3** The wave energy flux, Surtsey, Iceland. Left scale: kilowatts per meter of crest length. Resolution: hourly. Dates: January 1 to December 31, 2013.

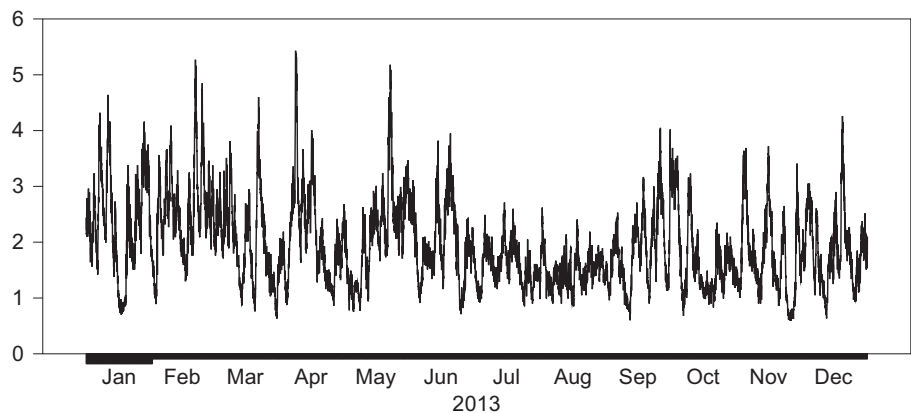


**Figure 7.4** The significant wave height, Santa Rosa Island, California. Left scale: meters. Resolution: hourly. Dates: January 1 to December 31, 2013.

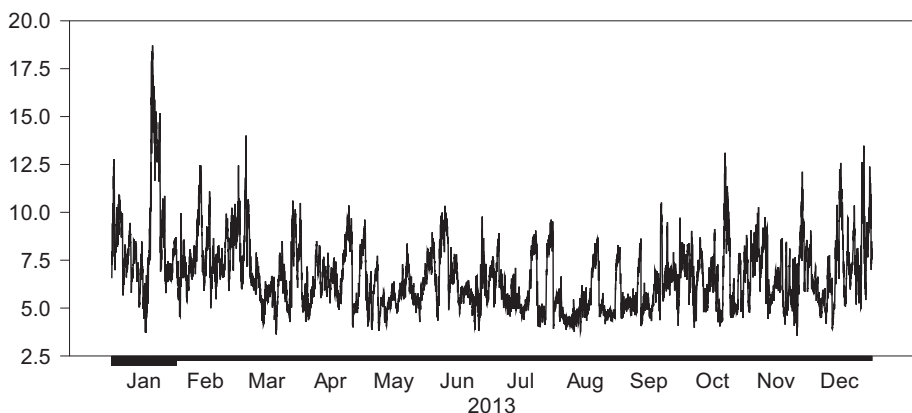


**Figure 7.5** The mean wave period, Santa Rosa Island, California. Left scale: seconds. Resolution: hourly. Dates: January 1 to December 31, 2013.

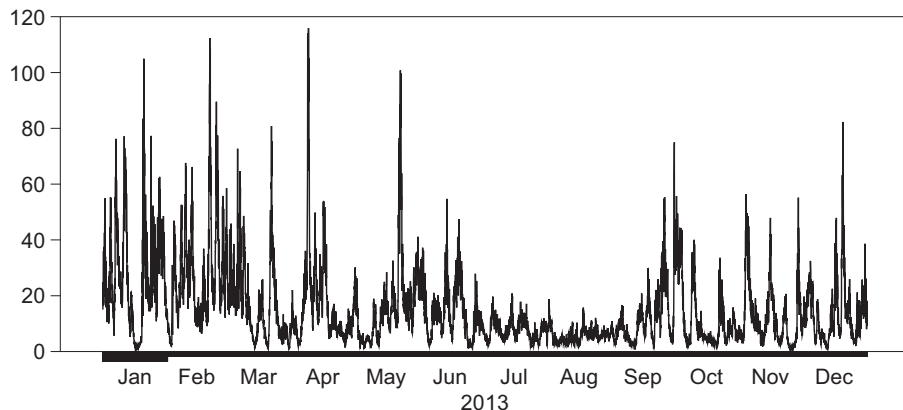


**Figure 7.6** The wave energy flux, Santa Rosa Island, California. Left scale: kilowatts per meter of crest length. Resolution: hourly. Dates: January 1 to December 31, 2013.

Figs. 7.4–7.6 are for Santa Rosa Island, located off the coast of California (latitude 33.67°N, longitude 120.21°W), at a depth of 1020 m. This data set is complete; no interpolation was needed.

The wave height shows two main features. There is strong seasonality, with much higher values occurring from October through mid-April. The months from late April through early October are more quiescent. The second feature is nonlinear variability: irregular transitions between high and low values, with large outliers, typically during winter storms. The wave period also shows some evidence of seasonality, with higher values in the autumn and winter. The flux, by construction, is more volatile than either of its components, and is notable for its intermittency, with abrupt transitions between high and low states, and occasional extreme outliers.

In addition to seasonality, some studies have found evidence of other longer-term patterns in wave data. Stopa et al. (2011) conducted an analysis for sites in Hawaii over periods of three decades. They report not only strong seasonal cycles but also evidence for the Arctic and Antarctic oscillations, the El Niño southern oscillation, and the Madden-Julian oscillation in both the wind and wave fields.

### 7.3 The physics models

The physics models originate in the late 1940s. Early works by Phillips (1957, 1958) and Miles (1957) identified the relationship between wind and waves, incorporating both turbulent wind flows and wave dissipation. The models were developed more fully in the 1960s with the contributions of Pierson and Moskowitz (1964). By the 1970s, hemispheric wave models had become operational. The second generation models, which were developed in the 1980s, incorporated nonlinear wave–wave interactions (Hasselmann et al., 1976, 1980, 1985). The third generation models,

developed over the decade 1984–94, incorporate all the relevant physics—forcing by wind, wave transfer, dissipation, shoaling, bottom friction, currents, and bathymetry. For summaries of the major elements, see Janssen (1991, 2004, 2007), Komen et al. (1994).

The action balance equation forms the core of the models. Let  $N$  denote the wave action density, let  $t$  denote time, let  $x, y$  denote the Cartesian coordinates, let  $\sigma$  denote the intrinsic frequency, and let  $\theta$  denote the wave propagation direction. Let  $C_g$  denote the wave action propagation speed in  $(x, y, \sigma, \theta)$  space. Let  $S$  denote the combined source and sink terms. In deep water, the three major components of  $S$  are the input by wind ( $S_{IN}$ ), nonlinear wave–wave interactions ( $S_{NL}$ ), and wave dissipation through white capping ( $S_{WC}$ ). In shallow water,  $S$  includes the effects of bottom friction ( $S_{BF}$ ) and shoaling-induced breaking ( $S_{BR}$ ). At larger scales, in deep water, swells can dissipate without actually breaking. Although the specification differs in particular models, the action balance equation is generally of the form:

$$\frac{\partial N}{\partial t} + \frac{\partial C_{g,x}N}{\partial x} + \frac{\partial C_{g,y}N}{\partial y} + \frac{\partial C_{g,\sigma}N}{\partial \sigma} + \frac{\partial C_{g,\theta}N}{\partial \theta} = S; \\ S = [(S_{IN}) + (S_{NL}) + (S_{WC}) + (S_{BF}) + (S_{BR})] \quad (7.2)$$

The model output—technically the predicted wave spectra with amplitudes associated with frequencies and propagation—can be decomposed into the wave height and period, along with the propagation direction and other terms.

More recent innovations include two-way coupling between the ocean surface and the atmosphere (Janssen, 1989). Another new development in the physics literature is the modeling of extreme waves. The energy balance equation characterizes the mean state, but not the probability distribution. The probability distribution of the wave height shows heavier tails than in the Gaussian normal, with evidence of excess kurtosis. High kurtosis has been found to correlate with the probability of freak waves (Mori and Janssen, 2006).

There are several large-scale wave models in operation, which produce regular forecasts. The WAVEWATCH III (WW3) model is run by the National Oceanic and Atmospheric Administration ([www.noaa.gov](http://www.noaa.gov)). The design for the model originates with Tolman (1991). Additional documentation and new developments are reviewed in Tolman and Chalikov (1996), and Tolman (2006, 2008). As of 2016, the resolution of the model is 50-km grids, and it incorporates regional domains into the northern hemisphere at resolutions of 18 and 7 km. The physics has been updated to include nonlinear resonant interactions, wave field refraction, and ice volume. Wind inputs are provided by the Global Forecast System (GFS) weather model (<http://weather.rap.ucar.edu/model/?model=gfs>), run by the National Center for Atmospheric Research. The model forecasts are run over horizons of up to 126 h, in 3-h steps, along with 6 h hindcasts, four times a day. The regional North Atlantic Hurricane model produces 72 h forecasts. The output is available at the following Website: <http://polar.ncep.noaa.gov/waves/index2.shtml>. The forecasted values include the wave height and the mean and peak wave periods.

A second large-scale model is maintained by the European Center for Medium-range Weather Forecasts (ECMWF, [www.ecmwf.int](http://www.ecmwf.int)). The model currently comprises 36 frequency bins and propagation directions. The average resolution of the grids is 28 km. The forecasts are generated using a coupled atmosphere-ocean model, which includes simulations of the general circulation of the ocean and the associated atmospheric-ocean processes. Wind inputs are based on the Integrated Forecasting System, a comprehensive Earth-system model developed at ECMWF. Detailed documentation on the model is available at the following Website: [http://www.ecmwf.int/sites/default/files/IFS\\_CY40R1\\_Part7.pdf](http://www.ecmwf.int/sites/default/files/IFS_CY40R1_Part7.pdf). Forecasts are produced over horizons of 48 h, again in 3-h steps. The forecasted values include the wave height, and the mean and zero-crossing wave periods.

SWAN (Simulating Waves Near shore) is a smaller, high resolution model developed at Delft University of Technology, designed to simulate the propagation of waves in shallow near-shore areas ([Booij et al., 1999](#); [Holthuijsen, 2007](#)). There are some differences between SWAN and the larger models. For instance, while WW3 uses an explicit propagation scheme in the action balance equation, SWAN uses an implicit numerical scheme. Documentation on SWAN is available at the main Website: <http://www.swan.tudelft.nl>. The manual is also available at: <http://falk.ucsd.edu/modeling/swanuse.pdf>.

SWAN has the advantage that it can be mounted on smaller computers and used for regional forecasting and analysis. In many studies, SWAN has been coupled with WW3 or other larger models, in effect combining the relative strengths of both.

The physics models have been subjected to extensive empirical testing, although in many cases this has involved model hindcasts, i.e., retrospective simulations, so that the forecasts are for the current period rather than for future values. Tests of SWAN in [Rogers et al. \(2007\)](#) find root mean squared errors (RMSEs) in the range of 0.22–0.31 m for a set of buoys off California. In [Chawla et al. \(2012\)](#), hindcasts for the wave height using WW3 at 23 sites find close agreement between the buoy data and the simulations, although the performance of the model is better in deeper water. In shallow water, unresolved bathymetry and other coastal features were found to reduce model accuracy. The RMSEs ranged from 0.21 to 0.55 m in the Atlantic and the Gulf of Mexico, but were generally higher in the Pacific, 0.33 to 0.57.

Tests of forecasts and hindcasts using WW3 and SWAN in [Garcia-Medina et al. \(2013\)](#) find a high correlation between the model simulation and buoy data in the Pacific Northwest. The normalized RMSE for the wave height ranges from 0.22 to 0.31 m, which translate into proportional errors of 13%–23%, although higher errors are found for some periods. This study also finds a slow deterioration in forecast accuracy over horizons ranging as long as 72 h. At some locations, the errors initially rise, but then simply fluctuate, with little discernible trend.

Since the late 1990s, the ECMWF model forecasts have been validated against buoy data on a regular basis ([Janssen et al., 1997](#)). The RMSE is found to be fairly high, even at short horizons, but the error increases only very gradually as the horizon extends out to several days. In this respect, one of the key strengths of the physics models is that they can predict over long horizons. A possible enhancement is to make the forecasts more probabilistic, using ensembles and Monte Carlo experiments ([Saetra and Bidlot, 2004](#); [Roulston et al., 2005](#)).

To illustrate the properties of the physics models, Figs. 7.7–7.10 show simulations for the wave height and period for the Iceland and Santa Rosa Island locations, using the ECMWF model. Comparing these with the actual values (Figs. 7.1, 7.2, 7.4 and 7.5), the model simulations are quite close to the observations. At Iceland, the correlation between the model simulation and the actual value is 0.98 for the wave height and 0.92 for the period. At Santa Rosa, the correlations are 0.99 for the wave height and 0.93 for the period.

While physics model hindcasts are generally closely correlated with buoy data, they are also significantly smoother. This can be viewed as a limitation of the models, but it may also constitute a strength in particular situations. Wave farms are by definition spread out over much wider areas. The physics models appear to be very effective

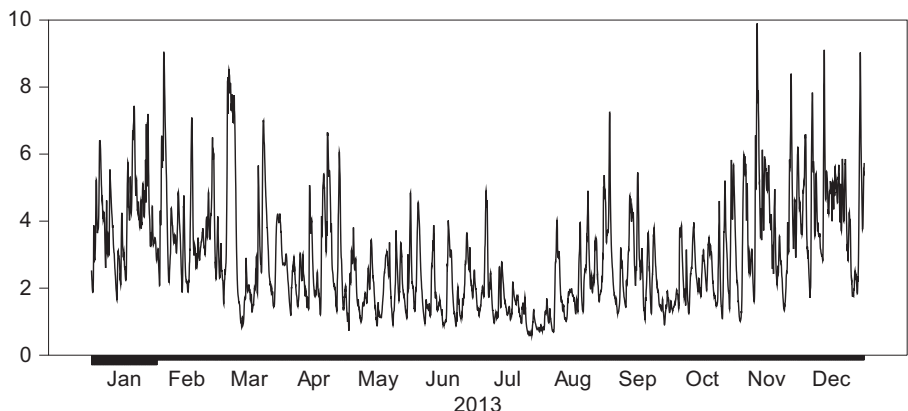


**Figure 7.7** The ECMWF model simulation for the wave height, Surtsey, Iceland. Left scale: meters. Resolution: hourly. Dates: January 1 to December 31, 2013.

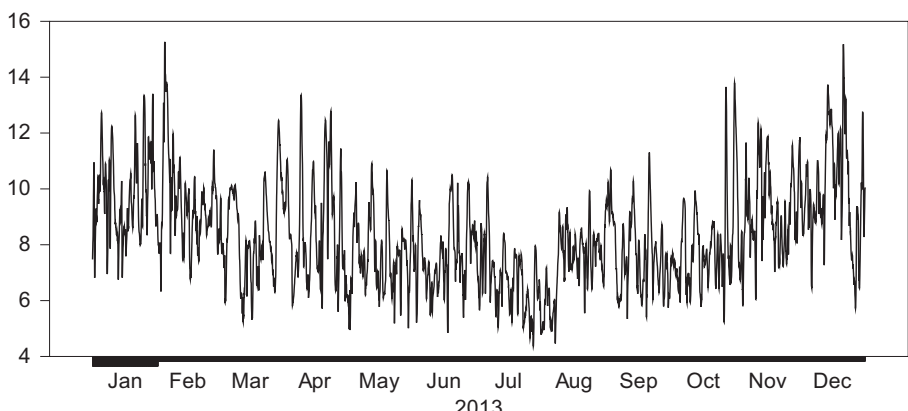


**Figure 7.8** The ECMWF model simulation for the wave period, Surtsey, Iceland. Left scale: seconds. Resolution: hourly. Dates: January 1 to December 31, 2013.

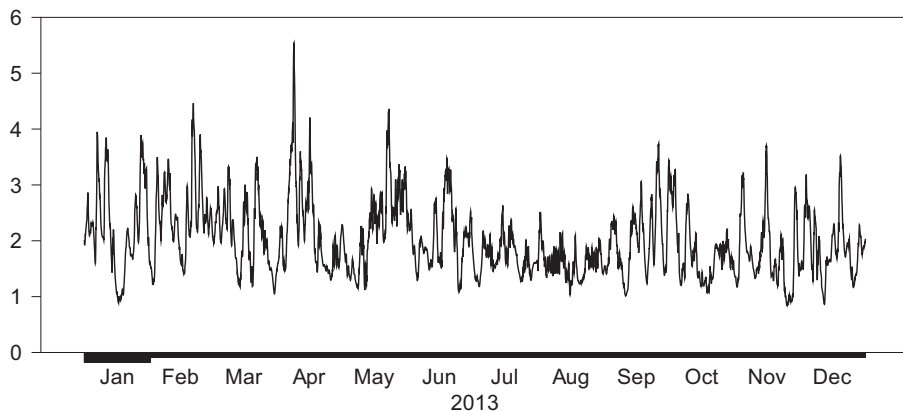


**Figure 7.9** The ECMWF model simulation for the wave height, Santa Rosa Island, California. Left scale: meters. Resolution: hourly. Dates: January 1 to December 31, 2013.

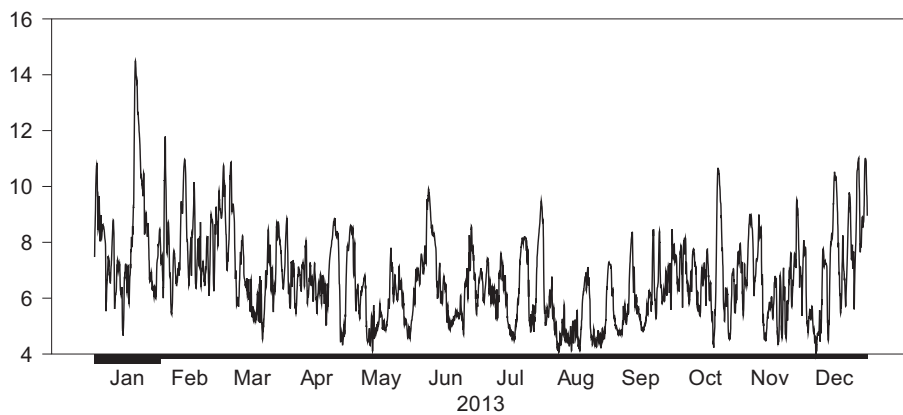


**Figure 7.10** The ECMWF model simulation for the wave period, Santa Rosa Island, California. Left scale: seconds. Resolution: hourly. Dates: January 1 to December 31, 2013.

at capturing the wave parameters over larger regions, even if they fail to reproduce all the variability observed at individual buoys.

## 7.4 Statistical and time series models

Statistical models have become popular in part because of advances in forecasting technology. As new techniques such as neural networks became available in inexpensive software packages, it was straightforward to apply these to buoy data sets. Early studies like [Deo and Naidu \(1998\)](#) compared the forecasting properties of neural

networks and statistical models for the wave height, over horizons of 3–24 h. These results were extended to multiple sites and deeper locations in Deo et al. (2001), and to breaking waves in Deo and Jagdale (2003). Makarynskyy (2004) extended this work to cover both the wave height and the wave period, again using neural nets. Londhe and Panchang (2006) used neural nets and data from several buoys to forecast over a range of horizons up to 24 h. They found a high degree of correlation between actual wave measurements and forecasts over the first 6 h, although the correlation falls off as the horizon extends. An interesting aspect of this study is that the nets were trained over a moving window of recent data. Limiting the training period to observations within a single week was found to produce more accurate forecasts. Zamani et al. (2008) compared neural networks with other type of artificial intelligence models, and find that the nets actually yield more accurate predictions. Tseng et al. (2007) applied neural nets to typhoon surge forecasting.

Malmberg et al. (2005) used regressions estimated by Kalman Filter (Kalman, 1960), although this analysis is limited to near-surface ocean wind speeds rather than waves. The key innovation in this study is that the regression coefficients are time-varying. This is an important point, and in this respect later studies have often specifically allowed both regression coefficients and the input and bias weights in neural nets to vary over time. The Kalman filter is not the only way to do this. Another technique that has shown considerable promise is estimating over a moving window. This is discussed in other contexts in Rossi and Inoue (2012).

While neural networks and regressions have been the most popular methods, other techniques have also been used. Several studies have used genetic programming: Gaur and Deo (2008); Surabhi and Deo (2008); Nitsure et al. (2012); Rao et al. (2013). Ghorbani et al. (2010) compare genetic programming and neural networks, finding that both perform well over intervals ranging from a few hours to a few days. Mahjoobi and Mosabbeb (2009) use support vector machines. Ozger (2010) combines wavelets with fuzzy logic. Ibarra-Berastegi et al. (2015) use random forests. Probabilistic forecasting is introduced in Pinson et al. (2012).

## 7.5 Physics versus statistics

When studies have compared different types of time series models against each other, the degree of accuracy has often been found to be very similar. In this sense, in wave energy the contest is not so much between different types of time series models as between statistical and physics-based methods. Physics and time series models have particular strengths and weaknesses. The time series models can only be used where in situ data sets are available. A reasonable critique is that they do not incorporate any understanding of the underlying causal mechanisms. However, they have been found to predict very accurately over the short horizons needed for reserve planning. By comparison, large-scale physics models can forecast over much wider areas and are more effective over long horizons. A widely noted issue in wave analysis is that buoy data sets are often incomplete, with large numbers of missing values. In this respect,

one of the strengths of the physics models is that hindcasts provide an effective means of interpolation.

In Reikard et al. (2011), forecasts of the ECMWF model were compared with forecasts from time series models at 13 sites, over horizons of 1–12 h. The main finding was that the time series model predicted more accurately over short horizons (1–4 h), while the physics model was more accurate over long horizons (6 h and above). The convergence point, i.e., the horizon at which the two methods yielded comparable degrees of accuracy, was 5–6 h. The most likely explanation is that the time series models capture proximate dependence in the data, while the physics models capture underlying signals at lower frequencies.

It is of course possible to combine physics and statistical methods. Several methods are investigated in the following works: Woodcock and Engel (2005), Woodcock and Greenslade (2006) and Durrant et al. (2008). These studies use physics model forecasts and then apply a sequence of statistical corrections to improve accuracy. One of these, the operational consensus forecast, combines the predictions from an ensemble of several models. The finding was an improvement in forecast accuracy of 20%–30% in deep water, and as much as 60%–70% in shallow water. A related idea is the model output statistics method, introduced in meteorology in the early 1970s (Glahn and Lowry, 1972), which involves using statistical methods to correct the bias. When these methods are combined, the finding was an improvement of roughly one-third in forecast accuracy at a 24 h horizon. Further analysis in other studies found that using a model output statistics approach yielded more accurate forecasts over the first 48 h than either physics or time series models alone.

## 7.6 Wave energy converters

One issue in wave energy is that there is no single dominant technology. Instead, a variety of wave energy converter (WEC) designs have been proposed. A concise summary of the literature is available in Falcao (2010) and has recently been updated in Uihlein and Magagna (2016). Some of these technologies are well established; others remain hypothetical or under development. Several technologies have evolved to the point where it is possible to calculate conversion matrices.

Surface attenuators are already in use. One example is the Pelamis P2 device (Retzler, 2006; Henderson, 2006; Yemm et al., 2012). This converter consists of semi-submerged cylindrical sections, moored so as to lie perpendicular to the wave front. Table 7.1 shows the Pelamis power matrix. The power rises as a function of the wave height. The machine attains its maximum power of 750 kW for wave height values of 5.5 m and wave period values of 6.5–12 s. Above this threshold, the power levels off, and declines for longer values of the period.

Conversion matrices for several other WECs were calculated in Babarit et al. (2012). Point absorber designs include the floating two body heaving converter, which consists of a torus sliding along a vertical spar, and heave buoy arrays, which consist of several buoys connected to a reference structure. The heave buoy array design can

**Table 7.1 Conversion matrix for the Pelamis P2 device**

Significant wave height (meters)	Wave period (seconds)																	
	5.0	5.5	6.0	6.5	7.0	7.5	8.0	8.5	9.0	9.5	10.0	10.5	11.0	11.5	12.0	12.5	13.0	
1.0		22	29	34	37	38	38	37	35	32	29	26	23	21				
1.5	32	50	65	76	83	86	86	83	78	72	65	59	53	47	42	37	33	
2.0	57	88	115	136	148	153	152	147	138	127	116	104	93	83	74	66	59	
2.5	89	138	180	212	231	238	238	230	216	199	181	163	146	130	115	103	92	
3.0	129	198	260	305	332	340	332	315	292	266	240	219	210	188	167	149	132	
3.5		270	354	415	438	440	424	404	377	362	326	292	260	230	215	203	180	
4.0			462	502	540	546	530	499	475	429	384	366	339	301	267	237	213	
4.5				544	635	642	648	628	590	562	528	473	432	382	356	338	300	266
5.0					739	726	731	707	687	670	607	557	521	472	417	369	348	328
5.5						750	750	750	750	737	667	658	586	530	496	446	395	355
6.0							750	750	750	750	750	711	633	619	558	512	470	415
6.5								750	750	750	750	750	743	658	621	579	512	481
7.0									750	750	750	750	750	750	676	613	584	525
7.5										750	750	750	750	750	750	686	622	593
8.0											750	750	750	750	750	750	690	625

Power is in kilowatts.

operate in deep or shallow water. Shallow water versions are already in use; a case in point is the Wavestar device in Denmark ([www.wavestar.com](http://www.wavestar.com)). In shallow water, the bottom-fixed heave buoy array consists of a jack-up structure, mounted on the seabed, with many floating buoys attached to fixed rocker arms. A third type of WEC is an oscillating device, which typically has one end moored to the seabed, while the other end is free to move. Electricity is generated by the relative motion of the oscillating component.

In a more general sense, it should be possible to compute power matrices for a wide range of WECs using well-established engineering principles. A floating body has six degrees of freedom: heave (up and down motion), surge (motion in the same line as wave propagation), sway (side to side motion), roll, pitch, and yaw. The power is captured primarily by the heave direction. The equations of motion include the excitation, radiation, hydrostatic stiffness and power take off forces, and damping mechanisms.

The most recent innovations in this field have been SNL-SWAN, and WEC-SIM, simulation tools developed at Sandia National Laboratory ([www.sandia.gov](http://www.sandia.gov)) and National Renewable Energy Laboratory (Ruehl et al., 2013, 2014; Porter et al., 2014; Ruehl et al., 2014). WEC-SIM allows modeling of a range of converters, based on mass, moment of inertia, and the equations of motion. Empirical tests have found close agreement between the simulated power and experiments with scale models. SNL-SWAN simulates the power output from wave farms consisting of multiple converters in the same area. At the present time, this research is ongoing.

The conversion matrices differ in the amount of power than can be produced, but for the most part show several common features. First, the relationship between the power and the wave parameters is nonlinear. The power generally rises as a function of the wave height, but then levels off above a given threshold. The power also initially rises as a function of the wave period, but then peaks, and falls off as the period increases. The same point is made in Falcao (2010), who notes that the power initially rises, then declines as a function of the wavelength.

Second, the resulting power output from converters is smoother and more predictable than the flux. Figs. 7.10–7.16 show the power output calculated for the Iceland and Santa Rosa Island sites, using three types of converters, the attenuator, a heave buoy array designed to operate in deep water, and a three-body oscillating flap device. The matrices for the latter two were from Babarit et al. (2012). The original values were at a resolution of 0.5 m, but were interpolated to 0.1 m using a linear method. The data in these calculations are a composite of the actual buoy data and ECMWF model simulations over a 12-month period. The power output assumes 150 converters.

Because of the high energy conditions off the Icelandic coast, the Pelamis frequently operates close to its peak rating during the winter months. The extreme outliers characteristic of the flux are not in evidence. Despite the smoothing effect of many converters over a wide area, however, the power output still exhibits nonlinear variability. All three converters show evidence of large ramp events, i.e., transitions between states of low and high energy. There are also lesser outliers and considerable volatility even at intermediate power levels.

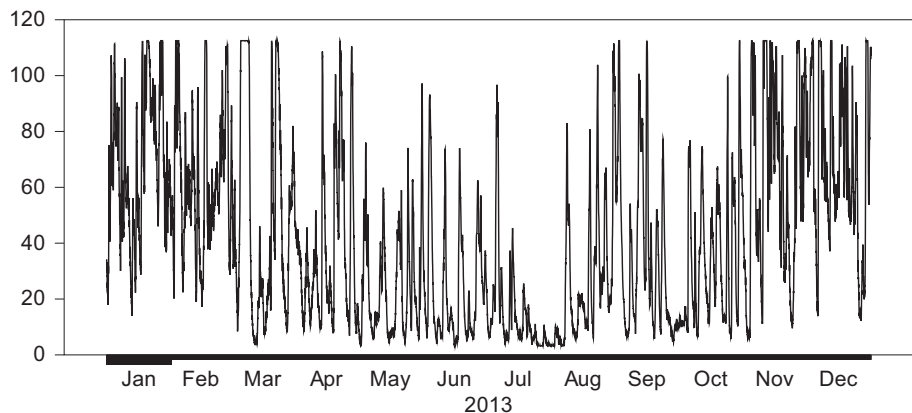


**Figure 7.11** The power output from the Pelamis, Surtsey, Iceland. Left scale: MW, 150 converters. Resolution: hourly. Dates: January 1 to December 31, 2013.

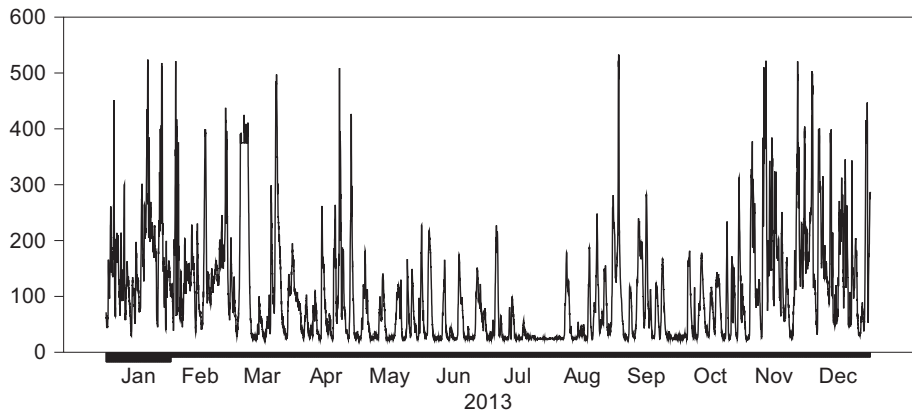


**Figure 7.12** The power output from the heave buoy array, Surtsey, Iceland. Left scale: MW, 150 converters. Resolution: hourly. Dates: January 1 to December 31, 2013.

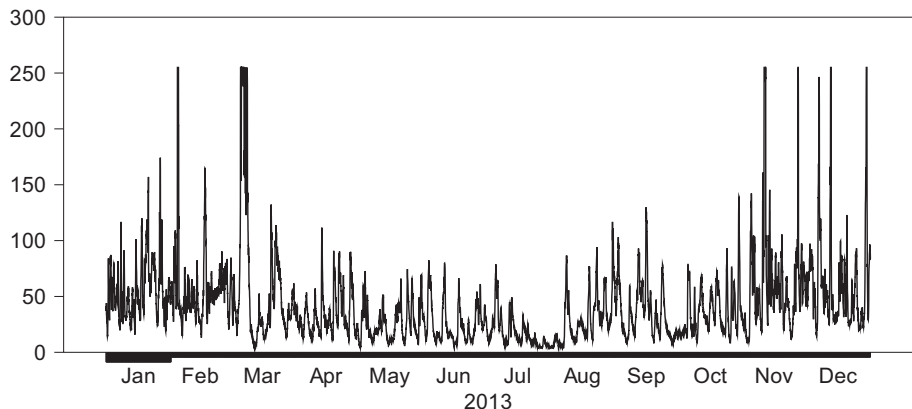


**Figure 7.13** The power output from the three-body oscillating flap device, Surtsey, Iceland. Left scale: MW, 150 converters. Resolution: hourly. Dates: January 1 to December 31, 2013.

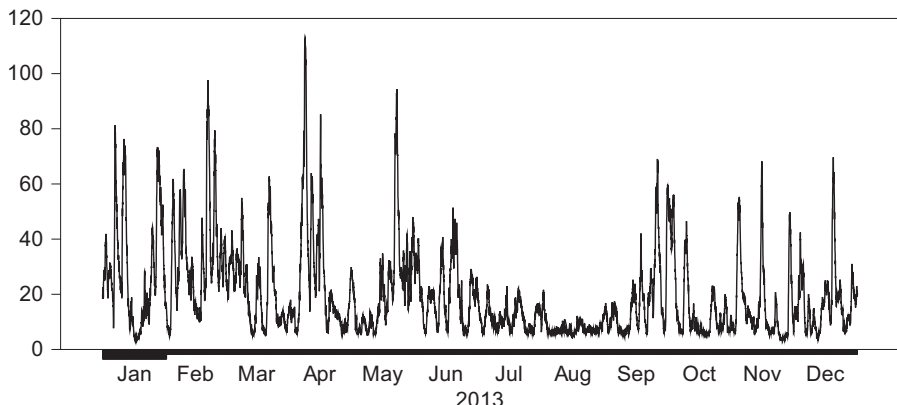


**Figure 7.14** The power output from the Pelamis, Santa Rosa Island, California. Left scale: MW, 150 converters. Resolution: hourly. Dates: January 1 to December 31, 2013.

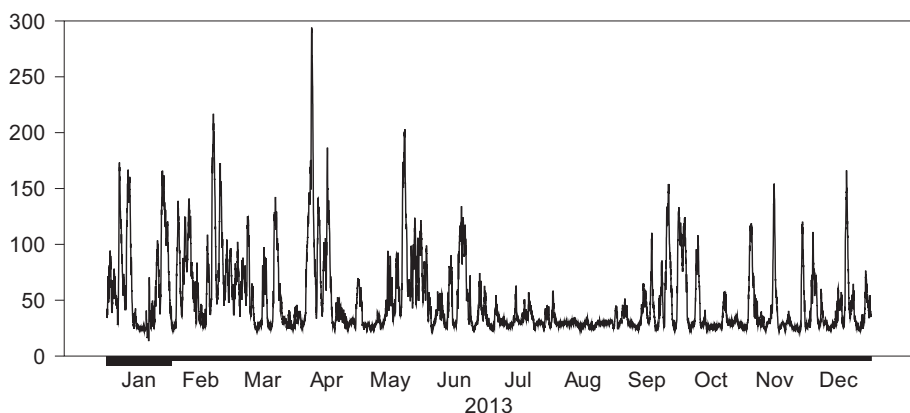


**Figure 7.15** The power output from the heave buoy array, Santa Rosa Island, California. Left scale: MW, 150 converters. Resolution: hourly. Dates: January 1 to December 31, 2013.

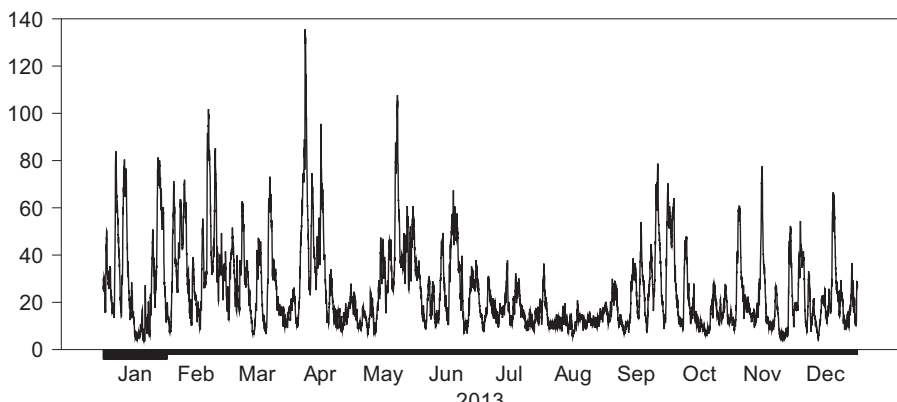


**Figure 7.16** The power output from the three-body oscillating flap device, Santa Rosa Island, California. Left scale: MW, 150 converters. Resolution: hourly. Dates: January 1 to December 31, 2013.

## 7.7 Simulating wave farms

Wave farms should in principle be more predictable than time series from individual buoys. [Brekken et al. \(2012\)](#) propose using the wave spectrum to simulate height and period over the broader areas spanned by wave farms. The conclusion is that the variability of waves in a farm is much lower than for an individual WEC. The same methodology was used in [Parkinson et al. \(2015\)](#) to simulate wave farms in the Pacific Northwest. The original 1-h data available from the buoys were converted to time series at resolutions of 1–15 min, and averaged out to 24 h. The reduced variability is found to yield major improvements in forecast accuracy, achieving a substantial reduction in reserve costs.

[Reikard et al. \(2015a,b\)](#) used a somewhat different methodology to simulate wave farms in two locations. Wave farms in the Vancouver area were simulated using weighted averages of colocated buoys; missing data were interpolated using SWAN hindcasts. The forecast errors for the power output at the 1 h horizon were found to be in the range of 8%–9% in deeper water and 10%–12% nearer to the coast. In the Pacific Northwest, wave farms were created using buoy time series and hindcasts of the ECMWF model. Because the model simulations are smoother than the buoy data, noise series were superimposed, to more realistically recreate wave conditions. The power output was then simulated using three WECs. One finding was that the forecast error at the simulated wave farms was only in the range of 5%–7%, much lower than the flux at the same buoy sites. Further, at the 1 h horizon, the forecast error for large-scale wave farms is 39%–40% lower than at individual buoys.

## 7.8 Conclusions

As the field continues to advance, several major findings have emerged. First in the ongoing debate between physics and time series models, the choice of methods depends primarily on the horizon. In the United States and Canada, balancing reserves are usually calculated at a 1 h horizon. The horizons used in Europe are generally somewhat longer. Forecasts 4–5 h in advance are used for real-time operation, i.e., the time required to switch on alternate sources. Forecasts 24–36 h ahead are used to determine the available running reserve for the day-ahead market. Time series models, have proven to be more accurate at the short horizons needed for reserve planning and energy trading. Physics models have been found to be more accurate at horizons beyond the first few hours. Further, the accuracy of their forecasts decays only very slowly over long horizons. Combining the two methods may be useful under particular circumstances. This can be done using the model output statistics approach, or by including physics model forecasts in regressions or neural nets. In general, though, the recommendation is to use time series models for short-term forecasts and physics models for long-term planning.

Second, there are some key differences between the wave flux and the power output from converters. The flux is a multiplicative function of the period and wave height squared. The power output is a nonlinear function of the wave height and period. It is generally smoother, with fewer extreme values.

Another reason why wave farms should be more predictable than buoy data is that they are spread out over wider areas. Simulations of wave farms suggest that the improvement in forecast accuracy could be considerable. Although there are few comparisons of waves with other forms of renewable energy, there is a vast literature on wind and solar power, which has generally reported much larger forecast errors than found for wave farms. This indicates that waves may be significantly less expensive than other forms of renewable energy, at least in terms of reserves.

There are of course several unresolved issues. To date, only a small number of wave farm simulations have been run, so that the conclusions pertain primarily to particular areas. More simulations, over wider areas, are needed. Perhaps the main limitation of the existing work however is that data from actual wave farms has not been made available for research. The findings from simulation studies will no doubt be refined as wave farms come on line and data become available.

## References

- Arinaga, R.A., Cheung, K.F., 2012. Atlas of global wave energy from 10 years of reanalysis and hindcast data. *Renewable Energy* 39, 49–64.
- Babarit, A., Hals, J., Muliawan, M.J., Kurniawan, A., Moan, T., Krokstad, J., 2012. Numerical benchmarking study of a selection of wave energy converters. *Renewable Energy* 41, 44–63.
- Booij, N., Ris, R.C., Holthuijsen, L.H., 1999. A third-generation wave model for coastal regions: model description and validation. *Journal of Geophysical Research* 104, 7649–7666.
- Brekken, T.K.A., Ozkan-Haller, H.T., Simmons, A., 2012. A methodology for large-scale ocean wave power time-series generation. *IEEE Journal of Oceanic Engineering* 37, 294–300.
- Chawla, A., Spindler, D.M., Tolman, H.L., 2012. Validation of a thirty year wave hindcast using the Climate Forecast System Reanalysis winds. *Ocean Modeling* 70, 189–206.
- Deo, M.C., Jagdale, S.S., 2003. Prediction of breaking waves with neural networks. *Ocean Engineering* 30, 1163–1178.
- Deo, M.C., Naidu, C.S., 1998. Real time wave forecasting using neural networks. *Ocean Engineering* 26, 191–203.
- Deo, M.C., Jha, A., Chaphekar, A.S., Ravikant, K., 2001. Neural networks for wave forecasting. *Ocean Engineering* 28, 889–898.
- Durrant, T.H., Woodcock, F., Greenslade, D.J.M., 2008. Consensus forecasts of modeled wave parameters. *Weather and Forecasting* 24, 492–503.
- Esteban, M., Leary, D., 2011. Current developments and future prospects of off shore wind and ocean energy. *Applied Energy* 90, 128–136.
- Falcao, A., 2010. Wave energy utilization: a review of the technologies. *Renewable and Sustainable Energy Reviews* 14, 899–918.
- Garcia-Medina, G., Ozkan-Haller, H.T., Ruggiero, P., Oskamp, J., 2013. An inner-shelf wave forecasting system for the U.S. Pacific Northwest. *Weather and Forecasting* 28, 681–703.

- Gaur, S., Deo, M.C., 2008. Real-time wave forecasting using genetic programming. *Ocean Engineering* 35, 1166–1172.
- Glahn, H.R., Lowry, D.A., 1972. The use of model output statistics (MOS) in objective weather forecasting. *Journal of Applied Meteorology* 11, 1203–1211.
- Ghorbani, M.A., Khatibi, R., Aytek, A., Makarynskyy, O., Shiri, J., 2010. Sea water level forecasting using genetic programming and comparing the performance with artificial neural networks. *Computers and Geosciences* 36, 620–627.
- Hasselmann, K., Ross, D.B., Müller, P., Sell, W., 1976. A parametric wave prediction model. *Journal of Physical Oceanography* 6, 200–228.
- Hasselmann, D.E., Duncel, M., Ewing, J.A., 1980. Directional wave spectra observed during JONSWAP 1973. *Journal of Physical Oceanography* 10, 1264–1280.
- Hasselmann, S., Hasselmann, K., Allender, J.H., Barnett, T.P., 1985. Computations and parameterizations of the non-linear energy transfer in a gravity wave spectrum. Part II: parameterizations of the non-linear energy transfer for application in wave models. *Journal of Physical Oceanography* 15, 1378–1391.
- Henderson, R., 2006. Design, simulation, and testing of a novel hydraulic power take-off system for the Pelamis wave energy converter. *Renewable Energy* 31, 271–283.
- Holthuijsen, L.H., 2007. Waves in Oceanic and Coastal Waters. Cambridge University press.
- Ibarra-Berastegi, G., Saenz, J., Esnaola, G., Ezcurra, A., Ulazia, A., 2015. Short-term forecasting of the wave energy flux: analogues, random forests and physics-based models. *Ocean Engineering* 104, 530–539.
- Janssen, P.A.E.M., 1989. Wave-induced stress and the drag of air over sea waves. *Journal of Physical Oceanography* 19, 745–754.
- Janssen, P.A.E.M., 1991. Quasi-linear theory of wind-wave generation applied to wave forecasting. *Journal of Physical Oceanography* 21, 1631–1642.
- Janssen, P.A.E.M., 2004. The Interaction of Ocean Waves and Wind. Cambridge University Press, Cambridge.
- Janssen, P.A.E.M., 2007. Progress in ocean wave forecasting. *Journal of Computational Physics* 227, 3572–3594.
- Janssen, P.A.E.M., Hansen, B., Bidlot, J.-R., 1997. Verification of the ECMWF wave forecasting system against buoy and altimeter data. *Weather and Forecasting* 12, 763–784.
- Kalman, R.E., 1960. A new approach to linear filtering and prediction problems. *Transactions of the American Society of Mechanical Engineers – Journal of Basic Engineering* 83D, 35–45.
- Komen, G.J., Cavalieri, L., Donelan, M., Hasselmann, K., Hasselmann, S., Janssen, P.A.E.M., 1994. Dynamics and Modelling of Ocean Waves. Cambridge University Press.
- Londhe, S.N., Panchang, V., 2006. One-day wave forecasts based on artificial neural networks. *Journal of Atmospheric and Oceanic Technology* 23, 1593–1603.
- Mahjoobi, J., Mosabeb, E.A., 2009. Prediction of significant wave height using regressive support vector machines. *Ocean Engineering* 36, 339–347.
- Makarynskyy, O., 2004. Improving wave predictions with artificial neural networks. *Ocean Engineering* 31, 709–724.
- Malmberg, A., Holst, U., Holst, J., 2005. Forecasting near-surface ocean winds with Kalman filter techniques. *Ocean Engineering* 32, 273–291.
- Miles, J.W., 1957. On the generation of surface waves by shear flows. *Journal of Fluid Mechanics* 3, 185–204.
- Mori, N., Janssen, P.A.E.M., 2006. On kurtosis and occurrence probability of freak waves. *Journal of Physical Oceanography* 36, 1471–1483.

- Nitsure, S.P., Londhe, S.N., Khare, K.C., 2012. Wave forecasts using wind information and genetic programming. *Ocean Engineering* 54, 61–69.
- Ozger, M., 2010. Significant wave height forecasting using wavelet fuzzy logic approach. *Ocean Engineering* 37, 1443–1451.
- Parkinson, S., Dragoon, K., Reikard, G., Garcia-Medina, G., Ozkan-Haller, H.T., Brekken, T.K.A., 2015. Integrating ocean wave energy at large-scales: a study of the US Pacific Northwest. *Renewable Energy* 76, 551–559.
- Phillips, O.M., 1957. On the generation of waves by a turbulent wind. *Journal of Fluid Mechanics* 2, 417–445.
- Phillips, O.M., 1958. The equilibrium range in the spectrum of wind-generated waves. *Journal of Fluid Mechanics* 4, 426–434.
- Pierson, W.J., Moskowitz, L., 1964. A proposed spectral form for fully developed wind-seas based on the similarity theory of S.A. Kitaigorodskii. *Journal of Geophysical Research* 69, 5181–5190.
- Pinson, P., Reikard, G., Bidlot, J.R., 2012. Probabilistic forecasting of the wave energy flux. *Applied Energy* 93, 364–370.
- Porter, A., Ruehl, K., Chartrand, C., 2014. Further development of SNL-SWAN, a validated wave energy converter array modeling tool. In: Proceedings of the 2nd Marine Energy Technology Symposium, Seattle, WA, USA, 2014.
- Rao, A.D., Sinha, M., Basu, S., 2013. Bay of Bengal wave forecast based on genetic algorithm: a comparison of univariate and multivariate approaches. *Applied Mathematical Modelling* 37, 4232–4244.
- Reikard, G., Pinson, P., Bidlot, J.R., 2011. Forecasting ocean wave energy: the ECMWF wave model and time series methods. *Ocean Engineering* 38, 1089–1099.
- Reikard, G., Robertson, B., Hiles, C., Buckham, B., Bidlot, J.R., 2015a. Simulating and forecasting ocean wave energy in Western Canada. *Ocean Engineering* 103, 223–236.
- Reikard, G., Robertson, B., Bidlot, J.-R., 2015b. Combining wave energy with wind and solar: short-term forecasting. *Renewable Energy* 81 (2015), 442–456.
- Retzler, C., 2006. Measurements of the slow drift dynamics of a model Pelamis wave energy converter. *Renewable Energy* 31, 257–269.
- Robertson, B., Hiles, C., Buckham, B., 2014. Characterizing the nearshore energy resources on the west coast of Vancouver Island. *Renewable Energy* 71, 665–678.
- Rogers, W.E., Kaihatu, J.M., Hsu, L., Jensen, R.E., Dykes, J.D., Holland, K.T., 2007. Forecasting and hindcasting waves with the SWAN model in the Southern California Bight. *Coastal Engineering* 54, 1–15.
- Roulston, M.S., Ellepola, J., von Hardenberg, J., Smith, L.A., 2005. Forecasting wave height probabilities with numerical weather prediction models. *Ocean Engineering* 32, 1841–1863.
- Rossi, B., Inoue, A., 2012. Out-of-sample forecast tests robust to the choice of window size. *Journal of Business and Economic Statistics* 30, 432–453.
- Ruehl, K., Porter, A., Posner, A., Roberts, J., 2013. Development of SNL-SWAN, a validated wave energy converter array modeling tool. In: Presented at the EWTEC 2013, Denmark, 2013.
- Ruehl, K., Michelen, C., Kanner, S., Lawson, M., Yu, Y.H., 2014. Preliminary verification and validation of WEC-Sim, an open source wave energy converter design tool. In: National Renewable Energy Laboratory Conference Paper NREL/CP-5000-61531.
- Saetra, O., Bidlot, J.-R., 2004. On the potential benefit of using probabilistic forecasts for waves and marine winds based on the ECMWF ensemble prediction system. *Weather and Forecasting* 19, 673–689.

- Stopa, J.E., Cheung, K.F., Chen, Y.L., 2011. Assessment of wave energy resources in Hawaii. *Renewable Energy* 35, 554–567.
- Surabhi, G., Deo, M.C., 2008. Real time wave forecasting using genetic programming. *Ocean Engineering* 35, 1166–1172.
- Tolman, H.L., 1991. A third-generation model for wind waves on slowly varying, unsteady and inhomogeneous depths and currents. *Journal of Physical Oceanography* 24, 782–797.
- Tolman, H.L., Chalikov, D., 1996. Source terms in a third-generation wind wave model. *Journal of Physical Oceanography* 26, 2497–2518.
- Tolman, H.L., 2006. Development of a Multi-Grid Version of WAVEWATCH III. Technical Report 256. National Oceanographic and Atmospheric Administration.
- Tolman, H.L., 2008. A mosaic approach to wind wave modeling. *Ocean Modelling* 25, 35–47.
- Tseng, C.M., Jan, C.D., Wang, J.S., Wang, C.M., 2007. Application of artificial neural networks in typhoon surge forecasting. *Ocean Engineering* 34, 1757–1768.
- Uihlein, A., Magagna, D., 2016. Wave and tidal current energy: a review of the current state of research beyond technology. *Renewable and Sustainable Energy Reviews* 58, 1070–1081.
- Woodcock, F., Engel, C., 2005. Operational consensus forecasts. *Weather and Forecasting* 20, 101–111.
- Woodcock, F., Greenslade, D.J.M., 2006. Consensus of numerical forecasts of significant wave heights. *Weather and Forecasting* 22, 792–803.
- Yemm, R., Pizer, D., Retzler, C., Henderson, R., 2012. Pelamis: experience from concept to connection. *Philosophical Transactions of the Royal Society* 370, 365–380.
- Zamani, A., Solomatine, D., Azimian, A., Heemink, A., 2008. Learning from data for wind-wave forecasting. *Ocean Engineering* 35, 953–962.

# Forecasting intrahourly variability of wind generation

8

Claire L. Vincent<sup>1</sup>, Pierre-Julien Trombe<sup>2</sup>

<sup>1</sup>The University of Melbourne, Melbourne, VIC, Australia; <sup>2</sup>Vattenfall Windkraft A/S, Esbjerg, Denmark

## 8.1 Introduction

Wind power fluctuations occurring within the hour had until recently received little attention. Under relatively small wind power penetration levels, these fluctuations could easily be absorbed by power systems. However, under future scenarios with penetration levels above 20% or 30% as already observed today in some regions of the world (e.g., Denmark), the integration of wind power into power systems will require more frequent balancing operations as well as subhourly scheduling of power generators to accommodate this variability (NREL, 2010). Forecasting the intrahourly variability of the wind power is an essential prerequisite to those operations. In addition, correct simulation or modeling of power fluctuations and their correlations in space and time is essential for building realistic power systems models (e.g., Sørensen et al., 2008) and for judicious planning of the location of new wind power capacity. An illustration of a 24-h episode of wind power fluctuations is shown in Fig. 8.1.

The wind power variability seen in Fig. 8.1 stems from variability in the wind itself. The wind varies on all time and space scales from turbulence to seasonal and interannual scales. Turbulent eddies with spatial scales of tens to hundreds of meters and temporal scales of seconds to minutes are always present in the atmosphere and are caused by changes in the wind speed with height and the thermal stratification of the atmosphere. On the timescales relevant to wind power forecasting and integration—from a few minutes up to several hours—wind fluctuations are governed by physical processes such as gravity waves, cold fronts, storms, cellular convection, convective rolls, low level jets, or sea breezes. A time series of wind speed from a meteorological mast in the North Sea for a 1-month period is shown in Fig. 8.2. In Fig. 8.3, a power spectrum based on the same data is shown. When plotted on a log–log axis, the power spectrum shows a classical spectral slope of  $-5/3$  (indicated by the dashed black line) that has been found as a universal feature of the atmosphere in numerous scientific studies (e.g., Nastrom et al., 1984; Larsén et al., 2013). This spectrum is, however, the result of a widely varying set of atmospheric conditions, and in certain circumstances, the variability will be greatly enhanced relative to the mean conditions. The contribution to the spectrum from timescales shorter than 1 h is indicated by shading. This contribution, as calculated on a sliding window through the month, is shown in the lower panel of Fig. 8.2, where it is clear that the degree of intrahourly wind fluctuations is by no means constant with time. The amount of variability changes with the

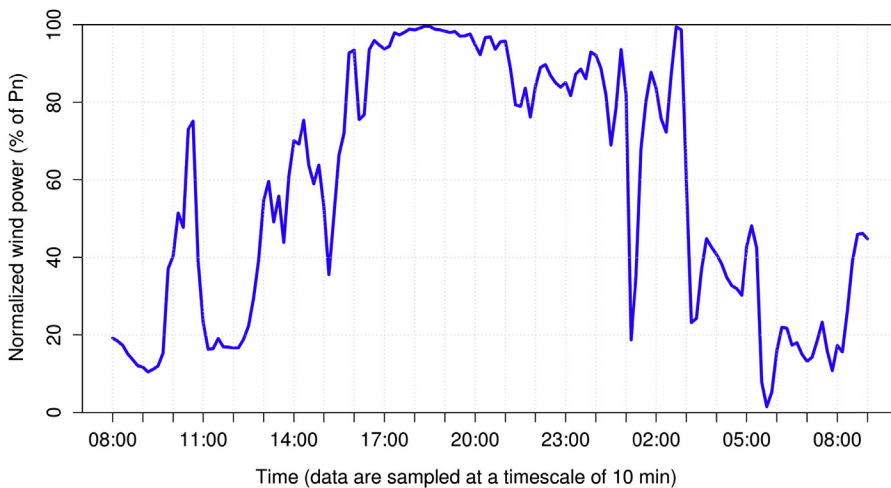


**Figure 8.1** Wind power sampled over 10-min intervals at the Horns Rev 1 wind farm. Data provided by Vattenfall Windkraft A/S.

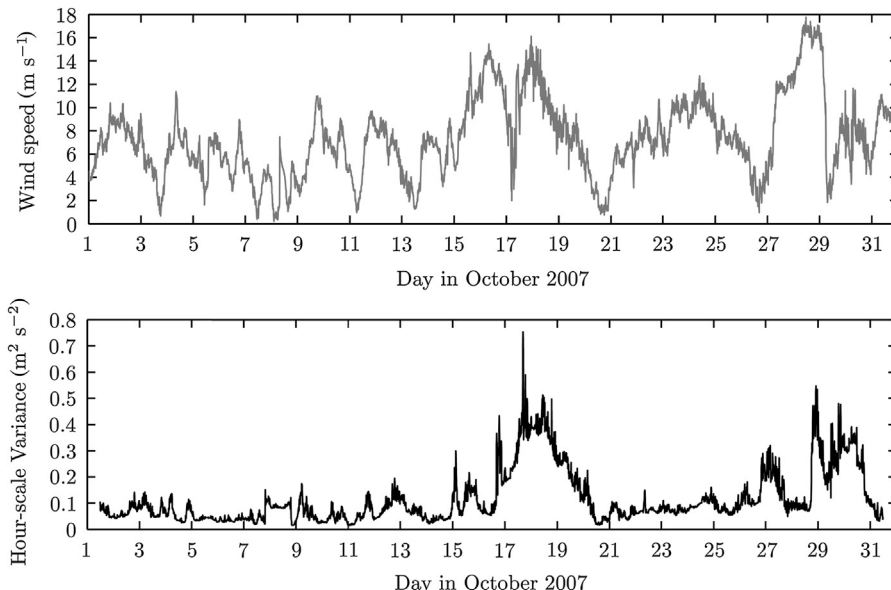


**Figure 8.2** Upper panel: Time series of wind speed at a height of 116 m, measured at the Egmond aan Zee wind farm from 1 to 31 of October 2007. Lower panel: Contribution to the total variance from timescales between 20 min and 1 hour.

Created using data downloaded from <http://www.noordzeewind.nl/en/knowledge/reportsdata>.

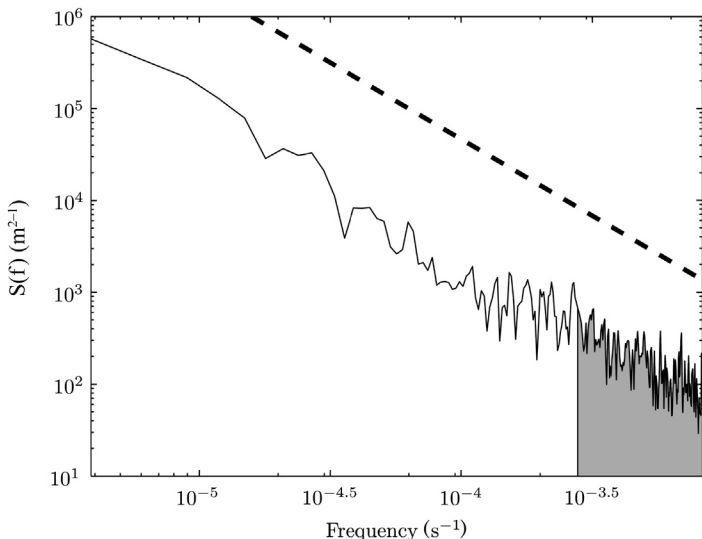


**Figure 8.3** Wind speed spectrum, based on the times series shown in Fig. 8.2. The shaded area indicates the contribution to the total variance from timescales between 20 min and 1 h.

Although not shown on a log–log axis, the shaded area should extend down to zero. The dashed line indicates a spectral slope of  $-5/3$ .

Created using data downloaded from <http://www.noordzeewind.nl/en/knowledge/reportsdata>.

evolving large-scale weather patterns and their interaction with smaller scale features at the surface.

When the wind varies, the wind power also varies. Variations in wind speed, however, are modified by the wind turbine power curve. Wind speed fluctuations below the cut-in wind speed of  $4 \text{ m s}^{-1}$  are of little consequence, as are those occurring above the rated speed of the turbine (around  $15 \text{ m s}^{-1}$ ). The steepest section of the wind turbine power curve occurs at a wind speed of around  $7\text{--}9 \text{ m s}^{-1}$ , and in this range fluctuations in wind speed will be amplified by the wind turbine power curve. Apart from the obvious effect of the shape of the power curve on mapping wind fluctuations to power fluctuations, the wind farm also acts to smooth out the fastest wind speed fluctuations both through weighted averaging of the wind over the rotor area, and due to the aggregation of wind power over the spatial extent of a wind farm (Sørensen et al., 2008). However, this smoothing does not completely remove the effect of fluctuations on the timescale of a few minutes, particularly for large offshore wind farms where the high concentration of turbines within a small geographical area means that wind and power fluctuations can be highly correlated. In this chapter, we focus on the meteorological drivers and statistical modeling of intrahourly wind power variability. We do not cover smoothing from the wind turbine rotor or geographical aggregation.

On the hourly timescale, wind fluctuations can be highly correlated across large numbers of turbines spread over large geographical areas, leading to large power fluctuations (Holttinen et al., 2011). The effect of large power fluctuations can be partly mitigated by accurate forecasts that either explicitly predict large power fluctuations or that predict both the mean and statistical properties of the power (e.g., Pinson et al., 2008; Trombe et al., 2014a).

In this chapter, we will start by reviewing the observational evidence and physical drivers of intrahourly wind variability. Then we will review statistical and physical forecasting models with respect to their strategies for incorporating the variability of the wind speed, including the outlook for generating explicit variability forecasts. Strategies for considering the spatial correlations between intrahourly fluctuations will then be considered, followed by a brief discussion of the possibilities for utilizing information about the wind variability for improving wind farm operations and scheduling. This chapter focuses mainly on variability in the wind itself, and only briefly covers the mapping of wind variability to power variability.

## 8.2 Meteorological causes of hour-scale wind variability

Intrahourly wind variability—here defined as wind variability on scales of a few minutes to an hour—is caused by atmospheric phenomena with spatial scales of around a kilometer up to tens of kilometers. There are numerous phenomena that can introduce variability into the wind on these scales. We review a few of them here:

**Open cellular convection** (see Fig. 8.4) was shown by [Vincent et al. \(2012a\)](#) to be associated with hour-scale wind fluctuations over the North Sea. Using observations and mesoscale modeling, they found that the rising air in the cloudy cell walls was associated with surface convergence that could explain horizontal wind variability with an amplitude of  $5\text{--}10 \text{ m s}^{-1}$ . As the field of cellular convection moves over a point location such as a wind farm, the spatial variability is experienced at the point as temporal variability. Open cellular convection occurs when very cold air is advected over comparatively warm sea water. For example, this situation typically occurs over the North Sea in late autumn and early winter, when the sea water still retains some heat from the preceding summer. A related phenomenon that can introduce intrahourly variability into the surface wind is convective rolls, which occur in a similar environment to open cellular convection but with higher values of background wind shear ([LeMone, 1973](#)).

A case of **gravity waves** over the sea in stable atmospheric conditions was investigated by [Larsén et al. \(2011\)](#). They showed regular wave patterns in the 10-m wind field measured by a satellite-mounted synthetic aperture radar covering an extensive part of the waters surrounding Denmark. The fluctuations had an amplitude of several meter per second and were consistent with observations from meteorological masts near the Nysted Wind Farm in the southern part of the Baltic Sea that showed wind fluctuations at 10 m, 40 m, and 65 m above sea level with amplitudes of around  $2 \text{ m s}^{-1}$  and a period of around 20 min. Similar results were reported near Long Island, New York, by [Sethuraman \(1980\)](#). Gravity waves are unlikely to cause fluctuations as large as convective processes occurring in unstable atmospheric conditions, but are nonetheless an important contributor to hour-scale wind variability. This is especially the case due to their highly organized structure, which could lead to correlated fluctuations at neighboring sites.

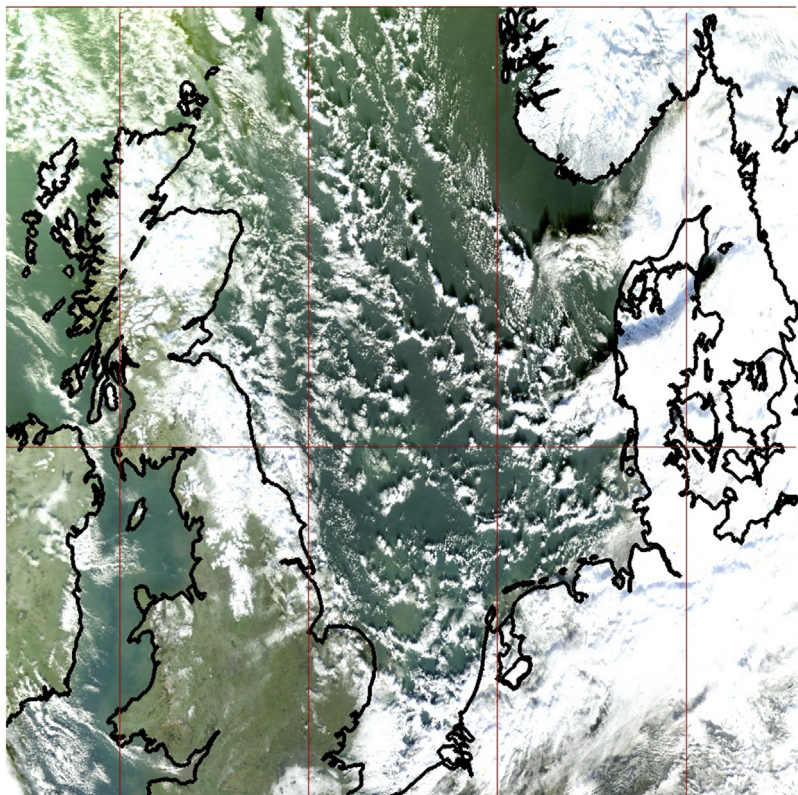


**Figure 8.4** Visual satellite picture showing regular pattern of cellular convection over the North Sea, leading to sustained hour-scale wind fluctuations.  
Created using data downloaded from <http://ladsweb.nascom.nasa.gov>.

The **sea breeze** circulation is the response of the atmosphere to differential heating of the land and sea. During the afternoon, radiative heating over the land causes air to rise, creating a positive pressure anomaly aloft and a circulation with flow toward the land at the surface and flow toward the sea aloft. During the night, a reverse process occurs, with a weak flow toward the sea at the surface. Although the sea breeze circulation is predominantly a diurnal effect, it can also influence smaller scales when, for example, convergence of the sea breeze front with the background flow results in squall lines or showers near the coast. Wind variability relating to the sea breeze circulation is especially relevant to wind energy because coastal areas are typically favorable areas for wind farm development. The impact of the sea breeze on offshore wind energy resource assessment in the North Sea region was examined by Steele et al. (2014), who suggested that some aspects of the sea breeze could influence wind farms up to 200 km offshore. They showed that at the Egmond aan Zee wind farm in the southern North Sea, the amplitude of the diurnal wind power cycle on days with a corkscrew sea breeze (where there is an along-shore component to the background

flow such that surface divergence at the coast is strengthened by the sea breeze) was more than double that on days without a sea breeze.

**Low level jets** are regions of elevated horizontal wind speed within the lower few hundred meters of the atmospheric boundary layer. Low level jets are of particular interest to wind energy because they can affect the typical hub heights of large wind turbines. Furthermore, they can cause high levels of vertical wind shear around the boundaries of the jet region that can lead to extreme turbulent loading on wind turbine blades. Low-level jets occur both over the land and over the sea. There is a diversity of hypothesized mechanisms for low-level jet formation, including inertial oscillations, nocturnal cooling, and interactions with steep topography. [Nunalee and Basu \(2014\)](#) gives a good overview of formation mechanisms on- and offshore, and showed clear observations of low-level jets on the northeastern US coast from both vertical wind profiles and mesoscale modeling. Like the sea breeze, low-level jets are a diurnal feature, but may project onto higher frequencies, particularly if the jet boundary is near the turbine hub height.

### 8.3 Observing hour-scale wind variability

Intrahourly wind variability can easily be observed in a time series of observations from a meteorological mast, but such observations are spatially sparse, expensive to collect and cannot be extended over a wide geographical area. Maps of the mean wind have been successfully created from satellite-mounted radar measurements (e.g., [Badger et al., 2010](#)), but the temporally sparse data from polar-orbiting satellites make it difficult to exploit such data sets for mapping the temporal variability of the wind. Thus, from a data availability perspective, it is more challenging to characterize the variability of the wind than the mean and distribution of the wind speed that are typically used in resource assessment studies.

Several studies have used observational data to study the variability of the wind on timescales of minutes to hours. For example, [Vincent et al. \(2011\)](#) used long time series of wind speed over the North Sea and adaptive spectra to express the variability of the wind as functions of wind direction, precipitation, rain rate, time of year and air–sea temperature difference. Their most striking result was that severe wind variability events on these timescales were much more prevalent in flow from the sea than in flow from the land, which was consistent with earlier work of [Akhatov \(2007\)](#), who showed that severe power fluctuations at the Horns Rev I wind farm in the Danish North Sea were most pronounced in flow from the sea. [Woods et al. \(2013\)](#) used a stochastic model to relate the wind variability to nearby measurement sites by applying a filter that retained the low-frequency part of the wind speed spectrum (that driven by synoptic scale weather systems), while decreasing the correlation between the high frequencies as the separation distance between sites increased.

In another study, [Vincent et al. \(2012a\)](#) and [Larsén et al. \(2013\)](#) showed that open cellular convection over the North Sea could be associated with large, hour-scale wind fluctuations and an increase in the wind speed spectrum over the timescales of minutes

to hours. An example of open cellular convection that was associated with severe wind fluctuations at a large offshore wind farm in the North Sea is shown in Fig. 8.4. The updrafts in the cloudy cell walls of the cellular convection induce regular wind fluctuations with a spatial scale of 10–80 km and a temporal scale of minutes to hours.

Describing the wind variability in time series observations requires an objective way to measure the time-evolving nature of the fluctuations. For example, the time series in Fig. 8.2 (lower panel) shows the contribution to the variance from timescales of 20 min to 1 h, calculated as the area under the power spectrum between the relevant frequencies, where the power spectrum is calculated on a sliding window of length 24 h. Davy et al. (2010) developed an index of wind variability by applying a band-pass filter to time series of wind speed observations, then calculating the standard deviation of the band-pass filtered signal on a 6-h moving window. An alternative approach was proposed by Vincent et al. (2010), who used adaptive spectral analysis based on an empirical decomposition and application of the Hilbert transform to calculate a time-evolving spectrum as a function of frequency and time, then integrated the spectrum between a pair of frequencies to create an index of variability. Their index represented an upper bound on the amplitude of fluctuations if all oscillatory components were in phase.

## 8.4 Forecasting wind power variability

Among the first research works investigating the predictability of intrahourly wind power fluctuations, there are several applications to offshore wind farms. Given the look-ahead time of 10 min that they address, the sole inputs to the different models are local observations of wind power generation and nacelle winds. Models range from autoregressive time series models with a new parametric predictive density of wind power (Pinson, 2012) to more complex models accounting for changes in the dynamical pattern of the fluctuations, so-called regime-switching models (Pinson et al., 2008). Explanatory variables can be used to control the transitions between regimes as in Gallego et al. (2011) who highlighted the influence of the wind direction on the variability regime of the wind power. Alternatively, a Markovian approach is possible that considers the transitions between regimes to be implicitly governed by some unobservable weather process (Pinson and Madsen, 2012). An interesting aspect of regime-switching models is that they can describe a complex process by a sequence of discrete states, each characterized by a different variability level, hence delivering highly interpretable information to forecast end users. Finally, these studies highlighted that an important factor in the limited predictability of wind power generation beyond lead times of 10 min is the lack of appropriate observations of forthcoming changes in the weather conditions.

Onshore wind farms can form a dense network of weather sensors. In that setup, wind farms located upwind can collect valuable information to improve the predictability of the power generation at nearby wind farms. However, so-called upwind observations are rarely available offshore. Instead, it has been proposed that other sources of observations can be used to fill this gap. In Trombe et al. (2014a), two weather radars were used to monitor the passage of precipitation events in the vicinity of an offshore wind farm

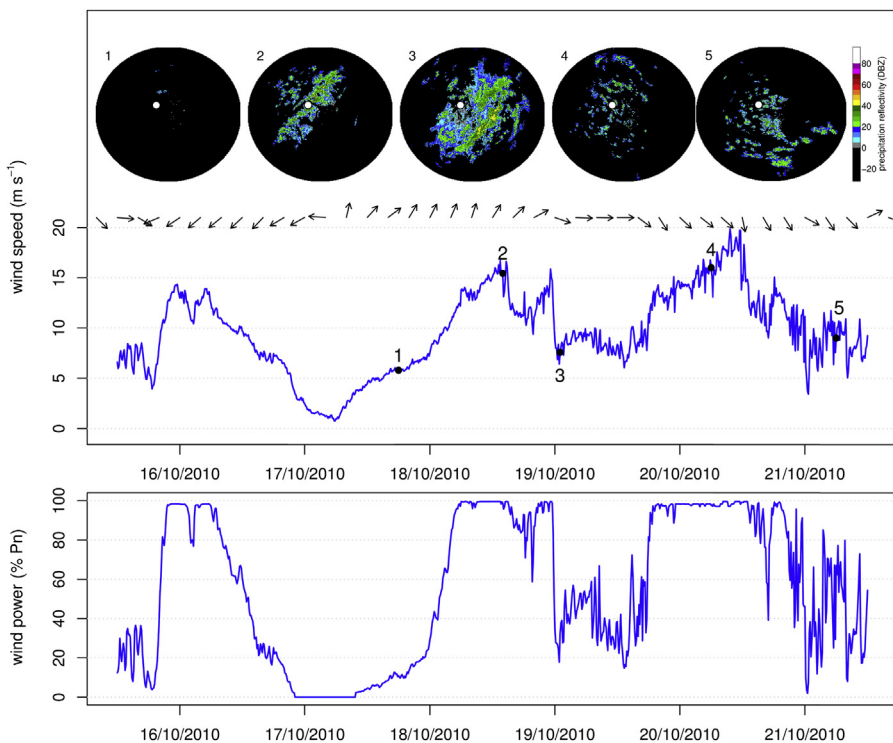


**Figure 8.5** Radar images showing spatial precipitation patterns and associated wind and power fluctuations.

Weather radar images were provided by the Danish Meteorological Institute. Time series of wind speed and direction and wind power generation were provided by Vattenfall Vindkraft A/S.

sited some 15 km away from the western coast of Denmark. An example of such an event is shown in Fig. 8.5. This event depicts a cold front moving from the North Sea and following a northwesterly trajectory as it passes across the wind farm (represented by the white dot on the weather radar images). There is a clear increase in the variability level of both the wind speed and wind power after the leading edge of the front has crossed the wind farm. In Trombe et al. (2014b), a data mining approach was proposed for classifying precipitation events with respect to the associated level of wind power variability observed when they pass in the vicinity of the wind farm. Precipitation was described by a set of attributes featuring its global intensity, spatial homogeneity, and horizontal motion. The most important attributes associated with a high wind power variability were found to be the motion direction and speed, as well as the maximum intensity of the precipitation event. This later research work concluded on the need to improve the characterization of precipitation over multiple scales, by identifying small precipitation cells embedded into large precipitation systems, for instance. This would potentially enable a better decoupling of the contribution of small- and large-scale weather phenomena to wind power variability.

While [Trombe et al. \(2014a\)](#) used local information from observations to predict the wind variability, an alternative approach based on large-scale weather patterns has been proposed in [Davy et al. \(2010\)](#) and [Ellis et al. \(2015\)](#). They expressed the degree of wind variability using a six hourly moving window of a band-pass filtered time series of observed wind speed, and examined different statistical models for relating wind variability to large-scale weather patterns. As a way of reducing the complexity of the large scale, gridded meteorological data, they calculated empirical orthogonal functions (EOFs) of meteorological fields including temperature, wind, and planetary boundary layer height and built their models using time series of the coefficients of the first eight EOFs. They found that of the models they tested, random forest models gave the best prediction of local wind variability. The implication of their result is that the local wind variability is strongly influenced by changes in weather pattern on a much larger scale.

Statistical models are unlikely to be able to forecast wind variability conditions up to 24 h into the future which are relevant to next-day bidding of wind power on electricity markets such as the Nordic power exchange. For these longer look-ahead times, numerical weather prediction (NWP) models can also be used to predict subhourly variability when run with a horizontal grid spacing of less than about 5 km. For example, [Skamarock \(2004\)](#) showed that the Weather Research and Forecasting (WRF) model could produce realistic atmospheric spectra up to a spatial scale of around seven times the horizontal grid spacing, so that spatial variability on a scale of a few tens of kilometers or a temporal scale of tens of minutes to a few hours can be at least partly resolved. [Vincent et al. \(2012a\)](#) showed that the WRF model could be used to simulate the hour-scale wind variability associated with open cellular convection, while [Larsén et al. \(2011\)](#) demonstrated that the same model could be used to model intrahourly variability generated by gravity waves. Despite this evidence that intrahourly wind variability can be successfully modeled using physical modeling strategies, such models are unlikely to compete with statistical models for very short-term forecasts with look-ahead periods of less than a few hours due to the spin-up and computational demands of such models. Furthermore, these models will not forecast the exact phase of individual wind fluctuations, but will instead produce a single stochastic realization (or a set of stochastic realizations) of the statistical properties of the wind. Such modeling has particular application to next-day forecasts of, for example, severe wind variability.

A topic that has received considerably more attention than intrahourly variability forecasting is ramp forecasting. Wind power or wind speed ramps are usually defined as a change in wind speed or power exceeding some threshold within a given time window (e.g., [Potter et al., 2009](#)). Ramp forecasting overlaps with variability forecasting, but is not always the same. For example, consider the time series of wind speed and variability in [Fig. 8.2](#). Note the sudden changes in wind speed on October 17 and 29, which are both accompanied by a spike in intrahourly variability, and then followed by a prolonged episode of high wind variability lasting more than 24 h. This is a typical scenario in the midlatitudes. A front passes through, causing a change of

air mass and large change in wind speed and direction. After the initial front and its associated ramp in wind speed have moved through, a cold postfrontal air mass may become established with showers, gustiness, and unstable conditions lasting for several days. Despite these differences, many ideas from ramp forecasting may be relevant to variability forecasting. For example, [Gallego et al. \(2013\)](#) proposed moving away from a binary ramp forecast to a continuous wavelet-based ramp function. Such a function could equally well be applied to variability, where variability is seen as a group of alternating ramp-up and ramp-down events.

## 8.5 Correlation between wind fluctuations at spatially distributed sites

Wind fluctuations on a timescale of minutes to hours are related to meteorological features with a spatial scale of kilometers to tens of kilometers. These spatial scales are commensurate with the scale of a large offshore wind farm, or the spacing of groups of turbines on land. For example, the Horns Rev I wind farm covers an area of  $5 \times 3.8$  km. This means that correlations between fluctuations in wind speed can be high among groups of turbines or pairs of wind farms. The implication of these spatial correlations is that to quantify the expected wind power variability over a geographic area, the correlations between neighboring sites must be taken into consideration. In general, the correlation between pairs of sites decreases as the distance between them increases.

There have been several recent efforts to quantify change in the correlation (often as a function of frequency, where it is called the coherence) over large distances. [St. Martin et al. \(2015\)](#) used networks of observational sites in Canada, Northwestern US, and Southeastern Australia covering horizontal extents of 354–5344 km to calculate correlation as a function of separation distance for different timescales, where the different timescales were extracted from the data by a high-pass filtering operation. Their work helped to quantify the fact that as the separation distance decreases, the timescale on which fluctuations show significant correlations also decreases. They found that for timescales shorter than around a day, the degree of smoothing that could be attained through aggregation of turbines over a geographical area increased as the timescales under consideration decrease.

Correlations between wind variability for pairs of sites separated by distances of 1–30 km were studied by [Woods et al. \(2011\)](#) using 84 measurement towers in Southeast Australia. They fitted expressions for the coherence and phase spectra—that is, the magnitude and phase of the complex cross-spectrum. The coherence decayed as a function of frequency, where the decay rate was a function of separation distance and wind speed standard deviation, while the phase depended on the angle between the wind and the line connecting the two sites as well as the separation distance and wind speed. By including the standard deviation of the wind speed, as well as the wind direction, they partly take into account the variation of coherence and phase

spectra with weather patterns. They suggest that the forms of their models will apply in other regions, even though the fitted parameter values are expected to vary between regions.

In similar studies, [Vincent et al. \(2012b\)](#) and [Larsén et al. \(2013\)](#) studied the coherence between pairs of meteorological masts in the North and Baltic Seas. Over the sea, the coherence is likely to be higher than over the land for long separation distances due to the homogeneous surface conditions. [Vincent et al. \(2012b\)](#) fitted the cospectrum and quadrature spectrum (that is, the real and imaginary parts of the complex cross-spectrum) to data from pairs of meteorological masts separated by distances of 2.13–12.4 km. They found that cospectra and quadrature spectra collapsed onto a single curve for the different separation distances when the frequency axis was normalized by the separation distance divided by the mean wind speed—that is, when they accounted for the time taken for fluctuations to be advected between the two sites by the mean wind. Expressions for the cospectrum and quadrature spectrum were fitted based on separation distance, wind speed, and angle between the mean wind and separation angle. Both the expressions of [Woods et al. \(2011\)](#) and that of [Vincent et al. \(2012b\)](#) would be suitable for statistical simulation of wind power production over geographically distributed areas over the land or sea.

Interestingly, [Vincent et al. \(2012b\)](#) removed days with nonstationary wind conditions from their analysis—that is, days where the range of wind speeds during the day was more than  $12 \text{ m s}^{-1}$  or the range of wind directions greater than 90 degrees. This meant that days with severe wind variability may have been neglected from the analysis. [Larsén et al. \(2013\)](#) showed that on days with open cellular convection over the North Sea, the power spectrum contained extra energy on timescales of minutes to a few hours. In this case, there is potential for higher correlations between sites over the sea as a result of organized patterns of cloudiness and convection with spatial scales of tens of kilometers.

## 8.6 Using wind variability information to improve wind farm operations and scheduling

Forecasts of wind variability can be used to mitigate the economic and technical challenges of the fluctuating supply from wind farms. Deficits in wind power due to unforeseen fluctuations in the wind speed must be compensated for using conventional generators with fast ramping capability, by managing the wind power supply itself, or by demand side management ([Grünewald et al., 2015](#)). Alternatively, climatological predictions of wind variability can be used to mitigate wind power fluctuations at the wind farm design stage.

One proposed method is to use a flexible dispatch margin, where wind farms are under scheduled in the short-term energy market, leaving some wind energy in reserve to balance system uncertainty. For example, [Cardell and Anderson \(2015\)](#) demonstrated that by using a flexible dispatch margin, both system and market performance

was improved, including less reliance on other generators to balance wind power fluctuations and less price spikes. In examining a flexible dispatch margin for systems with 10%, 20%, and 30% wind power penetration, they found modest system benefits for the 10% penetration case, but a significant decrease in variability for the 30% penetration case. Although they did not use an explicit variability forecast, information about the expected variability (as well as the expected uncertainty) can be used to inform decisions about the amount of wind power held in reserve for balancing fluctuations.

Wind power variability can also be partially mitigated at the site assessment and planning stage of wind farms. For example, [Reichenberg et al. \(2014\)](#) used gridded wind speed simulations from an atmospheric model with a horizontal resolution of 11 km to show that wind power fluctuations could be reduced by planning the spatial distribution of wind farms to minimize the correlation between power fluctuations.

## 8.7 Conclusions and future developments

Intrahourly wind variability is an atmospheric phenomenon that causes various technical and economic challenges for wind farm integration. In electricity systems with low levels of wind power, intrahourly fluctuations are likely to be absorbed by the system with few technical challenges, but with increasing levels of wind energy penetration, managing these fluctuations is likely to require further attention. Intrahourly wind variability is a particular concern for large offshore wind farms, where a large number of turbines are usually installed within a small geographical area, leading to correlated fluctuations between many turbines. In this chapter, we have focused on variability in the wind speed itself. The mapping between variability in wind speed and variability in wind power is nonlinear due to the shape of the power curve, and due to damping of fluctuations by the turbine rotor and aggregation of power across wind farms and geographic regions.

Many wind power forecasting models include an estimation of the variability or uncertainty of the wind speed. However, explicitly forecasting intrahourly wind variability requires a special blend of statistical and physical modeling. Recent attempts to explicitly forecast the wind variability have included predictors such as the wind speed time series itself, large-scale weather pattern and local information about approaching weather regimes from rain radars. NWP models have been used to explicitly simulate some aspects of wind and power variability and could be used for day-ahead forecasts of intrahourly variability.

Intrahourly wind variability has a tangible and potentially severe impact on wind power generation, but the frameworks for using wind power variability forecasts to alleviate this impact are still in a developmental stage. Using wind power variability forecasts as inputs to flexible dispatch systems on short-term electricity markets is a promising use for variability forecasts—that is, the higher the predicted amplitude of the variability, the more wind power that needs to be withheld for possible system balancing. Likewise, information about the predicted wind variability during the coming 24 h (along with information about the predicted uncertainty) could help optimize bidding on the day-ahead electricity markets.

## Acknowledgments

C Vincent's contribution to this chapter was funded by the Australian Research Council's Centres of Excellence program (CE110001028). The authors are grateful to Vattenfall Vindkraft A/S for use of the wind speed and power data, the Danish Meteorological Institute for the weather radar images and to Nordseewind for use of measurements from the Egmond aan Zee wind farm (available online at <http://www.noordzeewind.nl/en/knowledge/reportsdata/>). The satellite image in Fig. 8.4 was created using MODIS satellite data downloaded from <http://ladsweb.nascom.nasa.gov>.

## References

- Akhmatov, V., 2007. Influence of wind direction on intense power fluctuations in large offshore windfarms in the north sea. *Wind Engineering* 31 (1), 59–64. <http://dx.doi.org/10.1260/030952407780811384>.
- Badger, M., Badger, J., Nielsen, M., Bay Hasager, C., Pena, A., 2010. Wind class sampling of satellite SAR imagery for offshore wind resource mapping. *Journal of Applied Meteorology and Climatology* 49, 2474–2491. <http://dx.doi.org/10.1175/2010JAMC2523.1>.
- Cardell, J.B., Anderson, C.L., 2015. A flexible dispatch margin for wind integration. *IEEE Transactions on Power Systems* 30 (3), 1501–1510.
- Davy, R.J., Woods, M.J., Russell, C.J., Coppin, P.A., 2010. Statistical downscaling of wind variability from meteorological fields. *Boundary-layer Meteorology* 135 (1), 161–175. <http://dx.doi.org/10.1007/s10546-009-9462-7>.
- Ellis, N., Davy, R., Troccoli, A., 2015. Predicting wind power variability events using different statistical methods driven by regional atmospheric model output. *Wind Energy* 18, 1611–1628. <http://dx.doi.org/10.1002/we.1779>.
- Gallego, C., Pinson, P., Madsen, H., Costa, A., Cuerva, A., 2011. Influence of local wind speed and direction on wind power dynamics—application to offshore very short-term forecasting. *Applied Energy* 88 (11), 4087–4096.
- Gallego, C., Costa, A., Cuerva, Á., Landberg, L., Greaves, B., Collins, J., 2013. A wavelet-based approach for large wind power ramp characterisation. *Wind Energy* 16 (2), 257–278. <http://dx.doi.org/10.1002/we.550>.
- Grünewald, P., McKenna, E., Thomson, M., 2015. Going with the wind: temporal characteristics of potential wind curtailment in Ireland in 2020 and opportunities for demand response. *IET Renewable Power Generation* 9 (1), 66–77. <http://dx.doi.org/10.1049/iet-rpg.2013.0320>.
- Holttinen, H., Meibom, P., Orths, A., Lange, B., O'Malley, M., Tande, J.O., Estanqueiro, A., Gomez, E., Soder, L., Strbac, G., Smith, J.C., van Hulle, F., 2011. Impacts of large amounts of wind power on design and operation of power systems, results of IEA collaboration. *Wind Energy* 14, 179–192. <http://dx.doi.org/10.1002/we>.
- Larsén, X.G., Vincent, C., Larsen, S., 2013. Spectral structure of mesoscale winds over the water. *Quarterly Journal of the Royal Meteorological Society* 139, 685–700. <http://dx.doi.org/10.1002/qj.2003>.
- Larsén, X.G., Larsen, S., Badger, M., 2011. A case-study of mesoscale spectra of wind and temperature, observed and simulated. *Quarterly Journal of the Royal Meteorological Society* 137 (654), 264–274. <http://dx.doi.org/10.1002/qj.739>.
- LeMone, M.A., 1973. The structure and dynamics of horizontal roll vortices in the planetary boundary layer. *Journal of the Atmospheric Sciences* 30, 1077–1091. [http://dx.doi.org/10.1175/1520-0469\(1973\)030<1077:TSADOH>2.0.CO;2](http://dx.doi.org/10.1175/1520-0469(1973)030<1077:TSADOH>2.0.CO;2).

- Nastrom, G.D., Gage, K.S., Jasperson, W.H., 1984. Kinetic energy spectrum of large- and mesoscale atmospheric processes. *Nature* 310, 36–38.
- NREL, 2010. Western Wind and Solar Integration Study, NREL/SR-550-47434. Work performed by GE Energy, Schenectady, NY. National Renewable Energy Laboratory, Golden, CO.
- Nunalee, C.G., Basu, S., 2014. Mesoscale modeling of coastal low-level jets: implications for offshore wind resource estimation. *Wind Energy* 17, 1199–1216.
- Pinson, P., 2012. Very-short-term probabilistic forecasting of wind power with generalized Logit–Normal distributions. *Journal of the Royal Statistical Society: Series C (Applied Statistics)* 61 (4), 555–576.
- Pinson, P., Madsen, H., 2012. Adaptive modelling and forecasting of offshore wind power fluctuations with Markov-switching autoregressive models. *Journal of Forecasting* 31, 281–313. <http://dx.doi.org/10.1002/for.1194>.
- Pinson, P., Christensen, L.E.a., Madsen, H., Sørensen, P.E., Donovan, M.H., Jensen, L.E., 2008. Regime-switching modelling of the fluctuations of offshore wind generation. *Journal of Wind Engineering and Industrial Aerodynamics* 96 (12), 2327–2347. <http://dx.doi.org/10.1016/j.jweia.2008.03.010>.
- Potter, C., Grimit, E., Nijssen, B., 2009. Potential benefits of a dedicated probabilistic rapid ramp event forecast tool. In: Power Systems Conference and Exposition, 2009. PSCE '09. IEEE/PES, pp. 1–5. <http://dx.doi.org/10.1109/PSCE.2009.4840109>.
- Reichenberg, L., Johnsson, F., Odenberger, M., 2014. Dampening variations in wind power generation—the effect of optimizing geographic location of generating sites. *Wind Energy* 1631–1643.
- Sethuraman, S., 1980. A case of persistent breaking of internal gravity waves in the atmospheric surface layer over the ocean. *Boundary-layer Meteorology* 19 (1), 67–80. <http://dx.doi.org/10.1007/BF00120311>.
- Skamarock, W.C., 2004. Evaluating mesoscale NWP models using kinetic energy spectra. *Monthly Weather Review* 132 (12), 3019–3032. <http://dx.doi.org/10.1175/MWR2830.1>.
- Sørensen, P., Cutululis, N.A., Vigueras-Rodríguez, A., Madsen, H., Pinson, P., Jensen, L.E., Hjerrild, J., Donovan, M., 2008. Modelling of power fluctuations from large offshore wind farms. *Wind Energy* 11 (1), 29–43. <http://dx.doi.org/10.1002/we.246>.
- St Martin, C.M., Lundquist, J.K., Handschy, M.a., 2015. Variability of interconnected wind plants: correlation length and its dependence on variability time scale. *Environmental Research Letters* 10 (4), 044004. <http://dx.doi.org/10.1088/1748-9326/10/4/044004>.
- Steele, C., Dorling, S., von Glasgow, R., Bacon, J., 2014. Modelling sea-breeze climatologies and interactions on coasts in the southern north sea: implications for offshore wind energy. *Quarterly Journal of the Royal Meteorology Society*. <http://dx.doi.org/10.1002/qj.2482>.
- Trombe, P.-J., Pinson, P., Vincent, C., Bøvith, T., Cutululis, N.A., Draxl, C., Giebel, G., Hahmann, A.N., Jensen, N.E., Jensen, B.P., et al., 2014a. Weather radars—the new eyes for offshore wind farms? *Wind Energy* 17 (11), 1767–1787.
- Trombe, P.-J., Pinson, P., Madsen, H., 2014b. Automatic classification of offshore wind regimes with weather radar observations. *IEEE Journal of Selected Topics in Applied Earth Observations and Remote Sensing* 7 (1), 116–125.
- Vincent, C., Giebel, G., Pinson, P., Madsen, H., 2010. Resolving nonstationary spectral information in wind speed time series using the hilbert-huang transform. *Journal of Applied Meteorology and Climatology* 49 (2), 253–267. <http://dx.doi.org/10.1175/2009JAMC2058.1>.
- Vincent, C.L., Pinson, P., Giebel, G., 2011. Wind fluctuations over the north sea. *International Journal of Climatology* 31 (11), 1584–1595. <http://dx.doi.org/10.1002/joc.2175>.

- Vincent, C.L., Hahmann, A.N., Kelly, M.C., 2012a. Idealized mesoscale model simulations of open cellular convection over the sea. *Boundary-layer Meteorology* 142 (1), 103–121. <http://dx.doi.org/10.1007/s10546-011-9664-7>.
- Vincent, C.L., Larsén, X.G., Larsen, S.E., Sørensen, P., 2012b. Cross-spectra over the sea from observations and mesoscale modelling. *Boundary-layer Meteorology* 146 (2), 297–318. <http://dx.doi.org/10.1007/s10546-012-9754-1>.
- Woods, M.J., Davy, R.J., Russell, C.J., Coppin, P.A., 2011. Cross-spectrum of wind speed for Meso-Gamma scales in the upper surface layer over South-eastern Australia. *Boundary-layer Meteorology* 141 (1), 93–116. <http://dx.doi.org/10.1007/s10546-011-9632-2>.
- Woods, M.J., Russell, C.J., Davy, R.J., Coppin, P.A., 2013. Simulation of wind power at several locations using a measured time-series of wind speed. *IEEE Transactions on Power Systems* 28 (1), 219–226. <http://dx.doi.org/10.1109/TPWRS.2012.2207467>.

# Characterization of forecast errors and benchmarking of renewable energy forecasts

9

*Stefano Alessandrini<sup>1</sup>, Simone Sperati<sup>2</sup>*

<sup>1</sup>National Center for Atmospheric Research (NCAR), Boulder, CO, United States; <sup>2</sup>Ricerca Sistema Energetico (RSE) SpA, Milano, Italy

## 9.1 Introduction

The scientific community has studied wind and solar power forecasting for a relatively short period, since the first papers on these topics have been published in the early 1980s (Brown et al., 1984; Jensenius and Cotton, 1981). Furthermore, most of the forecasting systems commonly adopted when focusing on the prediction period between 6 h and 7 days ahead are based on statistically postprocessing meteorological forecasts (generally wind and solar radiation). Thus, wind and solar predictions accuracy is strongly dependent on the meteorological forecasts quality, which is improving in the last decades. The main reasons for these improvements are the increasing computational power, a better quality and availability of meteorological observations, and the use of more effective data-assimilation techniques. For all these reasons, benchmark exercises involving the comparisons of different techniques of wind and solar power forecasting are important for understanding the state of the art and the developments of a recent and continuously evolving scientific topic.

In the literature, some comparisons between model performance and forecasting approaches dedicated to wind and solar power forecasting have been presented. For instance, in Zamo et al. (2014a) the authors propose a benchmark of solar photovoltaic (PV) forecasting statistical methods for hourly PV electricity production, while in Zamo et al. (2014b) the same authors analyze the performance of eight forecasting methods for probabilistic PV forecasting using predictors from an ensemble numerical weather prediction (NWP) system. Three independent validations of global horizontal irradiance (GHI) multiday forecasting models based on NWP are carried out in Perez et al. (2013). The validations were conducted in the United States, Canada, and Europe.

In Texier and Girard (2009) the authors show the results of a study regarding different wind power forecasting (WPF) services over the same period and on the same two-wind farms. In De Giorgi et al. (2014), different hybrid forecasting methods applied to wind power prediction are compared, evaluating the performances of least-squares support vector machine (LS-SVM) with wavelet decomposition and hybrid artificial neural network (ANN)-based methods.

Finally, in [Hong et al. \(2014\)](#) the authors present the results of the first Global Energy Forecasting Competition (GEFCom, 2012), which was based on wind power and electric load forecasting. An upgraded edition of GEFCom was launched in 2014 with additional topics such as solar power and electric price forecasting.

Furthermore, in recent years, two important projects were dedicated to the topic of benchmarking renewable energy forecasts. The first is European R&D project ANEMOS (ENK5-CT-2002-00665), which had the aim of improving the accuracy of short-term WPF technology ([Kariniotakis et al., 2004](#)). In the ANEMOS framework, 11 state-of-the-art models were run for 6 test cases across Europe with different terrain characteristics and evaluated under an appropriate protocol ([Madsen et al., 2005](#)). This can be considered as the first attempt carried out between 2003 and 2005, when this topic was still at its early stage in terms of popularity, to establish the average quality level of the most advanced wind power prediction systems at that time.

The second project is the European Cooperation in Science and Technology (COST) Action ES1002 Weather Intelligence for Renewable Energies (“WIRE”) organized with the scope of defining the requirements to be fulfilled by the weather information for forecasting wind and solar energy production in the short-term horizon (i.e., from 0 to 72 h ahead). WIRE organized a benchmark exercise aiming to validate the performance of a wide range of modeling approaches for both wind and solar generation forecasting ([Sperati et al., 2015](#)).

The results of these two last mentioned projects are presented and discussed.

## 9.2 ANEMOS benchmark

This section is intended to be a summary of what extensively reported in [Kariniotakis et al. \(2004\)](#) to allow a comparison with the more recent WIRE benchmark, which will be also described in the following sections.

### 9.2.1 Setup and data description

The ANEMOS benchmark exercise was carried out in the period 2003–2004 to establish the performance of the state-of-the-art wind-power predictions systems commonly adopted at that time. A common and appropriate evaluation protocol was adopted to evaluate the different models applied on different test cases across Europe. The results of this benchmark have been and still are an important reference for the scientific community and the private sector to compare the quality of the systems developed afterward.

The test cases include several years of measurements from six wind farms in different topographic conditions (offshore, flat, semicomplex, and complex terrain) and NWP from models such as Hirlam, Aladin, and Skiron. Prediction systems, such as Prediktor, Previento, Sipreolico, CENER’s LocalPred, applied on these test cases, were used by system operators for operational forecasting activity.

The wind farms selected for the benchmark are located in four different European countries and are reported in the following list with some technical details:

- The Wusterhusen wind farm is placed on flat-terrain (Ruggedness Index, RIX index = 0, [Mortensen et al., 2006](#)) in the northeastern part of Germany 20 and 8 km from the shoreline of the Baltic Sea in Germany; two turbines, total nominal power (NP) equal 2 MW. The data set covers the period from January 1, 1999 to December 31, 2000.
- The Alaiz wind farm is located in Spain (Pamplona area) in a very complex terrain with a rated capacity of 33.09 MW. The data set covers all of 2001 with NWP data as for the Sotavento wind farm. The RIX index is equal to 15.
- Sotavento wind farm is located in complex terrain (RIX index = 7) in Spain (Galicia region) with a large number of different turbines with a rated capacity ranging from 600 to 1320 kW. The total NP is 17.56 MW.
- The Klim wind farm is located in Denmark (Jutland). It consists of 35 Vestas V44 600 kW turbines with a total rated capacity of 21.0 MW. The data set covers a period from January 1, 1999 to April 30, 2003. The RIX index is equal to 0.
- The Tunø is an offshore wind farm situated 6 km of the east coast of Jutland (Denmark) with a total rated capacity of 5.0 MW. The measured data only consist of production data and cover a period from March 18, 2002 onto April 30, 2003. The RIX index is equal to 0.
- The Golagh wind farm is located in Ireland (Donegal County) and has rated capacity of 15.0 MW. Measured power data are available for a period from August 1, 2002 onto March 31, 2003. The RIX index is equal to 7.3.

Off-line power forecasts, built by using the same NWP input, were provided by 11 models. As already mentioned, the chosen wind farms represent a wide range of topographic conditions. In fact, one of the Spanish wind farms is placed in complex terrain, the second Spanish and the Irish wind farms are placed in semicomplex terrain, and the three remaining wind farms are all situated in simple terrain.

The available data for each wind farm include measured total production and NWP values of wind speed and wind direction interpolated to the site. For all the wind farms, detailed layout and contour and roughness maps have been collected together with the manufacturer's power and thrust curves of the turbines.

### **9.2.2 Forecast evaluation**

The following actions have been taken to appropriately compare different forecasting models:

- Common NWP for each test case
- Same wind farm measurements (power production, wind speed and direction)
- A training period and an independent test period defined for each test case. The evaluation presented hereafter refers to the selected test periods
- Predictions are calculated from the same initialization time (00 UTC) to compare model performances
- The performance metrics used for the evaluations are the following: Mean absolute error (MAE) normalized by the wind farm's NP (NMAE), determination coefficient ( $R^2$ ), and percentage of errors lower than 10% of the NP.

Hereafter we report an analysis of NMAE of the different forecasting models (indicated by a number) as a function of forecast lead time for each wind farm.

### 9.2.2.1 Wusterhusen test case (*Fig. 9.1*)

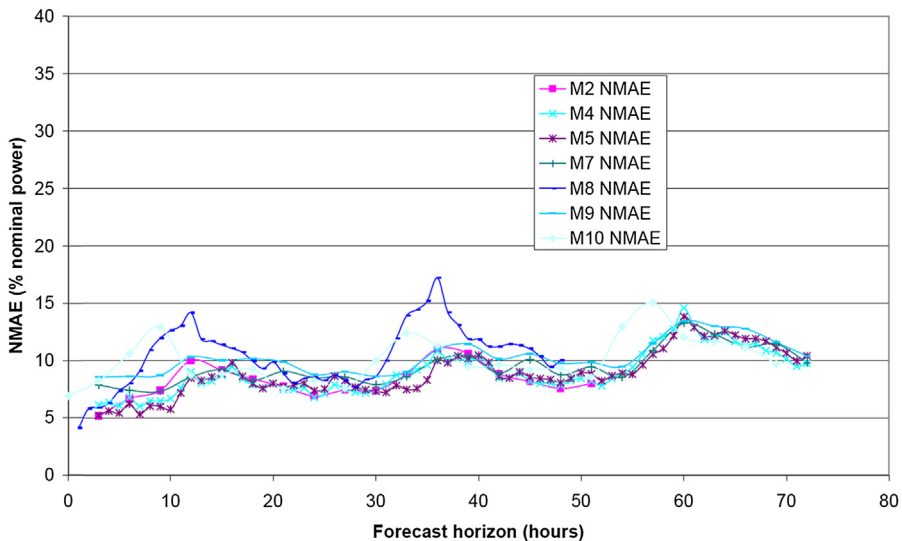


**Figure 9.1** Normalized mean absolute error (NMAE) for Wusterhusen test case by Kariniotakis et al. (2004).

All forecasting models exhibit an NMAE (except for model 8) lower than 15%. NMAE tends to increase with forecast lead time following a diurnal cycle with three maximum values at 12, 36, and 60 h. This is likely due to a lower predictability of the meteorological parameter at those hours. In fact, convective processes in the boundary layer are usually more enhanced during early afternoon hours. These processes are difficult to be correctly simulated by the numerical weather prediction models.

### 9.2.2.2 Alaiz test case (*Fig. 9.2*)

Alaiz test case is characterized by a high terrain complexity, as shown by the RIX value. The wind farm predictability is pretty low with values of NMAE, ranging from 20% to 35%. There is also a higher dispersion between different models. In fact, the lower wind farm's predictability enhances the influence of different models setup on the final accuracy.

### 9.2.2.3 Sotavento test case (*Fig. 9.3*)

Almost all the models show a peak of NMAE around 15 UTC; this can be again attributed to the presence of convective processes in the boundary layer.

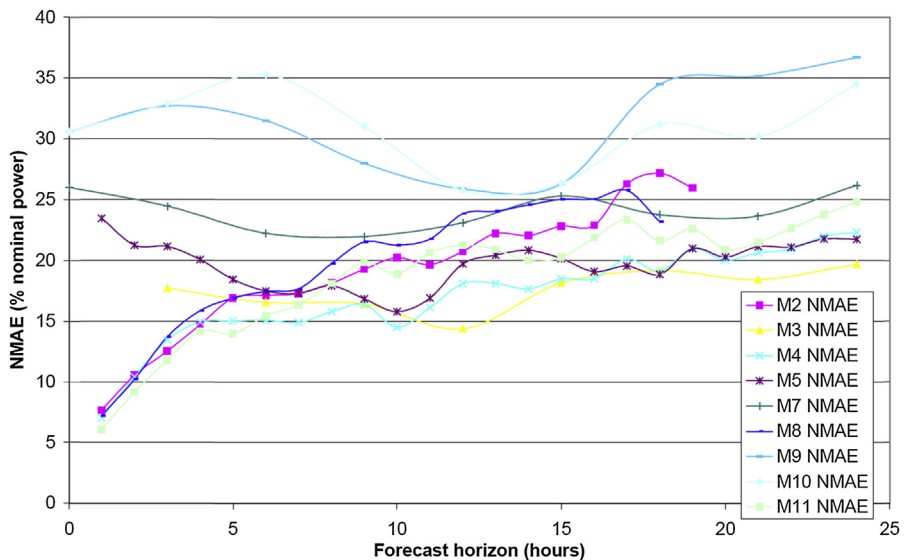


**Figure 9.2** Normalized mean absolute error (NMAE) for Alaiz test case by Kariniotakis et al. (2004).

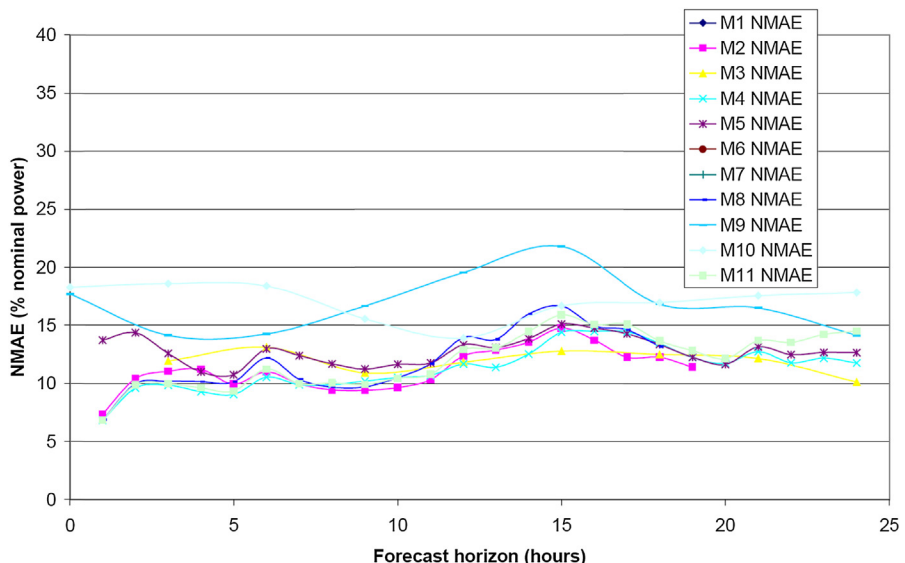


**Figure 9.3** Normalized mean absolute error (NMAE) for Sotavento test case by Kariniotakis et al. (2004).

### 9.2.2.4 Klim test case (Fig. 9.4)

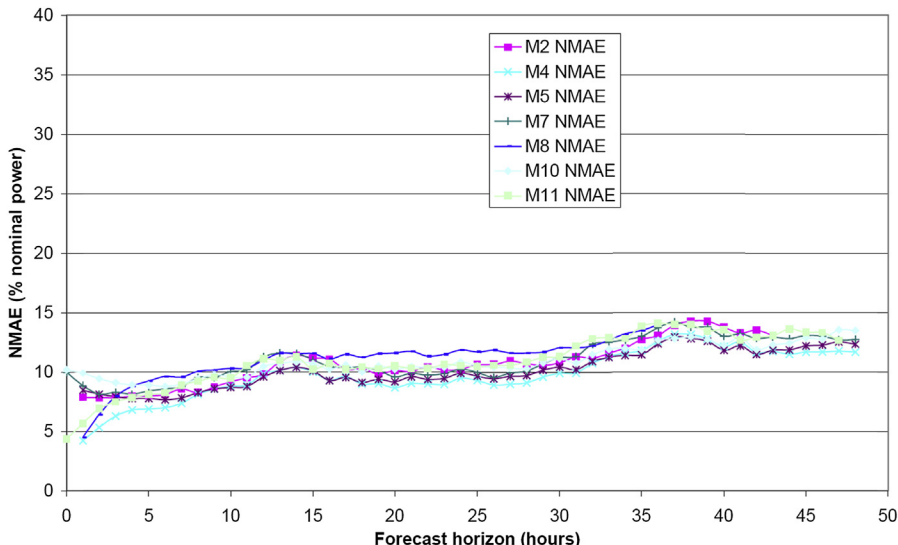


**Figure 9.4** Normalized mean absolute error (NMAE) for Klim test case by Kariniotakis et al. (2004).

The Klim wind farm shows the lower values of NMAE, below 15% for all forecast horizons; the different prediction models exhibit almost the same performances. Almost all the models show very similar performances.

### 9.2.2.5 Tunø Knob (offshore) test case (Fig. 9.5)

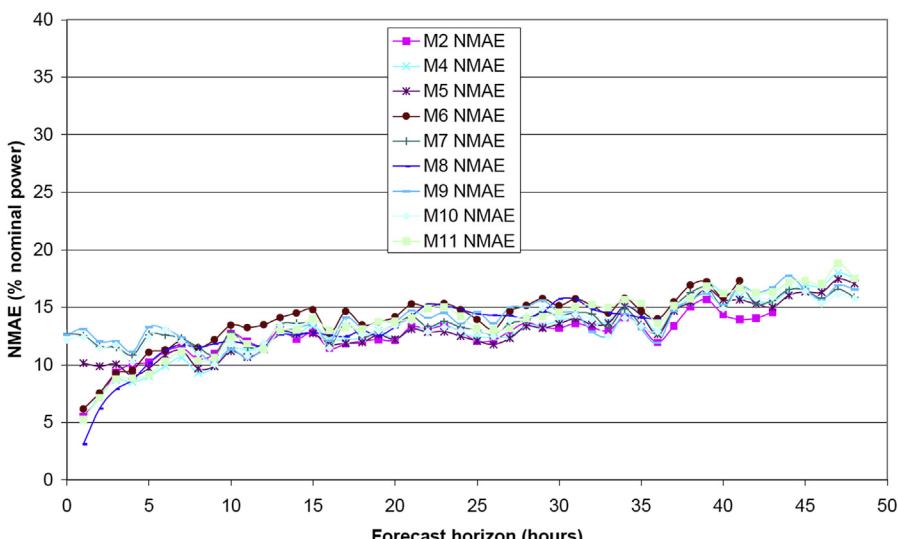


**Figure 9.5** Normalized mean absolute error (NMAE) for Tunø test case by Kariniotakis et al. (2004).

Low values of the NMAE with very low dispersion between the different prediction models can be seen. A constant increase of the NMAE with the forecast horizon is also clear.

### 9.2.2.6 Golagh test case (*Fig. 9.6*)

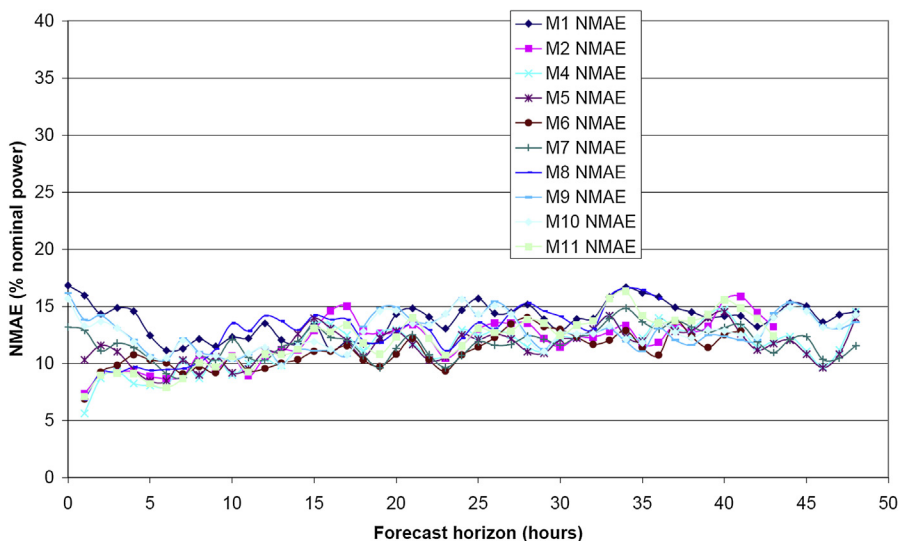


**Figure 9.6** Normalized mean absolute error (NMAE) for Golagh test case by Kariniotakis et al. (2004).

The NMAE values for the Golagh wind farm are less dependent on the forecast horizon than for the other wind farms. The range of variation of NMAE for 24 h horizon is 10%–16%, being comparable for longer forecast horizons.

The main evident conclusion coming out from these test cases is the strong dependence of predictability upon the terrain complexity. The performance of the prediction models is related to the complexity of the terrain. *Fig. 9.7* represents the average value of the NMAE for the 12 h forecast horizon as a function of RIX index, for each test case.

Higher RIX values correspond to higher values of NMAE. It is also demonstrated that offshore wind farms (Tunø Knob) do not necessarily guarantee a better predictability than wind farms on flat terrain in similar climatic conditions.

Different performances between test cases could also be attributed to the use of different prediction models. In fact, the NWP used in the test case has been provided by the meteorological services of the different countries (Germany, Spain, Denmark, and Ireland). However, some of the cases, Alaiz and Sotavento, have the NWP obtained with the same model and the increase of NMAE with RIX still appears.

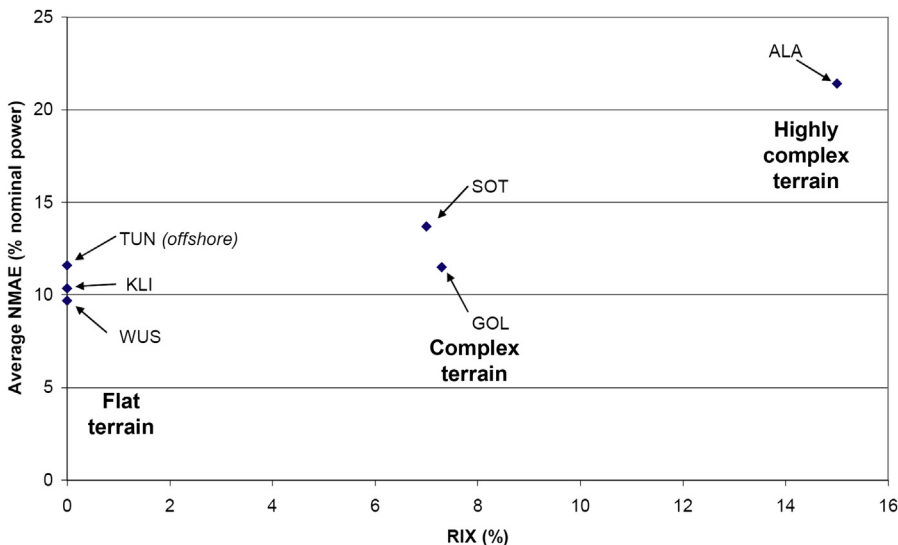


**Figure 9.7** Average normalized mean absolute error (NMAE) for 12 h forecast horizon versus RIX at each test case. Qualitative comparison over six wind farms: Tunø Knob (TUN), Klim (KLI), Wusterhusen (WUS), Sotavento (SOT), Golagh (GOL), Alaiz (ALA) by [Kariniotakis et al. \(2004\)](#).

## 9.3 WIRE benchmark

### 9.3.1 Setup and data description

The WIRE benchmark was organized with the scope of proposing a starting point toward the development of an international benchmarking platform, suitable for all possible applications in the renewable energy forecasting field. In fact, it was the first time that a wide range of both wind and solar, deterministic and probabilistic power forecasting techniques were evaluated under a common framework and compared on different, real test cases with varying topographical and meteorological conditions. This allowed understanding potential differences in the predictability of the two resources, which is information of primary importance for power system operators. Also, it was possible evaluating the improvements achieved by WPF technologies in the last 10 years, comparing the performances obtained with new techniques to those emerged from ANEMOS on the same case study.

The **WIRE benchmark** was announced in January 2013, setting a deadline for the submission of results at the end of June 2013. Overall, 33 participants from research institutions, meteorological services, or universities all over Europe applied for the exercise. Some applications came also from the United States, Australia, Japan, and India. A total of 18 submission were finally received, most of them only for the wind or PV part of the exercise and only a few for both. Three participants also decided to deliver probabilistic wind power forecasts.

Two wind farms and two PV plants were chosen as representative of different meteorological and topographical conditions. The Abruzzo wind farm is located in a complex terrain area in central Italy and has NP of about 100 MW, while Klim is an onshore wind farm located in Northern Denmark, in flat terrain, with NP equal to 21 MW. The two PV plants are both located in suburban areas of relatively large cities. The first one is located in Milano (Northern Italy) and the second one in Catania (Southern Italy), where solar irradiance availability is generally higher than in Northern Italy. Both plants are made with the same PV components and have NP of 5.21 kW. The location of each power plant is shown in Fig. 9.8.

The data sets covered a period of 1.5 or 2 years depending on the case. The organizers defined training and test periods for each one as shown in Table 9.1.

Full hourly power data were available to the participants for the training periods, while for the validation periods measured, data were masked for the first half of each month. Specifically, a 14-day masking with missing observations was imposed to reduce potential cheating attempts. The masked periods were then used for the evaluation, discarding forecasts received for the second half of each month. In this way, it was still possible for the participants to apply a rolling month by month retraining without having the possibility of adjusting and unfairly improve their predictions.

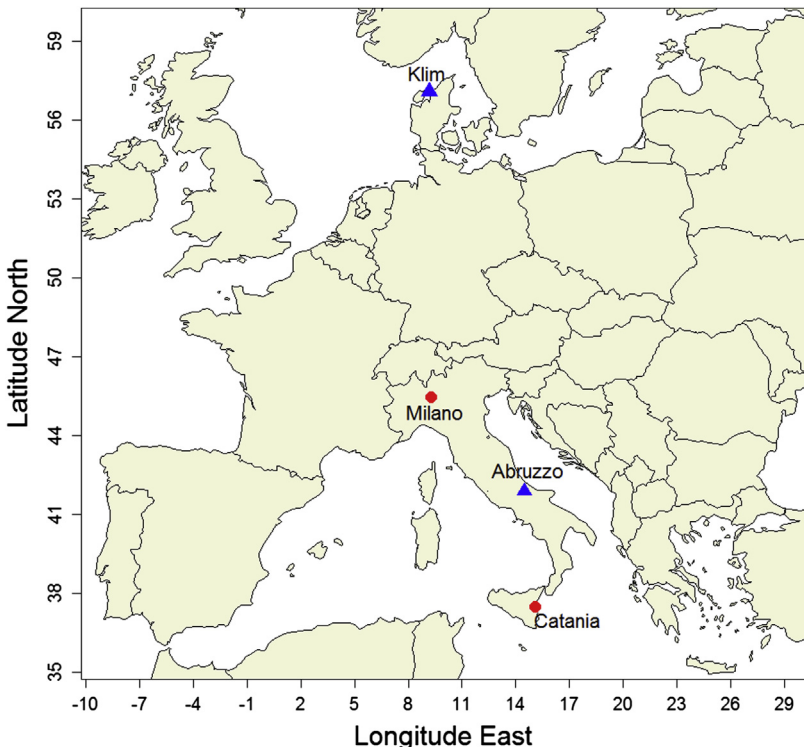


**Figure 9.8** Locations of the wind farms (triangles) and the photovoltaic plants (circles).

**Table 9.1 Training/test period definitions for the different data sets**

Power plant	Training period	Test period
Abruzzo	January 1–December 31, 2010	January 1–December 31, 2011
Klim	January 1–December 31, 2001	January 1–December 31, 2002
Milano	July 1–December 31, 2010	January 1–December 31, 2011
Catania	January 1–December 31, 2010	January 1–December 31, 2011

The organizers also provided forecast data. For Abruzzo, the participants were free to use meteorological data from the European Center for Medium-Range Weather Forecasts (ECMWF) deterministic model on the period between 0 and 72 h ahead runs starting at 12 UTC with 3-hourly frequency and 0.125 degrees horizontal resolution. The meteorological variables provided were wind speed and wind direction at 10 m height, temperature at 2 m height, boundary layer height, and mean sea level pressure. For Klim, the same meteorological data by the Danish HIRLAM model used in the frame of ANEMOS were provided. HIRLAM data have 0.15 degrees spatial resolution. The model was nested on the ECMWF meteorological fields, which served as initial and boundary conditions, performing a hourly, 0–48 h ahead run every 6 h (i.e., at 0, 6, 12, and 18 UTC). Wind speed, wind direction, and temperature were extracted at model levels 30 and 31 (i.e., corresponding to about 148 m and 30 m, respectively). The ECMWF deterministic model configuration at that time was TL511, with about 40 km spatial resolution. In both cases, data were interpolated at the wind farm position.

For Milano, forecast data of GHI, total cloud cover, and temperature at 2 m height were obtained by the ECMWF deterministic model and provided to the participants, along with measurements of GHI, direct normal irradiance, and T2M. The forecast runs were initialized at 12 UTC, with 3 h time-steps for the period 0–72 h ahead and a grid spacing equal to 0.125 degrees. Measured data of the same variables were provided for Catania, along with forecast data obtained using the regional atmospheric modeling system (RAMS) model (Pielke et al., 1992). RAMS was configured with two nested grids of 15 and 5 km horizontal resolution, respectively. The model was run starting at 0 UTC with hourly temporal resolution and nested on the 6 h ECMWF boundary fields with 0.125 degrees spatial resolution. Model parameterizations included the Harrington radiation scheme (Harrington, 1997) and activation of bulk microphysics to account for full moisture complexity.

### 9.3.2 Modeling approaches

The participants were free to use their own model data in addition to those provided by the organizers. All the modeling approaches used in the benchmark are reported in [Table 9.2](#).

**Table 9.2 List of all the forecasting methods used by the participants**

Wind	Photovoltaic	Wind (probabilistic)
Own meteorological model + Kalman filter, artificial neural network (ANN), and ensemble learning	WIRE model data + linear regression (random forest)	Own meteorological model + Kalman filter, ANN, and ensemble learning
Combination of HIRLAM and GFS + wake parameterization based on atmospheric stability + density corrected power curve + ANN	Own meteorological model + output correction using tendency of past production	WIRE data + conditional kernel density estimation with a quantile-copula estimator
WIRE data + nonlinear function approximation between wind speed and direction to wind power output	GFS + Model output statistics + conversion to power	WIRE data + local quantile regression using wind speed and wind direction as predictors
WIRE data + support vector machine (SVM)	WIRE data + SVM	
WIRE data + ANN	WIRE data + ANN	
WIRE data + power curve obtained by linear interpolation between fitting power values	Linear regression global horizontal irradiance—solar power	
Computational Fluid Dynamics model	WIRE data + quantile regression to estimate clear sky production, irradiation, and medium temperature + linear regression to explain clear sky production	
WIRE data + average of ensemble ANN initialized with different weights	WIRE data + linear regression model	
WIRE data + combination of time series and approximation	Combination of WIRE data and WRF ARW model using initial and boundary conditions from NCEP GFS + Gaussian generalized linear model	
Physical modeling and advanced statistical postprocessing + combination model applied on different prediction feeds		

*ARW*, Advanced Research *WRF*; *GFS*, Global Forecast System; *NCEP*, National Centers for Environmental Prediction; *WIRE*, Weather Intelligence for Renewable Energies; *WRF*, Weather Research and Forecasting.

### 9.3.3 Forecast evaluation

The ranking of the results was based on the MAE, which is expressed as follows:

$$\text{MAE} = \frac{1}{N} \sum_{i=1}^N |o_i - f_i|$$

where  $o_i$  is the  $i$ th observed value and  $f_i$  the  $i$ th forecasted value. MAE allows measuring the average error magnitude in the forecasts. Aiming to perform further evaluation of the best result and to check for statistically significant differences with the second best, the Diebold-Mariano (DM) test ([Diebold and Mariano, 2012](#)) was also computed. The DM test allows comparing the accuracy of two competing forecasts, testing the null hypothesis H0 (i.e., the two forecasts have the same level of accuracy) versus the alternative hypothesis H1 (i.e., the second result is actually less accurate than the first one). A resulting p value close or equal to one does not allow to draw conclusions and one simply cannot reject the null hypothesis, while very low p-values allow accepting H1. DM test was applied on the residuals, putting the data over all the lead times together.

Probabilistic forecasts were evaluated and ranked using the continuous ranked probability score (CRPS). The CRPS is a common verification index that compares a full probabilistic distribution with the observations, when both are represented as cumulative distribution functions (CDFs) ([Hersbach, 2002](#)), and it is expressed as follows:

$$\text{CRPS} = \frac{1}{N} \sum_{i=1}^N \int_{-\infty}^{\infty} \left( F_i^f(x) - F_i^0(x) \right)^2 dx$$

where  $F_i^f(x)$  is the CDF of the probabilistic forecasts for the  $i$ th value at each time-step and  $F_i^0(x)$  is the CDF of the measurements. CRPS is then the mean squared error of the cumulative distribution and can be reduced to the MAE for a deterministic forecast. The index was computed through numerical integration techniques based on a discretization of the forecast CDF. The CRPS is a negative-oriented score with the same dimension as the forecasted variable.

[Fig. 9.9](#) reports the results for the wind cases. For Abruzzo, the evaluation was carried out on 0–72 h ahead forecast lead times with 3-h time-steps. For Klim, hourly 0–48 h ahead forecasts were evaluated considering all four initialization times together. In both cases, MAE values were also calculated on the whole forecast range for the ranking and reported in the figure.

Except for some outliers, similar MAE trends are observed for both cases. Abruzzo shows significant differences between the lowest and the highest MAE, which span in about 4 or 5 MAE/NP percentage points, depending on the lead time. This is less evident for Klim, where lower dispersion of the error values is observed (i.e., about 1–2 MAE/NP percentage point, depending on the lead time).

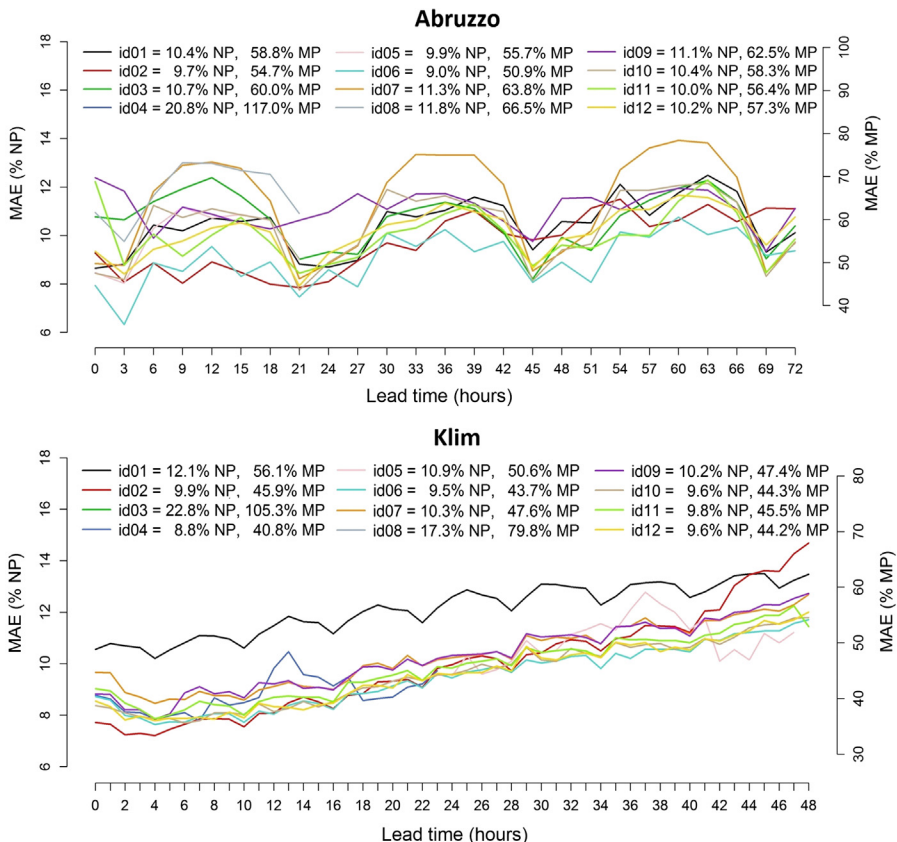


**Figure 9.9** Error trends of the 0–72 h ahead wind power forecasts starting at 12 UTC for Abruzzo (above) and of the 0–48 h ahead wind power forecasts starting at 0, 6, 12, and 18 UTC for Klim (below). The MAE/NP % and MAE/MP % are reported. *MAE*, mean absolute error; *MP*, mean power; *NP*, nominal power.

In both cases the best result was achieved by the same participant, who obtained a best score of 9.0% MAE/NP (50.9% MAE/MP) for Abruzzo and 9.5% MAE/NP (43.7% MAE/MP) for Klim. The outcome of 8.8% MAE/NP achieved by id04 for Klim was not considered, since the participant just provided forecasts for the 0–23 h ahead horizon without considering longer lead times. The DM test applied comparing the first two best results allowed rejecting the hypothesis of same forecast accuracy for both Abruzzo and Klim.

The winning forecasting method was based on using meteorological data provided by WIRE, followed by application of two statistical approaches combining ANNs and generalized linear models (GLMs) (Dobschinski, 2014). The two approaches were used separately to learn the nonlinear relation between the historical weather forecasts and the power measurements. The ANN consisted in a feedforward multilayer perceptron with one hidden layer and was optimized with the Levenberg–Marquardt

algorithm. In the GLM, a logit function was applied as a link function, and the response variable (i.e., wind power) was assumed to be binomially distributed. Wind power production data were normalized between 0 and 1 by division with NP. All the meteorological forecasts were standardized and used as model input together with information about the time of day. ANN and GLM used the same set of input data. Before training the models, power data was filtered manually with respect to nonplausible values. The outputs of the ANN and GLM were finally averaged to get a wind power forecast for each wind farm.

Overall, Abruzzo is characterized by a strong daily cycle of power production, which is not observed at Klim. Higher errors during evening and night hours at Abruzzo are due to higher production during those hours. In fact, the average wind power at 0 UTC was 6% higher than that at 12 UTC. The more defined increase of NMAE over lead time observed at Klim is probably related to the kind of error characterizing the meteorological forecasts. Being located on flat terrain, the meteorological forecasts for Klim are affected by lower representativeness errors (e.g., bad representations of topography, land use, kinematic winds etc.), which on the contrary are higher for complex-terrain sites such as Abruzzo. These kinds of error mask those caused by the decreasing predictability of the atmospheric flows over lead time more at Abruzzo than at Klim.

Solar power results were computed on forecast data filtered using solar elevation, discarding those in correspondence of lead times with solar height equal to zero. For Milano, an additional filter was imposed to discard a small set of unphysical power values in the test period. The results for Milano and Catania are reported in Fig. 9.10. Forecasts for Milano were evaluated for the 3–72 h ahead horizon with 3-hourly time-steps, while for Catania hourly forecast data from 1 to 72 h ahead were considered.

Most of the forecasting models show common trends with forecast errors reaching their peaks at 12 UTC of each forecast day. The differences between the error values are higher in Catania, where they reach about 5% MAE/NP. Also in this case the best result was achieved by the same participant, with 7% MAE/NP (26% MAE/MP) for Milano and 5.4% MAE/NP (14.8% MAE/MP) for Catania. The winning method was based on using WIRE meteorological data as input, applying then a quantile regression to estimate a clear sky production, a clear sky irradiance, and a medium temperature following Bacher et al. (2009). A linear regression was also applied to explain the rate of observed clear sky production. For Catania the participant applied an additional step of performing a bias correction with a quantile regression, based on the lead time and forecasted power. This last step was not applied to the Milano case due to the reduced amount of available data. For both solar cases the DM test applied for comparison with the second best result returned p values close to 1, making it difficult to state whether one model was actually more accurate than the other one. Looking at Fig. 9.10, one could notice that solar power forecasting error trends are strongly dependent on the daily cycle. This is due to the solar elevation trend that partly masks lead time-dependent errors. Also, the meteorological model's skill in forecasting solar irradiance and cloud coverage is not strongly dependent on lead time, and this is reflected on the power predictions.

Probabilistic forecasts were provided by few participants for the wind test cases, in terms of quantiles of the wind power probability density function (PDF) with 3-h

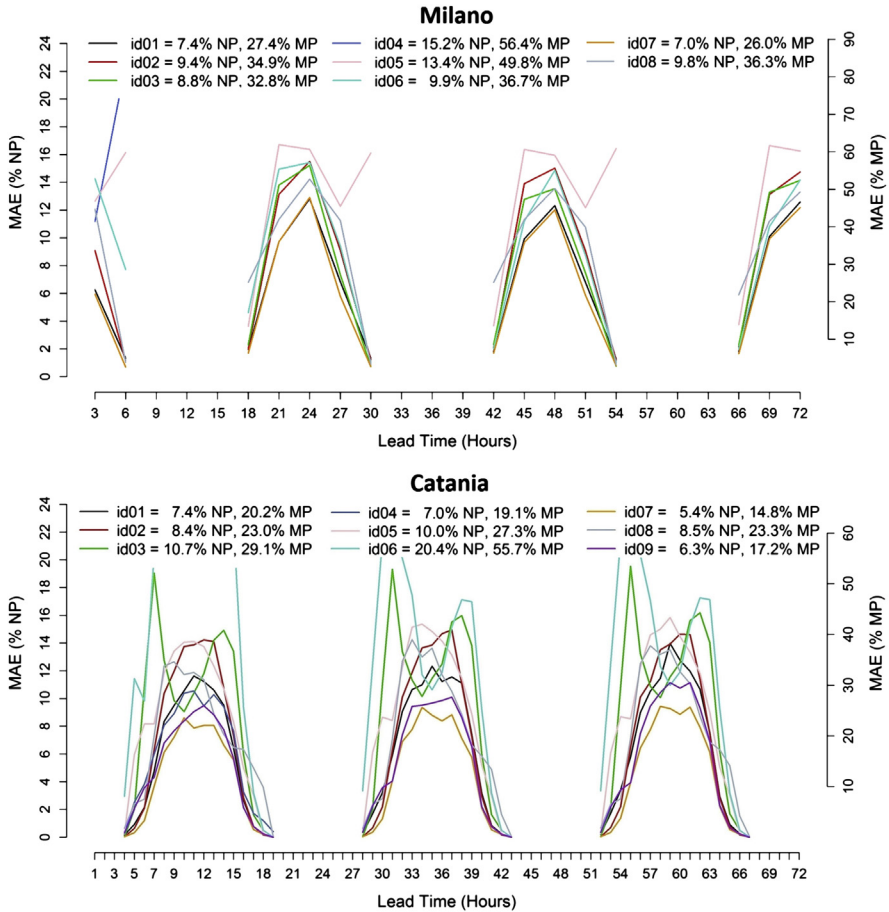


**Figure 9.10** Error trends of the 3–72 h ahead solar power forecasts starting at 12 UTC for Milano (above) and of the 1–72 h ahead solar power forecasts starting at 0 UTC for Catania (below). The MAE/NP % and MAE/MP % are reported. *MAE*, mean absolute error; *MP*, mean power; *NP*, nominal power.

time-steps. For Abruzzo, two participants provided 19 quantiles from 5% to 95%, while the third one provided nine quantiles from 10% to 90%.

Fig. 9.11 shows the CRPS as a percentage of NP and MP, calculated at each of the 3-hourly, 0–72 h ahead time-steps for the Abruzzo case and at each 3-hourly, 0–48 h ahead intervals for Klim.

The results reflect what was observed in the deterministic evaluation. In fact, a significant diurnal cycle is evident for Abruzzo, showing better scores during morning hours. For Klim the trend is instead more linear.

Bootstrap confidence bars are added on the winning error trends for each test case to check for statistically significant differences between the models. In the case of Abruzzo, for most of the time-steps the winning model does not appear significantly

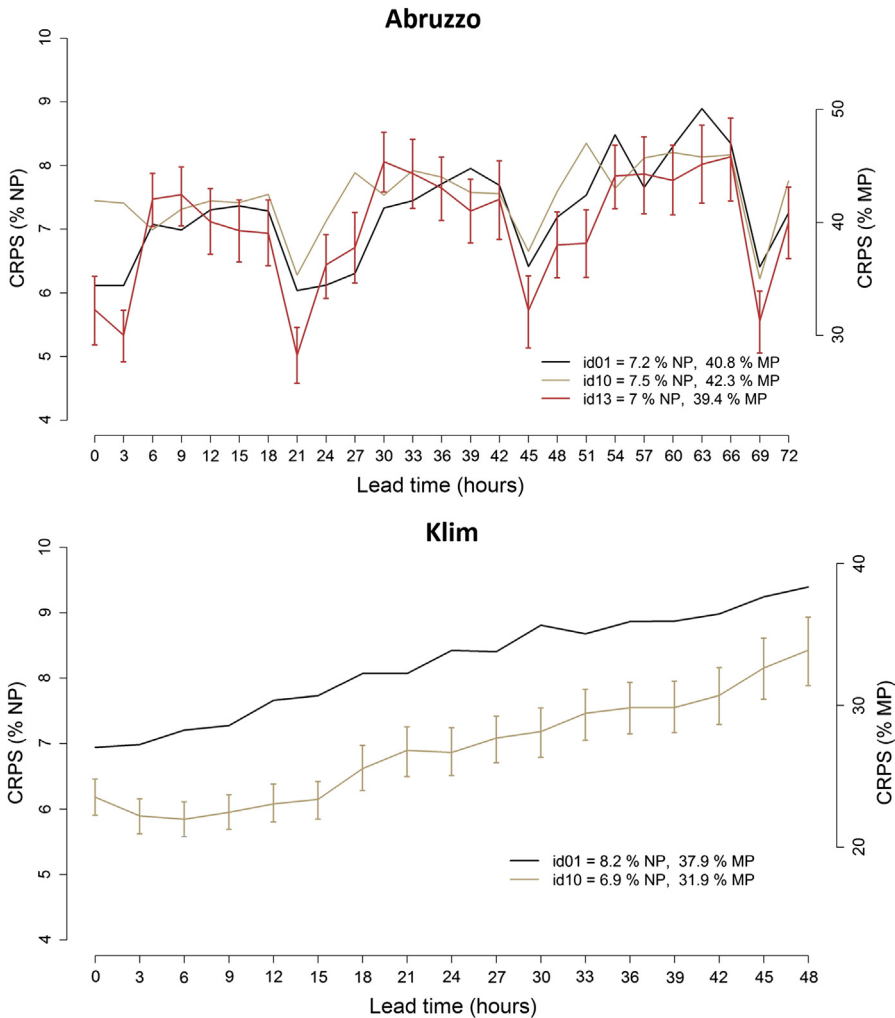


**Figure 9.11** Continuous ranked probability score (CRPS) trends of the 0–72 h ahead probabilistic wind power forecasts starting at 12 UTC for Abruzzo (above) and of the 0–48 h ahead probabilistic wind power forecasts starting at 0, 6, 12 and 18 UTC for Klim (below). The CRPS/NP % and CRPS/MP % are reported. *MP*, mean power; *NP*, nominal power.

better than the others, in particular during the worst performance periods during night hours. For Klim, on the contrary, the differences between the two models are statistically significant for every lead time. The winning method used on Abruzzo was a local quantile regression with wind speed and wind direction as predictors (Bremnes, 2004). On Klim, conditional kernel density estimation with a quantile-copula estimator was applied, using forecasted wind speed and direction, hour of the day, and forecast lead time as inputs (Bessa et al., 2012). 5%–95% quantiles were computed from the forecasted PDF using numerical integration.

### 9.3.4 Comparison with ANEMOS benchmark and high-resolution model run

Deterministic forecast data for the Klim wind case are the same used back in 2002 by the ANEMOS benchmark. At that time, the horizontal resolution of the HIRLAM model was equal to 0.15 degrees. HIRLAM was nested on the ECMWF boundary conditions fields with 0.5 degrees resolution. Fig. 9.12 shows a comparison between the new results obtained during the WIRE benchmark and the results obtained in (Kariniotakis et al., 2004). It should be noticed that the amount of available data in (Kariniotakis et al., 2004) was higher. In fact, the training period consisted of 2 years of data and forecast evaluation was performed on a subsequent 2-year period. In Fig. 9.12, it is possible observing the MAE as a function of forecast lead time of the two best forecasts from the ANEMOS benchmark and the WIRE one. In this comparison data for lead time 0 are missing, in fact it was not evaluated at that time.

The diagram shows that B1 and B2 (i.e., the best forecast of the WIRE benchmark) are generally better in terms of MAE than A1 and A2 (i.e., the best forecasts issued for the ANEMOS benchmark). This happens in particular for the forecast horizon from 24 to 48 h ahead. Also, during ANEMOS, some participants used models with autoadaptive capabilities, which can benefit, e.g., from using available online data. This is evident looking at the behavior of A1, which outperforms the others up to 5 h ahead. The performance of A1 degrades then at longer lead times, remaining lower (higher MAE) than those of B1 and B2. This is likely due to improvements in the statistical postprocessing methods adopted by B1 and B2.

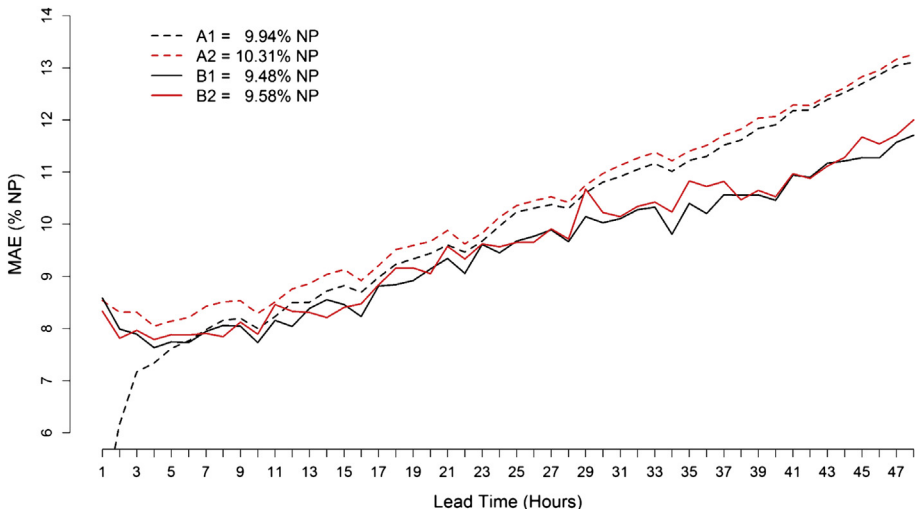


**Figure 9.12** Comparison between new and old results in term of MAE/NP as a function of forecast lead time (1–48 h ahead) for the wind power forecasts issued at 0, 6, 12, and 18 UTC for the Klim test case. A1, A2 and B1, B2 are the best two forecasts of the ANEMOS benchmark and the Weather Intelligence for Renewable Energies benchmark, respectively. MAE, mean absolute error; NP, nominal power.

In addition, aiming to investigate the potential improvement achievable by using higher resolution forecasts for the same power plant, the organizers performed a new forecast run using RAMS. These forecasts were not provided for the exercise and were only used for comparison. In this case, ECMWF reforecast data with 0.25 degrees horizontal resolution were retrieved for the same 2-year period. The RAMS run was started at 12 UTC using two nested grids with horizontal resolution of 12 km and 4 km, respectively. Hence, both boundary conditions and the limited-area model were run at a higher resolution than in 2003. The organizers applied a post-processing system based on ANN on both RAMS and HIRLAM outputs. In this way, the postprocessing model was similar to the one used by the winner in the WIRE benchmark except for the GLM part. For this test the organizers maintained the same conditions imposed on the participants (i.e., missing data for the first 14 days of each month of the test period). In Fig. 9.13 the results obtained by all participants are shown in gray. The dashed line refers to the model chain RAMS + ANN, and the black line is the error trend of HIRLAM + ANN.

RAMS + ANN shows an overall improvement over the best result emerged from the benchmark, obtaining an MAE/NP about 5% smaller. HIRLAM + ANN showed similar results to those of the other participants.

Also, the DM test returned a very low p value and thus allowed rejecting the null hypothesis. The result of RAMS + ANN demonstrate the benefits of using higher spatial resolution forecasts, both for the boundary conditions (which have improved in the last 10 years because of continuous developments to the ECMWF deterministic model) and for the limited-area model.

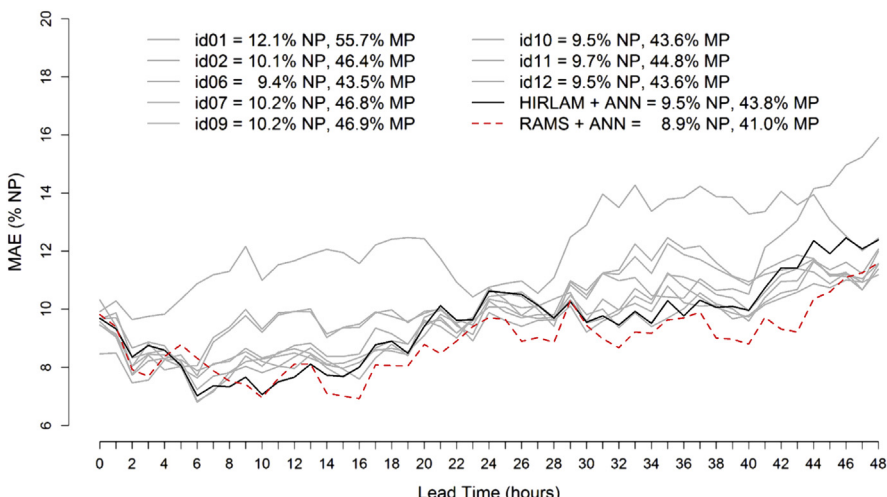


**Figure 9.13** Error trends of the 0–48 h ahead wind power forecasts starting at 12 UTC for the Klim test case. The MAE/NP % and MAE/MP % are reported. ANN, artificial neural network; MAE, mean absolute error; MP, mean power; NP, nominal power; RAMS, regional atmospheric modeling system.

## 9.4 Discussion and conclusions

In this chapter we have summarized the results of the ANEMOS benchmark exercise (carried out in 2003) and of the WIRE benchmark (carried out in 2013).

The ANEMOS benchmark was the first model competition for wind power prediction in Europe. NWP models were providing wind (speed and direction) forecast at each wind farm. Statistical postprocessing techniques were able to compute wind power forecast by using time series of past forecast and power observations. One of the main findings of the exercise is the dependence of the accuracy of power predictions on complexity of the terrain. For complex terrain, higher NMAE values above 35% for 24 h horizon and higher dispersion of the prediction model errors were obtained. In flat terrain NMAE values were below 10% for 24 h horizon. The performances on offshore wind farms were pretty similar to those of wind farms located on flat terrain in a similar climatology. In every test case a different prediction model obtained the best performance. This means that it is quite hard to define a general rule or a specific forecasting system to obtain the best performance on every test case.

The WIRE benchmark gathered contributions from a wide range of countries. For wind power, the best result reported a 9.0% MAE/NP (50.9% MAE/MP) on the Abruzzo test case, on a 0–72 h ahead forecast horizon. On the Klim case, a 9.5% MAE/NP (43.7% MAE/MP) was observed on a 0–48 h ahead forecast range. As previously stated, the two power plants are highly different in terms of topography and climatology. Abruzzo lies in a complex-terrain site in central Italy, while Klim in a flat-terrain site in Northern Denmark. Subsequently, wind energy is, in principle, more easily predictable on Klim. Furthermore, the representativeness errors of the meteorological model, mainly due to the more complex topography of Abruzzo, mask the decreasing predictability associated with the increasing forecast lead time. As a consequence, the average MAEs obtained by the participants on the first and on the third day ahead look quite similar. However, it should be considered that the meteorological data provided for the Klim case were generated back in 2001 and 2002. The MAE/NP obtained for Abruzzo, using more recent ECMWF global model data with 0.125 degrees resolution for a complex-terrain site, followed by an effective postprocessing system, appeared slightly lower than what was achieved for Klim. However, the Klim wind farm has a higher load factor than Abruzzo, and subsequently the resulting MAE/MP value was around 7% lower for Klim.

The results for Klim are similar to those obtained during the ANEMOS benchmark. A comparison between the WIRE benchmark and the results shown in ([Kariniotakis et al., 2004](#)) indicate that some improvements in the statistical postprocessing techniques have been achieved since 2003. The problem of having less recent and lower spatial resolution forecast data for Klim was investigated performing a higher resolution RAMS model run using ECMWF reforecasts data with 0.25 degrees horizontal resolution as boundary conditions. Then, a postprocessing system based on an ANN was applied. The results showed an improvement over the best result of the WIRE benchmark of 5.3% MAE/NP. The same postprocessing was also applied on the HIR-LAM data for comparison, showing MAE/NP values similar to those obtained during

the exercise. This allowed concluding that in the Klim case, a source of improvement with respect to past forecasting systems, is given by an increase in horizontal resolution of both the boundary conditions and the limited-area model. Also, better accuracy achieved by the ECMWF forecast system in the last 10 years, not only related to the spatial resolution, but also to other model developments should be considered.

For solar power, the best result reported a 7.0% MAE/NP (26% MAE/MP) on the Milano case, for the 3–72 h ahead forecast range and a 5.4% MAE/NP (14.8% MAE/MP) on Catania, for the 1–72 h ahead forecast horizon. Also in this case the power plants are located in areas with different predictability conditions. The Milano power plant is influenced by higher levels of pollution from the surrounding suburban area, where the presence of aerosol particles influences solar radiation intensity at the ground. Catania is located in Sicily, where the average solar irradiance intensity is usually higher than in Northern Italy. In fact, the average GHI measured at the Milano power plant for the whole test period was equal to  $165.6 \text{ W/m}^2$ , while  $203.7 \text{ W/m}^2$  were measured in Catania. As a consequence, Catania shows better predictability conditions. The role of the Etna volcano is, however, relevant for Catania in terms of releasing volcanic ash, which may influence the power production and are difficult to consider in a forecasting system. Furthermore, concerning Milano, the lower availability of data should be taken into account.

Solar energy appears overall more predictable than wind energy, as demonstrated by lower error values especially for Catania. This is due to higher predictability of the solar radiation forcing in clear sky conditions. The higher predictability for solar PV farms compared to wind farms could not be generally confirmed for other climatic conditions, i.e., Northern Europe where the frequency of cloudy days could be higher than in Milano and Catania.

The outcome of the probabilistic forecasting part of the WIRE benchmark, where just a few submissions were received, could be considered as a still limited capability of the community to produce this kind of forecasts. Anyway, the results were coherent with those of the deterministic application in term of performance quality dependence with the terrain complexity.

Finally, the impression is that a substantial source of improvement of renewable power forecasts in the last 10 years should be attributed to the NWP. In fact, testing the same postprocessing technique on older lower spatial resolution and on newer higher spatial resolution meteorological data allowed getting better results. It is tricky to draw certain conclusions from a single test case; however, an increase in model performance due to higher resolution and better accuracy appears reasonable. Also, improvements in the statistical modeling seem plausible, as noticeable by the comparison with previous applications on the same model data. Regarding the different modeling techniques, in the case of wind power the most effective methods proved to be based on machine learning algorithms, which can be applied effectively to deal with nonlinear relations between weather parameters and power production. Fewer participants applied machine learning techniques in the solar forecasting contest, where linear regressions were most used. In particular, quantile regression provided the best performances despite requiring low computational efforts.

## References

- Bacher, P., Madsen, H., Nielsen, H.A., 2009. Online short-term solar power forecasting. *Solar Energy* 83, 1772–1783.
- Benchmarking Exercise on Short-Term Forecasting Models for Renewable Generation. Available online: [http://www.wire1002.ch/fileadmin/user\\_upload/Documents/ES1002\\_Benchmark\\_announcement\\_v6.pdf](http://www.wire1002.ch/fileadmin/user_upload/Documents/ES1002_Benchmark_announcement_v6.pdf).
- Bessa, R.J., Miranda, V., Botterud, A., Zhou, Z., Wang, J., 2012. Time-adaptive quantile-copula for wind power probabilistic forecasting. *Renewable Energy* 40, 29–39.
- Bremnes, J.B., 2004. Probabilistic wind power forecasts using local quantile regression. *Wind Energy* 7, 47–54.
- Brown, B.G., Katz, R.W., Murphy, A.H., 1984. Time series models to simulate and forecast wind speed and wind power. *Journal of Climate and Applied Meteorology* 23 (8), 1184–1195.
- De Giorgi, M.G., Campilongo, S., Ficarella, A., Congedo, P.M., 2014. Comparison between wind power prediction models based on wavelet decomposition with least-squares support vector machine (LS-SVM) and artificial neural network (ANN). *Energies* 7, 5251–5272.
- Diebold, F.X., Mariano, R.S., 2012. Comparing predictive accuracy. *Journal of Business & Economic Statistics* 13, 253–265.
- Dobschinski, J., November 2014. How good is my forecast? Comparability of wind power forecast errors. In: Proceedings of the 13th International Workshop on Large Scale Integration of Wind Power into Power Systems as Well as on Transmission Networks for Offshore Wind Farms, Berlin, Germany, pp. 11–13.
- Harrington, J.Y., 1997. The Effects of Radiative and Microphysical Processes on Simulated Warm and Transition-Season Arctic Stratus (Ph.D. thesis). Colorado State University, Fort Collins, CO, USA.
- Hersbach, H., 2002. Decomposition of the continuous ranked probability score for ensemble prediction systems. *Weather and Forecasting* 15, 559–570.
- Hong, T., Pinson, P., Fan, S., 2014. Global energy forecasting competition 2012. *International Journal of Forecasting* 30, 357–363.
- Jensenius, J., Cotton, G.F., 1981. The development and testing of automated solar energy forecasts based on the model output statistics (MOS) technique. In: 1st Workshop on Terrestrial Solar Resource Forecasting and on Use of Satellites for Terrestrial Solar Resource Assessment, Washington, DC.
- Kariniotakis, G., Martí, I., Casas, D., Pinson, P., Nielsen, T.S., Madsen, H., Giebel, G., Usaola, J., Sanchez, I., Palomares, A.M., et al., November 2004. What performance can be expected by short-term wind power prediction models depending on site characteristics?. In: Proceedings of the European Wind Energy Conference (EWEC), London, UK, pp. 22–25.
- Madsen, H., Pinson, P., Kariniotakis, G., Nielsen, H.A., Nielsen, T.S., 2005. Standardizing the performance evaluation of short-term wind power prediction models. *Wind Engineering* 29, 475–489.
- Mortensen, N.G., Bowen, A.J., Antoniou, I., February 2006. Improving WAsP predictions in (too) complex terrain. In: Proceedings of the 2006 European Wind Energy Conference and Exhibition. EWEA.
- Perez, R., Lorenz, E., Pelland, S., Beauharnois, M., Knowe, G.V., Hemker Jr., K., Heinemann, D., Remund, J., Muller, S.C., Traunmuller, W., Steinmauer, G., Pozo, D., Ruiz-Arias, J.A., Lara-Fanego, V., Ramirez-Santigosa, L., Gaston-Romero, M., Pomares, L.M., 2013. Comparison of numerical weather prediction solar irradiance forecasts in the US, Canada and Europe. *Solar Energy* 94, 305–326.

- Pielke, R.A., Cotton, W.R., Walko, R.L., Tremback, C.J., Lyons, W.A., Grasso, L.D., Nicholls, M.E., Moran, M.D., Wesley, D.A., Lee, T.J., et al., 1992. A comprehensive meteorological modeling system—RAMS. *Meteorology and Atmospheric Physics* 49, 69–91.
- Sperati, S., Alessandrini, S., Pinson, P., Kariniotakis, G., 2015. The “weather intelligence for renewable energies” benchmarking exercise on short-term forecasting of wind and solar power generation. *Energies* 8, 9594–9619.
- Texier, O., Girard, N., March 2009. Wind power forecasting: a practical evaluation study of different wind power prediction services. In: Proceedings of the European Wind Energy Conference and Exhibition, Marseille, France, pp. 16–19.
- Zamo, M., Mestre, O., Arbogast, P., Pannekoucke, O., 2014a. A benchmark of statistical regression methods for short-term forecasting of photovoltaic electricity production, part I: deterministic forecast of hourly production. *Solar Energy* 105, 792–803.
- Zamo, M., Mestre, O., Arbogast, P., Pannekoucke, O., 2014b. A benchmark of statistical regression methods for short-term forecasting of photovoltaic electricity production, part II: probabilistic forecast of daily production. *Solar Energy* 105, 804–816.

# Wind power in electricity markets and the value of forecasting

10

Nicoló Mazzi<sup>1</sup>, Pierre Pinson<sup>2</sup>

<sup>1</sup>University of Padova, Padova, Italy; <sup>2</sup>Technical University of Denmark, Kgs. Lyngby, Denmark

## 10.1 Introduction

Forecasts are to be used as input to decision-making. Today, when it comes to renewable energy generation, such decisions are increasingly made in a liberalized electricity market environment, where future power generation has to be offered through contracts and auction mechanisms, hence based on forecasts. Taking the example of the European Nordic region, in 2014 around 84% of all electricity exchanges were made through Nord Pool. These markets were mainly designed considering the needs of conventional plants which, due to a limited flexibility, have to settle in advance on their production schedule.

Since renewable energy sources are to eventually participate in market mechanisms under the same rules than that for conventional generators, mismatches between contracted generation and actual deliveries may induce financial penalties. Indeed, the energy production from wind and solar power plants can be predicted with a limited accuracy that degrades with further lead times. This, in addition to uncertainties in market prices, yield uncertain market returns. However, even under such high levels of uncertainty, renewable energy producers may make optimal use of all information available, either in a deterministic or probabilistic form. It is our aim here to describe these processes of decision-making in electricity markets based on forecast information, also allowing to assess the value of various types of forecasts perceived by market participants.

Such problem of participation of renewable energy producers in electricity markets has received increasing attention over the last decade, mainly considering the case of wind power generation. One of the very first work in that field was that of [Bathurst et al. \(2002\)](#), which showed that, even using naive models for wind power forecasts, the expected profit can be increased by means of risk analysis. Consequently, many alternative and complementary proposals were made for obtaining optimal participation strategies and to assess the value of probabilistic forecast information in electricity markets. For instance, the aim of [Bremnes \(2004\)](#) was to show that one could find an optimal quantile forecasts that would be the best forecasts to use for market participation. This naturally justified the idea of further developing probabilistic forecasting methods, so as to be able to obtain such optimal quantiles. Focusing on expected revenue maximization and risk management, [Pinson et al. \(2007\)](#) gave analytical expressions for the optimal amount of contracted energy based on probabilistic forecasts, by

giving focus on the utility function of market participants. As a bridge between forecast quality and value in electricity markets, Bitar et al. (2012) presented an extensive analysis on this topic, highlighting the link between the expected profit and quality measure for the input wind power forecasts.

Our aim here is to describe the framework of market participation for renewable energy producers and to show how forecasts information directly translates to market value for these participants. As a basis for the development and discussion, we will consider the case of wind power producers, though similar developments could be made for solar power. This chapter is structured as follows. Section 10.2 introduced the reader to the basic concepts of competitive electricity markets, focusing on their structure and underlying timeline. These concepts are translated into equations in Section 10.3, by formulating the market revenue of wind power producers. Section 10.4 presents different offering strategies that a market participant may apply, depending on the available information of future wind power production. Then, in Section 10.5, the different trading strategies are tested and compared in a case study. Finally, conclusions are drawn in Section 10.6.

## 10.2 Electricity market context

Over the last decades, power systems moved from a centralized organization to new frameworks that aim to enhance competition. Initially, state-owned and vertically integrated companies were in charge of the management of the whole power system, from generation to retail. Then, aiming in privatizing the electricity supply sector and attracting new investors, deregulation processes have occurred worldwide. The key feature of the processes was the separation between activities of generation, transmission, distribution and retail, while banning the vertical integration among different sectors. Competition has been promoted mainly in generation and retail, while the transmission sector is still a natural monopoly, because of the prohibitive investment cost of transmission lines. The essential role of operation and management of the transmission grid is carry out by noncommercial entities, called transmission system operator (TSO) in Europe and independent system operator (ISO) in the United States.

The aim of this section is to introduce the reader to the concepts of electricity markets and their timeline. It is structured as follows. Section 10.2.1 presents the general structure of electricity markets, distinguishing between futures markets and electricity pools. Sections 10.2.2, 10.2.3 and 10.2.4 present the main trading stages of an electricity pool, i.e., day-ahead, intraday, and balancing markets, respectively.

### 10.2.1 Overview of various markets and their timeline

In electricity markets, two different trading floors are typically available, depending on the proximity of the trading. Medium/long-term markets (i.e., futures markets) allow trading on long-term horizons. The market participants can trade both physical and financial products, those by mean of forward contracts and options. A forward contract is signed between a seller who undertakes to produce a certain amount of energy

and a buyer who consumes that energy. Forward contracts are usually standard products, e.g., base load contracts include all the hours of the contracted time span, whereas peak load contracts only hours with high demand, typically from 8 a.m. to 7 p.m. of working days. Forward contracts can be associated with options. An option allows the buyer to decide after the agreement whether to benefit or not of the forward contract.

Differently, short-term markets (i.e., electricity pools) allow the trading of electricity on a daily and hourly horizon. Generally, they include several trading floors, i.e., day-ahead, intraday adjustment, and balancing market. Power producers can participate both in futures market and electricity pools. Usually a part of the capacity of thermal plants is contracted in medium/long contracts, since these ensure fixed revenues for the producers, avoiding the uncertainties of short-term trading. Remaining capacity is usually contracted in electricity pools. Contrariwise, renewable energy plants, e.g., wind farms and solar plants, have a stochastic nature and can be predicted with a limited accuracy. Therefore, they are not suitable for long-term contracts, as it is hard to guarantee a certain level of production, long time before the real-time operation. In this section we will focus on the participation of stochastic producers in electricity pools, neglecting futures market.

### **10.2.2 Day-ahead market mechanism**

The day-ahead market hosts transactions for selling and buying electric energy 1 day prior to delivery day. Buyers and sellers submit their offers to a market operator, which acts as central counterpart. A market offer includes a quantity of energy and the price at which the market participant is willing to contract this amount of energy. In case of sell/buy offers/bids, the price denotes the minimum/maximum price at which the seller/buyer is willing to provide/consume electricity. All sell offers are ranked in price-increasing order, to build a cumulative selling curve. The cumulative buying curve is carried out similarly, by ordering buy bids in price-decreasing order. The intersection between the two curves identifies the market-clearing price and volume. All the offers on the left of the clearing volume are accepted, while all the offers on the right are rejected. Accepted offers/bids are, generally, remunerated at the clearing price, disregarding the offer/bid price.

The day-ahead market gate closure occurs the day before the delivery day, usually at 12 a.m. The day-ahead market includes 24 separate auctions, one per each hour of the day. After the gate closure the market operator clears the market and informs each seller/buyer of their production/consumption schedule.

### **10.2.3 Intraday adjustment and continuous trading**

The intraday market is the market for sale/purchase energy during the day of delivery. It opens after the day-ahead market gate closure and closes from hours to minutes prior to energy delivery. Intraday market can be a useful tool for market participants to adjust their positions. Conventional producers may access the market to fix an infeasible schedule, since intertemporal constraints (e.g., ramping constraints) cannot, usually, be directly included in the market offers. On the other hand, stochastic producers can use this additional trading floor to modify their market position as their forecasts

may be more accurate, closer to real-time operation. Trading in the intraday market is, generally, continuous. The negotiation mechanism is based on automatic matching of demand bids and supply offers, which allows a continuous submission of new offers/bids during the whole session. Similarly to the day-ahead market, the intraday market is managed by the market operator.

#### 10.2.4 Balancing market mechanism

The balancing market is the last stage for trading electric energy. It plays an essential role, as production and consumption levels must match during the operation of electric power systems. This is a key feature, given that, at the moment, storage of large quantities of electric energy is not economically convenient.

Balancing markets are generally single-period markets, i.e., a separate session for each trading period. They allow the possibility to trade, in addition to electric energy *ancillary services* (e.g., voltage control) needed to maintain the stability of the electric system.

Conventional producers, usually, participate at the balancing market for providing regulating power, both in upward (i.e., increasing production) and downward (i.e., decreasing production) directions. Differently, stochastic producers, access the balancing stage to settle deviations from contracted production. These deviations are priced differently, depending on the pricing imbalance system of the market. We can distinguish between single-price imbalance system and two-price imbalance system.

In a single-price imbalance system the deviations are settled at the market price, disregarding the sign of producer imbalances (i.e., excess or lack of production). As a general rule, the balancing price is higher/lower than the day-ahead market price if the system is in up/downregulation, i.e., when a lack/excess of power production occurs. This price settlement leads to arbitrage opportunities for power producers. For instance, when the producer and the system imbalance are of opposite sign (i.e., when the power producer deviation helps to reduce the whole system imbalance), the producer receives a bonus for its deviation. Conversely, when the two imbalances occur in the same direction, the producer is penalized. Fig. 10.1a shows the arbitrage opportunity as function of the producer imbalance and the system status (up- or downregulation).

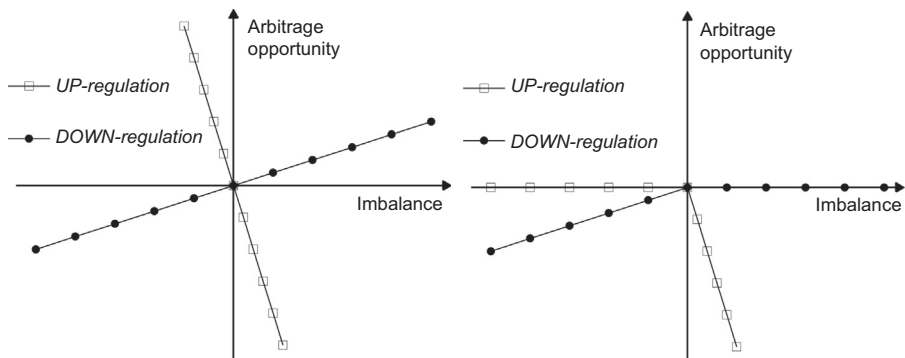


**Figure 10.1** Arbitrage opportunity for different imbalance settlement schemes.

In a dual-price imbalance system, deviations from the production schedule are traded at different prices, conditional upon the imbalance sign. When the deviation of the producer and system imbalance occur in opposite directions (i.e., the producer helps in reducing the system imbalance), its deviation is traded at the day-ahead market price, avoiding possible bonuses. Conversely, when the two imbalances occur in the same direction, the deviation of the producer is priced at the balancing market price (i.e., usually penalized). Fig. 10.1b shows the absence of arbitrage opportunity in a two-price imbalance system.

## 10.3 From market revenue to forecast value

In this section we will translate into equations the qualitative concepts of electricity pools introduced in Section 10.2. This section is structured as follows. Section 10.3.1 presents the assumptions that define the framework of the trading problem. The formulation of market revenues are developed in Section 10.3.2, while Section 10.3.3 presents a performance parameter that helps in comparing different trading strategies.

### 10.3.1 Assumptions

Let us introduce some assumptions that allow us to simplify the structure of the market and define the framework of the analysis.

- A1 The wind power producer trades only in the day-ahead market and in the balancing market, while the intraday trading is neglected.
- A2 The producer is risk neutral, i.e., he aims to maximize his profit, disregarding possible huge losses.
- A3 The producer is price taker, i.e., he cannot influence market equilibrium with his behavior.
- A4 The producer offer its energy generation at zero marginal cost.
- A5 The producer is provided with the cumulative distribution function  $F_E(\cdot)$  of future wind power production  $E$ . This writes

$$F_E(e) = \mathbb{P}(E \leq e) = \int_0^e f_E(x) dx, \quad (10.1)$$

where  $f_E(\cdot)$  is the probability density function

$$f_E(x) = \frac{\mathbb{P}(x < E < x + dx)}{dx}. \quad (10.2)$$

Assumptions A1, A3, and A5 are necessary for obtaining an analytical solution of the wind power producer profit maximization problem (Morales et al., 2013) and have been used in several studies (Bremnes, 2004; Pinson et al., 2007; Zugno et al., 2013a). As alternative, the problem can be formulated as a stochastic optimization problem (Morales et al., 2010; Rahimiyan et al., 2011), which can be easily extended by including the intraday trading. On the other hand, assumptions A2 and A4 are not

strictly required for the analytical formulation of the problem, but they help the reader in focusing on the fundamental concepts. However, risk aversion can be added subsequently, as Zugno et al. (2013a) show in their work, by anchoring the market quantity to the expected value of wind power production, either in the decision space or the probability space. When the problem is formulated using stochastic optimization, risk aversion can be included by adding the Conditional Value At Risk in the objective function (Morales et al., 2010; Rahimian et al., 2011).

### 10.3.2 Formulation of market revenues

Let  $\lambda$  and  $q$  denote prices and energy quantities, respectively. Then, let D and B be the subscripts denoting the day-ahead and the balancing market, respectively. Moreover, let us denote with  $t$  the time of placing offers (i.e., day-ahead market closure) and with  $k$  the time delay between  $t$  and the real-time operation. In each trading period  $k$  the wind power producer can submit an offer in the day-ahead market, specifying the amount of energy  $q^D$  he or she is willing to contract. The market revenue  $\rho_k$  of a market participant is computed as

$$\rho_k = \rho_k^D + \rho_k^B = \lambda_k^D q_k^D + \lambda_k^B q_k^B. \quad (10.3)$$

The quantities contracted in the two market stages, i.e.,  $q_k^D$  and  $q_k^B$ , are linked by

$$q_k^B = E_k - q_k^D, \quad (10.4)$$

where  $E_k$  is the wind power production measured during the hourly interval  $k$ . Eq. (10.4) shows that the quantity contracted at the balancing stage, i.e.,  $q_k^B$ , is not a decision variable. Indeed,  $E_k$  is not under control of the power producer and  $q_k^D$  is fixed at balancing stage. By rearranging Eq. (10.3),

$$\rho_k = \lambda_k^D q_k^D + \lambda_k^B (E_k - q_k^D) = \lambda_k^D E_k - (\lambda_k^B - \lambda_k^D)(q_k^D - E_k) = \lambda_k^D E_k - L_k. \quad (10.5)$$

The first term of Eq. (10.5), i.e.,  $\lambda_k^D E_k$ , is the product between the day-ahead market price and the effective wind power production during interval  $k$ . It represents the profit that the producer may have in case of perfect information, i.e., if he could know at  $t$  the wind production at  $t+k$ . Differently, the term  $L_k$  represents the penalties for imbalance creation, and it is always positive (in a dual-price settlement scheme). Therefore,  $\lambda_k^D E_k$  is the maximum profit that can be reached by the wind power producer. Note that all these considerations are true only for a dual-price settlement scheme ( $L_k$  can be either positive or negative in a single-pricing scheme).

### 10.3.3 Linkage to forecast value

Let us introduce a performance parameter that represents a coherent measure to access the effectiveness of a market offering strategy. As shown in Section 10.3.2, the profit

of the power producer can be seen as the sum between the profit in case of perfect information ( $\lambda_k^D E_k$ ), which represents the upper limit and the imbalance penalty term ( $L_k$ ). The first term is the maximum profit that could be reached by the power producer in each trading period, and it can be used as reference. The performance ratio  $\gamma_{t+k}$  of an offering strategy during interval  $k$ , is defined as

$$\gamma_{t+k} = \frac{\rho_k}{\lambda_k^D E_k} = 1 - \frac{L_k}{\lambda_k^D E_k}. \quad (10.6)$$

However, the result of specific strategy in a single time interval may not be the statistically significant. Therefore, the performance ratio  $\gamma$  is usually evaluated over  $N$  days, i.e.,

$$\gamma = \sum_{t=1}^N \sum_{k=13}^{36} \gamma_{t+k}. \quad (10.7)$$

The upper limit of  $\gamma$  is 1, which is obtained when the power producer is never penalized for its imbalances, during the  $N$  days of reference. Note that  $\gamma$  is not bounded inferiorly. As for [Section 10.3.2](#), all these considerations are true only for a dual-price settlement scheme.

## 10.4 Formulation of offering strategies

In this section we will develop different trading strategies of a wind power producer who aims to maximize his or her market revenue. The section is developed as follows. [Section 10.4.1](#) presents some basic offering strategies that can be used as a benchmark. Then, [Sections 10.4.2 and 10.4.3](#) present optimal offering strategies for the single-price and the dual-price imbalance settlement, respectively.

### 10.4.1 Benchmark offering strategies

At the time of placing bids, the wind power producer does not know exactly the future amount of wind power production. However, he can be provided with forecasts, either deterministic or probabilistic. Depending on the information that the producer may have available at  $t$ , we can identify three different categories of offering strategy. In category 1 we include the strategies that a power producer may develop when no forecasts of  $E_k$  are available. Then, in category 2 we consider the offering strategies based on point forecasts of  $E_k$ . Finally, in category 3, we include offering strategies based on probabilistic forecasts of  $E_k$ . An example of probabilistic forecasts and point forecasts is shown in [Fig. 10.2](#).

Strategy of category 1 should not require forecasts of  $E_k$ . However, the power producer can use past observations to develop a naive forecast model. We consider two different strategies in this category. The first, called Strategy 1A, proposes to offer at day-ahead stage the average value of wind power production over the previous

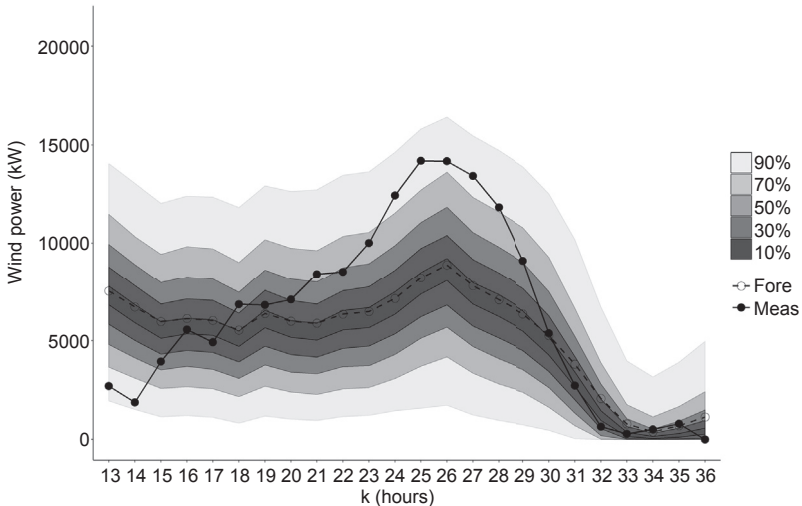


**Figure 10.2** Probabilistic and point forecasts for June 7, 2014.

years. A capacity factor  $c_f$  is evaluated, as the ratio between average measured production and total installed capacity ( $\bar{E}$ ). Then, the value of  $q_k^D$  is computed as

$$q_k^D = c_f \bar{E} \quad (10.8)$$

The second, i.e., Strategy 1B, suggests to use wind power production measured at  $t$ , as a representative for future values of  $E_k$ . This writes

$$q_k^D = E_t \quad (10.9)$$

When more information is available to the power producer, he or she may try to exploit this additional information to increase his expected market profit. In case of Strategy 2, this additional information is provided in the form of deterministic (point) forecasts. Point forecasts represent the expected value of future wind power production, i.e.,  $\hat{E}_k = \int_0^{\bar{E}} xf_{E_k}(x)dx$ . In Strategy 2 the market quantity offer is

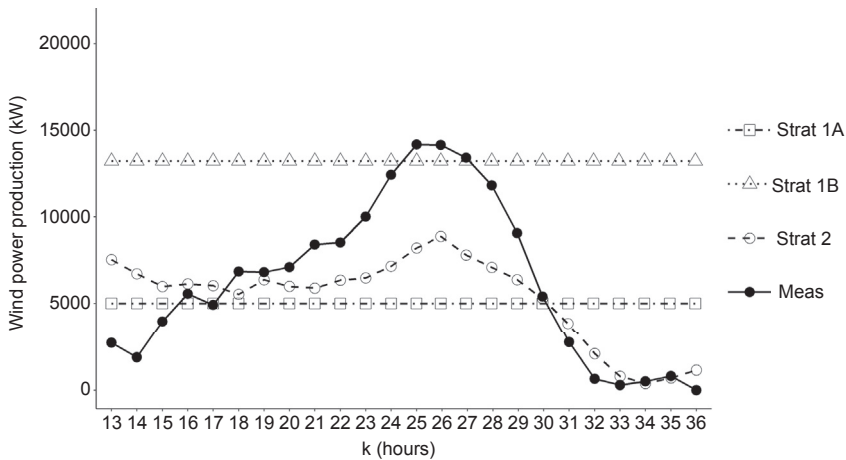
$$q_k^D = \hat{E}_k \quad (10.10)$$

**Example 4.1.** Let us consider an onshore wind farm of 21 MW located in Denmark, having a capacity factor  $c_f$  of 24%. Then, let us suppose that at 12 a.m. of June 6, 2014, the producer has to trade in the day-ahead market the wind power production for the following day. Following Strategy 1A would result in offering

$$q_k^D = 5004 \text{ kW}, \quad \forall k \in [13, 36], \quad (10.11)$$

**Table 10.1 Point forecasts of wind power production for June 7, 2014**

$k$	13	14	15	16	17	18	19	20
$\hat{E}_{t+k t}[\text{kW}]$	7542	6720	5981	6138	6033	5539	6387	5994
$k$	21	22	23	24	25	26	27	28
$\hat{E}_{t+k t}[\text{kW}]$	5895	6354	6484	7153	8219	8883	7806	7094
$k$	29	30	31	32	33	34	35	36
$\hat{E}_{t+k t}[\text{kW}]$	6382	5290	3833	2084	788	386	694	1142

**Figure 10.3** Different offering strategies for June 7, 2014.

while under strategy 1B, market offer would be

$$q_k^D = 13222 \text{ kW}, \quad \forall k \in [13, 36] \quad (10.12)$$

Differently, Strategy 2 required the point forecasts of  $E_k$ , shown in [Table 10.1](#).

The energy quantities contracted by the three offering strategies are graphically shown in [Fig. 10.3](#). Moreover, [Table 10.2](#) gives the exact value of market offers for the first 8-hourly interval.

#### 10.4.2 Trading strategies in a single-price imbalance system

In a single-price imbalance system, deviations from day-ahead contracted schedule are priced at the balancing market price, disregarding the sign of the imbalance. Let us introduce the *expected monetary value* (EMV), defined in decision theory as the

**Table 10.2 Day-ahead market offers under different strategies, expressed in kW**

$k$	13	14	15	16	17	18	19	20
Strategy 1A	5000	5000	5000	5000	5000	5000	5000	5000
Strategy 1B	13,222	13,222	13,222	13,222	13,222	13,222	13,222	13,222
Strategy 2	7542	6720	5981	6138	6033	5539	6387	5994

expected profit due to a specific decision. The EMV for the wind power producer can be obtained by computing the expectation of Eq. (10.5), i.e.,

$$\mathbb{E}[\rho_k] = \lambda_k^D \mathbb{E}[E_k] + (\lambda_k^B - \lambda_k^D) (\mathbb{E}[E_k] - q_k^D). \quad (10.13)$$

The market prices ( $\lambda_k^D$  and  $\lambda_k^B$ ) are initially assumed to be known at time  $t$ . Then, this strong assumption will be relaxed. When trying to maximize Eq. (10.13), three possible events may occur,

1. If  $\lambda_k^B > \lambda_k^D$ , the term  $(\lambda_k^B - \lambda_k^D)$  of Eq. (10.13) is positive. Therefore, the producer increases his or her profit in expectation when he or she has an excess of production at the balancing stage. This leads the producer to sell nothing at the day-ahead stage and to wait for selling his or her whole production at the balancing one ( $q_k^{D*} = 0$ );
2. If  $\lambda_k^B < \lambda_k^D$ , the term  $(\lambda_k^B - \lambda_k^D)$  of Eq. (10.13) is negative. In this situation the producer offers all his capacity ( $\bar{E}$ ) in the day-ahead market ( $q_k^{D*} = \bar{E}$ ). Doing that, he maximizes the volume of the negative imbalance than he can settle at the balancing stage ( $q_k^B = E_k - \bar{E}$ );
3. If  $\lambda_k^B = \lambda_k^D$ , the term  $(\lambda_k^B - \lambda_k^D)$  of Eq. (10.13) is null and any decision leads to the same expected profit.

All the three events lead to trivial solutions. When market prices are given, the optimal market offer  $q_k^{D*}$  is only determined by arbitrage possibility, since  $\mathbb{E}[E_k]$  does not influence its optimal level.

Let us now relax the assumption of known and deterministic prices. Indeed, we consider both the day-ahead and the balancing market prices as random variables with known probability density function. The EMV is obtained by introducing price expectation in Eq. (10.13), i.e.,

$$\mathbb{E}[\rho_k] = \mathbb{E}[\lambda_k^D] \mathbb{E}[E_k] + \mathbb{E}[\lambda_k^B - \lambda_k^D] (\mathbb{E}[E_k] - q_k^D). \quad (10.14)$$

As for deterministic prices, let us distinguish between three possible situations:

1. If  $\mathbb{E}[\lambda_k^B - \lambda_k^D] > 0$ , optimal bid is  $q_k^{D*} = 0$ ;
2. If  $\mathbb{E}[\lambda_k^B - \lambda_k^D] < 0$ , optimal bid is  $q_k^{D*} = \bar{E}$ ; and
3. If  $\mathbb{E}[\lambda_k^B - \lambda_k^D] = 0$ , each bid yields to the same EMV.

Even when the market prices are considered as random variables, the optimal level of  $q_k^{D*}$  is not influenced by the forecast of wind power production. Indeed, this settlement scheme pushes the producer to offer, at day-ahead stage, nothing or the whole capacity, depending on the expected value of market prices.

### 10.4.3 Trading strategies in a two-price imbalance system

In a two-price imbalance settlement scheme, deviations from the contracted generation schedule are priced differently depending on the mutual sign of the producer's imbalance and the system's imbalance. Therefore, we introduce two artificial market prices that allow to represent the imbalance sign of the system. The first, called upregulation price ( $\lambda_k^{UP}$ ), is equal to the balancing market price when upregulation energy is required and to the day-ahead market one otherwise. This writes

$$\lambda_k^{UP} = \begin{cases} \lambda_k^B & \text{if } \lambda_k^B \geq \lambda_k^D \\ \lambda_k^D & \text{if } \lambda_k^B < \lambda_k^D \end{cases} \quad (10.15)$$

Conversely, downregulation price ( $\lambda_k^{DW}$ ) is equal to the balancing market price when the system needs downregulation energy and to the day-ahead market one otherwise, i.e.,

$$\lambda_k^{DW} = \begin{cases} \lambda_k^D & \text{if } \lambda_k^B \geq \lambda_k^D \\ \lambda_k^B & \text{if } \lambda_k^B < \lambda_k^D \end{cases} \quad (10.16)$$

Then, let us define the differential prices  $\psi_k^{UP}$  and  $\psi_k^{DW}$  as the difference between the up- and downregulation market prices and the day-ahead market price, respectively. This writes

$$\psi_k^{UP} = \lambda^{UP} - \lambda_k^D \geq 0 \quad (10.17)$$

$$\psi_k^{DW} = \lambda^{DW} - \lambda_k^D \leq 0 \quad (10.18)$$

These differential prices allow to simplify the notation of the imbalance cost  $\lambda_k^D$  of the stochastic producer. Negative imbalances are priced at  $\psi_k^{UP}$ , while positive imbalances at  $\psi_k^{DW}$ . Therefore,  $\lambda_k^D$  is evaluated as

$$L_k = \begin{cases} \psi_k^{UP}(q_k^D - E_k) & \text{if } q_k^D \geq E_k \\ \psi_k^{DW}(q_k^D - E_k) & \text{if } q_k^D < E_k \end{cases} \quad (10.19)$$

The value of  $L_k$  is always positive, indeed.

1. If  $q_k^D > E_k$ , the terms  $(q_k^D - E_k)$  and  $\psi_k^{DW}$  are both negative. This yields to a positive value of  $L_k$ ;
2. If  $q_k^D < E_k$ , the terms  $(q_k^D - E_k)$  and  $\psi_k^{UP}$  are both positive. As before, this yields to a positive value of  $L_k$ ;
3. If  $q_k^D = E_k$ , trivial.

The EMV can be written as the difference of two terms, i.e.,  $\lambda^D \mathbb{E}[E_k]$  and  $\mathbb{E}[L_k]$ , which are respectively the expected profit in case of perfect information and the expected opportunity loss called EOL. The EOL is the loss of profit introduced by uncertainties, i.e., all the stochastic processes that the power producer can predict only with a limited accuracy.

As stated before, the term  $\lambda^D E_k$  is not under control of the wind power producer. Therefore the problem of maximizing the EMV is equivalent to minimizing the EOL. Let us now write explicitly the expectation of the EOL by moving to the probability space of wind power production. The  $L_k$  is a piece-wise function, where  $E_k$  is a discontinuity point. Therefore, the integral form of the EOL is the sum of two integrals: the first (upregulation term) is defined for  $E_k \in [0, q_k^D]$ , while the second (downregulation term) for  $E_k \in [q_k^D, \bar{E}]$ . Let us, initially, assume known and deterministic market prices. Under such assumption, the EOL is

$$\text{EOL}_k = \int_0^{q_k^D} \psi_k^{UP}(q_k^D - x) f_{E_k}(x) dx + \int_{q_k^D}^{\bar{E}} \psi_k^{DW}(q_k^D - x) f_{E_k}(x) dx, \quad (10.20)$$

where  $f_{E_k}(\cdot)$  is the probability density function of the wind power production. The minimum of the EOL can be computed by deriving Eq. (10.20) with respect to  $q_k^D$  and by setting it to 0. The solution yields to the following expression for the optimal quantile  $q_k^{D*}$

$$q_k^{D*} = F_{E_k}^{-1} \left( \frac{|\psi_k^{DW}|}{|\psi_k^{DW}| + \psi_k^{UP}} \right), \quad (10.21)$$

where  $F_{E_k}^{-1}(\cdot)$  is the inverse of the cumulative density function of wind power production.

Let us now relax the assumption of deterministic prices. The extended integral form of the EOL to the probability space of stochastic prices is

$$\begin{aligned} \text{EOL}_k = & \int_0^{q_k^D} \int_0^\infty y(q_k^D - x) f_{E_k}(x) f_{\psi_k^{UP}}(y) dx dy \\ & + \int_{q_k^D}^{\bar{E}} \int_{-\infty}^0 y(q_k^D - x) f_{E_k}(x) f_{\psi_k^{DW}}(y) dx dy. \end{aligned} \quad (10.22)$$

Similar to Eq. (10.21), the optimal level of the day-ahead contracted energy is (Bremnes, 2004; Linnet, 2005)

$$q_k^D = F_{E_k}^{-1} \left( \frac{|\hat{\psi}_k^{\text{DW}}|}{|\hat{\psi}_k^{\text{DW}}| + \hat{\psi}_k^{\text{UP}}} \right) = F_{E_k}^{-1}(\alpha_{t+k}^*) \quad (10.23)$$

where

$$\hat{\psi}_k^{\text{UP}} = \int_0^\infty y f_{\hat{\psi}_k^{\text{UP}}}(y) dy \quad (10.24)$$

$$\hat{\psi}_k^{\text{DW}} = \int_{-\infty}^0 y f_{\hat{\psi}_k^{\text{DW}}}(y) dy \quad (10.25)$$

Eq. (10.23) shows that the behavior of a strategic producer in a dual-price settlement is to overestimate future wind power production when  $|\hat{\psi}_k^{\text{DW}}| > \hat{\psi}_k^{\text{UP}}$ , and underestimate it if  $|\hat{\psi}_k^{\text{DW}}| < \hat{\psi}_k^{\text{UP}}$ . However, the balancing market prices are hard to forecast with high accuracy, since they generally show a high degree of stochasticity. Then, we want to analyze how the quality of wind power forecasts may affect the optimal value of the EOL. First, we compute the value of the EOL when  $q_k^D = q_k^{D*}$  (Bitar et al., 2012)

$$\text{EOL}_k^* = -\hat{\psi}_k^{\text{UP}} \int_0^{q_k^{D*}} x f_{E_k}(x) dx + |\hat{\psi}_k^{\text{DW}}| \int_{q_k^{D*}}^{\bar{E}} x f_{E_k}(x) dx \quad (10.26)$$

Then, we apply the change of variable  $y = F_{E_k}(x)$ , thus leading to

$$\text{EOL}_k^* = -\hat{\psi}_k^{\text{UP}} \int_0^{\alpha_{t+k}^*} F_{E_k}^{-1}(y) dy + |\hat{\psi}_k^{\text{DW}}| \int_{\alpha_{t+k}^*}^1 F_{E_k}^{-1}(y) dy \quad (10.27)$$

Fig. 10.4 provides a graphical interpretation of the two integrals of Eqs. (10.27), when for sake of clarity, the wind farm capacity  $\bar{E}$ , has been set to 1 MW.  $I1$  and  $I2$  of Fig. 10.4 are computed as

$$I1 = \int_0^{\alpha_{t+k}^*} F_{E_k}^{-1}(y) dy = \int_0^{q_k^{D*}} x f_{E_k}(x) dx \quad (10.28a)$$

$$I2 = \int_{\alpha_{t+k}^*}^1 F_{E_k}^{-1}(y) dy = \int_{q_k^{D*}}^{\bar{E}} x f_{E_k}(x) dx \quad (10.28b)$$

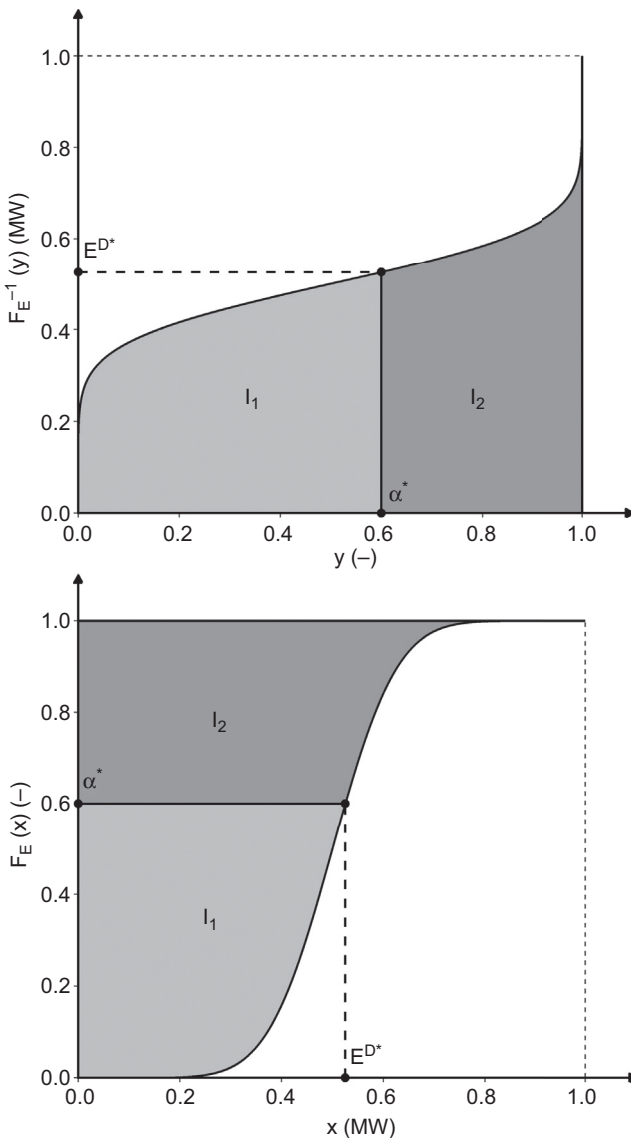


**Figure 10.4** Integral form interpretation of  $EOL_{t+k}^*$  ( $\bar{E} = 1\text{MW}$ ).

For a complete and wider analysis of this topic, we refer the interested reader to Bitar et al. (2012).

**Example 4.2.** Let us consider that the expectations of the differential prices (in \euro/MWh) are:

$$\hat{\psi}^{\text{UP}} = 10, \quad \hat{\psi}^{\text{DW}} = -10 \quad (10.29)$$

which lead to a nominal level of the optimal quantile of 0.5 ( $\alpha^* = 0.5$ ). Let us now consider 2 different cumulative distribution functions with the same expected value but different variance:

$$F_E^a(x) = \begin{cases} 0, & \text{if } x < 0 \\ 1, & \text{if } x > 1 \\ x, & \text{otherwise} \end{cases} \quad (10.30)$$

$$F_E^b(x) = \begin{cases} 0, & \text{if } x < 0.25 \\ 1, & \text{if } x > 0.75 \\ \frac{x - 0.25}{0.5}, & \text{otherwise} \end{cases} \quad (10.31)$$

In both cases the optimal quantile is  $E^{D^*} = 0.5$  MW. The integrals  $I_1$  and  $I_2$  are straightforward to compute for uniform distributions and led to the following results:

$$I_1^a = 0.125 \text{ MWh} \quad I_1^b = 0.1875 \text{ MWh} \quad (10.32a)$$

$$I_2^a = 0.375 \text{ MWh} \quad I_2^b = 0.3125 \text{ MWh} \quad (10.32b)$$

The reader may refer to Fig. 10.5 for a graphical interpretation of the results. We can now compute the optimal EOL for the two cases:

$$\text{EOL}^{a*} = -\psi^{\text{UP}} I_1^a + |\hat{\psi}^{\text{DW}}| I_2^a = 2.50 \text{ €/MWh} \quad (10.33a)$$

$$\text{EOL}^{b*} = -\psi^{\text{UP}} I_1^b + |\hat{\psi}^{\text{DW}}| I_2^b = 1.25 \text{ €/MWh} \quad (10.33b)$$

## 10.5 Test case exemplification

A test case based on real data can help in understanding concretely the differences between different offering strategies and the value of wind power forecasts, either deterministic or probabilistic.

### 10.5.1 Experimental setup

The test case analyses different possible offering strategies of a 21-MW wind farm located in Western Denmark. For this wind farm, both point forecasts and probabilistic forecasts, in form of 19 quantiles and measured values of wind power production, are available for the whole 2014. Market prices of zone *DK1* of Nord Pool Spot are used

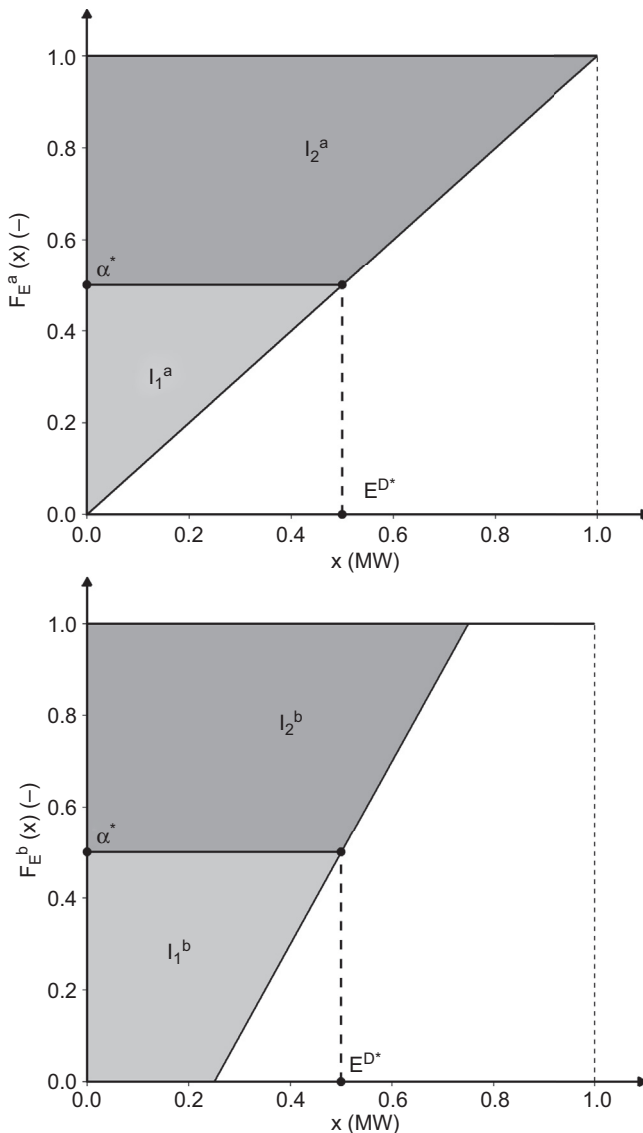


**Figure 10.5** Integral form interpretation of Example 4.2.

for both day-ahead and balancing market prices. All the assumptions of [Section 10.3.1](#) are still valid. Five different offering strategies are considered for the test case:

- Strategy 1: naive forecasts
  - Strategy 1A (*capacity factor model*)
  - Strategy 1B (*persistence model*)
- Strategy 2: point forecasts
- Strategy 3: probabilistic forecasts

The producer has to develop a strategy for estimating the nominal level  $\alpha_{t+k}$  of the optimal quantile:

$$\alpha_{t+k} = \frac{|\hat{\psi}_k^{\text{DW}}|}{|\hat{\psi}_k^{\text{DW}}| + \hat{\psi}_k^{\text{UP}}} \quad (10.34)$$

The expected price for up(down)-regulation can be evaluated as the product between the expected price, known that the system is in up(down)-regulation and the probability of system to be in up(down)-regulation. In this test case we consider two simple models for the estimation of  $\alpha_{t+k}$ :

- Strategy 3A: The producer uses the historical market prices of the previous year to evaluate of the optimal  $\alpha_{t+k}$ . Bimonthly averages for each of the 24 trading hours are obtained by analyzing market data of 2013 (*fixed average*).
- Strategy 3B: Optimal  $\alpha$  is estimated from the last  $n_{ts}$  market prices available at the moment of placing bids, for each specific trading hour. In this test case we chose a time span of 30 days (*moving average*).

[Fig. 10.6](#) shows the different values of  $\alpha$  over a year for the sixth trading interval (from 5 to 6 a.m.) for strategy 3A (solid line) and 3B (dashed line).

For each strategy we evaluated the total revenue over a year, called  $\rho$ . The total revenue, following the approach of [Section 10.3.2](#), can be split into two terms: the revenue in case of perfect information, called  $\rho_{PI}$ , and the imbalance penalties term,  $\rho_L$ . The difference between  $\rho_{PI}$ , which is common among each trading strategy, and  $\rho_L$  gives the total revenue. The values of  $\rho_{PI}$  and  $\rho_L$  for the whole year ( $t \in [1, 365]$  and  $k \in [13, 36]$ ) can be computed as follow:

$$\rho_{PI} = \sum_{t=1}^{365} \sum_{k=13}^{36} \lambda^D E_k, \quad (10.35)$$

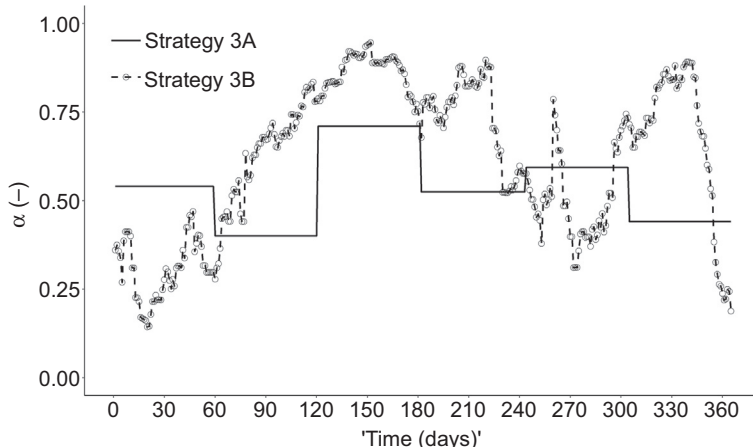


**Figure 10.6** Coefficient  $\alpha$  estimated by mean of strategies 3A and 3B, sixth trading hour.

$$\rho_L = \sum_{t=1}^{365} \sum_{k=13}^{36} L_{t+k} \quad (10.36)$$

### 10.5.2 Trading results and value of various forecasts

The cumulative values of the imbalance penalties term  $\rho_L$  for the different strategies are displayed in Fig. 10.7.

The results of each trading strategy are shown in Fig. 10.8 and Table 10.3.

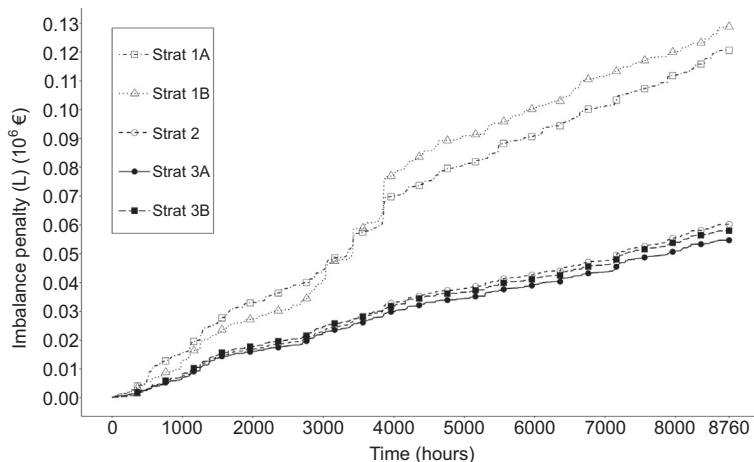


**Figure 10.7** Cumulative imbalance penalties for different strategies.

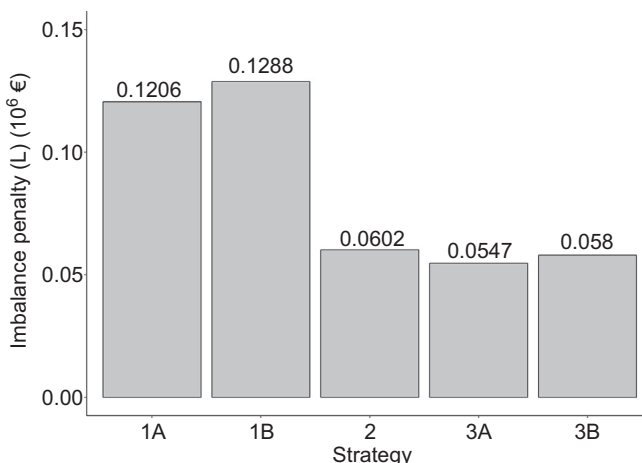


**Figure 10.8** Bar plot of imbalance penalties for different strategies.

**Table 10.3 Revenues and performance ratio of each trading strategy**

Strategy	$\rho_{PI}$ [10 <sup>6</sup> €]	$\rho_L$ [10 <sup>6</sup> €]	$\rho$ [10 <sup>6</sup> €]	$\gamma$ [%]
1A	1.256	0.121	1.135	90.40
1B	1.256	0.129	1.127	89.74
2	1.256	0.060	1.196	95.20
3A	1.256	0.055	1.201	95.64
3B	1.256	0.058	1.198	95.38

Analyzing the results, the improvement that forecasts give in terms of reducing the imbalance penalties term is clear. We notice that the term  $\rho_L$  is more than the double in case of naive forecast (Strategies 1A and 1B) compare to point forecast (Strategy 2). The penalty term is further decreased when probabilistic forecasts are available. If we take producer 2 as reference,  $\rho_L$  is reduced of around 4% for strategy 3B and 9% for strategy 3A. The difference, mainly if we analyze the performance ratio, may not appear so significant to the reader; nevertheless, for this test case we used very simple methods for the estimation of optimal  $\alpha$ . More advances models can help in increasing the performance. Furthermore, in [Zugno et al. \(2013a\)](#) the authors show how the effectiveness of this strategy can be improved by modeling the risk aversion of the wind power producer.

## 10.6 Overall conclusions and perspectives

In this chapter we presented the trading problem of a wind power producer. Here we consider that the stochastic producer has to access the electricity market under the same rules of conventional generators, thus becoming responsible of its deviations. We have shown how the wind power producer can exploit information from wind and market price forecasts, to maximize his or her expected profit. The stochastic producer offers in the day-ahead market (which ensures more high and stable prices), considering his forecasts on balancing market prices. We have shown how he can exploit all the information he has available and how it can affect his or her profit. We developed our analysis under assumptions that may not be always acceptable, e.g., assumption A3 (price taker). We refer the interested reader to [Zugno et al. \(2013b\)](#) and [Baringo and Conejo \(2013\)](#), where a stochastic mathematical program with equilibrium constraints is used to model the price-maker behavior, both at day-ahead stage and balancing stage ([Zugno et al., 2013b](#)). Furthermore, this chapter considers the typical structure of European electricity markets. Our assumption of uniform prices is not more true if considering US electricity markets. The reader is referred to [Botterud et al. \(2012\)](#) for a formulation of the trading problem of wind production in locational marginal price markets.

## References

- Baringo, L., Conejo, A.J., 2013. Strategic offering for a wind power producer. *IEEE Transactions on Power Systems* 28 (4), 4645–4654.
- Bathurst, G.N., Weatherill, J., Strbac, G., 2002. Trading wind generation in short term energy markets. *IEEE Transactions on Power Systems* 17 (3), 782–789.
- Bitar, E.Y., Rajagopal, R., Khargonekar, P.P., Poolla, K., Varaiya, P., 2012. Bringing wind energy to market. *IEEE Transactions on Power Systems* 27 (3), 1225–1235.
- Botterud, A., Zhou, Z., Wang, J., Bessa, R.J., Keko, H., Sumaili, J., Miranda, V., 2012. Wind power trading under uncertainty in Imp markets. *IEEE Transactions on Power Systems* 27 (2), 894–903.
- Bremnes, J.B., 2004. Probabilistic wind power forecasts using local quantile regression. *Wind Energy* 7 (1), 47–54.
- Linnet, U., 2005. Tools Supporting Wind Energy Trade in Deregulated Markets (Ph.D. thesis). Technical University of Denmark, DTU, DK-2800 Kgs. Lyngby, Denmark.
- Morales, J.M., Conejo, A.J., Madsen, H., Pinson, P., Zugno, M., 2013. Integrating Renewables in Electricity Markets: Operational Problems, vol. 205. Springer Science & Business Media.
- Morales, J.M., Conejo, A.J., Pérez-Ruiz, J., 2010. Short-term trading for a wind power producer. *IEEE Transactions on Power Systems* 25 (1), 554–564.
- Pinson, P., Chevallier, C., Kariniotakis, G.N., 2007. Trading wind generation from short-term probabilistic forecasts of wind power. *IEEE Transactions on Power Systems* 22 (3), 1148–1156.
- Rahimian, M., Morales, J.M., Conejo, A.J., 2011. Evaluating alternative offering strategies for wind producers in a pool. *Applied Energy* 88 (12), 4918–4926.
- Zugno, M., Jónsson, T., Pinson, P., 2013a. Trading wind energy on the basis of probabilistic forecasts both of wind generation and of market quantities. *Wind Energy* 16 (6), 909–926.
- Zugno, M., Morales, J.M., Pinson, P., Madsen, H., 2013b. Pool strategy of a price-maker wind power producer. *IEEE Transactions on Power Systems* 28 (3), 3440–3450.

# Forecasting and setting power system operating reserves

11

Manuel Matos<sup>1,2</sup>, Ricardo Bessa<sup>1</sup>, Audun Botterud<sup>3</sup>, Zhi Zhou<sup>3</sup>

<sup>1</sup>INESC Technology and Science (INESC TEC), Porto, Portugal; <sup>2</sup>University of Porto, Portugal;

<sup>3</sup>Argonne National Laboratory, Argonne, IL, United States

## 11.1 Introduction

Power systems work in a permanent equilibrium between generation and load, and this balance is managed to maintain the frequency in the stipulated value. So, when, for instance, load increases, generation must also increase and that is why generation units are scheduled in advance to follow the forecasted load. Small variations around the forecasted situations lead to small frequency variations that are counteracted by an adequate variation in the generation managed by automatic regulation of the machines (primary and secondary, through Automatic Generation Control). Large variations, however, like the ones originated by sudden units' disconnection, require the availability of additional power that could be mobilized, to first contain frequency deviations and then restore the frequency value (UCTE, 2004).

More recently, with the deployment of large amounts of power coming from variable renewable energy sources (RES, initially wind power, now also solar photovoltaic power), the correction of forecasting errors gained increasing importance. This is a new situation in power systems, although the names and basic concepts of reserves remain more or less the same, leading to a situation where forecasting errors are compensated by tertiary reserve, originally a replacement reserve when secondary reserve is mobilized.

In any case, the estimation of the necessary reserves is a crucial aspect of modern power system operation, namely due to the uncertainty of renewable sources, requiring adequate methodologies able to calculate and manage the risk associated with a specific reserve. Probabilistic methodologies are not new in this topic, but the inclusion in the models of probabilistic forecasts of RES variable generation paves the way to a comprehensible approach that fulfills the already-mentioned requirements, namely when they are combined with decision-aid methodologies.

### 11.1.1 Overview of existing methodologies

In the power systems planning time domain, several methods exist to assess the adequacy of power system generation, which can be divided in two main groups: the analytical methods and the simulation methods.

The analytical methods describe the system behavior through a mathematical model and assess the power system reliability by convolving the generation with the load and

compute the expected values of reliability indices (Billinton and Allan, 1984). The main advantage of these methods, which made them popular in the 80's, was its low computational effort.

The simulation methods, based on nonchronological and chronological Monte Carlo methods, compute the reliability indices by random sampling scenarios or snapshots of system states (Billinton and Li, 1994). The main advantage of these methods, which made them very attractive for power system planning studies, is the possibility to include multiple system dependencies and characteristics, electrical and nonelectrical. Recent research consists of extending these methods to include renewable generation and demand response (Matos et al., 2009; Bremermann et al., 2014).

For the operational time domain, analytical methods seem to be more adequate since decisions about the short-term reserve requirements must be made in a very short time (which is a key requirement for operators). In fact, until recently, the methods employed by the system operators (SOs) to define the operating reserve needs were deterministic. Some historical examples are deterministic rule from the “Union for the Co-ordination of Transmission of Electricity” (UCTE) that depends only on the size of the typical load variations and was insensitive to the level of wind power penetration of the system (UCTE, 2004); (b) PJM that considered underforecasted load forecast error based on the 80th percentile of a rolling 3-year underforecast average plus forced outage rate (FOR) component (PJM, 2010); maintaining reserves equal to the single largest contingency in the system (N-1 rule)—variants of this rule has been applied by many SOs.

With the rapid increase in RES penetration in recent years, it became clear that this type of rules was no longer acceptable and a revision of the reserve setting procedures should be promoted. For instance, ERCOT (the Independent SO in Texas) in 2009 started to use the following rule: monthly nonspinning reserve requirements are set equal to the 95% percentile of the historical total forecast error (Maggio, 2009); more recently, in 2014 ERCOT an operating reserve demand curve (ORDC) in its real-time (RT) market (ERCOT, 2013), which depends in part on historical forecasting errors; REE [the Spanish Transmission System Operator (TSO)] started to study the inclusion of the load and wind forecast error distributions in setting the operating reserve (Torre, 2010; Holttinen et al., 2012). Similar efforts are being undertaken in other countries as well, such as Portugal (Bessa et al., 2012a,b), Germany, and Belgium<sup>1</sup> (Holttinen et al., 2012).

Early probabilistic methods in the scientific literature that incorporate uncertainty from renewable energy (mainly wind power) assumed that the forecast errors follow a Gaussian distribution (Söder, 1993; Doherty and O’Malley, 2005; Ortega-Vazquez and Kirschen, 2009). These methodologies were generalized in Matos and Bessa (2011) to include nonparametric wind power forecasts and derive a set of decision-making strategies for modeling decision-maker preferences (e.g., nonlinear trade-off between risk and reserve cost). Analytical methods based on convolution of several uncertainties were also described in subsequent publications (Menemenlis et al.,

<sup>1</sup> See the report “Potential cross-border balancing cooperation between the Belgian, Dutch and German electricity Transmission System operators” elaborated by the Institute of Power Systems and Power Economics and E-Bridge Consulting (online available at: [http://www.tennet.eu/nl/fileadmin/downloads/About\\_Tennet/Publications/Technical\\_Publications/balancing/141008\\_Final\\_report.pdf](http://www.tennet.eu/nl/fileadmin/downloads/About_Tennet/Publications/Technical_Publications/balancing/141008_Final_report.pdf)).

2012). Following this approach (Hedayati-Mehdiabadi et al., 2015), proposed two stages of reserve scheduling method: (1) estimates the flexibility margin from wind power plants and (2) a larger set of wind power scenarios are evaluated to ensure the adequacy of the scheduled energy and reserve margins.

Recent work has been focused in intrahourly variability. For instance, Negnevitsky et al. (2014) propose a risk-based strategy that takes into account steady-state voltage and branch evaluations, as well as frequency response adequacy. Furthermore, in Rahmann et al. (2016) a probabilistic methodology to quantify different types of operating reserves by including probabilistic information about load and wind variability is proposed. In Nosair and Bouffard (2015), a modeling framework is also described to quantify intrahourly RES variability.

The outcome from these probabilistic methods can also be included as constraints in the unit commitment (UC) problem. One example is the probabilistic constraint converted into equivalent deterministic inequalities constraints proposed by Restrepo and Galiana (2011) for a deterministic UC model. Moreover, stochastic UC formulations that account for the uncertainty in renewable energy have received substantial attention in the academic literature (e.g., Bouffard and Galiana, 2008; Tuohy et al., 2009; Ruiz et al., 2009; Morales et al., 2009; Papavasiliou et al., 2011; Wang et al., 2011). However, the reported benefits from stochastic UC formulations vary. For instance Wang et al. (2011), showed that a deterministic UC with dynamic reserve rules (point forecast minus 10% quantile and 5% of the load) obtain an operating cost close to the one obtained by a stochastic UC model.

Finally, it is important to mention that the integration of RES in the power system requires a revision of reserve categories and probably to a creation of new reserve categories that are expected to handle events related with large forecast errors and rapid generation ramps. In the United States, reserve products traded in electricity markets included regulation, spinning, and nonspinning reserves. However, the ability to maintain sufficient operational flexibility is gaining increasing attention. In fact, so-called flexi-ramp products have already been introduced in the CAISO and MISO markets in addition to the traditional reserve products (Xu and Tretheway, 2012; Navid and Rosenwald, 2013). Flexi-ramp reserves are meant to ensure that sufficient ramping capacity is available in RT dispatch, accounting for the uncertainty in renewable energy and other resources and its impact on operational ramping requirements. An example from Europe is Spain, where a forth category of reserve (deviation reserve) was created to handle large deviations (above 300 MWh) between scheduled generation and the forecasted demand (Holttinen et al., 2012). Extreme events, such as wind power curtailment due to wind speed above cut out value (e.g., between 25 and 30 m/s), might also require specific methodologies. For instance, in Lin et al. (2012) a high-resolution tool, which considers the spatial distribution of wind power plants, is proposed to simulate power reduction trajectories in a minute-to-minute time resolution under extreme wind speed events.

An important distinction between European and US electricity markets is that in most European market reserves are scheduled separately ahead of the energy market clearing, whereas in the United States, reserves and energy are typically jointly cooptimized within the same market clearing problem.

### 11.1.2 Aims and structure of this chapter

Our overall objective is to describe two probabilistic modeling approaches for setting the operating reserve requirements in power systems (and electricity markets) with separated and joint dispatch of electrical energy and ancillary services offers. Both methods take advantage of probabilistic forecasts for RES and employ analytical convolutions to determine the system generation margin (SGM). After explaining the integration of different uncertainty forecast products in [Section 11.2](#), the specifics of the probabilistic frameworks are described in [Section 11.3](#). These methods are applied to two different case studies in Europe and the United States: Portugal and Illinois power systems, in [Section 11.4](#). The chapter ends with an outlook regarding further developments in this topic and changes in the power system sector.

## 11.2 Integration of uncertainty forecasts in operating reserve estimation

In the literature, it is well established that wind and solar power forecast errors at the power plant level are not appropriately represented by a Gaussian distribution. Typically, the probability density functions of forecast errors are skewed, have a large peak around zero, and high kurtosis compared to a Gaussian distribution ([Lange, 2005](#); [Alessandrini et al., 2015](#)). In some cases, the classical central limit theorem (CTL) is used to support the assumption of Gaussian forecast errors for wind and solar power forecasts at the regional/national level. However, the classical CTL assumes the i.i.d. real valued random variables have a common distribution function ([Sen and Singer, 1994](#)), which is not valid for wind and solar forecast errors since their distribution's shape changes from site to site ([Pinson, 2006](#)). Even at the wind power plant level, the probability distribution of the wind farm's aggregate power cannot be characterized using the classical CLT ([He et al., 2014](#)).

Under these statistical characteristics, the renewable energy uncertainty should be modeled without a direct assumption of the Gaussian distribution for the errors. The uncertainty of the deterministic (or point) forecast can be approached by different representations. The most common representation is a nonparametric probabilistic forecast represented by quantiles, intervals, or probability density functions ([Bessa et al., 2012a,b](#)). The other two representations take the form of risk indices ([Pinson et al., 2009](#)) linked with the forecast accuracy and trajectories (or short-term scenarios) incorporating temporal and/or spatial interdependence structure of forecast errors ([Tastu et al., 2015](#)).

Typically, the renewable energy uncertainty in the reserve requirements setting problem is represented by a nonparametric probabilistic forecast, which takes the form of a set of quantiles ([Matos and Bessa, 2011](#); [Zhou and Botterud, 2014](#)). This corresponds to have a discrete representation of the cumulative distribution function (*cdf*)  $F_{t+k|t}$  generated at time instant  $t$  for look-ahead time  $t+k$ . In this representation, an exponential interpolation is required for the distribution tails ([Andersen, 2009](#)). Other methods, such as semiparametric regression can directly provide the full

probability distribution ([Pinson, 2012](#)), which can reduce the modeling error of the uncertainty in reserves setting problems. The forecasted wind generation can also be represented through its probability mass function (*pmf*). The *pmf* can be approximated by assigning the midpoint between two consecutive quantiles to the area between the two percentiles (probability).

The other two possible representations, forecast risk indices and trajectories, are not usually used as inputs for this problem. The risk index is a qualitative measure about an a priori warning on expected level of forecast error. The risk index may be more easily understood than probabilistic forecasts and can also be related with information about the potential magnitude of prediction errors. However, it is only a single numerical value that informs on the spread of the wind power forecasts respectively at a given period, thus only provides information on the confidence of the point forecasts. From these risk indices, it is possible to define the most accurate and least accurate that the total wind power forecast error is ever expected to be. In the reserve setting work the goal is to use the probability distribution with all the possible values of wind generation for the forecast time horizon and associated probabilities.

The scenarios representation respects the forecasted density/cumulative probability functions for the forecast time horizon but also informs on the development of the prediction errors through the set of look-ahead times. This information is valuable for time-dependent decision problems such as UC. However, in general, the reserve management problem consists in setting the reserves for each hour independently, and so in this problem the use of the scenario representation is not justified. Another disadvantage of the scenarios is the impossibility to compute the required number of scenarios necessary to adequately represent the temporal evolution of uncertainty. Nevertheless, this uncertainty representation is widely used in stochastic UC problems (e.g. [Bouffard and Galiana, 2008](#); [Morales et al., 2009](#); [Papavasiliou et al., 2011](#); [Wang et al., 2011](#)), and it was also applied to the reserve setting problem ([Saez-Gallego et al., 2014](#)). Finally, it is also possible to construct simultaneous predictions intervals (or quantile trajectories) from temporal trajectories and integrate this information in reserve setting tools that can use a quantile modeling of the renewable energy uncertainty ([Bessa, ;2015](#)).

## 11.3 Conceptual frameworks

### 11.3.1 Modeling assumptions

To build a probabilistic model to estimate the operating reserve requirements, several modeling assumptions should be evaluated for statistical correctness, as discussed in this subsection.

#### 11.3.1.1 Independency of forecast errors

The methodology proposed in this chapter assumes renewable generation and load forecast errors are independent. Here, it is important to stress that independence assumption is for forecast errors and not for the dependency between renewable

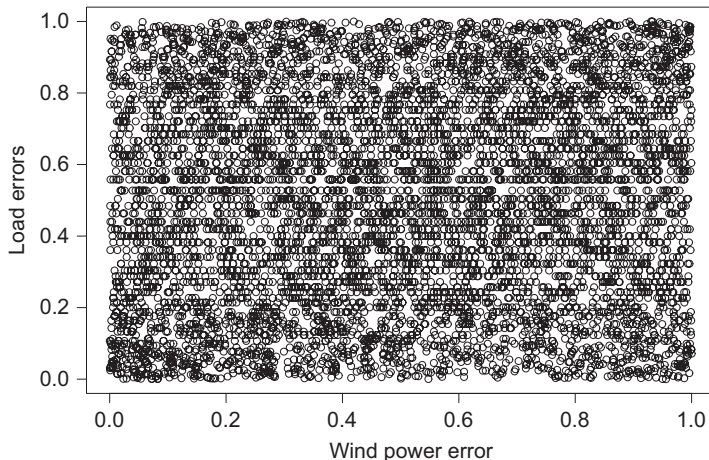


**Figure 11.1** Scatter plot between load and forecast errors in DK1 area of Denmark.

generation and load time series. So far, there is no evidence in the literature and available data that support the hypothesis that the forecast errors of renewable generation and load are dependent, as well as that the forecast error of wind and solar generation are dependent.

Fig. 11.1 depicts a scatter plot that relates the day-ahead (DA) wind and load forecast errors in control area DK1 in Denmark<sup>2</sup> for the first 10 months of 2015. The observed errors were transformed with the empirical *cdf* to the unit interval, which enables a better visualization of nonlinear dependencies. This plot shows, empirically, that the assumption of independence may be valid for this data. The Kendall rank correlation coefficient is 0.044, which shows a very weak dependency.

#### 11.3.1.2 Unplanned outages of wind turbines

The modeling of each wind turbine unplanned outage is computationally heavy. The alternative is an approximation, assuming that all the wind turbines are identical (with the same failure rate  $\lambda$  and unit size). For systems with high levels of wind generation and consequently high number of wind turbines, this approximation is acceptable. With this approximation and considering maintenance, the model becomes the simple Markov model.

For this model, where all the units are equal, the Binomial distribution can be used to build the capacity outage probability table (COPT) (Billinton and Allan, 1984). In this case the Binomial distribution is the following:

$$P(M = m|n, 1 - \lambda) = \frac{n!}{m!(n-m)!} \cdot (1 - \lambda)^m \cdot \lambda^{n-m} \quad (11.1)$$

<sup>2</sup> Data downloaded from: <http://www.nordpoolspot.com/historical-market-data/>.

where  $P$  is the probability that  $m$  turbines (out of  $n$ ) are in operation;  $\lambda$  the failure rate of each turbine. Because the subject is operating reserve, the outage replacement rate (ORR) should be used instead of the forced outage rate (FOR) (Billinton and Allan, 1984). The ORR represents the probability that a unit fails and is not replaced during the lead time  $T$ . The lead time is the period of time that generation cannot be replaced with the start of “offline” reserve units. The ORR is computed from the failure rate using the relation  $\text{ORR} \approx \lambda \cdot T$ .

Assuming a very high number of wind turbines, equal size units, and very low failure rate, the hypotheses of doing only a small adjustment on the forecasted distribution is reasonable. This approximation will enable a reduction of the computational complexity without compromising the accuracy of the model. The approximation can be evaluated for a system with the following characteristics: the number of wind turbines is 2000; the failure rate is between 1 and 10 failures per year; and the lead time is between 1 and 24 h. Assuming that each wind turbine has a rated power of 1.5 MW, the total capacity is 3000 MW. The mean and standard deviation of the COPT are given in Table 11.1.

The rate between the mean minus of the  $4\sigma$  (only 0.005% of generation is below this value) and the rated power is a very high percentage value, even for the worst case with a very high failure rate and lead time. This shows the low importance of a complex modeling of wind turbines outages in the operating domain. The *cdf* of the forecasted wind power can be adjusted using the mean value of the COPT to capture the effect of wind turbines’ outages.

### 11.3.1.3 Unplanned outages of conventional generation

The conventional generation (e.g., thermal power plants) operating points are defined by the market clearing or other dispatch mechanism, and its uncertainty is associated to unplanned outages. This uncertainty is represented by a *pmf* analogous to the COPT.

Several analytical methods that construct explicitly the COPT can be found in the literature. They can be further divided into two categories: the discrete and continuous distribution methods. A comparison between different approaches can be found in (Mazundar and Gaver, 1984; Alavi-Sereshki and Singh, 1991), where the authors concluded a low

**Table 11.1 Mean and standard deviation of the binomial distribution for the system**

Lead time (h)	$\lambda$ (failures/ year)	Mean (MW)	$\sigma$ (MW)	$4\sigma$ (MW)	(Mean – $4\sigma$ )/rated power
1	1	2999.658	0.716	2.866	0.998
24	1	2991.780	3.506	14.025	0.992
1	10	2996.575	2.265	9.060	0.995
24	10	2917.808	10.950	43.801	0.958

$$\text{where } E(M) = n \cdot (1 - \text{ORR}) \cdot 1.5 \quad \sigma(M) = \sqrt{n \cdot (1 - \text{ORR}) \cdot \text{ORR} \cdot 1.5}$$

accuracy of the continuous distributions methods when compared to other methods. In [Ghajar and Billinton \(1993\)](#), several methods for the evaluation of the marginal outage costs using the COPT were compared. The authors concluded that the fast Fourier transform (FFT) algorithm proposed by [Allan et al. \(1981\)](#) provides the best accuracy for all operating reserves in a reasonable amount of computational time.

The main idea with the FFT algorithm is to transform the unit capacity tables into the frequency domain using the FFT and to convolve using a point by point multiplication. In the end of the algorithm the inverse FFT algorithm is used to produce the final COPT. Following the units representation model for operating reserve described in [Billinton and Allan \(1984\)](#), each unit is only represented by two states (on or off) with the corresponding probability and the possibility of repairing the unit during the lead time is not considered. This method is computationally attractive since the computational time grows linearly with the number of units in the system.

As explained in the previous section, the ORR should be used instead of the FOR, so the expected value of the probabilities of failure during the lead time is very low. The ORR is calculated directly from the failure rate  $\lambda$  that can be estimated from a historical database of outages. Nevertheless, statistical postprocessing is recommended to adjust the failure rate. Assuming a Poisson distribution, it is possible to derive an upper bound for the failure rate directly from the probability of  $x$  failures or less in a total time  $t$  for a given confidence level ([Billinton and Allan, 1992](#)):

$$P_x = \sum_{k=0}^x \frac{(\lambda \cdot t)^k \cdot e^{-\lambda \cdot t}}{k!} \quad (11.2)$$

For example, for a confidence level of 95%, a generation unit with zero failures has an upper failure rate  $\lambda'$  equal to:

$$1 - 0.95 = e^{-\lambda' \cdot t} \Leftrightarrow \lambda' = \frac{3}{t} \quad (11.3)$$

#### 11.3.1.4 Load uncertainty

The most common representation of load uncertainty is by a Gaussian distribution with a given standard deviation and zero mean ([Billinton and Huang, 2008; Xie et al., 2017](#)). However, nonparametric representations, such as quantiles, may be more appropriate to represent uncertainty ([Xie et al., 2017](#)), particularly for load time series at the low voltage level ([BenTaieb et al., 2015](#)). In both cases, the mean and variance of the Gaussian distribution, or the quantiles, should be derived by a conditional estimator or model ([Liu et al., 2017](#)).

The representation through a set of quantiles is more useful for the convolution with the FFT, which will be explained in the next section. Nevertheless, the load forecast uncertainty represented by a Gaussian distribution can be approximated using a discrete interval method.

### **11.3.2 Separated energy and ancillary services market clearing**

#### **11.3.2.1 Framework**

In the current structures of most European electricity markets, the DA market session accepts bids for energy (generation and consumption in the next day) and sets closing price and quantity that correspond to the basic transactions. These quantities can be later adjusted through the day, in a set of intraday market sessions, but they are first subject to a validation process by the TSO regarding congestion and voltage limits issues. The TSO may need to change some of the approved transactions to obtain a viable diary program that corresponds to the technically feasible solution closer to the market results.

The next step is the ancillary services market for the next and current day, where the TSO sets values for the necessary reserves, taking into account the load level, the generation mix, and the relevant uncertainties (unit's failures, load forecasting, and renewables forecasting), to reduce the risk of loss of load to acceptable (very low) levels. Cost is not the main concern, but it is also part of the equation, since excessive reserves will be an economic burden to the consumers.

In this framework, and using the UCTE/ENTSO-E categories (UCTE, 2004), operational reserve includes secondary and tertiary reserves, so the bidding is normally made for the specified secondary reserve, with some additional rules applying (e.g., 2/3 of the reserve band for upward reserve, 1/3 to downward reserve), namely to the maximum tertiary reserve that could be mobilized if needed. These aspects are not discussed in the present chapter, where the main focus is to establish a relation between operational reserve and the risk of loss of load, as a basis to a decision-making process that may assume different formulations.

#### **11.3.2.2 Methodology to estimate system generation margin**

The SGM is the amount that the total system generation capacity exceeds the system load, which is also a random variable. The inputs to calculate the SGM are the probability distribution of renewable and conventional generation and load. Fig. 11.2 depicts the inputs and outputs of a robust reserve setting (RRS) tool developed for the Portuguese power system in the framework of the FP6 European Project ANEMOS.plus. In the Portuguese case, probabilistic forecasts are modeled separately for each RES technology, and the unplanned unavailability of hydropump storage is also considered in the COPT. A new suggestion of the regulation reserve requirements is produced either when a new market dispatch or a probabilistic forecast is available.

The first step is to compute the *pmf* of the sum of all RES technologies and conventional generation for each look-ahead time step. Assuming independence between all r.v. (in other words, between the all uncertainties), the sum can be computed by applying the convolution definition. The following equation shows an example for wind ( $W$ ) and conventional generation ( $C$ ):

$$P_G(W + C = z) = \sum_{k=-\infty}^{\infty} P_W(W = z - k) \cdot P_C(C = k) \quad (11.4)$$

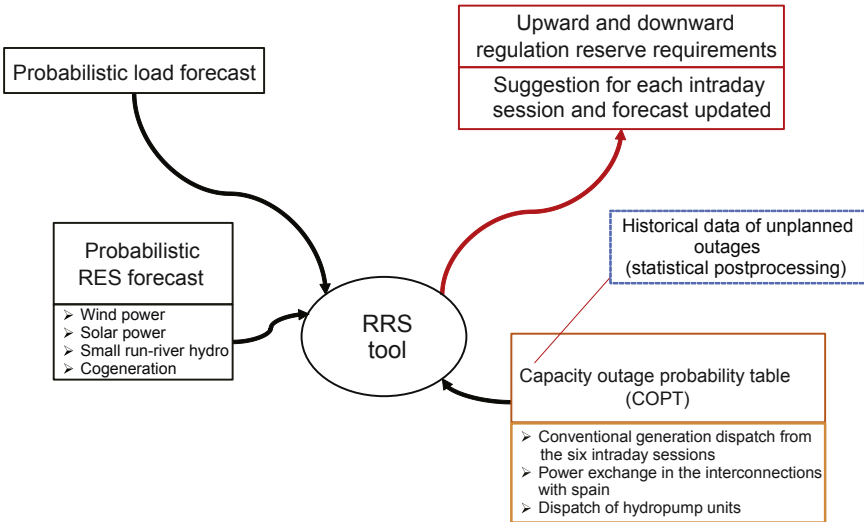


**Figure 11.2** Inputs and outputs from the robust reserve setting (RRS) tool.  
RES, renewable energy sources.

The direct convolution operation is computationally expensive in problems with a *pmf* characterized by a high number of points. As an example, if the *pmf* consists 50 points, the product in Eq. (11.4) is performed 441 times (all possible combinations). A more efficient way to compute the convolution is in the frequency domain with the FFT method (Springer, 1979). The method used to convolve two r.v. using FFT was adapted from the one described in (Kohl and Ruckdeschel, 2014). Note the convolution with the FFT is applied sequentially to each sum of r.v. from the generation side.

The system load is also calculated by summing the r.v. associated to the load probabilistic forecast with the COPT created with the ORR of hydropump units.

Finally, the SGM is the difference between the total generation ( $G$ ) and the load ( $L$ ), which also requires a convolution:

$$P_M(G - L = z) = \sum_{k=-\infty}^{\infty} P_G(G = z + k) \cdot P_L(L = k) \quad (11.5)$$

The SGM distribution is a discrete probability distribution for each time step, represented by its *pmf*, depicted in Fig. 11.3 for three cases: (1) no reserve; (2) 800 MW of upward reserve; and (3) 1000 MW of upward reserve. It is important to note the probability function of Fig. 11.3 is discrete, i.e., represented by a set of points and corresponding probability.

At this point, risk attributes related to the amount of loss of load or excess of generation, and meaningful for the SO, can be computed from the SGM. Following the approach described in Matos and Bessa (2011), the idea is to characterize the SGM distribution from Fig. 11.3 by a set of risk attributes, to give meaningful information to the operator about the impact of a potential reserve level. The classical measures in

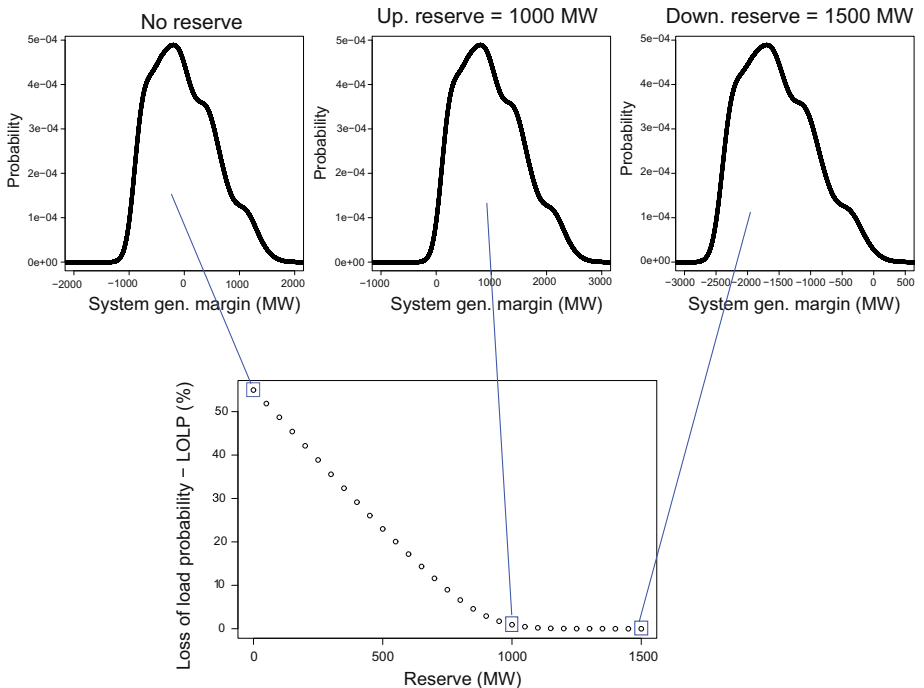


**Figure 11.3** Probability mass function of a system generation margin and LOLP versus reserve curve.

reliability Billinton and Allan (1984) can be calculated from the SGM distribution, e.g., loss of load probability (LOLP), loss of load expectation (LOLE), or the expected power not supplied. Risk indices related with the positive system margin can also be computed. In that situation, risk represents the probability of having excess generation to satisfy the load in the short term. The three *pmf*'s in the top of Fig. 11.3 correspond to a point in the risk—reserve curve of Fig. 11.3.

For instance, LOLP that represents the probability of the system load exceeding the available generation in a given period of time, has value 49% for the situation depicted in Fig. 11.3, if no reserve is scheduled in the system. Considering two possible upward reserve levels, 800 and 1000 MW, the SGM distribution has a horizontal translation, as depicted in Fig. 11.3. The risk decreases as the level of operating reserve increases, LOLP equal to 6.6% with 800 MW of reserve and equal to 0.9% when reserve is equal to 1000 MW.

As a result from the exercise depicted in Fig. 11.3, curves (represented by points) with reserve as a function of risk can be obtained. For instance, if we take the cumulative distribution of the SGM, a direct reading of LOLP and LOLE is possible for each reserve level. Fig. 11.3 illustrates that three points from this curve correspond to the SGM with three different reserve levels. Similar curves can be constructed for other risk metrics (Bessa and Matos, 2010).

### 11.3.2.3 Decision-making strategy

In this framework, there are no optimal solutions that could be found by a mathematical assessment (it is impossible to minimize simultaneously risk and cost). The purpose of the decision-aid phase is to support the decision maker in balancing between risk and cost and find the preferred solution for the reserve needs.

The simplest approach is to compare the risk measure with a threshold value and accept the corresponding cost. This method is generally accepted by SOs since it is common in power system planning (i.e., evaluate the adequacy of the generation units in providing the required reserve). For instance, the Governments of France and UK have set a tolerability threshold for the LOLE of 3 h per year that means a system security level of 99.97% ([RTE, 2014](#); [European Commission, 2014](#)).

This reference risk should be maintained through each hour of the scheduling horizon, therefore the reserve is adjusted in each hour to maintain a uniform risk level. The result is the same; either the objective is to minimize the cost or the reserve level. The decision rule can be formulated as follows:

$$\begin{aligned} \min \quad & r_i \\ \text{suj.} \quad & \text{Risk}_i(r_i) \leq \text{Risk}_{\text{ref}} \end{aligned} \tag{11.6}$$

For instance, in [Fig. 11.3](#), an LOLP equal to 0.45% would require a reserve level of at least 1050 MW.

The main drawback of this approach is the lack of intuitive interpretation of the risk indices and therefore is not easy to define a reference level. Also from an economic perspective, this solution is not “optimal” because the reserve cost is not taken into account. More elaborated decision-making strategies that use information about the trade-off between reserve cost and risk can be found in ([Matos and Bessa, 2011](#)).

### 11.3.3 Joint energy and ancillary services market clearing

#### 11.3.3.1 Framework

In this section, we describe a joint energy and reserve market clearing in a two settlement electricity market, commonly used in U.S. ISO/RTO electricity markets. We also introduce a probabilistic ORDC that is used in the market clearing. The concept of an ORDC has existed in the academic literature for quite a while (e.g. [Hogan, 2005](#)) but was only recently introduced in actual market operations in Texas in 2014 ([ERCOT, 2013](#)). In [Zhou and Botterud \(2014\)](#) we proposed a method to account for the uncertainty in wind power forecasts when deriving ORDCs, as outlined briefly in this section.

The market operation includes a DA market and an RT market, which are cleared in sequence. At the DA stage, the market is solved by UC and ED models based on supply and demand bids for energy and reserve, and DA wind power forecasts. The demand for reserves is modeled by an ORDC, which is developed to associate the price that a SO should pay for reserve to the economic/reliability benefit it provides to the system, as discussed in more detail in the next section. The market clearing model

cooptimizes energy and reserves simultaneously, which is common in US electricity markets. After the DA market, the SO has a chance to revise the commitment schedule by adjusting the status of fast units. The procedure is called Reliability Assessment Commitment (RAC). At this stage, the wind power forecasts and ORDCs are updated accordingly. After the RAC procedure, the RT ED is executed with the realized wind power supply and with an updated ORDC based on the latest probabilistic forecasts.

The commitment of generating units to provide energy and operating reserves is a key procedure for SOs to ensure that sufficient capacity is available to handle demand in real time, given uncertainty and variability in supply and demand resources. We use a UC model to investigate the use of ORDC and joint energy and reserve optimization in electricity market operations. The model maximizes the total social welfare over a preset period of time, usually 24 h. The social welfare is defined as the difference between the economic benefits of reserves and the system's operating cost, assuming that there is no demand response for energy. At a high level, the mathematical formulation can be described as:

Maximize: economic benefits of reserves – (fuel cost + start-up cost + unserved energy cost)

Subject to:

1. Energy balance constraints;
2. Operating reserve supply–demand balance constraints; and
3. UC constraints, such as ramping, minimum up/down constraints, etc.

The UC problem is formulated as a mixed integer linear programming problem with stepwise thermal unit cost functions and ORDC. The prices of energy and reserves are the dual variables of the energy balance constraints and operating reserve balance constraints, respectively, in the ED stage, whose formulation is a linear programming problem because the integer variables (UC schedule) are fixed.

### **11.3.3.2 Methodology for developing an operating reserve demand curve**

The ORDC is derived from the SGM distribution ( $P_M(M = m)$ ), which is developed with a similar method to the one introduced in [Section 11.3.2](#). There are three sources of uncertainties: forced outages of conventional generation, load forecast uncertainty, and wind power forecast uncertainty. They are assumed independent. Note that since the ORDC is derived before the market clearing, the set of committed thermal generators must be estimated. This is done based on the net load forecast and a merit order list of the thermal generators, as explained in detail in [Zhou and Botterud \(2014\)](#). Given the pmf's of wind forecasts ( $P_W(W = w)$ ), load forecasts ( $P_L(L = l)$ ), and the set of conventional generation units expected to be committed ( $P_G(G = g)$ ), the distribution of the SGM can be developed by the convolution of the distributions of the three sources of uncertainty, as follows:

$$\begin{aligned} P_M(M = m) &= P_M(W + G + (-L) = m) \\ &= \sum_{l=-\infty}^{\infty} \sum_{g=-\infty}^{\infty} P_W(W = m + l - g) \cdot P_G(G = g) \cdot P_L(L = l) \end{aligned} \quad (11.7)$$

When the SGM is negative, it means there is a supply shortage. With a certainty amount of reserves added, the SGM increases, and the probability of lost load decreases. In this way, we can develop the LOLP, which is the cumulative probability that the generation margin is less than zero, that is  $P(M + R < 0)$ . Then, the price that a SO should pay for reserves can be represented as follows:

$$\text{Price}(r) = \text{LOLP}(r, m) * \text{VOLL} \quad (11.8)$$

where  $r$  is the level of reserve,  $m$  is the amount of generation margin,  $\text{LOLP}(r, m)$  is the LOLP given the total of the amount of reserve and SGM, and value of loss load (VOLL) is the value of lost load. Sampling levels of reserve from 0 to the amount  $T$ , where additional reserve does not provide significant additional value to the system, an ORDC can be developed, as showed in Fig. 11.5.

Fig. 11.5 shows a ten-step ORDC curve, derived from Fig. 11.4 with equal length of reserve increments. In Fig. 11.5,  $P_0$  corresponds to the product of VOLL and LOLP when there is no reserve. This means that if the price of offered reserve is equal to or greater than  $P_0$ , it would not purchase reserves because the cost is higher than the benefit provided to the system. By including the ORDC in the joint market clearing formulation for energy and reserves, the optimization will consider the trade-off

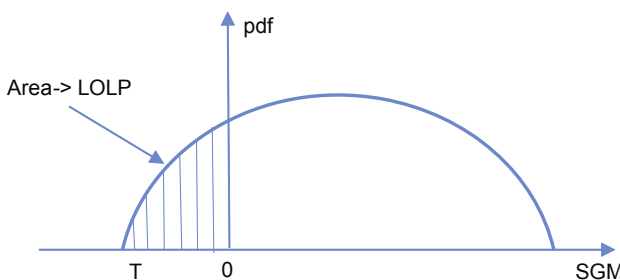


**Figure 11.4** Generation margin probability distribution. *LOLP*, loss of load probability; *pdf*, probability distribution function; *SGM*, system generation margin.

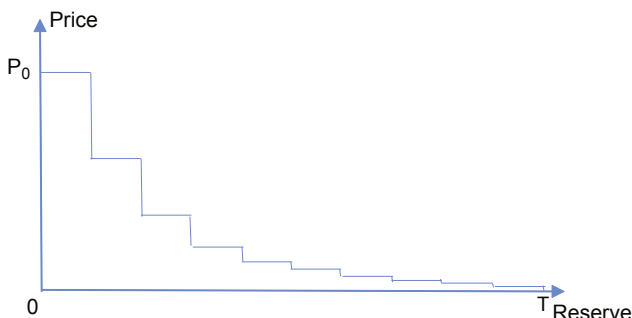


**Figure 11.5** A stepwise operating reserve demand curve.

between the cost and benefits of reserves along with the cost of meeting the load in the system. The benefit of reserves corresponds to the integral under the ORDC curve up to the cleared reserve level. Note that the ORDC curve in Fig. 11.5 is very similar to the LOLP curve in Fig. 11.3, only that the ORDC curve is multiplied with VOLL, which enables the integration of the curve into the market clearing formulation for economic optimal scheduling of resources for both energy and reserves. For more details on the development of the stepwise ORDC, we refer to Zhou and Botterud (2014).

## 11.4 Illustrative results

This section presents a set of illustrative results for the methodologies described in Section 11.3 covering the two types of reserve setting models: (1) separated energy and reserve market clearing (Portuguese test case) and (2) joint clearing of energy and reserve with ORDC (Illinois test case).

### 11.4.1 Separated energy and ancillary services market clearing

#### 11.4.1.1 Assumptions

The results presented in this section were collected during the demonstration for the Portuguese Transmission System Operator, in the framework of the EU Project ANEMOS.plus, and for the period between end of 2010 and mid-2011. The capacity mix in the Portuguese power system in the end of 2010 was 4.578 GW of hydrogen generation, 7.407 GW of thermal generation, and 6.077 GW of generation under a tariff remuneration scheme. The generation under a tariff remuneration scheme is minihydro (0.414 GW), CHP (1.687 GW), wind generation (3.854 GW), and photovoltaic (0.123 GW). In 2010 the maximum peak power was 9.403 GW. Around 17% of the total consumption was wind generation. Wind power is remunerated with a fixed feed-in tariff and does not participate in the electricity market.

The reserve that is estimated by the tool is tertiary reserve (*reserva de regulação* in Portuguese), which was mainly used to handle imbalances between load and generation in each hourly interval.

The RRS tool results are compared with the following deterministic rules:

- Rule 1 (rule in place during 2010–11 in Portugal): upward reserve equal to 2% of the forecasted load plus the largest unit in the system (435 MW); downward reserve equal to 2% of the forecasted load.
- Rule 2: rule 1 plus 20% of the wind power point forecast for both upward and downward reserve

#### 11.4.1.2 Illustrative results

The tertiary reserve suggested by the RRS tool (with a maximum LOLP equal to 0.5% defined by the decision maker) for the intraday markets was compared to the reserve effectively mobilized. Since for each intraday session a new reserve value is suggested, for illustrative purposes only the most recent reserve suggestion is showed.

**Fig. 11.6** depicts the suggested downward reserve by the RRS tool and deterministic rules, and mobilized reserve (historical data publicly available in [www.mercado.ren.pt](http://www.mercado.ren.pt)) for October 11, 2010. Both deterministic rules suggested reserve levels below the mobilized reserve in almost every hour. The reserve suggested by the RRS tool avoids situations with insufficient reserve in the system.

It is important to stress that the goal is not to predict the mobilized reserve but to conduct a risk analysis and suggest a reserve level in accordance with the desired risk threshold. In this day, the deterministic rules have a probability of generation deficit much higher than 0.5% since the reserve levels are lower than those suggested by the RRS tool. Another disadvantage of the deterministic rules is their inability to provide information about risk.

**Fig. 11.7** depicts the estimated upward reserve requirements for November 27, 2010. In the last period of the day, there is a significant increase in mobilized reserve, and only the RRS tool detects this requirement and suggests appropriate reserve levels. The two deterministic rules suggest insufficient reserves in the last hours of the day.

**Fig. 11.8** shows the downward reserve suggested for December 10, 2010. As in previous days, both deterministic rules suggest insufficient reserve levels compared to the mobilized reserve. The reserve suggested by the tool is always above the mobilized one and shows a pattern consistent with the variation of the mobilized reserve, e.g.,

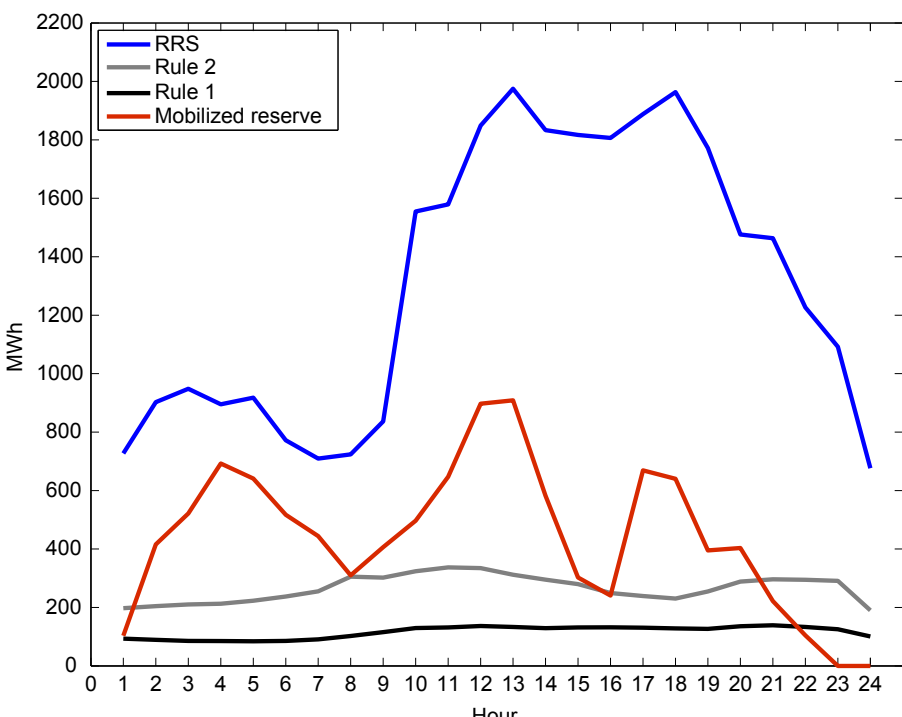


**Figure 11.6** Suggested downward reserve for of October 11, 2010.

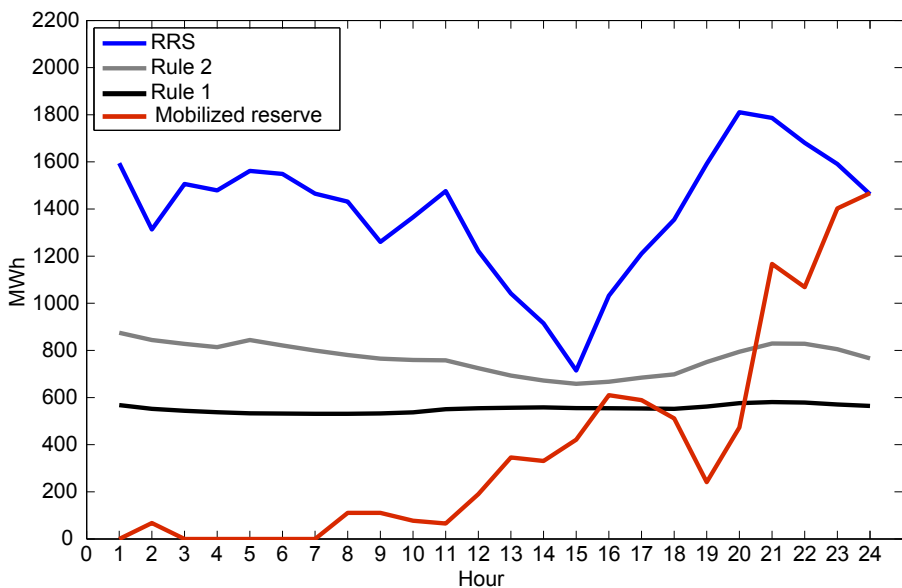


Figure 11.7 Suggested upward reserve for November 27, 2010.

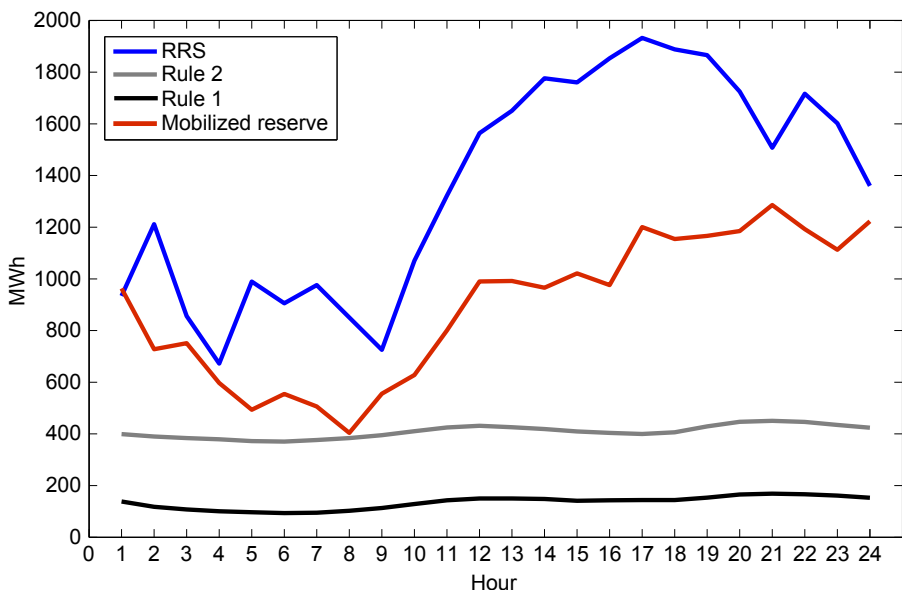


Figure 11.8 Suggested downward reserve for December 10, 2010.

there is an increase in mobilized reserve between 9h00 and 24h00, and this is also accompanied by the suggested reserve.

These three days illustrate situations where the reserve suggested by deterministic rules is below the mobilized reserve, which can lead to operating scenarios with high risk. However, opposite situations can also occur. That is, there may be situations in which the reserve level suggested by the rules is excessive, leading to a risk much lower than 0.5%. Such situations are illustrated in Fig. 11.9 (February 12, 2011) and Fig. 11.10 (April 29, 2011).

In Fig. 11.9, the reserve suggested by the deterministic rules was always sufficient. However, the suggested reserve level, in some hours, is much higher than reserve suggested by the tool and actually mobilized. In these situations, the risk associated with rules is less than the risk desired by the operator. The conclusions for Fig. 11.10 are analogous.

Importantly, in all cases presented, the reserve suggested by deterministic rules presents only slight variations between hours. This characteristic is a further disadvantage of deterministic rules because it suggests a lower sensitivity in relation to the time-varying power system operating conditions. For instance, it is expected that in hours with high uncertainty associated to RES, the suggested reserve is higher compared to hours where uncertainty is lower.

#### 11.4.1.3 Overall risk assessment

The main requirement for a risk-based reserve setting tool is to have a match between the predefined risk value and the observed number of insufficient reserve situations

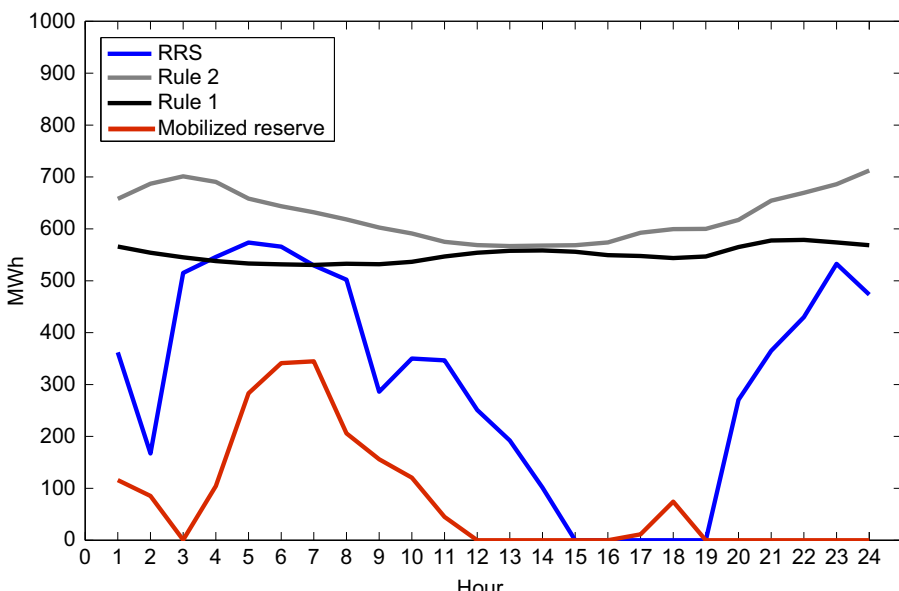


**Figure 11.9** Suggested upward reserve for February 12, 2011.

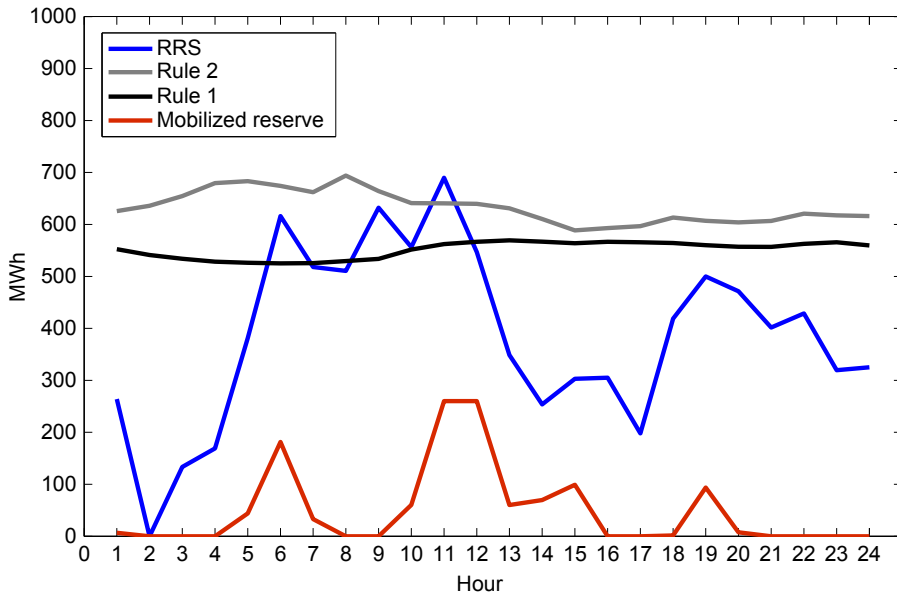


**Figure 11.10** Suggested upward reserve for April 29, 2011.

(i.e., mobilized reserve greater than suggested reserve) for an evaluation period (Bessa et al., 2012a,b). For an 8-month period, Table 11.2 compares the predetermined risk level and the number of situations where the suggested reserve was insufficient. The results show that the RRS tool is well calibrated for the upward direction, and deterministic rules lead to high risk. In the case of downward reserve, the number of hours with insufficient reserve is higher than the predefined risk. This deviation is related to the quality of the probabilistic forecasts; a more detailed discussion of these results can be found in Bessa et al. (2012a,b). Finally, the risk of deterministic rules for the downward reserve is very high, indicating that the suggested reserve is often insufficient.

### 11.4.2 Joint energy and ancillary services market clearing

#### 11.4.2.1 Assumptions

The market simulation is conducted on a simplified power system for the US state of Illinois from 2006 to 2007, to study the potential effects of using the ORDC to

**Table 11.2 Number of situations with insufficient suggested reserve for a predefined risk threshold equal to 0.5%**

Predefined risk threshold = 0.5%	RRS (%)	Rule 1 (%)	Rule 2 (%)
Upward reserve	0.40	2.46	0.78
Downward reserve	3.27	55.87	34.36

accommodate wind power variability and uncertainty under a large-scale expansion of wind power. The system consists of 210 thermal power plants. The thermal unit data include max/min output, minimum on/off times, and the cost of cold/warm start-ups. For the detailed information sources of heat rate curves, fuel costs, max/min output, etc., we refer to Zhou and Botterud (2014), Botterud et al. (2013) and Zhou et al. (2013). The total thermal capacity is 41,380 MW, 10.6% higher than the peak load. We assume that the VOLL is 3500 \$/MWh. The percentage of spinning reserve is set to 50% of the total operating reserve requirement, with the rest being met by non-spinning resources.

The total installed capacity of wind power in the system is assumed 14,000 MW. Under this assumption, wind power provides 20% of the in-state load and 16.6% of the total load including export in the simulation period July–October. The wind power data correspond to wind power forecasts and realized wind power generation for 15 hypothetical locations in the state of Illinois for 2006 from the Eastern Wind Integration and Transmission Study (EWITS). For details of time series of wind power generation, we refer to Brower (2009). In this analysis, we used the DA wind power point forecast from EWITS in the DA market clearing and a 1 h ahead persistence point forecast for the RAC operation. We focus primarily on DA results below.

#### 11.4.2.2 Illustrative results

##### 1. Development of the ORDC

Figs. 11.11 and 11.12 illustrate the development of the ORDC for the first hour of July 24, 2006 in the DA market. In Fig. 11.11, the three graphs in the top row are, from left to right, the probability distributions of load, wind power, and conventional generation. The convolution of the three stochastic variables derives the probability distribution of the SGM for that hour in the lower graph, as explained in Section 11.3.3. The area of the section to the left of zero is the LOLP if there is no reserve. As operating reserves are added, the SGM distribution function is shifted to the right, accordingly, and the LOLP becomes smaller. Then, based on Eq. (11.8), pairs of prices and reserve demand quantities can be sampled from the generation margin distribution to form a demand curve (Fig. 11.12).

In this analysis, it is assumed that thermal units bid their operating costs for energy, without separate bids for reserve. However, the opportunity cost of energy is reflected in the cooptimized market clearing. Therefore, the operating reserve and energy prices are determined by both the risk/uncertainty level of the system and the available capacity for energy and reserves. As long as the system uncertainty level is low and there is surplus capacity, the prices would remain low. If the uncertainty level is high and there is supply scarcity in the system, the prices would be high for both energy and reserves. As showed in Fig. 11.12, if additional capacity is scheduled as reserve, the system risk level would become lower, and the marginal prices for the next unit of reserve will be lower (or at least stay the same because of the stepwise representation). In this case, the algorithm considers the risk of load curtailment and the additional cost of committing more capacity to derive the optimal dispatch schedule. The resulting prices for energy and reserve reflect the state of the system and the corresponding risk of load curtailment and therefore provide better price signals than traditional formulations with price inelastic operating reserve requirements. Moreover, the joint optimization of energy and reserves ensure efficient use of the available resources in the system.

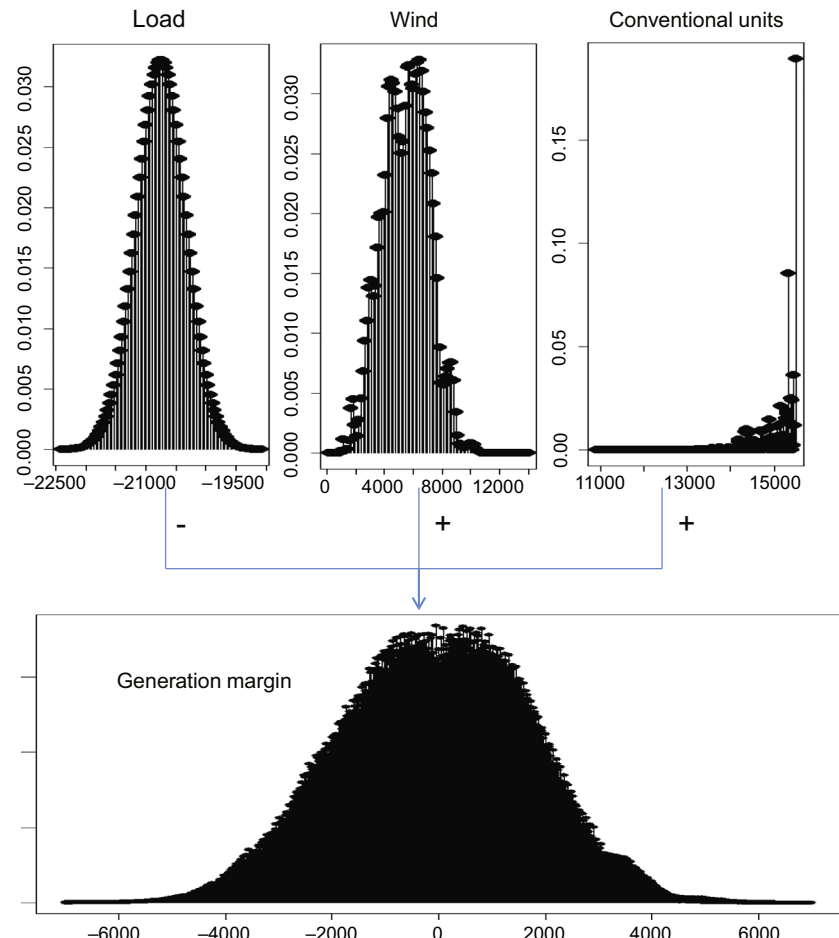


**Figure 11.11** An example of system generation margin (SGM) probability distribution (hour 1 on July 24, 2006).

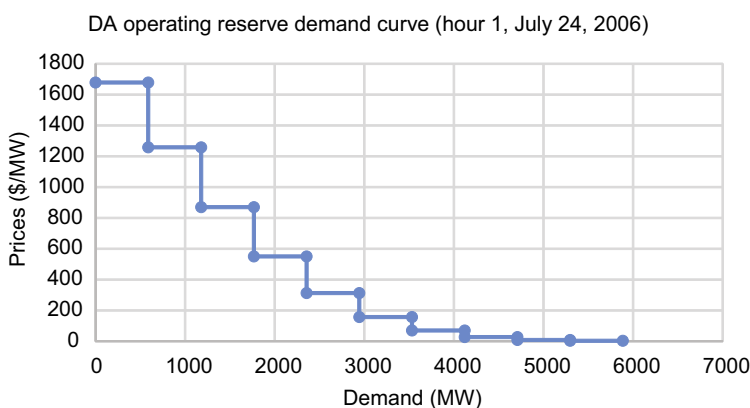


**Figure 11.12** An example of operating reserve demand curve (hour 1 on July 24, 2006).

## 2. System operation analysis

To evaluate and compare the performance of the proposed model, four cases with different reserve strategies are implemented: labeled as PF (perfect forecast), DR (dynamic reserve), FR (fixed reserve), and DC (demand curve). Case PF serves as a benchmark and uses no reserve other than a fixed contingency reserve (equal to the largest generator of 1146 MW) because it assumes a perfect forecast for wind and load. In addition to the contingency reserve, case DR uses a dynamic reserve strategy, which sets the additional amount of hourly operating reserve equal to the difference between the 50% and 1% quantile of the probabilistic wind power forecasts. Likewise, case FR uses a fixed reserve strategy, which sets the amount of additional hourly operating reserves equal to the average of the additional dynamic reserve in case DR. Case DC uses the proposed ORDC to set the amount of the reserve requirement dynamically on the basis of system conditions. Specifically, when developing the ORDC, we assume that the load is normally distributed with a mean equal to the realized load data and standard deviation equal to 2% of the hourly load at the DA stage. The load distribution in the RAC stage is similar but with 1% variance to reflect a smaller load forecasting error than at the DA stage.

**Fig. 11.13** compares the amount of cleared operating reserves for the four cases. It is higher in all hours for the DC strategy as compared to the other three cases. The reason is that the SO purchases available capacity as operating reserve as long as the additional cost is lower than the reliability benefit. Moreover, during peak hours, the scheduled amount of reserves from the DC strategy is higher than that found using other models because more thermal units are committed during peak hours. This makes the probability of forced outages higher, which is one of the determinant factors to determine the LOLP and the corresponding demand curve for reserves. The scheduled reserve under the DR strategy, which also considers the uncertainty in the wind forecast, follows a similar pattern as in the DC case but with a lower level of reserves. The other two cases apply a constant amount of reserves across all the hours of the day, regardless of the forecasted uncertainty level.

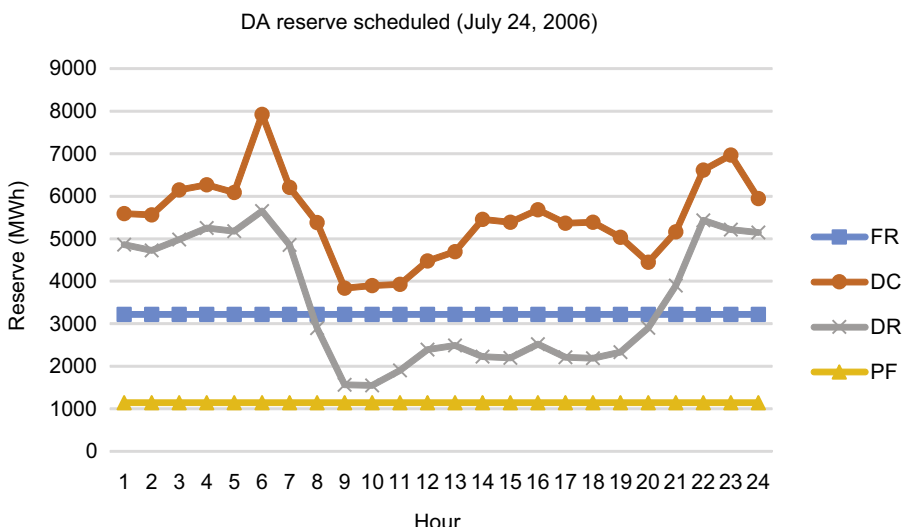


**Figure 11.13** Total reserve quantity in the day-ahead (DA) market on July 24, 2006.

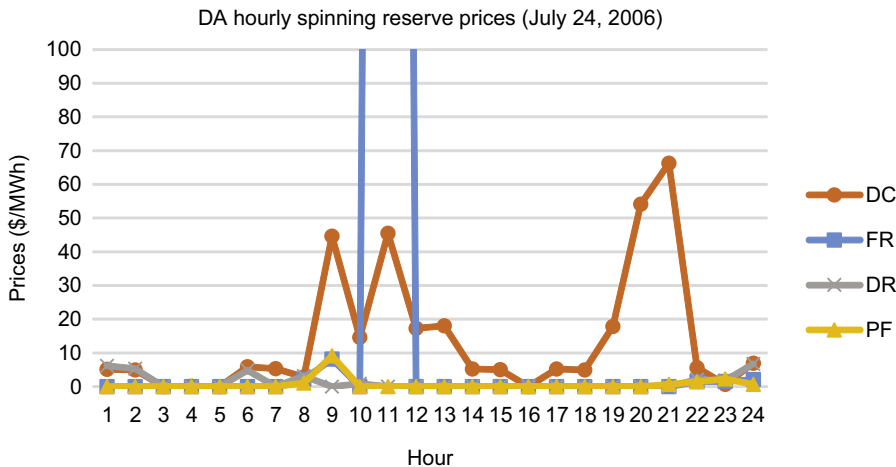


**Figure 11.14** Hourly spinning reserve prices in the day-ahead (DA) market on July 24th, 2006.

Reserve and energy prices of the four cases on July 24, 2006 are shown in Figs. 11.14 and 11.15, respectively. In terms of reserve prices, those from the DC model are generally higher than in the cases without the demand curve. The reason is that, in the DC case, all available capacity from committed units that can be used for reserve is accounted for when the SO clears the market. In turn, this means that all units have the opportunity to get compensated if they have the capability to provide operating reserve, as long as the marginal cost of additional reserve is lower than the benefit in terms of increased reliability. This differs from cases with a preset, fixed operating reserve requirement, where generation units may oftentimes not

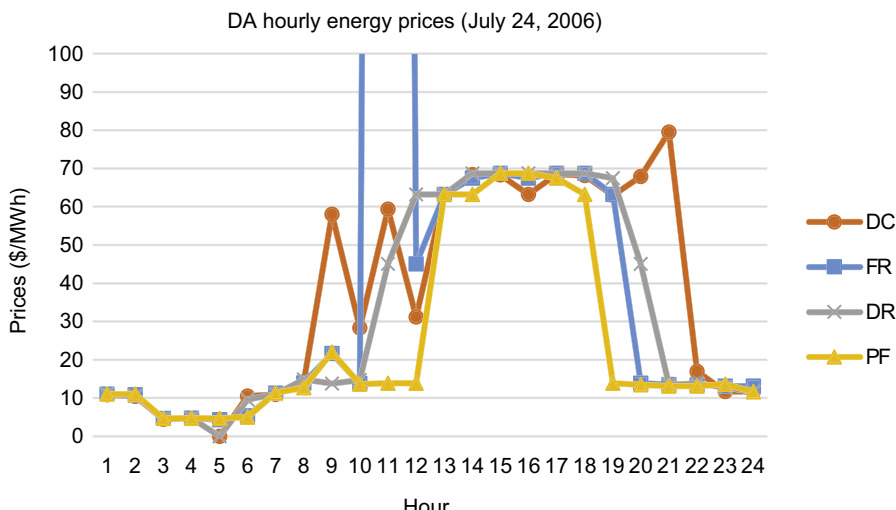


**Figure 11.15** Hourly energy prices in the day-ahead (DA) market on July 24th, 2006.

be compensated for having reserve capacity available, even if they contribute to improve system reliability. Therefore, the DC model offers a more equitable approach to compensating the generation capacity for providing reserve through a market mechanism. The operating reserve prices are close to zero for the other cases in most of the hours. The main exception is for the FR strategy, which sees a large price spike in hour 11 because of shortage of reserves, which brings the price up to the administratively determined penalty cost, assumed to be \$1100/MW-h for reserve shortfalls.

The operating reserve strategy also influences energy prices (Fig. 11.14). For the DC strategy, the figure shows that there is a close link between the reserve and energy prices. For instance, both markets see high prices in hours 20–21 in case DC. Moreover, the energy price for the DC strategy tends to be higher than for the other cases in hours where the reserve prices are high, indicating scarcity in the system. In general, the cooptimization of energy and reserves along with the ORDC ensure that the prices for both reserves and energy in the system reflect the level of forecast uncertainty for wind and load and the likelihood of forced outages for thermal generators, as well as the cost of supply.

Finally, Fig. 11.16 shows the estimated hourly LOLP at the DA stage based on the amounts of scheduled reserve in each case (Fig. 11.13). The DC strategy maintains a low and relatively constant LOLP level throughout the day. In contrast, for all the other strategies, there is a high variation in the estimated LOLPs. Cases PF and DR show high LOLPs during peak hours, where wind uncertainty is low and the need for reserves is primarily driven by forced outages of thermal units due to the high number of committed generators. This aspect is only adequately accounted for in the DC strategy through the probabilistic representation of forced outages. The FR strategy obtains a lower LOLP during the peak hours than the DR strategy because of the fixed amount of additional wind reserve. Finally, note that Fig. 11.16 overestimates the actual system LOLP since the SO usually can schedule additional resources if needed, i.e., beyond the scheduled operating reserves, in the recommitment and dispatch procedures that take place between the DA and RT markets.

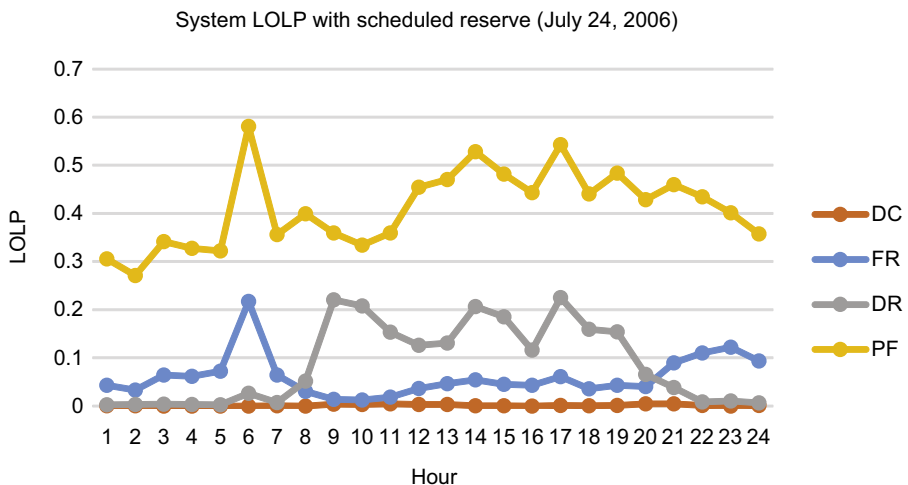


**Figure 11.16** Hourly system loss of load probability (LOLP) in the DA market on July 24, 2006.

### 11.4.3 Qualitative analysis of the methodologies

The two methodologies, one for separated/sequential markets and the other for joint/cooptimized markets, described in [Section 11.3](#), share a similar probabilistic approach. Both methods are based on convolutions (that assume independence of random variables) and calculate the SGM separately for each hour, despite the differences in how the markets are operated. This shows that a standard probabilistic framework can be easily adapted to handle different electricity market structures and include alternative cost functions for reserve procurement.

The separated approach ([Section 11.3.2](#)), more suitable for European markets, handles cost and risk separately mainly because the regulatory framework induces SO to operate the power system with very low risk. Nevertheless, linear and nonlinear trade-offs between reserve cost and risk can easily be included in the tool, depending on the risk preferences of the SO ([Matos and Bessa, 2011](#)).

The joint ORDC approach ([Section 11.3.3](#)) from the United States converts LOLP to economic terms, which enables cooptimization of energy and reserves. In this case, the representation of risk preferences is primarily reflected in the choice of VOLL, which in turn influences the demand for operating reserves. In general, cooptimization has certain benefits in terms of optimal resource scheduling to meet energy and reserve needs, and the ORDC approach contributes to improve the market efficiency. A thorough discussion of the pros and cons of cooptimization in electricity markets is available in [Kirschen and Strbac \(2004\)](#) and [Read \(2010\)](#).

## 11.5 A look into the future

Recently, SOs have been very active in integration of renewable energy uncertainty forecasts into system management functions, with most of the work focused on reserve setting and UC policies. A large number of SOs already generate internally or purchase point and probabilistic forecasts for renewable generation, and their goal is to embed this information in power flow and load-generation balancing software.

It is to be noted that all these successful developments were mostly focused on the traditional paradigm of managing the electric power system. The increasing integration of distributed energy resources (DERs) at the distribution network level significantly poses new challenges and a need to consider future actors in the systems (e.g., DER aggregators), as well as flexible DER owned by the Distribution System Operator (DSO) (e.g., storage). Furthermore, the progressive integration of RES in energy and ancillary services markets, which we have discussed in this chapter, may require a complete redefinition of the market structures and induce changes in reserve setting and procurement mechanisms. Some recent trends related to RES, DER, and the balancing of supply and demand in the power system are briefly described below.

One trend is the design of DA stochastic market dispatch mechanisms that aim at maximizing market efficiency by anticipating expected system balancing costs from renewable energy forecast errors (e.g., [Morales et al., 2014a](#)). In this framework, the electrical generation from stochastic generators (e.g., wind or solar generation) is

modeled by a set of scenarios, characterized by a vector of power values and a probability of occurrence. A new merit order to offers is designed where flexible generators may be dispatched out of merit order in the DA market to guarantee that sufficient capacity is available in RT to deal with energy imbalances (Morales et al., 2014b). In this scenario, the reserve setting problem is embedded in the market dispatch through a stochastic formulation, but it means a radical change in electricity markets rules and mechanisms.

The flexibility from demand-side resources is being extensively studied in the literature and at the industrial level in several smart grid test pilots. From the SO perspective, forecasting the load participation in ancillary services might be a difficult task. Several factors (e.g., nature of the load, control algorithms, aggregation size) could make it difficult to deliver the contracted energy or reserve capacity (Kirby and O’Malley, 2011). Therefore, it is important to develop mechanisms, such as probabilistic offers (Kirby and O’Malley, 2011) or complex offers (O’Connell et al., 2016), that mitigate this problem since this new resource, even when aggregated, will introduce two sources of uncertainty: (1) the load profile will become more variable and uncertain, which might result in a higher load forecast error; (2) reserve from demand response resources might have some level of unavailability that should be modeled by the reserve setting methodologies.

In this context, operational flexibility modeling at different voltage levels will play an important role. This flexibility should be characterized by available capacity, available storage energy, and power ramp rate (or response time). One recently proposed modeling approach is the Power Nodes model that allows a detailed functional modeling of DER units such as storage units (e.g., batteries, flywheels) and dispatchable conventional and RES generation (Ulbig and Andersson, 2015). On top of these flexibility modeling methods, it is possible to design a new generation of tools for setting the reserve/flexibility inter- and intrahourly requirements (Nosair and Bouffard, 2015; Dvorkin et al., 2014), considering also the multitemporal nature of some resources.

Finally, the activation of reserve capacity by the SO that is connected to the distribution networks may create technical problems in the DSO management tasks (Rivero et al., 2015). In the future, the coordination between SO and DSO in terms of reserve activation needs to be improved since both entities might explore distributed DER connected to the distribution grid for different (and sometimes conflicting) purposes, such as voltage control, congestion management, and frequency balancing.

## Acknowledgments

This work is financed by the FCT—Fundação para a Ciência e a Tecnologia (Portuguese Foundation for Science and Technology) within project UID/EEA/50014/2013 and by the US Department of Energy, Office of Energy Efficiency and Renewable Energy through its Wind and Water Power Program.

## References

- Alavi-Sereshki, M., Singh, C., 1991. A generalized continuous distribution approach for generating capacity reliability evaluation and its applications. *IEEE Transactions on Power Systems* 6 (2), 16–22.
- Alessandrinini, S., Delle Monache, L., Sperati, S., Cervone, G., 2015. An analog ensemble for short-term probabilistic solar power forecast. *Applied Energy* 157, 95–110.
- Allan, R., Leite da Silva, A., Abu-Nasser, A., Burchett, R., 1981. Discrete convolution in power system reliability. *IEEE Transactions on Reliability* 30 (5), 452–456.
- Andersen, P., 2009. Optimal Operation of a Wind-Storage Power System under Market Conditions (Master thesis). Technical University of Denmark.
- BenTaieb, S., Huser, R., Hyndman, R., Genton, M., 2015. Forecasting Uncertainty in Electricity Smart Meter Data by Boosting Additive Quantile Regression. Monash University. No 12/15 Working Paper.
- Bessa, R.J., Miranda, V., Botterud, A., Zhou, Z., Wang, J., 2012a. Time-adaptive quantile-copula for wind power probabilistic forecasting. *Renewable Energy* 40 (1), 29–39.
- Bessa, R., Matos, M.A., 2010. Dealing with wind power forecast uncertainty. In: Proceedings of the 25th Mini-Euro Conference on Uncertainty and Robustness in Planning and Decision Making.
- Bessa, R.J., 2015. From marginal to simultaneous prediction intervals of wind power. In: Proceedings of the 18th Intelligent Systems Applications to Power Systems Conference and Debate (ISAP 2015), Porto, Portugal.
- Bessa, R.J., Matos, M., Costa, I.C., Bremermann, L., Franchin, I.G., Pestana, R., Machado, N., Waldl, H., Wichmann, C., 2012b. Reserve setting and steady-state security assessment using wind power uncertainty forecast: a case study. *IEEE Transactions on Sustainable Energy* 3 (4), 827–836.
- Billinton, R., Allan, R.N., 1984. Reliability Evaluation of Power Systems. Plenum Press, New York and London.
- Billinton, R., Allan, R.N., 1992. Reliability Evaluation of Engineering Systems. Plenum Press, New York.
- Billinton, R., Huang, D., 2008. Effects of load forecast uncertainty on bulk electric system reliability evaluation. *IEEE Transactions on Power Systems* 23 (2), 418–425.
- Billinton, R., Li, W., 1994. Reliability Assessment of Electric Power Systems Using Monte Carlo Methods. Springer Science & Business Media.
- Botterud, A., Zhou, Z., Wang, J., Sumaili, J., Keko, H., Mendes, J., Bessa, R.J., Miranda, V., 2013. Demand dispatch and probabilistic wind power forecasting in unit commitment and economic dispatch: a case study of Illinois. *IEEE Transactions on Sustainable Energy* 4 (1), 250–261.
- Bouffard, F., Galiana, F.D., 2008. Stochastic security for operations planning with significant wind power generation. *IEEE Transactions on Power Systems* 23 (2), 306–316.
- Bremermann, L.E., Matos, M., Lopes, J.A.P., Rosa, M., 2014. Electric vehicle models for evaluating the security of supply. *Electric Power Systems Research* 111, 32–39.
- Brower, M., 2009. Development of Eastern Regional Wind Resource and Wind Plant Output Datasets. NREL Subcontract Report NREL/SR-550-46764.
- Doherty, R., O’Malley, M., 2005. A new approach to quantify reserve demand in systems with significant installed wind capacity. *IEEE Transactions on Power Systems* 20 (2), 587–595.
- Dvorkin, Y., Kirschen, D.S., Ortega-Vazquez, M.A., 2014. Assessing flexibility requirements in power systems. *IET Generation, Transmission & Distribution* 8 (11), 1820–1830.

- ERCOT, 2013. Methodology for implementing operating reserve demand curve (ORDC) to calculate real-time reserve price adder, fifth draft. Electric Reliability Council of Texas (ERCOT).
- European Commission, 2014. United Kingdom Electricity Market Reform – Capacity Market. C (2014) 5083 Final.
- Ghajar, R., Billinton, R., 1993. Comparison of alternative techniques for evaluating the marginal outage costs of generating systems. *IEEE Transactions on Power Systems* 8 (4), 1550–1556.
- He, M., Yang, L., Zhang, J., Vittal, V., 2014. A spatio-temporal analysis approach for short-term forecast of wind farm generation. *IEEE Transactions on Power Systems* 29 (4), 1611–1622.
- Hedayati-Mehdiabadi, M., Zhang, J., Hedman, K.W., 2015. Wind power dispatch margin for flexible energy and reserve scheduling with increased wind generation. *IEEE Transactions on Sustainable Energy* 6 (4), 1543–1552.
- Hogan, W.W., 2005. On an “Energy Only” Electricity Market Design for Resource Adequacy. Harvard University. Working Paper.
- Holttinen, H., Milligan, M., Ela, E., Menemenlis, N., Dobschinski, J., Rawn, B., et al., 2012. Methodologies to determine operating reserves due to increased wind power. *IEEE Transactions on Sustainable Energy* 3 (4), 713–723.
- Kirby, B., O’Malley, M., 2011. Load Participation in Ancillary Services: Workshop Report. US Department of Energy.
- Kirschen, D.S., Strbac, G., 2004. Fundamentals of Power System Economics. John Wiley & Sons.
- Kohl, M., Ruckdeschel, P., 2014. General purpose convolution algorithm for distributions in S4-classes by means of FFT. *Journal of Statistical Software* 59 (4), 1–24.
- Lange, M., 2005. On the uncertainty of wind power predictions – analysis of the forecast accuracy and statistical distribution of errors. *Journal of Solar Energy Engineering* 127 (2), 177–184.
- Lin, J., Sun, Y.Z., Cheng, L., Gao, W.Z., 2012. Assessment of the power reduction of wind farms under extreme wind condition by a high resolution simulation model. *Applied Energy* 96, 21–32.
- Liu, B., Nowotarski, J., Hong, T., Weron, R., 2017. Probabilistic load forecasting via Quantile Regression Averaging on sister forecasts. *IEEE Transactions on Smart Grid* 8 (2), 730–737.
- Maggio, D., 2009. Integrating wind forecasting into market operation – ERCOT. Presentation at Utility Wind Integration Group (UWIG) Workshop, Phoenix, USA.
- Matos, M., Bessa, R.J., 2011. Setting the operating reserve using probabilistic wind power forecasts. *IEEE Transactions on Power Systems* 26 (2), 594–603.
- Matos, M., Lopes, J.P., Rosa, M., Ferreira, R., da Silva, A.L., Sales, W., et al., 2009. Probabilistic evaluation of reserve requirements of generating systems with renewable power sources: the Portuguese and Spanish cases. *International Journal of Electrical Power & Energy Systems* 31 (9), 562–569.
- Mazundar, M., Gaver, D., 1984. A Comparison of algorithms for computing power generating system reliability indices. *IEEE Transactions on Power Apparatus and Systems* 103 (1), 92–99.
- Menemenlis, N., Huneault, M., Robitaille, A., 2012. Computation of dynamic operating balancing reserve for wind power integration for the time-horizon 1–48 hours. *IEEE Transactions on Sustainable Energy* 3 (4), 692–702.
- Morales, J.M., Conejo, A.J., Pérez-Ruiz, J., 2009. Economic valuation of reserves in power systems with high penetration of wind power. *IEEE Transactions on Power Systems* 24 (2), 900–910.

- Morales, J.M., Zugno, M., Pineda, S., Pinson, P., 2014a. Electricity market clearing with improved scheduling of stochastic production. *European Journal of Operational Research* 235 (3), 765–774.
- Morales, J.M., Zugno, M., Pineda, S., Pinson, P., 2014b. Redefining the merit order of stochastic generation in forward markets. *IEEE Transactions on Power Systems* 29 (2), 992–993.
- Navid, N., Rosenwald, G., 2013. Ramp capability product design for MISO markets. *MISO Market Development and Analysis* [Online]. Available from: <https://www.misoenergy.org/Library/Repository/Communication%20Material/Key%20Presentations%20and%20Whitepapers/Ramp%20Product%20Conceptual%20Design%20Whitepaper.pdf>.
- Negnevitsky, M., Nguyen, D.H., Piekutowski, M., 2014. Risk assessment for power system operation planning with high wind power penetration. *IEEE Transactions on Power Systems* 30 (3), 1359–1368.
- Nosair, H., Bouffard, F., 2015. Flexibility envelopes for power system operational planning. *IEEE Transactions on Sustainable Energy* 6 (3), 800–809.
- O'Connell, N., Pinson, P., Madsen, H., O'Malley, M., 2016. Economic dispatch of demand-side balancing through asymmetric block offers. *IEEE Transactions on Power Systems* 31 (4), 2999–3007.
- Ortega-Vazquez, M., Kirschen, D.S., 2009. Estimating the spinning reserve requirements in systems with significant wind power generation penetration. *IEEE Transactions on Power Systems* 24 (1), 114–124.
- Papavasiliou, A., Oren, S.S., O'Neill, R.P., 2011. Reserve requirements for wind power integration: a scenario-based stochastic programming framework. *IEEE Transactions on Power Systems* 26 (4), 2197–2206.
- Pinson, P., 2006. Estimation of the Uncertainty in Wind Power Forecasting (Doctoral dissertation). École Nationale Supérieure des Mines de Paris.
- Pinson, P., 2012. Very-short-term probabilistic forecasting of wind power with generalized logit-normal distributions. *Journal of the Royal Statistical Society: Series C (Applied Statistics)* 61 (4), 555–576.
- Pinson, P., Nielsen, H.A., Madsen, H., Kariniotakis, G., 2009. Skill forecasting from ensemble predictions of wind power. *Applied Energy* 86 (7), 1326–1334.
- PJM, 2010. PJM Manual 13. Emergency Operations. Revision 39.
- Rahmann, C., Heinemann, A., Torres, R., 2016. Quantifying operating reserves with wind power: towards probabilistic-dynamic approaches. *IET Generation, Transmission & Distribution* 10 (2), 366–373.
- Read, E.G., 2010. Co-optimization of energy and ancillary service markets. In: *Handbook of Power Systems I*. Springer Berlin Heidelberg, pp. 307–327.
- Restrepo, J.F., Galíana, F.D., 2011. Assessing the yearly impact of wind power through a new hybrid deterministic/stochastic unit commitment. *IEEE Transactions on Power Systems* 26 (1), 401–410.
- Rivero, E., Six, D., Gerard, H., 2015. Assessment of Future Market Architectures and Regulatory Frameworks for Network Integration of DRES – The Future Roles of DSOs. FP7 EU Project evolvDSO, Deliverable Report D1.4.
- RTE, 2014. Generation Adequacy Report on the Electricity Supply-Demand Balance in France (Technical Report).
- Ruiz, P., Philbrick, C.R., Sauer, P.W., March 2009. Wind power day-ahead uncertainty management through stochastic unit commitment policies. In: *Power Systems Conference and Exposition, 2009. PSCE'09. IEEE/PES*. IEEE, pp. 1–9.
- Saez-Gallego, J., Morales, J.M., Madsen, H., Jónsson, T., 2014. Determining reserve requirements in DK1 area of Nord Pool using a probabilistic approach. *Energy* 74, 682–693.

- Sen, P.K., Singer, J.M., 1994. Large Sample Methods in Statistics: An Introduction with Applications, vol. 25. CRC Press.
- Söder, L., 1993. Reserve margin planning in a wind-hydro-thermal power system. *IEEE Transactions on Power Systems* 8 (2), 564–571.
- Springer, M.D., 1979. The Algebra of Random Variables. John Wiley and Sons, New York.
- Tastu, J., Pinson, P., Madsen, H., 2015. Space-Time Trajectories of Wind Power Generation: Parameterized Precision Matrices under a Gaussian Copula Approach. In: *Lecture Notes in Statistics: Modeling and Stochastic Learning for Forecasting in High Dimension*. Springer, pp. 267–296.
- Torre, M., 2010. Managing uncertainty at REE. Presentation at Utility Wind Integration Group (UWIG), Albuquerque, USA.
- Tuohy, A., Meibom, P., Denny, E., O’Malley, M., 2009. Unit commitment for systems with significant wind penetration. *IEEE Transactions on Power Systems* 24 (2), 592–601.
- UCTE, 2004. Operating Handbook – Policies P1: Load-Frequency Control and Performance.
- Ulbig, A., Andersson, G., 2015. Analyzing operational flexibility of electric power systems. *International Journal of Electrical Power & Energy Systems* 72, 155–164.
- Wang, J., Botterud, A., Bessa, R., Keko, H., Carvalho, L., Issicaba, D., Sumaili, J., Miranda, V., 2011. Wind power forecasting uncertainty and unit commitment. *Applied Energy* 88 (11), 4014–4023.
- Xie, J., Hong, T., Laing, T., Kang, C., 2017. On normality assumption in Residual simulation for probabilistic load forecasting. *IEEE Transactions on Smart Grid* (in press).
- Xu, L., Tretheway, D., 2012. Flexible Ramping Products. California ISO. [Online]. Available from: <https://www.caiso.com/Documents/DraftFinalProposal-FlexibleRampingProduct.pdf>.
- Zhou, Z., Botterud, A., 2014. Dynamic scheduling of operating reserves in co-optimized electricity markets with wind power. *IEEE Transactions on Power Systems* 29 (1), 160–171.
- Zhou, Z., Botterud, A., Wang, J., Bessa, R.J., Keko, H., Sumaili, J., Miranda, V., 2013. Application of probabilistic wind power forecasting in electricity markets. *Wind Energy* 16 (3), 321–338.

# Forecasting for storage management

12

*Edgardo D. Castronuovo*

University Carlos III de Madrid, Leganés (Madrid), Spain

## 12.1 Introduction

Wind and solar powers have received major boosts in many countries that aim to exploit these renewable resources. Wind farms and solar plants have spread over the last decades in accordance with the interest of the community. The intensification of these types of power generation allows, among other important advantages, the use of renewable energy resources, the reduction of CO<sub>2</sub> emissions and the utilization of local energy supplies. In terms of installed capacity, wind farms have increased from 1743 MW in 1990 to 370 GW in 2014 worldwide (a 21,227% increase). In Europe, over the same time period, the installed capacity has risen from 439 MW to 129 GW (a 29,160% increase) (EWEA, 2009). In the United States, the installed capacity of wind farms has increased from approximately 1200 MW in 1990 (US-DOE, 2008) to 66 GW in 2014 (a 5500% increase) (AWEA, 2010; Global Wind Energy Council, 2015). In China, the installed capacity of wind-based generators increased from 146 MW in 1997 to 114.6 GW in 2014 (a 78,490% increase) (Global Wind Energy Council, 2015; Wind Power, 2010). Solar photovoltaic (PV) cells have experienced similar rates of increase. Although it was negligible in 1990, in 2013, the total installed PV capacity was more than 50 GW, including 17.5 GW in Europe, 18.3 GW in China, and 12 GW in the United States (IEA, 2014a; Observ'ER, 2014). Today, solar thermal generation is mainly led by two countries, Spain and the United States. Of the 3.6 GW installed worldwide at the beginning of 2014, 2.3 GW was in Spain and 900 MW was in the United States (an additional 700 MW was added to the United States' capacity in early 2014) (IEA, 2014b).

However, the large amount of energy from renewable sources that cannot be controlled requires that additional operational tools be developed to ensure that this resource is used effectively. Renewable generation can modify the dynamic and static behavior of an electric system (as described in Banakar et al., 2008; Albadi and El-Saadany, 2010, and others). One of the main problems associated with solar and wind power generation is that it is impossible to predict the generation profiles of plants in the future with precision due to the limited controllability of these technologies and the variability of the energy resources. It is only possible to control the variations of solar thermal generation, by using thermal storage. The intrinsic error in the statistical prediction methods that have been used to estimate the probable future production of wind and solar power results in deviations from the expected generation.

The influence of the prediction method on forecasts of the wind and solar PV production has been analyzed in many studies (including Doherty and O’Malley, 2005; Koeppel and Korpas, 2008; Matevosyan and Soder, 2007; Pinson et al., 2009a,b and previous chapters of this book). The variations in the amount of power produced must be compensated for to maintain the balance of generation, load, and losses.

In recent years, the use of storage devices for complementing the production from renewable resources that cannot be controlled has generated high expectations among the industrial and scientific communities. Storage plants can increase the flexibility of wind and solar plants and therefore support the present trend of worldwide expansion. The objectives of complementing renewable production with storage are different for large grids and for isolated systems. In large and interconnected systems, storage devices can be used to complement power production to obtain a better profit, improve the operational flexibility, and recover the reliability indexes that ensure secure operation. In isolated grids, storage capacity is mainly used to guarantee the stability of the system to probable variations in wind and solar power production. In the next section, general formulations of optimization problems used to improve the operation of storage with solar and wind power plants are provided. Then, this chapter presents some of the main studies in the literature relating to the complementarity of storage and power from uncontrollable renewable resources and classifies them on the basis of their objectives. The pumped storage plant is the primary type of storage considered because it is the storage mechanism that is the most frequently used in practice and in the specific literature.

## 12.2 Mathematical formulations

When possible trajectories of the amount of energy to be generated in the next hours and of the prices at which the energy is sold are available, the optimal operation of a renewable plant and a storage device can be determined using Eqs. (12.1)–(12.9). In this optimal formulation, the storage device is completely dedicated to the combined operation and considered electrically close to the renewable plant.

$$\text{Max} \sum_{i=1}^n (c_i t P_{oi} - cst P_{ci}) \quad (12.1)$$

s.t.

$$P_{oi} = P_{og_i} + P_{di} \quad (12.2)$$

$$P_i = P_{og_i} + P_{ci} \quad (12.3)$$

$$E_{i+1} = E_i + t \left( \eta_c P_{ci} - \frac{P_{di}}{\eta_d} \right) \quad (12.4)$$

$$E_1 = E_1^{esp} \quad (12.5)$$

$$E_{n+1} = E_{n+1}^{esp} \quad (12.6)$$

$$Pc^L \leq Pd_i \leq Pd^U \quad (12.7)$$

$$Pd^L \leq Pd_i \leq \min\left(Pd^U, \eta_d \frac{E_i}{t}\right) \quad (12.8)$$

$$0 \leq E_i \leq E^U \quad (12.9)$$

where  $i = 1, \dots, n$ .

The variables are vectors that express the following:  $Po$  is the total amount of hourly active powers delivered to the network by the renewable-storage ensemble;  $Pc$  is the hourly amount of active powers delivered by the renewable producer to be stored;  $Pog$  is the amount of hourly active powers delivered directly to the network by the renewable facility;  $Pd$  is the amount of hourly active powers delivered by the storage facility to the network; and  $E$  is the amount of energy stored in the storage device per hour. The constraints are as follows:  $c$  is a vector of hourly active power prices;  $cs$  is the cost of operating the storage system;  $\eta_c$  and  $\eta_d$  are the efficiencies of charging and discharging the storage device, respectively;  $t$  is the length of each discretization interval;  $E_1^{esp}$  and  $E_{n+1}^{esp}$  are the initial and final amounts of energy in the storage device, respectively;  $P$  is a vector of the power available from the considered renewable producer each hour;  $Pc^L$  and  $Pc^U$  are the lower and upper power limits of the charging capacity of the storage system, respectively;  $Pd^L$  and  $Pd^U$  are the lower and upper production power limits of the storage device, respectively;  $E^U$  is the reservoir's storage capacity; and  $n$  is the number of discretization intervals.

Objective function (Eq. 12.1) maximizes the profit when energy is sold and decreases the cost of operating the storage device. In many cases, the operating costs of storage are low and can be neglected. The total power injected into the system is provided partially by the renewable producer and partially by the storage (Eq. 12.2). The power available in the renewable device can be delivered directly to the system or stored (Eq. 12.3). At the beginning of the next period, the energy stored in the device can be increased or decreased by charging or discharging it (Eq. 12.4). The initial and final levels of energy in the storage device are defined in Eqs. (12.5) and (12.6), respectively. The storage device has upper and lower limits on the amount of energy it can store or discharge (Eqs. 12.7 and 12.8). However, discharging is only possible if there is energy stored in the storage device (Eq. 12.8). Finally, there are upper and lower limits on the amount of energy in the storage device (Eq. 12.9).

The production of power from the renewable resources, such as wind and solar power, that cannot be completely controlled, which are considered in this study, is difficult to adapt to current markets. Markets generally work with firm expectations for production. However, in these plants, power is only obtainable when the primary

source of energy (wind or solar radiation) is available. The storage device allows shifts in the available energy so that the energy from renewable resources is sold during the market's most profitable periods. Deviation costs, which are associated with penalties for producing more or less than the expected amount of energy, can also be considered in the formulation when they are present in the market regulations. The optimization problem given by Eqs. (12.1)–(12.9) was proposed by [Castronovo and Lopes \(2004a\)](#), among others; it can be adapted to the particular characteristics of a storage device, renewable plant, and remuneration scheme. This formulation can be used in statistical analyses that optimize possible operating scenarios using Monte Carlo or similar approaches. Once simulations have been performed, statistical parameters (medium values, standard deviations, quantiles, etc.) can be calculated from the optimal results.

Alternatively, the conditions for the optimal operation of the storage device can be determined from the expected statistical variations in the amount of renewable energy produced. A large (in comparison with the renewable plant) storage device is considered in this case. This storage device operates as usual (storing energy when the price is low and selling it when the price is high) and reserves a portion of its capacity for compensating for the variations in the production of energy from renewable resources in the region. A reserve of energy and power must be kept, as shown in Eqs. (12.10)–(12.16).

$$\text{Max} \sum_{i=1}^n (c_{it}Po_i - c_{it}Pc_i) \quad (12.10)$$

s.t.

$$E_{i+1} = E_i + t \left( \eta_c P c_i - \frac{P d_i}{\eta_d} \right) \quad (12.11)$$

$$E_1 = E_1^{esp} \quad (12.12)$$

$$E_{n+1} = E_{n+1}^{esp} \quad (12.13)$$

$$Pd^L \leq Pd_i \leq \min \left[ (Pd^U - RP^m), \eta_d \frac{E_i}{t} \right] \quad (12.14)$$

$$Pc^L \leq Pc_i \leq (Pc^U - RP^M) \quad (12.15)$$

$$RE \leq E_i \leq (E^U - RE) \quad (12.16)$$

where  $i = 1, \dots, n$ .  $RP^m$  and  $RP^M$  are the active power reserved for discharging and charging the storage device, respectively, and  $RE$  is the energy reserve to be maintained in the storage device at all periods.

In Eq. (12.10), the maximum profit made by operating the storage device is sought. The storage plant sells energy during the most profitable periods and buys energy at lower prices. This operation is performed by the storage owner in accordance with external remuneration schemes (markets, government payments, etc.) and independently of the actions of the renewable producer. Therefore, Eqs. (12.2) and (12.3) in the first formulation (which are related to the control of renewable resources) are not applicable here. Eqs. (12.11)–(12.13) are similar to Eqs. (12.4)–(12.6).

The storage device acts as a load for the system when it charges and as a producer when it discharges. In a previous agreement (which may or may not include economic payments), the storage device compensates for certain unwanted deviations in the renewable production. Therefore, it cannot discharge at its maximum power capacity; possible decreases in the renewable production must be compensated for by additional production by the storage device, as shown in Eq. (12.14). In the same way, a reserve charge must be maintained in the storage device to compensate for an overproduction by the renewable plant or plants, as shown in Eq. (12.15). An energy reserve must be kept in the storage device in lower and upper real limits, to compensate for an amount of renewable energy that is too high or too low. The amount of power and energy reserves, needed for compensating for variations in the production of an individual renewable plant or a cluster of plants, can be calculated from production deviations obtained from conventional statistical functions, quantiles, or other statistical methods. In Castronovo et al. (2014), different quantiles of the production distributions of two real wind farms are compensated for using a hydro-pumped storage plant in accordance with Eqs. (12.10)–(12.16).

The formulations given in Eqs. (12.1)–(12.9) and Eqs. (12.10)–(12.16) correspond to generic optimization problems that can be adapted to different storage devices, remuneration schemes, and plants that generate energy from uncontrollable sources. Due to the advantages of cooperation between renewable production and storage, many studies have been described in the literature; they use approaches that are similar to the one presented in this paper and other alternatives. In the following sections, some of these studies and uses of storage devices to compensate for variations in the amount of energy produced by solar and wind plants are analyzed in a methodological review.

## 12.3 Coordinating renewable producers and hydro-pumped storage for optimal participation in the market

In large systems, storage can be coordinated with wind farms and solar plants to improve the alternatives for controlling the productions. In this coordination process, the main concerns are related to the operability of the combined systems and their interactions with the electricity marketplace. The large-scale integration of wind farms and solar power into a system requires a solution to several operational and economic problems that relate to the assimilation of energy from sources that are not completely

controllable. Cooperation with storage devices can improve the flexibility and profitability of renewable production (Estanqueiro et al., 2007) when it works adequately. In some cases, the use of generic storage devices is a good choice for preliminary studies. Bathurst and Strbac (2003) analyze the optimal dispatch of an electrical energy storage facility by considering short-term power exchanges and the penalties for the imbalances expected of a wind farm. A sensitivity analysis that considers several ranges of storage capacities and different market parameters is performed as part of the study.

However, in general, the advantages of cooperation depend on the type of storage available in the system. In Zhao et al. (2015), the most common storage devices and their ability to cooperate with wind and solar power are reviewed. Hydro-pumped storage accounts for more than 99% of the bulk storage capacity worldwide, which is approximately 127 GW (Dhillon et al., 2014). This type of coordination is described most frequently in the literature. The present chapter is centered on the cooperation of solar and wind energy providers and hydro-pumped storage facilities.

Hydro-pumped storage plants allow the storage of large amounts of electricity generated between periods of operation with relatively low losses (20%–30%) during the storage cycle. A pumping station uses electricity to raise water from a lower reservoir to an upper one; the station acts as a load on the system. In that way, some of the electric energy is stored in the water's height. When the system requires this energy (or when the prices are most favorable) a hydroelectric generator injects part of the stored energy into the grid. In some countries, hydro-pumped storage plants execute interseasonal storage cycles. However, in most cases, the storage cycle is performed on a daily or weekly basis. In addition, the storage capacity of these plants can be used to compensate for variations in wind power production to balance the integrated operation (Castronovo and Lopes, 2004a,b,c). Due to the significant penetration of wind plants (which is greater than that of solar plants) and pumped storage, many studies of cooperation between wind farms and hydro-pumped storage plants have been conducted. A description of various optimization techniques for scheduling the use of wind power and hydro-pumped storage is presented in Dhillon et al. (2014).

Economic profits can be expected from the cooperation of wind farms and pumped storage facilities. In Castronovo and Lopes (2004a), a new approach to coordinating a wind power plant with a hydro-pumped storage station is proposed. The goal of the algorithm is to calculate the optimal combined operation of a wind farm and a pumped storage plant in a large integrated system. Probable restrictions on the output production and the operational constraints of the machines are included in the formulation of the problem. The output restrictions can be represented as being applicable to certain hours or the whole day. The stochastic characteristics of the wind production forecast are included in the model by means of wind power time-series scenarios. Using the remuneration tariffs for the wind power generated in Portugal, the predicted yearly average economic gain of the joint strategy is between 425.3 and 716.9 k€ for the analyzed test cases.

Koeppel and Korpas (2008) analyze the addition of a storage device in the same location of an intermittent wind generator in northern Norway, to compensate for

variations in the power generated due to forecasting errors. The algorithm estimates possible errors in the production for the next periods and calculates the requirements of the storage device. The cooperation method can also be used with other types of intermittent generator, such as PV installations. The results show the advantages of the approach when the energy storage device is used appropriately.

Sometimes, the objective of the analysis is to find a way to enclose the wind production within narrow limits by using the storage device's capacity to make the wind farm's operation approximates conventional generation. In this way, the formulation of the problem assists the owner of a wind hydro-storage generating facility by improving the quality of the estimates of the amount of energy that can be offered to the market in each of the next hours and the confidence intervals of these calculations. The stochastic nature of wind production is represented in this type of approach. In [Castronuovo and Lopes \(2004b\)](#), an optimization problem is formulated and solved with the goal of enclosing the wind power produced between narrow limits. Cooperating with a pumped storage plant increases the control of the wind power producer, enabling participation in the market and reducing the amount of energy losses.

From an economic perspective, the use of storage devices can be compared with that of financial tools. [Hedman et al. \(2006\)](#) evaluate the options of using a hydro-pumped storage plant to reduce the uncertainty in wind production and of purchasing call/put options for protection from this uncertainty. In the analysis, the wind farm and the pumped storage have the same owner and the Black-Scholes options pricing model is used. Real data, which are extracted from the PJM transmission organization (price data) and from a wind location in Sutherland, United States (wind speed data), are used in the study. The results show that in some situations, purchasing options are financially competitive with using a pumped storage plant. However, the authors highlight the fact that a complete and competitive options purchasing market does not currently exist in the deregulated electric industry of the United States. [Ngoc et al. \(2009\)](#) also propose an adequate consideration of the cost of unbalancing the system, allowing a better approximation of the actual electricity market.

In most systems, the future price of wind energy depends on the electricity market results and, therefore, is best represented by a stochastic variable. In [Gao et al. \(2009\)](#), future prices and the amount of wind power generated are considered as stochastic variables. Pump action is represented by discrete values due to the connection and disconnection of pumps that are not continuously controllable. A stochastic characterization is performed using the collocation method, and realistic data are used to test the proposed algorithm. The result of the comparison of the expected profits is that joint operation is beneficial for both wind and pumped storage facilities.

The uncertainty in market prices and wind generation can be analyzed using a two-stage stochastic programming approach. In [Garcia-Gonzalez et al. \(2008\)](#), the optimal bids for the day-ahead market are calculated, also considering the probable coordination of the wind farm with a pump storage facility. The approach is tested using price previsions for the Spanish daily market. The additional use of a storage facility increases wind farm profits, as the pumped storage plant provides a hedge against

production uncertainty and more efficient operation, by storing energy during off-peak hours to increase the amount of energy sold during peak hours. An improved representation of this combined operation is presented in [Garcia-Gonzalez and IEEE \(2008\)](#).

[Dursun and Alboyaci \(2010\)](#) analyze the contribution of wind hydro-pumped storage systems to meeting Turkey's demand for electric energy. The Turkish economy has been increasing at an annual rate of approximately 7%–10% since 2000. According to the study, wind–hydro solutions not only guarantee that the demand for electricity from the local grid is continuously met but also minimize the dependence on imported fuel and, therefore, reduce the negative effects of using fossil fuels.

Depending on the economic structure of the electricity market, the advantages of combining wind farms and pumped storage facilities can provide very different or nonexistent gains. [Tuohy et al. \(2009\)](#) examine the operation of a power system in Ireland with and without a storage unit for various levels of wind power, focusing on the cost savings associated with the wind farms in the system. The analysis is performed in cases extracted from the All Island Grid Study with the addition of a hypothetical pumped storage plant to the grid. The best results were obtained when a large amount of wind power was produced. However, this economic study does not recommend the construction of a new storage plant in Ireland.

Using pumped energy storage to compensate for variations in wind power production can increase the value of a storage plant. [Muche \(2009\)](#) proposes a new valuation of the pumped storage plants considering this fact. The paper considers the activity of a storage plant in the spot market in both day-ahead and intraday operations. The pumped storage plant is validated using a stochastic analysis of probable scenarios of operation obtained from daily optimizations based on different price profiles. The proposed validation is matched with a classic investment appraisal, which takes the cash flow expected from an investment as the basis for the value of the storage plant. In the simulations, the conventional procedure results in substantially lower contribution margins and, therefore, leads to a misvaluation of the investment because it does not consider the scope of future actions. The proposed method can be extended to a portfolio of power plants. [Vennemann et al. \(2010\)](#) analyze the benefits associated with pumped storage plants, including their coordination with wind farms. The study is centered in Germany and concludes by highlighting the importance of these plants for the system's adequate operation. In addition, the authors suggest that more than 14,000 MW could be introduced into the German system in the next years if adequate incentives are considered in the market.

In [Castronuovo et al. \(2014\)](#), an integrated method of determining the optimal schedule for an existing large storage plant that cooperates with a wind farm or a cluster of wind farms is presented. The analysis includes the conventional daily cycle of operation of the storage plant. The storage plant is now in operation; it was built to operate economically in the market. An integrated approach involving three functions is proposed; it considers the gains that result from operating in the spot market, the minimization of variations in the renewable production, and the reduction of costs due to imbalances costs. In this analysis, different cases are represented using typical data from the year 2008 of the Spanish electricity market. Different quantiles are considered in the study. The results show how convenient combined action is.

The gain obtained from the cooperation between wind farms and storage facilities is strongly related to the error in the forecasting prevision of wind production. Because forecasts of wind production can be represented using different quantiles, deciding what level of error should be compensated for involves a risk for the wind farm owner. [Bourry et al. \(2009\)](#) analyze different risk-based strategies for coordinating wind farms and hydro-pumped storage facilities in electricity markets. A method for assessing the risk of intraday scheduling and operating the plant in an electricity market is proposed in the paper. In [Murage and Anderson \(2014\)](#), cooperation between a large wind farm and a hydro-pumped storage facility in Kenya is proposed. Different wind scenarios are related using Markov transition probabilities. This formulation reduces wind shortcuts and improves the benefits of cooperation.

The ability to store power can improve the operation of renewable energy plants that use solar power. Currently, there are two main systems for using solar power in the electrical system: PV panels and solar thermal plants.

Solar thermal generation has an implicit storage capacity because of the thermal cycle performed when electric power is produced. Solar thermal plants (also called concentrating solar plants) concentrate solar radiation in a fluid by heating it. Then, the fluid (generally oil) transfers its heat to water, producing overheated steam. The steam moves a conventional thermal generator, producing electricity. Different thermal storage alternatives are possible; these include direct storage of saturated or superheated steam in pressure vessels, saturated water thermal storage systems, thermocline storage systems using tanks containing rocks and sand, tanks of hot oil, tanks of molten salts, and other proposals ([Medrano et al., 2010](#)). Few references can be found that discuss the optimal operation of solar thermal plants into the system, which may be due to the reduced penetration of these types of producers. In [Wittmann et al. \(2011\)](#), a price-driven strategy for operating a solar thermal plant in a way that optimizes its energy production is proposed. In [Usaola \(2012\)](#), the storage capacities of such plants are used to improve the profits of operating in a spot market. Several scenarios are considered in the analysis, and the simulations show the benefits of using the storage ability.

In [Mekmuangthong and Premrudeepreechacharn \(2015\)](#), the combined operation of a PV plant and a hydro-pumped storage facility is analyzed. The system is operated in an interseasonal cycle that results in energetic and economic gains. The optimal size of the storage plant is calculated. However, most part of the studies considers both PV plants and wind farms for obtaining the best coordination with hydro-pumping storage devices. A combined operation of a microgrid containing a wind farm, a PV facility and a pumped storage facility is proposed by [Oskouei and Yazdankhah \(2015\)](#). The uncertainty in wind generation is forecasted using an autoregressive-moving average (ARMA) model, and various scenarios are generated using a Weibull distribution function. For individual amounts of PV power generated and market prices, the probability density function (pdf) is a normally distributed random function. The algorithm reduces the unexpected variations in the amounts of PV and wind power generated and increments the profit of their combined operation. ARMA models and scenarios generated using Weibull distribution functions are also used in [Parastegari et al. \(2015\)](#) to model the uncertainty in wind generation. In this study, wind farms, PV generation,

a pumped storage plant, and other devices are integrated to identify the best operation scheme in terms of both energy and reserve markets. The proposed method increases the profit and reduces the risk in the generation process.

## 12.4 The cooperation of renewable producers and storage facilities in isolated systems

In isolated systems, the introduction of intermittent renewable energy (such as wind or solar energy) can be more complex than it is in large interconnected systems. In isolated systems, the main concerns regarding large amounts of energy that are not completely controllable relate to dynamic security restrictions. Wind parks and solar plants are generally unable to assist in maintaining the frequency and voltage of the system within tight margins. Therefore, storage devices can perform an important role in balancing the amounts of power and energy in the system (Khatibi et al., 2008).

Wind is generally more readily available on islands. The wind speed is higher and varies more smoothly near the sea, allowing the development of efficient wind farms. In addition to this, pumped storage facilities are used in isolated systems to improve their efficiency and security, increasing the capacity of control necessary for the grid to operate adequately. Several authors have analyzed applications of isolated systems that include wind power and pumped storage. A real case based on the Multi-purpose Socorridos system located on Madeira Island, Portugal, is studied in Vieira and Ramos (2008). Different weather conditions are considered by using winter and summer profiles.

Pumped storage capacity can also improve the dynamic conduct of an isolated system that uses wind power. The stochastic nature of wind power production and the constraints associated with its dynamic security must be considered in this case. Brown et al. (2008) aim at determining the optimal energy and power capacities of a storage facility and consider several probable operational scenarios. The fixed and operational costs of the generation plants and the pumped storage devices in a real island system are included in the analysis. In the simulations, the optimal storage capacity of the pumped storage facility was found to be only 17% of the installed wind capacity and equivalent to 1.33 h of wind farm full production.

The energy in many isolated grids is mainly supplied by conventional diesel-based generators. Currently, wind power is included in some of these grids, which improves the efficiency of the electric supply. Pumped storage facilities can enhance the performance of systems in which wind power has penetrated to a medium or high level. Abbey and Joos (2009) develop a stochastic optimization approach to calculate the optimal size of a storage plant for minimizing the amount of energy dumped into an isolated diesel–wind system. When the system operates, the diesel plant controls both the frequency and the voltage. The formulation of the problem considers different levels of wind penetration, possible load and wind power generation scenarios, and three diesel operating strategies: minimum loading (using a dumped load), new low-load diesel technologies (such as electronic fuel injectors), and diesel unit

commitment (which allows the diesel generator to be disconnected during some periods). The introduction of storage devices does not significantly influence the cost of the energy served. However, the results show that the addition of a storage facility considerably improves the sustainable approach to serving the energy needs of remote communities.

The combined operation of a PV plant, a wind farm, and a hydro-pumped storage facility on a remote island is studied in [Ma et al. \(2014\)](#). Medium values of the amounts of PV, wind, and water resources are used to calculate the optimal operation of this hybrid system. In [Ntomaris and Bakirtzis \(2015\)](#), PV, wind, and conventional thermal generation are combined with a hydro-pumped storage plant for optimal operation in Crete, Greece. Eleven generation scenarios are examined. The combined operation reduces the expected cost of the system by approximately 19%.

Isolated grids can also be present in continental territories. In [Ramos and Ramos \(2009\)](#), a Portuguese village that uses wind power production, solar generation, and pumped storage capacity is analyzed. The village actually has pumped storage capacity to supply the water requirements of the population, and it is isolated from the national grid. The study analyzes the possibility of interconnection with the external grid and/or the introduction of an additional hydroelectric turbine in the water circuit. From an economic perspective, the interconnection is profitable if the distance to the grid is less than 31.6 km. In this analysis, the inclusion of an additional hydroelectric turbine is not found to be profitable (because it requires additional reinforcement in the water circuit) in either the isolated or the interconnected solution.

In [Fonseca and Schlueter \(2013\)](#), the integration of wind power, PV generation, and a storage plant in a tall building in Caracas, Venezuela, is proposed. The building receives limited amounts of electricity and water from distribution grids. Two pumped storage systems located between floors one to six and seven to nine are proposed. Different scenarios are analyzed. The study supports the economic and technical feasibility of the project and the benefits of its implementation.

## 12.5 Storage sizing

An important issue is determining the optimal size of the storage elements required by a particular system. A large storage capacity generally results in larger investment costs, reducing the feasibility of the enterprise. [Castronovo and Lopes \(2004c\)](#) analyze the optimal size of the coupled water reservoir required for the optimal operation of a wind farm with additional hydro-pumped water storage capacity. The proposed formulation of the optimization problem is fully explicated, which allows the algorithm to be applied to different electric systems.

For an integrated action, the optimal size of the storage reservoir and the size of each storage element must be calculated on the basis of the characteristics of the system and the expected amount of error in forecasts of the wind farm's production. In [Bludszuweit et al. \(2008\)](#), a Beta distribution is compared with a Gaussian distribution; the results show that the former distribution is advantageous for representing real data from two wind farms. In the proposed approach, the optimal amount of energy

storage is calculated using the pdf of the forecast error. The results show that the energy loss is proportional to the integral of the tail of the pdf. Therefore, the tail of the pdf must be especially precise.

In [Pinson et al. \(2009\)](#), the optimal size of the storage device is calculated by using economic data from the Danish regulation market. The storage device acts as a buffer by absorbing the fluctuations in the wind farm's production, in the day-ahead market. The results of yearly simulations show how important the accepted level of economic risk is in a calculation of the optimal size of a storage facility.

[Wu et al. \(2014\)](#) propose an optimization algorithm that minimizes the total cost of the storage device and the penalties associated with uninstructed variations. Three pdf's are compared in the analysis: a normal pdf, a mixed pdf based on the Laplace approximation, and a proposed quantile distribution. The results show that normal distribution is less appropriate for calculating the optimal size of the reservoir.

## 12.6 Reliability studies of the combined operation of wind power plants and storage facilities

The reliability of a power system can be changed when a large number of wind farms is included. Storage devices can help improve the reliability of the system's operation, maintaining adequate values of the system's security indices. A method of evaluating the reliability of the Roy Billinton test system with wind energy and storage devices using Monte Carlo simulations is proposed by [Hu et al. \(2009\)](#). The study incorporates random generating unit failures and calculates the most common reliability indexes (loss of load expectation and loss of energy expectation). The results show that energy storage devices can improve the system's reliability in addition to reducing the possibility of wind energy curtailment. [Sioshansi et al. \(2014\)](#) present a method of estimating the capacity value of a storage device that captures the effects of system shortages on the state of the charge of the storage device in subsequent periods. The method is applied to five utility systems in the United States: Pacific Gas and Electric, Southern California Edison, NV Energy, the Public Service Company of New Mexico, and FirstEnergy. The proposed method is compared with others in the literature, and the reliability indexes are better. A method for calculating the capacity value of a solar thermal plant is proposed by [Usaola \(2013\)](#). Reliability indexes are calculated using series of daily average values from an ARMA model. The results show that the capacity credit decreases with the penetration level and is higher for dispersed plants and higher storage capacities.

## 12.7 Conclusion

In recent years, renewable power facilities have been integrated into most electric power systems. Although this type of power generation has many advantages, it also introduces new paradigms into the system's operation, especially when the percentage of renewable power that is not controllable in the generation matrix is significant. Complementing wind and solar power with storage devices can enhance

the controllability of the system. The present study summarizes some of the most significant literature published in the field of cooperation of solar and wind power with pumped storage. Several objectives were analyzed: improving benefits into the market, reducing penalties for variable production, sizing storage spaces, studying reliability, cooperating in isolated grids, etc. The papers analyzed evidence the importance of this topic to applications of electric power.

## Acknowledgment

This work was performed within the research project *RESMART 2014/00338/001*, of the Ministry of Science and Technology of Spain.

## References

- AWEA, 2010. Market Update Factsheet.
- Abbey, C., Joos, G., February 2009. A stochastic optimization approach to rating of energy storage systems in wind-diesel isolated grids. *IEEE Transactions on Power Systems* 24, 418–426.
- Albadri, M.H., El-Saadany, E.F., June 2010. Overview of wind power intermittency impacts on power systems. *Electric Power Systems Research* 80, 627–632.
- Banakar, H., et al., February 2008. Impacts of wind power minute-to-minute variations on power system operation. *IEEE Transactions on Power Systems* 23, 150–160.
- Bathurst, G.N., Strbac, G., 2003. Value of combining energy storage and wind in short-term energy and balancing markets. *Electric Power Systems Research* 67, 1–8.
- Bludszuweit, H., et al., August 2008. Statistical analysis of wind power forecast error. *IEEE Transactions on Power Systems* 23, 983–991.
- Bourry, F., et al., 2009. Risk-based strategies for wind/pumped-hydro coordination under electricity markets. *PowerTech*. <http://dx.doi.org/10.1109/PTC.2009.5282276>.
- Brown, P.D., et al., May 2008. Optimization of pumped storage capacity in an isolated power system with large renewable penetration. *IEEE Transactions on Power Systems* 23, 523–531.
- Castronuovo, E.D., Lopes, J.A.P., 2004a. On the optimization of the daily operation of a wind-hydro power plant. *Ieee Transactions on Power Systems* 19, 1599–1606.
- Castronuovo, E.D., Lopes, J.A.P., 2004b. Bounding active power generation of a wind-hydro power plant. In: 2004 International Conference on Probabilistic Methods Applied to Power Systems, pp. 705–710.
- Castronuovo, E.D., Lopes, J.A.P., 2004c. Optimal operation and hydro storage sizing of a wind-hydro power plant. *International Journal of Electrical Power & Energy Systems* 26, 771–778.
- Castronuovo, E.D., Usaola, J., Bessa, R., Matos, M., Costa, I.C., Bremermann, L., Lugaro, J., Kariniotakis, G., June 2014. An integrated approach for optimal coordination of wind power and hydro pumping storage. *Wind Energy* 17 (6), 829–852.
- Dhillon, J., Kumar, A., Singal, S.K., February 2014. Optimization methods applied for wind-PSP operation and scheduling under deregulated market: a review. *Renewable and Sustainable Energy Reviews* 30, 682–700.
- Doherty, R., O'Malley, M., 2005. A new approach to quantify reserve demand in systems with significant installed wind capacity. *IEEE Transactions on Power Systems* 20, 587–595.

- Dursun, B., Alboyaci, B., September 2010. The contribution of wind-hydro pumped storage systems in meeting Turkey's electric energy demand. *Renewable & Sustainable Energy Reviews* 14, 1979–1988.
- EWEA, 2009. Wind Energy – The Facts.
- Estanqueiro, A.I., et al., 2007. Barriers (and solutions...) to very high wind penetration in power systems. In: 2007 IEEE Power Engineering Society General Meeting, vols. 1–10, pp. 2103–2109.
- Fonseca, J.A., Schlueter, A., May 2013. Novel approach for decentralized energy supply and energy storage of tall buildings in Latin America based on renewable energy sources: case study – informal vertical community Torre David, Caracas – Venezuela. *Energy* 53, 93–105.
- Gao, F., et al., 2009. Wind generation scheduling with pump storage unit by collocation method. In: 2009 IEEE Power & Energy Society General Meeting, vols. 1–8, pp. 2634–2641.
- Garcia-Gonzalez, J., et al., May 2008. Stochastic joint optimization of wind generation and pumped-storage units in an electricity market. *IEEE Transactions on Power Systems* 23, 460–468.
- Garcia-Gonzalez, J., IEEE, 2008. Hedging strategies for wind renewable generation in electricity markets. In: 2008 IEEE Power & Energy Society General Meeting, vols. 1–11, pp. 3494–3499.
- Global Wind Energy Council, 2015. <http://www.gwec.net>.
- Hedman, K.W., et al., 2006. Comparing Hedging Methods for Wind Power: Using Pumped Storage Hydro Units Vs. Options Purchasing.
- Hu, P., et al., August 2009. Reliability evaluation of generating systems containing wind power and energy storage. *IET Generation Transmission & Distribution* 3, 783–791.
- IEA, 2014a. PVPS Report – Snapshot of Global PV 1992–2013. Report IEA-PVPS T1-24.
- IEA, 2014b. Technology Roadmap – Solar Thermal Electricity.
- Khatibi, M., et al., 2008. An analysis for increasing the penetration of renewable energies by optimal sizing of pumped-storage power plants. Electric Power Conference (EPEC). <http://dx.doi.org/10.1109/EPC.2008.4763324>.
- Koeppel, G., Korpas, M., December 2008. Improving the network infeed accuracy of non-dispatchable generators with energy storage devices. *Electric Power Systems Research* 78, 2024–2036.
- Ma, T., Yang, H., Lu, L., Peng, J., September 2014. Technical feasibility study on a standalone hybrid solar-wind system with pumped hydro storage for a remote island in Hong Kong. *Renewable Energy* 69, 7–15.
- Matevosyan, J., Soder, L., May–June 2007. Short-term hydropower planning coordinated with wind power in areas with congestion problems. *Wind Energy* 10, 195–208.
- Medrano, M., Gil, A., Martorell, I., Potau, X., Cabeza, L.F., January 2010. State of the art on high-temperature thermal energy storage for power generation. Part 2—Case studies. *Renewable and Sustainable Energy Reviews* 14, 56–72.
- Mekmuangthong, C., Premrudeepreechacharn, S., August 2015. Optimization for operation and design of solar-hydro pump energy storage using GAMS. *Applied Mechanics and Materials* 781, 346–350.
- Muche, T., November 2009. A real option-based simulation model to evaluate investments in pump storage plants. *Energy Policy* 37, 4851–4862.
- Murage, M.W., Anderson, C.L., March 2014. Contribution of pumped hydro storage to integration of wind power in Kenya: an optimal control approach. *Renewable Energy* 63, 698–707.
- Ngoc, P.D.N., et al., 2009. Optimal operation for a wind-hydro power plant to participate to ancillary services. *Industrial Technology*. <http://dx.doi.org/10.1109/ICIT.2009.4939699>.

- Ntomaris, A.V., Bakirtzis, A.G., 2015. Stochastic day-ahead scheduling of thermal and hybrid units in insular power systems with high wind penetration. In: PowerTech. Eindhoven, 29 June–2 July 2015.
- Observ'ER, 2014. The State of Renewable Energies in Europe. Available online at: <http://www.energies-renouvelables.org/>.
- Oskouei, M.Z., Yazdankhah, A.S., November 2015. Scenario-based stochastic optimal operation of wind, photovoltaic, pump-storage hybrid system in frequency-based pricing. *Energy Conversion and Management* 105, 1105–1114.
- Parastegari, M., Hooshmand, R.-A., Khodabakhshian, A., Zare, A.-H., January 2015. Joint operation of wind farm, photovoltaic, pump-storage and energy storage devices in energy and reserve markets. *International Journal of Electrical Power & Energy Systems* 64, 275–284.
- Pinson, P., et al., January 2009a. From probabilistic forecasts to statistical scenarios of short-term wind power production. *Wind Energy* 12, 51–62.
- Pinson, P., et al., 2009b. Dynamic sizing of energy storage for hedging wind power forecast uncertainty. In: 2009 IEEE Power & Energy Society General Meeting, vols. 1–8, pp. 1760–1767.
- Ramos, J.S., Ramos, H.M., February 2009. Sustainable application of renewable sources in water pumping systems: optimized energy system configuration. *Energy Policy* 37, 633–643.
- Sioshansi, R., Madaeni, S.H., Denholm, P., January 2014. A dynamic programming approach to estimate the capacity value of energy storage. *IEEE Transactions on Power Systems* 29 (1), 395–403.
- Tuohy, A., et al., 2009. Impact of pumped storage on power systems with increasing wind penetration. In: 2009 IEEE Power & Energy Society General Meeting, vols. 1–8, pp. 2642–2649.
- US-DOE, 2008. 20% Wind Energy by 2030.
- Usaola, J., January 2012. Operation of concentrating solar power plants with storage in spot electricity markets. *IET Renewable Power Generation* 6 (1), 59–66.
- Usaola, J., November 2013. Capacity credit of concentrating solar power. *IET Renewable Power Generation* 7 (6), 680–688.
- Vennemann, P., et al., 2010. Pumped Storage Plants in the Future Power Supply System, vol. 1. VGB Powertech, pp. 44–49.
- Vieira, F., Ramos, H.M., November 2008. Hybrid solution and pump-storage optimization in water supply system efficiency: a case study. *Energy Policy* 36, 4142–4148.
- Wind Power, 2010. Wind Energy Data for China – General Data.
- Wittmann, M., Eck, M., Pitz-Paal, R., Müller-Steinhagen, H., April 2011. Methodology for optimized operation strategies of solar thermal power plants with integrated heat storage. *Solar Energy* 85, 653–659.
- Wu, J., Zhang, B., Li, H., Li, Z., Chen, Y., Miao, X., February 2014. Statistical distribution for wind power forecast error and its application to determine optimal size of energy storage system. *International Journal of Electrical Power & Energy Systems* 55, 100–107.
- Zhao, H., Wu, Q., Hu, S., Xu, H., Rasmussen, C.N., January 2015. Review of energy storage system for wind power integration support. *Applied Energy* 137 (1), 545–553.

# Dynamic line rating forecasting

13

Romain Dupin, Andrea Michiorri

MINES ParisTech PSL - Research University Centre PERSEE: Centre for Processes, Renewable Energies and Energy Systems, Sophia Antipolis, France

## 13.1 Introduction

The current carrying capacity, or ampacity, of bare overhead conductors is limited for several security reasons, such as network stability or the thermal limit of the conductor. This last one is, most of the time, the most restrictive one. The temperature of a conductor is, as explained in detail in Section 2.2, the result of an energy balance between the heat dissipated by Joule effect, the heat gained by solar radiation, and the heat exchanged with the environment by convective and radiative heat exchange. High temperatures, caused by the Joule effect, can lead to the annealing of the conductive material, reducing its strength and increasing its resistance. Before this the thermal elongation will deform the conductor increasing the sag and reducing the clearance to the ground, as shown in Fig. 13.1.

To avoid this, a maximal core temperature is defined in association with the maximal admitted sag value. At this point, it is possible to set a maximal current which, according to the value of external parameters, will always maintain the conductor's sag within safety values.

Traditionally conservative annual or seasonal values for external weather parameters such as wind speed and air temperature are used to calculate a static rating (SR) for a circuit. This value is usually calculated for each class of conductor, for each season,

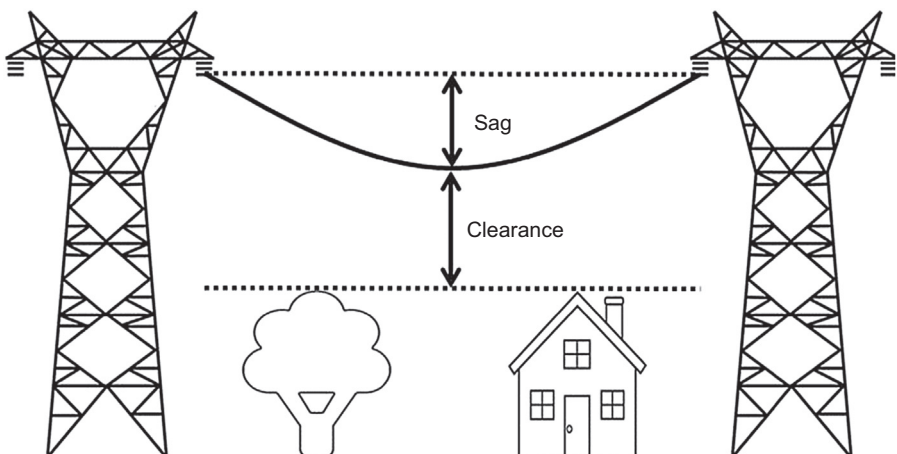


Figure 13.1 Representation of the sag and the clearance distance for an overhead line.

and for each country. This approach has the double advantage of facilitating the management of the network and of increasing safety, thanks to the fact that protection settings are changed few times per year. On the other side, a large current-carrying capacity is not exploited and in a little number of cases, clearance limits are breached.

When a line is often congested because of outages or of load or generation growth, network reinforcing is often the only option available to network operators. Reinforcing can take the form of a simple retensioning of the line (increase the mechanical tension of the conductors to bear higher temperatures), reconductoring (replacing the existing conductors with higher ampacity ones), increasing the voltage of the line, or building a new line. All these options are more or less expensive and the last one, the construction of a new line, is particularly difficult because of growing environmental concerns and regulations.

For this reason, it is observed a growing interest in dynamic line rating (DLR), the use of a variable ampacity for overhead lines based on real-time environmental conditions. This can increase the ampacity of up to 200% of the SR, especially in wind conditions or during the night, when congestions can be caused by wind power production or evening peak demand.

Several tools have been designed to estimate the rating in real time; however, this chapter will focus on the forecast for DLR. This is particularly important since most of the operating decisions of a transmission system operator are taken at least one day before their applications.

In this chapter, the calculation methods of the rating of a line will be first described. In a second part, we will present different devices used for DLR calculation. Then, a presentation of the problem of DLR forecast, and some proposed methods will be assessed. Finally, we will show the benefits of the DLR and its forecasts presented in the literature.

## 13.2 Dynamic line rating calculations

### 13.2.1 Influence of core temperature on sag of the line

The sag of a span of an overhead line can be calculated analytically with a catenary equation or with its parabolic approximation as described in ([electricalengineeringinfo](#)) and presented in [Eq. \(13.1\)](#), where:  $L$  (m) is the span length,  $mg$  ( $\text{N m}^{-1}$ ) is its weight per unit, and  $H$  ( $\text{kg m}^{-1}$ ) is the mechanical axial tension.

$$\text{Sag} \approx \frac{mgL^2}{8H} \quad (13.1)$$

Considering no elongation in the conductor, the mechanical axial tension can be calculated as in [Eq. \(13.2\)](#), where the thermal–tensional equilibrium of the conductor between a state 1 and a state 2 is presented:

$$0 = A(T_{c2} - T_{c1}) + B\left(\frac{1}{H_1^2} - \frac{1}{H_2^2}\right) - H_1 - H_2 \quad (13.2)$$

In this equation,  $A$  ( $\text{kg m s}^{-2}\text{K}^{-1}$ ) and  $B$  ( $\text{kg}^3 \text{m}^3 \text{s}^{-6}$ ) are parameters depending on conductor properties such as the Young Modulus and the cross-sectional area.  $T_c$  (K) is the temperature at the core of the line. One of the two states is used as a reference and can be the condition of the cable at the moment of the tensioning or a standard condition such as the core temperature of the cable equal to 20°C.

### 13.2.2 Dynamic thermal model

The previous equation links the sag of the conductor with its temperature. It is now necessary to show the relationship between the temperature and the current carried by the conductor. This is described in the thermal model of the conductor, at the core of ampacity calculation. The two standards used for the calculation of the core temperature of an overhead line depending on weather characteristics, the IEEE standard (IEEE, 1993), and the CIGRE standard (CIGRE, 2002), are similar in their approach. When simplifications are applied, such as neglecting the magnetic heating or the Corona heating, the following thermal balance is obtained:

$$R(T_c)I^2 + Q_s - (Q_c + Q_r) = mC_p \frac{dT_c}{dt} \quad (13.3)$$

where  $R(T_c)$  is the resistance per unit of length ( $\Omega\text{m}^{-1}$ ),  $Q_s$  is the solar heating ( $\text{W m}^{-1}$ ),  $Q_c$  is the convective cooling ( $\text{W m}^{-1}$ ),  $Q_r$  is the radiative cooling ( $\text{W m}^{-1}$ ),  $C_p$  is the specific heat capacity of the conductor's material ( $\text{J kg}^{-1} \text{K}^{-1}$ ), and  $I$  is the current flowing through the line. The term  $mC_p \frac{dT_c}{dt}$  ( $\text{W m}^{-1}$ ) represents the dynamic evolution of the temperature, modeled as a first-order system with a time constant equal to  $\tau = 1/mC_p$ , in general equal to 5–20 min according to the conductor and the initial conditions.

The difference between the two standards lies in the calculation of the convective cooling, depending on the wind speed. However, for low wind speed (i.e.,  $< 5 \text{m s}^{-1}$ ), the two models have similar results.

In Eq. (13.3), four weather parameters are considered to have an influence on the core temperature of the line:

- The wind speed  $W_s$  ( $\text{m s}^{-1}$ )
- The wind direction  $\varphi$  (rad)
- The ambient temperature  $T_a$  (K)
- The solar radiation  $S$  ( $\text{W m}^{-2}$ )

Other weather parameters such as precipitation or icing could also be considered for DLR calculations (Pytlak et al., 2009, 2011), even if they are most of the time neglected for line design SR.

### 13.2.3 Selection of the critical span

The environmental parameters mentioned above can change along the length of a line, resulting in a different ampacity for each span. Anyway, for each line a unique value

must be selected for the ampacity, and this value should be equal to the minimum ampacity observed on all the N spans of the line, as in Eq. (13.4):

$$DLR_{Line} = \min_{i \in [0, N]} (DLR_i) \quad (13.4)$$

Due to the difficulty to calculate the DLR at every position along the line, even if some methodologies are proposed (Michiorri et al., 2010), a set of critical spans is usually selected where the DLR devices are installed (Matus et al., 2012) and the minimal value of DLR is selected.

## 13.3 Dynamic line rating devices

As a means to determine the current rating of a line, it is needed to monitor the environment of the line or the line itself. For DLR, there are three different kinds of devices which have been developed:

- Weather measurements
- Online measurements
- Conductor clearance measurements

### 13.3.1 Ampacity estimation from meteorological measurements

The first kind of device, the direct weather measurement, is based on weather station that measures the weather characteristics and where the line rating is calculated from it. It is cost-effective because it is not mandatory to settle the device directly on the line. However, its measurements are made on a single point. However, this method is used little in practice because of the fact the whole length of the line is not monitored and some critical spans of the line could be neglected. Furthermore, the state of the conductor is only estimated, resulting in a reduced precision.

An illustration of those points is made in (Schell et al., 2011). For a line located in France, DLR results that are obtained with meteorological measurements, a Meteo France weather station located near the line, are compared with an online sag measurement device, measuring the DLR value for the whole length of the line. The calculations are made for a 3-day period and, during a 4-h period, the DLR value obtained with the direct weather measurements station is superior to the value given by the online device. More generally, on a year, the error of the DLR calculated with the measurements of the weather station could be up to 95% superior to the value given by the online device.

### 13.3.2 Ampacity estimation from live conductor measurements

In this case a measurement tool is mounted on the live conductor measuring one or more physical properties such as the core temperature, the mechanical tension, or the vibration frequency of the conductor.

Those tools are more complex and expensive to install and maintain because they imply an installation on the overhead line. Several different devices have been developed until now, and some examples are here presented:

A device able to measure the conductor temperature is the USi “Power Donut” ([Engelhardt and Basu, 1996](#)). It is composed of a weather station located on a pillar and a “donut” clamped on the conductor and powered by a battery recharged by magnetic induction. The donut measures the temperature at the surface of the line and the inclination of the line. These measurements are sent to the base station where they are coupled with the readings of the weather station to provide a precise estimate of the conductor ampacity.

Another similar device is the CAT-1 Transmission Line Monitoring System, which calculates accurate real-time rating with the measure of mechanical tension at the extremities of the line ([CAT-1](#))

A third solution is developed by Ampacimon, which created a device which collects vibration data and then calculates the sag of the line ([Ampacimon](#)).

All the examples mentioned above provide measurements on single spans of an overhead line, and several tools must be installed to monitor all potential bottlenecks. To overcome this, another solution consists in wrapping a fiber optic cable along the conductor, during manufacturing or on existing lines. The fiber optics provides accurate measurement of temperature or tension with a high spatial resolution (up to 2–5 m) for the whole length of the line ([Dakin et al., 1985](#)).

### **13.3.3 Ampacity estimation from conductor clearance measurements**

A third possibility is the use of devices located on the ground, and with which the sag of the line is measured. Most of the cases are based on visual observations: lasers used to measure the distance between the ground and the line ([Lasertech](#)); photos made with camera ([EPRI, 2001](#)); and GPS observations ([Mensah-Bonsu et al., 2002](#)).

In some cases, another parameter could be observed, the line sag being then deduced. As an example, in ([Physicalgrid](#)), the magnetic field of the line is used for such purpose.

## **13.4 Dynamic line rating forecasts**

### **13.4.1 Mathematical framework**

In general for forecast purposes, deterministic forecasts are used. They can be described as functions able to predict at time  $t$  for the horizon  $h$  a single-point value  $\hat{Y}_{t+h|t}$ , by taking into account the available information  $X_t$  at time  $t$  as shown in [Eq. \(13.5\)](#). However, currently, probabilistic forecasts are also more and more used, the probability associated with each possible future event being provided.

$$\hat{Y}_{t+h|t} = f(X_t) \quad (13.5)$$

For the case of a single-point forecast, the goal is usually to get a forecast as close as possible to the future observations, through the reduction of the root mean square error as an example. But the goal could be different, as the example of a forecast has a certain probability  $\tau \in [0,1]$  to be superior to the measurement. This last case, described in Eq. (13.6), corresponds to a quantile forecast  $\hat{Y}_{t+h|t}^\tau$ , and a special attention is given to it in this chapter. Indeed, due to security criteria, a risk criterion should be associated to a forecast associated to DLR. This leads to the fact the forecast should be, most of the time, inferior to the observation, the security limit being defined through the value of the quantile. As an example, with  $\tau = 0.02$ , there is a probability that the forecast is superior to the observation equal to 2%, which one may consider as an acceptable probability for medium-range forecasts. The quantile could also be selected depending on an evaluation of safety and benefits. As an example, in (Bucher et al., 2013), the authors study on a 30-bus network provided by IEEE, and they show the impact of different quantiles, from 1% to 10%, on the economic benefits and the number of situations where the N-1 criterion is not respected.

$$P\left(\hat{Y}_{t+h|t}^\tau > Y_{t+h}\right) = \tau \quad (13.6)$$

With regards to the outputs  $Y_{t+h}$ , in the case of DLR the unknown variable  $Y$  can be the conductor ampacity, the conductor temperature or the conductor sag. Two observations arise at this point. These variables are strongly dependent on the specific section of the line and to forecast a value acceptable for a whole circuit, the most conservative value along its path should be used as previously mentioned in Eq. (13.4). Ampacity is an implicit variable that cannot be measured but only estimated from other measurements and physical modeling such as the thermal models described in CIGRE (2002).

Regarding the inputs, they can be divided in static and dynamic inputs. Static inputs are relative to the conductor and environment characteristics such as the diameter of the conductor, its resistance, its orientation, its height from the ground, the ground roughness, and the altitude. These parameters are necessary to calculate an estimation of the ampacity when this is the parameter that will be predicted. Dynamic inputs are represented by measurements relative to the conductor such as tension, sag, or temperature in specific points of the line, by measurements of meteorological parameters such as wind speed, wind direction, air temperature, and solar radiation and in the case of medium-range forecasts, meteorological forecasts at the closest grid points for the same meteorological parameters can also be used.

An example of the physical problem to be modeled and of the available sources of information ( $X_t$ ) can be seen in Fig. 13.2, representing a map of a region crossed by an overhead line for what DLR want to be forecasted. The line is divided in  $N_c$  sections (e.g., 16) according to the orientation but also to the ground (roughness, obstacles). Along the line  $N_{mc}$  (e.g., 3) measurement point on the live conductor, represented by green triangles, are installed, with  $N_{ws}$  (e.g., 3) weather stations, represented by blue rectangles. Weather stations and live conductor measurements can be in the same location or in different locations. Furthermore, for each circuit section, it is

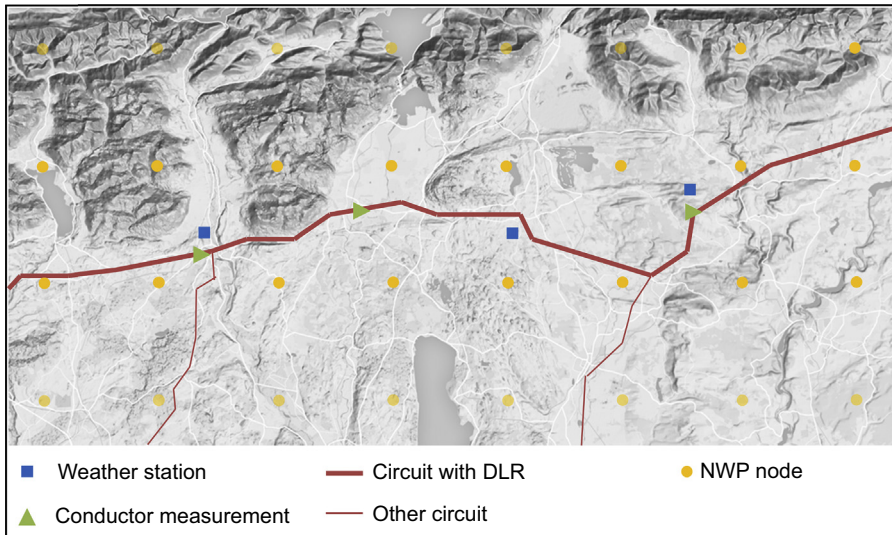


**Figure 13.2** Example of the physical problem to be modeled and of the available information sources. *DLR*, Dynamic line rating.

possible to identify the four closest points of the NWP grid, represented here as yellow circles, for a total of  $N_{nwp}$  (e.g., 18) grid points. Both weather stations and NWP provide information about the four main weather parameters: wind speed, wind direction, air temperature, and solar radiation. Weather stations can provide update readings with frequency  $f_{meas}$  (e.g., 1/h) while Numerical Weather Prediction (NWP) provide forecasts with a time resolution of  $f_{nwp}$  (eg: 1/3 h).

### 13.4.2 Dynamic line rating short-term forecast examples (0–6 h)

Several first attempts in the realization of a DLR forecast method were done in the early 90s, mainly focusing on short-term prediction:

Douglass developed a first method using the historic data (Douglass, 1988). The DLR is forecasted on a 1-h horizon as the DLR value that is exceeded 95% of the time during the previous hour.

In Foss and Maraio (1990), the DLR is forecasted for the next 4 h, the multiplication of its worst value during the last 4 h and a parameter, which represent the cyclic yearly and daily patterns for the weather conditions. This ratio is calculated as the historic ratio between the previous year average values of DLR at  $t$  and  $t+horizon$ ,  $t$  being the time when the prediction is made and  $h$  the horizon of the forecast.

More recently, in Zhang et al. (2002), Kim et al. (2006), and Wang et al. (2011), the focus has been made on methods using Monte Carlo simulations (MCSs): after the definition of a probability density function (pdf) associated with a future weather characteristics, a MCS is run for picking at each iteration weather parameters, and from them the associated DLR is calculated using the physical model (Fig. 13.3).

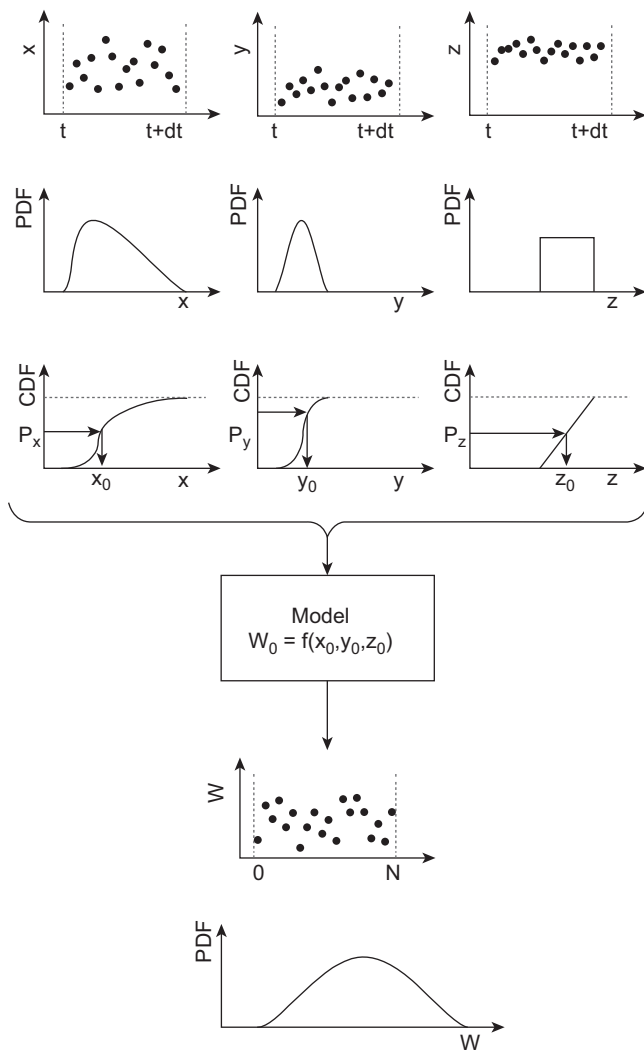


**Figure 13.3** Forecasted DLR probability density with Monte Carlo simulation.

Michiorri, A., Taylor, P.C., Jupe, S.C.E., Jan 2010. Overhead line real-time rating estimation algorithm: description and validation. Proceedings of the Institution of Mechanical Engineers, Part A—Journal of Power and Energy 224 (3), 293–304.

One of the difference between the studies is the selection of the used parameters, some of them having a pdf associated to ambient temperature being used in Wang et al. (2011), whereas a deterministic forecast of the same parameter is being used in Kim et al. (2006). Moreover, the characterization of the pdf's is made differently in each study. The format of the used pdf for each weather characteristics is different for each weather parameter, and a consensus appeared in literature recently for the choice of the pdf's, the parameters of those ones being found through an analysis of the past observations.

For the wind direction  $\varphi$ , the von Mises distribution appears as adapted because of the cyclic nature of the output (Eq. 13.7):

$$VM(\varphi|\mu, k) = \frac{1}{[2\pi * I_0(k)]} e^{k*\cos(\varphi-\mu_\varphi)} \quad (13.7)$$

where  $0 \leq k \leq \infty$ ,  $0 \leq \mu_\varphi \leq 2\pi$ ,  $0 \leq \varphi \leq 2\pi$ , and  $I_0$  is the zero-order Bessel function (Eq. 13.8):

$$I_0(k) = \sum_{p=0}^{\infty} \frac{1}{(p!)^2} \left(\frac{k}{2}\right)^{2p} \quad (13.8)$$

For the wind speed  $W_s$ , the Weibull distribution is widely used (Eq. 13.9):

$$Weib(W_s|\alpha, \beta) = \frac{\beta}{\alpha^\beta} W_s^{\beta-1} e^{-\left(\frac{W_s}{\alpha}\right)^\beta} \quad (13.9)$$

For the ambient temperature  $T_a$ , the normal distribution is used (Eq. 13.10):

$$f(T_a|\mu, \sigma) = \frac{1}{\sigma\sqrt{2\pi}} e^{-\frac{1}{2}\left(\frac{T_a-\mu}{\sigma}\right)^2} \quad (13.10)$$

For the solar radiation, no pdf has been used yet in the literature for DLR forecasts, deterministic forecasts being used instead.

### **13.4.3 Dynamic line rating medium-term forecast examples (6–48 h)**

As for short-term forecasts, few papers had been written on DLR medium-range forecasting. Contrary to the short-term forecasts, most of them consider weather forecasts, even if exceptions are to be noted.

As an example, in Hall and Deb (1988), a 1-week forecast model is developed by setting the forecasted ampacity as the sum of a deterministic compound obtained through Fourier analysis and a stochastic compound calculated with an autoregressive model of order 2.

With weather forecasts, different methods are proposed in the literature.

In Uski (2015a), only the ambient temperature is used, the wind speed and the solar radiation being considered as too unstable along the entire length of the whole line. Forecasts are made at several locations along the line, and for each, the forecast is considered as the physical model run with the same inputs as the one used for the calculation of the SR, except the temperature which is the one forecasted plus 5°C that offers a security margin.

In Sun et al. (2015), the author describes an analytical method providing the parameter of the pdf associated with the forecasted DLR. Considering the pdf is Gaussian, the

authors calculate its mean value  $E(\hat{Y}_{t+h|t})$  and its standard deviation  $\sigma(\hat{Y}_{t+h|t})$ . The used parameters are the ambient temperature  $T$ , the east–west compound of the wind speed  $U$ , the north–south compound of the wind speed  $V$ , through their mean value, and their standard deviations. The function  $f$  which describes the physical model of the IEEE standard (IEEE, 1993) is also used for ampacity calculations. Through a first-order Taylor series expansion, the authors use the following equation:

$$E(\hat{Y}_{t+h|t}) = f(E(T), E(U), E(V)) \quad (13.11)$$

$$\begin{aligned} \sigma(\hat{Y}_{t+h|t})^2 &= \left( \frac{\delta f(\cdot)}{\delta T} \Big|_{E(T)} \right)^2 Var(T) + \left( \frac{\delta f(\cdot)}{\delta U} \Big|_{E(U)} \right)^2 Var(U) \\ &\quad + \left( \frac{\delta f(\cdot)}{\delta V} \Big|_{E(V)} \right)^2 Var(V) \end{aligned} \quad (13.12)$$

In Michiorri and Taylor (2009) and Ringelband et al. (2012), an approach through the use of MCSs similar to the one proposed in the previous section is presented. However, contrary to short-term forecasts were only the past observations of weather parameters were used, here weather forecasts are considered for the setting of the pdf's parameters.

In Ringelband et al. (2012), a MCS is also run, but the used weather forecasts are forecast ensembles: for a given horizon,  $K$  forecasts are provided for each weather parameter, the inputs used for their calculations being slightly modified for each result. For the wind speed and the wind direction, the pdf is defined with a mixture model, a pdf being associated to each forecast of the ensemble ones and the parameters of the pdf's and the mixture models being found with the likelihood functions (Eqs. 13.13 and 13.14).

$$pr(\varphi) = \sum_{i=1}^K \omega_i * VM_i(\varphi|\mu_i, k_i) \quad (13.13)$$

$$pr(W_s) = \sum_{i=1}^K \omega_i * Weib_i(W_s|\alpha_i, \beta_i) \quad (13.14)$$

## 13.5 Benefits of dynamic line rating forecasting

DLR and DLR forecasts could unlock network capacity and so bring several advantages for the management of the network. Those could be summed up with the following points:

- The improvement of the coupling between electricity markets.
- The reduction of wind power curtailment due to congestions.
- The reduction of redispatching due to curtailment.
- The delay of network reinforcements due to increased generation or loads.
- The improvement of reliability.

### 13.5.1 Coupling of electricity market

In synchronous areas, the different electricity markets are connected through overhead lines or underground cables. Through them, a convergence of the electricity market is observed with a global reduction of the costs of electricity. Due to that, those lines bring important financial benefits and are strongly used. As an example, in 2012, the connections between France and Germany were enabling a convergence of the electricity costs on both the market 67% of the time, the line being used at its maximum capacity for the 33% of the remaining time ([Cross-border electricity, 2012](#)). In that context, the increase of the ampacity of the line could improve the economic benefits linked to the use of this asset.

For a specific case, in [Uski \(2015b\)](#), one of the interconnections between Sweden and Finland is studied. For an SLR of 1500 MW, the authors show that 97% of the time the DLR was superior to 1800 MW, i.e., a DLR superior to the SR of 20%. Moreover, for 500 h of congestion situations, the authors showed that the average cost of 50 €/MWh in Finland would be decreased of 4.7 €/MWh, thanks to the use of DLR.

### 13.5.2 Reduction of wind power curtailment

The value of the wind cooling a line connected to a wind power farm is highly correlated to the value of the wind responsible for its production of electricity ([Nguyen et al., 2014](#)). Because of that, through DLR, the transmission issues due to wind generation are solved by wind cooling.

This could lead to far less congestion issues ([Kazerooni et al., 2011a](#)) and to financial benefits, the wind farms generating more energy ([Wallnerström et al., 2015](#)).

In [Banerjee et al. \(2014\)](#), a reflection is addressed on day-ahead scheduling taking into account wind power forecasts and DLR. DLR forecasts are also considered, but the pdf's are considered as the same for each season, instead of a probabilistic forecast that provides one for each time step. Considering a 14-bus network and through a two-stage stochastic optimization, the authors study the impact of the reserve costs and of the line overloads on the total curtailed wind generation, depending on the presence or not of DLR.

### 13.5.3 Reduction of redispatching

In [Khaki et al. \(2010\)](#), the authors make an economic dispatch on a simplified network, calculating the savings done with DLR. The studied network is composed of three nodes, one load, and two generation nodes, one being a thermal plant producing expansive energy and the other one being a hydropower plant producing cheaper energy.

First, they run an economic dispatch where they minimize, in a first approach, the active losses in the lines. For that objective, the DLR, even if it offers a positive reduction, does not have a significant impact on the potential sparing.

Secondly, a similar optimization problem is solved, but now the goal is to minimize the cost of use of the two plants. The DLR allows the hydropower plant producing more energy by increasing the ampacity of the lines connecting it to the other nodes. For a week, It is shown that these costs are decreased from 1815 k\$/GWh to 1693 k\$/GWh.

Similar results are demonstrated in [Kazerooni et al. \(2011b\)](#). In that article, the studied case is a transmission network located in the Humber Estuary region, composed of

nine nodes: three nodes with gas generation; one with coal generation; two with wind generation.

By creating a set of scenarios describing the loads and generation on long periods, via Latin hypercube sampling, the constraint costs are analyzed depending on ampacity setting. For the winter period, with DLR, the constraint costs are to be expected to be reduced of around 53%.

### **13.5.4 Delay of network reinforcements due to both increased generation and demand**

In France, a study carried out by ERDF, **the main DSO**, (Minaud et al., 2013) estimated in 300 M€/GW and 100 M€/GW the connection cost for PV farms and wind farms, respectively. Those costs could be prohibitive for the introduction of renewable energies and DLR could make reduce the needed investments.

In [Wallnerström et al. \(2015\)](#), a wind farm is connected with a line being often congested, and two hypotheses are tried to solve this issue, the adding of a new line and the use of DLR. For a case of a wind farm with seven wind power plants, it is shown that the total curtailed energies with DLR or with a new line are the same. However, the financial benefits for a period of 20 years show, for this case, a financial gain with the DLR, whereas financial losses are incurred with the creation of a new line.

### **13.5.5 Mitigation of reliability issues**

DLR brings significant benefits for the reliability of the network.

In [Greenwood and Taylor \(2014\)](#), the reliability of four networks is estimated with a MCS through the calculation of the Loss of Load Expectation index (LOLE), which is the theoretical number of hours per year where the supply does not meet the demand. The studied cases are a 6-bus, a 14-bus, a 24-bus, and a 39-bus network defined by IEEE. The results show an important reduction of the LOLE, up to 67% when DLR is installed.

Also, during short periods of the year, the SR is inferior to the DLR. In [Heckenbergerova et al. \(2011\)](#), it is explained that the SR is generally defined such as it is only 5% of the time inferior to the DLR value. However it should be opposed to the reality of the field: in [Fu et al. \(2011\)](#), the SR is compared to the value of the DLR for a whole year on an Irish overhead line. For the winter period, the DLR is inferior to the SR 40% of the time. In addition to the increase of the ampacity most of the time, DLR would seldom decrease the ampacity to a value inferior to the SR, safer for the operation of the network.

## **13.6 Conclusions**

The DLR has several interests from the point of view of the grid operators: it improves the risk indexes, decrease the number of congestion issues, allows a higher renewable energy penetration rate, and brings economic benefits.

Forecasting the ampacity of the lines would allow a full exploitation of that technology, and this question has been addressed in several papers. However, the lack

of diversity in the exposed used methods for the construction of those models and the absence of comparison between them leads to the conclusion far more research is to be done in that area.

Also, most of the studies dealing with the potential DLR benefits for the grid operators are made taking into account the measures of the DLR. However, those values are far superior to the DLR forecasts, made in accordance with security criteria. Thus, the obtained results are optimist, but not realistic, and it is needed to be corrected in future research.

## References

- Ampacimon. Available: <http://www.ampacimon.com/product/>.
- Banerjee, B., Jayaweera, D., Islam, S.M., 2014. Optimal scheduling with dynamic line ratings and intermittent wind power. In: PES General Meeting| Conference & Exposition, 2014 IEEE, pp. 1–5.
- Bucher, M.A., Vrakopoulou, M., Andersson, G., 2013. Probabilistic N–1 security assessment incorporating dynamic line ratings. In: Proceedings of the 2013 IEEE Power and Energy Society General Meeting, Vancouver Canada, pp. 21–25.
- CAT-1 Transmission line monitoring system, In: (Ed.) Nexans.USA.
- CIGRE, W., 2002. In: 12, Thermal Behaviour of Overhead Conductors, Tech.. Brochure.
- Cross-border electricity exchanges—use and management of interconnections in 2012. Commission de Régulation de l'Énergie, 2012.
- Dakin, J., Pratt, D., Bibby, G., Ross, J., 1985. Distributed optical fibre Raman temperature sensor using a semiconductor light source and detector. Electronics Letters 21, 569–570.
- Douglass, D.A., 1988. Weather-dependent versus static thermal line ratings [power overhead lines]. IEEE Transactions on Power Delivery 3, 742–753.
- <http://www.electricalengineeringinfo.com/2015/01/what-is-sag-tension-in-electrical-transmission-lines.html>.
- Engelhardt, J., Basu, S., 1996. Design, installation, and field experience with an overhead transmission dynamic line rating system. In: Transmission and Distribution Conference, 1996. Proceedings, 1996 IEEE, pp. 366–370.
- EPRI, 2001. Video Sagometer Application Guide.
- Foss, S.D., Maraio, R., 1990. Dynamic line rating in the operating environment. IEEE Transactions on Power Delivery 5, 1095–1105.
- Fu, J., Morrow, D.J., Abdelkader, S., Fow, B., 2011. Impact of dynamic line rating on power systems. In: UPEC, Soest.
- Greenwood, D.M., Taylor, P.C., 2014. Investigating the impact of real-time thermal ratings on power network reliability. IEEE Transactions 29, 2460–2468.
- Hall, J.F., Deb, A.K., 1988. Prediction of overhead transmission line ampacity by stochastic and deterministic models. IEEE Transactions 3, 789–800.
- Heckenbergerova, J., Musilek, P., Filimonenkov, K., 2011. Assessment of seasonal static thermal ratings of overhead transmission conductors. In: Power and Energy Society General Meeting, San Diego.
- IEEE, 1993. Standard for Calculating the Current–Temperature Relationship of Bare Overhead Conductors. Transmission and Distribution Committee of the IEEE Power Engineering Society IEEE Std 738-1993.

- Kazerooni, A.K., Mutale, J., Perry, M., Venkatesan, S., Morrice, D., 2011a. Dynamic thermal rating application to facilitate wind energy integration. In: PowerTech, 2011 IEEE Trondheim, pp. 1–7.
- Kazerooni, A.K., Mutale, M.P.J., Venkatesan, S., Morrice, D., 2011b. Dynamic thermal rating application to facilitate wind energy integration. In: PowerTech, Trondheim.
- Khaki, M., Musilek, P., Heckenbergerova, J., Koval, D., 2010. Electric power system cost/loss optimization using dynamic thermal rating and linear programming. In: EPEC, Halifax, NS.
- Kim, D.-M., Cho, J.-M., Lee, H.-S., Jung, H.-S., Kim, J.-O., 2006. Prediction of dynamic line rating based on assessment risk by time series weather model. In: Probabilistic Methods Applied to Power Systems, 2006. PMAPS 2006. International Conference on, pp. 1–7.
- Kim, D.M., Cho, J.M., Lee, H.S., Jung, H.S., Kim, J.O., 2006. Prediction of dynamic line rating based on assessment risk by time series weather model. In: PMAPS, Stockholm.
- Lasertech, [www.lasertech.com](http://www.lasertech.com), ed.
- Matus, M., Sáez, D., Favley, M., Suazo-Martínez, C., Moya, J., Jiménez-Estévez, G., et al., 2012. Identification of critical spans for monitoring systems in dynamic thermal rating. *IEEE Transactions on Power Delivery* 27, 1002–1009.
- Mensah-Bonsu, C., Krekeler, U.F., Heydt, G.T., Hoverson, Y., Schillicci, J., Agrawal, B.L., 2002. Application of the Global Positioning System to the Measurement of Overhead Power Transmission Conductor Sag, vol. 17.
- Michiorri, A., Taylor, P.C., 2009. Forecasting real-time ratings for electricity distribution networks using weather forecast data. In: Electricity Distribution-part 1, 2009. CIRE 2009. 20th International Conference and Exhibition on, pp. 1–4.
- Michiorri, A., Taylor, P., Jupe, S., 2010. Overhead line real-time rating estimation algorithm: description and validation. Proceedings of the Institution of Mechanical Engineers, A: Journal of Power and Energy 224, 293–304.
- Minaud, A., Gaudin, C., Karsenti, L., 2013. Analysis of the options to reduce the integration costs of renewable generation in the distribution networks. Part 1: impact of PV development in France and global analysis of considered alternatives to reinforcement. In: Electricity Distribution (CIRED 2013), 22nd International Conference and Exhibition on, pp. 1–4.
- Nguyen, H.-M., Lambin, J.-J., Vassort, F., Lilien, J.-L., 2014. Operational experience with dynamic line rating forecast-based solutions to increase usable network transfer capacity. In: Proceedings of the 45th Session of the Council on Large Electric Systems (CIGRE). Physicalgrid, <http://www.physicalgrid.com/rt-tlms.html>, ed.
- Pytlak, P., Musilek, P., Lozowski, E., 2009. Precipitation-based conductor cooling model for dynamic thermal rating systems. In: Electrical Power & Energy Conference (EPEC), 2009 IEEE, pp. 1–7.
- Pytlak, P., Musilek, P., Lozowski, E., Toth, J., 2011. Modelling precipitation cooling of overhead conductors. *Electric Power Systems Research* 81, 2147–2154.
- Ringelband, T., Schäfer, P., Moser, A., 2012. Probabilistic ampacity forecasting for overhead lines using weather forecast ensemble. *Electrical Engineering* 95, 99–107.
- Schell, P., Nguyen, H., Lilien, J., 2011. Quantifying the limits of weather based dynamic line rating methods. In: *IEEE Transactions*, Halifax.
- Sun, X., Luh, P.B., Cheung, K.W., Guan, W., 2015. Probabilistic forecasting of dynamic line rating for over-head transmission lines. In: Power & Energy Society General Meeting, 2015 IEEE, pp. 1–5.
- Uski, S., 2015a. Dynamic line rating forecastability for conservative day-ahead line rating values. In: Industrial Electronics Society, IECON 2015-41st Annual Conference of the IEEE, pp. 003738–003742.

- Uski, S., 2015b. Estimation method for dynamic line rating potential and economic benefits. *International Journal of Electrical Power & Energy Systems* 65, 76–82.
- Wallnerström, C.J., Huang, Y., Söder, L., 2015. Impact from Dynamic Line Rating on Wind Power Integration, vol. 6.
- Wang, K., Sheng, G., Jiang, X., 2011. Risk assessment of transmission dynamic line rating based on Monte Carlo. In: Power Engineering and Automation Conference (PEAM), 2011 IEEE, pp. 398–402.
- Zhang, J., Pu, J., McCalley, J.D., Stern, H., Gallus Jr., W.A., 2002. A Bayesian approach for short-term transmission line thermal overload risk assessment. *IEEE Transactions on Power Delivery* 17, 770–778.

# The role of predictability in the investment phase of wind farms

14

Javier Sanz Rodrigo<sup>1</sup>, Laura Frías Paredes<sup>1</sup>, Robin Girard<sup>2</sup>, George Kariniotakis<sup>2</sup>, Kevin Laquaine<sup>2</sup>, Nicole Stoffels<sup>3</sup>, Lueder von Bremen<sup>3</sup>

<sup>1</sup>National Renewable Energy Centre (CENER), Sarriguren, Spain; <sup>2</sup>MINES Paris Tech, Sophia Antipolis, France; <sup>3</sup>University of Oldenburg, Oldenburg, Germany

## 14.1 Introduction

The use of wind power forecasting is normally associated with the operational phase of a wind farm in connection to different end uses and prediction horizons (Wang et al., 2011). In the very short term, from seconds to six hours, forecasts are useful to predict sudden events such as ramps that can be managed by turbine and wind farm control (Mendes et al., 2013). In the range from 6 h to 2–3 days, short-term forecasting is used by transmission system operators (TSO) for power system management (scheduling, reserves planning, congestion management, etc.) (Giebel et al., 2011). Wind farm operators use day-ahead and intraday forecasts for trading in the energy market (Pinson et al., 2007). Medium-term forecasting up to a week ahead is used for operation and maintenance planning of wind farms (Jacobsen and Rubjerg, 2005), conventional power plants, or transmission lines. Long-term weather forecasting beyond a week-ahead is particularly interesting to support offshore wind farms servicing logistics during the construction and operation phases (Scholz-Reiter et al., 2010). Finally, very long-term seasonal and decadal wind climate forecasting is relevant to inform wind energy investors about the volatility of the future wind resource and how this risk can have an impact on the return of investment (Soret et al., 2015).

Wind power forecasting is a matter of temporal scales as an inherent characteristic of the wind speed variability of the weather (Lange and Focken, 2005). From seasonal scales driven by global circulation weather patterns to daily cycles due to temperature changes and to subminute turbulence variations generated by local topography, wind power integration is a multiscale problem. Managing the variability of wind generation is a key aspect for an optimal integration of wind power in the electrical grid, especially when large penetration is sought as it is the case for European targets of 20% share of renewables by 2020. According to the European Wind Energy Association (EWEA), wind energy is expected to contribute with 15.7%–18.4% of EU's energy demand (EWEA, 2011) in 2020.

Large wind power penetration and efficient wind farm operation require early consideration of the impact of wind power deployment from site to regional/country and continental levels. Spatial planning aspects are typically considered during the resource assessment phase, when wind energy prospecting meets the geopolitical and environmental constraints of the area of interest. Traditionally, this activity is aided

by the use of a wind atlas embedded in a geographical information system (GIS, see for instance: [Dutra and Szklo, 2008](#); [Dvorak et al., 2010](#)) that, in a layered format, accounts for all the geographical information relevant for wind energy deployment: wind resource, terrain elevation, land use, political boundaries, transmission lines, environmentally restricted areas, etc. The wind resource layer is often reduced to two variables, the wind speed and the wind power density, both averaged over the 20-year expected lifetime of a wind farm. This rather limited information is useful to classify a site in terms of energy potential but does not include any information about the quality of this energy in terms of grid integration, turbine safety, or operational costs. Only by introducing wind power variability and predictability aspects in spatial planning tools, it is possible to obtain an integrated vision of the cost of wind energy throughout the deployment life cycle ([IRENA, 2012](#)). This enriched wind atlas allows a more comprehensive planning of wind energy deployment considering, as much as possible, all the stakeholders interests in a seamless modeling framework.

This chapter shows some test cases from the EU project SAFEWIND on different ways that the planning phase of wind farms can benefit from early knowledge of wind power predictability. The interest is focused on day-ahead short-term forecasting, as the most relevant range for TSOs and wind energy traders.

We shall use the term predictability assessment when we quantify wind predictability during the planning phase of a wind farm ([Sanz Rodrigo et al., 2013](#)). This can be associated to the prediction of the hub-height wind speed (the meteorological wind resource), the gross wind power from a specified turbine power-curve model, or the net wind power output, which includes wind farm losses due to wake effects and other environmental aspects that are site and wind farm layout specific.

## 14.2 A model chain for wind resource and predictability assessment

Wind power predictability assessment is done using roughly the same tools of the operational forecasting environment but applied, in hindcast mode, to virtual time series of wind power production that have been generated with resource-assessment models. Similar to wind resource assessment, the characterization of predictability depends on the resolution of the model used to generate the time series. Then, we can speak about regional or large-scale predictability in connection to reanalysis data, with several tens of kilometers of horizontal resolution or local-scale predictability in connection to site measurements ([Sanz Rodrigo et al., 2013](#)).

In the context of spatial planning and project financing, a wind atlas methodology should use a consistent modeling framework to deal with both hindcast and forecast simulations. The core model is a numerical weather prediction (NWP) model, driven by Global Circulation Models (GCMs) outputs produced by met-offices such as NCEP/NCAR in the United States or ECMWF in Europe ([Kalnay et al., 1996](#); [Dee et al., 2011](#)). GCMs are used, with data assimilation systems, to resolve the large-scale fields of the weather, at resolutions of several tens to hundreds of kilometers, to define the state of the atmosphere at typically 6-hourly intervals (so-called analyses in forecasting and reanalysis in hindcasting). NWPs operating at regional scale refine

the weather patterns to produce forecasts at mesoscale level, at resolutions of several kilometers and hourly time steps (Hahmann et al., 2014). Even though there are meso-scale models that can proceed with physical downscaling to microscale levels, due to the computational cost, all the subgrid scales are not resolved but rather parameterized, i.e., semiempirical formulation is used to fill the subgrid gap, which is not simulated by the meteorological models. This will typically result in wind speed bias in complex terrain areas because of unresolved speedups generated by the subgrid topography. Microscale models can be used to correct this bias and simulate wake effects from wind farms (Badger et al., 2013).

When dynamic data from the wind farm are available in almost-real time, it can be used to build statistical models, so-called Model Output Statistics (MOS), which act as a transfer function between the NWP outputs and the wind power predictions. These tools are more efficient than full-physical models and have proven very effective at removing systematic errors coming from both the NWP and the wind farm power curve. This is the standard approach for operational short-term deterministic wind power forecasting. Probabilistic forecasting constitutes an important field of research as it allows the introduction of uncertainty in the prediction. An up-to-date review of wind power forecasting models can be found in Giebel et al. (2011) and Foley et al. (2012). During the planning phase of a wind farm, MOS models can be used in connection with virtual time series of wind power production generated by a microscale model of the wind farm driven by onsite met mast wind observations. These short-term observations can be extended back in time to a long-term period making use of statistical tools such as measure—correlate—predict methods (Rogers et al., 2005) or statistical downscaling techniques that relate historical measured or simulated databases with the local measurements (Vanvyve et al., 2015).

## 14.3 The value of predictability in spatial planning

The spatiotemporal characteristics of wind predictability can be exploited to contribute to a more efficient and secure integration of wind energy in the power grid. Hence, smart consideration of meteorological aspects can not only promote optimum use of the wind energy potential but can also contribute to important savings in operational costs. For instance, at site level, it is possible that the market value of wind power of a certain wind farm decreases if the wind power day-ahead wind power predictions are very inaccurate although the wind resource is very good.

At larger scales, temporal variability decreases and predictability increases because of spatial error smoothing, i.e., the correlation between forecast errors becomes weaker with distance and the predictability of a region is always better than that of a single wind farm (Focken et al., 2002). Hence, a large wind power operator finds market benefits in distributing the wind farm portfolio along large areas whose wind patterns are maximally uncorrelated. This way, a compensation of forecasting errors takes place and leads to significant improvements in the aggregated predictability and market revenues. This portfolio effect is also beneficial for the TSOs in reducing the balancing costs associated with reserves and congestion management. This can be especially advantageous in the development of a European grid with a unified energy market, where strong cross-border interconnections allow an efficient exchange of energy across the EU. Hence,

higher penetration of renewable energy generation is possible, reducing energy supply risks and lowering the electricity prices (EWEA, 2009; Rombauts et al., 2011).

Improvements in day-ahead wind power forecasting were very significant in the first decade of 2000. Lange et al. (2006) report wind power forecasting errors, in terms of root-mean-square error (RMSE) in % of installed capacity, in the E.ON Netz area of the German grid improving from 10% in 2001% to 6.5% in 2006. For Germany, this error is of the order of 5% while for an individual wind farm in complex terrain the error can be as high as 20% (Giebel et al., 2011).

### 14.3.1 Large-scale wind power predictability mapping

Producing GIS-based predictability information is a basic need for the initial integration of this information in spatial planning tools. To this end, NWPs are compared to reanalysis data making use of a generic power curve. A test case is presented to show this methodology applied to a European domain for a simulation of 1 year.

The COSMO-EU model by the German Weather Service (DWD) provides forecasts and analyses on a  $4.1 \times 7$  km grid (COSMO, 2011). The domain has  $735 \times 625$  grid points, hence 459,375 grid points in total. Forecasts are started at 00 UTC and are produced up to 72 h at an hourly resolution.

The presented data cover the year 2010. For the conversion from wind speed to wind power at approximately 68.8 m height (model level 38), a mean of two different power curves is used, namely: the Enercon E82 and the Vestas V90/2.

Based on the COSMO-EU data and a wind power conversion with a mean power curve assuming a homogenous wind farm distribution, forecast errors are calculated (Madsen et al., 2005): the mean absolute error (MAE) and the RMSE, normalized by the load factor (mean wind power production), for every grid point at a European scale (Fig. 14.1). The difference between these two statistical values lies mainly in the sensitivity toward outliers. The RMSE is more sensitive to the largest errors and outliers (Wilks, 2011). Besides, the annual mean the statistical values are averaged over the different seasons to account for the strong seasonal variations in wind power production.

The forecast error maps (Fig. 14.1) immediately make clear that the forecast error is very much dependent on the local orography. The more complex the terrain, the larger the forecast errors. However, not only the orography has an influence on the forecast error, but also some meteorological phenomena.

Local effects such as the Mistral winds in Southern France or cutoff lows in the Mediterranean play an important role and result in high wind power during the year. Cutoff lows, also named cold air pool, are a meteorological phenomenon and the result of a polar belt trough in the upper air flow extending down to the surface. The frequency of these phenomena was rather high in 2010 (Wetterzentrale, 2012). Especially the cutoff low is difficult to forecast. Hence, forecast errors in the Mediterranean close to Southern Italy are high.

Fig. 14.1 shows the MAE averaged over 2010 for two different forecast horizons: 1-day and 3-day ahead. Wind power forecast errors strongly depend on the load

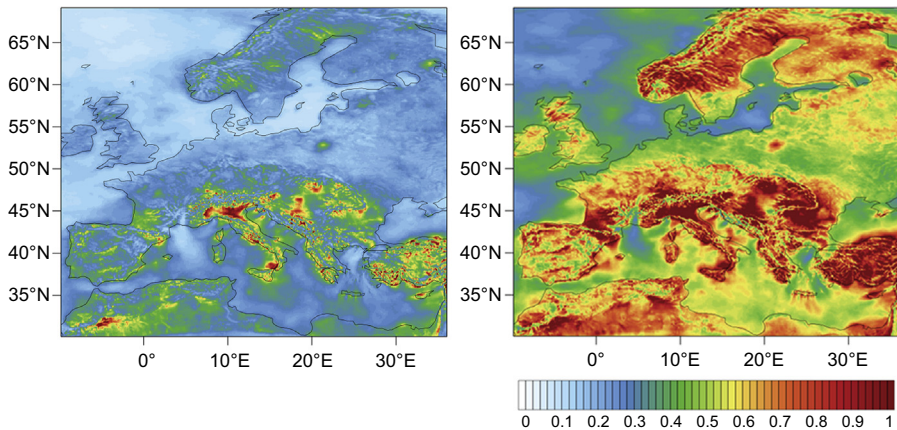


**Figure 14.1** Mean absolute error of the wind power forecast normalized with the load factor for 2010 for forecast day 1 (left) and day 3 (right).

From Sanz Rodrigo, J., Frías Paredes, L., Stoffels, N., von Bremen, L., 2013. Wind power predictability assessment from large to local scale. European Wind Energy Conference EWEA-2013, Wien, Austria, February 2013.

factor which itself depends on the topography. Especially, areas of complex terrain have a faster forecast error development than, e.g., the northern offshore regions. In the Mediterranean, especially the cutoff lows lead to much larger forecast errors than in other offshore regions. In contrast to the cutoff lows the Mistral is well predictable. For the first 24 h the forecast errors are smaller than 0.3, except for areas of very complex terrain. In these regions the orography is mainly responsible for the forecast errors. Systematic errors are neglectable here. On day 3, even the coastal regions have high forecast errors and only few offshore regions have a small forecast error.

There is a significant difference between the small wind power production during summer and the large wind power production, especially offshore, during winter (not shown). Fig. 14.2 shows the seasonal RMSE for summer and winter for forecast day 2. The RMSE was chosen because it accounts better for large forecast errors and emphasizes the differences between the seasons. It becomes very clear, that during the summer period with smaller wind power output, the relative forecast errors are much higher than during the winter season. Even the northern offshore regions have a high forecast error in summer than, e.g., the onshore regions in Northern Germany. While the RMSE is also small for the complete German and Danish coast in winter, the same regions have very high errors in summer. Every site which has slightly complex terrain shows high error values in summer. One exception is, once again, the south of France, where the forecast errors in the Mistral region seem to be constantly small over the year. This region is characterized by high wind speeds and hence high wind power. The small forecast errors are a result of the good predictability of the Mistral winds.

Single wind farm forecasts have high forecast errors. Pooling wind farms over a region, e.g., a TSO zone, helps to smooth out forecast errors. Therefore the forecast error was once again calculated out of spatially smoothed time series. The results are shown in Fig. 14.3 in

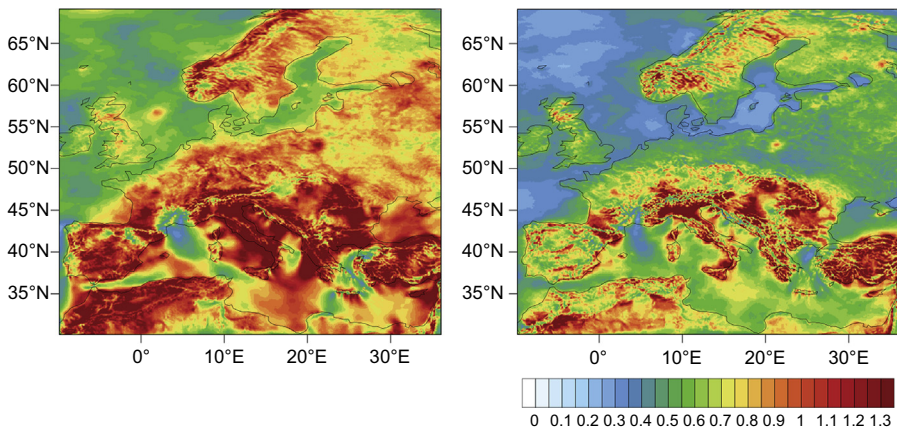


**Figure 14.2** Wind power forecast root-mean-square error normalized with the load factor and averaged over the summer season (top) and the winter season (bottom) for forecast day 2.  
From Sanz Rodrigo, J., Frías Paredes, L., Stoffels, N., von Bremen, L., 2013. Wind power predictability assessment from large to local scale. European Wind Energy Conference EWEA-2013, Wien, Austria, February 2013.

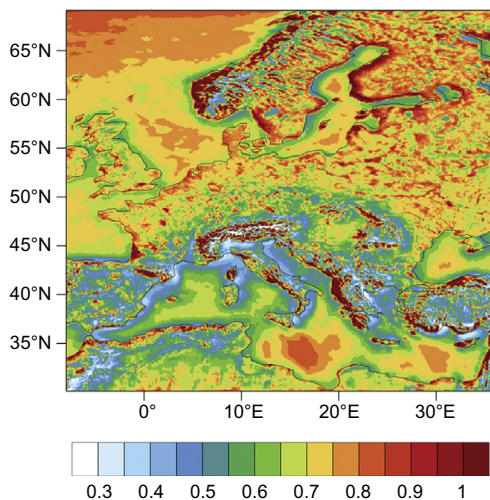


**Figure 14.3** Smoothing factor [100-km smoothed root-mean-square error (RMSE)/local RMSE] for forecast day 2 normalized with the load factor.  
From Sanz Rodrigo, J., Frías Paredes, L., Stoffels, N., von Bremen, L., 2013. Wind power predictability assessment from large to local scale. European Wind Energy Conference EWEA-2013, Wien, Austria, February 2013.

terms of a smoothing factor defined as the ratio of the yearly RMSE over a radius of 100 km and the yearly RMSE of each local grid point. In some regions of complex terrain the smoothing effect leads to error reductions of 50%. The coastal regions in Northern Germany also show significant reductions of approximately 40%. This result is very

promising when the aim is not to forecast the wind power for a single wind farm but rather for a portfolio of wind farms spread over larger regions. This smoothing effect does not only reduce the variability and the forecast error, but also the need of adding other forms of energy to the grid to compensate for the fluctuations in wind power generation. In the future the demand of storage capacity may also be decreased by pooling wind farms together.

### **14.3.2 Local-scale wind farm predictability**

When evaluating the return of investment, the developer will primarily consider the price of electricity expected in the next 20 years, something which depends on the regulatory framework of the electricity market. In countries like Spain, the wind farm operator is obliged to provide a day-ahead forecast of the energy production to help the TSO manage the power system. In a liberalized energy market, the market operator sets an hourly electricity price as well as imbalance tariffs for down- and upregulation. If the system, in a specific situation, requires up/downregulation, and the electricity producer is below/above the forecasted (traded) production, a penalization will be issued which is proportional to the deviation and the cost of regulating up/down. These penalties are naturally linked with the level of wind power predictability of the wind farm: the higher the predictability, the lower the penalization and the faster the return of investment.

The question is, can we anticipate the economic impact of predictability during the planning phase to take it into account in the feasibility study of the wind farm? To answer this question, it is necessary to develop a methodology that can make use of the available information of the site during the planning phase. The target variable is the predictability of the wind farm since this is ultimately linked with the trading benefits. Hence, an essential aspect of the study is to evaluate the methodology using onsite data from both the planning and the operational phases.

The case study comprises two wind farms in Spain, one in the North (WF1), in complex terrain, comprising 45 wind turbines and a total power of 32.05 MW and one in the South (WF2), in simple terrain, comprising 14 turbines and a total power of 28 MW. The available data correspond to a year-long period in both the planning and the operational phase. Comparing the wind speed and directional distributions of the planning and operational phases, it is noticed that while WF1 shows a similar wind climate in both phases, WF2 show a significant changes of the speed distribution because of large interannual variability of the synoptic activity of the region next to the Strait of Gibraltar.

A wind farm model is built based on the WAsP wind atlas methodology ([Troen and Petersen, 1989](#)) applied to the onsite mast measurements, the standard model used by the wind industry, to build virtual time series similarly as it is done by the Prediktor wind power forecasting model ([Landberg, 1999](#)). Wind farm wake efficiencies are averaged values considering the wind speed distribution of each wind direction sector. Hence, the same wake efficiency is adopted regardless of the instantaneous wind speed. Electrical and availability energy losses are not included since this cannot be evaluated from the available data, and they are typically not included in forecasting models.

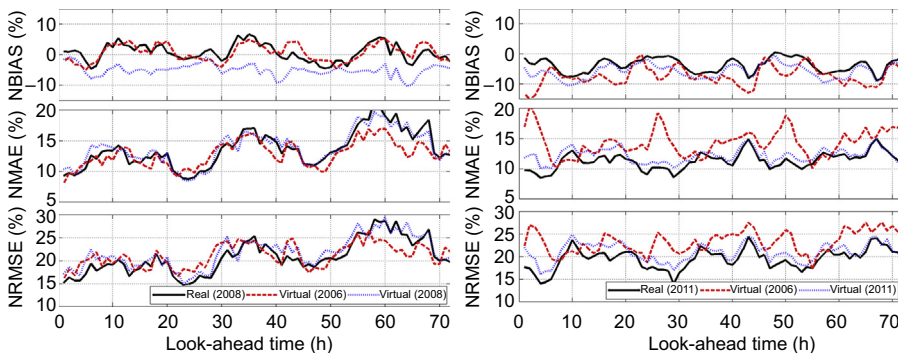
The generated virtual production data are used as input to CENER's LocalPred deterministic forecasting model (Martí et al., 2003). LocalPred is based on NWP inputs from the Skiron mesoscale model, forced with Global Forecasting System (GFS) forecasts and a MOS module that is trained based on wind farm (virtual in this case) production data. The first 6 months of the period are used for training and the remaining 6 months for evaluation. The methodology adopted in this study can be easily assimilated by the wind energy industry since it is based on models that are widely used already in the resource assessment phase (Irigoyen et al., 2011).

Fig. 14.4 shows the dependency of the forecasting errors with the look-ahead time for WF1 and WF2, respectively. The errors from the real production data are compared with those obtained from the virtual production data from the planning and operational phases.

Daily cycles of the errors are observed since the forecasting model is initialized once a day allowing for the highlighting of the intraday error variability of the GFS input data. These cycles are quite repeatable from year to year in WF1 as a result of the similitude of wind climate observed between the planning and operational phases. This is not the case in WF2 where a distinct daily pattern is observed in both phases.

Despite the larger wind climate variability observed in WF2, predictability is higher because of the much simpler local topography that results in higher performance of the mesoscale model. The error growth is also less pronounced in WF2.

In the context of predictability assessment, we shall focus on mean errors over a given prediction horizon. Table 14.1 shows mean errors for the first 3 days of prediction. The bias normalized by the installed wind power capacity (NBIAS) show more scatter in the results owing to the inherent error compensation of this metric. In the case of WF1 the differences between the virtual and the real normalized mean absolute error (NMAE) or normalized root mean square error (NRMSE) in the first 2 days of



**Figure 14.4** Wind power forecasting error versus look-ahead time for WF1 (left) and WF2 (right). The predictability from the “real” operational production data is compared with the predictability from the “virtual” production data generated from the wind speed measurements during the planning (2006 in both WF1 and WF2) and operational (2008 in WF1 and 2011 in WF2) phases.

From Sanz Rodrigo, J., Frías Paredes, L., Stoffels, N., von Bremen, L., 2013. Wind power predictability assessment from large to local scale. European Wind Energy Conference EWEA-2013, Wien, Austria, February 2013.

**Table 14.1 Mean daily forecasting errors from the real and virtual time series of wind power production data for WF1 and WF2**

	WF1			WF2		
	Real (2008)	Virtual (2006)	Virtual (2008)	Real (2011)	Virtual (2006)	Virtual (2011)
<b>NBIAS (%)</b>						
0–24 h	0.9	0.5	−4.7	−3.9	−8.1	−6.3
24–48 h	0.9	0.7	−4.9	−3.7	−7.4	−5.5
48–72 h	0.0	0.5	−5.7	−3.8	−7.0	−5.8
<b>NMAE (%)</b>						
0–24 h	11.4	11.2	11.9	10.7	13.7	12.2
24–48 h	13.3	13.1	13.4	11.2	14.3	11.9
48–72 h	16.1	14.0	15.9	11.9	14.9	12.5
<b>NRMSE (%)</b>						
0–24 h	17.8	19.1	19.0	19.0	22.1	21.0
24–48 h	20.3	21.5	21.4	19.2	23.4	20.6
48–72 h	24.0	22.5	24.7	20.1	24.1	21.1

NBIAS, NMAE and NRMSE errors normalized by installed wind power capacity.

From Sanz Rodrigo, J., Frías Paredes, L., Stoffels, N., von Bremen, L., 2013. Wind power predictability assessment from large to local scale. European Wind Energy Conference EWEA-2013, Wien, Austria, February 2013.

prediction is within 0.2/1.3% and 0.5/1.3% from the planning and operational phases, respectively. The corresponding differences for WF2 are 3.2/4.3% and 1.4/2.1%, larger than WF1 because of the large differences in wind climate observed in WF2. Similarly to wind resource assessment, the impact of interannual variability on predictability needs to be determined to produce robust long-term estimates.

### 14.3.3 Predictability in the decision-making process of a wind energy developer

Girard et al. (2013) analyzed the financial benefit of increasing predictability from a producer's point of view. The analysis was based on a simplified market model with real-world wind power production and day-ahead market data from the Elspot market. The considered study builds upon a case study in Western Denmark. This area is characterized by high wind potential and rather flat landscapes. It was chosen because of the high number of wind farms located there and the existence of sufficiently long tracks of data (4 years) to permit us to produce results with a statistical meaning. The considered wind farms are represented in Fig. 14.5.

It is shown that the financial loss due to imbalance costs, induced by imperfect predictions, represents a low share of revenue in the day-ahead market. Only an increase in predictability resulting from aggregation could lead to a substantial increase in benefits.

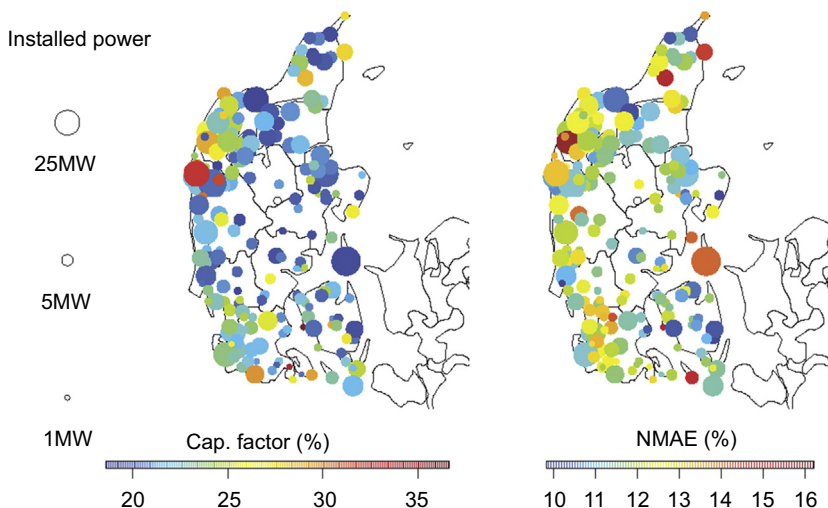


**Figure 14.5** Location of the wind farms in the case study of Western Denmark. Circle size represents installed wind farm capacity. The color code gives the capacity factor (left), as well as the day-ahead normalized mean absolute error (NMAE) (right), both in (% Nominal Power). From Girard, R., Laquaine, K., Kariniotakis, G., 2013. Assessment of wind power predictability as a decision factor in the investment phase of wind farms. Applied Energy 101, 609–617.

In this paper, the potential gains have been quantified through the modeling of the relationship that exists between total revenue, the capacity factor, and predictability. The results are shown in Fig. 14.6.

The associated sensitivity analysis showed that in a case when aggregation is not considered, only 0.02% of the revenue's variance can be explained by predictability, while in a case where aggregation is considered, this proportion reaches 0.15%. This low benefit from predictability is explained partly by the level of imbalance costs and partly by the strong positive correlation that exists between prediction errors and the capacity factor. Ultimately, this implies that in the resource assessment phase, lower predictability will typically go hand in hand with a high associated capacity factor. This makes predictability less relevant than capacity factor in the resource assessment phase, at least from a wind power producer's point of view. Note that there is a difference between considering predictability in the resource assessment phase and considering predictability for an operational wind farm. In the second case, not treated in this paper, the capacity factor is fixed and the role of predictability is different.

Market imbalance cost reduction is not the only benefit a wind power producer can obtain from predictability. Within the operation and maintenance cost breakdown, predictability can play a more important role, especially for offshore wind farms, where the lack of predictability leads not only to market imbalance costs but also to loss of availability due to downtime periods (turbines not accessible because of bad weather that was not well predicted in the maintenance strategy). Still, apart from specific rules

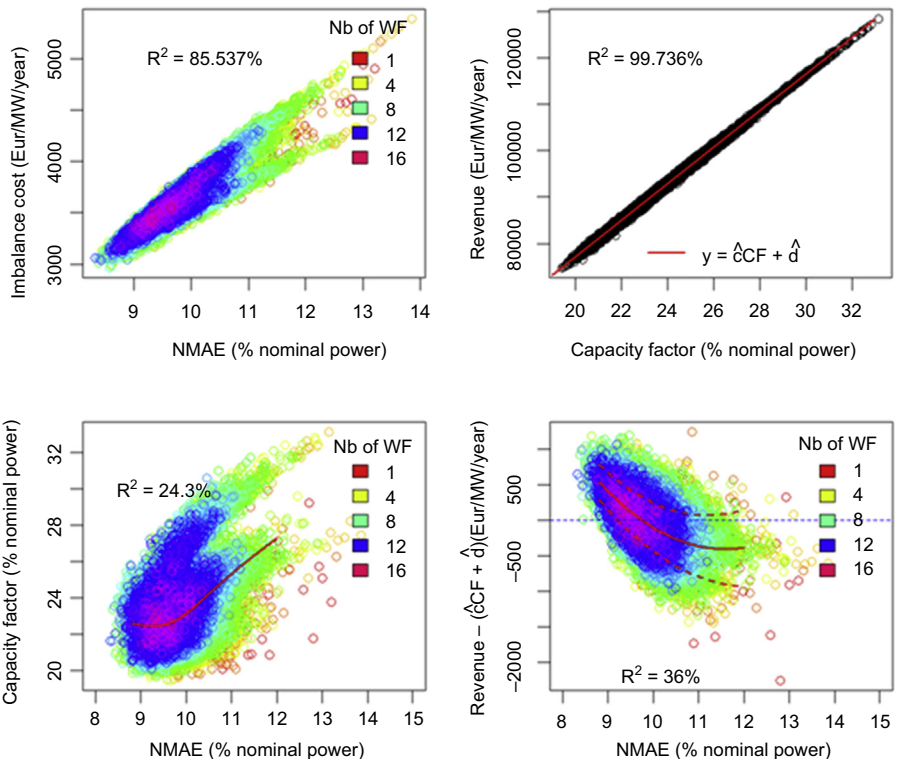


**Figure 14.6** Relations between capacity factor, imbalance cost, revenue, predictability, and the number of wind farms in the portfolio. The solid red lines in the two upper graphs are obtained through linear regression (the corresponding determination coefficients are given). For the bottom-left plot, it is obtained using local polynomial fitting, while for the bottom-right plot it is obtained through second-order polynomial estimation (associated  $R^2$  is given). The red dashed lines on the right give the conditional quantiles (90% upper and 10% lower) obtained with second-order polynomial models. The color code gives the number of wind farms within a given cluster.

From Girard, R., Laquaine, K., Kariniotakis, G., 2013. Assessment of wind power predictability as a decision factor in the investment phase of wind farms. Applied Energy 101, 609–617.

in tenders for wind power installation projects, market imbalance costs constitute the only incentive for producers toward achieving more predictability.

While the results of this paper show the market's incentive action on wind power producers toward achieving greater predictability, it does not quantify the benefit of predictability from the system's point of view. Indeed, the effectiveness of the market measure does not necessarily coincide with the value of predictability with respect to the electric system and might miss the benefits and costs brought about by longer-term investment. Further work should contain a systemic analysis in the spirit of the capacity value (Keane et al., 2011) to reveal the intrinsic value of increasing predictability for a given system at a given level of predictability.

Girard et al. (2013) also provided a prospective analysis, based mainly on the relationship that exists between imbalance prices, spot prices, and aggregation of prediction errors in the system. Under the assumption that the market mechanism will remain the same in the future, it is shown that the benefit of predictability for an independent producer participating in the electricity market is unlikely to increase.

It is also shown that the obtained results would not be different with a larger spatial smoothing effect that could result from the consideration of a larger area. However, this result depends on the analyzed Nordpool market. Alternative market mechanisms, e.g., based on nodal pricing, would most likely give fundamentally different results. The analysis of such cases with respect to predictability makes part of the perspectives of this work.

#### **14.3.4 Portfolio effect in wind energy trading**

It is well known by wind farm operators that higher revenues are obtained by participating in the energy market with a cluster rather than with the individual wind farms, a process sometimes called upscaling. Because of error compensation from uncorrelated predictabilities, the aggregated is almost always lower than the individual predictability. For an optimum portfolio effect, the operator must know how to combine the wind farms in terms of the economic impact in the market.

Focken et al. (2002) analyzed the effect of spatial smoothing on wind power predictability over German regions. The analysis showed that the magnitude of the error reduction depends more on the regional size than on the number of wind farms. For a region of a diameter of 370 km an error reduction of 63% was found by aggregating predictions from 50 sites. Above this number a saturation level is reached where the error cannot be further decreased by aggregation. Extending the influence area beyond national borders is definitively an appealing perspective to further decrease the error reduction.

In support of the findings of Focken et al. (2002), a case study is presented next to illustrate how this portfolio effect works in practice and put in value the extra benefits found when participating in a hypothetic European market instead of a national market. Let us assume that the Iberian electricity daily market rules are adopted, wherein the market operator sets an hourly electricity price as well as imbalance tariffs for down- and upregulation. If the system in a specific situation requires up/downregulation and the electricity producer is below/above the forecasted (traded) production, a penalization will be issued, which is proportional to the deviation and the cost of regulating up/down. Likewise, the operator can obtain profit from deviations that go in favor of the system regulation.

An Irish operator owns 12 wind farms, totaling 202 MW, in Ireland and Northern Ireland and participates in the Irish electricity market. He has the opportunity to buy several wind farms in France (3) and Spain (2) and participate in the European market with 284 MW. He wants to assess the benefits of the portfolio effect when participating in the Irish and the EU markets. To this end, the (Iberian) market tariffs along the year 2008 are used to assess the economic impact of different clustering scenarios. A synchronized database of wind farm productions from these 17 wind farms is used

together with their respective wind power forecasts produced with CENER's LocalPred model (Frias et al., 2009). The integrated capacity factor is 0.25 for both the Irish and the EU cases.

The optimization of the clustering process begins by selecting one wind farm as a seed and then aggregating sequentially the wind farm whose combination with the cluster results in the highest predictability. This optimization variable is monitored with the day-ahead MAE, normalized by the rated power of the cluster (*NMAE*). The lack of predictability results in system imbalance costs and penalties for the wind energy operator. The cost of predictability is measured as the difference between the final profit from the market and the profit for perfect prediction. Fig. 14.7 shows the *NMAE* and the cost of predictability in €/MWh for the Irish and EU test cases.

The individual wind farms have predictabilities in the range 7.5%–22%. A wind farm situated in the SE quadrant of Ireland and having a predictability level close to the mean value of this range is selected as seed for the optimization process. By combination of this wind farm with each one of the other farms of the portfolio reductions in the *NMAE* of 1%–3.3% are observed. The pair with the lowest *NMAE* is selected and the clustering process continues by adding a third wind farm and so on. In the Irish case, the *NMAE* finds a minimum after adding the ninth wind farm with a cluster predictability of 7.8% (error reduction of 42%). Adding more wind farms results in a slight increase of the error (error saturation due to high correlation in the ensemble).

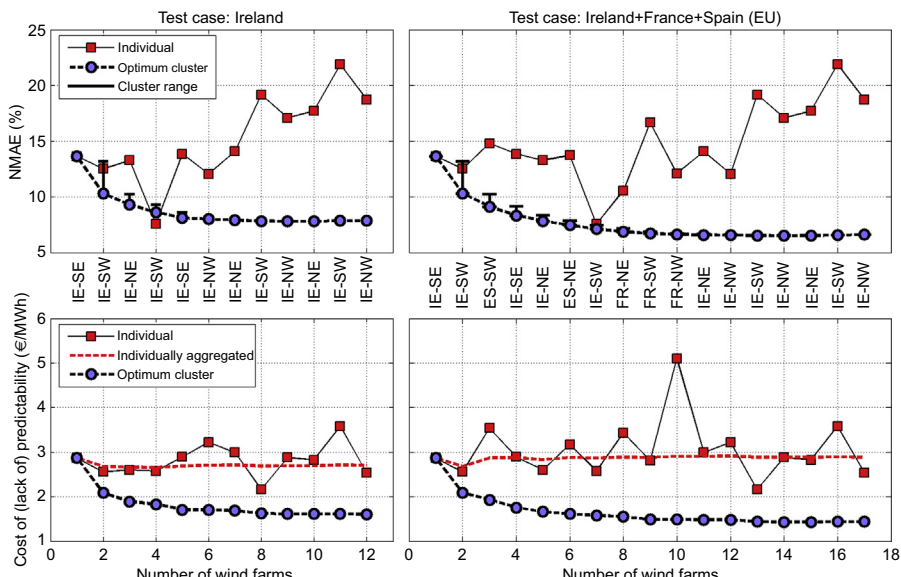


**Figure 14.7** Predictability in normalized mean absolute error (*NMAE*) (up) and cost of the lack of predictability (down) for the Irish (left) and EU test cases when participating in the market with individual wind farms and with optimum clusters. The geographical location of each newly aggregated wind farm to the cluster is provided between the upper and lower graphs (IE: Ireland, FR: France, ES: Spain).

It is not surprising that the wind farms with the largest errors are added at the end of the optimization process.

In the EU scenario, the operator includes two wind farms in Spain and three in France, extending the spatial coverage of his portfolio to a wider range of wind climates. The wind climates of the North and South of Europe are characterized by a mean synoptic weather activity of opposite sign, typically resulting in optimally uncorrelated winds. As a result, the cluster predictability can be further reduced to 6.5% (error reduction of 52%), obtained after aggregating the 14th wind farm. The economic impact of the portfolio effect results in penalties of 1.62 and 1.43 €/MWh for the Irish and EU cases, respectively, while if the individual wind farms participate in the market the penalties range from 2 to 5 €/MWh. It is worth noticing that the 10th wind farm added to the EU cluster has the maximum individual cost with a moderate predictability level. This is due to a particularly unfavorable combination of forecasting errors and balancing costs in this particular yearly integration. When this wind farm participates in the cluster, this high individual cost in fact produces a slightly positive economic impact.

In terms of the revenues obtained by the operator for year 2008, considering perfect prediction the total profit would be 13.9 and 19.3 M€ for the Irish and EU cases. The lack of predictability respectively results in 0.63 (4.53%) and 0.94 (4.86%) M€ losses if individual wind farms participate in the market and 0.37 (2.69%) and 0.47 (2.42%) M€ losses if participating with the optimized cluster. The savings introduced by the portfolio effect are therefore not negligible: 0.26 and 0.47 M€/year (if 2008 is considered a representative year). The wider the spreading of the wind farm distribution across Europe is, the better performance of the portfolio effect.

## 14.4 Conclusions

The EU project SAFEWIND builds on results from previous EU projects Anemos and Anemos.plus, altogether 10 years' worth of research and demonstration activities on wind power forecasting. An innovative aspect of the project looks into the consideration of forecasting during the planning phase of wind power, the wind resource assessment phase, and how early assessment of the economic and technological impact of wind power forecasting can contribute to better planning decisions.

Spatial planning instruments such as wind atlases are progressively integrating more spatiotemporal information to build decision-making scenarios that span the life cycle of wind energy projects. These decision-support systems can efficiently promote wind energy based on a comprehensive integration of end-user requirements, which considers sometimes conflicting aspects: technological, economic, environmental, and social. While the selection of the optimum wind energy locations shall be generally based on reducing the cost of energy, other criteria can be adopted depending on the relative influence of the different aspects at regional level. Nevertheless, regardless of the spatial planning strategy, decisions will be highly influenced by the meteorological fingerprint of wind energy.

Forecasting models are run on hindcast mode to produce predictability-related information that can be used to anticipate operational costs and produce a better assessment of the cost benefit of wind energy deployment. Several case studies have been presented to illustrate this approach considering different end-user perspectives.

Meteorological mesoscale models give us the opportunity to evaluate wind power predictability and other forecast skills. In addition to a large capacity factor, small wind variability is also desirable for wind power integration. Hence, forecast skill maps can provide useful information for spatial planning and to analyze the sources of forecast errors, either by topographical effects or meteorological phenomena.

From the developer's perspective, including predictability as a decision factor in the planning phase of a wind farm has a very low weight compared to the capacity factor, which is evidently the main feasibility driver. For the case of Denmark, only when wind farm aggregation is considered, predictability can become more important but only explains 0.15% of the total revenues variance. Nevertheless, predictability can be already assessed during the planning phase to provide an indicator of the quality of wind for grid integration purposes.

A pan-European electricity market offers great advantage for wind energy traders that can benefit from portfolio effects in larger domains. In the case study presented, moving from Ireland to a Western European domain that includes a few wind farms in France and Spain implies a decrease of around 10% in the aggregated prediction error and in the associated market penalties.

While the SAFEWIND project focused on analyzing the impact of short-term predictability on spatial planning, there are other relevant predictability aspects that should be considered during the investment phase of a wind farm. The uncertainty on the wind resource assessment is transformed to financial risk reducing significantly the project value. Beyond the epistemic uncertainty due to limitations of the model chain, there is always an aleatoric uncertainty due to the inherent variability of the wind resource. The aleatoric uncertainty cannot be reduced but needs to be quantified properly. Uncertainty on the future climate due to interannual variability and climate change is difficult to assess. Climate prediction models are used to assess the seasonal to decadal predictability to determine if a certain region will experience significant deviations with respect to the historic average wind resource ([Soret et al., 2015](#)).

## References

- Badger, J., Volker, P., Ott, S., Réthoré, P.-E., Hahmann, A., Hasager, C., Prospathopoulos, J., Sieros, C., June 2013. Wake modeling combining mesoscale and microscale models. In: International Conference on Aerodynamics of Offshore Wind Energy Systems and Wakes, ICOWES, Lyngby, Denmark.
- COSMO [Online]. 10. 04. 2011–11. 10. 2011. <http://www.cosmo-model.org/>.
- Dee, D.P., et al., 2011. The ERA-Interim reanalysis: configuration and performance of the data assimilation system. *Quarterly Journal of the Royal Meteorological Society* 137, 553–597.
- Dutra, R., Szklo, A., 2008. Assessing long-term incentive programs for implementing wind power in Brazil using GIS rule-based methods. *Renewable Energy* 33, 2507–2515.

- Dvorak, M.J., Archer, C.L., Jacobson, M.Z., 2010. California offshore wind energy potential. *Renewable Energy* 35, 1244–1254.
- EWEA, May 2009. Integrating Wind, Developing Europe's Power Market for the Large-Scale Integration of Wind Power. TradeWind Final Report, second ed. 102 pp.
- EWEA, July 2011. Pure Power, Wind Energy Targets for 2020 and 2030. European Wind Energy Association Report, 96 pp.
- Focken, U., Lange, M., Mönnich, K., Waldl, H.-P., Beyer, H.G., Luig, A., 2002. Short-term prediction of the aggregated power output of wind farms—a statistical analysis of the reduction of the prediction error by spatial smoothing effects. *Journal of Wind Engineering & Industrial Aerodynamics* 90, 231–246.
- Foley, A.M., Leahy, P.G., Marvuglia, A., McKeogh, E.J., 2012. Current methods and advances in forecasting of wind power generation. *Renewable Energy* 37, 1–8.
- Frías, L., Pascal, E., Irigoyen, U., Cantero, E., Loureiro, Y., Lozano, S., Fernandes, P.M., Martí, I., March 2009. Support Vector Machines in the wind energy framework. A new model for wind energy forecasting. In: Proceedings of EWEC-09, Marseille (France).
- Giebel, G., Brownsword, R., Kariniotakis, G., Denhard, M., Draxl, C., 2011. The state-of-the-art in short-term prediction of wind power. Deliverable D1.2 of the FP7-ANEMOS-plus project. In: A Literature Overview, second ed. 109 pp.
- Girard, R., Laquaine, K., Kariniotakis, G., 2013. Assessment of wind power predictability as a decision factor in the investment phase of wind farms. *Applied Energy* 101, 609–617.
- Hahmann, A.N., et al., March 2014. Validation and comparison of numerical wind atlas methods: the South African example. In: European Wind Energy Conference EWEA-2014, Barcelona, Spain.
- IRENA, June 2012. Renewable Energy Technologies: Cost Analysis Series. In: Volume 1: Power Sector. Issue 5/5 Wind Power. IRENA Working Paper.
- Irigoyen, U., Cantero, E., Correia, P., Frías, L., Loureiro, Y., Lozano, S., Pascal, E., Sanz Rodrigo, J., March 2011. Navarre virtual wind series: physical mesoscale downscaling wind WAsP. In: Methodology and Validation, Proceedings of EWEC-11, Brussels (Belgium).
- Jacobsen, V., Rubjerg, M., October 2005. Offshore Wind Farms—the Need for Metocean Data. Copenhagen Offshore Wind.
- Kalnay, E., Kanamitsu, M., Kistler, R., Collins, W., Deaven, D., Gandin, L., Iredell, M., Saha, S., White, G., Woollen, J., et al., 1996. The NCEP/NCAR 40-year reanalysis project. *Bulletin of the American Meteorological Society* 77, 437–471.
- Keane, A., Milligan, M., Dent, C., Hasche, B., D'Annunzio, C., Dragoon, K., Holttinen, H., Samaan, N., Soder, L., O'Malley, M., 2011. Capacity value of wind power. *IEEE Transactions on Power Systems* 26, 564–572.
- Landberg, L., 1999. Short-term prediction of the power production from wind farms. *Journal of Wind Engineering & Industrial Aerodynamics* 80, 207–220.
- Lange, M., Focken, U., 2005. Physical Approach to Short-term Wind Power Prediction, first ed. Springer. 220 pp.
- Lange, B., Rohrig, K., Ernst, B., Schlägl, F., Cali Ü, J.R., Moradi, J., February 2006. Wind power prediction in Germany—recent advances and future challenges. In: Proceedings of the European Wind Energy Conference and Exhibition, Athens (Greece).
- Madsen, H., et al., 2005. Standardizing the performance of short-term wind prediction models. *Wind Engineering* 29, 475–489.
- Martí, I., Usaola, J., et al., June 2003. Wind power prediction in complex terrain. LocalPred and Sipreólico. In: Proceedings of EWEC-03, Madrid, Spain.

- Mendes, J., Sumaili, J., Bessa, R., Keko, H., Miranda, V., Botterud, A., Zhou, Z., December 2013. Very Short-Term Wind Power Forecasting: State-of-the-Art. Report from Argonne National Laboratory, ANS/DIS-14/6.
- Pinson, P., Chevallier, C., Karioniotakis, G., 2007. Trading wind generation from short-term probabilistic forecasts of wind power. *IEEE Transactions on Power Systems* 22 (3), 1148–1156.
- Rogers, A.L., Rogers, J.W., Manwell, J.F., 2005. Comparison of the performance of four measure-correlate-predict algorithms. *Journal of Wind Engineering & Industrial Aerodynamics* 93, 243–264.
- Rombauts, Y., Delarue, E., D'haeseleer, E., 2011. Optimal portfolio-theory-based allocation of wind power: taking into account cross-border transmission-capacity constraints. *Renewable Energy* 36, 2374–2387.
- Scholz-Reiter, B., Lütjen, M., Heger, J., Schweizer, A., 2010. Planning and control of logistics for offshore wind farms. *Advances in Mathematical and Computational Methods* 242–247. ISSN:1792–6114.
- Sanz Rodrigo, J., Frías Paredes, L., Stoffels, N., von Bremen, L., February 2013. Wind power predictability assessment from large to local scale. In: European Wind Energy Conference EWEA-2013, Wien, Austria.
- Soret, A., Torralba, V., Davis, M., Doblas-Reyes, F., Gonzalez-Reviriego, N., 2–3 June 2015. Climate predictions for site selection: a new generation of risk management tools. In: EWEA Resource Assessment Workshop, Helsinki, Finland.
- Troen, I., Petersen, E.L., 1989. European Wind Atlas. Risø National Laboratory, Roskilde, Denmark, ISBN 87-550-1482-8, 656 pp.
- Vanvyve, E., Delle Monache, L., Rife, D., Monaghan, A., Pinto, J., 2015. Wind resource estimates with an analog ensemble approach. *Renewable Energy* 74, 761–773.
- Wang, X., Guo, P., Huang, X., 2011. A review of wind power forecasting models. *Energy Procedia* 12, 770–778.
- Wetterzentrale. 09. 03. 2012. [http://www.wetterzentrale.de/topkarten/tkn\\_av.html](http://www.wetterzentrale.de/topkarten/tkn_av.html).
- Wilks, D.S., 2011. Statistical Methods in the Atmospheric Sciences. In: International Geophysics Series, vol. 100. Oxford Academic Press.

# Index

*'Note:* Page numbers followed by “f” indicate figures, “t” indicate tables.’

## A

- ABL. *See* Atmospheric boundary layer (ABL)  
Abruzzo wind farm, 243  
Adaptive Network based Fuzzy Inference System models (ANFIS models), 67  
Adiabatic cooling, 5  
Aerosol  
    direct effect, 16–17  
    indirect effect, 18  
    optical properties, 164–167  
Aerosol optical depth (AOD), 162–163, 168f, 169t  
AESO. *See* Alberta Electric System Operator (AESO)  
AI techniques. *See* Artificial intelligence techniques (AI techniques)  
Air temperature, 325–326  
Alaiz test case, 238, 239f  
Alaiz wind farm, 237  
Alberta Electric System Operator (AESO), 84  
All Sky Infrared Visible Analyzer (ASIVA), 155  
All-sky camera, 153, 154f  
    short-term forecasting based on, 153  
    system, 170, 171f  
    types, 154–156  
All-Sky imager, 155  
All-sky imaging for cloud determination, 156  
Ampacity, 325, 330  
    estimation  
        from conductor clearance measurements, 329  
        from live conductor measurements, 328–329  
    from meteorological measurements, 328  
    variable, 326  
Analog ensemble technique (AnEn), 20  
Analog method. *See*  $k$ -nearest neighbors ( $k$ -NN)  
Analogs, 131–132, 186  
Analytical methods, 279–281  
Ancillary services market clearing  
    joint energy, 290–293, 297–302, 299f–301f  
    separated energy and, 287–290, 293–297, 294f–297f, 297t  
ANEMOS  
    benchmark, 236–241, 251–252, 251f  
    European project, 59  
    forecast evaluation, 237–241  
    framework, 236  
    projects and other major R&D activities, 92–94  
    setup and data description, 236–237  
AnEn. *See* Analog ensemble technique (AnEn)  
ANFIS models. *See* Adaptive Network based Fuzzy Inference System models (ANFIS models)  
ANNs. *See* Artificial neural networks (ANNs)  
AOD. *See* Aerosol optical depth (AOD)  
AR. *See* Autoregression (AR)  
AR process. *See* AutoRegressive process (AR process)  
ARIMA. *See* Autoregressive integrated moving average (ARIMA)  
ARIMAX. *See* Autoregressive integrated moving average models with exogenous variable (ARIMAX)  
ARMA models. *See* Autoregressive moving average models (ARMA models)

- Artificial intelligence techniques  
 (AI techniques), 122–132  
 ANNs, 123–130, 125t–126t  
 $k$ -NN, 130–132, 131f
- Artificial neural networks (ANNs), 61,  
 123–130, 186, 235  
 artificial neuron transfer functions,  
 125t–126t  
 multilayer perceptron, 129–130, 130f  
 simple perceptron, 127–129, 128f
- ASIVA. *See* All Sky Infrared Visible Analyzer (ASIVA)
- Atmosphere, 3
- Atmosphere-ocean model, 204
- Atmospheric  
 chaos, 7–8  
 motion, 3–5, 4f  
 phenomena, 222  
 turbulence, 37  
 variables, 13
- Atmospheric boundary layer (ABL), 35–36
- Attenuator, 210
- Autoregression (AR), 112–113
- Autoregressive integrated moving average (ARIMA), 67, 112–113, 120–122
- Autoregressive integrated moving average models with exogenous variable (ARIMAX), 122
- Autoregressive models, 115–116, 186
- Autoregressive moving average models (ARMA models), 64–65, 112–113, 317–318
- AutoRegressive process (AR process), 64
- Axons, 123–124
- B**
- Back propagation-learning (BPL), 129
- Balancing market mechanism, 262–263, 262f
- Band-pass filter, 225
- Benchmarking of renewable energy forecasts
- ANEMOS benchmark, 236–241  
 forecasting systems, 235  
 WIRE benchmark, 242–252
- Beta distribution, 319–320
- Bias, 124
- Bias normalized by installed wind power capacity (NBIAS), 348–349
- Big Data problem, weather forecasting as, 22
- Binomial distribution, 284–285
- Block-matching techniques, 188
- Bonneville Power Administration (BPA), 85
- Boundary layer depth detection from lidars, 46–49
- Box-Jenkins forecasting, 64, 67
- BPA. *See* Bonneville Power Administration (BPA)
- BPL. *See* Back propagation-learning (BPL)
- C**
- Calibration, 33
- Canadian Wind Energy Association, 59–60
- Capacity factor, 350
- Capacity outage probability table (COPT), 284–285
- Carrier-to-noise ratio detection (CNR detection), 33–36
- CAT-1 Transmission Line Monitoring System, 329
- CBH. *See* Cloud base height (CBH)
- CCD. *See* Charge-coupled device (CCD)
- CDFs. *See* Cumulative distribution functions (CDFs)
- Ceilometer, 173
- CENER’s LocalPred deterministic forecasting model, 348, 353
- Central limit theorem (CTL), 282
- Centro de Investigaciones Energéticas, Medioambientales y Tecnológicas (CIEMAT), 170
- CF. *See* Circle factor (CF)
- CFD. *See* Computational fluid dynamics (CFD)
- Charge-coupled device (CCD), 153–154
- CIEMAT. *See* Centro de Investigaciones Energéticas, Medioambientales y Tecnológicas (CIEMAT)
- CIGRE standard, 327
- Circle factor (CF), 159–160
- Clear-sky index-based persistence forecast, 187
- Clear-sky models (CSMs), 112
- Climatological use of Doppler wind lidar measurements, 35–37, 36f
- Closed-loop postprocessing, 191

- Cloud, 160–164, 162t–163t, 164f  
aerosol optical properties, 164–167  
cloud-index models, 181–182  
coverage, 156–159, 157f, 159f  
detection of raindrops, 159–160, 160f  
height estimation, 164, 165f  
whole-sky images, 158f
- Cloud base height (CBH), 160–161, 164, 173
- Cloud Imager, 154–155
- Cloud motion vectors (CMV), 172–173, 187  
forecasting approaches based on, 188–190, 189f
- Cloud physical properties algorithm (CPP algorithm), 181
- CMOS camera. *See* Complementary metal oxide semiconductor camera (CMOS camera)
- CMV. *See* Cloud motion vectors (CMV)
- CNR detection. *See* Carrier-to-noise ratio detection (CNR detection)
- Coherence, 228–229
- Coherent  
detection, 30, 32  
wind lidar, 32
- Cold air pool. *See* Cutoff lows
- Complementary metal oxide semiconductor camera (CMOS camera), 153–154
- Computational fluid dynamics (CFD), 61–62
- Concentrated solar power (CSP), 171–172
- Concentrated solar thermal electricity (CSTE), 182
- Concentrated-PV (CPV), 182
- Concentrating solar plants. *See* Solar thermal plants
- Conceptual frameworks  
joint energy and ancillary services market clearing, 290–293  
modeling assumptions, 283–286  
separated energy and ancillary services market clearing, 287–290
- Conductor clearance measurements, ampacity estimation from, 329
- Conductors, 325–326
- Continuous ranked probability score (CRPS), 246, 250f
- Conventional generation, unplanned outages of, 285–286
- Conventional producers, 261–262
- Converters, 210
- Cooperation in Science and Technology (COST), 236
- COPT. *See* Capacity outage probability table (COPT)
- Core temperature on sag of line, 326–327
- Coriolis force, 3–4
- Correlation between wind fluctuations at spatially distributed sites, 228–229
- COSMO-EU model, 344
- Cospectrum, 229
- COST. *See* Cooperation in Science and Technology (COST)
- Coupled  
atmosphere-hydrology models, 12  
models, 12
- CPP algorithm. *See* Cloud physical properties algorithm (CPP algorithm)
- CPV. *See* Concentrated-PV (CPV)
- Critical span, selection of, 327–328
- Critical success index (CSI), 84
- CRPS. *See* Continuous ranked probability score (CRPS)
- CSMs. *See* Clear-sky models (CSMs)
- CSP. *See* Concentrated solar power (CSP)
- CSTE. *See* Concentrated solar thermal electricity (CSTE)
- CTL. *See* Central limit theorem (CTL)
- Cumulative distribution functions (CDFs), 246
- Cumulus parameterizations, 14
- Cup anemometers, 33, 35
- Cutoff lows, 344
- D**
- DA. *See* Day-ahead (DA)
- Data assimilation (DA), 7, 10–11  
EnKF, 11  
hybrid approaches, 11  
nudging, 10  
variational assimilation techniques, 10–11
- Data preprocessing, 144–145
- Day-ahead (DA), 284  
market, 290–291  
market mechanism, 261  
wind power, 298

- DC. *See* Demand curve (DC)
- Decision-making, 259, 290  
predictability in, 349–352
- Demand curve (DC), 300–302
- Dendrites, 123–124
- Department of Energy (DOE), 93
- Deterministic rules, 280, 294, 296
- Deutsches Zentrum für Luft-und Raumfahrt (DLR), 170
- Deviation costs, 311–312
- DHI. *See* Diffuse horizontal irradiance (DHI)
- DICast forecast, 21f
- Diebold-Mariano test (DM test), 246
- Diffuse component (DIF component), 16
- Diffuse horizontal irradiance (DHI), 182
- Direct clear-sky index, 173
- Direct normal irradiance (DNI), 16, 112, 171, 182
- Direct Normal Irradiance Nowcasting (DNICast), 153, 170  
solar resource and forecasting  
methodology, 170–176, 172f
- DLR. *See* Deutsches Zentrum für Luft-und Raumfahrt (DLR); Dynamic line rating (DLR)
- DM test. *See* Diebold-Mariano test (DM test)
- DNI. *See* Direct normal irradiance (DNI)
- DNICast. *See* Direct Normal Irradiance Nowcasting (DNICast)
- DOE. *See* Department of Energy (DOE)
- Doppler lidar, 44, 49  
probes, 43–44  
system, 30–31
- Doppler spectra, 51
- Doppler wind lidar measurements, 35–37, 36f  
numerical turbulence reconstruction  
method from, 39–40  
turbulent properties from vertically pointing  
Doppler lidar, 40–44, 43f
- Doppler-shifted  
backscattered radiation, 30  
frequency, 30
- Downregulation price, 269
- Downscaling procedure, 61–62
- DR. *See* Dynamic reserve (DR)
- Dual-Doppler lidars, 49
- Dual-price imbalance system, 263
- Dynamic  
solver, 13  
thermal model, 327
- Dynamic line rating (DLR), 326, 331f  
benefits of DLR forecasting, 334–336  
calculations, 326–328  
devices, 328–329  
forecasts, 329–334  
sag and clearance distance for overhead  
line, 325f
- Dynamic reserve (DR), 300–302
- E**
- Earth-system model, 204
- Eastern Wind Integration and Transmission Study (EWITS), 298
- ECMWF. *See* European Centre for Medium-Range Weather Forecast (ECMWF)
- ECMWF Ensemble Prediction System (EPS), 91
- Electricity market(s), 259–260, 281, 287  
context, 260–263  
balancing market mechanism, 262–263  
day-ahead market mechanism, 261  
intraday adjustment and continuous  
trading, 261–262  
markets and their timeline, 260–261  
coupling of, 334–335
- Electricity Reliability Council Of Texas (ERCOT), 84, 280
- Empirical methods, 181
- Empirical orthogonal functions (EOFs), 227
- EMV. *See* Expected monetary value (EMV)
- Energy  
balance equation, 203  
joint, 290–291, 297–302  
methodology for developing ORDC, 291–293
- production, 259
- separated, 287, 293–297  
decision-making strategy, 290  
methodology to estimating SGM, 287–289
- Energy reserve (RE), 312–313
- EnKF. *See* Ensemble Kalman filter (EnKF)
- Ensemble Kalman filter (EnKF), 11
- Ensemble modeling, 19–20

- EOFs. *See* Empirical orthogonal functions (EOFs)
- EOL. *See* Expected opportunity loss (EOL)
- EOT. *See* Equation of time (EOT)
- EPS. *See* ECMWF Ensemble Prediction System (EPS)
- Equation of time (EOT), 16
- ERCOT. *See* Electricity Reliability Council Of Texas (ERCOT)
- EU project SAFEWIND, 342
- European Centre for Medium-Range Weather Forecast (ECMWF), 135–144, 204, 205f–206f, 244
- European Wind Energy Association (EWEA), 341
- eWind, 77
- EWITS. *See* Eastern Wind Integration and Transmission Study (EWITS)
- eXclusive-OR (XOR), 129, 129t
- Exemplification, test case, 273–277
- experimental setup, 273–276, 276f
  - trading results and value of forecasts, 276–277, 276f, 277t
- Exogenous data, 135–144
- Expected monetary value (EMV), 267–268, 270
- Expected opportunity loss (EOL), 270
- Extrinsic calibration, 169
- F**
- Fabry-Pérot etalon, 32
- Fast Fourier transform algorithm (FFT algorithm), 285–286
- FDDA nudging schemes. *See* Four-dimensional data assimilation nudging schemes (FDDA nudging schemes)
- FFT algorithm. *See* Fast Fourier transform algorithm (FFT algorithm)
- Field of view (FoV), 154–155
- “Firing” of neuron, 123–124
- Fixed reserve (FR), 300–302
- Flexi-ramp, 281
- Forced outage rate (FOR), 280, 284–285
- Forces rising motion, 5
- Forecast(s)/forecasting, 204, 259
- assessment, 146
  - based on spatial and temporal information, 187–191
- based only on temporal information, 186–191
- DLR, 331–336
- error(s), 248
- maps, 344
- evaluation, 237–241, 246–250, 247f, 249f
- increasing forecasting spatial coverage, 145
- independency of forecast errors, 283–284
- integration of uncertainty forecasts in operating reserve estimation, 282–283
- intrahourly variability of wind generation, 219–233
- market revenue to forecast value, 263–265
- quality, 259–260
- systems, 235
- timescales, 60–61
- trading results and value of forecasts, 276–277, 276f, 277t
- waves, 199
- wind power variability, 225–228
- of wind variability, 229
- Forward contracts, 260–261
- Four-dimensional data assimilation nudging schemes (FDDA nudging schemes), 10
- Four-dimensional variational DA schemes (4D-Var schemes), 10–11
- FoV. *See* Field of view (FoV)
- FR. *See* Fixed reserve (FR)
- G**
- GAs. *See* Genetic algorithms (GAs)
- Gaussian distribution, 282, 286
- GCMs. *See* Global Circulation Models (GCMs)
- GEFCom. *See* Global Energy Forecasting Competition (GEFCom)
- Generalized linear models (GLMs), 247–248
- Generalized multidimensional state estimate methodology, 75
- Generic storage devices, 313–314
- Genetic algorithms (GAs), 123
- Genetic programming, 207
- Geographical information system (GIS), 341–342
- Geometrical calibration of all-sky cameras, 167–169

- Geostationary meteorological satellites, 179  
*GFS. See Global forecast system (GFS)*  
*GH Forecaster*, 77  
*GHI. See Global horizontal irradiance (GHI)*  
*GIS. See Geographical information system (GIS)*  
*GLMs. See Generalized linear models (GLMs)*  
 Global Circulation Models (GCMs), 342–343  
 Global Energy Forecasting Competition (GEFCom), 236  
 Global forecast system (GFS), 203, 348  
 Global horizontal irradiance (GHI), 16, 132, 171, 182, 235  
 Global positioning system tracking, 9  
 Global tilted irradiance (GTI), 182  
 Golagh test case, 241, 241f  
 Golagh wind farm, 237  
 Gravity waves, 222, 227  
 Grid spacing, 15  
 Ground-based remote sensing instruments, 47–48  
*GTI. See Global tilted irradiance (GTI)*
- H**  
 Hadley circulation, 3–4  
*HDR-ASIS. See High-dynamic-range all-sky imaging system (HDR-ASIS)*  
 Heave buoy array design, 208–210  
 Heliosat methods, 181  
 Heliosat-4 method, 181  
 Heterodyne wind lidar, measuring principles for, 31–32, 31f  
*High resOlution Numerical wind EnergY Model for On-and Offshore forecasting (HONEYMOON)*, 91  
 High-dynamic-range all-sky imaging system (HDR-ASIS), 155  
 High-resolution model run, 251–252  
*HIRlam Power prediction Model (HIRPOM)*, 71  
*HONEYMOON. See High resOlution Numerical wind EnergY Model for On-and Offshore forecasting (HONEYMOON)*  
 Hour-scale wind variability  
   meteorological causes of, 222–224  
   observing, 224–225
- Hue saturation intensity (HSI), 156–157  
 Hybrid approaches, 11  
 Hybrid system (HS), 118, 132–135, 134f  
 Hydro-pumped storage for optimal participation in market, 313–318
- I**  
*ICI system*, 154–155  
*iEnKF. See Inverted Kalman Filter technique (iEnKF)*  
 Image processing techniques  
   cloud properties, 156–167  
*IMM. See Informatics and Mathematical Modeling (IMM)*  
 In situ pyranometric measurements, 186, 191  
 In-phase/quadrature-phase detection scheme (IQ scheme), 32  
 Independent system operators (ISOs), 111, 260  
 Informatics and Mathematical Modeling (IMM), 76  
 Inter Tropical Convergence Zone, 3–4  
 Inter-Quantile Range (IQR), 88  
 Intraday  
   adjustment, 261–262  
   market, 261–262  
 Intrahourly wind variability, 222  
 Intrinsic calibration, 167  
 Inverse FFT algorithm, 286  
 Inverted Kalman Filter technique (iEnKF), 75  
 Investment phase of wind farms  
   mean absolute error of wind power forecast, 345f  
   mean daily forecasting errors, 349t  
   model chain for wind resource, 342–343  
   predictability assessment, 342–343  
   TSO, 341  
   value of predictability in spatial planning, 343–354  
   wind power forecasting, 341, 348f  
*IQ scheme. See In-phase/quadrature-phase detection scheme (IQ scheme)*  
*IQR. See Inter-Quantile Range (IQR)*  
 Isolated grids, 310  
 ISOs. *See Independent system operators (ISOs)*

**J**

Joule effect, 325

**K**

$k$ -nearest neighbors ( $k$ -NN), 130–132, 131f, 160–161, 186

Kalman Filter (KF), 11, 64  
ensemble, 74–75  
technique, 191, 192f

Kendall rank correlation coefficient, 284

Klim test case, 240, 240f

Klim wind farm, 237

Kolmogorov hypothesis, 41–42

Koninklijk Nederlands Meteorologisch Instituut (KNMI), 181

**L**

Land surface models (LSMs), 14

Large-scale wind power predictability mapping, 344–347

Laser-based techniques, 31

LAWEPS. *See* Local Area Wind Energy Prediction System (LAWEPS)

Lead time, 284–285

Least-squares support vector machine (LS-SVM), 235

Light detection and ranging (lidars), 30  
boundary layer depth detection from, 46–49

lidar-based remote sensing devices, 30  
for meteorological applications, 30  
systems, 31  
wind gusts from, 44–46

Line-of-sight (LOS), 30

Linear filter, 114

Linear nonstationary models, 120–122  
ARIMAX, 122

autoregressive integrated moving average models, 120–122

Linear stationary models, 115–119, 120t  
autoregressive models, 115–116  
mixed autoregressive moving average models, 117–119, 118f

moving average models, 116

Live conductor measurements, ampacity estimation from, 328–329

Load uncertainty, 286

Local Area Wind Energy Prediction System (LAWEPS), 72

Local Circulation Assessment and

Prediction System model (LOCALS model), 72

Local quantile regression (LQR), 88

Local-scale wind farm predictability, 347–349

LocalPred, 348

LOCALS model. *See* Local Circulation Assessment and Prediction System model (LOCALS model)

Logic Theorist, 122–123

LOLE. *See* Loss of load expectation (LOLE)

LOLP. *See* Loss of load probability (LOLP)

Long-range WindScanner master computer software (LRMCS), 51

Long-range WindScanner system (LRWS system), 49–51, 50f

Longwave radiation, 13–14

Longwave radiative transfer, 13–14

Lorentzian function, 38

LOS. *See* Line-of-sight (LOS)

Loss of load expectation (LOLE), 288–289, 336

Loss of load probability (LOLP), 288–289, 292

Low level jets, 224

Low-pass filtered detector signal, 32

LQR. *See* Local quantile regression (LQR)

LRMCS. *See* Long-range WindScanner master computer software (LRMCS)

LRWS system. *See* Long-range WindScanner system (LRWS system)

LS-SVM. *See* Least-squares support vector machine (LS-SVM)

LSMs. *See* Land surface models (LSMs)

Lucas–Kanade method, 188

**M**

MA. *See* Moving averages (MA)

MACC. *See* Monitoring Atmosphere

Composition and Climate (MACC)

Machine learning algorithms, 131

MAE. *See* Mean absolute error (MAE)

MAE/NP values, 252, 252f

Many ADALINEs (MADALINE), 129

Markets

prices, 268

revenue to forecast value, 263–265

- Markets (Continued)**
- assumptions, 263–264
  - formulation of market revenues, 264
  - linkage to forecast value, 264–265
  - and timeline, 260–261
- Markovian approach, 225
- Mathematical framework, 329–331
- Maximal core temperature, 325
- McClellan models, 176
- MCSs. *See* Monte Carlo simulations (MCSs)
- Mean absolute error (MAE), 81, 237, 246, 344
- Mean wave period, 199–200, 200f–201f
- Measurement methodologies for wind energy
- boundary layer depth detection from lidars, 46–49
  - climatological use of Doppler wind lidar measurements, 35–37
  - coherent fiber-based scanning wind lidars, 31
  - lidars for meteorological applications, 30
  - LRWS system and short-range
    - WindScanner systems, 49–52
    - measuring principles for heterodyne wind lidar, 31–32
    - turbulence estimation from wind lidar measurements, 37–46
    - wind lidar calibration, 33–35
    - wind measurement using classical cup anemometry, 29f
- Mechanical axial tension, 326
- Medium-term forecast examples, DLR, 333–334
- Medium/long-term markets, 260–261
- Mesoscale modeling, improvements in, 69–74
- Mesoscale networks, 8–9
- Meteorological Aerodrome Report (METAR), 8–9
- Meteorological geostationary, satellite SSI retrieval from, 181–186
- Meteorological masts, 29
- Meteorological measurements, ampacity estimation from, 328
- Meteorology for renewable energy forecasting, 3–8
- atmospheric chaos, 7–8
  - atmospheric motion, 3–5, 4f
  - prediction across scales, 5–7, 6f
- Meteosat Second Generation Cloud Physical Properties (MSGCPP), 181
- Metrology, 33
- Microphysics parameterizations, 14
- Microscale models, 342–343
- MINES ParisTech/ARMINES, 76–77
- Mixed autoregressive moving average models, 117–118, 118f
- with exogenous variables, 119
- MLPs. *See* Multilayer perceptrons (MLPs)
- Mobotix Q24 cameras, 170
- Model chain, 61–63
- Model output statistics (MOS), 18, 61, 186, 343
- Monin-Obukhov similarity theory, 14
- Monitoring Atmosphere Composition and Climate (MACC), 181
- Monte Carlo techniques, 37, 39, 280, 311–312
- Monte Carlo simulations (MCSs), 320, 331, 332f
- MOS. *See* Model output statistics (MOS)
- Moving averages (MA), 112–113, 116
- MSEPS. *See* Multi-Scheme Ensemble Prediction System (MSEPS)
- MSGCPP. *See* Meteosat Second Generation Cloud Physical Properties (MSGCPP)
- Multi-purpose Socorridos system, 318
- Multi-Scheme Ensemble Prediction System (MSEPS), 71, 75
- Multilayer perceptrons (MLPs), 123, 129–130, 130f
- N**
- N-1 rule, 280
- NAM model. *See* North American Mesoscale model (NAM model)
- National Digital Forecast Database (NDFD), 135–144
- National Oceanic and Atmospheric Administration (NOAA), 93
- National Renewable Energy Laboratory (NREL), 181, 210
- National Solar Radiation Database (NSRDB), 181
- Navier–Stokes equations, 4–5, 22

- NBIAS. *See* Bias normalized by installed wind power capacity (NBIAS)
- NDFD. *See* National Digital Forecast Database (NDFD)
- Near IR (NIR), 155
- Negotiation mechanism, 261–262
- Net wind power output. *See* Specified turbine power-curve model
- Network
- neural, 68, 206–207
  - reinforcements delay to increasing generation and demand, 336
  - stability, 325
- Neurons, 123–124
- Newtonian relaxation, 10
- NIR. *See* Near IR (NIR)
- NMAE. *See* Normalized mean absolute error (NMAE)
- NOAA. *See* National Oceanic and Atmospheric Administration (NOAA)
- Nonlinear variability, 202
- Nonlinear wave–wave interactions, 202–203
- Nonparametric probabilistic forecast, 282–283
- Normalized mean absolute error (NMAE), 237, 242f, 348–349
- Normalized root mean square error (NRMSE), 348–349
- North American Mesoscale model (NAM model), 79–80, 135–144
- NREL. *See* National Renewable Energy Laboratory (NREL)
- NRMSE. *See* Normalized root mean square error (NRMSE)
- NSRDB. *See* National Solar Radiation Database (NSRDB)
- Nudging, 10
- Numerical turbulence reconstruction method, 39–40, 40f
- Numerical weather prediction model (NWP model), 4–5, 59–61, 112, 179, 227, 235, 342–343
- configuration for specific applications, 15–16
  - coupled models, 12
  - DA, 10–11
  - fundamentals, 12–13
- improvements in, 69–74
- model development, 16–18
- observational data, 8–10, 9f
- short-term prediction models with, 75–80
- standard physics available in, 13–14
- NWP model. *See* Numerical weather prediction model (NWP model)
- O**
- Objective function, 311
- Observing Systems Capability Analysis and Review (OSCAR), 179
- OcamCalib toolbox, 167–169
- Off-line power forecasts, 237
- Offering strategy, 264–265
- formulation, 265–273
  - benchmark offering strategies, 265–267, 266f–267f, 267t–268t
  - trading strategies in single-price imbalance system, 267–269, 272f, 274f–275f
- Open cellular convection, 222, 223f
- Operating reserve
- estimation, 282–283
  - strategy, 300–302
- Operating reserve demand curve (ORDC), 280, 290
- development, 298, 299f
  - joint ORDC approach, 303
  - methodology for developing, 291–293, 292f
- Operational time domain, 280
- Optical flow techniques, 188
- Optimal combination of forecasts, 78
- Optimization of clustering process, 353
- Optimized solar forecasting, mathematical methods for
- AI techniques, 122–132
  - hybrid systems, 132–135, 134f
  - regression methods, 112–122
  - state of art in solar forecasting, 135–146
- ORDC. *See* Operating reserve demand curve (ORDC)
- ORR. *See* Outage replacement rate (ORR)
- OSCAR. *See* Observing Systems Capability Analysis and Review (OSCAR)
- Outage replacement rate (ORR), 284–286

**P**

- Parameterizations, 13
- PBL. *See* Planetary boundary layer (PBL)
- pdf. *See* Probability density function (pdf)
- Pearson correlation, 190
- Pelamis P2 device, 208, 209t
- Perceptron learning rule, 127–128, 128t
- Perfect forecast (PF), 300–302
- Phase spectra, 228–229
- Photovoltaics (PV), 136t–143t
- energy, 182, 235
  - installations, 184
  - plants, 243, 243f
  - production monitoring systems, 179
  - simulation models, 193
- Physical
- approach, 59–60
  - solar model, 181
- Physics-based models, 199, 202–208
- PJM transmission organization, 280
- Plane-of-array irradiance (POAI), 182
- Planetary boundary layer (PBL), 14
- Plataforma Solar de Almeria (PSA), 153, 170
- pmf*. *See* Probability mass function (*pmf*)
- POAI. *See* Plane-of-array irradiance (POAI)
- Poisson distribution, 286
- Pooling wind farms, 345–347
- “Popcorn” cumulus clouds, 5
- Portfolio effect in wind energy trading, 352–354
- Postprocessing
- method, 18–19
  - of satellite-based forecasts, 191, 192f
- POW’WOW. *See* Prediction of Waves, Wakes and Offshore Wind (POW’WOW)
- Power
- fluctuations, 219, 221
  - spectrum, 225
  - traders, 59
- Power system, 260, 279
- conceptual frameworks, 283–293
  - existing methodologies, 279–281
  - integration of uncertainty forecasts in operating reserve estimation, 282–283
  - joint energy and ancillary services market clearing, 297–302
- qualitative analysis of methodologies, 303
- separated energy and ancillary services market clearing, 293–297
- SGM, 281
- Preceptron
- multilayer, 129–130, 130f
  - simple, 127–129, 128f
- Precipitable water (PW), 165–166
- Predictability, 353f
- assessment, 342–343
  - in decision-making process of wind energy developer, 349–352
  - value in spatial planning, 343–354
- Prediction of Waves, Wakes and Offshore Wind (POW’WOW), 92
- Prediction risk index, 92
- Prediktor, 63, 75–76, 236
- Probabilistic
- forecasts/forecasting, 19–20, 19f, 21f, 145, 248–249, 259–260
  - methods, 280–281
- Probability density function (pdf), 19–20, 248–249, 263, 270, 282, 317–318, 331
- Probability mass function (*pmf*), 282–283, 288
- PSA. *See* Plataforma Solar de Almeria (PSA)
- Pulsed wind lidar, 35–36
- Pumped energy storage, 316
- Pumped storage
- capacity, 318
  - facilities, 318–319
  - plant, 310, 316
- Pumping station, 314
- PV. *See* Photovoltaics (PV)
- PW. *See* Precipitable water (PW)

**Q**

- Quadrature spectrum, 229
- Qualitative analysis of methodologies, 303

**R**

- RAC. *See* Reliability Assessment Commitment (RAC)
- Radiance images, 179
- Radiation parameterizations, 13–14
- Radiosonde-based methods, 47–48
- Raindrops detection, 159–160, 160f

- Ramp forecasts/forecasting, 83–86, 85f, 145
- RAMS model. *See* Regional atmospheric modeling system model (RAMS model)
- Ranked Probability Skill Score (RPSS), 84
- Rapid Update Cycle model (RUC model), 84
- Rawinsondes, 9
- RE. *See* Energy reserve (RE)
- Real-time (RT), 280, 290–291
- Recursive least squares algorithm (RLS algorithm), 78
- Red-Green-Blue (RGB), 156
- Redispatching, reduction of, 335
- Regime-switching models, 225
- Regional atmospheric modeling system model (RAMS model), 244
- Regression methods, 112–122, 114f  
linear nonstationary models, 120–122  
linear stationary models, 115–119
- Reliability Assessment Commitment (RAC), 290–291
- Reliability issues, mitigation of, 336
- Renewable energy, 282–283  
plants, 261  
producers, 259–260
- Renewable energy forecasting, 242. *See also* Short-term solar power forecasting; Wave energy forecasting  
benchmarking of  
ANEMOS benchmark, 236–241  
forecasting systems, 235  
WIRE benchmark, 242–252  
configuring NWP to problem, 12–18  
meteorology for, 3–8  
observational data and assimilation into NWP models, 8–12  
planning for validation, 20–22  
postprocessing method, 18–19  
probabilistic forecasting, 19–20  
weather forecasting as big data problem, 22
- Renewable energy sources (RES), 259, 279
- Renewable generation, 309–310
- Renewable resources, 3, 311–312
- RES. *See* Renewable energy sources (RES)
- Reserve scheduling method, 280–281
- RGB. *See* Red-Green-Blue (RGB)
- Risk index, 283
- Risk-based strategy, 281
- RIX index. *See* Ruggedness Index (RIX index)
- RLS algorithm. *See* Recursive least squares algorithm (RLS algorithm)
- RMSE. *See* Root mean square error (RMSE)
- Robust reserve setting tool (RRS tool), 287, 288f, 294
- Root mean square error (RMSE), 72, 184, 204, 344–345, 346f
- Rossby waves, 5
- RPSS. *See* Ranked Probability Skill Score (RPSS)
- RRS tool. *See* Robust reserve setting tool (RRS tool)
- RT. *See* Real-time (RT)
- RUC model. *See* Rapid Update Cycle model (RUC model)
- Ruggedness Index (RIX index), 237
- S**
- S input by wind ( $S_{IN}$ ), 203
- Sag of line, core temperature on, 326–327
- Sandia National Laboratory, 210
- Satellite images of reflectance, 182
- Satellite-based forecasting, 179. *See also* Renewable energy forecasting  
different approaches  
forecast based on spatial and temporal information, 187–191  
forecast based only on temporal information, 186–187  
postprocessing of, 191, 192f
- Satellite-derived SSI, 179
- Sea breeze circulation, 223–224
- Semiempirical methods, 181
- Semiparametric regression, 282–283
- Separated approach, 303
- SERG. *See* Sustainable Energy Research Group (SERG)
- SGM. *See* System generation margin (SGM)
- Shoaling-induced breaking ( $S_{BR}$ ), 203
- Short-range WindScanner system, 49, 50f, 51–52
- Short-term forecasting based on all-sky cameras, 153. *See also* Dynamic line rating (DLR)  
geometrical calibration of all-sky cameras, 167–169

- Short-term forecasting based on all-sky cameras (*Continued*)  
 image processing techniques, 156–167  
 map of short-term forecasted direct normal irradiance, 175f  
 sky camera systems, 153–156  
 solar resource and forecasting methodology, 170–176, 172f
- Short-term markets, 261
- Short-term prediction models with NWPs, 75–80  
 approach to Prediktor, 76  
 DNV GL’s short-term energy forecasting service, 77  
 modeling wind speed *vs.* wind power, 78–80  
 models using NWP data, 75  
 optimal combination of forecasts, 78
- Short-term solar power forecasting. *See also*  
 Renewable energy forecasting  
 different approaches for satellite-based forecasting, 186–191  
 postprocessing of satellite-based forecasts, 191  
 spatial and time scales of Earth observation systems, 180f  
 SSI retrieval from meteorological geostationary satellite, 181–186  
 view of geostationary meteorological satellites, 180f
- Shortwave radiative, 13–14
- Signal filtering, 37–39
- Signal-to-noise ratio (SNR), 35–36
- Simple perceptron, 127–129, 128f
- Simulating wave farms, 213
- Simulating Waves Near shore (SWAN), 204
- Simulation methods, 280
- $S_{IN}$ . *See* S input by wind ( $S_{IN}$ )
- Single scattering albedo (SSA), 165–166
- Single wind farm forecasts, 345–347
- Single-price imbalance system, 262  
 trading strategies in single-price imbalance system, 267–269, 272f, 274f–275f
- Sky camera systems, 153–156  
 all-sky camera types, 154–156
- Small Unmanned Meteorological Observer (SUMO), 74
- Smoothing factor, 345–347, 346f
- SNR. *See* Signal-to-noise ratio (SNR)
- Social welfare, 291
- Soil properties, 14
- Solar forecasting, 111, 179, 180f, 188  
 data preprocessing, 144–145  
 exogenous data, 135–144  
 forecast assessment, 146  
 forecasting solar irradiance and PV power generation, 136t–143t  
 increasing forecasting spatial coverage, 145  
 probabilistic forecasts, 145  
 ramp forecasts, 145  
 state of art in, 135–146
- Solar plants, 318
- Solar power(s), 309  
 forecasts/forecasting, 184, 235  
 from SSI to, 182–184
- Solar radiation, 5, 325
- Solar resource, 3  
 and forecasting, 153, 170–176, 172f
- Solar thermal generation, 317  
 plants, 317
- Solar-forced circulation, 3–4
- Soleksat forecast, 188
- Solmirus All Sky Infrared Visible Analyzer, 155
- SOs. *See* System operators (SOs)
- Sotavento test case, 238, 239f
- Sotavento wind farm, 237
- Space-filling observation method, 39
- Spatial discretization, 15
- Spatial information, forecast based on, 187–191
- Spatial planning aspects, 341–342  
 value of predictability in, 343–354
- Spatially distributed sites, correlation between wind fluctuations at, 228–229
- Spatio-temporal characteristics of wind predictability, 343  
 forecasting, 82–83  
 approaches based on statistical modeling of spatiotemporal variability, 190–191
- Specified turbine power-curve model, 342
- Spectral methods, 13
- SR. *See* Static rating (SR)
- SSA. *See* Single scattering albedo (SSA)

- SSI. *See* Surface solar irradiance (SSI)
- Standard measure of wave power, 199–200
- Standard probabilistic framework, 303
- State-of-the-art wind-power predictions system, 236
- Static rating (SR), 325–326
- Statistical learning methods, 7
- Statistical modeling of spatiotemporal variability, 190–191
- Statistical models, 206–207
- Statistical power curve modeling, 80
- Statistical regression model, 18
- Statistical time series models, 187
- Statistics model, 207–208
- Stochastic Lagrangian model, 39
- Storage
- device, 310, 313, 315, 320
  - plants, 310
- Storage management, forecasting for cooperation of renewable producers and storage facilities, 318–319
- coordinating renewable producers and hydro-pumped storage, 313–318
- mathematical formulations, 310–313
- reliability studies, 320
- renewable generation, 309–310
- storage sizing, 319–320
- Subgrid gap, 342–343
- SUMO. *See* Small Unmanned Meteorological Observer (SUMO)
- Surface solar irradiance (SSI), 179
- retrieval from meteorological geostationary satellite, 183f
  - approaches, 181–182
  - characteristics of SSI retrieval from satellite, 184, 185t
  - local combination with in situ pyranometric measurements, 186
  - from SSI to solar power, 182–184
- Sustainable Energy Research Group (SERG), 77
- SWAN. *See* Simulating Waves Near shore (SWAN)
- Swc. *See* White capping (Swc)
- System generation margin (SGM), 281
- methodology to estimating, 287–289, 288f–289f
- System operation analysis, 300–302, 300f–301f
- System operators (SOs), 280
- T**
- Thermal plants, 261
- Thermal–tensional equilibrium, 326
- Three-dimensional variational DA schemes (3D-Var schemes), 10–11
- Three-dimensional wind field (3D wind field), 29, 30f
- 3D wind velocity, 30
- Time series models
- continuous, 261–262
  - results and value of forecasts, 276–277, 276f, 277t
  - strategies in single-price imbalance system, 267–269, 272f, 274f–275f
- Time series models, 64–68, 206–207
- improvements, 68
  - for very–short-term forecasting, 64–68
- TIs. *See* Turbulent intensities (TIs)
- TKE. *See* Turbulent kinetic energy level (TKE)
- Transfer function, 124–127, 125t–126t
- Transmission system operators (TSOs), 59, 260, 280, 341
- Truncated Taylor series, 13
- TSOs. *See* Transmission system operators (TSOs)
- Tunø, offshore wind farm, 237
- Tunø Knob (offshore) test case, 240–241, 240f
- Turbine control, 60
- Turbulence estimation from wind lidar
- measurements, 37–46
  - numerical turbulence reconstruction method, 39–40
  - signal filtering and consequence for turbulence estimation, 37–39
  - turbulent properties from vertically pointing doppler lidar, 40–44
  - wind gusts from lidar, 44–46
- Turbulent intensities (TIs), 40
- Turbulent kinetic energy level (TKE), 39
- U**
- UCTE/ENTSO-E categories, 287
- Uncertainty
- integration of uncertainty forecasts in operating reserve estimation, 282–283
  - load, 286
  - of renewable sources, 279–281

- Union for the Co-ordination of Transmission of Electricity (UCTE), 280
- Unit commitment (UC), 281, 291
- University California San Diego (UCSD), 155
- Upregulation price, 269
- Upscaling models, 80–82, 352
- V**
- Value of loss load (VOLL), 292
- Variability
- forecasting, 85–86
  - index, 189
  - test, 190
- Variational assimilation techniques, 10–11
- Vestas V164 turbine, 29
- VIS/IR Whole Sky Imager, 155
- W**
- Warmer tropical atmosphere, 3–4
- Wave
- energy, 199
  - flux, 199–200, 201f–202f
  - farms, 205–206
  - forecasting, 199
  - height, 202
- Wave energy converters (WEC), 208–210
- power output from heave buoy array, 211f–212f
  - power output from Pelamis, 211f–212f
  - power output from three-body oscillating flap device, 211f–212f
- Wave energy forecasting. *See also* Renewable energy forecasting
- characteristics of data, 199–202
  - mean wave period, 200f–201f
  - significant wave height, 200f–201f
  - wave energy flux, 201f–202f
- physics models, 202–206
- physics *vs.* statistics, 207–208
- simulating wave farms, 213
- statistical and time series models, 206–207
- WEC, 208–210
- WAVEWATCH III model (WW3 model), 203
- WCS. *See* WindScanner Client Software (WCS)
- Weather and wind Energy PROGnosis (WEPROG), 77
- Weather forecasts, 333
- Weather Intelligence for Renewable Energies (WIRE), 236
- benchmark
- ANEMOS benchmark and high-resolution model run, 251–252
  - forecast evaluation, 246–250
  - modeling approaches, 244, 245t
  - setup and data description, 242–244, 244t
- WIRE ES1002, 93
- Weather Research and Forecasting model (WRF model), 16, 135–144, 227
- WRF-solar model, 16–18, 17f
- WEC. *See* Wave energy converters (WEC)
- WEFRUC. *See* Wind Energy Forecast Rapid Update Cycle (WEFRUC)
- Weibull distribution, 332
- WEPROG. *See* Weather and wind Energy PROGnosis (WEPROG)
- WEST. *See* Wind Energy Simulation Toolkit (WEST)
- WFIP. *See* Wind Forecast Improvement Project (WFIP)
- White capping (Swc), 203
- White noise process, 114
- Whole Sky Camera, 155
- Whole Sky Imager (WSI), 155
- Whole-sky InfraRed Cloud-Measuring System (WSIRCMS), 155
- Wind, 318
- farm(s), 222, 237, 243, 243f
  - fluctuations, 219–221
  - correlation between wind fluctuations at spatially distributed sites, 228–229
- lidars, 30, 48
- calibration, 33–35, 34f
  - turbulence estimation from wind lidar measurements, 37–46
- measurements, 29
- parks, 318
- resource, 3
- model chain for, 342–343
- speed, 61–62, 225–226, 226f, 325–326
- fluctuations, 221
  - modeling, 78–80
  - ramps, 227–228

- turbine(s)  
  mechanics, 64  
  unplanned outages of, 284–285, 285t
- variability, 222–224  
  information, 229–230  
  in time series observations, 225
- Wind energy deployment, 341–342
- Wind Energy Forecast Rapid Update Cycle (WEFRUC), 77
- Wind Energy Simulation Toolkit (WEST), 73
- Wind Forecast Improvement Project (WFIP), 93
- Wind power, 225–226, 226f, 309, 326  
  challenges, 60  
  in electricity markets, 259–278  
  fluctuations, 219  
  integration, 341  
  modeling, 78–80  
  predictions  
    accuracy level of, 81t  
    Ensemble Kalman filtering, 74–75  
    improvements in NWP and mesoscale  
      modeling, 69–74  
      meteorological modeling for, 69–75, 69f  
    ramps, 227–228  
  reduction of wind power curtailment, 335  
  reliability studies of combined operation of  
    wind power plants, 320  
  uncertainty of, 86–92, 87f  
    ensemble forecasts, risk indices, and  
      scenarios, 89–92  
    statistical approaches, 86–89
- Wind power forecasting (WPF), 59, 235,  
  341
- ANEMOS projects and other major R&D  
  activities, 92–94
- forecast timescales, 60–61
- forecasting approaches, 62f
- meteorological modeling for wind power  
  predictions, 69–75
- model chain, 61–63
- ramp forecasting, 83–85, 85f
- short-term prediction models with NWPs,  
  75–80
- spatio-temporal forecasting, 82–83
- time series models, 64–68
- uncertainty of wind power predictions,  
  86–92
- upscaling models, 80–82
- variability forecasting, 85–86
- Wind power predicting tool (WPPT), 70–71
- WindCube V2, 39
- WindScanner Client Software (WCS),  
  50–51
- WindScanners, 30f  
  LRWS system, 49–51, 50f  
  short-range WindScanner system, 49, 50f,  
  51–52  
  WindScanner.dk project, 49
- WIRE. *See* Weather Intelligence for  
  Renewable Energies (WIRE)
- Wissenschaftliches Mess-und  
  EvaluierungsProgramm (WMEP),  
  77
- WLS70 lidar, 35–36
- World Meteorological Organization  
  (WMO), 179
- WPF. *See* Wind power forecasting (WPF)
- WPPT. *See* Wind power predicting tool  
  (WPPT)
- WRF model. *See* Weather Research and  
  Forecasting model (WRF model)
- WSI. *See* Whole Sky Imager (WSI)
- WSIRCMS. *See* Whole-sky InfraRed  
  Cloud-Measuring System  
  (WSIRCMS)
- Wusterhusen  
  test case, 238, 238f  
  wind farm, 237
- WW3 model. *See* WAVEWATCH III model  
  (WW3 model)
- X**
- XOR. *See* eXclusive-OR (XOR)
- Y**
- Young Modulus, 327